

David S. Epp *Editor*

Special Topics in Structural Dynamics & Experimental Techniques, Volume 5

Proceedings of the 38th IMAC, A Conference
and Exposition on Structural Dynamics 2020



Conference Proceedings of the Society for Experimental Mechanics Series

Series Editor

Kristin B. Zimmerman, Ph.D.
Society for Experimental Mechanics, Inc.,
Bethel, CT, USA

The Conference Proceedings of the Society for Experimental Mechanics Series presents early findings and case studies from a wide range of fundamental and applied work across the broad range of fields that comprise Experimental Mechanics. Series volumes follow the principle tracks or focus topics featured in each of the Society's two annual conferences: IMAC, A Conference and Exposition on Structural Dynamics, and the Society's Annual Conference & Exposition and will address critical areas of interest to researchers and design engineers working in all areas of Structural Dynamics, Solid Mechanics and Materials Research.

More information about this series at <http://www.springer.com/series/8922>

David S. Epp
Editor

Special Topics in Structural Dynamics & Experimental Techniques, Volume 5

Proceedings of the 38th IMAC, A Conference and Exposition
on Structural Dynamics 2020

Editor

David S. Epp
Sandia National Laboratory
Albuquerque, NM, USA

ISSN 2191-5644 ISSN 2191-5652 (electronic)
Conference Proceedings of the Society for Experimental Mechanics Series
ISBN 978-3-030-47708-0 ISBN 978-3-030-47709-7 (eBook)
<https://doi.org/10.1007/978-3-030-47709-7>

© The Society for Experimental Mechanics, Inc. 2021

This work is subject to copyright. All rights are reserved by the Publisher, whether the whole or part of the material is concerned, specifically the rights of translation, reprinting, reuse of illustrations, recitation, broadcasting, reproduction on microfilms or in any other physical way, and transmission or information storage and retrieval, electronic adaptation, computer software, or by similar or dissimilar methodology now known or hereafter developed. The use of general descriptive names, registered names, trademarks, service marks, etc. in this publication does not imply, even in the absence of a specific statement, that such names are exempt from the relevant protective laws and regulations and therefore free for general use. The publisher, the authors and the editors are safe to assume that the advice and information in this book are believed to be true and accurate at the date of publication. Neither the publisher nor the authors or the editors give a warranty, express or implied, with respect to the material contained herein or for any errors or omissions that may have been made. The publisher remains neutral with regard to jurisdictional claims in published maps and institutional affiliations.

This Springer imprint is published by the registered company Springer Nature Switzerland AG
The registered company address is: Gewerbestrasse 11, 6330 Cham, Switzerland

Preface

Special Topics in Structural Dynamics & Experimental Techniques represents one of eight volumes of technical papers presented at the 38th IMAC, A Conference and Exposition on Structural Dynamics, organized by the Society for Experimental Mechanics, and held in Houston, Texas, February 10–13, 2020. The full proceedings also include volumes on *Nonlinear Structures and Systems*; *Dynamics of Civil Structures*; *Model Validation and Uncertainty Quantification*; *Dynamic Substructures*; *Rotating Machinery, Optical Methods & Scanning LDV Methods*; *Sensors and Instrumentation, Aircraft/Aerospace, Energy Harvesting & Dynamic Environments Testing*; and *Topics in Modal Analysis & Testing*.

Each collection presents early findings from experimental and computational investigations on an important area within Structural Dynamics. *Special Topics in Structural Dynamics & Experimental Techniques* represents papers highlighting new advances and enabling technologies for Experimental Techniques, Finite Element Techniques, and System Identification.

The organizers would like to thank the authors, presenters, session organizers, and session chairs for their participation in this track.

Albuquerque, NM, USA

David Epp

Contents

1	Benfield-Hruda Damping and Residual Vectors	1
	Paul Blesloch, Scott Sharp, and William Zornik	
2	Harmonic Forcing of Damped Non-homogeneous Euler-Bernoulli Beams	11
	Arnaldo J. Mazzei Jr. and Richard A. Scott	
3	Characterization of Fatigue in Integrated Tuned Mass-Dampers	25
	Srikar M. Srivatsa and Daniel J. Inman	
4	Dynamic Identification of Masonry Arch Bridges Using Multiple Methodologies	37
	Semih Gonen and S. Soyoz	
5	Using Impact Testing for Production Quality Control	49
	Shawn Richardson, Jason Tyler, Randall Spears, and Mark Richardson	
6	A Tutorial on Analysis Techniques for Deriving Mechanical Shock and Vibration Environmental Specifications from Field Data	59
	Jerome S. Cap	
7	Design and Characterization of a Multi-purpose Duffing Oscillator with Flexible Parameter Selection	81
	Markus J. Hochrainer and Anton M. Puhwein	
8	Modeling Viscoelastic Behavior in Transient Analyses	89
	Paul Blesloch and Eric Austin	
9	Extensions to NIFO and CRP to Estimate Frequency-Independent Nonlinear Parameters	99
	Michael Kwarta and Matthew S. Allen	
10	System Characterization and Design Using Mechanical Impedance Representations	121
	Alexandra C. Karlicek, Brandon J. Dilworth, and J. Gregory McDaniel	
11	Analysis of Full-Field Response from a Multi-Shaker Test	129
	Dagny Beale, Brian Owens, and Ryan Schultz	
12	Calibration of Shaker Electro-mechanical Models	133
	Ryan Schultz	
13	A Low-Cost Excitation System for Operational Modal Analysis (OMA)	145
	Max Gille, Johannes Maierhofer, and Daniel J. Rixen	
14	Reconciling the Difference Between Test and Real Environments: Improving Fixture Design Based on Modal Strain	153
	Scott A. Smith and Matthew R.W. Brake	
15	A Video-Based Course on Random Vibrations	161
	Pernille Lysgaard and Rune Brincker	

16	Vibration-Based Non-Destructive Techniques for a 3-Level Characterization of Damages in Cables	165
	Abdou Dia, Lamine Dieng, and Laurent Gaillet	
17	Power Grid Time Synchronization for Phase-Sensitive Vibration Measurements	173
	Ferrill T. Rushton, Eugene H. Lin, Jessica Y. Chan, Adam J. Wachtor, Eric B. Flynn, and Nick Lieven	
18	Transmission Simulator Based MIMO Response Reconstruction for Vehicle Subcomponents	189
	Christopher A. Schumann, Matthew S. Allen, Washington J. DeLima, and Eric Dodgen	
19	Exploring Uncertainties in Multi-Input-Multi-Output (MIMO) Testing	197
	James Woodall, Maimuna Hossain, Arup Maji, John Pott, and Fernando Moreu	
20	Experimental Evaluation of the Inertia Properties of Large Diesel Engines	205
	Mohammad Afzal, Kari Saine, Claus Paro, and Eddy Dascotte	
21	Dynamic Performance and Uncertainty Analysis of a Piezometaelastic Structure for Vibration Control and Energy Harvesting	215
	Leticia H. Maki, Make S. Valencia, and Paulo S. Varoto	
22	Assessing Predictive Capabilities for Nonlinear Dynamic Structural Responses	233
	Liliana C. Haus, B. Evan Saunders, Jonathan E. Acosta, Thomas E. Allard, Kyle A. Brindley, and Andrew J. Morello	
23	Identify Loose Footings of Machines Using Model Updating-Based Method	255
	Shih-Yin Chien, Zhen Wah Chew, and Yum Ji Chan	
24	Bayesian Finite Element Model Updating Using a Population Markov Chain Monte Carlo Algorithm	259
	M. Sherri, I. Boulkaibet, T. Marwala, and M. I. Friswell	
25	Modal Analysis of the Box Assembly with Removable Component in Two Configurations	271
	Levi H. Manring, Brian P. Mann, and John F. Schultze	
26	Using the SWAT Method for Reconstructing Forces on a Drop Shock Table to Better Inform Finite Element Simulations	283
	Brian A. Ferri, Tyler F. Schoenherr, and Ryan Jennings	
27	Pointless Grading and Digital Content Delivery as Educational Differentiators: A Case Study for Noise and Vibration Courses	301
	Andrew R. Barnard	
28	Toward Extracting Multidimensional Kinematics from SWIFT Experiments	305
	Ethan Billingsley, Robert Billette, Yolnan Chen, Christopher Tilger, Michael Murphy, and Mike Bowden	
29	An Acceleration-Based Approach to Force Limiting a Random Vibration Test	315
	T. Van Fossen and K. Napolitano	
30	Frequency Based Substructuring on Resonant Plate	327
	Erica M. Jacobson, Jason R. Blough, James P. DeClerck, Charles D. Van Karsen, and David Soine	
31	A Data-Driven Approach to the Impedance Matched Multi-Axis Test Method	335
	Kevin J. Moreno, Vijaya V. N. Sriram Malladi, and Pablo A. Tarazaga	
32	An Automated Topology Optimization Platform Through a Collaborative Project Between Academia and Industry	341
	Karolina Ohstrom, Seth Law, Alec Maxwell, Zhaoshuo Jiang, Juan Caicedo, Haley Sims, Nick Sherrow-Groves, and Nate Warner	
33	Shaker-Amplifier System Characterization	351
	Greta Colford, Kevin Craft, Andy Morello, Dustin Harvey, Colin Haynes, and Stuart Taylor	

Chapter 1

Benfield-Hruda Damping and Residual Vectors



Paul Blelloch, Scott Sharp, and William Zornik

Abstract The Benfield-Hruda component mode synthesis (CMS) method is commonly used in the coupled loads analysis (CLA) community because it provides a very convenient means of applying component mode damping to selected components. However, since it is a CMS method, it results in approximate, rather than exact, system modes. In this paper, we will show that the approximation in the Benfield-Hruda modes can result in unacceptable errors in the calculation of residual vectors, resulting in incorrect quasi-static responses. A solution is proposed and demonstrated. This uses the Benfield-Hruda method for damping synthesis but not to calculate the system modes. It results in a much more robust convergence of results and eliminates the issue with residual vectors.

Keywords Damping · Coupled loads analysis · Simulation · Component mode synthesis

Acronyms

CMS component mode synthesis
CLA coupled loads analysis
DOF degree of freedom

1.1 Introduction

One of the most difficult-to-define things to model in any structural dynamic analysis is the damping. The simplest approach is to assume a fixed modal damping applied to each system mode, sometimes called diagonal or system mode damping. This approach is straightforward but does not easily allow for the incorporation of either localized damping, such as that arising from isolators, or for knowledge of damping in the modes of one or more components. The most commonly used method for addressing the second issue is the Benfield-Hruda component mode synthesis (CMS) method [1, 2]. This first calculates a set of “intermediate” modes by removing the component modes from the system. It then reassembles the system using the intermediate modes and the component modes that had been removed and calculates the system modes. These system modes are approximate, but the advantage of the process is that damping can be applied to both the “intermediate” modes and the component modes separately, which is then transformed into a fully coupled damping matrix in the space of the system modes. This provides a very natural method for incorporating knowledge of component mode damping into a system-level damping matrix.

The biggest disadvantage of the Benfield-Hruda method is that the system modes are approximations, and while they do converge on the “exact” system modes as the number of intermediate modes are increased, this convergence can be slow and it is difficult to know a priori how many intermediate modes to calculate. In the absence of residual vectors, this

P. Blelloch (✉)
ATA Engineering Inc., San Diego, CA, USA
e-mail: paul.blelloch@ata-e.com

S. Sharp · W. Zornik
Northrop Grumman Innovation Systems, Chandler, AZ, USA
e-mail: Scott.Sharp@ngc.com; William.Zornik@ngc.com

slow convergence is not a large problem because it is not necessarily critical that system modes be exact. However, in this paper, we will show that the method that commercial versions of the popular Nastran finite element solver package use to calculate residual modes [3] are only correct for exact normal modes, and do not necessarily work with Benfield-Hruda modes. This can result in very significant errors in quasi-static results, even when the system modes might otherwise appear to be sufficiently accurate. This makes the convergence properties of the Benfield-Hruda method much more critical, and an impractical number of intermediate modes may be required to converge on an acceptably accurate solution.

A very simple correction is proposed. This is to calculate the intermediate modes and system modes separately, and directly transform the intermediate mode damping to the system modes. This approach avoids calculating approximate Benfield-Hruda modes, and therefore completely avoids the issue with residual vectors. The convergence is now only with respect to the damping matrix, but we will show that this is very robust and that a relatively small number of intermediate modes will typically result in very small errors. This approach can be numerically more expensive than the traditional Benfield-Hruda approach, since it requires two eigensolutions on the full assembled matrices, but in practice, it is typically less expensive since the number of intermediate modes required is so much fewer. The approach has been implemented in DMAP and applied to a small number of small and large example problems.

This paper is organized as follows: First, we show the equations for the traditional Benfield-Hruda method and how these are used to synthesize a system damping matrix. This is followed by a development of the equations used to calculate residual vectors in commercial versions of Nastran, with an explanation of why these only work for the case of exact normal modes. Finally, we present the equations for the proposed correction. The main body of the paper then consists of two examples that demonstrate the issue with the traditional Benfield-Hruda method along with the accuracy of the proposed solution.

1.2 Review of Benfield-Hruda Component Mode Synthesis

The Benfield-Hruda modal synthesis method is predicated on the system model having some number of degrees of freedom (DOFs) that are identified as component modes from upstream components. These are not necessarily (and, in fact, rarely are) all the component modes, but they are just those component modes for which modal damping will be applied. However, for the purposes of this discussion, we refer to these DOFs as the component mode DOFs. The first step in the Benfield-Hruda method, therefore, is to identify the component mode DOFs and partition the left-hand side of the system equations of motion as follows¹:

$$\begin{bmatrix} M_{11} & M_{12} \\ M_{12}^T & M_{22} \end{bmatrix} \begin{Bmatrix} \ddot{x}_1 \\ \ddot{x}_2 \end{Bmatrix} + \begin{bmatrix} K_{11} & K_{12} \\ K_{12}^T & K_{22} \end{bmatrix} \begin{Bmatrix} x_1 \\ x_2 \end{Bmatrix} \quad (1.1)$$

where (x_2) are the component mode DOFs, and (x_1) are the remaining DOFs. An eigensolution on the remaining DOFs (x_1) is then performed to calculate the intermediate modes² $[\tilde{\Phi}_1]$ so that

$$[\tilde{\Phi}_1]^T [K_{11}] [\tilde{\Phi}_1] = [\Omega_1^2], [\tilde{\Phi}_1]^T [M_{11}] [\tilde{\Phi}_1] = [I] \quad (1.2)$$

The assembled equations are then expressed in terms of the intermediate modes and the component modes as

$$\begin{bmatrix} I & M_{12}\tilde{\Phi}_1 \\ \tilde{\Phi}_1^T M_{12}^T & M_{22} \end{bmatrix} \begin{Bmatrix} \ddot{q}_1 \\ \ddot{x}_2 \end{Bmatrix} + \begin{bmatrix} \Omega_1^2 & K_{12}\tilde{\Phi}_1 \\ \tilde{\Phi}_1^T K_{12}^T & K_{22} \end{bmatrix} \begin{Bmatrix} q_1 \\ x_2 \end{Bmatrix} \quad (1.3)$$

Now, a second eigensolution is performed on the assembled equations so that

$$\begin{bmatrix} \Phi_1 \\ \Phi_2 \end{bmatrix}^T \begin{bmatrix} I & K_{12}\Phi_1 \\ \Phi_1^T K_{12}^T & K_{22} \end{bmatrix} \begin{bmatrix} \Phi_1 \\ \Phi_2 \end{bmatrix} = [\Omega^2] \quad (1.4)$$

¹For the case where the component modes are associated with a Hurty/Craig-Bampton component, the K_{12} is zero, M_{22} is the identity, and $K_{22} = \Omega_2^2$, where Ω_2 is the diagonal matrix of component modal frequencies.

²Note that K_{11} and M_{11} include the physical stiffness and mass matrices from all components, so these are sometimes referred to as mass-loaded modes.

$$\begin{bmatrix} \Phi_1 \\ \Phi_2 \end{bmatrix}^T \begin{bmatrix} I & M_{12}\Phi_1 \\ \Phi_1^T M_{12}^T & M_{22} \end{bmatrix} \begin{bmatrix} \Phi_1 \\ \Phi_2 \end{bmatrix} = [I] \quad (1.5)$$

The matrix $[\Omega^2]$ is the diagonal matrix of system frequencies squared, and the system modes are $\begin{bmatrix} \tilde{\Phi}_1 \Phi_1 \\ \Phi_2 \end{bmatrix}$. In the limit where all modes are retained at the intermediate eigensolution, the Benfield-Hruda modes will be identical to the system modes that would have been calculated with a single eigensolution.³ If the intermediate modes are truncated, the secondary eigensolution will produce system modes that are an approximation to the single-eigensolution modes. There is not much advantage to the two-step synthesis process, except that it allows damping to be assigned to both the intermediate and component modes as follows⁴:

$$[B] = \begin{bmatrix} 2\xi_1\Omega_1 & 0 \\ 0 & 2\xi_2\Omega_2 \end{bmatrix} \quad (1.6)$$

This damping can then be transformed into the system modal coordinates as follows:

$$[B_{hh}] = \begin{bmatrix} \Phi_1 \\ \Phi_2 \end{bmatrix}^T \begin{bmatrix} 2\xi_1\Omega_1 & 0 \\ 0 & 2\xi_2\Omega_2 \end{bmatrix} \begin{bmatrix} \Phi_1 \\ \Phi_2 \end{bmatrix} \quad (1.7)$$

Note that while the damping matrix in the space of intermediate and component modes is diagonal (uncoupled), the damping matrix in the space of the final system modes ($[B_{hh}]$) is fully coupled.

The advantage of the Benfield-Hruda damping synthesis is that it allows the user to choose a subset of component modes for component modal damping while applying damping to the remaining DOFs in a way that is as close to system damping as possible.

1.3 Benfield-Hruda and Residual Vectors

Residual vectors are used in Nastran to approximate the contribution of neglected modes [3, 4]. They provide a capability that is equivalent in many ways to mode acceleration data recovery [5]. The basic equations are fairly simple. The first step is to orthogonalize the applied loads with regards to the calculated modes as follows:

$$\hat{P} = (I - M\Phi\hat{M}^{-1}\Phi^T)P \quad (1.8)$$

where

M - Physical mass matrix

Φ - Retained eigenvectors

\hat{M} - Diagonal generalized mass matrix (usually identity)

P - Applied load matrix (includes inertial load vectors)

Note that \hat{P} is orthogonal to the normal modes Φ in the sense that $\Phi^T \hat{P} = (\Phi^T - \Phi^T)P = 0$. This is true for any shape Φ , as long as $\hat{M} = \Phi^T M \Phi$.

The next step calculates the shapes associated with the orthogonalized loads:

³Because the Benfield-Hruda modes are only identical to the system modes when all intermediate modes are included; the user needs to be careful to include enough intermediate modes to get an accurate solution.

⁴The Benfield-Hruda method is not limited to diagonal component mode damping ($2\xi_1\Omega_1$). The component can have a fully populated damping matrix if available. It is also possible to have discrete damping elements distributed anywhere in the structure that result in additional coupled damping terms. However, the most common application is with diagonal damping for both the component and the intermediate modes, which still results in a fully coupled damping matrix at the system mode level.

$$\hat{R} = K^{-1}\hat{P} \quad (1.9)$$

The deflection due to any set of shapes Φ is $X = \Phi\hat{K}^{-1}\Phi^T P$, where $\hat{K} = \Phi^T K \Phi$. The residual solution is then the exact solution $K^{-1}P$, minus the contribution of the shapes $\Phi\hat{K}^{-1}\Phi^T P$, or,

$$\hat{R} = \left(K^{-1} - \Phi\hat{K}^{-1}\Phi^T \right) P \quad (1.10)$$

Equation (1.9) is only correct if the right-hand sides of (1.9) and (1.10) are equal, or if $K^{-1}\hat{P} = \left(K^{-1} - \Phi\hat{K}^{-1}\Phi^T \right) P$. Substituting in for \hat{P} from Eq. (1.8) leads to the following identity:

$$\left(I - K\Phi\hat{K}^{-1}\Phi^T \right) P = \left(I - M\Phi\hat{M}^{-1}\Phi^T \right) P \quad (1.11)$$

This is true if $K\Phi\hat{K}^{-1} = M\Phi\hat{M}^{-1}$. If the columns of Φ are eigenvectors, and \hat{K} is a diagonal matrix of eigenvalues λ_i , then $K\Phi\hat{K}^{-1} = M\Phi\hat{M}^{-1}$ can be rewritten as $[K]\{\phi_i\} - \lambda_i[M]\{\phi_i\} = 0$, which is the generalized eigenvalue problem. So, $K\Phi\hat{K}^{-1} = M\Phi\hat{M}^{-1}$ is true if and only if the columns of Φ are eigenvectors. This shows that although residual vectors can be developed relative to any set of basis functions, the residual vectors calculated in Nastran are only correct if the basis functions are, in fact, the exact modes of the system. Residual vectors will work for basic vectors that are not solutions to the eigenvalue problem if they are calculated from Eq. (1.10), but not if they are calculated as the solution of Eq. (1.9).

It has proven to be the case in practice that the small error in Benfield-Hruda synthesized mode shapes results in sufficient errors in the residual vectors that quasi-static results using a combination of Benfield-Hruda modes and residual vectors can have very significant errors. While the errors are very much case-specific, attempts to correct them by increasing the frequency cutoff of the intermediate modes are difficult to implement. In the next section we propose a solution, and in the following two sections demonstrate the solution by example.

1.4 Proposed Solution

There are a few potential solutions to the fact that residual vectors calculated in Nastran are not correct for Benfield-Hruda synthesized mode shapes. These include the following:

1. Keep increasing the frequency cutoff of the intermediate modes until the errors are sufficiently small.
2. Start with the exact system modes and use these to approximate the intermediate modes, rather than starting with intermediate modes to synthesize system modes. This might use a method similar to the one documented in previous work [6].
3. Calculate system and intermediate modes separately and just use the intermediate modes to map damping.

Both methods 2 and 3 solve the issue with residual vectors, since both use the “exact” system modes, which satisfy Eq. (1.11). This results in residual vectors that are complete with respect to the system modes and therefore generate correct quasi-static results.

As mentioned previously, the first solution has proven to be very unsatisfactory. The convergence of the Benfield-Hruda modes using quasi-static responses as a metric can be extremely slow. In practice, the only feasible way to ensure convergence is to calculate “all” intermediate modes. This is only practical in a model that is constructed of superelements, such that the size of the system matrices are moderate, but even in that case the number of intermediate modes required can be very large and numerically inefficient. This is illustrated in the second example.

The second method is feasible and would only require solving the full eigensolution once, since the intermediate modes could be approximated based on a relatively small number of system modes. However, the method outlined in [6], is fairly complex, can be numerically sensitive, and would require significant development.

The third method is effectively a brute force method. It neither uses the intermediate modes to approximate the system modes, nor does it use the system modes to approximate the intermediate modes. It does require two full eigensolutions, but for most practical problems this is not an issue. In practice, it has proven to be much faster than the approach of increasing intermediate modal frequency cutoff and it is robust in the sense that no studies are required to demonstrate convergence.

To implement this method, the user starts by partitioning the matrices into component modes DOF $\{x_2\}$ and all other DOF $\{x_1\}$ as in Eq. (1.1). The user solves for the intermediate modes $[\Phi_1]$ as is Eq. (1.2). The method now diverges by not assembling the system consisting of intermediate and component modes as in Eq. (1.3). Instead, the system modes Φ are calculated directly from Eq. (1.1) such that

$$\begin{bmatrix} \Phi_1 \\ \Phi_2 \end{bmatrix}^T \begin{bmatrix} K_{11} & K_{12} \\ K_{12}^T & K_{22} \end{bmatrix} \begin{bmatrix} \Phi_1 \\ \Phi_2 \end{bmatrix} = [\Omega^2] \quad (1.12)$$

$$\begin{bmatrix} \Phi_1 \\ \Phi_2 \end{bmatrix}^T \begin{bmatrix} M_{11} & M_{12} \\ M_{12}^T & M_{22} \end{bmatrix} \begin{bmatrix} \Phi_1 \\ \Phi_2 \end{bmatrix} = [I] \quad (1.13)$$

Note that these are exact system modes and not approximations. The goal is now to map damping from the intermediate modes to the system modes. Noting from Eq. (1.2) that $[\tilde{\Phi}_1]^T [M_{11}] [\tilde{\Phi}_1] = [I]$, so the pseudo-inverse of $[\tilde{\Phi}_1]$ is $[\tilde{\Phi}_1]^T [M_{11}]$. The intermediate modes $[\tilde{\Phi}_1]$ can therefore be mapped to the system modes $[\Phi_1]$ by pre and post-multiplying by $[\tilde{\Phi}_1]^T [M_{11}] [\Phi_1]$ which is the cross-orthogonality between intermediate and system modes relative to the $[M_{11}]$ partition of the mass matrix. The Benfield-Hruda damping can then be expressed as follows:

$$[B_{hh}] = \begin{bmatrix} [\tilde{\Phi}_1]^T [M_{11}] [\Phi_1] \\ \Phi_2 \end{bmatrix}^T \begin{bmatrix} 2\xi_1 \Omega_1 & 0 \\ 0 & 2\xi_2 \Omega_2 \end{bmatrix} \begin{bmatrix} [\tilde{\Phi}_1]^T [M_{11}] [\Phi_1] \\ \Phi_2 \end{bmatrix} \quad (1.14)$$

This approach requires two eigensolutions to calculate both the intermediate modes $[\tilde{\Phi}_1]$ and the system modes $\begin{bmatrix} \Phi_1 \\ \Phi_2 \end{bmatrix}$; however, there is no need to retain a large number of intermediate modes, and since the system modes are exact there is no issue with residual vectors. In practice, the method has been found to be very robust and efficient relative to worrying about modal convergence using a traditional Benfield-Hruda method.

1.5 First Example

As a first example, consider the Northrop Grumman Omega launch illustrated in exploded view in Fig. 1.1. For this example, the cryogenic third stage is simulated, with bending moments recovered in an element connecting the two liquid tanks.

A simulation was performed for an empty cryogenic third stage, with axial thrust ramped up over 1 s and held steady over 1 s on both engines. The third-stage model contains a Hurty/Craig-Bampton of the payload, and a Hurty/Craig-Bampton model of each of the two engines. The remainder of the model is represented by standard finite elements.

The transient bending moment in plane 1 on end A of a beam connecting the two liquid tanks was recovered. All solutions used system modes to 60 Hz and a residual vector associated with the engine thrust. The baseline was run without Benfield-Hruda CMS. Traditional Benfield-Hruda solutions were then run based on intermediate frequency cutoffs of 60 Hz, 100 Hz, 200 Hz, 500 Hz and 1000 Hz. The alternate Benfield-Hruda solution was run with intermediate frequency cutoff of 60 Hz. The run times are summarized in Table 1.1. The traditional Benfield-Hruda solution with intermediate modes to 60 Hz takes only slightly longer than the baseline solution, and the alternate Benfield-Hruda solution with intermediate modes to 60 Hz only takes a little longer than that. Increasing the frequency cutoff of the intermediate modes, however, significantly increases the run time.

Now consider the transient bending moment solution plotted in Fig. 1.2. The alternate Benfield-Hruda solution is effectively exact. The error in the traditional Benfield-Hruda solution is about 13% for frequency cutoffs of either 60 or 100 Hz, but drops to less than 1% for frequency cutoffs of 200 Hz or higher.

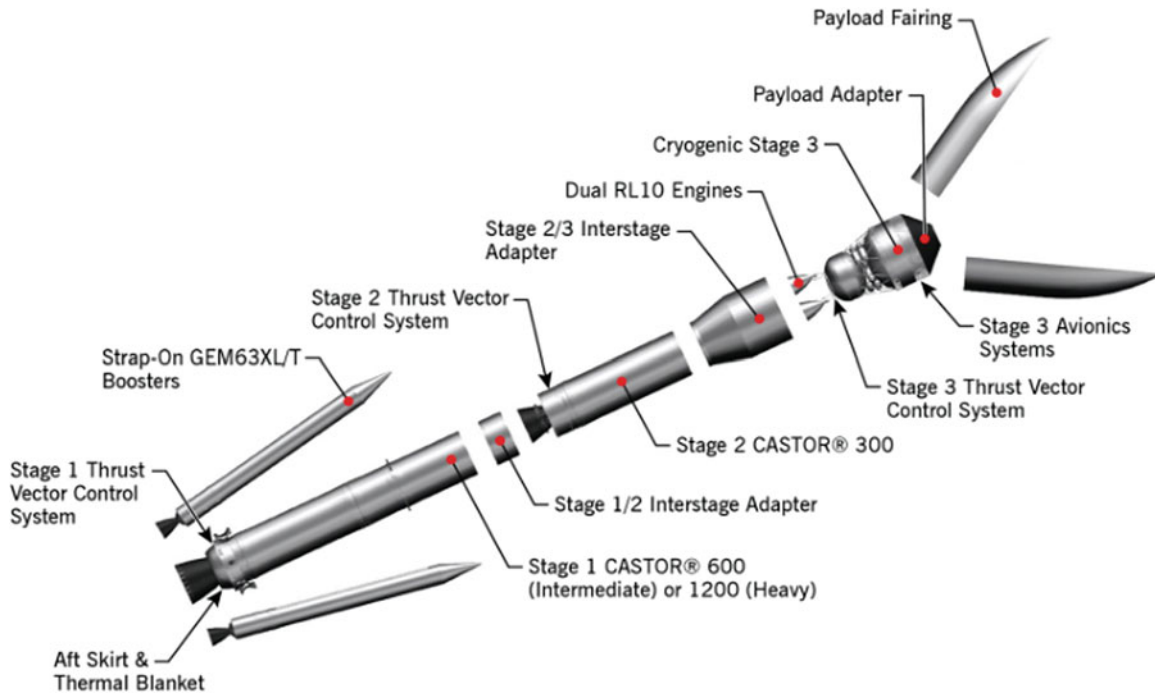


Fig. 1.1 Expanded view of Northrop Grumman Omega Launch Vehicle (<https://www.rollcall.com/sponsored-content/omega-rocket-air-force-pursuit/>)

Table 1.1 Comparison of run times for various Benfield-Hruda solutions

Case	Run Time
No Benfield-Hruda	0:16
Traditional Benfield-Hruda (60 Hz)	0:18
Traditional Benfield-Hruda (100 Hz)	0:30
Traditional Benfield-Hruda (200 Hz)	1:10
Traditional Benfield-Hruda (500 Hz)	5:07
Traditional Benfield-Hruda (1.000 Hz)	9:34
Alternate Benfield-Hruda (60 Hz)	0:25

For this particular output, an intermediate frequency cutoff of 200 Hz ($4\times$ the system frequency cutoff of 60 Hz) gives an acceptable answer. However, in practice it is rarely practical to perform this type of convergence study, and every output will converge at a different rate. The alternate Benfield-Hruda, which uses “exact” system modes has effectively no error.

The error in the Benfield-Hruda system frequencies as function of intermediate mode frequency cutoff is illustrated in Fig. 1.3. The error does decrease, although it is difficult to map frequency error to error in transient results.

For this example, the intermediate mode damping was set to 10%, the damping on the two engine component modes to 5%, and the damping on the payload modes to 1%. Since the traditional Benfield-Hruda solution with intermediate modes to 1000 Hz is converged, it was treated as the “truth” solution for damping. The error in diagonal damping ratios for each of the other Benfield-Hruda solutions are plotted in Fig. 1.4. The error in damping ratios also decreases as the intermediate modal frequency cutoff increases. All solutions except for the two with a 60 Hz intermediate mode cutoff frequency have negligible error. The alternate solution with a 60 Hz cutoff has a lower error than the traditional solution with a 60 Hz cutoff (1% versus 3%). These errors are probably negligible and well within the uncertainty in damping.

1.6 Second Example

The second example consists of a substructured model of a large launch vehicle. The assembled matrices have approximately 40,000 DOFs, meaning that it is feasible, although painful, to calculate all the intermediate modes. In this case, the exact solution was the traditional Benfield-Hruda solution retaining all the intermediate modes. A total of 2165 system modes were

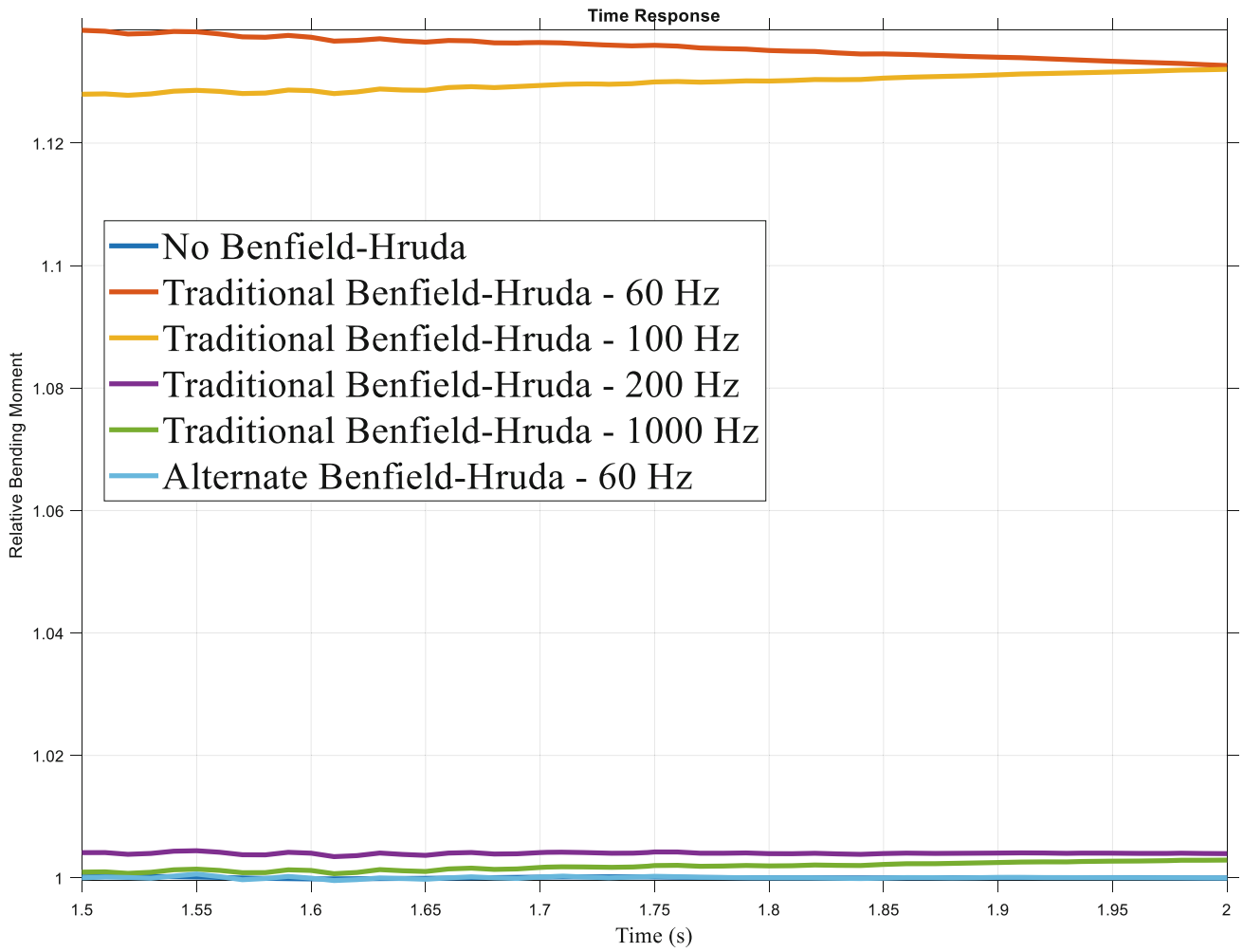


Fig. 1.2 “Steady-state” bending moment for various Benfield-Hruda solutions

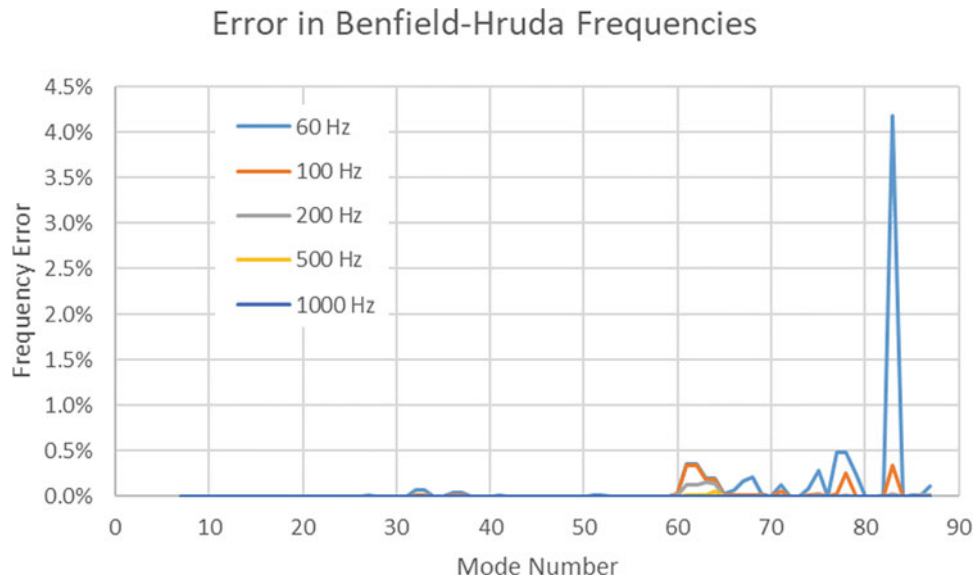


Fig. 1.3 Error in Benfield-Hruda system mode frequencies for different intermediate mode frequency cutoffs

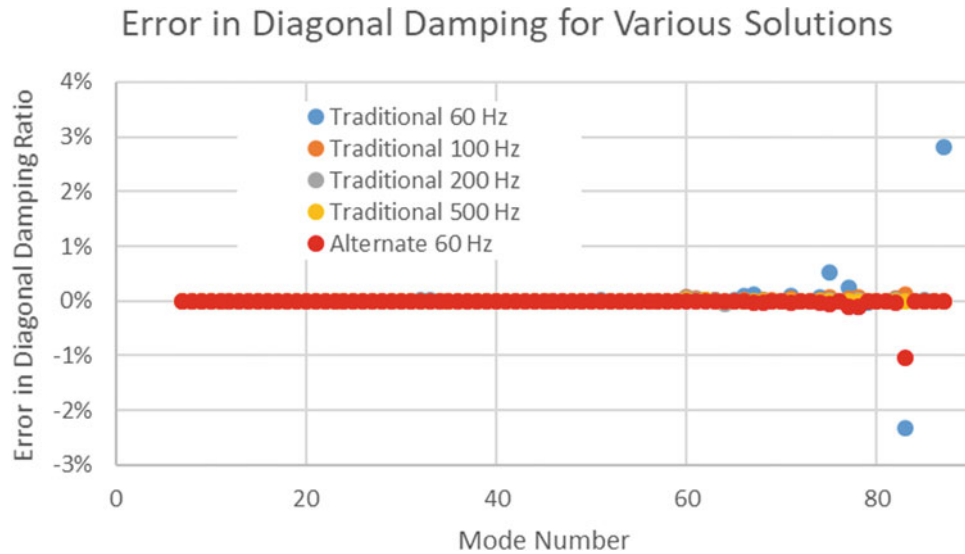


Fig. 1.4 Error in Benfield-Hruda diagonal damping ratios for different solutions

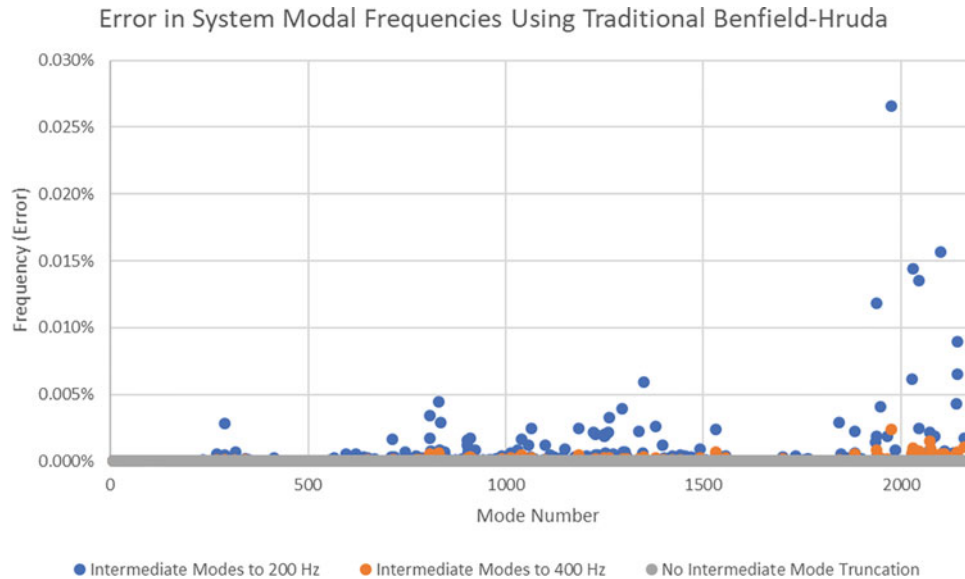


Fig. 1.5 Error in Benfield-Hruda system mode frequencies for different intermediate frequency cutoffs

calculated up to 60 Hz. The Benfield-Hruda solution was then repeated with intermediate frequency cutoffs of 200 Hz and 400 Hz. The error in system mode frequencies are Fig. 1.5. The frequencies are all fairly close.

Again treating the traditional Benfield-Hruda with no intermediate frequency cutoff as the truth, the error in the diagonal damping ratios for traditional Benfield-Hruda with either 200 or 400 Hz cutoff and the alternate Benfield-Hruda with either 65 Hz or 120 Hz cutoff were calculated and are plotted Fig. 1.6. In this case, all diagonal damping ratio errors are fairly small, but the alternate Benfield-Hruda results are much closer, even with an intermediate frequency cutoff of 65 Hz.

This demonstrates that the alternate method is feasible on a large model, and that the diagonal damping ratios are very accurate.

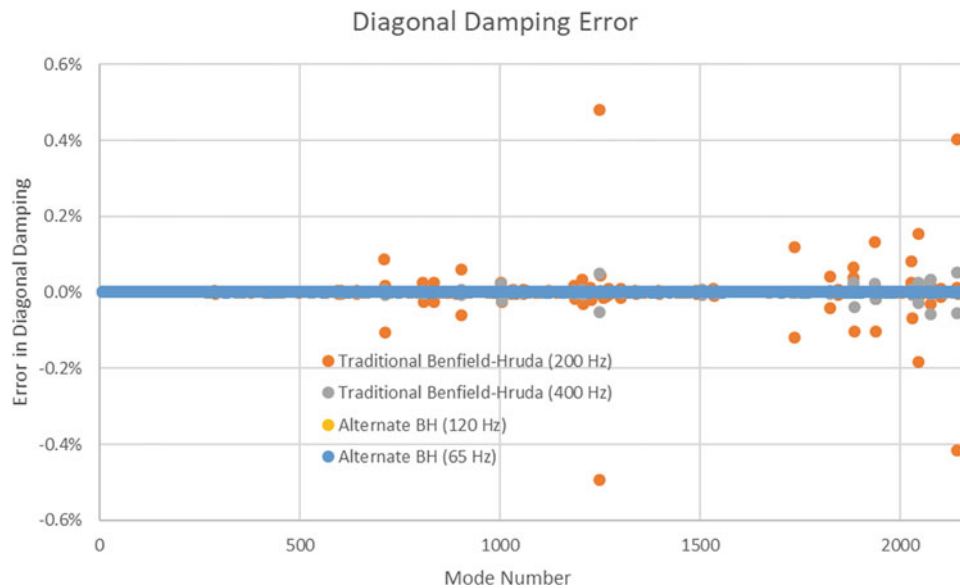


Fig. 1.6 Error in Benfield-Hruda diagonal damping ratios for different models

1.7 Summary

It has been demonstrated that errors introduced in the Benfield-Hruda component mode synthesis method can result in residual vectors that do not correctly capture steady-state response. An alternate procedure, which calculates the system and intermediate modes separately has been suggested. This method eliminates the problem with the residual vectors by using “exact” system modes while still allowing for the Benfield-Hruda damping synthesis method to be applied. Two examples were used to demonstrate the shortcomings in the traditional method and the performance of the alternate method. The first example showed how the use of a traditional Benfield-Hruda method can result in significant errors in quasi-static internal loads when using residual vectors, and how this error is eliminated using the alternate method. The second example illustrates the accuracy of the damping achieved using the alternate method for a large launch vehicle model.

References

1. Benfield, W.A., Hruda, R.F., *Vibration analysis of structures by component mode substitution* AIAA J., Vol. 7, pp. 1255–1261, 1971
2. Blesloch, P.A., Tengler, N.: *Application of hruda-benfield method to component damping for STS coupled loads*. 35th AIAA/ASME/ASCE/AHS/ACS Structures, Structural Dynamics and Materials Conference, April 18–20, 1994, Hilton Head, South Carolina (1994)
3. Rose, T.: *Using residual vectors in MSC/Nastran dynamic analysis to improve accuracy*. MSC World Users’ Conference (1991)
4. Roy, N., Girard, A.: *Impact of residual modes in structural dynamics*. European Conference on Spacecraft Structures, Materials & Mechanical Testing, Noordwijk, The Netherlands, May 10–12 (2005)
5. Dickens, J.M., Nakagawa, J.M., Wittbrodt, M.J.: *A critique of mode acceleration and modal truncation augmentation methods for modal response analysis*. *Comput. Struct.* **62**(6), (1997)
6. Blesloch, P.A., Flanigan, C.C.: *A time domain approach for spacecraft reanalysis*. Proceedings of the AIAA/ASME/ASCE/AHS/ASC 33rd Structures, Structural Dynamics and Materials Conference, April 13–15, 1992, Dallas, Texas (1992)

Chapter 2

Harmonic Forcing of Damped Non-homogeneous Euler-Bernoulli Beams



Arnaldo J. Mazzei Jr. and Richard A. Scott

Abstract This work is an extension of previous studies on vibrations of non-homogeneous structures. It also explores the use of logistic functions. In the studies, frequency response functions (FRFs) were determined for segmented structures, using analytic and numerical approaches. The structures are composed of stacked cells, which are made of different materials and may have different geometric properties. Here the steady state response, due to harmonic forcing, of a segmented damped Euler-Bernoulli beam is investigated. FRFs for the system are sought via two methods. The first uses the displacement differential equations for each segment. Boundary and interface continuity conditions are used to determine the constants involved in the solutions. Then the response, as a function of forcing frequency, can be obtained. This procedure is unwieldy. In addition, determining particular integrals can become cumbersome for arbitrary spatial variations. The second approach uses logistic functions to model the segment discontinuities. The result is a single partial differential equation with variable coefficients. Approaches for numerical solutions are then developed with the aid of MAPLE[®] software. For free-fixed boundary conditions, spatially constant force and viscous damping, excellent agreement is found between the methods. The numerical approach is then used to obtain the FRF for the case of a spatially varying force.

Keywords Segmented beams · Layered structures · Logistic functions · Resonances of non-homogenous structures

Nomenclature

A	Cross-section area (A_i , cross-section area for i -th material)
a_i	Non-dimensional parameters related to beam properties
B_i	Constants of integration
C_i	Viscous damping coefficient per unit length
CD_i	Non-dimensional damping coefficient
E	Young's modulus (E_i , Young's modulus for i -th material)
f_i	Non-dimensional logistic functions
F_i	Forcing functions (force per unit length)
G_i	Non-dimensional spatial forcing functions
g_i	Non-dimensional forcing functions
I	Area moment of inertia of the beam cross section (I_i , moment of inertia of i -cell)
K	Non-dimensional logistic function parameter
$K_{1,i}$	Non-dimensional ODE parameters related to beam properties
L	Length of beam (L_i , length of i -th cell)
R_i	Non-dimensional spatial functions
t	Time
u	Non-dimensional transverse displacement of the beam, $u = w/L$

A. J. Mazzei Jr. (✉)

Department of Mechanical Engineering, C. S. Mott Engineering and Science Center, Kettering University, Flint, MI, USA
e-mail: amazzei@kettering.edu

R. A. Scott

University of Michigan, Ann Arbor, MI, USA
e-mail: car@umich.edu

x	Longitudinal co-ordinate
w	Transverse displacement of the beam
α, β	Non-dimensional ODE coefficients
γ	Non-dimensional viscosity coefficient
η	Non-dimensional structural damping coefficient
λ	Complex frequency, $\lambda = (a + bI)$
ξ	Non-dimensional spatial co-ordinate, $\xi = x/L$
ρ	Mass density (ρ_i , density value for i -th material)
τ	Non-dimensional time, $\tau = \Omega_0 t$
Ω_0	Reference frequency

2.1 Introduction

This work adds to a series (see references [1, 2]) on transverse vibrations of layered beams. Here the main interest is the vibration analysis, both theoretical and numerical, of segmented damped beams. The media of interest are structures with different materials and varying cross-sections, which are layered in cells and may be uniform or not.

The objective is the determination of frequency response functions (FRFs). Here, Euler-Bernoulli theory is used for a two-segment configuration under harmonic forcing.

To treat the problem two approaches are discussed. In the first, analytic solutions are derived for the differential equations for each segment. The constants involved are determined using boundary and interface continuity conditions. The response, at a given location, can then be obtained as a function of forcing frequency (FRF). Note that the procedure can become unwieldy for arbitrary spatial variations. In the second, the discrete cell properties are modeled by continuously varying functions, specifically logistic functions. This provides the advantage of working with a single differential equation (albeit one with variable coefficients). The differential equation is then solved numerically by means of MAPLE^{®1} software.

Similar analytical and numerical approaches were applied to undamped beams in references [1] and [2] (Euler-Bernoulli and Timoshenko models). Overall results showed that the numerical method worked very well, for both beam models, when compared to the analytical solutions.

In the following a brief literature review is given. For vibrations of layered beams one may refer to the list given in references [1] and [2]. Solids composed by discrete layers are studied in references [3], [4], [5] and [6]. Also, a recent article [7] provides a review of references on this subject. Vibrations of damped Euler-Bernoulli beams are treated in reference [8]. There the model consists of a uniform elastically supported beam, which incorporates different dissipation mechanisms. The oscillatory character of solutions is investigated. In reference [9] estimates for the solutions of an abstract second order evolution equation are given. Applications to models of an elastic beam (possibly non-homogeneous), with a frequency-proportional damping, are discussed. Damping mechanisms on beams are studied in reference [10], where different models of dissipation are presented to account for experimentally observed behavior. Damping effect on beam vibrations is also discussed in reference [11], where the dissipation mechanism is due to air. Minimal influence is observed. The response of internally damped cantilever beams to sinusoidal vibration is given in reference [12]. An expression for the magnitude of the force transmitted to the ends of the beams is derived when both a primary and a secondary force are employed to excite the beams at arbitrary positions. It is demonstrated that the transmitted force can be attenuated significantly through broad ranges of frequency when the primary and secondary forces are of equal magnitude and their location is chosen suitably. Reference [13] treats the spectrum of Euler-Bernoulli beam equation with Kelvin-Voigt damping. Under some assumptions on the coefficients, it is shown that the essential spectrum contains continuous spectrum only, and the point spectrum consists of isolated eigenvalues of finite algebraic multiplicity. The asymptotic behavior of eigenvalues is presented. Damping effects on Timoshenko beams can be found in reference [14]. The numerical analyses provided for outlining the relevant influences on the dynamic response associated to any singular damping mechanism and also the evaluation of the modal critical damping values.

2.2 Basic Structure

The equation of motion for a viscously damped Euler-Bernoulli beam is given below. Figure 2.1 exhibits the underlying variables.

¹www.maplesoft.com

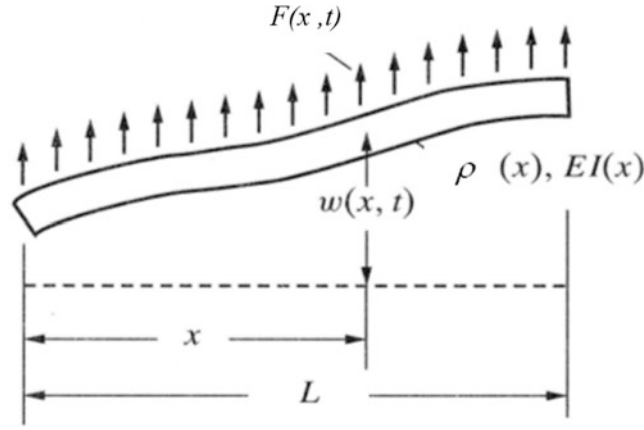


Fig. 2.1 Beam element

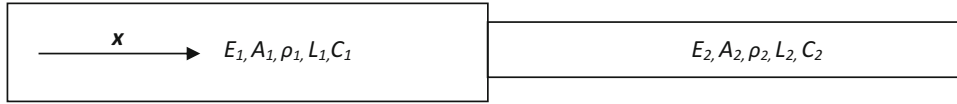


Fig. 2.2 Layered beam

$$\frac{\partial^2}{\partial x^2} \left(E(x)I(x) \frac{\partial^2 w(x, t)}{\partial x^2} \right) + \rho(x)A(x) \frac{\partial^2 w(x, t)}{\partial t^2} + C(x) \frac{\partial w(x, t)}{\partial t} = F(x, t) \quad (2.1)$$

The beam is assumed to be under a damping force, with $C(x)$ representing a varying viscous damping coefficient per unit length. Material type can be either homogeneous or a non-homogeneous.

In the following the configuration discussed consists of a beam composed of two cells. Consider the beam shown in Fig. 2.2 which has two cells of different materials. E , ρ , and A may vary in a discontinuous manner. The segments are under transverse loads f_1 and f_2 (force per unit length) and viscous damping forces (per unit length, damping coefficients C_1 and C_2).

Approaches for obtaining the steady state response, due to harmonic forcing, are sought next.

2.3 Solution Approaches

In non-dimensional form, eq. (2.1) can be written as:

$$\frac{\partial^2}{\partial \xi^2} \left(f_1(\xi) f_2(\xi) \frac{\partial^2 u(\xi, \tau)}{\partial \xi^2} \right) + f_3(\xi) f_4(\xi) \frac{\partial^2 u(\xi, \tau)}{\partial \tau^2} + (CD) f_5(\xi) \frac{\partial u(\xi, \tau)}{\partial \tau} = g(\xi, \tau) \quad (2.2)$$

where: $\tau = \Omega_0 t$, $\Omega_0 = \sqrt{\frac{E_1 I_1}{\rho_1 A_1 L^4}}$, $\xi = \frac{x}{L}$, $u(\xi, \tau) = \frac{w(x, t)}{L}$, $CD = C_1 \sqrt{\frac{L^4}{\rho_1 A_1 E_1 I_1}}$, $g(\xi, \tau) = F(x, t) \frac{L^3}{E_1 I_1}$, $E(x) = E_1 f_1(\xi)$, $I(x) = I_1 f_2(\xi)$, $\rho(x) = \rho_1 f_3(\xi)$, $A(x) = A_1 f_4(\xi)$, $C(x) = C_1 f_5(\xi)$. f_i are functions representing the transitions from one cell to another. (For the continuous variation approach logistic functions will be utilized, details are given below.)

For harmonic forcing with frequency λ :

$$g(\xi, \tau) = G(\xi) e^{\lambda \tau} \quad (2.3)$$

One can assume solutions of the following form:

$$u(\xi, \tau) = R(\xi) e^{\lambda \tau} \quad (2.4)$$

This leads to:

$$\frac{d^2}{d\xi^2} \left(f_1(\xi) f_2(\xi) \frac{d^2 R(\xi)}{d\xi^2} \right) + \lambda^2 f_3(\xi) f_4(\xi) R(\xi) + \lambda(CD) f_5(\xi) R(\xi) = G(\xi) \quad (2.5)$$

Taking $\lambda = (a + bI)$ and separating real and imaginary parts, after some manipulation, gives:

$$\frac{d^2}{d\xi^2} \left(f_1(\xi) f_2(\xi) \frac{d^2 R(\xi)}{d\xi^2} \right) - \left(b^2 f_3(\xi) f_4(\xi) + \frac{CD^2 (f_5(\xi))^2}{4 f_3(\xi) f_4(\xi)} \right) R(\xi) = G(\xi) \quad (2.6)$$

The result, eq. (2.6), is a non-homogeneous ordinary differential equation with variable coefficients. Analytic and numerical solutions are discussed next.

2.3.1 Analytical Approach

For constant properties in each segment, eq. (2.6) can be written as a system of n -equations, where n is the number of cells. For two cells:

$$\frac{d^4 R_i(\xi)}{d\xi^4} - \left(K_{1,i} b^2 + K_{2,i} \frac{CD^2}{4} \right) R_i(\xi) = K_{3,i} G_1(\xi), \quad i = 1, 2 \quad (2.7)$$

where: $K_{1,1} = 1, K_{2,1} = 1, K_{3,1} = 1, K_{1,2} = \frac{a_3 a_4}{a_1 a_2}, K_{2,2} = \frac{a_5^2}{a_1 a_2 a_3 a_4}, K_{3,2} = \frac{a_6}{a_1 a_2}, a_1 = \frac{E_2}{E_1}, a_2 = \frac{l_2}{l_1}, a_3 = \frac{\rho_2}{\rho_1}, a_4 = \frac{A_2}{A_1}, a_5 = \frac{CD_2}{CD_1}, a_6 = \frac{G_2}{G_1}$.

General solutions to the linear differential eqs. (2.7) involve solutions to the homogeneous equations and ‘‘particular integrals’’. For arbitrary forcing $G_i(\xi)$, finding tractable particular solutions may pose a problem. Consequently, a constant spatial force is discussed here. (Non-constant spatial forcing is treated later numerically.)

The following forcing is considered: $G_1(\xi) = G_{1,0}, G_2(\xi) = G_{2,0}; G_{1,0}, G_{2,0}$ constants.

Then the general solutions can be written:

$$R_1(\xi) = B_1 \cos(\alpha \xi) + B_2 e^{\alpha \xi} + B_3 \sin(\alpha \xi) + B_4 e^{-\alpha \xi} - \frac{G_{1,0}}{\alpha^4} \quad (2.8)$$

$$R_2(\xi) = B_5 \cos(\beta \xi) + B_6 e^{\beta \xi} + B_7 \sin(\beta \xi) + B_8 e^{-\beta \xi} - K_{3,2} \frac{G_{1,0}}{\beta^4} \quad (2.9)$$

Where B_i are constants to be determined and $\alpha^4 = \left(K_{1,1} b^2 + K_{2,1} \frac{CD^2}{4} \right), \beta^4 = \left(K_{1,2} b^2 + K_{2,2} \frac{CD^2}{4} \right)$.

The overall analytic solution requires that the boundary conditions be defined. Two sets are considered below.

Free-Fixed Boundary Conditions

For these conditions the moment and shear free end at $\xi = 0$ gives: $\frac{d^2 R_1(\xi)}{d\xi^2} \Big|_{\xi=0} = 0$ and $\frac{d^3 R_1(\xi)}{d\xi^3} \Big|_{\xi=0} = 0$. The fixed boundary condition at $\xi = 1$ gives: $R_2(1) = 0$ and $\frac{dR_2(\xi)}{d\xi} \Big|_{\xi=1} = 0$. Interface continuity conditions (assuming the cells have the same length) provide: $R_1(\xi) = R_2(\xi), \xi = 0.5$ (displacement continuity), $\frac{dR_1(\xi)}{d\xi} = \frac{dR_2(\xi)}{d\xi}, \xi = 0.5$ (slope continuity), $\frac{d^2 R_1(\xi)}{d\xi^2} =$

$a_1 a_2 \frac{d^2 R_2(\xi)}{d\xi^2}$, $\xi = 0.5$ (moment continuity) and $\frac{d^3 R_1(\xi)}{d\xi^3} = a_1 a_2 \frac{d^3 R_2(\xi)}{d\xi^3}$, $\xi = 0.5$ (shear continuity). These conditions lead to a system of algebraic equations, which in matrix form can be written as:

$$[A] \{B\} = \{G\} \quad (2.10)$$

Where:

$$[A] = \begin{bmatrix} -\alpha^2 & \alpha^2 & 0 & \alpha^2 & 0 & 0 & 0 & 0 \\ 0 & \alpha^3 & -\alpha^3 & -\alpha^3 & 0 & 0 & 0 & 0 \\ 0 & 0 & 0 & 0 & \cos(\beta) & e^\beta & \sin(\beta) & e^{-\beta} \\ 0 & 0 & 0 & 0 & -\beta \sin(\beta) & \beta e^\beta & \beta \cos(\beta) & -\beta e^{-\beta} \\ \cos(0.5\alpha) & e^{0.5\alpha} & \sin(0.5\alpha) & e^{-0.5\alpha} & -\cos(0.5\beta) & -e^{0.5\beta} & -\sin(0.5\beta) & -e^{-0.5\beta} \\ -\alpha \sin(0.5\alpha) & \alpha e^{0.5\alpha} & \alpha \cos(0.5\alpha) & -\alpha e^{-0.5\alpha} & \beta \sin(0.5\beta) & -\beta e^{0.5\beta} & -\beta \cos(0.5\beta) & \beta e^{-0.5\beta} \\ -\alpha^2 \cos(0.5\alpha) & \alpha^2 e^{0.5\alpha} & -\alpha^2 \sin(0.5\alpha) & \alpha^2 e^{-0.5\alpha} & al a_2 \beta^2 \cos(0.5\beta) & -al a_2 \beta^2 e^{0.5\beta} & al a_2 \beta^2 \sin(0.5\beta) & -al a_2 \beta^2 e^{-0.5\beta} \\ \alpha^3 \sin(0.5\alpha) & \alpha^3 e^{0.5\alpha} & -\alpha^3 \cos(0.5\alpha) & -\alpha^3 e^{-0.5\alpha} & -al a_2 \beta^3 \sin(0.5\beta) & -al a_2 \beta^3 e^{0.5\beta} & al a_2 \beta^3 \cos(0.5\beta) & al a_2 \beta^3 e^{-0.5\beta} \end{bmatrix}$$

$$\{B\} = \begin{bmatrix} B_1 \\ B_2 \\ B_3 \\ B_4 \\ B_5 \\ B_6 \\ B_7 \\ B_8 \end{bmatrix} \quad \{G\} = \begin{bmatrix} 0 \\ 0 \\ \frac{K_{3,2} G_{1,0}}{\beta^4} \\ 0 \\ -\frac{\alpha^4 G_{1,0} K_{3,2} - \beta^4 G_{1,0}}{\alpha^4 \beta^4} \\ 0 \\ 0 \\ 0 \end{bmatrix}$$

Note that natural frequencies can be found on setting the determinant of $[A]$ to zero.

Fixed-Fixed Boundary Conditions

For fixed-fixed conditions, $R_1(\xi) = 0$, $\xi = 0$ and $\left. \frac{dR_1(\xi)}{d\xi} \right|_{\xi=0} = 0$. In this case, the matrices in eq. (2.10) are:

$$[A] = \begin{bmatrix} 1 & 1 & 0 & 1 & 0 & 0 & 0 & 0 \\ 0 & \alpha & \alpha & -\alpha & 0 & 0 & 0 & 0 \\ 0 & 0 & 0 & 0 & \cos(\beta) & e^\beta & \sin(\beta) & e^{-\beta} \\ 0 & 0 & 0 & 0 & -\beta \sin(\beta) & \beta e^\beta & \beta \cos(\beta) & -\beta e^{-\beta} \\ \cos(0.5\alpha) & e^{0.5\alpha} & \sin(0.5\alpha) & e^{-0.5\alpha} & -\cos(0.5\beta) & -e^{0.5\beta} & -\sin(0.5\beta) & -e^{-0.5\beta} \\ -\alpha \sin(0.5\alpha) & \alpha e^{0.5\alpha} & \alpha \cos(0.5\alpha) & -\alpha e^{-0.5\alpha} & \beta \sin(0.5\beta) & -\beta e^{0.5\beta} & -\beta \cos(0.5\beta) & \beta e^{-0.5\beta} \\ -\alpha^2 \cos(0.5\alpha) & \alpha^2 e^{0.5\alpha} & -\alpha^2 \sin(0.5\alpha) & \alpha^2 e^{-0.5\alpha} & al a_2 \beta^2 \cos(0.5\beta) & -al a_2 \beta^2 e^{0.5\beta} & al a_2 \beta^2 \sin(0.5\beta) & -al a_2 \beta^2 e^{-0.5\beta} \\ \alpha^3 \sin(0.5\alpha) & \alpha^3 e^{0.5\alpha} & -\alpha^3 \cos(0.5\alpha) & -\alpha^3 e^{-0.5\alpha} & -al a_2 \beta^3 \sin(0.5\beta) & -al a_2 \beta^3 e^{0.5\beta} & al a_2 \beta^3 \cos(0.5\beta) & al a_2 \beta^3 e^{-0.5\beta} \end{bmatrix}$$

$$\{B\} = \begin{bmatrix} B_1 \\ B_2 \\ B_3 \\ B_4 \\ B_5 \\ B_6 \\ B_7 \\ B_8 \end{bmatrix} \quad \{G\} = \begin{bmatrix} \frac{G_{1,0}}{\alpha^4} \\ 0 \\ \frac{K_{3,2} G_{1,0}}{\beta^4} \\ 0 \\ -\frac{\alpha^4 G_{1,0} K_{3,2} - \beta^4 G_{1,0}}{\alpha^4 \beta^4} \\ 0 \\ 0 \\ 0 \end{bmatrix}$$

2.3.2 Numerical Approach

For the numerical approach, a continuous variation model is used. With this model, transitions from one cell to another are modeled via logistic functions. Here these functions, f_i , in non-dimensional form, are taken to be:

$$f_i(\xi) = 1 + \left(\frac{\delta_2 - \delta_1}{\delta_1} \right) \left(\frac{1}{2} + \frac{1}{2} \tanh \left(K \left(\xi - \frac{1}{2} \right) \right) \right), i = 1, 2, 3, 4, 5 \quad (2.11)$$

δ_j represents a material property, geometric property or damping (E , I , ρ , A or C). K controls the sharpness of the transition from one cell to another in the function. A large value corresponding to a sharper transition at $\xi = \frac{1}{2}$.

Substituting eqs. (2.11) into (6) leads to a differential equation, with variable coefficients, which may not have analytic solutions. Given the material layout and cross section variation, i.e., the corresponding logistic functions, a MAPLE[®] routine can be used to obtain numerical approximations to the FRF of the system. This is done by monitoring the response for different values of the frequency b . Resonances can also be obtained via a forced-motion approach (see reference [15]). It consists of using MAPLE[®]'s two-point boundary value solver to solve a forced motion problem. A constant value for the forcing function G is assumed and the frequency b is varied. By observing the mid-span deflection of the beam, resonant frequencies can be found on noting where changes in sign occur.

The approaches are illustrated in the following numerical examples.

2.4 Numerical Examples

Consider the beam shown in Fig. 2.2 and assume the following materials: Aluminum ($E_1 = 71 \text{ GPa}$, $\rho_1 = 2710 \text{ Kg} / \text{m}^3$) and Silicon Carbide ($E_2 = 210 \text{ GPa}$, $\rho_2 = 3100 \text{ Kg} / \text{m}^3$). These values are taken from a paper in the field [16].

2.4.1 Free-Fixed Boundary Conditions

For the free-fixed case, the determinant of $[A]$ in eq. (2.10) leads to the following values for the first two non-dimensional natural frequencies: $b = 5.7228$ and $b = 27.3930$. (The following parameters apply: $a_1 = 2.9577$, $a_2 = a_4 = a_5 = a_6 = 1.0000$, $a_3 = 1.1439$, $G_{1,0} = 1.0000$, $CD = 1.0000$).

Using eq. (2.10) to determine the values of the constants B_i , and eq. (2.8), allows for the calculation of the FRF for the system. Setting $\xi = 0.50$ (beam mid-span), amplitudes can be calculated for different values of the non-dimensional frequency b .

The frequency response function, spanning the first two natural frequencies, for the mid-point of the beam is shown in Fig. 2.3.

For the continuous variation model and using the numerical values given above, the continuously varying functions are shown in Fig. 2.4 (note: $K = 500$).

Assuming a value of I for the external forcing $G(\xi)$ and using the forced-motion approach ([15]), the resultant deflections are plotted below for two distinct values of the frequency b .

The resonance frequencies are taken to occur at $b = 5.9$ and $b = 27.5$, as seen in Fig. 2.5.

Amplitudes for the response at the center of the beam can be monitored from eq. (2.6). The approach leads to the numerical FRF shown in Fig. 2.6 (dots on the plot).

The figure shows an overlap of the numerical results and the results from the analytical approach (eq. (2.8)). It is seen that very good agreement is obtained, the first two resonances and amplitude values correspond well.

From the numerical FRF, the damping ratio of the system, corresponding to the non-dimensional value of damping $CD = 1.0000$, can be estimated. The method used here is the half-power bandwidth [17], applied to the first mode, which, although only applicable to lightly damped single degree of freedom systems, is frequently applied to well-separated modes of multi-degree of freedom systems. It leads to a ratio of approximately 2%.

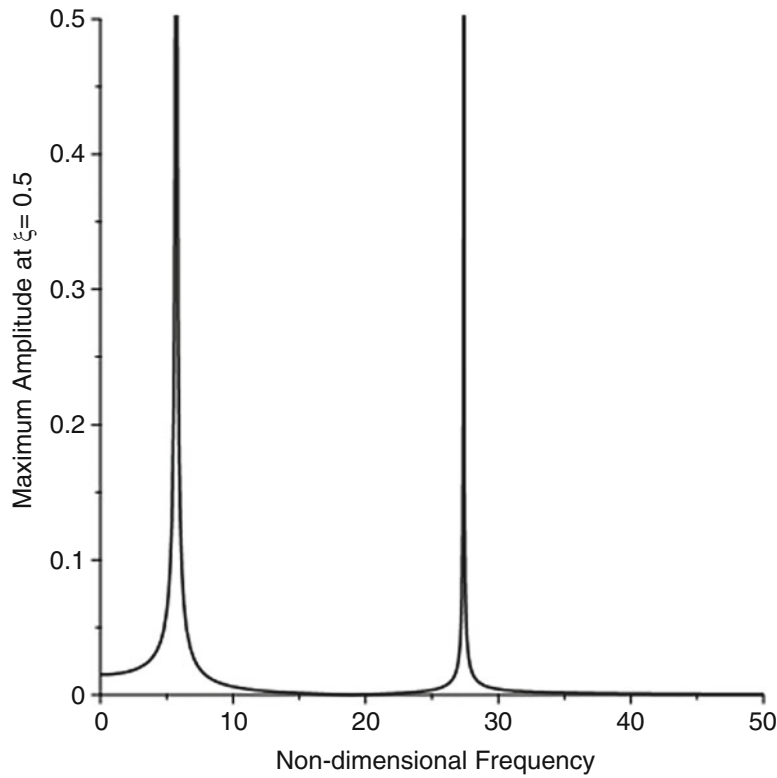


Fig. 2.3 FRF for non-homogeneous beam at mid-point – Free/Fixed

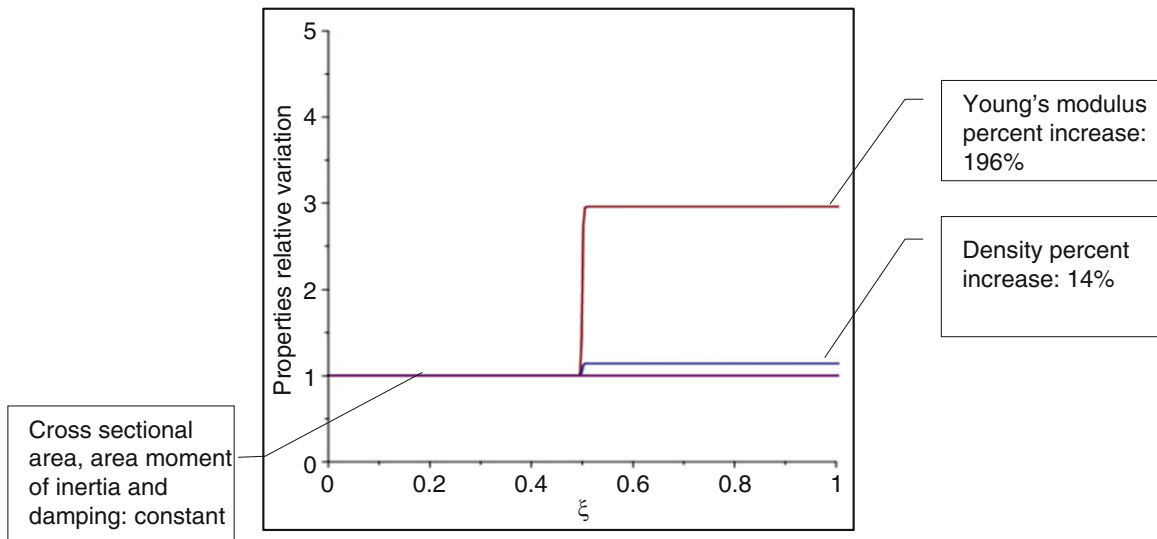


Fig. 2.4 Relative properties variation for two-cell beam

2.4.2 Fixed-Fixed Boundary Conditions

For the fixed-fixed case, the determinant of $[A]$ in eq. (2.10) gives the natural frequencies: $b = 27.40$ and $b = 79.49$. Eqs. (2.10) and (2.8) lead to the FRF for the system, which is shown in Fig. 2.7.

The numerical FRF for this case is seen in Fig. 2.8. The overlap of the numerical results and the results from the analytical approach show that good agreement is obtained for the first frequency and amplitude values, with the second one not quite

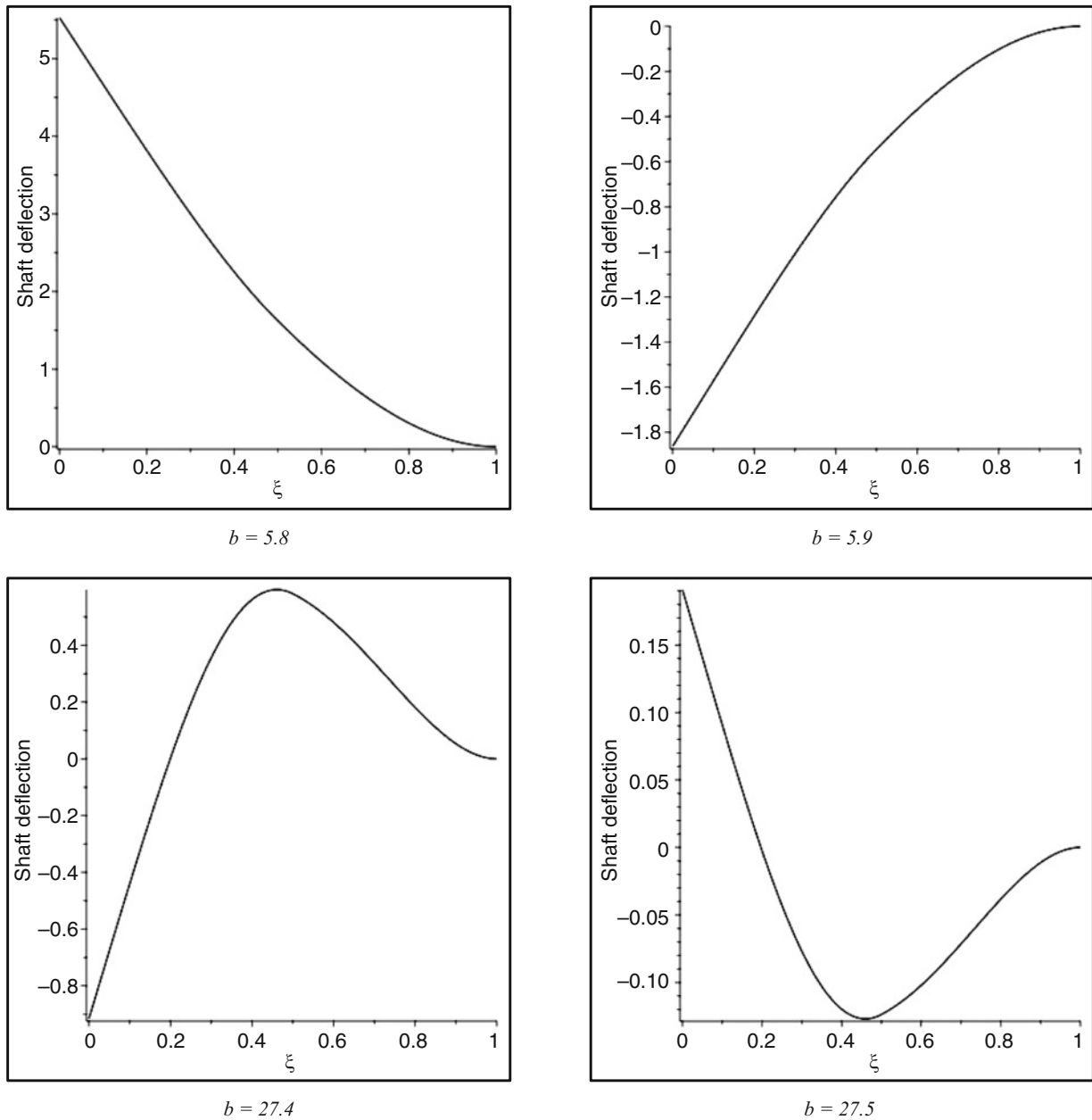


Fig. 2.5 Beam deflections for distinct values of b – Free-Fixed: first and second resonance

given the amplitudes seen in the analytical approach (similar results were obtained for the non-damped case, see reference [1]).

An example is now given in which the spatial force is non-constant. Consider a variable force given by the exponential function: $G(\xi) = e^{-\xi^2}$. The results can be found using the continuous variation model. The FRFs for this case are seen in Fig. 2.9.

2.5 PDE Direct Numerical Approach

Equation (2.2) could be tackled directly via a PDE solver. To this end, here an attempt is made using MAPLE® software.

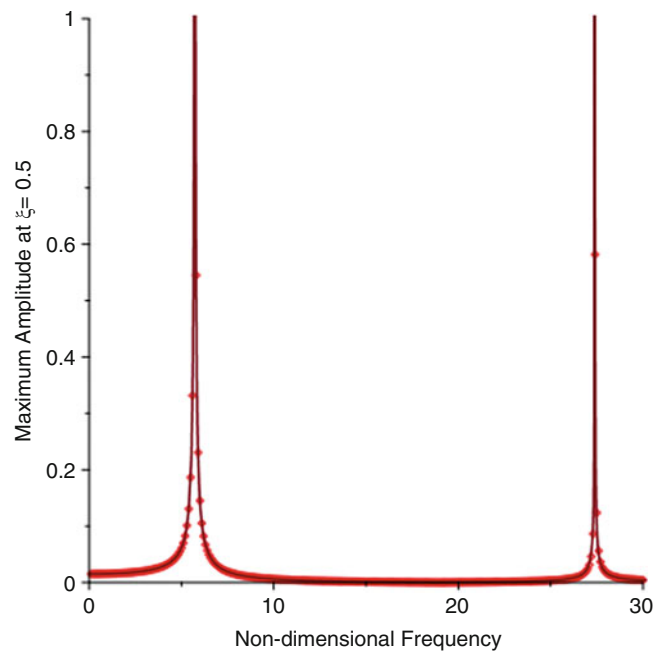


Fig. 2.6 Results comparison – numerical and analytical approaches – Free/Fixed

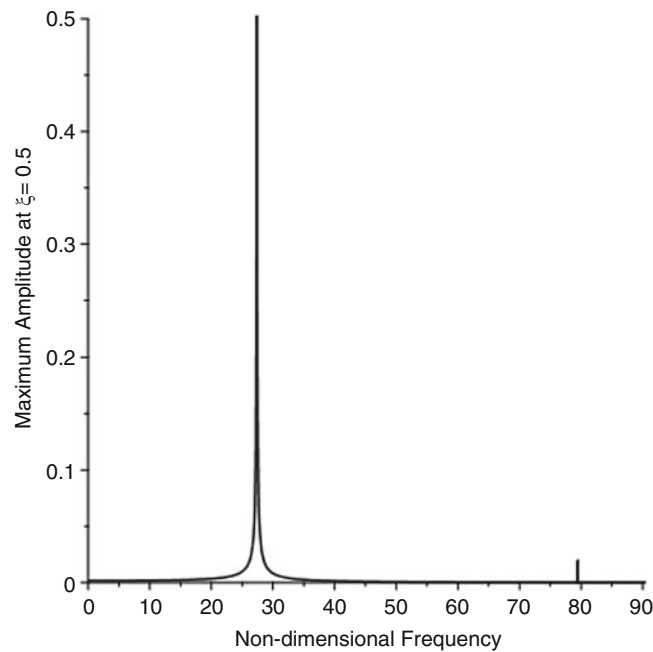


Fig. 2.7 FRF for non-homogeneous beam at mid-point – Fixed/Fixed

On running the numerical routine, it was noticed that convergence of the PDE solver is better achieved with less abrupt changes on the logistic functions. Therefore, here, these functions will be used with a value of $K = 100$. In addition, the beam is subjected to harmonic forcing: $g(\xi, \tau) = \sin(\nu\tau)$ and $CD = 0.1000$ (approximately a damping ratio of 0.2%).

Figure 2.10 shows overlaps for the FRFs obtained using the ODE and PDE solutions. Both cases are illustrated. Note that good agreement is seen for the resonances with some variation on the amplitudes.

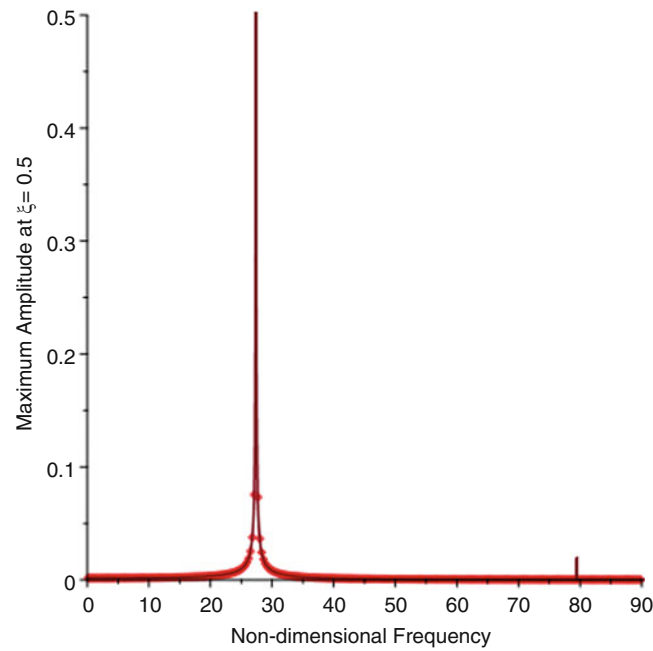


Fig. 2.8 Results comparison – numerical and analytical approaches – Fixed/Fixed

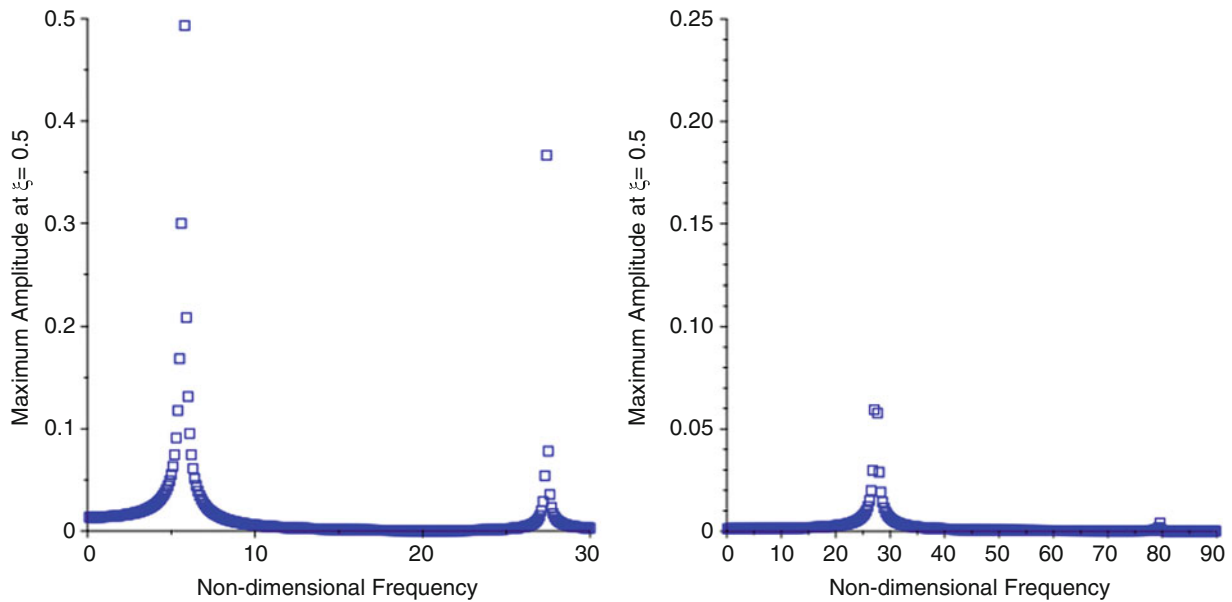


Fig. 2.9 FRFs for exponential force – Free/Fixed (a), Fixed/Fixed (b)

2.6 A More Complete Model

For cases involving lighter, stronger and more flexible beams, subjected to vibration problems, energy losses due to damping effects become very important. When dealing with such cases, the viscous damping approach discussed above may not be adequate to fully model the behavior of such structures. The model leads to uniform damping rates, which are generally not observed, since damping rates in beams tend to increase with frequency (see, for instance, [18]).

In order to address this issue, a more complete model for the damped beam is presented in the following. The basic viscously damped Euler-Bernoulli equation is modified to include extra energy dissipation mechanisms. The first one includes a Kelvin-Voigt (internal) mechanism and the second one a structural damping. These mechanisms are discussed

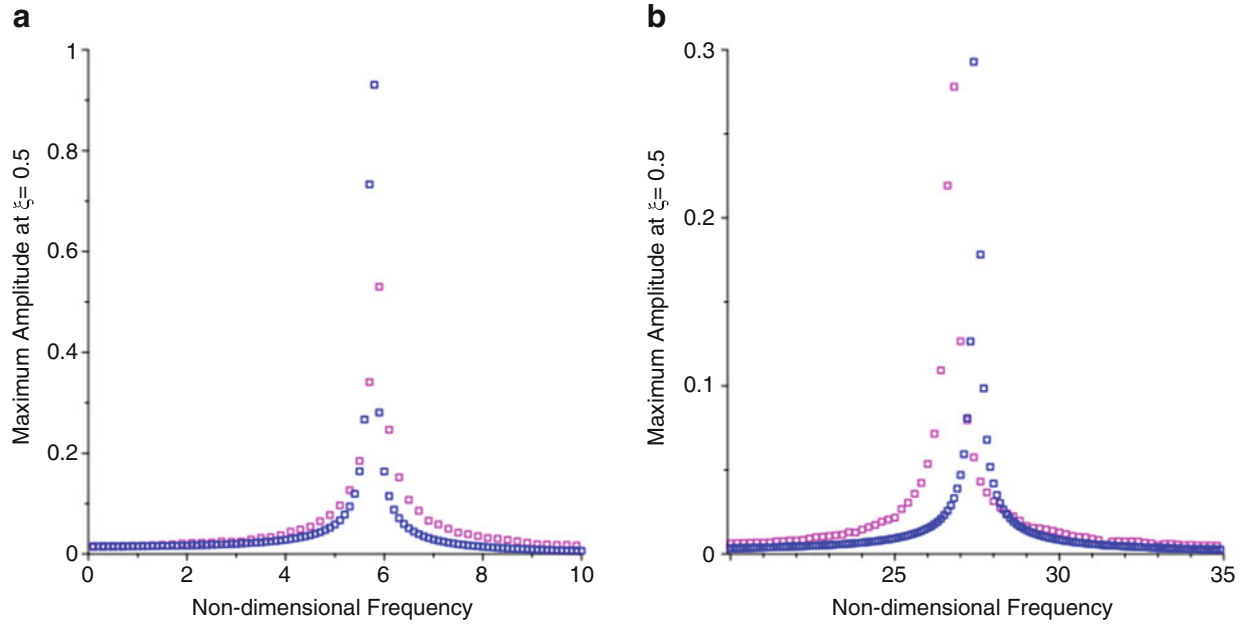


Fig. 2.10 FRFs comparison: ODE versus PDE solutions – Free/Fixed (a), Fixed/Fixed (b)

in details in reference [19]. Note that in the study it was observed, via experiments, that a predominantly linear relationship between the damping rate and the frequency exists; a behavior which was described as “structural damping”.

The modified equation, in non-dimensional form, then becomes:

$$\begin{aligned} \frac{\partial^2}{\partial \xi^2} \left(f_1(\xi) f_2(\xi) \frac{\partial^2 u(\xi, \tau)}{\partial \xi^2} \right) + f_3(\xi) f_4(\xi) \frac{\partial^2 u(\xi, \tau)}{\partial \tau^2} + (CD) f_5(\xi) \frac{\partial u(\xi, \tau)}{\partial \tau} - \gamma f_6(\xi) \frac{\partial^3 u(\xi, \tau)}{\partial \tau \partial \xi^2} \\ + \eta \frac{\partial^2}{\partial \xi^2} \left(f_2(\xi) f_7(\xi) \frac{\partial^3 u(\xi, \tau)}{\partial \tau \partial \xi^2} \right) = g(\xi, \tau) \end{aligned} \quad (2.12)$$

Where η is a non-dimensional viscosity coefficient, γ is a non-dimensional structural damping coefficient and $f_6(\xi)$ and $f_7(\xi)$ are non-dimensional logistic functions describing variations of these damping mechanisms from one cell to another.

Inclusion of Kelvin-Voigt damping requires that the boundary conditions for the problem be revisited [10]. Here the displacement solutions are assumed to be sufficiently smooth, so that the conditions utilized for the previous model still apply (see [20]).

As discussed above, for the case of stacked beams, analytic solutions for eq. (2.12) may not be feasible.

In this section, the continuous variation approach is employed to obtain direct numerical solutions to the equation. MAPLE® PDE solver is employed.

Consider the same 2-cell beam given above and the following parameters: $g(\xi, \tau) = \sin(\nu\tau)$, $K = 100$, $CD = 0.1000$ (damping ratio of 0.2%), $\gamma = 0.1000$, $\eta = 0.1000$. (For simplicity, damping coefficients are taken to have the same values in both cells.) The logistic functions assumed are: $f_6(\xi) = f_7(\xi) = 1.0000$ (A) and $f_6(\xi) = f_7(\xi) = 1 + \left(1 + \tanh\left(K \left(\xi - \frac{1}{2} \right) \right) \right)$ (B).

Figure 2.11 shows the FRFs for these cases with free-fixed boundary conditions. Only the first mode is shown, since the procedure did not capture large amplitudes at the expected second frequency. It is conjectured that the damping caused the amplitudes to be small and not significantly distinct to stand out in the numerical routine. (Decreasing damping values showed increased amplitudes around expected resonance.)

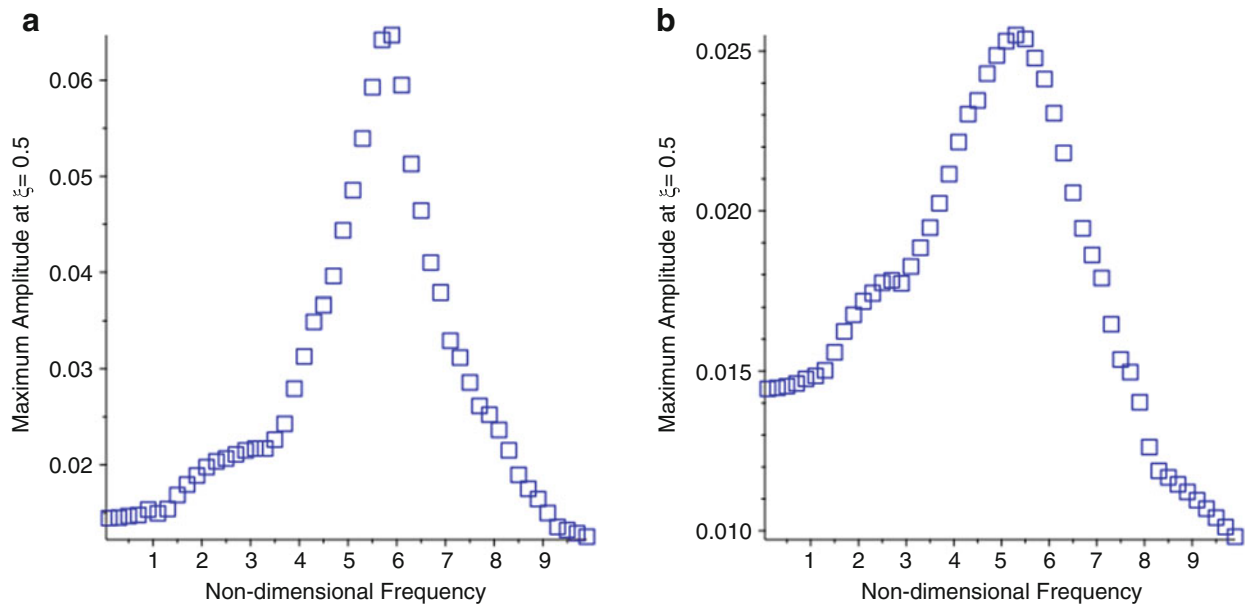


Fig. 2.11 FRFs for expanded model – Free/Fixed

2.7 Conclusions

Modeling discrete property variations via continuously varying functions, in conjunction with numerical solutions, has been shown to lead to good results for resonant frequencies and FRFs of viscously damped layered beams subject to harmonic excitation.

A numerical approach was conducted using MAPLE[®] software, which shows to lead to accurate solutions based on a comparison to analytical results for a specific case.

Two sets of boundary conditions were studied. Namely, free-fixed and fixed-fixed for a uniform two-cell beam made of aluminum and silicon-carbide.

Very good agreement was observed for both cases, with some variation on the amplitudes for the FRFs.

Comparing numerical solutions from two approaches, using ODE and PDE solvers and continuously varying functions, also showed good agreement.

Lastly, a model involving internal and structural damping, in addition to viscous damping was introduced. Numerical results were shown to be feasible for specific cases, using the numerical PDE solver provided by MAPLE[®] software.

References

1. Mazzei, A. J., & Scott, R. A.: Harmonic forcing of a two-segment Euler-Bernoulli Beam. *Special Topics in Structural Dynamics, Volume 6: Proceedings of the 35th IMAC, A Conference and Exposition on Structural Dynamics 2017*, N. Dervilis, ed., Springer International Publishing, Cham, pp. 1–15, (2017)
2. Mazzei, A. J., & Scott, R. A.: Harmonic forcing of a two-segment Timoshenko Beam. *Special Topics in Structural Dynamics, Volume 5, N. Dervilis, ed., Springer International Publishing*, pp. 1–15, (2019)
3. Lee, E.H., Yang, W.H.: On waves in composite materials with periodic structure. *SIAM J. Appl. Math.* **25**(3), 492–499 (1973)
4. Hussein, M.I., Hulbert, G.M., Scott, R.A.: Dispersive Elastodynamics of 1D banded materials and structures: analysis. *J. Sound Vib.* **289**(4–5), 779–806 (July 2)
5. Hussein, M.I., Hulbert, G.M., Scott, R.A.: Dispersive Elastodynamics of 1D banded materials and structures: design. *J. Sound Vib.* **307**(3–5), 865–893 (June 11)
6. Vasseur, J. O., Deymier, P., Sukhovich, A., Merheb, B., Hladky-Hennion, A. C., & Hussein, M. I.: Phononic band structures and transmission coefficients: methods and approaches. *Acoustic Metamaterials and Phononic Crystals*, P.A. Deymier, ed., Springer Berlin Heidelberg, pp. 329–372, (2013)
7. Hussein, M.I., Leamy, M.J., Ruzzene, M.: Dynamics of Phononic materials and structures: historical origins, recent Progress, and future outlook. *Appl. Mech. Rev.* **66**(4), 040802–040802–38 (2014)

8. Leopold, H.: Vibration of the Euler-Bernoulli Beam with Allowance for Dampings. Proceedings of the World Congress on Engineering, London, England, (2008)
9. Di Blasio, G., Kunisch, K., Sinestrari, E.: Mathematical models for the elastic beam with structural damping. *Appl. Anal.* **48**(1–4), 133–156 (1993)
10. Banks, H. T., & Inman, D.: On Damping Mechanisms in Beams, 383904, NASA, Hampton, VA, United States, (1989)
11. Filipiak, J., Solarz, L., Zubko, K.: Analysis of damping effect on beam vibration. *Mol. Quantum Acoust.* **27**, (2006)
12. Snowdon, C.: Response of internally damped cantilever beams to sinusoidal vibration. *J. Acoust. Soc. Am.* **38**, (1965)
13. Zhang, G.-D., Guo, B.-Z.: On the Spectrum of Euler–Bernoulli beam equation with Kelvin–Voigt damping. *J. Math. Anal. Appl.* **374**(1), 210–229 (2011)
14. Capsoni, A., Maria Viganò, G., Bani-Hani, K.: On damping effects in Timoshenko beams. *Int. J. Mech. Sci.* **73**, 27–39 (2013)
15. Mazzei, A.J., Scott, R.A.: On the effects of non-homogeneous materials on the vibrations and static stability of tapered shafts. *J. Vib. Control.* **19**(5), 771–786 (2013)
16. Chiu, T.C., Erdogan, F.: One-dimensional wave propagation in a functionally graded elastic medium. *J. Sound Vib.* **222**(3), 453–487 (1999)
17. Chopra, A. K.: *Dynamics of Structures: Theory and Applications to Earthquake Engineering*, Pearson, Hoboken, NJ, (2017)
18. Bishop, R.E.D.: The treatment of damping forces in vibration theory. *J. R. Aeronaut. Soc.* **59**(539), 738–742 (1955)
19. Russell, D.: 4. On mathematical models for the elastic beam with frequency-proportional damping. *Control and Estimation in Distributed Parameter Systems*, Society for Industrial and Applied Maths, pp. 125–169, (1992)
20. Lang, H., & Leyendecker, S.: Complex frequency response for linear beams with Kelvin-Voigt viscoelastic material. 4th Joint International Conference on Multibody System Dynamics, Montréal, Québec, Canada, (2016)

Arnaldo J. Mazzei Jr. is a Prof. of Mechanical Engineering at Kettering University. He received his Ph.D. in Mechanical Eng. from the University of Michigan. Currently he teaches courses in Vehicle Dynamics, Chassis Systems, Vibrations and CAE. Research interests: Automotive Engineering, System Dynamics and Vibrations. He is an active member of SAE and SEM.

Chapter 3

Characterization of Fatigue in Integrated Tuned Mass-Dampers



Srikar M. Srivatsa and Daniel J. Inman

Abstract Recent work concerned with passive vibration suppression in structural systems has focused on the development of metastructures. Metastructures (also called architected materials) are a type of mechanical metamaterial: an object arranged or constructed in such a manner that it has traits unachievable by its constituent material. Metastructures often consist of embedded spring mass systems made from small beams with a tip mass or chiral lattice structures with mass inserts. The goal of a metastructures design is to reduce vibrations of the host structure. It does this using the absorber action of the embedded spring mass systems. The embedded tuned mass dampers (TMDs) then become prone to sustaining failure by fatigue. While many recent papers discuss various geometric and material designs, very few if any address the issues of fatigue of the embedded absorbers. This paper makes an initial investigation into the relationship between the TMDs' geometric parameters and their fatigue performance with the goal of improving the design and implementation metastructures. A sensitivity analysis was performed to identify the geometric TMD parameter with the largest impact on natural frequency and stress concentration. Analytical models for natural frequency and maximum stress were developed for the TMDs and compared to finite element models. The analytical models were substantiated by the FEA models for some of the perturbed parameters, indicating that further work would be needed to confirm that, for a given parameter, a certain trend in natural frequency indicates an anticipatable trend in stress.

Keywords Vibration suppression · Metamaterial · Fatigue · Structural dynamics · Geometric optimization

3.1 Introduction

3.1.1 Background

Mechanical metamaterials have been at the forefront of novel materials design over the past couple of decades. Mechanical metamaterials are fundamentally defined by deliberately arranging traditional materials in a specific fashion, giving them characteristics unachievable by the constituent materials. The characteristics or number of input materials can vary, as can the nature and applications of the output traits. As such, mechanical metamaterials as diverse as those with negative Poisson's Ratios [1] to those with seemingly fluid-like behavior [2] have been developed. A spinoff of metamaterials, known as metastructures, have larger-scale modifications allowing for capabilities that traditional structures would not have.

A specific type of metastructure, previously detailed in a paper by Reichl et. Al [3], in addition to Reichl's doctoral dissertation [4], contains integrated tuned mass dampers (TMDs) used to mitigate vibrations experienced by the larger structure. This structure is a simple beam, fixed at one end, with periodic cavities for the TMDs (Fig. 3.1, p. 2). These TMDs have been developed to redirect and dissipate energy transferred through the structure during vibrations, thereby reducing the effects of cyclic loading and excess vibrations on the overall structure. Depending on the usage of a given structure, the implementation of integrated TMDs can allow for increased service lifetimes and reduced cumulative damage. Tuned mass dampers are already used in a variety of engineered systems to counteract the effects of excess vibrations [5]; structures

S. M. Srivatsa
Sibley School of Mechanical and Aerospace Engineering, Cornell University, Ithaca, NY, USA
e-mail: srisri@umich.edu

D. J. Inman (✉)
Department of Aerospace Engineering, University of Michigan, Ann Arbor, MI, USA
e-mail: daninman@umich.edu

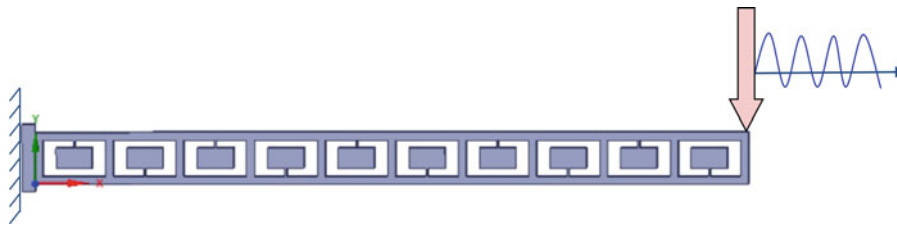


Fig. 3.1 The host structure used to examine tuned mass dampers (TMDs) in this study consists of ten TMDs mounted within the cavities of a beam, much like a metastructure from Reichl’s past work [3]. The TMDs consist of point masses attached to “integrated damped springs”, which alternate in their connection point to the beam from the top face to the bottom face. The beam is fixed at one end and loaded at the cantilevered end; the frequency of the load applied at the free end can differ. This structure is not tuned to suppress vibrations at a specific frequency, like a metastructure

with embedded TMDs would thus have an additional measure of localized vibration suppression. In metastructures, the suppression of vibrations at a given frequency is achieved by changing the geometries of the individual TMDs.

3.1.2 Motivation

The energy that is redirected by the integrated TMDs is ultimately dissipated through their oscillation. However, this induced cyclic motion would indicate that the TMDs undergo the detrimental effects of cyclic loading over a sustained period of time. Thus, it is likely that the TMDs are prone to failure by fatigue. More specifically, this fatigue is likely to be perpetuated by stress concentrations caused by the unique geometry of the TMDs. As per the crack-propagation mode of fatigue, the repeated oscillation of the TMDs is likely to cause the repeated re-opening of any cracks that may form at any stress concentration sites. These cracks would eventually grow to the point of fast fracture, indicating a catastrophic failure of the loaded body [6]. While other methods of analyzing fatigue failure could also be applicable to these TMDs, the presence of these anticipated stress concentrations necessitates the use of the crack propagation method in this study.

Some common engineering solutions exist to mitigate failure by crack propagation. The addition of fillets—rounded corners which lessen the impact of cyclic loading on the repeated opening of any pre-existing cracks—is an applicable solution for the TMDs studied herein [7]. However, fillets may only lessen the likelihood and immediacy of fatigue failure, rather than eliminate it outright. Recall that the application of structurally-integrated TMDs requires tuning them to suppress vibrations at a given frequency, and that this tuning is accomplished by modifying the TMDs’ geometries. The nature of the stress concentrations observed in the TMDs will thus depend not only on the nature of loading experienced by the overall structure, but on the local geometries. The impact of both the loading scenario and the local geometries is likely to be exacerbated as a result of the TMDs’ local dynamics, which will be distinct from those of the overall structure into which they are integrated. Because of this exacerbation, there might be a relationship between the tuned natural frequency of the TMD (itself a function of TMD size) and its fatigue performance, as indicated by the local stress concentration. The fatigue life of integrated TMDs in structures has not been thoroughly characterized, so understanding the potential outcomes of tuning the TMDs to a given resonant frequency would aid the implementation of metastructures in various engineering applications. This may be achieved by avoiding certain frequency ranges by sizing the TMDs appropriately or employing fatigue failure mitigation tactics—like the aforementioned fillets—to increase the TMDs’ service lifetimes.

3.2 Objectives

The primary goal of this study is to determine whether there may be any correlation between the natural frequency of the TMDs and any observed local stress concentrations (which would be indicative of fatigue performance). In the process of addressing this goal, the fidelity of commercial finite element software packages versus simpler analytical methods will be evaluated. Secondary goals include quantifying the effect of adding fillets to the TMDs to decrease stress concentrations, in addition to identifying methods to establish any natural frequency- stress concentration correlation outside of the range of geometries relevant to the metastructure examined in this study.

3.3 Caveats

A couple of key caveats limit the consideration of results from this study. The first and foremost is that the scope of this study is restricted by the finite range of values used to parametrize the TMD geometries. The range of values used in this study stem from the existing geometries of the baseline metastructure, and as such are applicable to any metastructure with the same ratios between its various baseline TMD geometries. However, the performance of a metastructure (or other system with integrated TMDs) with vastly different geometries cannot be directly correlated to the results of this study. Also, the structures used herein have not been tuned—that is, to ensure that the natural frequencies of the TMDs match those of the overall structure. The scope of this study is thus to evaluate the dynamic properties of the TMDs; the inclusion of the larger structure is necessary to observe the stress concentration results (which would be derived from a stress profile only observable with the entire assembly). A third caveat is that this study limits the consideration of fatigue performance to the quantification of any stress concentrations and assumes that existing relationships between stress concentrations in notches and fatigue life are applicable here due to their largely case-independent nature for common engineering metals [6].

3.4 Methods

3.4.1 Sensitivity Analysis

Understanding any potential relationship between the natural frequency of a given TMD and its fatigue performance when integrated with a larger structure depends on the specific geometry that contributes to a given TMD's natural frequency. As shown in Fig. 3.2c, there are multiple geometric features that can be modified to tune the TMDs studied herein. It is entirely possible that TMDs of different proportions may happen to have the same natural frequency, but that their fatigue performances may differ due to their differing individual geometries. It would thus help to understand the relative impacts of these individual geometries on the natural frequency and fatigue performance.

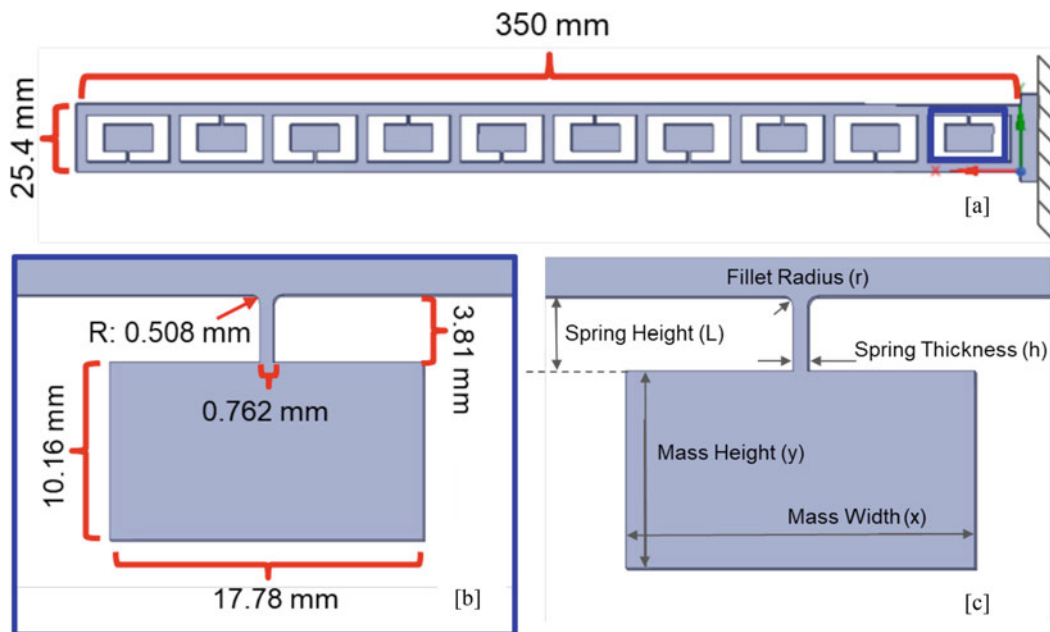


Fig. 3.2 The baseline dimensions of the structure examined herein are shown. The blue inset in (a) is expanded to show detail of the TMD in (b). The thickness of the structure into the page, in both (a) and (b), is 25.4 mm. Shown in (c) are the five TMD parameters chosen for perturbation in the sensitivity analysis

A sensitivity analysis can be used to identify the input geometries to which the outputs— in this case, natural frequency and fatigue performance— are most sensitive. This is accomplished by first establishing a set of baseline dimensions for the individual TMD unit (as shown in Fig. 3.2b). Each individual parameter is then perturbed by a series of fixed percent differences, with all other parameters held constant. The output properties are then computed for each of these perturbed geometries and compared to the baseline geometry’s outputs. This entire process is repeated until each input parameter has been through this process of perturbation. The input properties that cause the most dramatic changes in the output properties can hence be taken as the most sensitive input parameters. Throughout this entire process, the overall size of the metastructure beam (i.e. the frame inside which the individual TMDs are hosted) remains the same, as shown in Fig. 3.2a, for the sake of uniformity. Additionally, all ten TMDs on a given beam are kept at the same dimensions, despite it having been demonstrated that tuning individual mass dampers for different frequencies makes the metastructure effective over a larger range of frequencies [3].

While this is not a comprehensive method of evaluating the exact effect of all inputs through their full range of values, it nonetheless elucidates which TMD parameters affect natural frequency and stress concentration (and thus fatigue performance) the most. Since tuning the metastructures to absorb vibrations at a given frequency requires the adjustment of the individual TMDs’ geometries, a sensitivity analysis would indicate the potential tradeoffs of changing a given parameter to achieve a certain natural frequency by indicating to what degree that change impacts fatigue performance—or vice versa, by indicating the smallest possible geometry changes for a given fatigue performance improvement.

3.4.2 Analytical Modeling

A schematic model of the TMD allows for the derivation of equations for the mass-damper’s anticipated natural frequency and maximum stress. As shown in Fig. 3.3, the TMDs were simplified as a cantilever beam with a point mass at the free tip; the point mass in the schematic corresponds to the large mass portion of the TMD (referred to hereon as the point mass) while the beam itself corresponds to the damped spring portion of the TMD (referred to hereon as the spring). Note that this cantilever beam model is distinct from the cantilevered boundary conditions employed for the overall metastructure shown in Fig. 3.1.

By simplifying the TMD’s as such, the maximum stress can be defined using the static beam bending equation. It is anticipated that the maximum stress would occur at the fixed end, at either the top or bottom edge of the beam, as shown below:

$$S_{a/\max} = \frac{M (h/2)}{I} = \frac{6 (F_{eff}) (L)}{hh^2} \quad (3.1)$$

where F_{eff} indicates the effective inertial force caused by the oscillation of the point mass. This can be further broken down as such:

$$F_{eff} = (m_{point}) (A) (-2\pi\omega_n)^2 \quad (3.2)$$

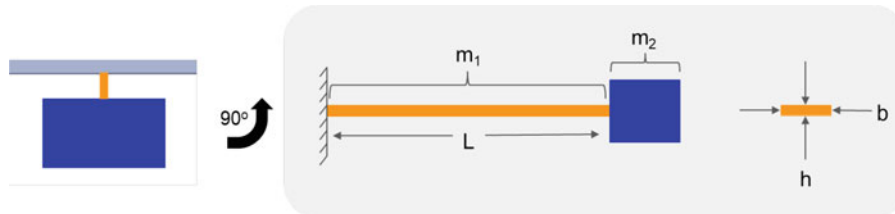


Fig. 3.3 The individual TMD shown on the left has been color-coded to distinguish the spring (in orange) from the point mass (in blue). The TMD was then rotated 90 degrees and simplified according to the schematic shown in the center. The simplification consists of a cantilevered beam (in orange), fixed at one end and with a point mass (in blue) at the free end. The image on the right indicates the cross-section of the cantilevered beam. Variables referred to herein are used in Eqs. 3.1, 3.2, 3.3, 3.4 and 3.5

where A is the amplitude of the point mass' side-to-side oscillations, ascertained from the FEA simulation's displacement outputs. On a TMD, the maximum stress from Eq. 3.1 would be at the corners between the damped spring and the frame of the metastructure, as shown in Fig. 3.4 below. Based solely on the relative orders of inputs in Eq. 3.1, one would anticipate that the spring thickness (h) has the largest impact on maximum stress. The point mass' dimensions (x & y) are of only first order, in comparison. While the analytical model itself does not directly provide an estimation of stress concentration, they do contribute to stress concentration in conjunction with maximum stress results from the FEA model (to be discussed further down).

The natural frequency of the individual TMDs can be determined from the schematic model by using the second-order ordinary differential equation that models a cantilever beam as a forced damped oscillator, shown below:

$$m\ddot{x} + b\dot{x} + kx = F_{eff}(t) \quad (3.3)$$

where F_{eff} is again the excitation derived from the inertial force of the point mass (not defined herein). From this equation, the expression for natural frequency can be derived using the effective cantilever beam stiffness and mass of the cantilever (m_{point}), accounting for the added impact of the point mass (m_{spring}):

$$\omega_n = \sqrt{\frac{k}{m}} = \sqrt{\frac{Ebh^3}{4L^3 * \left[m_{point} + \left(\frac{33m_{spring}}{140} \right) \right]}} \quad (3.4)$$

Like with Eq. 3.1, based on the relative orders of the input variables in Eq. 3.4 one would anticipate that the spring length (L) and thickness (h) contribute the most to affecting its natural frequency.

This natural frequency expression does not account for damping; the damped natural frequency uses a widely accepted value for metals of 0.01 [8] and is found as such:

$$\omega_d = \sqrt{\frac{(1 - \zeta^2) Ebh^3}{4L^3 * \left[m_{point} + \left(\frac{33m_{spring}}{140} \right) \right]}} \quad (3.5)$$

Note that these analytical considerations are a single-degree-of-freedom simplification of the TMD. While a multiple-degree-of-freedom system would certainly be capable of capturing the more complex geometry of the TMD, solving such a system is far more computationally expensive. Providing a simpler alternative to computation-heavy commercial FEA codes would allow for a quicker, rule-of-thumb-type consideration of TMDs' failure characteristics when being implemented in metastructures. However, this simplification of the TMD's dynamics includes the potential misrepresentation of some portions of the TMD—most notably, the portrayal of the damping mass as a point mass and ignoring its true inertial properties.

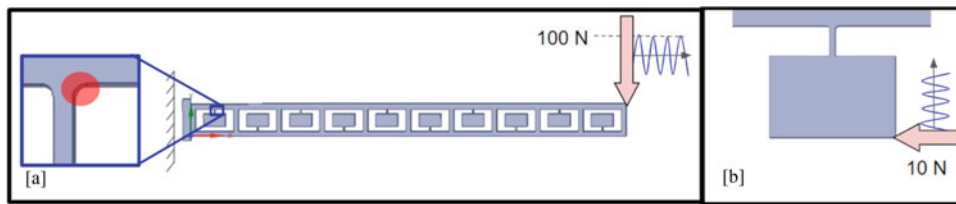


Fig. 3.4 The red circle in (a) denotes the location of the maximum stress anticipated, and observed, on the TMD closest to the fixed end of overall structure as modeled in FEA. This is indicated by the analytical expression for maximum stress (Eq. 3.1). The TMD-alone model (b) shows the location of the applied load, used solely to determine the dynamic properties in isolation

3.4.3 Finite Element Modeling

These analytical models were compared to results derived from commercial FEA software. The finite-element model was constructed in ANSYS Workbench (Ver. 18.1), using the Harmonic Response package. In this method, the software performs a modal analysis of the input structure to determine its modal properties, and then determines the structural response for a given range of frequencies.

Unlike previously described with metastructures and integrated TMDs, which are often made of polymers and fabricated using additive manufacturing methods due to their complex geometries [4], 6061-T6 Aluminum was used as a baseline material to evaluate the performance of the metastructure in this study. This choice was to ensure that the results pertaining to stress concentration could eventually be used with existing stress concentration-fatigue life relations. Fatigue life relations have only been extensively developed for traditional engineering materials, like steel and aluminum alloys, used most in fatigue-prone situations [7]. To accommodate this, the FEA model used the 6061-T6 aluminum material configuration present in the default ANSYS material libraries. This default material configuration included not only elasticity parameters, but also fatigue and plasticity considerations. The mesh contained 3D tetrahedral second-order elements, with an average element side length of approximately 1/1000 the overall structure's length and an element size $\frac{1}{4}$ of that near the base of the TMDs (where stress concentrations were to be expected). Again, the structure's inherent damping was taken as 0.01 [8], in order to allow for the production of a reasonable stress response at the resonant frequency.

Recall that the sensitivity analysis would perturb a given geometric input parameter of the TMDs by a series of fixed percentage differences, keeping all the other parameters at their baseline values, and then repeat the systematic perturbation for all of the five chosen geometric input parameters (Fig. 3.2c). Each observed parameter was perturbed by -5% , -1% , 1% , and 5% from its baseline value. A separate finite element model was computed for each perturbed case—indicating a total of 21 FEA models computed for of this study (4 perturbations each for the 5 geometries chosen, plus a baseline model). However, recall that the TMDs evaluated herein are not being tuned to the resonant frequency of the entire structure—especially because when the perturbations are conducted, only the perturbed parameter is modified while all others are held constant. In order to ascertain the dynamic properties of the TMDs in isolation, a model of just a TMD (independent of the larger structure) was used to find its natural frequency. The larger metastructure was used to identify stress concentration. As such, this indicates 2 models for each perturbed geometry—bringing the total number of FEA models computed to 42.

The aforementioned model parameters were applied uniformly across all the geometries evaluated as a part of the sensitivity analysis. The entire metastructure was fixed at one end and had an oscillating 100 N load applied at the cantilevered end (Fig. 3.4a). The range of frequencies applied for the oscillating load was from 0 to 1500 Hz, and the frequency and structural response of the first bending mode for the metastructure fell within this range. While this frequency was not considered for evaluating the dynamics of the TMD, it would be indicative of the structure's most excited state (and thus where the stress concentrations would be highest). When modeling the TMD alone, the back surface of the “base plate” was fixed and a dummy oscillating load was applied at one edge of the point mass' end face (Fig. 3.4b). The dummy load, applied with a range of frequencies from 0 to 3000 Hz, would be used solely to identify the resonant frequency at the first bending mode for the TMD.

Due to the stress distribution of the overall metastructure—being a fixed-cantilevered beam, the stress values of the metastructure frame would increase closer to the fixed end—the TMD closest to this fixed end was observed to have the highest local maximum stresses at its corners where it met the frame of the larger structure (Fig. 3.4a). While the maximum stress of a metastructure in each FEA model may not have been on or near a TMD, this maximum stress would not have contributed specifically to the fatigue of the TMDs—and was thus excluded from consideration in this study. As such, this corner location of the TMD closest to the structure's fixed end was consistently used to sample the maximum stress herein throughout all perturbations.

Developing the stress concentration factor depends on the parameter being perturbed. It follows the formula below:

$$K_t = \frac{\sigma_{max}}{S_a} \quad (3.6)$$

where a “true” maximum is divided by an “average” maximum. Herein, the maximum observed stress from the FEA model is used as the “true” maximum, while the maximum stress from the analytical model (Eq. 3.1) is used as the “average” maximum. This method allows for an accurate capture of the “average” maximum, since the discretization used to create the FEA model eliminates the two-dimensionality of the analytical model used to define the maximum stress.

3.5 Results

3.5.1 Fillet Radius Perturbation

The first parameter perturbed in this study was the radius of the fillet; the results from the FEA model are shown in Fig. 3.5a. The stress concentration results indicate that the impact of fillets is in line with literature and prior work regarding stress concentrations in round notches: with increasing fillet radius, the stress concentration decreases non-linearly and monotonically [7]. However, it does not appear that changing the fillet radius causes any perceptible trend or significant change in natural frequency, as seen in the results from the TMD-alone model (Fig. 3.5b). The analytical models defined herein do not accommodate for the fillet radius, so the FEA models' results cannot be compared directly to theory. However, a lack of significant change in natural frequency with changing fillet radius indicates that fillets can be employed to reduce stress concentrations in metastructures without affecting their dynamic properties—useful information for the potential real-world implementation of integrated TMDs.

3.5.2 Spring Parameter Perturbations

The next set of parameters perturbed in this study are the two dimensions of the spring examined herein: the spring thickness and height (parameters 'h' and 'L' in the schematic model in Fig. 3.2c, respectively). As with the fillet results, the natural frequency perturbation was conducted with the TMD alone, while the stress concentration results are from the model with the entire structure.

The natural frequency perturbation for the spring thickness (Fig. 3.6f, g) and spring height (Fig. 3.6a, b) are shown below, comparing FEA results with results of the analytical model. In both cases, the natural frequency trends derived from FEA match that of the analytical model. The relative magnitudes of natural frequency percent change between $\pm 1\%$ and $\pm 5\%$ perturbations, respectively, appear to be similar between the FEA and analytical models' results for both perturbed parameters as well. However, the actual values of natural frequency percent change are not consistent between both models. The analytical model appears to be more sensitive than the FEA model is, indicating that perhaps the single-degree-of-freedom consideration used to derive Eq. 3.5 for natural frequency may not be the most accurate depiction of the system's dynamics. This is further observed when the actual values of natural frequency are enumerated, such as for the spring height's values shown in Fig. 3.6e. Here, the dynamics of the TMD as described by the FEA model appear to diverge much further from the analytical model. Additionally, it can be noted that while the analytical model prescribes that the spring height and thickness are of equal order, the perturbation results from the FEA model fail to reflect this. Together, these results indicate even more so that the analytical model is not the most accurate picture of the TMD's dynamics. While the analytical model certainly does correctly capture the trend of natural frequency with changing geometric parameters, it does not accurately reflect the magnitude of these changes.

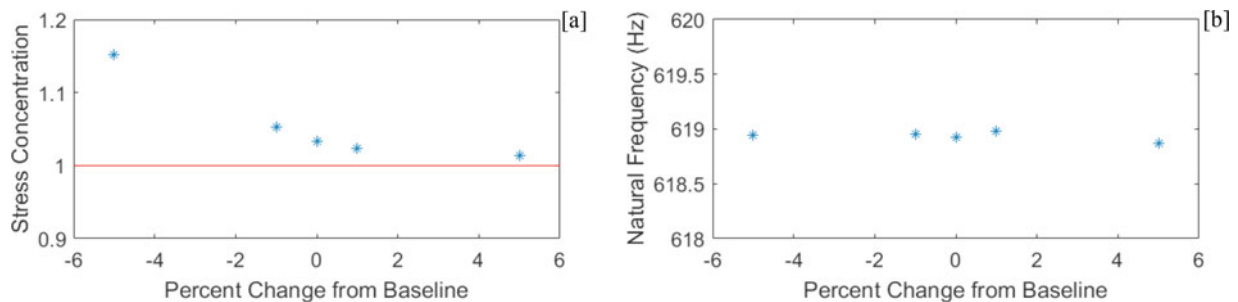


Fig. 3.5 Results of the fillet radius perturbation show a monotonic and non-linear trend in stress concentration (a), similar to that of existing notch-based stress concentration trends for similar geometries. The red line in the stress concentration plot indicates the minimum possible stress concentration. The lack of noticeable change in natural frequency (b) indicates that employing larger fillets indeed lowers the stress concentration without affecting dynamic properties (for the range of values tested herein)

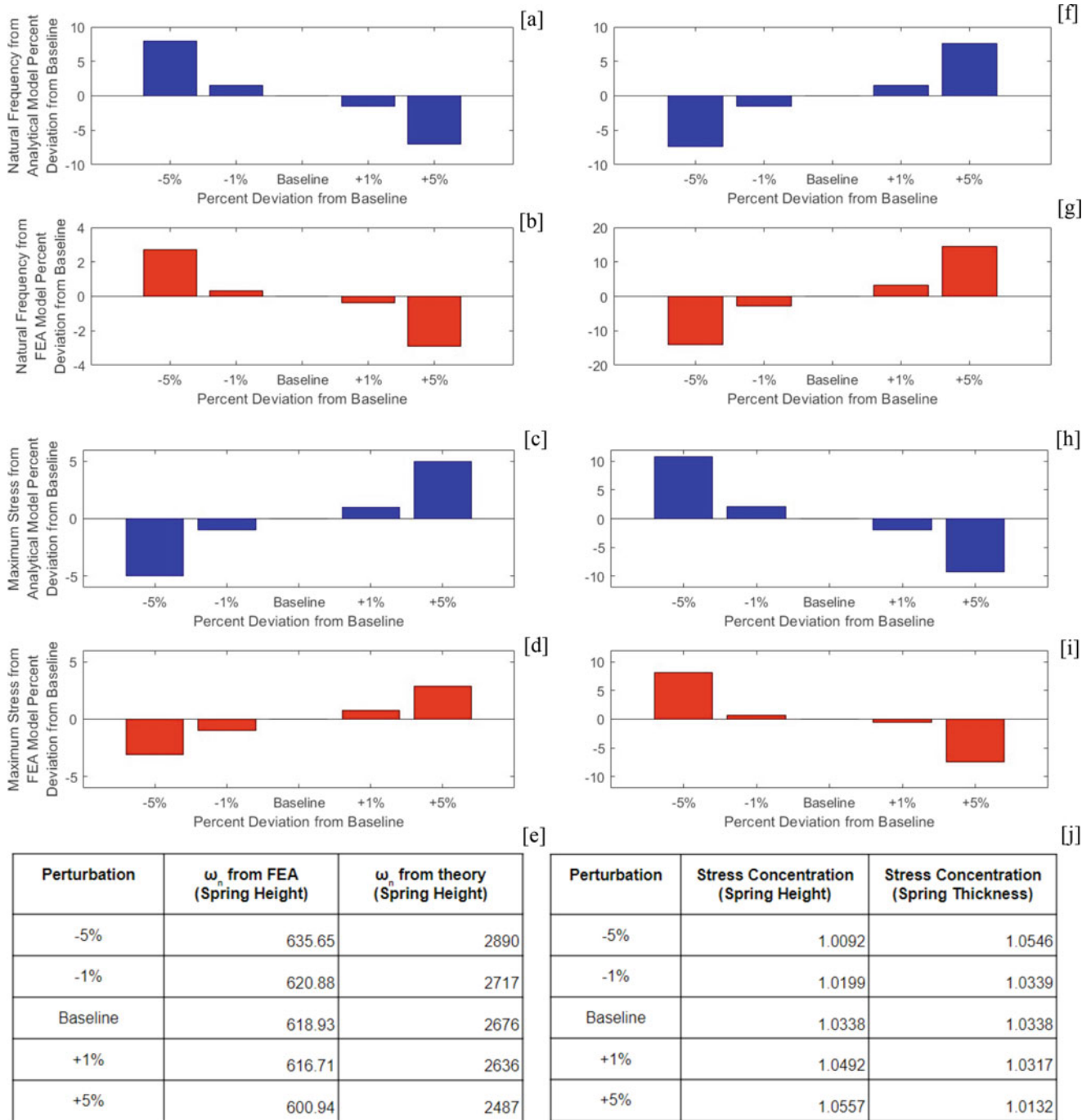


Fig. 3.6 The perturbations of spring height and spring thickness are shown. These include the natural frequency perturbations for spring height (analytical model in (a), FEA in (b)), spring thickness (analytical model in (f), FEA in (g)), as well the maximum stress perturbations for spring height (analytical model in (c), FEA in (d)) and spring thickness (analytical model in (h), FEA in (i))—all of which show agreement between theory and the FEA models. The actual natural frequency values from the perturbation for spring height are shown in (e), while the stress concentration perturbations are shown in (j)

The stress concentration results for the spring height and thickness perturbations also had their own sources of ambiguity. The “true” maximum stress for both parameters appears to trend in the same direction as the “average” maximum stress, indicating adherence between the FEA model and analytical formulation (Fig. 3.6c, d, h, i). However, the magnitudes of the trends are not even, indicating either that the analytical model does not fully capture the causes of stress concentrations at the base of the TMDs or that the method of sampling maximum stress based on the FEA model’s results may not be accurate. With specific regard to the fidelity of the FEA model, a lack of sufficient resolution would result in a “true” maximum stress that may be higher than indicated in the model. However, the magnitude of perturbation expressed in the “average” maximum stress values between the spring thickness and height matches the relative magnitudes of those values in the analytical model (Eq. 3.1).

In addition, the trend of the stress concentration factors themselves is in the opposite direction of “average” maximum stress (derived from theory) for both spring parameters (Fig. 3.6j). One would anticipate that a thicker beam, or a longer beam, would reduce the effect of vibrations on the maximum stress observed. While that reduction in maximum stress is indeed observed, the lack of adherence with the stress concentration factor may indicate that the implementation of TMDs would need to consider a tradeoff between the actual observed maximum stress (primarily associated with the propensity of yielding) and the resultant stress concentration factor (associated with the propensity of crack propagation). The fidelity of the FEA model’s accuracy may also be called into question, but a higher resolution model would only yield higher “true” maximum stress values. It is indefinite as to whether a higher resolution FEA model would yield a switch in the trend direction for stress concentration factor.

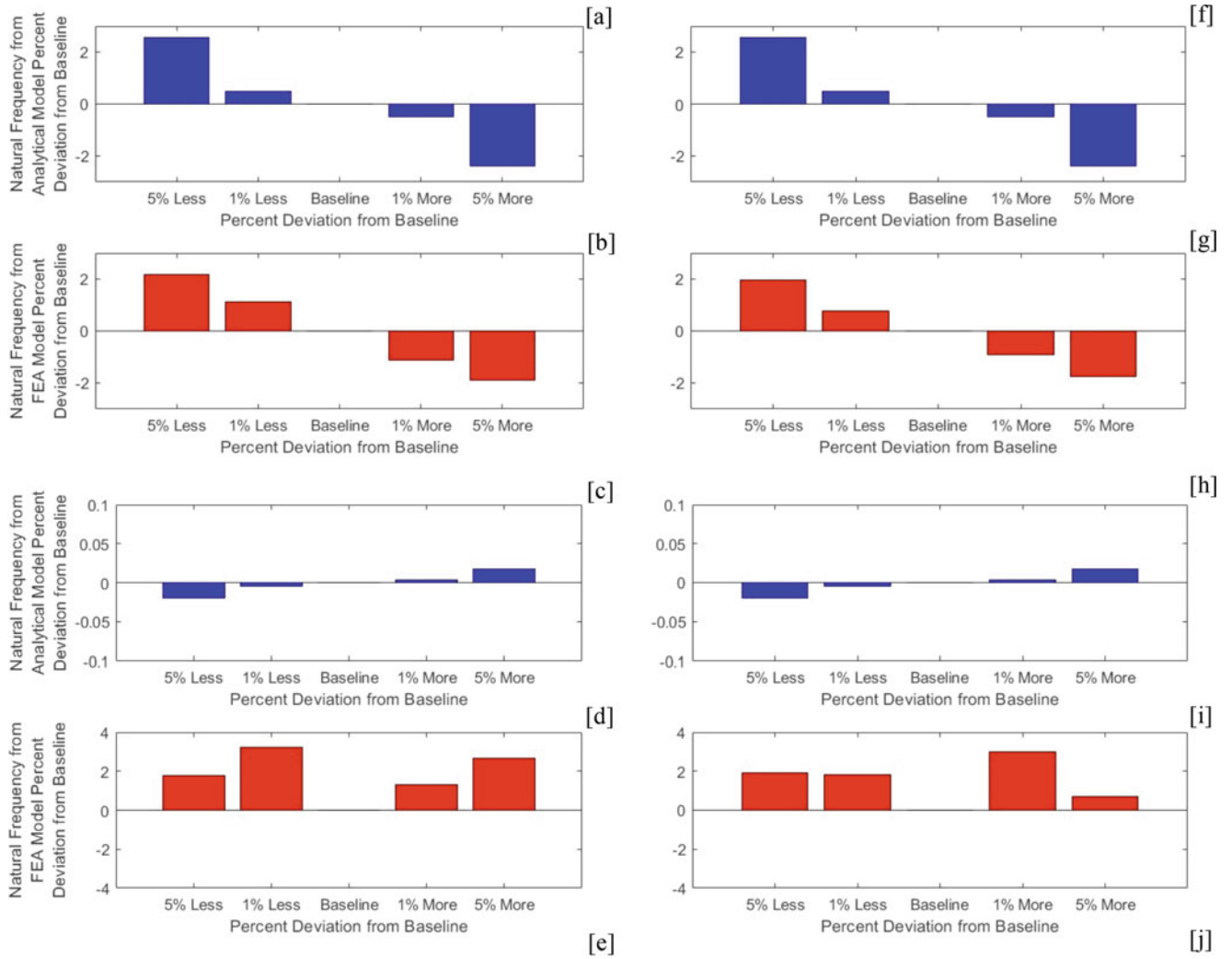
3.5.3 Point Mass Parameter Perturbations

Having examined the perturbation of the spring parameters, the last set of parameters perturbed in this study are the two considered dimensions of the mass: its width and height (parameters ‘x’ and ‘y’ in the schematic model in Fig. 3.2c, respectively). Again, the natural frequency perturbation was conducted with the TMD alone while the stress concentration results are from the model with the entire structure; these results are on p.9.

The natural frequency perturbation for the mass height (Fig. 3.7a, b) and mass width (Fig. 3.7f, g) are shown below, comparing FEA results with results of the analytical model. In both cases, the natural frequency trends derived from FEA match that of the analytical model. The relative magnitudes of natural frequency percent change between $\pm 1\%$ and $\pm 5\%$ perturbations, respectively, appear to be similar between the FEA and analytical models’ results for both perturbed parameters as well. Unlike with the spring parameters, the actual values of natural frequency percent change are consistent between both models– the analytical model appears to indicate the same degree of sensitivity as the FEA model. However, the actual values of natural frequency continue to differ, as shown for instance with the mass height parameters in Fig. e.

As with the spring parameters, the difference in values indicates that the single-degree-of-freedom model would not be accurate in depicting the actual dynamics of the system. However, when it comes to predicting the trend and relative impact of modifying the point mass’ dimensions in an effort to change the TMD’s dynamics, the analytical model appears to perform more accurately.

The stress concentration results for the mass height (Fig. 3.7c, d) and mass width (Fig. 3.7h, i) are shown below, indicating a lack of the anticipated trend in the “true” FEA results. This lack of a trend thus carries through to the stress concentration factors (Fig. 3.7j). In this case, it is likely (as with the spring parameters) that the resolution of the finite element model’s mesh was not enough to observe a “true” maximum stress value as high as it should be. However, the presence of “true” values higher on both sides of the baseline value sheds some doubt on this notion. Another potential cause of the lacking trend could be insufficient perturbation, wherein the $\pm 1\%$ and $\pm 5\%$ perturbations were not enough to cause a significant effect on the FEA model. If so, this brings into question the FEA model’s margin of error regarding stress concentration trends induced by all forms of parameter perturbation.



Perturbation	ω_n from FEA (Mass Height)	ω_n from theory (Mass Height)
-5%	652.93	2745
-1%	646.14	2689
Baseline	638.93	2676
+1%	631.86	2663
+5%	626.85	2612

Perturbation	Stress Concentration (Mass Height)	Stress Concentration (Mass Thickness)
-5%	1.0092	1.0546
-1%	1.0199	1.0339
Baseline	1.0338	1.0338
+1%	1.0492	1.0317
+5%	1.0557	1.0132

Fig. 3.7 The perturbations of mass height and width are shown. These include the natural frequency perturbations for mass height (analytical model in (a), FEA in (b)), mass thickness (analytical model in (f), FEA in (g))—all of which show some theory-FEA agreement. These also include the maximum stress perturbations for mass height (analytical model in (c), FEA in (d)) and mass thickness (analytical model in (h), FEA in (i))—none of which show agreement between theory and the FEA models. Note the difference in magnitude between analysis types for the maximum stress plots. The actual natural frequency values from the perturbation for spring height are shown in (e), while the stress concentration perturbations are shown in (j)

3.6 Conclusions

Overall, the analytical models defined herein appear to be supported by the finite element analysis results, indicating that simplified analytical models may be used to gauge the impact of geometry on the stress concentration properties of integrated TMDs. Furthermore, the trends observed in natural frequency indicate that, for certain parameters such as spring height or length, a certain change in natural frequency would indicate a corresponding change in stress concentration. Furthermore, it appears that the implementation of fillets affects stress concentration but not natural frequency, indicating that these commonly used implements to reduce stress concentrations would be useable for integrated TMD's.

However, these conclusions are limited by a lack of observed trend in stress concentration for the point mass parameters. This is likely attributed to the fidelity of the finite element model, but this is not confirmed. Additionally, the results do not provide evidence to suggest that these trends would necessarily be viable outside of the range of values evaluated herein. Especially as not all the FEA results express the anticipated trends from theory (which should persist within the bounds of linear-elastic mechanical behavior), the presence (or lack thereof) of any extrapolated trends can neither be affirmed or negated.

In addition to addressing these aforementioned limitations of this study, future work would focus on correlating the presence of stress concentrations to fatigue life. This would likely entail experimental confirmation of the existing notch-based stress concentration-fatigue life relations using existing methods, in addition to developing new computational or empirical methods to gauge fatigue performance from stress concentration results. Also, the analysis of TMDs tuned to the resonant frequency of their host structure would allow for the evaluation of fatigue life as a function of the overall metastructure, rather than just that of individual TMDs. In the vein of verifying key assumptions of this study, another goal of future work would be to experimentally determine the overall structure's damping properties, as well as those of the TMD alone, to determine the accuracy of the damping ratio of 0.01 assumed for the model.

Acknowledgments The author would like to acknowledge Dr. Katie Reichl, Dr. Lawren Gamble, and Ms. Brittany Essink for their technical guidance and background knowledge.

References

1. Ren, X., et al.: Auxetic metamaterials and structures: a review. *Smart Mater. Struct.* **27**(2), 023001 (2018). <https://doi.org/10.1088/1361-665x/aaa61c>
2. Kadic, M., et al.: On the practicability of Pentamode mechanical metamaterials. *Appl. Phys. Lett.* **100**(19), 191901 (July 2012). <https://doi.org/10.1063/1.4709436>
3. Reichl, K.K., Inman, D.J.: Lumped mass model of a 1D Metastructure for vibration suppression with no additional mass. *J. Sound Vib.* **403**, 75–89 (2017). <https://doi.org/10.1016/j.jsv.2017.05.026>
4. Reichl, K.: Active Metastructures for Light-Weight Vibration Suppression. 2018. University of Michigan, Ann Arbor, PhD dissertation. Deep Blue, <https://deepblue.lib.umich.edu/handle/2027.42/144044>.
5. Newland, David E.: VIBRATION OF THE LONDON MILLENNIUM FOOTBRIDGE. Department of Engineering, University of Cambridge, www2.eng.cam.ac.uk/~den/ICSV9_06.htm
6. Liu, M., et al.: An improved semi-analytical solution for stress at round-tip notches. *Eng. Fract. Mech.* **149**, 134–143 (2015). <https://doi.org/10.1016/j.engfracmech.2015.10.004>
7. Noda, N., et al.: Stress concentration factors for shoulder fillets in round and flat bars under various loads. *Int. J. Fatigue.* **19**(1), 75–84 (1997). [https://doi.org/10.1016/s0142-1123\(97\)82050-6](https://doi.org/10.1016/s0142-1123(97)82050-6)
8. Orban, F.: Damping of materials and members in structures. *J. Phys. Conf. Ser.* 5th Int. Workshop Multi-Rate Proces. Hysteresis. **268**, 1(1), (2011). <https://doi.org/10.1088/1742-6596/268/1/012022>.

Srikar M. Srivatsa is currently a first-year doctoral student in mechanical engineering at Cornell University. His current research interests are in studying novel computational methods for designing metamaterials. He received his Bachelors in mechanical engineering from the University of Michigan in May 2019.

Chapter 4

Dynamic Identification of Masonry Arch Bridges Using Multiple Methodologies



Semih Gonen and S. Soyoz

Abstract To reduce the significant uncertainties associated with finite element modeling of masonry structures, one of the most efficient and novel approaches is the system identification using ambient vibrations and the use of modal parameters for updating of the FEM models. This paper presents system identification of stone masonry arch bridges located in the northeastern part of Turkey. The collected signals were preprocessed for system identification, and then modal parameters of the structures were identified by processing the data separately in the frequency and time domains, using Enhanced Frequency Domain Decomposition (EFDD), Auto-Regressive Model (AR Model) and Multiple Signal Classification (MUSIC) methods. The results were presented and compared for three of the representative bridges, consisting of three, four and five arches, respectively. They indicate that AR models and MUSIC method are able to capture the modal frequencies estimated by the reliable EFDD method; however, the results of MUSIC method are subject to the user's methods, and this approach has not yet reached the required robustness for practical structural engineering applications.

Keywords Dynamic identification · Stone masonry · Arch bridges · In-situ testing · Non-destructive evaluation

4.1 Introduction

Assessment of historical structures is often followed by subsequent preservation and strengthening measures. Thus, realistic and rigorous structural assessment becomes more important in terms of protecting cultural heritage and using resources carefully. Structural assessment of masonry arch bridges located on the railway between Northern and Central parts of Turkey was to be performed using only finite element analysis; however, finite element modeling (FEM) of masonry structures comprises significant uncertainties in terms of material properties, boundary conditions, and different modeling assumptions. Since these uncertainties affect the results significantly and make generating an accurate FEM model a challenging task, they should be reduced as much as possible. In this context, one of the most efficient and novel approaches is system identification using ambient vibrations and the use of modal parameters for updating the FEM models. Dynamic identification, FEM updating and seismic performance assessment of the bridges mentioned above have been discussed elsewhere [1, 2]. This paper focuses only on rigorous system identification of selected bridges and compares the results obtained from different methodologies.

Dynamic identification tests were carried out under ambient vibration, hammer impact loading, and train passing conditions. The collected signals were preprocessed for system identification, and then modal parameters of the structures were identified by processing the data separately in the frequency and time domains, using MATLAB software. The results, obtained using the data under ambient vibration condition, were presented for three of the representative bridges, consisting of three, four and five arches, respectively. Because historical masonry structures are often more complicated and have higher stiffness than the standard shear-type buildings, dynamic identification presents a more challenging task for these structures. Thus, it is good practice not to rely on a single method but to confirm the identification results with other methods based on different principles. For this reason, Enhanced Frequency Domain Decomposition (EFDD) was performed in the frequency domain and the modal values were found with the methods using the Cross Power Spectral Density (CPSD) graphs and decay of the autocorrelation, whereas, in the time domain Auto-Regressive Model (AR Model) and Multiple Signal Classification

S. Gonen (✉) · S. Soyoz
Department of Civil Engineering, Boğaziçi University, TR, Bebek/Istanbul, Turkey
e-mail: serdar.soyoz@boun.edu.tr

(MUSIC) methods were employed. Finally, the results were compared to each other and recommendations were derived for future work.

It is possible to find examples of similar work in the literature and others have also emphasized the importance of using multiple methodologies in the analysis. Costa et al. [3] performed operational modal analysis of three different masonry arch bridges using EFDD and Stochastic Subspace Identification (SSI) and did numerical model updating. Aoki et al. [4] carried out a series of non-destructive, destructive and dynamic tests to determine the dynamic properties of the long masonry arch bridge and utilized them for modal updating procedure. Some other research exemplifies rigorous ambient vibration tests on concrete and iron bridges and the performance of various system identification methods [5, 6]. Magalhães et al. [7] introduced the topic of operational modal analysis by using three output-only modal identification algorithms on the data from a 280-meter long concrete arch bridge. Their use of different methods based on distinct principles revealed the uncertainty of the modal damping estimates and demonstrated the need for further research. Various instances that employ operational modal analysis for structural dynamic identification of monumental historical structures are available to the reader as well [8–11].

This paper contributes to understanding the dynamic properties of a large number of historical arch bridges built in the same period while highlighting the capabilities and drawbacks of the identification methods used. After a quick overview of the bridges and the manner of data collection, the paper outlines the various methods by which the data was manipulated and analyzed. It then presents the data obtained from the bridges and compares the information gained from the multiple interpretive methodologies. It concludes with a discussion of the various identification methodologies and emphasizes the benefit of using multiple approaches to enable accurate analysis.

4.2 Bridges & Ambient Vibration Survey

Bridges presented in this study represent a similar design: barrel arches, sandstone or limestone, mortar and infill as a building material, and a similar deck width of around five meters. Properties of the bridges are given in Table 4.1 and shown in Fig. 4.1. Of those, Bridge 13 (three arches), Bridge 41 (four arches), and Bridge 5 (five arches) have been selected as paradigms to present the results obtained from the analysis as they typify their respective groups and produced particularly clear results.

Instrumentation was performed using a cabled data acquisition system, force-balance accelerometers (FBA), and 24-bit recorders. Twelve FBA sensors were used for the ambient vibration survey of Bridge 13, while 20 FBA sensors were used in a single setup for Bridges 41 and 5. Sensors were placed over the arches and piers at the lateral edges on the deck in longitudinal, vertical and out-of-plane (transverse) directions with regard to the bridges' plane. It was thus possible to characterize vertical and transversal movements as well as rotations. An example of the sensor layout for Bridge 5 is provided in Fig. 4.2. Approximately 1 h of data was collected for each bridge under the bare condition, and a maximum of 7 min' data was taken under impact loading and train passing. The system's sampling frequency was configured to 200 Hz.

Table 4.1 List of presented bridges in this paper

ID	Location (km)	Spans (m)	Total Length (m)	Max Height (m)
5	21 + 689	6–10–10–6–6	64.3	17.55
13	30 + 153	8–8–8	40.7	13.70
41	360 + 292	10–10–10–10	59.3	10.77

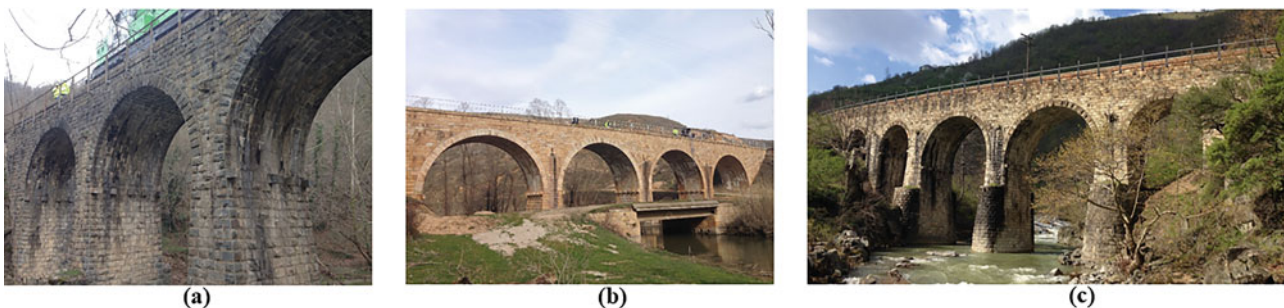


Fig. 4.1 Dynamically Identified Bridges: (a) Bridge 13, (b) Bridge 41 and (c) Bridge 5

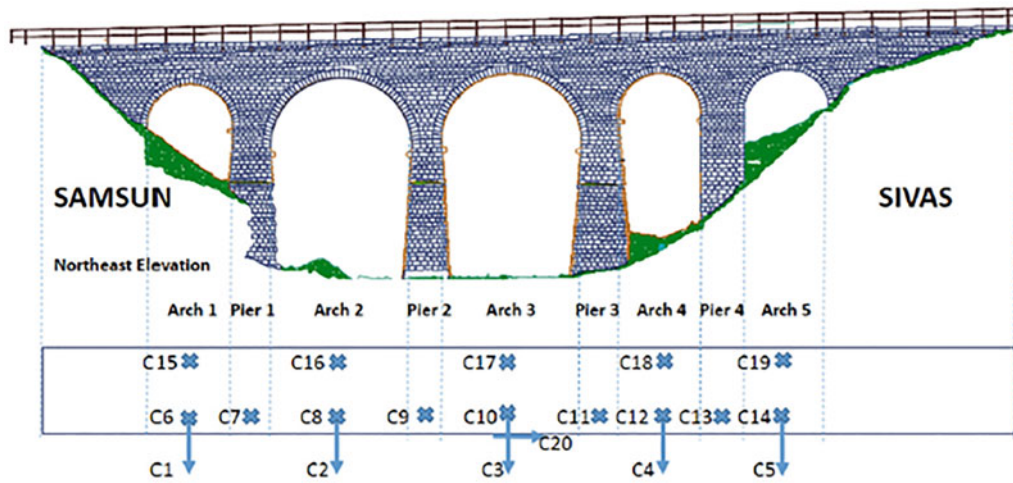


Fig. 4.2 Profile and sensor layout of Bridge 5

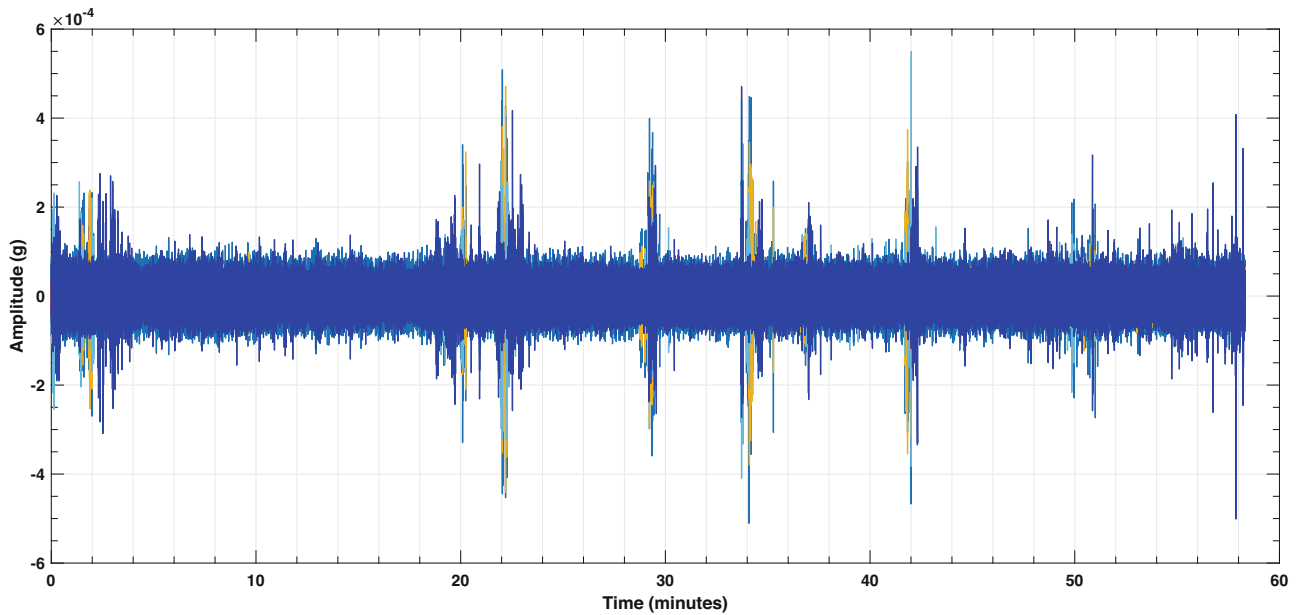


Fig. 4.3 Example of the processed ambient vibration data - in the bare condition

4.3 System Identification

4.3.1 Preprocessing

For structures with high stiffness such as masonry arch bridges, ambient vibration has small amplitudes and low signal-to-noise ratio. The noise changes the frequency content and the amplitudes of the Fourier spectra, also introduces spurious resonant peaks [12]. Thus, in this study, analysis of the noisy data collected from the bridges presented required signal processing before the identification procedure. Preprocessing included detrending, applying filters and decimation. An example of the processed ambient vibration data from a few channels is shown in Fig. 4.3.

First, existing trends in the data, if there are any, were removed from the data. Second, the acceleration data was integrated twice to find the displacement time histories. The raw data usually has non-zero final displacements, and this should be corrected by removing the low frequencies incrementally via the application of high-pass filters. The suggested increment for correction is 0.05 Hz. Third, it is often a good practice to check the Fourier Amplitude Spectrum of the data as it indicates the quality of the signal and whether the signal is noise dominant or not. If there were any frequencies in the

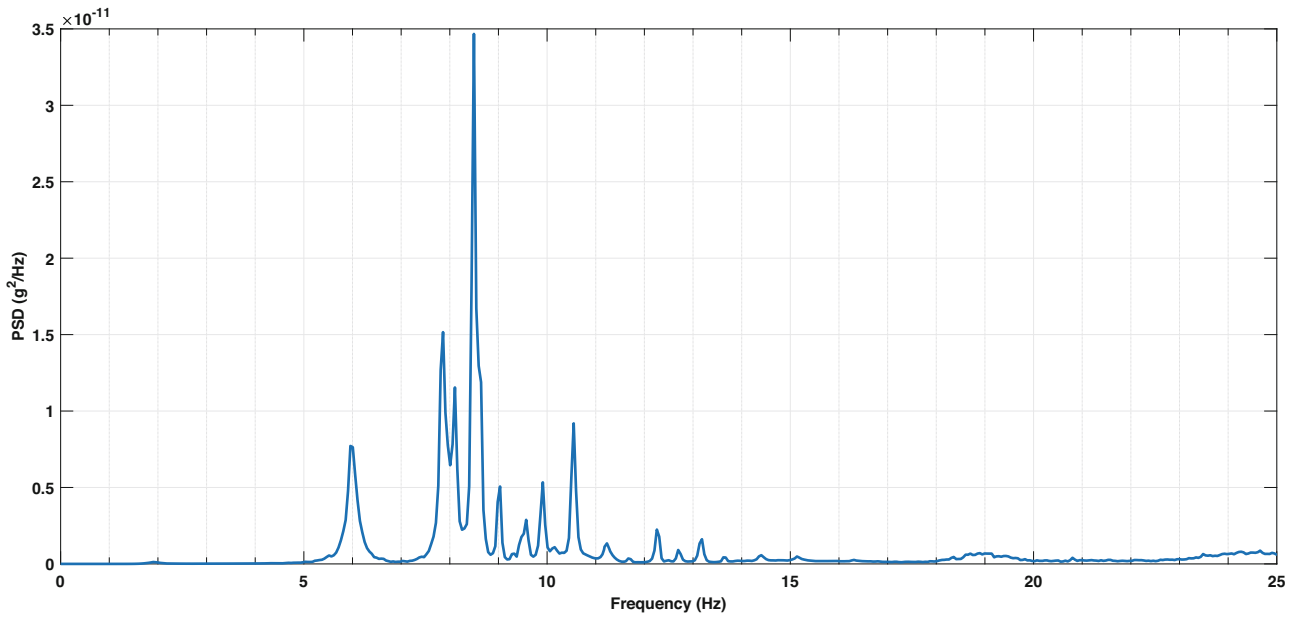


Fig. 4.4 Auto-spectrum of the whole data for Bridge 5

signal dominated by noise, such as those stemming from a working generator or an electrical connection, these frequencies might be eliminated by employing a band-pass filter around them. Finally, decimation was employed when dealing with long records in time-domain methods, as they tend to require more processing time. Decimation enabled shortening the data without losing information.

4.3.2 Enhanced Frequency Domain Decomposition (EFDD)

Frequency Domain Decomposition [13], is a non-parametric output-only modal identification technique. As its name suggests, it operates in the frequency domain and has the advantage of being fast and user-friendly. It also gives the user a feeling of the data they are dealing with through the use of spectral density functions. As the first step in implementing the identification algorithm, the Power Spectral Density (PSD) matrix was estimated. In this paper, PSD matrix estimation was done with the Welch method, using 4096 points for the Fast Fourier Transform (FFT), a Hanning window and a 50% overlapping. Then, the estimate of the output PSD, G_{yy} , was decomposed by taking the singular value decomposition (SVD) of the PSD matrix.

$$G_{yy}(\omega_j) = U_j S_j U_j^H \quad (4.1)$$

where U_j is an orthonormal matrix ($U_j U_j^H = I$) that contains the singular vectors of $G_{yy}(\omega_j)$ and S_j is a diagonal matrix containing the scalar singular values. Now the spectral matrix is decomposed into a set of auto spectral density functions, each corresponding to a single degree of freedom system. By plotting the first singular values for each frequency, a system's modal frequencies can be obtained via simple peak-picking, and the mode shapes were obtained using the first singular vectors at the corresponding frequency. Figure 4.4 presents an example of the auto-spectrum for Bridge 5.

Enhanced Frequency Domain Decomposition [14] is an improved version of the FDD technique and allows the identification of damping ratios. The PSD function was identified around the peak by comparing the mode shape estimate (the singular vector) with the singular vectors for the frequency lines around the peak. This comparison could be made using Modal Assurance Criterion (MAC), which measures the correlation between two modal vectors [15].

$$MAC_{\phi_1, \phi_2} = \frac{(\phi_1^T \phi_2)^2}{(\phi_1^T \phi_1) (\phi_2^T \phi_2)} \quad (4.2)$$

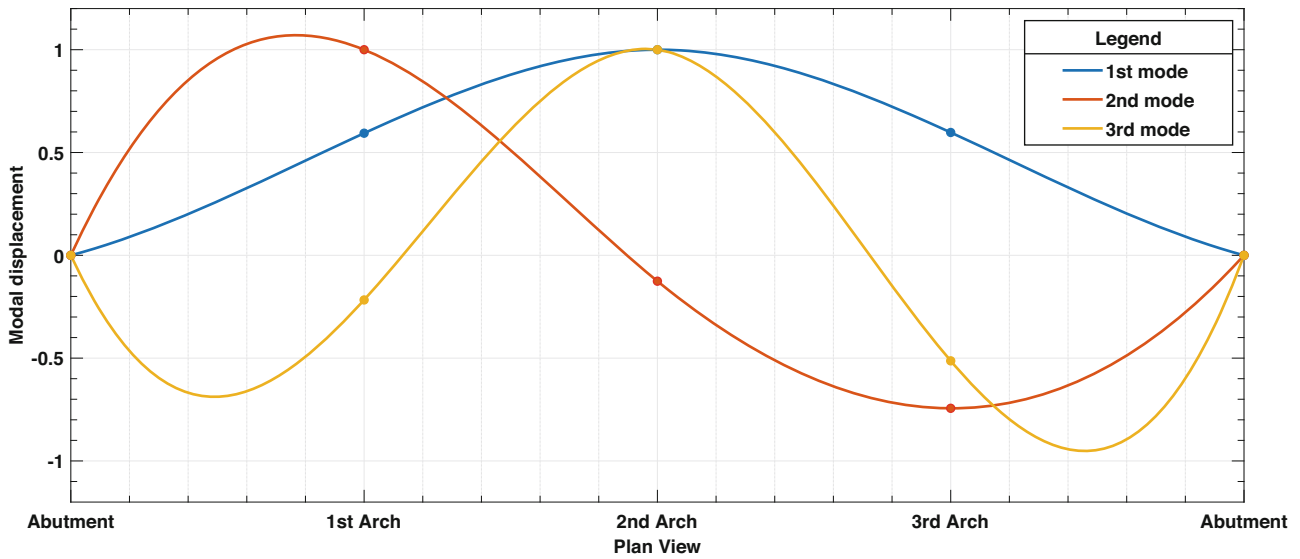


Fig. 4.5 Experimental out-of-plane mode shapes for Bridge 13

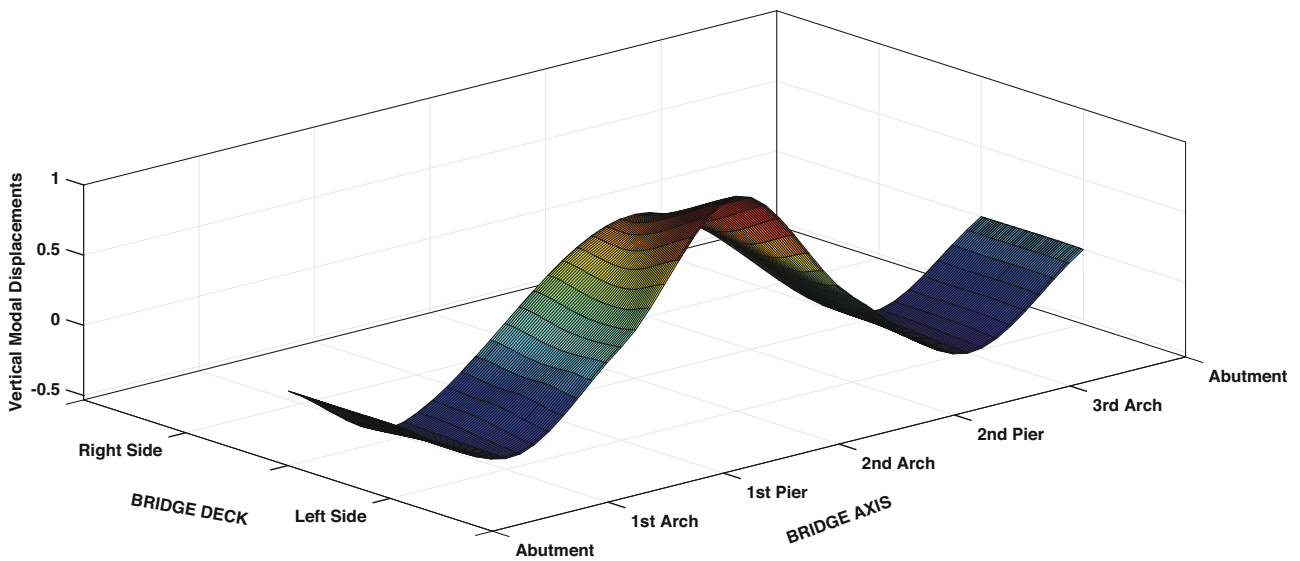


Fig. 4.6 Experimental first vertical mode shape for Bridge 13

The MAC value ranges between zero and one. As long as the singular vector has a high MAC value with the mode shape, the corresponding singular value belongs to the single degree of freedom (SDOF) density function. If the MAC value drops below the user-defined threshold for a certain frequency, then the search for matching parts of the auto spectral density function is stopped, and the rest of the values (the remaining part of the function) is set to zero. Then the natural frequency and damping are obtained by taking the spectral density function back to the time domain using Inverse Fast Fourier Transform (IFFT). Since the impulse response of a dynamic system and the system’s output correlation when excited by white noise are proportional, the modal damping ratio of the mode under investigation can be estimated by the logarithmic decrement of the free decaying auto-correlation function of the SDOF system. An improved estimate of the natural frequency is found by the crossing times of the function. The method is described in detail by Magalhães et al. [7]. The “results and discussion” section of this paper will present in detail the frequencies identified for the various bridges and their damping ratios; however, examples of the mode shape identification from singular vectors and damping identification from the impulse response function can be seen in Figs. 4.5, 4.6 and 4.7.

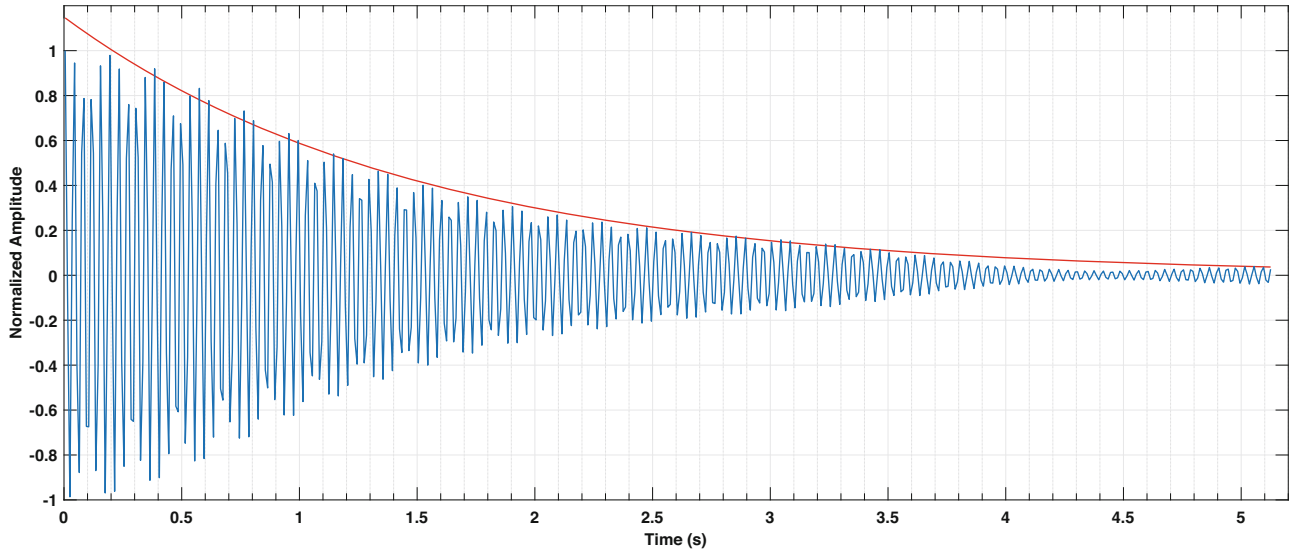


Fig. 4.7 Example of the impulse response function and damping envelope for damping identification, Bridge 13-out-of-plane mode, $\xi = 0.58\%$

4.3.3 Auto-Regressive (AR) Model

The time-domain methods available for operational modal analysis, extensively investigated elsewhere [16], are mainly based on discrete-time state-space models and auto-regressive moving average (ARMA) or auto-regressive (AR) models. Both methods are classified as parametric methods, but the subspace identification formulations such as Stochastic Subspace Identification use state-space models whereas the AR models use modal models. The former method is more commonly used in civil engineering applications, while the latter has been less frequently adopted by the civil engineering community [7].

To understand the AR model, it is necessary first to understand the modal model and discrete-time method. If we apply the Laplace transform to the equation of motion of a multi-degree of freedom (MDOF) system with zero initial conditions, we can relate the inputs with the output through a matrix called transfer function, $H(s)$, such that

$$Ms^2X(s) + CsX(s) + KX(s) = F(s) \quad (4.3)$$

$$H(s) = \frac{X(s)}{F(s)} = [Ms^2 + Cs + K]^{-1} \quad (4.4)$$

Algebraic manipulations allow the transfer function in Eq. 4.4 to be expressed as the sum of the contribution of the dynamic system modes, as given below for the case of non-proportional damping with the load at point i and the displacement at point j .

$$H_{ij} = \frac{X_j(s)}{F_i(s)} = \sum_{k=1}^n \left[\frac{\psi_{jk}\psi_{ik}}{m_{kk}^*(s - \lambda_k)} + \frac{\psi_{jk}^c\psi_{ik}^c}{m_{kk}^*(s - \lambda_k^c)} \right] \quad (4.5)$$

where ψ is the k^{th} complex mode shape, c denotes the complex conjugate, m is the k^{th} modal mass and λ_k is the k^{th} eigenvalue of the k^{th} modal response [17].

The discrete-time method for system identification, using discrete-time linear filters, is well known in electrical and systems engineering and can also be used in structural engineering [18]. Discrete-time models for single input-single output (SISO) systems can be expressed as:

$$y(t) = - \sum_{r=1}^m a_r y(t-r) + \sum_{s=1}^n b_s x(t-s) \quad (4.6)$$

$$A(q) \cdot y(t) = B(q) \cdot x(t) \xrightarrow{\text{yields}} y(t) = H(q) \cdot x(t) \quad (4.7)$$

Having defined the modal model and discrete-time method, the ARX Models (Auto-Regressive with Auxiliary Input) for SISO systems can be defined as below:

$$y(t) = \frac{B(q)}{A(q)} \cdot x(t) + e(t) \quad (4.8)$$

where $y(t)$ is the output time series, $x(t)$ is the input time series and $e(t)$ corresponds to zero-mean Gaussian noise. $H(q) = \frac{B(q)}{A(q)}$ represents the system transfer function.

The SISO system can be represented in another way by defining vectors as follows:

$$\varphi(t) = \begin{Bmatrix} -y(t-1) \\ \vdots \\ -y(t-m) \\ x(t) \\ x(t-1) \\ \vdots \\ x(t-n) \end{Bmatrix}_{(m+n+1) \times 1} \quad \text{and} \quad \theta = \begin{Bmatrix} a_1 \\ \vdots \\ a_m \\ b_0 \\ b_1 \\ \vdots \\ b_n \end{Bmatrix}_{(m+n+1) \times 1} \quad \Rightarrow \quad y(t) = \varphi^T(t) \cdot \theta \quad (4.9)$$

Once the SISO system is defined, the system identification can be achieved by using “One-Step Ahead Prediction.” That is, if we know all the parameters up to time $(t-1)$, one-step-ahead prediction $\hat{y}(t)$ of the output $y(t)$ at time t is:

$$\hat{y}(t) = \varphi^T(t) \cdot \theta \quad (4.10)$$

The difference between the estimated and recorded values of $y(t)$ — in other words, the error in the prediction $\varepsilon(t)$ — can be minimized to predict $\hat{y}(t)$ by means of the least-squares approximation (or using other methods such as Burg, Yule-Walker or Kalman filters inter alia). Differentiating the error function with respect to θ finally gives the Eq. 4.11:

$$\theta = \frac{\sum_{t=\max(m,n)+1}^N \varphi(t) \cdot y(t)}{\sum_{t=\max(m,n)+1}^N \varphi(t) \cdot \varphi^T(t)} \quad (4.11)$$

After finding the a and b coefficients using Eq. 4.11, the system’s poles (roots of $A(q)$) are found and utilized to determine the natural frequencies and damping ratios of the system [18]. This can either be achieved by using the formulas in the given reference or by using the pole-zero plot feature in MATLAB software. For the AR model estimation, the procedure is essentially the same as the ARX model except that the input is implicitly considered to be white noise.

The AR model method is known to improve the results obtainable from noisy data. However, the results are highly dependent on the chosen model order for the system. The model order theoretically should be twice the number of modes, since, for stable systems (with no negative damping), the poles appear in complex-conjugate pairs. Notwithstanding, higher model orders are required due to the presence of noise in the data. Thus, a practical approach would be to observe the system’s frequency response and the change of natural frequencies and damping ratios with increasing model order. For this purpose, a stabilization diagram is an effective and widely-used tool. Figure 4.8 represents an example of a stabilization diagram and the frequency response plot of the system, drawn together.

4.3.4 Multiple Signal Classification (MUSIC) Method

In the MUSIC method, the signal $x(t)$ is assumed to be composed of p complex exponentials in noise. It can be decomposed in terms of its signal and noise subspace components by using the eigenvalues and eigenvectors of the autocorrelation matrix.

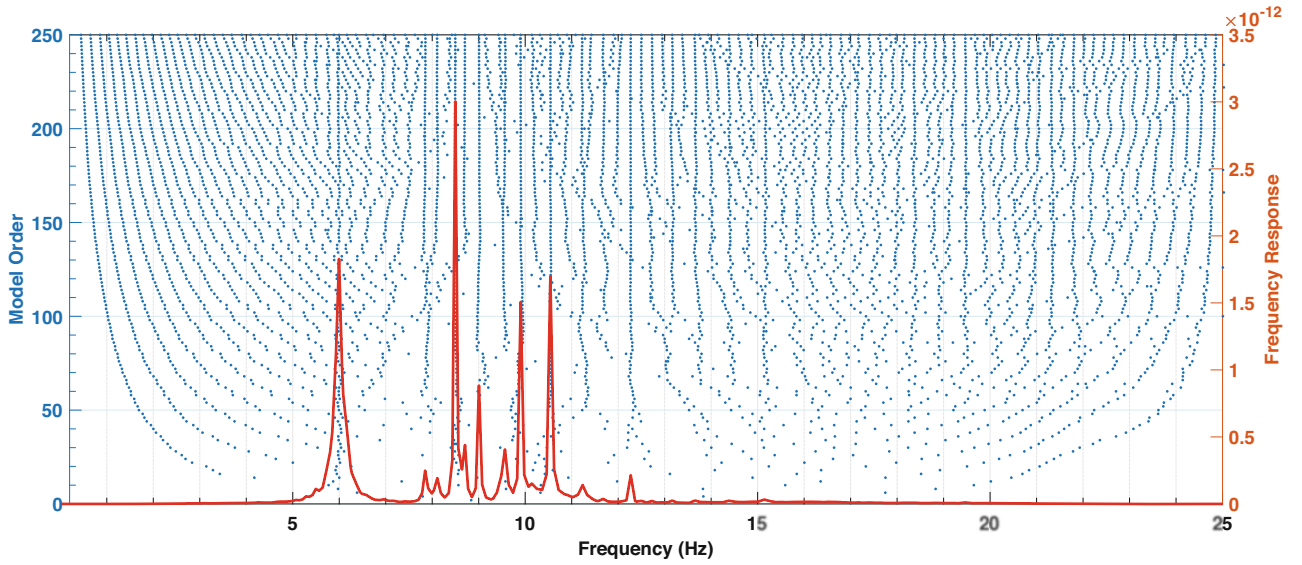


Fig. 4.8 Stabilization diagram for Bridge 5-Sensor 1 out-of-plane data

The autocorrelation matrix R_{xx} is defined by:

$$R_{xx} = \begin{bmatrix} R(0) & \cdots & R(M) \\ \vdots & \ddots & \vdots \\ R(-M) & \cdots & R(0) \end{bmatrix}_{(m+1) \cdot (m+1)}$$

where

$$R(\tau) = \frac{1}{N} \sum_{t=1}^N x(t) \cdot x(t - \tau) \quad (4.12)$$

and $\tau = [-M \dots M]$. Every stationary signal $x(t)$ can be expressed as a linear combination of the eigenvectors of its autocorrelation matrix [19]. Thus, we can write:

$$x(t) = \sum_i^m c_i \cdot S_i \quad (4.13)$$

where c_i is a constant and S_i is the i^{th} eigenvector.

It can be observed that the correlated components of the record $x(t)$, i.e., the signal, have much larger eigenvalues than the uncorrelated components, i.e., the noise. Also, the signal subspace is orthogonal to the noise subspace. Therefore, the signal and the noise can be separated by using the eigenvalues and eigenvectors of the correlation matrix [12, 20]. In addition to the MUSIC method in literature, the Pisarenko Harmonic Decomposition and Rotational Invariance Techniques (ESPRIT) are based on this principle; the theoretical background may be read in various textbooks on signal processing, e.g., Moon et al. [20].

Two important points should be noted concerning the MUSIC method. The first is the assumption that $x(t)$ is a stationary signal and hence does not change significantly with time. Therefore, the autocorrelation function R_{xx} is not a function of time, but only of the time lag between two components. Thus, if the record is not of ambient vibrations but rather represents a signal under transient loads such as earthquakes or blasts, this assumption is not valid. The second crucial part is the selection of the filter order (or the number of sinusoids) in the signal, M . The filter order M must be greater than p to represent the signal accurately, but it should not be too large; otherwise, it might represent the noise as well. Selecting the optimal filter order can be made via the simple method proposed by Safak [21].

Table 4.2 Dynamic identification results for Bridge 13

BRIDGE 13					
Mode shape	AR Model		EFDD		MUSIC
	f (Hz)	Damping ratio, ζ (%)	f (Hz)	Damping ratio, ζ (%)	f (Hz)
1st out-of-plane	6.23	0.38–1.33	6.23	0.45–1.00	6.20
2nd out-of-plane	8.37	0.73–2.40	8.37	0.97–1.30	8.40
3rd out-of-plane	9.98	0.43–1.11	9.99	0.79–1.14	9.96
1st vertical	16.66	0.88–1.84	16.68	1.64–5.22	N/A

Table 4.3 Dynamic identification results for Bridge 41

BRIDGE 41					
Mode shape	AR Model		EFDD		MUSIC
	f (Hz)	Damping ratio, ζ (%)	f (Hz)	Damping ratio, ζ (%)	f (Hz)
1st out-of-plane	5,72	1.80–2.78	5,71	1.22–4.44	5,96
2nd out-of-plane	8,49	1.06–1.88	8,50	1.02–1.56	8,50
3rd out-of-plane	12,18	1.04–1.99	12,11	1.16–3.57	12,11
4th out-of-plane	15,33	0.29–0.60	15,33	0.31–0.43	15,33
1st vertical	18,44	0.28	18,45	0.03–0.67	18,46

Table 4.4 Dynamic identification results for Bridge 5

BRIDGE 5					
Mode shape	AR Model		EFDD		MUSIC
	f (Hz)	Damping ratio, ζ (%)	f (Hz)	Damping ratio, ζ (%)	f (Hz)
1st out-of-plane	6,01	1.05–1.33	6,01	0.43–1.32	5,96
2nd out-of-plane	8,50	0.27–0.43	8,50	0.06–0.33	8,50
3rd out-of-plane	10,55	0.27–0.44	10,55	0.23–0.35	10,55
1st vertical	18,90	0.60–1.29	18,90	1.34–3.16	N/A

4.4 Results and Discussions

Dynamic identification results using the three different methods presented above are shown in Tables 4.2, 4.3 and 4.4. The examples of mode shape identification presented in the text already are representative of all the shapes rendered, which are very similar to each other for different methods; thus, additional examples will not be provided in this section. For the same reason, a comparison of mode shapes via MAC is not necessary here.

The results show that the identified modal frequencies are very close to each other, confirming the reliability of the results. For example, Fig. 4.9 presents a frequency response spectra comparison for Bridge 5 data. However, and significantly, the damping estimation turns out to be notably subjective — to the extent that it seems best to provide a range for the damping ratio rather than a single value.

The methodologies used in analysis present idiosyncratic issues in application and interpretation. In the case of damping estimation from EFDD, the method and data used alter the results. For example, using all the data available from all sensors or using only the out-of-plane data from the sensors in the transverse direction for damping estimation of the out-of-plane modes give different results. The reason for this is the slight change in the auto-spectrum for different data sets; as the auto-spectrum changes so does its IFFT and the damping estimation. Similarly, using an exponential fit to the Impulse Response Function (IRF) or IRF's envelope or using logarithmic decrement method with selection of a different number of peaks results in different values. As for the damping estimation from the AR Model, the data used and the model order assigned change the results. Generally, the higher the model order the smaller the damping ratio. Also, similar to the previous case, damping ratios estimated from out-of-plane data or vertical data do not match. Thus, utmost care is necessary both in implementing dynamic identification and in presenting the data derived.

The results obtained from the MUSIC method depend on the data used. For long records, e.g., several minutes' worth of data, employing even a moderate number of sensors renders the method impossible due to computational power limitations. Therefore, 60 minutes' worth of data was decimated four times, and the segmentation technique was used afterward. An average of the frequency response spectra obtained via MUSIC method was then used to estimate the system's fundamental frequencies. Although it was not possible to identify the first vertical modal frequencies from an average spectrum of the

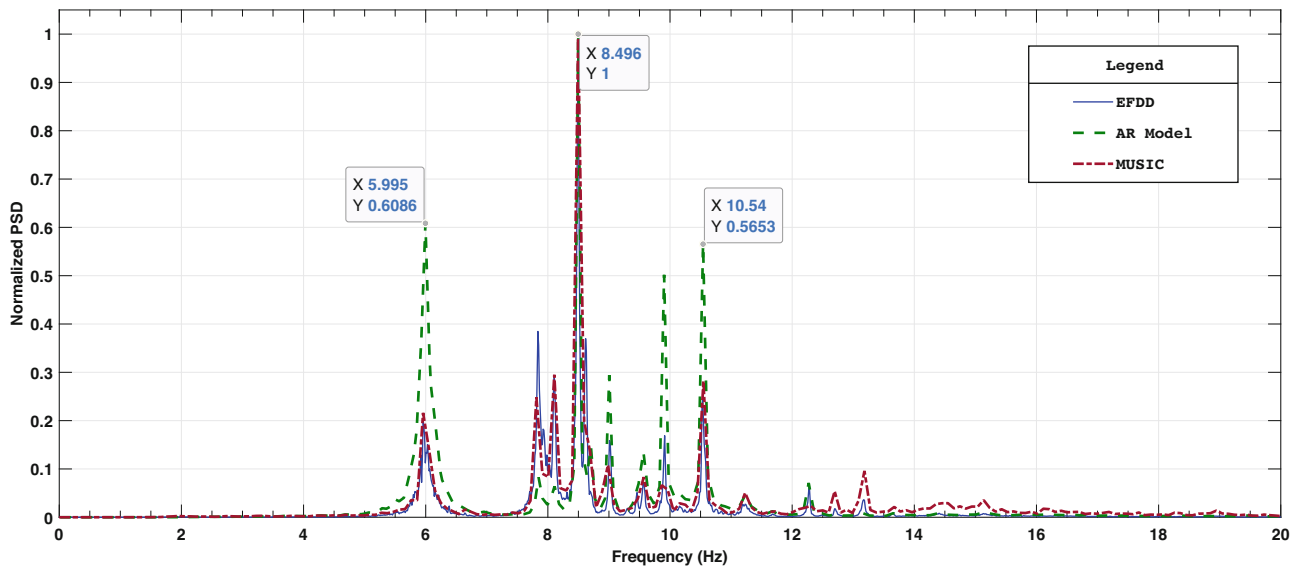


Fig. 4.9 Frequency response spectra comparison for out-of-plane data of Bridge 5

segmentation for Bridge 41 and Bridge 5, these frequencies could be determined when particular portions of the data were chosen. This again demonstrates the subjectivity of the method. Another observation was that the filter order and the length of the data do not change the frequency response spectrum significantly, in other words, as both quantities keep increasing the frequency response stabilizes quickly after the iteration starts. Depending on the data used and filter order chosen, the MUSIC method was capable of identifying the first three fundamental frequencies of Bridge 13 using only two seconds of data. This shows that the method is very promising. At the moment, however, the results are subject to the user's methods, and this approach has not yet reached the required robustness for practical structural engineering applications.

Another general observation concerns the sensor layout. As can be seen in other studies referenced in this paper, mode shapes of the masonry arch bridges are usually complex and multi-directional. That is, peaks in the frequency response spectrum representing the modal frequencies usually appear in spectra obtained from both out-of-plane and vertical data; therefore, making the engineer's work more difficult to distinguish between the structural modes. Also, observed mode shapes change depending on the bridge geometry. In the case of this paper, the first structural modes observed were out-of-plane. In the case of a longer bridge span and shallow arches, however, the dominant modes would probably be vertical and horizontal. In general, a careful 3D investigation of modal displacements is necessary since the planar view of the mode shapes can be misleading. Keeping that in mind and also considering that all the methods perform fairly well with a few minutes' worth of data collection, it would be advisable to perform ambient vibration testing with sensors put in horizontal, vertical and out-of-plane directions in a dense grid covering the bridge deck, using multiple setups. It should also be noted the sensors on the piers are necessary, but due to piers' high rigidity the record becomes very noisy at high frequencies.

4.5 Conclusion

This study presents information on the ambient vibration tests carried out to find the modal characteristics of masonry arch bridges under investigation, a brief explanation of the system identification methods used, results obtained from the different identification methodologies which provide important information for the practical application and the comparison of results.

Due to the large stiffness of masonry arch bridges and the low amplitudes of ambient vibrations, low signal-to-noise ratio makes characterization of the dynamic properties of the structures challenging. Because of noise, the frequency content of the signal changes and spurious resonant peaks occur in the frequency spectrum. Therefore, preprocessing of the signal is required and multiple different system identification methods operating in frequency and time domains used for cross-reference. The intention of this paper was not to select a winner amongst the presented methods but to introduce them to the reader and highlight the advantages and drawbacks of each method. As this study makes clear, because of the inherent complexity of masonry structures, it is good practice not to rely on a single method but rather to confirm the identification results with other methods based on different principles. The comparison of results reveals that all methods yield reasonable

estimates of the natural frequencies and the range of damping ratios, even though the damping estimation tends to be relatively subjective. Mode shape estimation, by contrast, is a difficult task and requires three-dimensional visualization; therefore, recommendations were given for ambient vibration testing of similar structures in the future. In the meantime, applying multiple methodologies to dynamic identification demonstrates the strengths and weaknesses of each analytical approach even as it suggests the same for the structures under study.

Acknowledgments The authors appreciate the financial support provided by Boğaziçi University Research Fund [grant number 12782]. We also appreciate the collaboration of ARUP-Istanbul office and Mr. Korkut Kaynardag and Mr. Emre Aytulun.

References

1. Soyoz, S., Karcioğlu, E., Aytulun, E., Kaynardag, K., Pevlan, S.C. & Karadeniz, A.: Dynamic identification- model updating-seismic performance assessment of stone arch bridges. Proceedings of the 4th Conference on Smart Monitoring, Assessment and Rehabilitation of Civil Structures. (2017)
2. Aytulun, E., Soyoz, S., Karcioğlu, E.: Comparison of nonlinear time history and pushover analyses for the assessment of Stone Arch Bridges. Proceedings of the 16th European Conference on Earthquake Engineering. (2018)
3. Costa, C., Arede, A., Costa, A., Caetano, E., Cunha, A., Magalhaes, F.: Updating numerical models of masonry arch bridges by operational model analysis. *Int. J. Archit. Herit.* 760–774 (2015)
4. Aoki, T., Sabia, D., Rivella, D., Komiya, T.: Structural characterization of a stone arch bridge by experimental tests and numerical model updating. *Int. J. Archit. Herit.* 227–250 (2007)
5. Andersen, P., Brincker, R., Peeters, B., Roeck, G. D., Hermans, L., & Krämer, C.: Comparison of system identification methods using ambient bridge test data. Proceedings of the 17th International Modal Analysis Conference (IMAC). Florida. (1999)
6. Gentile, C., Saisi, A.: Operational modal testing of historic structures at different levels of excitation. *Construct. Build. Mat.* 1273–1285 (2013)
7. Magalhães, F., Cunha, A.: Explaining operational modal analysis with data from an arch bridge. *Mech. Syst. Signal Process.* 1431–1450 (2011)
8. Ramos, L.F., Marques, L., Lourenco, P.B., De Roeck, G., Campos-Costa, A., Roque, J.: Monitoring historical masonry structures with operational modal analysis: two case studies. *Mech. Syst. Signal Process.* **24**(5), 1291–1305 (2010)
9. Formisano, A., Gilda, F., Raffaele, L., Mazzolani, F.M.: Numerical calibration of an easy method for seismic behaviour assessment on large scale of masonry building aggregates. *Adv. Eng. Softw.* **80**, 116–138 (2015)
10. Sesigür, H., Erol, G., Soyöz, S., Kaynardag, K., & Gönen, S.: Repair and Retrofit of Ketchaoua Mosque. Proceedings of the 10th International Conference on Structural Analysis of Historical Constructions, Leuven, Belgium, 13–15 September (2016)
11. Demirlioglu, K., Gonen, S., Soyoz, S. and Limongelli, M.P.: In-plane seismic response analyses of a historical brick masonry building using equivalent frame and 3D FEM modeling approaches. *Int J Archit Herit.* (2018)
12. Kaya, Y., Safak, E.: *Bull. Earthq. Eng.* **13**, 917 (2015). <https://doi.org/10.1007/s10518-014-9642-9>
13. Brincker, R., Zhang, L., & Andersen, P.: Modal identification of output-only systems using frequency domain decomposition. *Smart Mat Struct.* 441–445 (2001a)
14. Brincker, R., Ventura, C., & Andersen, P.: Damping estimation by frequency domain decomposition. Proceedings of the 19th International Modal Analysis Conference. (2001b)
15. Allemang, R.J., & Brown, D.L.: A correlation coefficient for modal vector analysis. Proceedings of the 1st International Modal Analysis Conference. Orlando, Florida. (1982)
16. Peeters, B.: System identification and damage detection in civil engineering. Ph.D. Thesis. Katholieke Universiteit Leuven. (2000)
17. Clough, R., Penzien, J.: Dynamics of Structures. McGraw-Hill Book Company, New York (1993)
18. Safak, E.: Identification of linear structures using discrete-time filters. *J. Struct. Eng. ASCE.* **117**, 3046–3085 (1991)
19. Loeve, M.: Probability Theory Vol. II, 4th ed., Graduate Texts in Mathematics. Springer-Verlag. (1978)
20. Moon, T.K., Stirling, W.C.: Mathematical Methods and Algorithms for Signal Processing. Prentice Hall, Upper Saddle River (2000)
21. Safak, E.: Analysis of real-time data from instrumented structures. Proceedings of the 13th World Conference on Earthquake Engineering. Vancouver. (2004)

Semih Gonen Graduated from Middle East Technical University (2011) and did his masters on Structural Analysis of Historical Constructions at Polytechnic University of Catalonia. Currently a Ph.D. candidate at Bogazici University in Structural Earthquake Engineering. Interested in structural health monitoring, special structures, artificial intelligence

Chapter 5

Using Impact Testing for Production Quality Control



Shawn Richardson, Jason Tyler, Randall Spears, and Mark Richardson

Abstract It is well known that when any physical property of a machine or structure changes, its modal parameters will also change. Modal frequency is the most sensitive parameter to changes in stiffness. If the stiffness of a test article is less than the stiffness of a properly assembled structure, its modal frequencies will be less than those of the properly assembled structure. If its stiffness is greater than the stiffness of a properly assembled structure, its modal frequencies will be greater than those of the properly assembled structure.

In this paper it is shown how a simple, low-cost *three-step* process can be used for pass-fail testing in a production environment, or for qualification testing of any assembled mechanical system. In the *first step*, the structure is impacted and Frequency Response Functions (FRFs) are calculated from the acquired force and response signals. In the *second step*, the FRFs are curve fit to obtain the modal frequencies of several modes of the structure. In the *third step*, the modal frequencies are *numerically compared* with the frequencies of a properly assembled structure.

A metric called the **Shape Difference Indicator (SDI)** is used to numerically compare two “*shapes*”. In this application, each “*shape*” contains the modal frequencies of several modes of the test article. A test article passes the qualification test when its SDI value with the shape of a correctly assembled article is “*close to 1*”.

In the example used for this paper, SDI is also used to search a database of modal frequency shapes. The search results are displayed in a *bar chart of SDI values* between the *current & archived* shapes of modal frequencies. Each shape in the database is associated with a *known amount of torque* applied to several cap screws that attach two aluminum plates together. When the modal frequencies of the test article fail to closely match those of a correctly assembled structure, the bar chart will also indicate how much torque must be applied to each cap screw to pass the test.

Keywords Frequency Response Function (FRF) · Modal Assurance Criterion (MAC) · Shape Difference Indicator (SDI) · Fault Correlation Tools (FaCTs™) · Experimental Modal Analysis mode shape (EMA mode shape)

5.1 Introduction

It is well known that the resonant vibration of any mechanical structure or system is closely correlated with its physical properties. In other words, if any physical property (mass, stiffness, damping) or its boundary condition changes, its resonant vibration will change to reflect the change in the physical property or boundary condition.

Each natural resonance is also called a mode of vibration. Each resonance is completely defined by its natural frequency, damping decay, and its distributed deflection shape. These parameters are commonly called the modal frequency, modal damping, and the mode shape of a resonance.

The frequency of a resonance is called its *natural frequency* because it is not dependent on the forces which cause the vibration. The same is true of modal damping and the mode shape. These three modal properties do not change unless a physical property or a boundary condition changes.

Modal frequency is the easiest parameter to estimate from experimental data. In a Frequency Response Function (FRF), each resonance is represented by a peak in the data. Modal frequencies are estimated by curve fitting experimental FRFs.

S. Richardson · J. Tyler · R. Spears · M. Richardson (✉)
Vibrant Technology, Inc., Centennial, CO, USA

e-mail: shawn.richardson@vibetech.com; jason.tyler@vibetech.com; randall.spears@vibetech.com; mark.richardson@vibetech.com

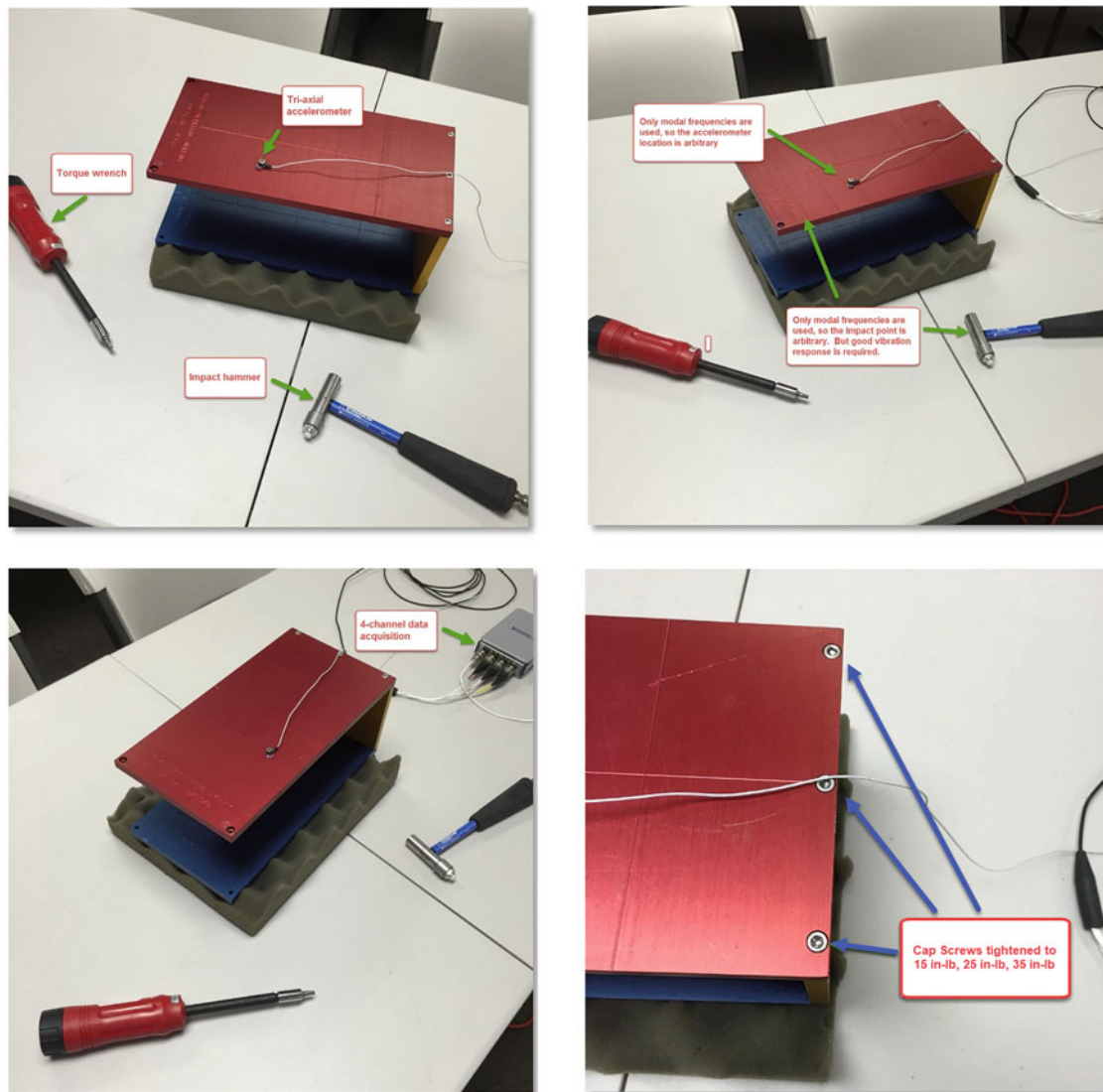


Fig. 5.1 Test article

Modal frequency is the most sensitive parameter to stiffness changes in a structure. If stiffness is increased anywhere in a structure, its modal frequencies will increase. If stiffness is decreased anywhere in a structure, its modal frequencies will decrease.

How much each modal frequency increases or decreases with a stiffness change depends on its mode shape and where the excitation forces are applied to the structure. If a force is applied where a mode shape has a non-zero component, that mode will be excited and participate in the resonant vibration. Ideally, if its mode shape is zero where the force is applied, that mode will not be excited and will not participate in the vibration.

In this example, different amounts of torque were applied to the three cap screws that attach the top plate to the back vertical plate of the Jim Beam structure shown in Fig. 5.1. This has the effect of changing the joint stiffness between the two plates. If the joint stiffness changes, the frequencies of some modes will also change.

Different amounts of torque were applied to the three cap screws and the frequencies of several modes were determined by curve fitting experimental FRFs associated with each set of torques. The experimental modal frequencies associated with each set of torques were then used to determine whether the Jim Beam was properly assembled. One set of torques was assumed to be the values required for a correctly assembled beam structure.

5.2 FaCTs™

The **Shape Difference Indicator (SDI)** metric was used to numerically compare two “*shapes*”, each containing modal frequencies corresponding to a different set of torques applied to the cap screws. SDI has values *between 0 & 1*. An SDI value *greater than 0.90* indicates a *strong correlation* between a pair of shapes. An SDI value *less than 0.90* indicates a *significant difference* between a pair of shapes.

SDI was used to search a database of archived modal frequency shapes; each shape associated with *known torque values* for the cap screws. Each cap screw was tightened using three different torque values, **15 in-lbs, 25 in-lbs, 35 in-lbs**. This gave a total of **27 different torque combinations** among the three cap screws.

Using SDI to search a database is called **Fault Correlation Tools** or **FaCTs™** [6]. With **FaCTs™**, the search results are displayed in a bar chart of the *ten highest SDI values* between the current & archived frequency shapes. The **FaCTs™** bar chart displays the ten SDI bars ordered from the highest to the lowest value. For this example, each bar was labeled with the three torque values associated with each frequency shape.

FaCTs™ can be used in two different ways.

1. To pass or fail a test article based on its modal frequencies versus a *baseline* set of frequencies
2. To identify the correct amounts of torque necessary to pass a test article when it fails

5.3 Test Setup

The Jim Beam was impact tested using a tri-axial accelerometer, an instrumented impact hammer, and a 4-channel acquisition system. The tri-axial accelerometer was attached to the top plate, and the impact force was applied to the top plate. FRFs between each of the three tri-axial responses and the impact force were then calculated. Finally, the three FRFs were curve fit to extract the modal frequencies of six modes of the plate. The six modal frequencies were then stored as “*shapes*” in an archival database.

This simple approach to qualification testing has several advantages,

1. Instead of an accelerometer, a non-contacting sensor such as a microphone or laser vibrometer could be used to measure the response
2. The impact force does not have to be measured. If it is not measured, Cross spectra between one of the responses and the others can be curve fit to obtain the modal frequencies
3. The location of the response sensor and the impact point can be different for each test
4. The only requirement for each test is that a resonance peak be present for each mode of interest in the FRFs or Cross spectra.

5.3.1 Active Impact & Response Points

The location of the tri-axial accelerometer and the impact point are both arbitrary since modal frequencies can be extracted from practically any FRF. However, *active points* should be chosen so that resonance peaks of the modes of interest are non-zero in the FRFs or Cross spectra.

If the mode shapes of the modes of interest are available, one method of locating the most *active points* on the top plate is to multiply the shapes together and display their product on a model of the test article. The shape product of six modes of the Jim Beam is shown in Figs. 5.2 and 5.3.

As shown in Fig. 5.2, the best locations for attaching the accelerometer and impacting the Jim Beam are on the two outer corners of the top plate. But if only the points in the middle of the top plate are considered, the best locations among those points are shown in Fig. 5.3. The active points shown in either Fig. 5.2 or 5.3 will provide valid measurements with resonance peaks for the six modes of interest in them.

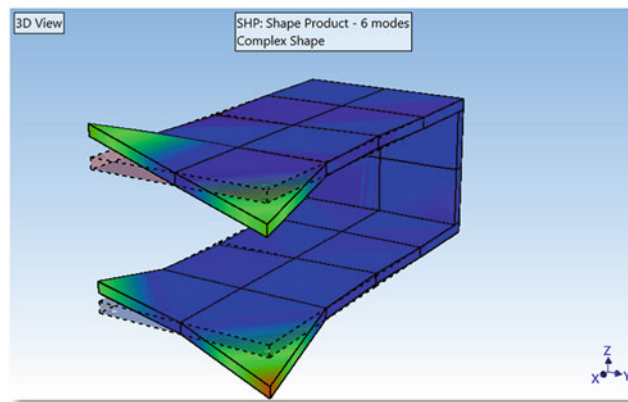


Fig. 5.2 Best locations for impact & responses

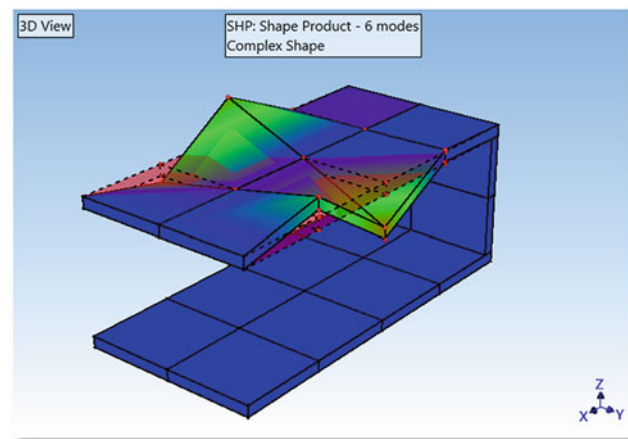


Fig. 5.3 Best mid-plate locations

5.3.2 MAC & SDI

The Modal Assurance Criterion (MAC) is a measure of the *co-linearity* of two shape vectors [1, 2]. If two shapes *lie on the same straight line*, they are *co-linear*, and *MAC equals 1.0*. If two shapes *do not lie on the same straight line*, they are *linearly independent*, and *MAC is less than 1.0*.

The Shape Different Indicator (SDI) is a measure of the *equality* of two shape vectors [3, 4]. If two shapes *have equal components*, *SDI equals 1.0*. If two shapes *do not have equal components*, *SDI is less than 1.0*. The following *rules of thumb* are used with SDI

SDI values → *between 0.0 & 1.0*

SDI = 1.0 → two shapes have *equal components*

SDI > 0.9 → two shapes are *similar*

SDI < 0.9 → two shapes are *different (some components are not equal)*

SDI can be used for comparing any pair of shape vectors that have numerical components. SDI has two advantages over MAC.

1. MAC measures the *co-linearity* of two shape vectors. Two shapes can be *unequal* but *still be co-linear*
2. MAC *cannot be used* to compare two shapes *having only one shape component*. MAC *equals 1* in those cases

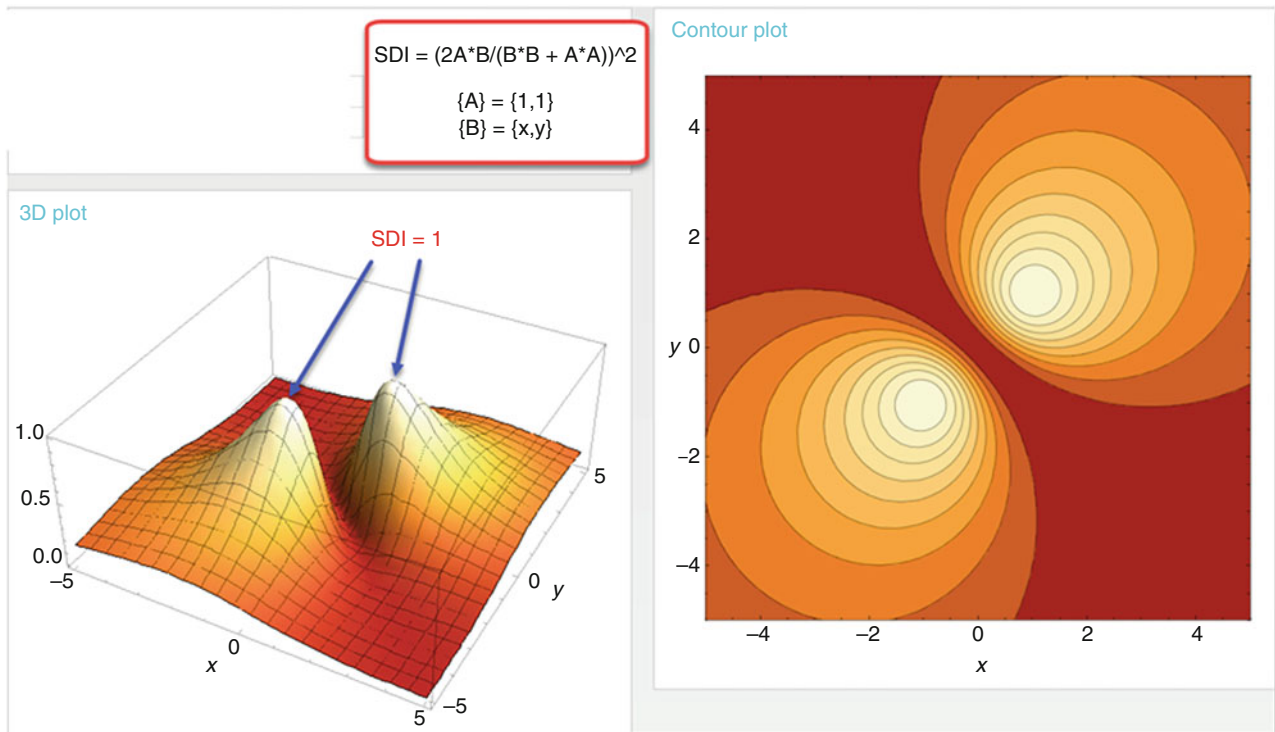


Fig. 5.4 SDI for $\{\mathbf{A}\} = \{1, 1\}$ $\{\mathbf{B}\} = \{x, y\}$. x - -5 to +5, y = -5 to +5

5.3.3 SDI Plot

In Fig. 5.4, SDI is plotted between two shape vectors $\{\mathbf{A}\} = \{1, 1\}$ and $\{\mathbf{B}\} = \{x, y\}$, where x & y have values for -5 to $+5$. $SDI = 1$ in only two places, where $\{\mathbf{B}\} = \{1, 1\}$ and $\{\mathbf{B}\} = \{-1, -1\}$. When $SDI = 1$, $\{\mathbf{A}\}$ & $\{\mathbf{B}\}$ have *equal components*, but one can be the *negative* of the other.

Notice that $SDI = 0$ at the *origin* $\{0, 0\}$. Also, for values of $\{\mathbf{A}\}$ & $\{\mathbf{B}\}$ *near to the origin*, SDI *decreases rapidly toward zero*. This means that when $\{\mathbf{A}\}$ & $\{\mathbf{B}\}$ have components with *small numbers* in them, SDI is a *more sensitive* measure of their difference. Likewise, when $\{\mathbf{A}\}$ & $\{\mathbf{B}\}$ have components with *large numbers* (like modal frequencies), SDI is a *less sensitive* measure of their difference.

5.3.4 SDI Sensitivity

The sensitivity of SDI is more clearly shown in Fig. 5.5. For large values of $\{v\}$, the SDI curve is “*very flat*”, meaning that it is less sensitive to the difference between $\{u\}$ & $\{v\}$. For small values of $\{v\}$, SDI decreases rapidly when $\{u\}$ & $\{v\}$ are different. The FaCTs database search will more accurately distinguish between shapes with modal frequencies in them if SDI is made more sensitive by replacing the modal frequencies with small numbers.

5.4 Pass-Fail Test

The following steps were used for Pass-Fail testing the Jim Beam

1. Impact the top plate and acquire the force signal and three response signals of the tri-axial accelerometer
2. Calculate three FRFs between the force & response signals
3. Curve fit the FRFs for the modal frequencies of six modes

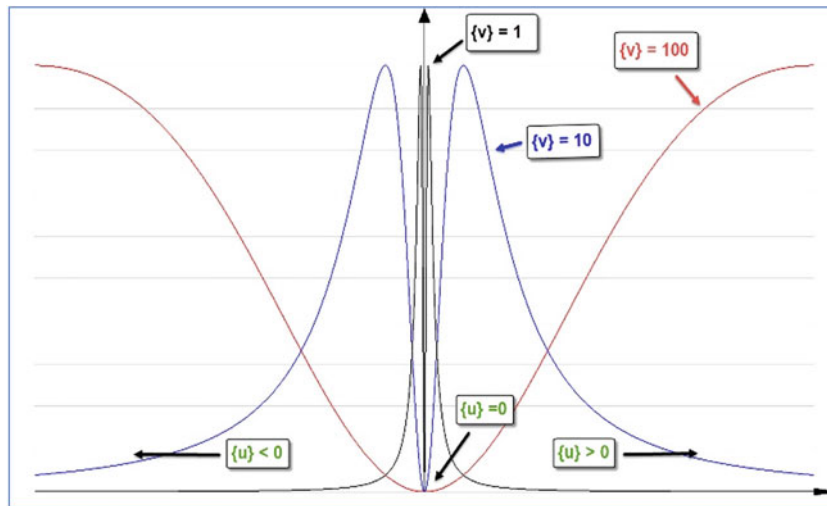


Fig. 5.5 Sensitivity of SDI

4. Use FaCTs to compare the modal frequencies of the six modes with the *baseline frequencies* of a properly assembled structure
5. If FaCTs is *less than 0.90*, the structure *fails* the assembly test
6. If the structure *fails* the test, **FaCTs** identifies the cap screw torque values required to pass the test

5.5 Torque Cases

The torque wrench shown in Fig. 5.1 was used to tighten each cap screw using a known amount of torque.

- Three torque values were applied to each screw; **15 in-lbs, 25 in-lbs, 35 in-lbs**
- Applying **3 different torques** to each screw gave a total of **27 different torque cases**
- With one of the torques applied to each screw, the structure was impacted and three FRFs were calculated between the impact force & the responses of the tri-axial accelerometer
- A total of **81 FRFs** were calculated from the impact & response data
- The FRFs for each torque case were curve fit and **6 modal frequencies** were archived in a database for each case

5.5.1 FRF Acquisition

FRFs were acquired with the 4-channel data acquisition hardware shown in Fig. 5.1. A typical acquisition of time waveforms and their resulting FRFs & Coherences is shown in Fig. 5.6.

5.6 Trend Plot and FaCTs Bars

A Trend Plot of the all 27 torque cases is shown on the left in Fig. 5.7. Assuming the correct torque for each cap screw is **25 in-lbs**, the FaCTs bar chart on the right in Fig. 5.7 shows the 10 torque cases with the highest FaCTs bars compared to the **25-25-25 case**.

The FaCTs bar for the **25-25-25 case** has a value of “1”. The remaining FaCTs bars are ordered from highest to lowest according to their SDI values, and each FaCTs bar is labeled with its three torque values.

The 10 FaCTs bars show how the torque of each screw must be changed in order to match the **25-25-25 case** and pass the test article. The torque corrections for the five highest FaCTs bars are,

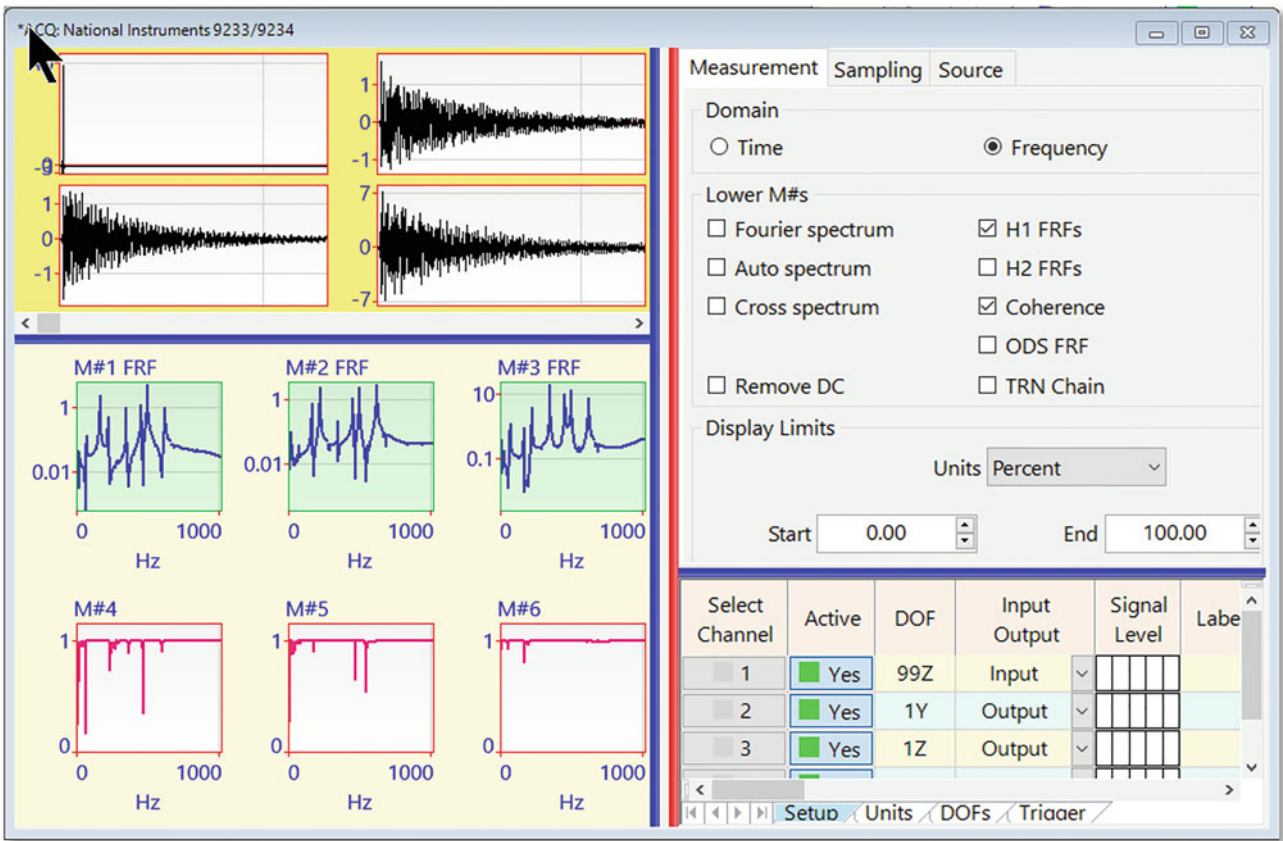


Fig. 5.6 Time waveforms, FRFs & coherences

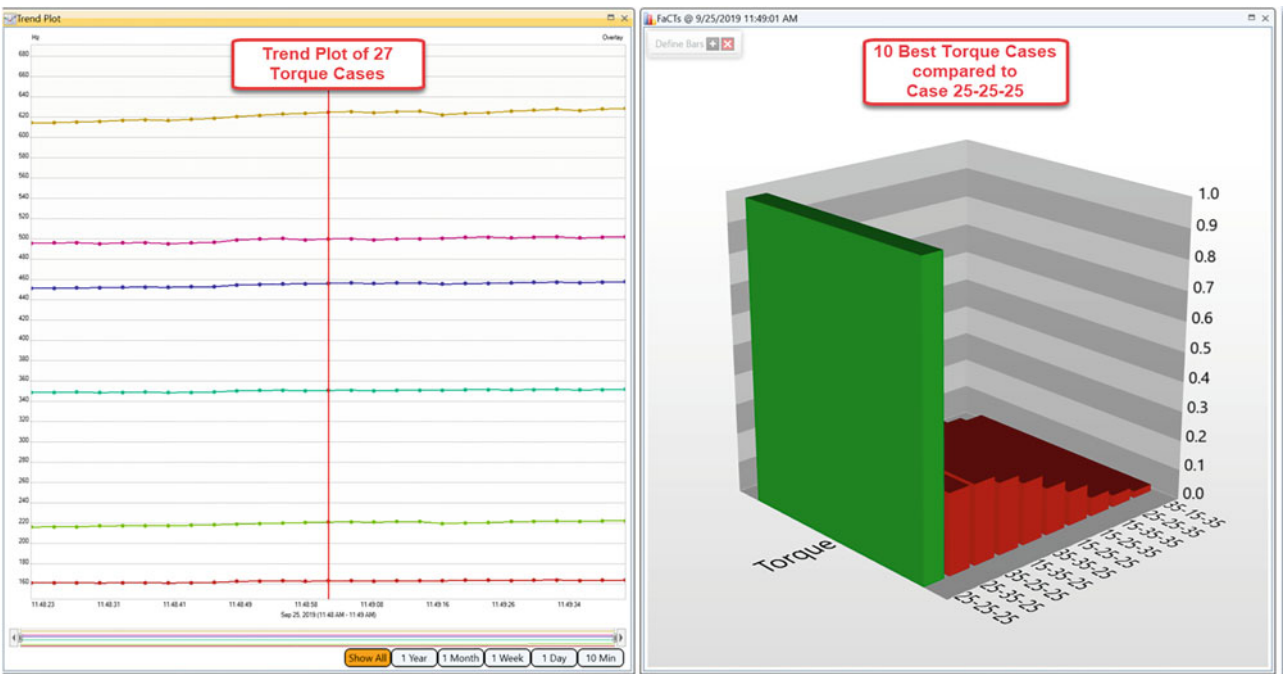


Fig. 5.7 Trend plot and FaCTs bars

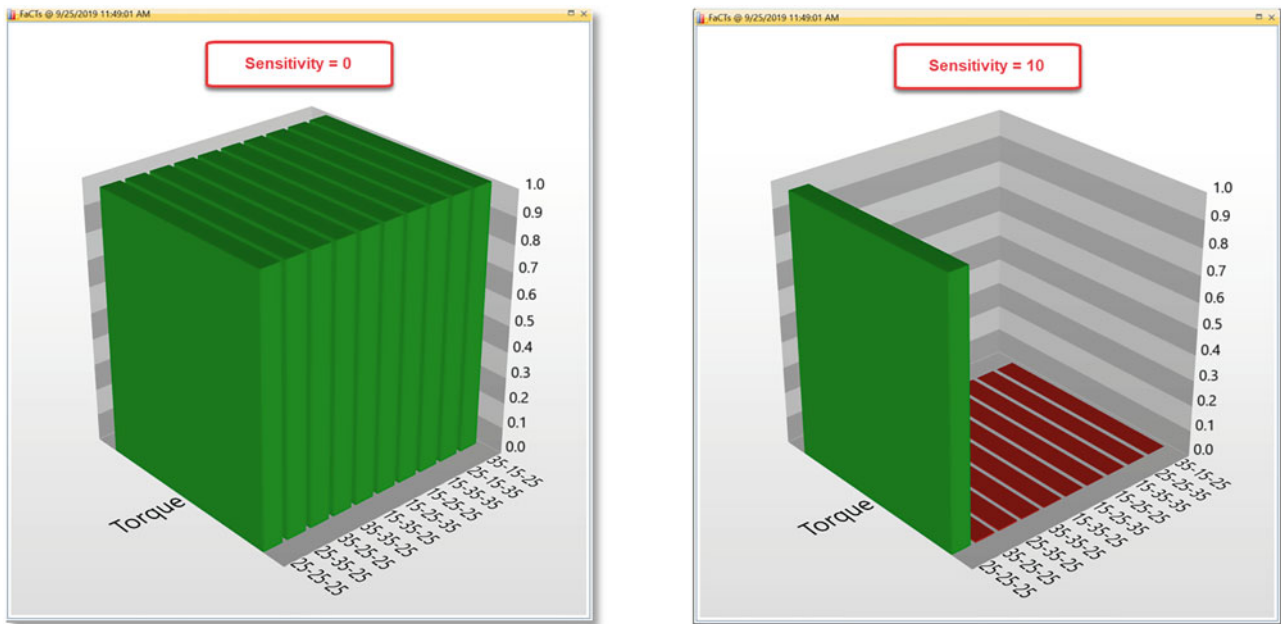


Fig. 5.8 FaCTs bars (Sensitivity = 0 & Sensitivity = 10)

25-35-25 case → less torque on the middle screw

35-25-25 case → less torque on the first screw

15-35-25 case → more torque on the first screw & less torque on the middle screw

35-35-25 case → less torque on the first & middle screws

15-25-25 case → more torque on the first screw

Anyone of these torque corrections would pass the test article in this simulated production test.

5.6.1 What About Sensitivity?

The modal frequencies have values between 160 Hz & 630 Hz. The SDI sensitivity graphs in Fig. 5.4 indicate that the SDI curve is “*very flat*” for these large numbers. Hence, FaCTs will not be very sensitive to small differences in these modal frequencies. In a previous paper [3], a formula was given for replacing large numbers with small numbers in the shapes so that they are closer to the origin where SDI is more sensitive for measuring the difference between two shapes.

FaCTs uses sensitivities between 0 and 10. For sensitivity = 0, the shape components are not changed, and hence SDI is not very sensitive to the frequency differences. For sensitivity = 1–10, the shape components are replaced with smaller numbers.

Figure 5.8 shows FaCTs bar charts for the two extreme cases; **sensitivity = 0** and **sensitivity = 10**. In both cases, the correct torque case **25-25-25 case** was still identified, having a FaCTs value of “**1**”. But when the maximum sensitivity is used, the FaCTs bars clearly distinguish the torque case of the properly assembled structure from the other torque cases.

5.7 Conclusion

In the example presented here, the three cap screws used to attach two plates of the Jim Beam together were tightened using a torque wrench. Three different amounts of torque were applied to each screw, using a *very small difference on only 10 in-lbs* between the different torques.

SDI was introduced as a new metric for comparing two sets of shape data in reference [3]. It was later used as part of the database search method in reference [5] to identify unbalance in rotating machinery, and in reference [4] to identify cap

screw torque values of a single cap screw from differences in modal frequencies. This paper extended the application in [4] by applying torque changes to three cap screws instead of just one.

SDI has two properties that make it useful for comparing two sets of shapes,

1. When SDI *equals 1* two shapes are either equal, or one is the negative of the other
2. When SDI is *less than 1*, the two shapes are not equal
3. SDI can be applied to shapes with *only one component*

SDI was used to search a database of shapes with modal frequencies in them. Each shape was associated with torques applied to the three cap screws used to attach the top and vertical plates of the Jim Beam structure together. The search method, called FaCTs™, displays a bar chart with up to the *ten highest SDI values* between the current shape and shapes archived in a database.

FaCTs identified the correct torque case from among 27 different cases, even with very small differences (10 in-lbs) between torque values. This confirmed that,

Experimentally determined modal frequencies can be used in a product test or qualification test to identify very small stiffness changes in an assembled structure.

Not only could FaCTs identify the correct torque case, but by ordering the 9 other cases according to their SDI values, FaCTs provided the torques necessary to pass a structure that initially fails a qualification test.

It was also shown that when two sets of shape data contain large numbers, as is the case with modal frequencies, SDI, and therefore FaCTs, can be made more sensitive to the difference between two shapes by replacing large shape values with smaller values.

The simplest use of SDI as a Pass-Fail indicator is to compare each current set of shape data with a *baseline* set of data acquired from a correctly assembled machine or structure. When SDI is *greater than 0.9*, the test article is correctly assembled and passes the qualification test. When SDI is *less than 0.9*, the difference between the *current & baseline* shapes is *significant* and the test article has failed the test.

FaCTs can be used in a wide variety of production testing or machine qualification testing environments since it provides an accurate way of comparing multiple sets of shape data. The bars in a FaCTs bar chart are easy to understand since they only have values between 0 and 1.

References

1. Allemang, R. J., Brown, D.L.: A correlation coefficient for modal vector analysis. Proceedings of the International Modal Analysis Conference (1982)
2. Allemang, R. J.: The Modal Assurance Criterion (MAC): Twenty years of use and abuse. Proceedings of the International Modal Analysis Conference (2002)
3. Richardson, S., Tyler, J., McHargue, P., Richardson, M.: A new measure of shape difference. IMAC XXXII, February 3–6, (2014)
4. Richardson, S., Tyler, J., Schwarz, B., McHargue, P., Richardson, M.: Using modal parameters for structural health monitoring. IMAC-XXXV January 30–February 2, 2017 Garden Grove, CA (2017)
5. Richardson, S., Richardson, M., Tyler, J., McHargue, P.: Using operating data to locate & quantify unbalance in rotating machinery. IMAC XXXIV, January 25–28, (2016)
6. FaCTs™ is a trademark of Vibrant Technology, Inc.



Chapter 6

A Tutorial on Analysis Techniques for Deriving Mechanical Shock and Vibration Environmental Specifications from Field Data

Jerome S. Cap

Abstract There is a wide variety of applications that subject systems to mechanical shock and vibration environments. How to best characterize those environments and generate the necessary system and component test specifications varies according to the nature of the underlying environment. The purpose of this paper is to provide the reader with an overview of some commonly used analysis techniques for a range of field environments including transportation and handling, aircraft carriage, and missile flight. The paper will also address statistical methods for defining the Maximum Predicted Environment and test control methods as they pertain to achieving the best possible system and component laboratory simulations.

Keywords Vibration · Shock · Random · Sinusoidal · Specifications

6.1 Introduction

Virtually every time a system moves, it experiences mechanical shock and vibration excitation. The intensity and spectral content of each environment depends on the type of system and the type of motion. This variety presents the analyst with the challenge of identifying (1) the tests and/or analyses best suited to measure input and response data at points of interest, (2) whether the data exhibits any anomalous content, (3) the appropriate spectral analysis, and (4) what is the best means of turning response data into a useful set of laboratory test specifications.

No paper can address every aspect of such a broad topic. Therefore, the purpose of this paper is to present a set of techniques that an analyst can consider using to create a credible set of test specifications. To keep the scope of this paper manageable, the focus will be on experimentally based specifications and single axis test specifications. However, some comments will be made on analytically derived responses and multi-axis system testing.

The references identified in this paper represent applied examples of the concepts described in this paper. A complete list of the papers associated with these topics would be exhaustive, so the reader is encouraged to refer to the references in these papers to gain a more in depth understanding of the underlying theories.

6.2 Overview of Field Environments

This paper will focus on the mechanical shock and vibration environments associated with ground and air cargo transportation, captive carry flight, and missile flight. However, this paper will be organized according to the temporal and spectral content rather than by the actual source of the excitation.

Sandia National Laboratories is a multi-mission laboratory managed and operated by National Technology and Engineering Solutions of Sandia, LLC., a wholly owned subsidiary of Honeywell International, Inc., for the U.S. Department of Energy's National Nuclear Security Administration under contract DE-NA0003525.

J. S. Cap (✉)
Sandia National Laboratories, Albuquerque, NM, USA
e-mail: jscap@sandia.gov

1. Random vibration
2. Sinusoidal vibration
3. Mixed random and sinusoidal vibration
4. Transients and shocks
5. Mixed shock and vibration

6.3 Random Vibration

There are many events for which the environment is almost totally comprised of random vibration. Two common examples include: (1) aircraft captive carry, and (2) the portions of powered missile flight associated with transonic and maximum dynamic pressure (max Q). Figure 6.1 presents examples of the acceleration waveforms associated with each of these environments.

Many random vibration waveforms are Gaussian or nearly Gaussian. A simple first order check for Gaussian content is to compute the Kurtosis, K , as shown in Eq. (6.1). For a perfectly Gaussian waveform $K = 3$. For the captive carry waveform in Fig. 6.1 the Kurtosis is 3.05. For transient waveforms such as the transonic/max Q waveform in Fig. 6.1 one should compute the Kurtosis using a sliding window.

$$K = \frac{\frac{1}{n} \sum_{i=1}^n (x_i - \bar{x})^4}{\left(\frac{1}{n} \sum_{i=1}^n (x_i - \bar{x})^2 \right)^2} \quad (6.1)$$

The most common means of presenting the spectral content is an Auto-Spectral Density (ASD) or in the case of a Multiple Input, Multiple Output (MIMO) system a Spectral Density Matrix (SDM). While there are several ASD estimators, Welch's Method [1] is perhaps the most common. The ASD analysis parameters include: sample rate (SR), block size (BS), overlap percentage, and window type. The analyst must select the block size that produces the desired frequency resolution ($\Delta f = SR/BS$), while ensuring that an adequate number of analysis blocks are used in the spectral density computation to ensure the desired Normalized Variance Error, NVE. Equation (6.2) presents the basic estimate of the normalized variance error as a function of the number of blocks, M , used in the ASD estimate.

$$NVE = 1/\sqrt{M} \quad (6.2)$$

A common estimate of the uncertainty in an ASD is $1 \pm 2*NVE$. Figure 6.2 shows how the NVE is related to the “hash” in an ASD and how using more blocks improves the ASD estimate. The analyst must decide how accurate they need the ASD to be and hence how many blocks of data should be used. Given a limited amount of data the trade-off is between

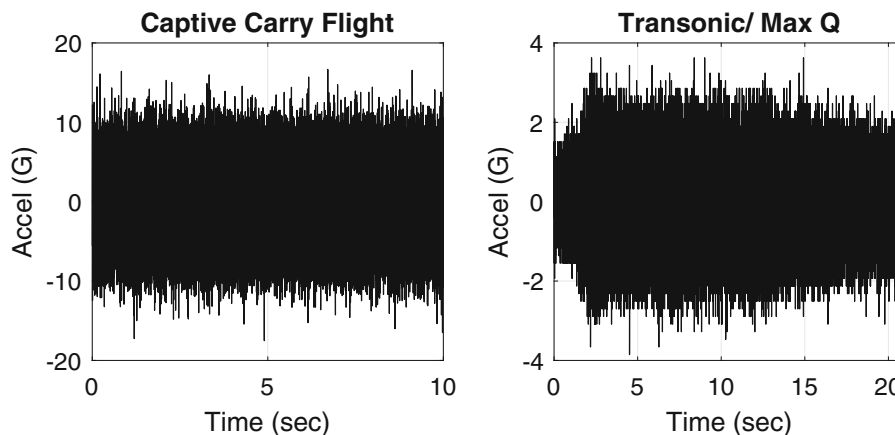


Fig. 6.1 Examples of random vibration environments

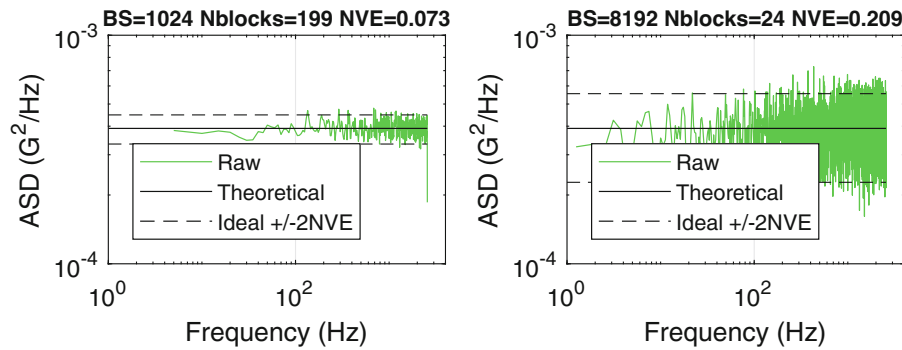


Fig. 6.2 Example of normalized variance error for two different number of analysis blocks

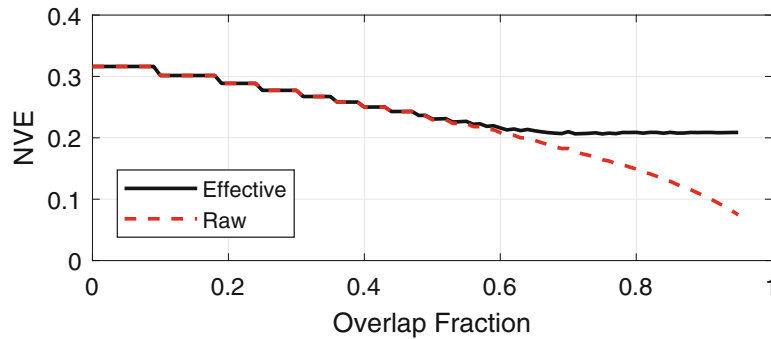


Fig. 6.3 Normalized variance error versus overlap fraction (Kaiser Window, $\alpha = 3$)

frequency resolution and NVE. Later in this paper the concept of using octal bandwidth ASDs to reduce variance error will be discussed.

Using overlapped blocks can help reduce the NVE, but the reader should note that overlap percentages greater than 50% yield diminishing returns on the effective number of blocks, M_{EFF} , that should be used in Eq. (6.2). The relationship between the raw and effective number of blocks [2] depends on the window used in the analysis and the fraction of overlap. Figure 6.3 presents this graphically for a Kaiser window with $\alpha = 3$. Increasing the fractional overlap increases the number of blocks and hence the raw NVE keeps getting better. However, the effective number of blocks and the corresponding NVE reach an asymptote (the steps in the curve indicate the incremental increase in the number of blocks).

While the initial estimate of the spectral density will have a linear bandwidth frequency resolution, linear bandwidth ASDs are often hashy due to a high NVE, which is an artifact of insufficient data for computing the ASD. One good approach for reducing the variance error is to re-average the ASD using $1/N$ -th octave frequency bands. This author recommends 1/sixth octave bands in keeping with the best practices described in NASA7005 [3], although the original paper on the topic [4] tied the bandwidth to the system damping in order to achieve a balance between the reduction in variance error with the bias error (i.e., the inadvertent rounding off of the peak and valleys associated with the true structural dynamic response). Figure 6.4 presents an example of a linear and 1/sixth octave ASD for the captive carry waveform shown in Fig. 6.1. The reader will note that the hash in the linear ASD is not present in the 1/sixth octave ASD.

When displaying an ASD, the analyst should always provide the root mean square acceleration (Grms) since this is the best means of interpreting the general intensity of the environment.

If the random vibration waveform is non-stationary, then the analyst must account for the effects of the non-stationarity on the spectral density estimate. One common technique is a Maxi-Max analysis. For a Maxi-Max analysis, the random vibration waveform is divided into segments and an ASD is computed for each segment. The segments can be overlapped using whatever percentage the analyst deems necessary to capture the time-varying nature of the environment.

How to best interpret the ensemble of Maxi-Max ASDs depends on how the analyst intends to use the results. For example, using the envelope of the ensemble of ASDs is best for insuring that any subsequent test specification is conservative. However, applying the envelope for the entire duration of the event could lead to excessive fatigue damage. The alternative is to use a fatigue damage model to either reduce the magnitude of the composite ASD and/or adjust the effective duration of the event until the resulting combination of level and duration produces the same fatigue damage as the underlying transient

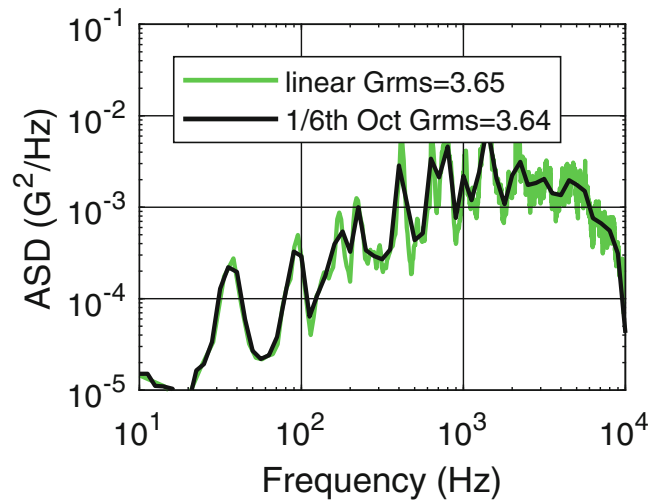


Fig. 6.4 Captive carry environment linear and 1/6th octave bandwidth ASDs

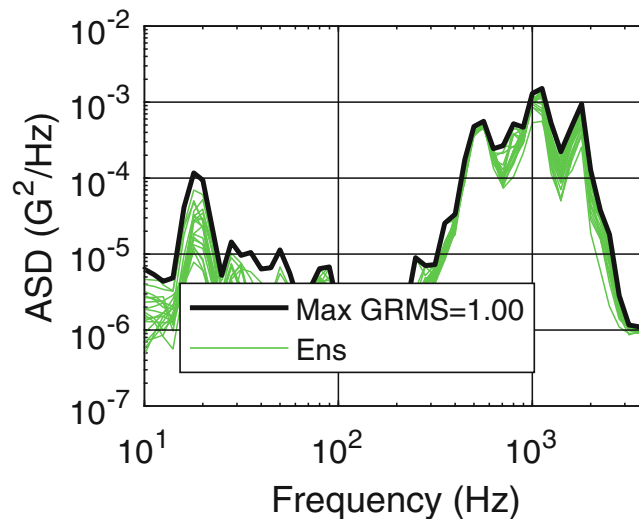


Fig. 6.5 Missile transonic/max Q flight ensemble of 1/6th octave bandwidth ASDs

environment. Figure 6.5 presents the ensemble of 1/6th octave Maxi-Max ASDs for the transonic/max Q waveform shown in Fig. 6.1 along with the underlying ensemble of individual ASDs.

6.4 Sinusoidal Vibration

Not counting rotating machinery, there are few pure sinusoidal environments, but perhaps the one that is potentially every bit as damaging as any random vibration environment is the swept sinusoidal environment associated with rocket motor resonant burn.

A good technique for analyzing sinusoidal data is the Waterfall Spectrum (WFS). A WFS is simply a series of Fourier Transforms (FTs) computed for windowed blocks of overlapped data. The resulting FT magnitudes can be scaled to produce the correct peak amplitude for a known sinusoidal input.

If the frequency and amplitude of the waveform are changing rapidly with time, the analyst can consider overlapping the analysis blocks to achieve finer time resolution. One can also zero pad the windowed blocks of data to achieve finer frequency resolution. Figure 6.6 presents an example of a motor resonant burn acceleration waveform and the resulting WFS.

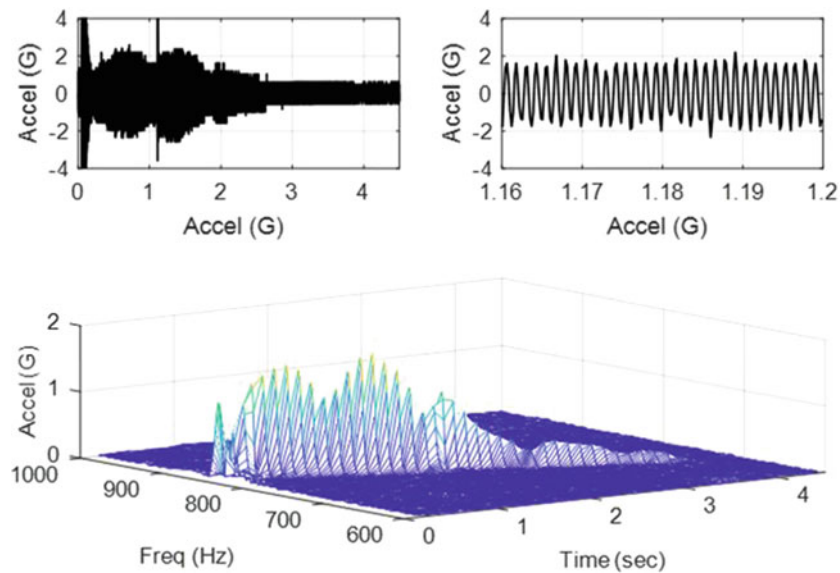


Fig. 6.6 Example of WFS for a motor resonant burn swept sinusoidal environment

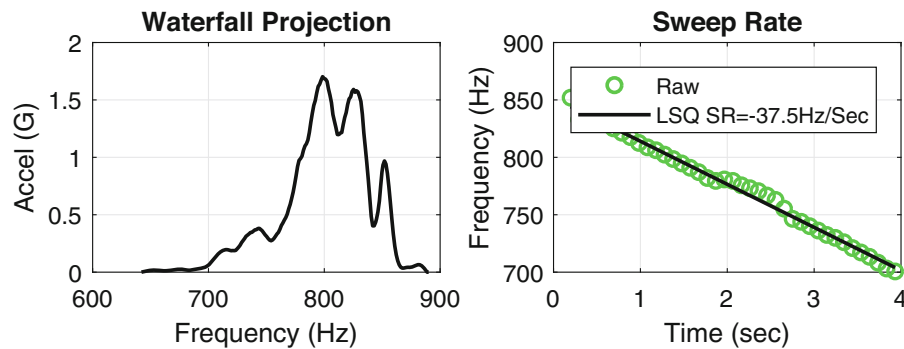


Fig. 6.7 Example of WFP and sweep rate estimate for a motor resonant burn swept sinusoidal environment

The envelope of the WFS for all time (denoted as a Waterfall Projection or WFP) can be used directly to define a laboratory swept sine test. The “ridgeline” of the WFS can be used to define the sweep rate. Figure 6.7 presents the WFP and ridgeline for the WFS shown in Fig. 6.6.

6.5 Mixed Random and Sinusoidal Vibration

Air transportation environments involving turboprop aircraft and helicopters contain a mixture of random and sinusoidal vibration. Sometimes what at first appears to be sinusoidal content can in fact be narrowband random. The least bit of shift in the RPMs associated with a multi-engine turboprop aircraft can result in a modulated nearly sinusoidal waveform that starts to look like a narrowband random waveform. A simple way to determine if a waveform is sinusoidal or narrowband random is to plot a histogram of the peaks for a bandpass filtered version of the waveform. The peaks for an ideal narrowband random waveform will follow a Rayleigh distribution whereas the peaks for an ideal sinusoidal waveform will have a constant amplitude. Many real-world waveforms fall somewhere in between these two ideal cases. Figure 6.8 presents an example of mixed sine on random vibration data (actually 60 Hz noise and its harmonics).

The key to analyzing a true sine-on-random content environment is to separate the sinusoidal content from the broadband random content. The separation can be done in the time domain by estimating the amplitude and frequency of the sinusoid and then subtracting that content from the raw waveform. In the frequency domain either ASDs or WFS can be used to

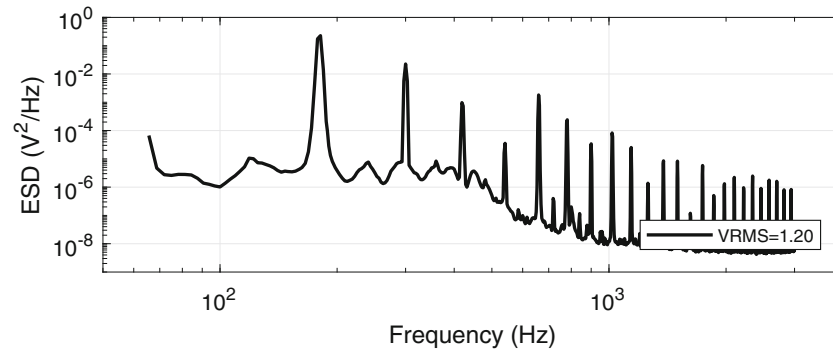


Fig. 6.8 Example of sine on random vibration environment

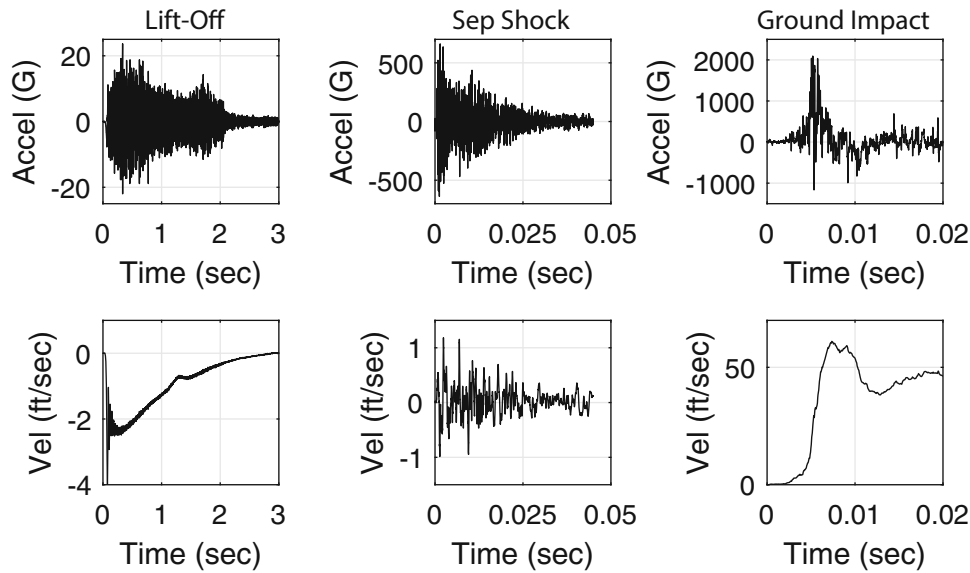


Fig. 6.9 Temporal waveforms for launch, stage separation, and ground impact environments

identify the magnitude of the sinusoidal content and then the corresponding spikes can be edited out to leave an estimate of the broadband random content.

6.6 Transients and Shocks

When an environment is too short to analyze using spectral densities, the analyst must start treating the environment as a shock. Events that fall into this category include: (1) missile launch transients, (2) pyrotechnically induced separation shocks, and (3) ground impact shocks. Figure 6.9 presents acceleration waveforms for each of these environments.

The most common means of characterizing the spectral content of a shock environment is the Shock Response Spectra (SRS) or the Pseudo Velocity Response Spectra (PVRS). Fourier Energy Spectrum (FES) and Input Energy Spectrum (IES) [5] are also used. SRS, PVRS, and IES all use Single Degree of Freedom (SDOF) oscillators to characterize the spectral content of the shock. In each case the analyst chooses the resonant frequencies of the SDOF oscillators (a minimum of 1/12th octave resolution is recommended) and the damping of the SDOF oscillator (in theory the damping should be set equal to the anticipated system damping but from a practical perspective values in the 3–5% range are typically used).

In the interest of brevity, this paper will focus on SRS. The SRS presented in this paper were computed using a Maxi-Max Absolute Acceleration (MMAA) algorithm with a 3% of critical damping ratio. Figure 6.10 presents the SRS for the environments shown in Fig. 6.9 (the damping ratios for these SRS varied so they are identified in the legends).

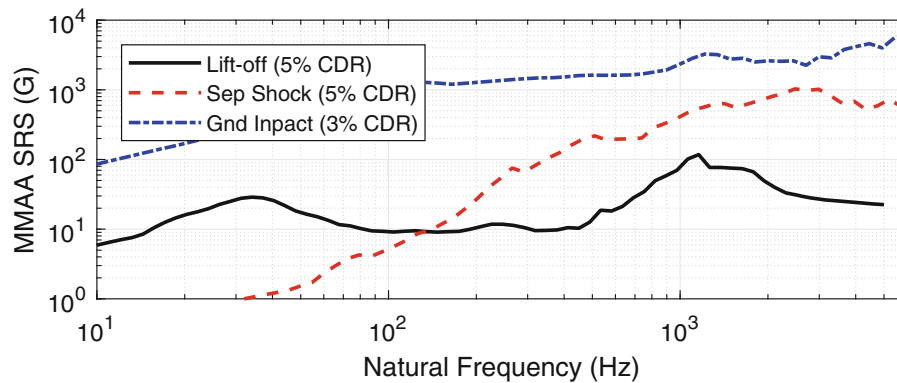


Fig. 6.10 SRS for launch, stage separation, and ground impact environments

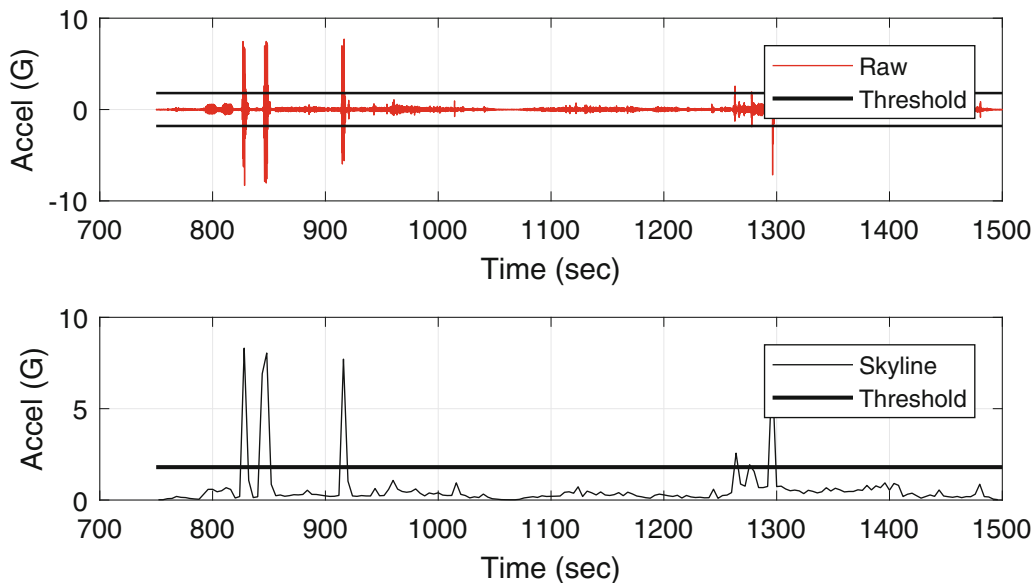


Fig. 6.11 Truck transportation acceleration and skyline data

6.7 Mixed Shock and Vibration

Perhaps the main feature of ground transportation environments is the fact that mechanical shocks of varying intensity are intermixed with quasi-stationary vibration. The upper plot in Fig. 6.11 presents an example of acceleration response data for a truck transportation road test.

The analyst must decide how to parse the data. One useful approach is a skyline plot. A skyline plot, like the one shown in the lower plot in Fig. 6.11, is simply a set of one or more metrics (peak G, rms G, Kurtosis, etc.) computed using sequential blocks of data. The analyst must choose the duration and overlap of the blocks to capture each shock event in a single block while not zooming out so far as to include significant random vibration content in with the shocks. The analyst should review every shock to avoid including electrical noise spikes and to look for signs of over-ranged accelerometers (the temptation with the large file sizes associated with transportation environments is to totally automate the process).

The analyst must also choose the threshold between shocks and vibration based on the character of the skyline plot. Unless the analyst is trying to establish the complete distribution of shocks, it is probably better to include a few low-level shocks in with the vibration environment rather than including vibration events in with the shocks.

All blocks that include shocks are extracted for analysis using a model such as SRS. Adjacent “shock” blocks should be concatenated (making sure to not double count overlapped portions) since they most likely are catching the same shock

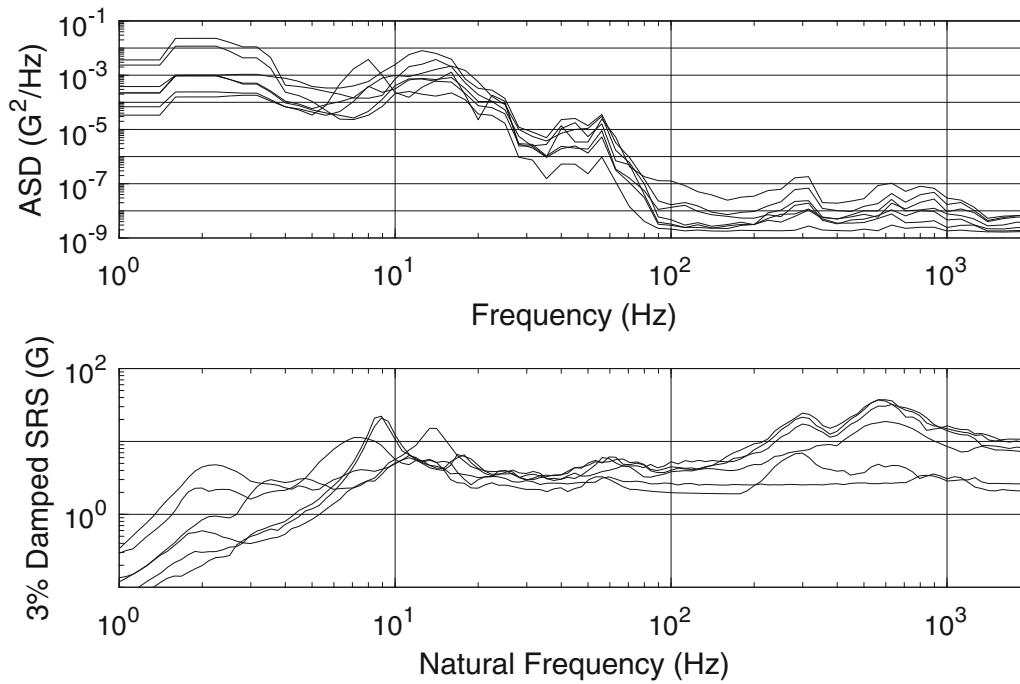


Fig. 6.12 ASD and SRS ensembles for the mixed shock and vibration truck transport environment

event. All blocks that include only vibration are concatenated (again making sure to not double count overlapped portions) and analyzed using ASDs. Figure 6.12 presents ensembles of ASDs and SRS for the acceleration waveform defined in Fig. 6.11.

6.8 Best Practices for Measuring Good Data During Field Tests

An important part of developing good test specifications is acquiring good data from the next assembly level tests and/or analyses. Acquiring good field data starts well before the test begins.

The analyst should use available knowledge about the intensity and spectral content of the field environment when choosing their transducers (typically accelerometers). The data acquisition system (DAS) should have good anti-aliasing filters and a sufficiently small bit resolution for the desired accuracy. A good rule of thumb for the digital noise floor of the DAS is $\frac{1}{2}$ bit. Equation (6.3) generates the bit resolution, G_{BR} , as a function of the number of bits, N , in the analog to digital converter (ADC) and the total amplitude range of the ADC, $Grange$. Equation (6.4) computes the theoretical noise floor ASD, S_{TNF} , where f_N is the Nyquist frequency ($1/2$ of the sample rate).

$$G_{BR} = Grange / (2^N - 1) \quad (6.3)$$

$$S_{TNF} = (G_{BR}/2)^2 / f_N \quad (6.4)$$

Sigma-Delta ADCs tend to be better than traditional ADCs, but they can be mis-applied.

Where possible, a noise transducer should be employed to identify whether spurious responses represent real mechanical response or electrical noise. Another good practice is to acquire a data set without any external stimulation to establish the noise floor of the DAS.

Lastly, independent measures of critical parameters are often useful. For example, using photometrics or laser displacement sensors to capture the rigid body response of a system can come in handy when assessing the accuracy of the accelerometers used on a test and can possibly be used to correct the low frequency response from piezoelectric accelerometers (since they cannot accurately measure rigid body acceleration).

6.9 Data Quality Checks

During the post-test review, the analyst should view data with a skeptical eye. The velocity is an excellent check on the credibility of any acceleration measurement. For tests in which the net velocity should be zero, any drift in the accelerometers represent potential error (small offsets in the acceleration data can usually be removed without fear that the remaining trace is bad). The anomalous acceleration data can be removed using techniques such as high pass filtering or curve fitting the anomalous content (this latter approach works better on the velocity waveform).

Spikes that can be traced to electrical noise (such as cross talk between the fire pulse and the accelerometer cables during a live fire pyrotechnic test) and/or content associated with 60 Hz line noise and its harmonics should also be removed.

6.10 Statistical Modeling

Most field tests have inherent test-to-test variability. Therefore, it is prudent to employ statistical models to define a Maximum Predicted Environment (MPE). The MPE should have a stated probability of occurrence and confidence interval.

Statistical models require multiple data sets measured under nominally the same conditions. For events such as captive carry this rarely happens. However, parametric models can be used to merge data from nominally different flight conditions if one understands the relationship between the parameters and the response data. For example, References [6, 7] document the relationship between dynamic pressure, Q , and the rms vibration response for the turbulent boundary layer flow associated with external captive carry. Figure 6.13 presents such a scaling model [8].

The upper plot shows an ensemble of as-measured ASDs, while the middle plot shows the linear relationship between Q and Grms for the raw ASDs, as well as the resulting Grms values scaled to the desired value of Q (the difference between the measured Grms values and the linear fit is assumed to represent the flight to flight variability). Equation (6.5) describes the scaling model. The bottom plot shows the resulting scaled ASDs where m_{MN} is the slope and b_{MN} is the y-intercept. The reader can see that the spread in the data is reduced, which generally results in a lower prediction of the MPE.

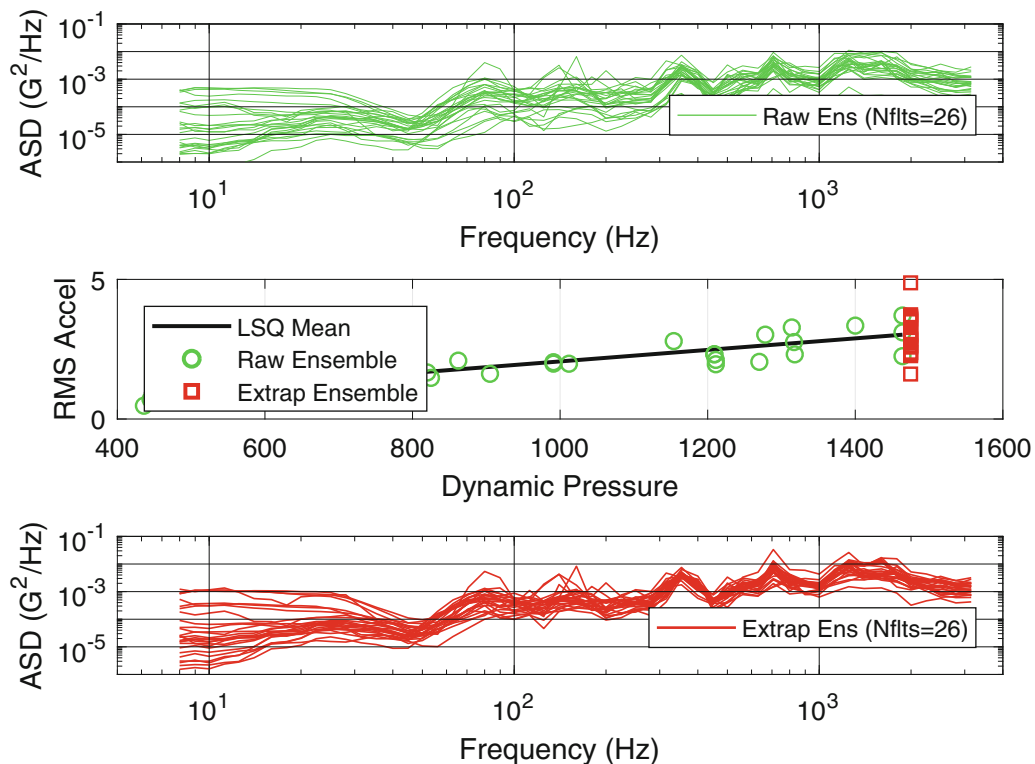


Fig. 6.13 Example of Q scaling model for external captive carry flight vibration [8]

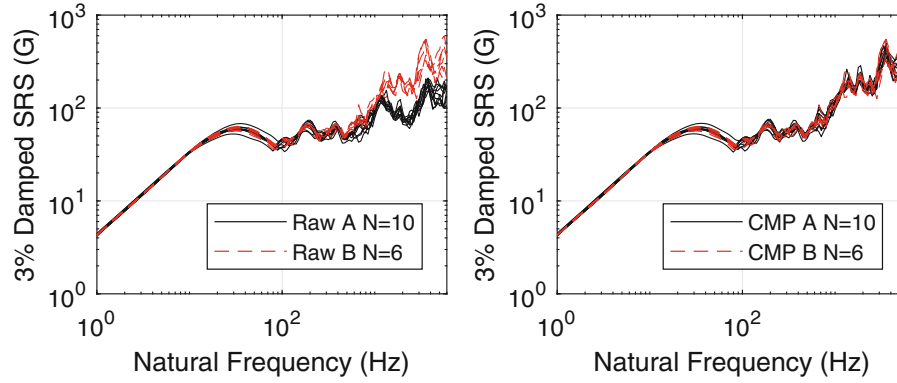


Fig. 6.14 Example of merging bifurcated data ensembles

$$G = m_{MN}Q + b_{MN} \quad (6.5)$$

Another common parametric model is used when data comes from systems having somewhat different geometries but essentially the same forcing functions. The resulting ensembles of response spectra will have similarities but also marked differences. The assumption is that the differences are described by the means for each system while the flight to flight variation is independent of which system was being flown. The technique for merging the two ensembles, $S_{ENS(A)}$ and $S_{ENS(B)}$, is a form of regression bootstrapping. Equations (6.6) and (6.7) are used to separate each ensemble into its respective mean, S_{MN} , and difference, S_{DIF} . Equation (6.8) shows how the sets of differences for both ensembles are added to the mean for ensemble B to create a composite ensemble, $S_{ENS(CMP)}$. Figure 6.14 shows an example of this technique applied to a bifurcated ensemble based on 16 nominally identical tests performed on the same test unit (the analysis was conducted on the log of the data).

$$S_{DIF(A)} = S_{ENS(A)} - S_{MN(A)} \quad (6.6)$$

$$S_{DIF(B)} = S_{ENS(B)} - S_{MN(B)} \quad (6.7)$$

$$S_{ENS(CMP)} = S_{MN(B)} + U [S_{DIF(A)}, S_{DIF(B)}] \quad (6.8)$$

Once the analyst has compiled a homogeneous ensemble of data, the next step is to choose the best statistical model. When sufficiently large data sets are available, the analysts can simply rank order the results and choose the spectrum (one frequency at a time) associated with the desired probability of occurrence. This approach is referred to as a Distribution Free Tolerance Limit (DFTL) or Empirical Tolerance Limit (ETL).

When the available data set is small, but there is evidence in support of a closed form analytical model, such as a normal or lognormal distribution, the solution becomes straightforward. Equation (6.9) presents the Normal Tolerance Limit (NTL) formulation presented in NASA7005 for computing the MPE estimate for a desired probability, P , and confidence, C , $X_{P/C}$ based on the mean (μ) and standard deviation (σ) of the raw ensemble [3]. There are both lookup tables and analytical models [9] for computing the value of k as a function of the number of flights and the desired probability and confidence.

$$X_{P/C} = \mu + k\sigma \quad (6.9)$$

The value of k becomes quite large for small numbers of spectrum to account for uncertainty in the estimates of the mean and standard deviation.

For small sample sizes (3–5), SMC-TR-06-11 [10] proposes that the user assume a standard deviation, σ , of 3 dB, thereby avoiding the adjustment in the NTL model associated with small sample sizes. Equation (6.10) presents this formulation for computing a scale factor, $L_{P/C}$, to be applied to the logmean of the data for the desired probability, P , and confidence, C , given the number of flights, N . For the P99/90 scale factor, $Z_P = 2.322$ and $Z_C = 1.282$.

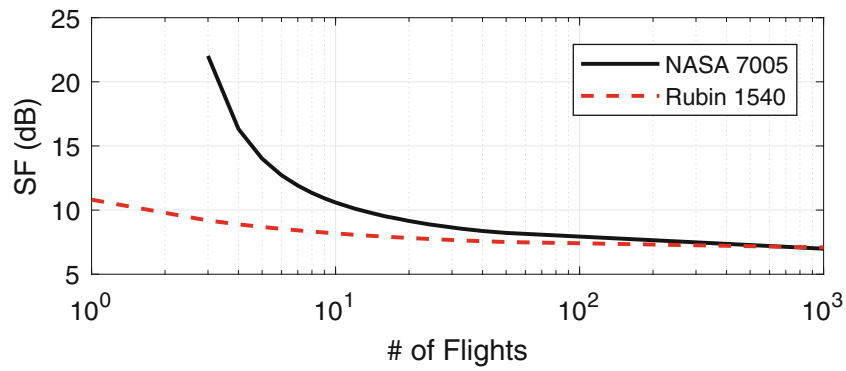


Fig. 6.15 Comparison of NASA and SMC statistical models

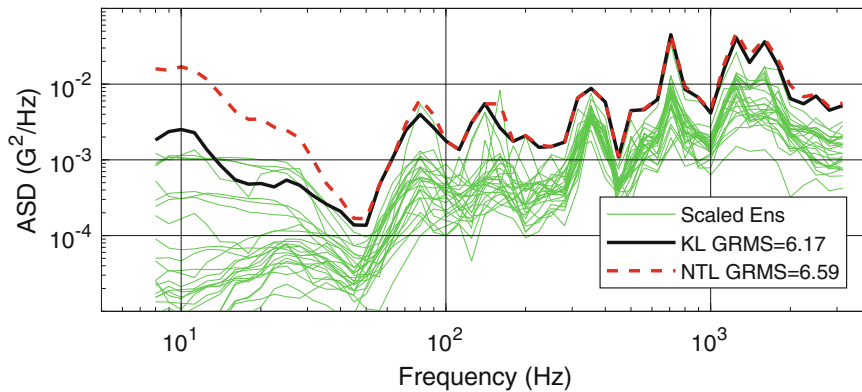


Fig. 6.16 Example of distribution and P99 value for 2000 realizations of an external captive carry environment [8]

$$L_{P/C} = \sigma \left(Z_P + Z_C/N^{1/2} \right) \text{ (dB)} \tag{6.10}$$

Figure 6.15 compares the dB scale factors relative to the sample means for the NASA7005 and SMC (Rubin 1540) models. The reader can see that the SMC and NASA models are identical for large values of N, but the SMC model calls for greatly reduced scale factors for small values of N.

The reader should understand that the standard deviation used in the SMC model was based on Trident I flight data [11]. Therefore, one should exercise caution when using this formulation for carriers other than launch vehicles.

Principal Component Mode Synthesis techniques such as a Karhunen-Loeve (KL) expansion model [12] fit a set of shape functions (such as Eigenvectors) to the ensemble of spectra and then generate large numbers of realizations by randomly varying the weighting of the shape functions. The analyst then simply ranks the realizations using a distribution free tolerance model and chooses the spectrum having the desired probability of occurrence, P. KL models work very well for ensembles having as few as 5–10 spectra.

Bootstrapping techniques can be used to improve the confidence in a KL model. The bootstrap technique resamples the original data with replacement to help the analyst understand what the MPE results would look like if a different ensemble had been measured in the first place. Generally, many bootstrap runs are conducted and the set of P percentile spectra from each bootstrap run are collected and rank ordered. The spectrum having the desired probability is used to represent that level of confidence in the MPE prediction.

Figure 6.16 compares the Q scaled ensemble from Fig. 6.13 against the P99/90 MPEs using the KL and NTL algorithms. Since the KL expansion model as defined in [12] uses a Gaussian seed to synthesize realizations it is not unexpected that it agrees with the NTL model for a relatively large ensemble size like the one used in this example.

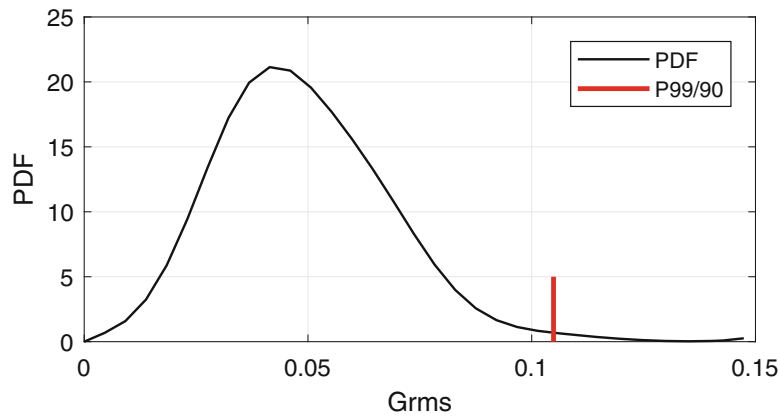


Fig. 6.17 Distribution of vibration intensity for an interstate road trip [13]

6.11 Duration

The final step in defining the MPE environment is establishing the effective duration. For fatigue inducing environments (random vibration, sinusoidal vibration, and multiple hit, low G shocks), the key is to define the anticipated service life and determine whether the intensity of the environment is constant or varies as a function of time. For example, Fig. 6.17 shows the Probability Distribution Function (PDF) of Grms levels for interstate truck transport [13] along with the P99/90 Grms value. Clearly the MPE level is not present for the entire duration of the road trip.

Captive carry flights have less variation for a given dynamic pressure, but a typical mission profile often includes only a few minutes of max Q flight and many hours of low Q flight associated with high altitude cruise.

In both cases there are two approaches for defining the duration: (1) define a stepped test schedule of levels by dividing the PDF into segments and durations with respect to the MPE levels, or (2) employ a test time compression model such as the Miner-Palmgren power law model shown in Eq. (6.11) to shorten the test duration.

$$D = \sum_{i=1}^n \Delta T_i G_i^b \quad (6.11)$$

Where ΔT_i and G_i are the distribution of field durations and amplitudes derived from the PDF and b is the fatigue exponent. $1/b$ is the slope of the fatigue stress vs cycles (S-N) curve.

Since raising the levels of the test beyond the MPE levels introduces the possibility of a false failure, it is recommended that the analyst first compress the times associated with the lower magnitude events. For the PDF shown in Fig. 6.17 and a fatigue coefficient of $b = 6.65$ (a typical value for a ductile material) a 1000-mile road trip (20 h) can be replicated with 1 h of testing at the P99/90 levels. This is consistent with guidance in Mil-Std-810 [6].

For low G, multiple occurrence shocks that produce fatigue damage, the same power law models can be used to estimate how many worst-case shocks must be applied to produce the same damage as the ensemble of field shocks [14].

For high G shocks having only a few occurrences, one can assume that any failures will be due to first passage failure and hence one hit in each direction of concern is theoretically sufficient. However, it is always prudent to apply as many hits as the underlying environment dictates.

6.12 Creating Component Responses from System Level Laboratory Tests

This section addresses the issues associated with deriving component specifications from system level laboratory tests. Shaker tests (especially single axis setups) rarely can replicate the true field environment owing to differences in boundary conditions and in how the inputs are applied. Multi-axis shaker tests and acoustic tests tend to do better, but even these methods can still fall short. Therefore, the most important thing to understand is how accurate the test is. Figure 6.18 presents the error associated with three system tests: (1) a MIMO acoustic test simulating missile launch [15], (2) a MIMO vibration test simulating external captive carry flight [16], and (3) a Single-Input-Multiple-Output (SIMO) shaker test simulating captive carry flight [17]. It is useful to have a scalar estimate of the overall error in the ensemble of responses. Equation

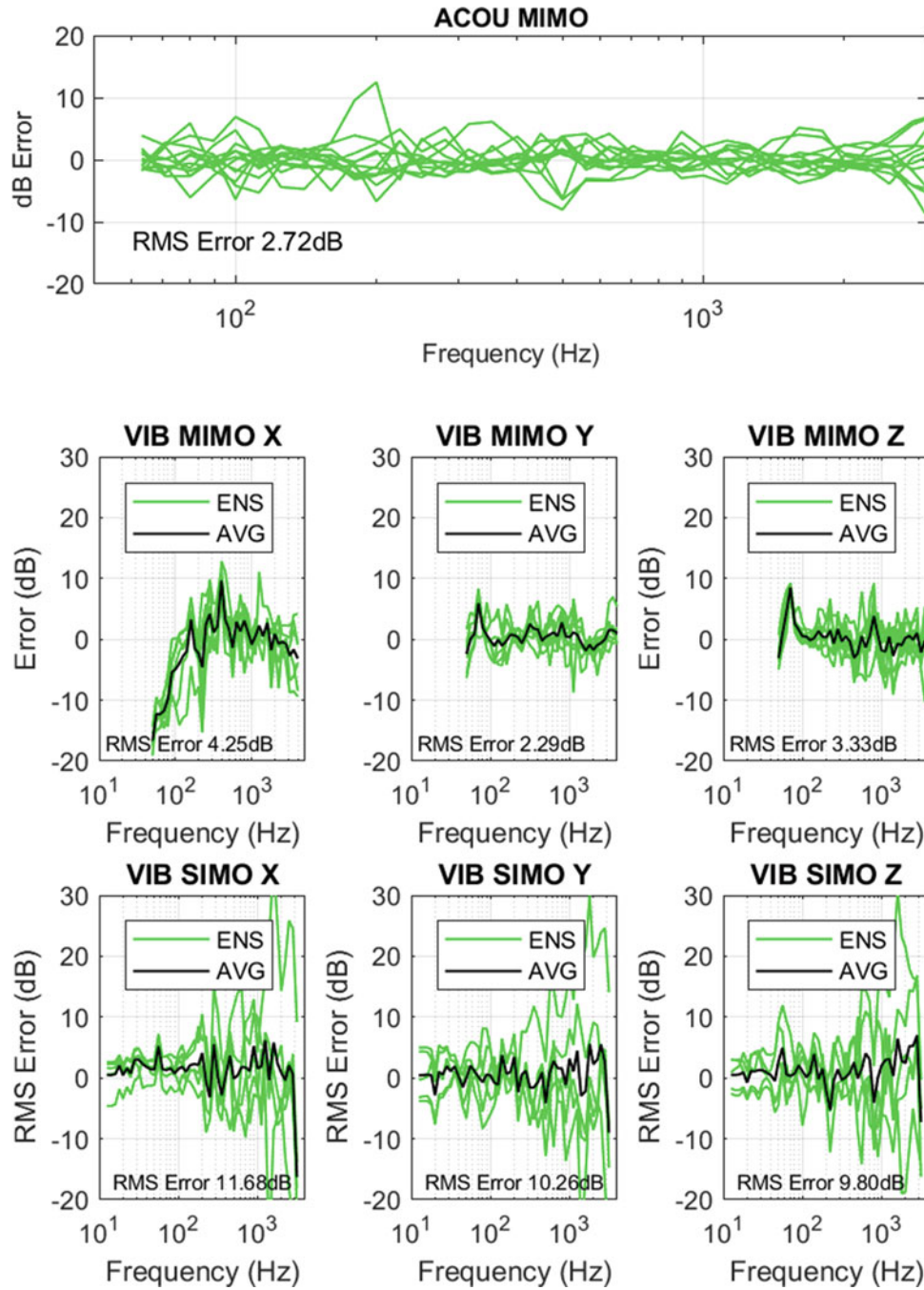


Fig. 6.18 Examples of the accuracy for three system tests

(6.12) computes the rms dB error, E_{RMSDB} , based on the sum of the rms dB ratios of the measured spectrum, S_M , divided by the desired spectra, S_R , normalized by the ratio of the k -th frequency bandwidth, $\Delta f(k)$ divided by the total frequency range, f_B . The rms dB error is presented for each ensemble in Fig. 6.18.

$$E_{RMSDB} = \left(\frac{1}{N} \right) \sum_{n=1}^N \left(\sqrt{\frac{\sum_{k=1}^K \left[\left(10 * \log \left(\frac{S^{(k)}_M}{S^{(k)}_R} \right) \right)^2 \Delta f(k) \right]}{f_B}} \right) \quad (6.12)$$

The SIMO was clearly less accurate than the MIMO tests, which is believed to be due to the limitations in the realism of the forcing function and boundary conditions.

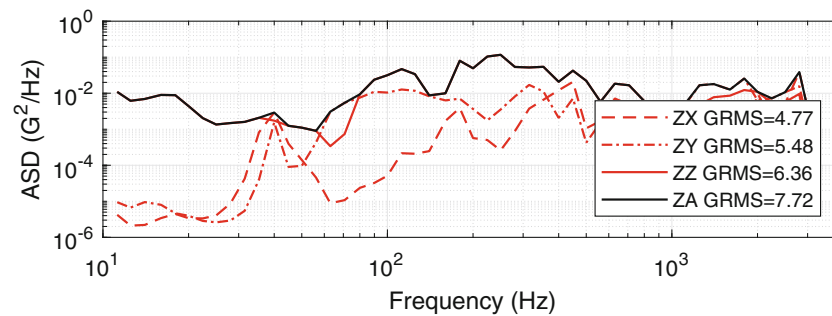


Fig. 6.19 In-axis and cross-axis responses for single axis shaker tests

These tests were based on multiple internal responses acquired from field tests. If one does not have the luxury of field data, then the only choice is to try for the best possible replication of the boundary conditions and inputs. In many cases the test engineer is forced to control the test on the shaker table using a generic specification. This latter approach tends to produce overly conservative responses because straight line specifications tend to over excite the fixed base resonant frequencies in the system [18].

When employing single axis testing, it is recommended that the final component responses be based on some combination of the in-axis and cross-axis responses (i.e., the Y axis response to the X, Y, and Z axis inputs). If the system test is based on a SIMO approach for matching multiple in-axis responses, then the cross-axis responses are simply artifacts of the test and the three responses should simply be enveloped. Conversely, if the system tests consist of three base inputs then one should assume that the cross-axis responses could be real and summing the three responses is recommended. Figure 6.19 presents an example of the envelope of the in-axis and cross-axis responses for a set of single axis SIMO shaker tests.

The analyst may choose to apply correction factors to data acquired from laboratory tests based on the known accuracy of the setup.

6.13 Obtaining System Responses from Analytical Models

Finite Element (FE) models have an advantage over laboratory tests since they can better replicate the boundary conditions and inputs associated with the field conditions. Conversely, FE models can have trouble capturing the true internal behavior. Shifts in resonant frequencies and errors in the damping values can adversely affect the accuracy of the model predictions. As was the case for system level laboratory tests, it is desirable to assess the model using data from a controlled experiment and make corrections as deemed appropriate.

6.14 Generation of Specifications

Given the MPE spectrum, the next step is to develop a practical test specification. Test labs prefer specifications consisting of relatively few straight-line segments. There are pros and cons to such an approach, so the analyst should use good judgment when developing such specifications.

When enveloping the raw MPE spectra one should allow for uncertainty in the MPE spectrum. If the MPE spectrum was based on a high statistical level (such as P99/90) then one does not really need to apply a cushion on the magnitude. However, it is common for field testing to be performed using one or two test assets. Furthermore, the full range of temperature extremes are rarely encountered during a field test. Therefore, including a cushion for left/right shifting of peaks in the MPE spectrum is recommended. If some measure of the variability exists it can be taken advantage of. If no such information is available, then one must use their best judgment. An automated algorithm was developed at Sandia that draws plateaus on top of the peaks in the spectrum and connects the plateaus with ramps. This approach works best with octal banded ASDs. For example, for a 1/sixth octave MPE ASD, using 1/third octave plateaus allows for 1/12th octave cushions on either side of the peaks in the MPE spectrum. The slope must be achievable in the test lab (24 dB/octave is a reasonable value). Figure 6.20 presents an example of the enveloping process. The algorithm technically uses the piecewise representation of the ASD, so the analyst

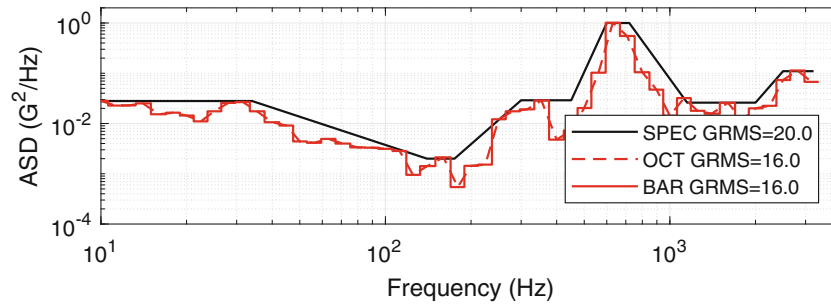


Fig. 6.20 Example of random vibration test specification & underlying MPE spectrum

must always keep in mind what the corresponding rectangular band version looks like. Both versions of the MPE ASD are provided in this example.

The final check on a random vibration specification is that the Grms of the specification should not significantly exceed the Grms of the underlying MPE spectrum. A 50% exceedance is on the high end of reasonable.

Applying this type of algorithm to WFPs or SRS does not work quite as well, since those types of spectra tend to have much shallower ramps and less pronounced peaks. The analyst can still use the basic concepts of plateaus and ramps and some measure of the overall increase in the “area under the curve”.

While ASDs and WFPs can be directly implemented in the vibration test lab, shocks require the synthesis of an acceleration waveform whose SRS matches the desired SRS within a given tolerance and meets the limitations of the shaker for acceleration, velocity, and displacement.

Common waveforms used in shock synthesis include (1) sums of decayed sinusoids, (2) half-sine modulated sinusoids (wavelets), and (3) windowed random. The basic algorithms for deriving several types of acceleration waveforms was worked out by David Smallwood [19]. Equation (6.13) presents the formulation for decayed sine shaker shocks where A_k are the tonal amplitudes, f_k are the tonal frequencies, and ζ_k are the tonal decay rates.

$$A(t) = \sum_{k=1}^N A_k e^{-2\pi\zeta_k f_k t} \sin(2\pi f_k t) \quad (6.13)$$

The basic parameters used for this example are:

1. Sample rate of ≈ 10 times the highest tonal frequency. The minimum recommended oversampling rate is ≈ 5 .
2. Duration equal to 8 times the period of the lowest tonal frequency. This allows the lowest tones to have enough oscillations to produce a good SRS analysis.
3. The exponential decay rate, ζ , was defined to force the waveform to decay to 5% of the initial peak value. This ensures that the shaker will essentially be at rest at the end of the test.
4. 6 tones/octave. While one can often match the desired SRS using as few as 3 tones/octave, using more tones tends to produce a better match for the desired SRS, reduce the peak acceleration, and provide a richer spectral content (the field environment is more likely to be random in content and hence exhibit a broadband spectral content). A Sandia study suggests a minimum tonal density of 4 tones/octave for 5% damped SRS and a minimum tonal density of 6 tones/octave for 3% damped SRS.
5. Alternate the polarity of every other tonal amplitude. This tends to produce a smoother SRS.

Figure 6.21 presents an example of a waveform constructed using sums of decayed sines.

6.15 Generation of Composite Specifications

The next topic is the combining of several specifications to reduce the number of unique tests. Component designers (and sometimes test engineers) often request this to save time and money. It is the job of the analyst to make sure that the resultant specification does not represent an over or under test. Therefore, how to handle this depends on the classes of specifications being combined.

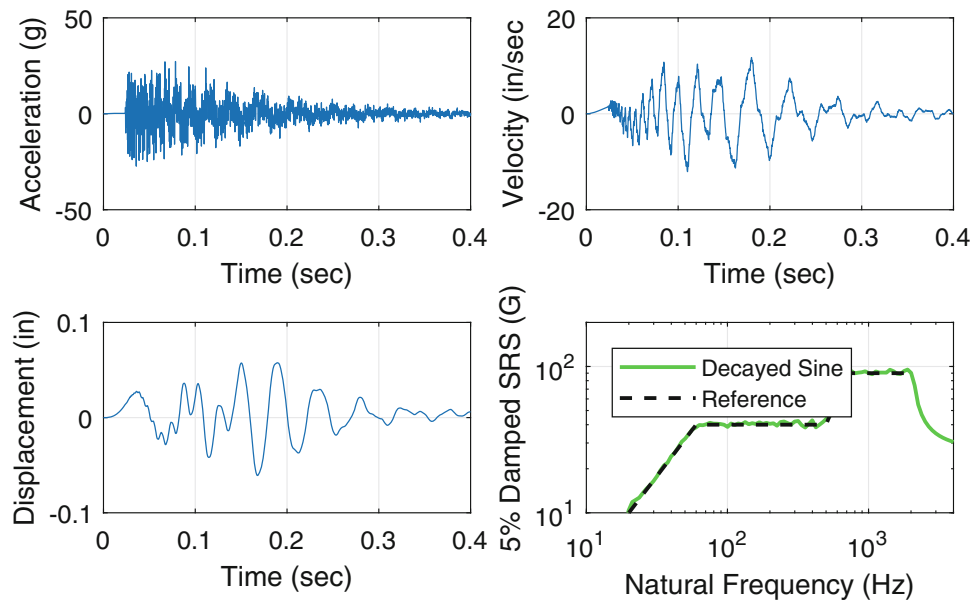


Fig. 6.21 Example of decayed sine shaker shock

For shocks that are assumed to produce first passage failure, the approach is to envelop the shocks of interest. The one warning is to avoid combining shocks with radically different spectral content, as this can make it difficult to implement the resulting combined shock in the lab.

The most common scheme combines two or more axis-specific specifications into a composite specification. The primary benefit of this approach is a reduced chance of the test engineer using the wrong specification for a test. However, this approach should be discouraged because all but one of the directions are being over tested. Therefore, it should not be done without consulting the component designer since there may be a “weak” direction that would have aligned with the lowest of the three axis-specific specifications. Furthermore, some testing schemes can generate responses in multiple directions (such as resonant fixture testing used to replicate a pyroshock environment) but achieving the desired 3-D levels usually benefits from having the correct levels for each direction.

One method for vibration and repetitive shocks is the combination of parallel environments (i.e., a component can expect to see one of a set of environments but not all of them). The best example is a set of specifications based on three different aircraft. This step is typically implemented at the request of the systems engineer. The recommended technique is based on having the final specification produce as little additional fatigue damage as possible above that of the most severe underlying specification. One means of achieving this goal is to use time compression models to adjust the duration of the specifications so that they are all the same duration and then envelope the specifications. Figure 6.22 presents an example of this process. This problem was chosen to demonstrate the concept of “decompression”. For frequencies above 400 Hz the duration of the driving ASD was shorter than the selected composite duration so the levels needed to conserve the total fatigue damage was lower.

Another method for vibration and repetitive shocks involves the combining of serial environments (i.e., environments that the component will experience in sequence). For this class of environments, the goal is to create a specification that produces as much fatigue damage as the sum of the underlying environments. One approach for accomplishing this is to employ a time compression fatigue model to the specifications of interest one frequency at a time. The lower level spectra are increased until they match the highest spectrum. The corresponding test durations are compressed according to the fatigue model. The resultant spectrum will have a different duration associated with each frequency line. At this point the analyst can either (1) keep this preliminary composite spectrum and define the test duration based on the longest of the frequency specific durations, or (2) raise the level of the composite spectrum until the equivalent duration for all frequencies is the same (typically the shortest of the preliminary frequency specific durations). Figure 6.23 presents the individual and final composite spectra using the latter approach.

One note to the reader regarding these techniques. Time compression models are not perfect so the more one compresses the original durations, the less credible the resulting specification will be. Furthermore, altering the shape of the spectrum will change how a component’s resonant modes are excited. Therefore, one should try and only combine specifications having

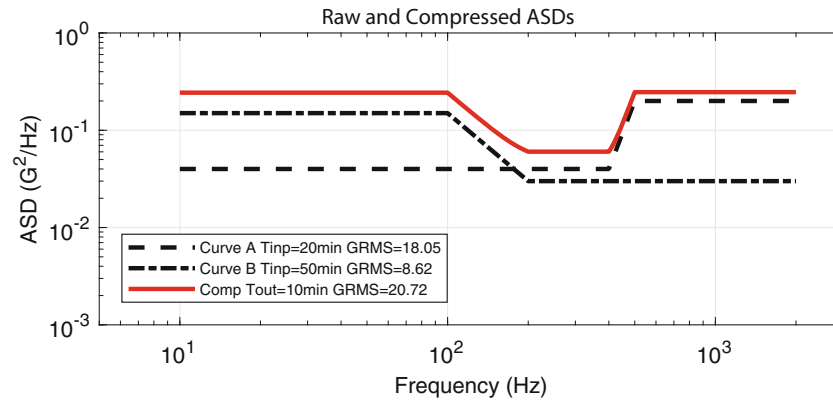


Fig. 6.22 Example of time compressed composite random vibration specification for parallel environments

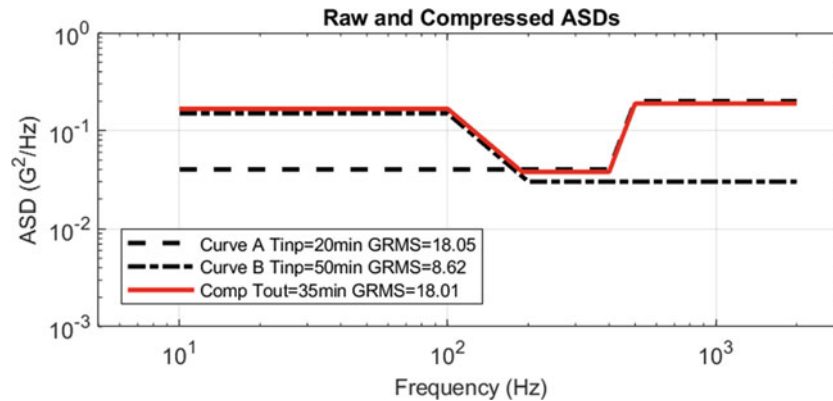


Fig. 6.23 Example of time compressed composite random vibration specification for serial environments

similar durations and spectral content. Similarly, one should only time compress long duration, low magnitude environments and never more than needed to make the lab test practical.

The last topic is the omission of benign environments. This should not be done without some form of damage model (preferably one involving a FE model), but at least one that involves the resonant modes of the component. The safest approach is to look for environments that have spectral content well below the lowest resonant frequency (which transportation environments often do). This tends to work in ones favor because those are also the longer duration environments so one gets the most benefit from omitting them.

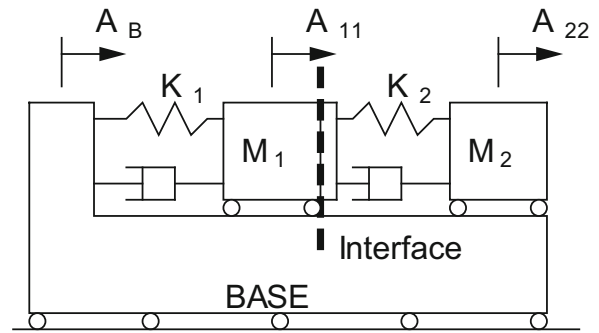
6.16 Component Testing Issues

The final step in the overall process is the implementation of the test specifications. There are numerous ways in which a test can go wrong, but often trouble can be averted by advanced planning by the component designer, the environments engineer, and the test engineer.

One issue is the upper frequency of the test. Best practices dictate that the specifications initially be defined out to the highest frequency for which the field data can be trusted and/or the response rolls off to negligible levels. However, it must also be recognized that shakers have issues controlling inputs above 2–3 kHz depending on the weight of the test article. Therefore, it may be necessary to truncate a specification or at the very least allow for wider tolerances above the frequency where the shaker dynamics begin to affect the controllability of the test.

The ideal approach is to use an analytical model such as a FE analysis to identify the frequency above which an incremental extension of the spectrum results in little or no increase in the overall stress. Obviously, such a prediction is only as good as the fidelity and resolution of the FE model, but in general a component having a dozen or so significant resonant modes in each axis below a given frequency will not need to be tested above that frequency, and only the very stiffest of components will not meet that criteria for a 3 kHz cutoff frequency.

Fig. 6.24 NASA TDOF force limiting model



Another issue is the testing of components having strong resonant behavior. As was discussed in the section on system testing, conducting base excitation tests using straight-line segment specifications will tend to over drive the fixed base resonant frequencies of the component. Applying a response limit during vibration testing based on knowledge of the component's response in the field will notch the input specification at the fixed base resonances in a manner that is similar to what occurs in the field and hence keep the component from being over tested.

If field response data do not exist, the NASA force limited vibration monograph [18] presents models for identifying how deep the notch should be. The NASA models assume that the maximum input force is related to the driving point impedances of the payload and the system. Figure 6.24 presents one of the NASA models, which assumes that the system, M_1 , and payload, M_2 , can be modeled as a Two Degree of Freedom (TDOF) system. Figure 6.25 presents an example for a TDOF coupled system consisting of an 11-lb payload with a 200 Hz resonant frequency and a 1000-lb system with a first resonant mode of 20 Hz. The upper plot in Fig. 6.25 shows the skeleton and dynamic mass lines associated with the driving point impedances for the payload and the skeleton mass line for the system. The middle plot in Fig. 6.25 presents the corresponding raw and notched input ASDs, while the lower plot presents the corresponding response ASDs for the payload.

The two points of interest in this analysis are: (1) notching is justified even though the mass of the payload is much less than the mass of the system (in part because the payload is stiffer), and (2) a 1% reduction in the overall Grms of the input specification results in a significant reduction in the response at the resonant frequency of the payload.

While shaker shocks cannot be actively response limited during the test, it is possible to adjust the input such that the responses of interest is kept within a desired range if one is permitted to measure transfer functions for the test setup ahead of time. One approach incorporates a Single-Input-Multiple-Output (SIMO) optimization scheme directly in the algorithm for synthesizing the input waveform composed of sums of decayed sinusoids to achieve the desired response at several locations of interest in a least squares sense [20].

The intensity of the input waveform can vary considerably depending on how the tonal frequencies interact with the system resonances. Therefore, when generating the inputs for a SIMO analysis, a Monte Carlo algorithm should be used to generate multiple combinations of tonal frequencies. Figure 6.26 shows a 3-DOF system consisting of an input and two SDOF oscillators. A set of 20 Monte Carlo SIMO simulations were performed. The one producing the best combination of a low rms dB error and minimum input peak acceleration was chosen. Figure 6.27 compares the raw and achieved inputs and responses.

One common approach that can result in inconsistent test results is the simultaneous testing of multiple components. Unless the fixture is extremely rigid, this approach will often result in different excitation levels for each component. At the very least the test engineer should monitor the response of each component, but ideally the control scheme should take those responses into account. Average control has some benefit, but if one needs to ensure each component is exposed to at least the desired levels, then a minimum extremal control scheme should be used.

Ironically, if one of the components is loosely fixtured during a minimum extremal control test, the control system will increase the input to bring the levels for that component within spec. This results in the inadvertent over testing of the other components, so it should only be employed for the testing of robust components. Good fixture design is the best defense against this, but response limiting can also be employed (which sort of defeats the purpose of minimum extremal control).

When trying to replicate a shock environment, the best approach is with a shaker owing to the ability to shape the spectral content. The main limitation of shakers is that the peak acceleration levels can only be a few hundred G's, the net velocity and displacement must be within the shaker's capabilities, and the upper frequency limit is 4–6 kHz.

One last comment on shaker shocks pertains to defining the duration. Again, the nature of SRS allows for a wide range of durations for the input acceleration waveform while still producing the desired SRS. Temporal moments [21] have been shown to be useful in producing laboratory shaker shocks that more closely replicate the duration of the field environments.

When shaker shock testing cannot achieve the desired levels and/or spectral content, the test engineer must resort to drop tables and resonant fixtures.

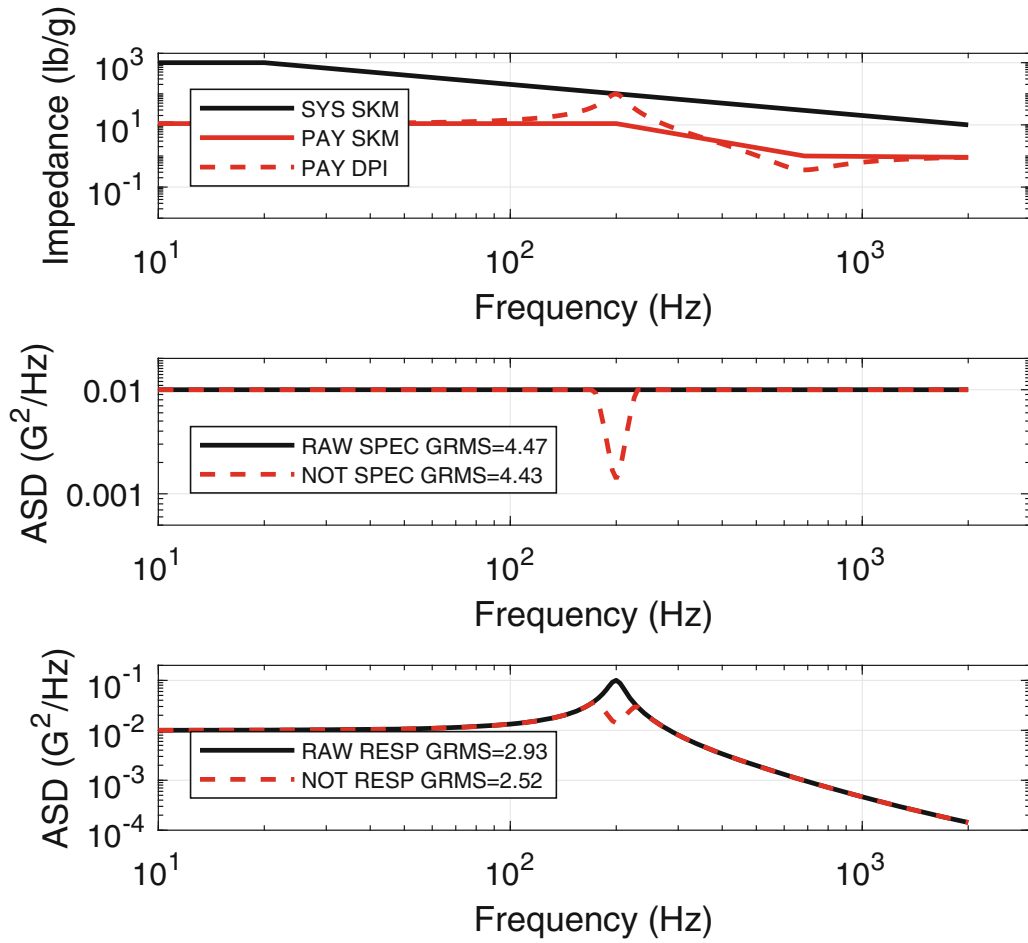


Fig. 6.25 Component raw and notched acceleration response spectra

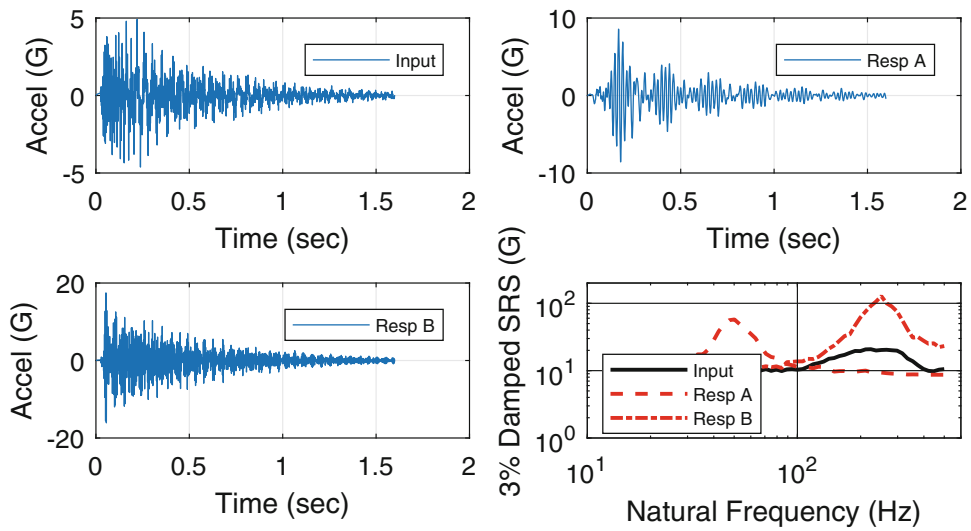


Fig. 6.26 3-DOF model for use in SIMO optimization example

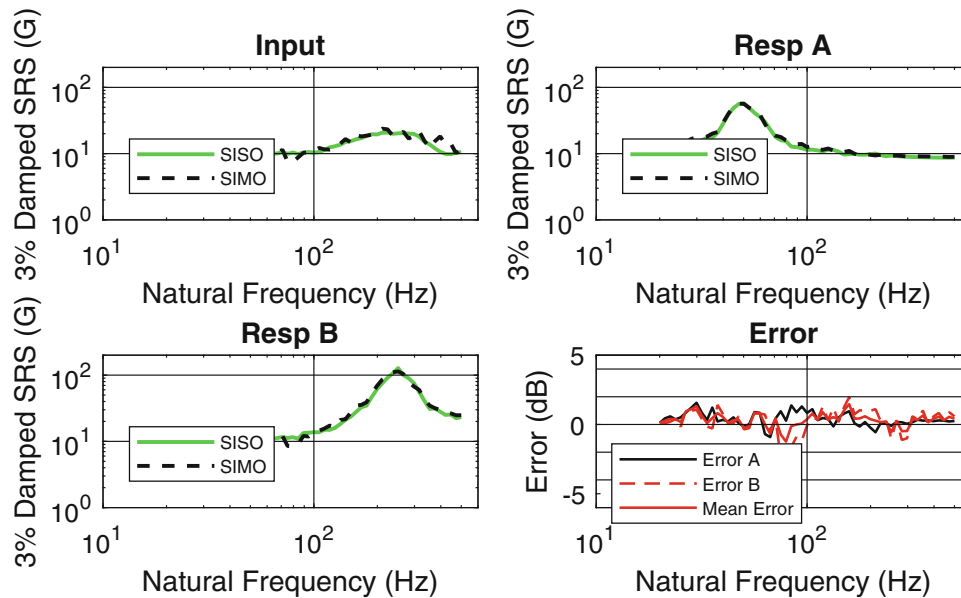


Fig. 6.27 SIMO shaker shock synthesis

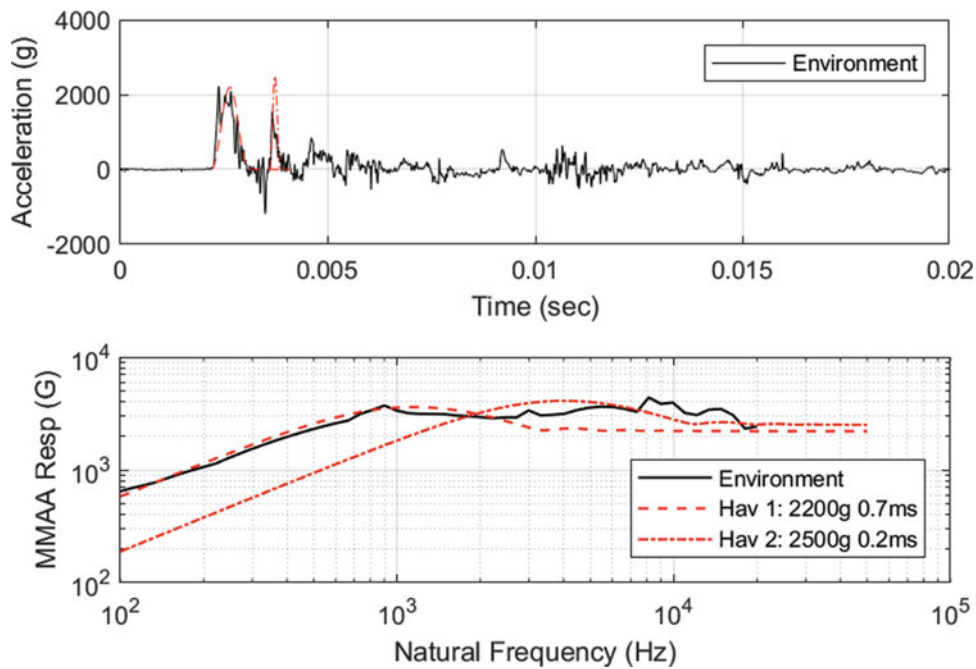


Fig. 6.28 Haversine drop shocks for ground impact field environment

Drop table shock testing is commonly employed owing to the ease of implementation. However, except for environments such as ground impact, which tend to have a significant one-sided acceleration content, the waveform generated by a drop table (a half-sine, haversine, or terminal peak sawtooth) rarely looks like the field environment. The sole criteria for using such a test is the assertion that a test is conservative if the SRS produced by the test exceeds the SRS of the test specification. This puts a lot of pressure on the belief in SRS as being the only possible damage metric. However, drop table testing will continue to be used so the analyst should at least try and achieve the best match for both the SRS and the peak acceleration.

Perhaps the greatest issue with drop table testing is the need to use a long duration and short duration drop shock to span the desired frequency range. Since these shocks must be done sequentially one does not excite the resonant frequencies of the component simultaneously. Figure 6.28 presents an example of this. The concept of mounting resonant fixtures on the drop

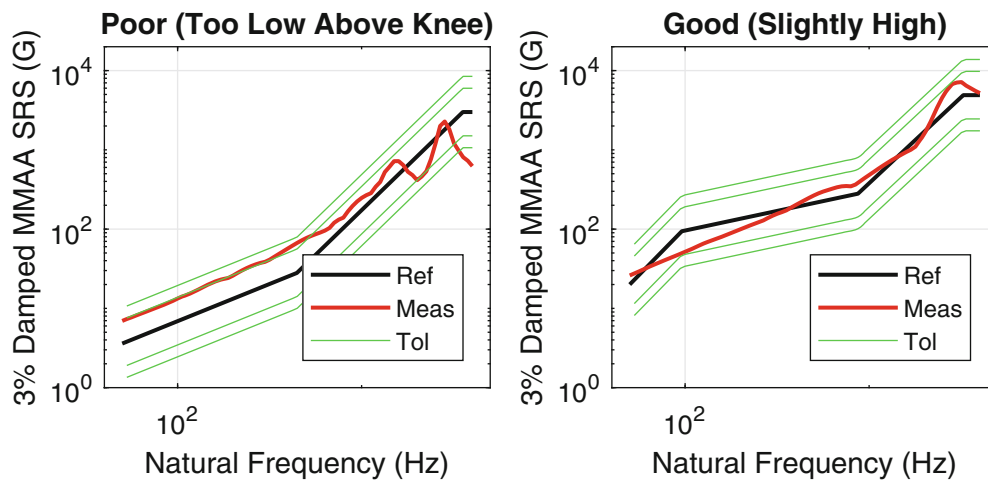


Fig. 6.29 Examples of resonant fixture tests

table (which would produce a waveform consisting of a low frequency haversine combined with a high frequency ringing waveform) has been studied and such an approach has promise for replacing the need for double haversines.

Resonant fixture testing produces oscillatory decaying waveforms that are very similar in nature to many field environments such as pyrotechnically induced shocks. However, the test engineer is limited to a waveform based on the fundamental resonant frequency of the fixture and perhaps some harmonics. Controlling the damping is also somewhat of an art. Therefore, the analyst and component designer must usually work with the test engineer to develop the best possible resonant fixture waveform and then focus on replicating that for the remainder of the test series. Figure 6.29 presents examples of poor and good resonant fixture tests.

6.17 Summary and Conclusions

This paper has covered many topics associated with the processing of field data and the development of laboratory test specifications. Although the topics have been covered at a fairly high level, the author hopes that the reader will appreciate the many concepts that one should consider when developing specifications. The referenced papers provide a more in-depth review of the techniques discussed.

References

1. Welch, P.D.: A direct digital method of power spectrum estimation. *IBM J. Res. Dev.* **5**(2), 141–156 (1961)
2. Nuttall, A.: Spectral Estimation by Means of Overlapped Fast Fourier Transform Processing of Windowed Data NUSC Rept. No. 4169. Naval Underwater Systems Center, New London
3. NASA-HDBK-7005, Dynamic Environmental Criteria, 4 December 2000
4. Piersol, A.G.: Optimum resolution bandwidth for spectral analysis of stationary random vibration data. *Shock. Vib.* **1**(1), 33–43 (1993)
5. Edwards, T.S.: Using work and energy to characterize mechanical shock. In: *Proceeding of the 74th Shock and Vibration Symposium* (2003)
6. Mil-Std-810G, Environmental Engineering Considerations and Laboratory Tests, 31 October 2008
7. Piersol, A.G.: Vibration and Acoustic Test Criteria for Captive Flight of Externally Carried Stores, AFFDL-TR-71-158. DTIC No. AD-893-005L, December 1971
8. Cap, J.S., C' de Baca, M.K., Skousen, T.L.: The derivation of maximum predicted environments for externally carried stores using a small number of flight tests. In: *Proceedings of the 84th Shock and Vibration Symposium*, Atlanta, Georgia, 3–7 November 2013
9. Owen, D.B.: Factors for One-Sided Tolerance Limits and for Variables Sampling Plans Sandia Monograph SC-R-607. Sandia Corp., Albuquerque (1963)
10. SMC-TR-06-11: Test Requirements for Launch, Upper Stage, and Space Vehicles, 6 September 2006
11. Pendelton, L.R., Henrikson, R.L.: Flight-to-flight variability in shock and vibration levels based on trident I flight data. In: *Proceedings of the 53rd Shock and Vibration Symposium, Classified Supplement (Unclassified paper)* (1983)
12. Cap, J.S., Paez, T.L.: A procedure for the generation of statistically significant transient signals. In: *Proceedings of the 75th Shock & Vibration Symposium*, Virginia Beach, 18–22 October 2004

13. Cap, J.S.: An on-road shock & vibration response test series utilizing worst case and statistical analysis techniques. In: Proceedings of the 68th Shock & Vibration Symposium, Baltimore, MD, November 1997
14. Cap, J.S., C' de Baca, M.K.: The derivation of appropriate laboratory vibration test durations and number of shock hits from non stationary field test data. In: Proceedings of the 86th Shock and Vibration Symposium, Orlando, FL, 5–8 October 2015 (coauthor: M. C de Baca)
15. Cap, J.S., Norman, S., Smallwood, D.O.: The Derivation of Multiple-Input-Multiple Output (MIMO) acoustic test specifications to simulate a missile flight. In: Proceedings of the 86th Shock and Vibration Symposium, Orlando, FL, 5–8 October 2015
16. Rohe, D.P., Nelson, G.D., Schultz, R.A.: Strategies for shaker placement for impedance-matched multi-axis testing. In: Walber, C., Walter, P., Seidlitz, S. (eds.) Sensors and Instrumentation, Aircraft/Aerospace, Energy Harvesting & Dynamic Environments Testing, Volume 7. Conference Proceedings of the Society for Experimental Mechanics Series. Springer, Cham (2020)
17. Cap, J.S.: A technique for the identification of the optimum inputs for a vibration or acoustic test. In: Proceedings of the 76th Shock & Vibration Symposium, Destin, FL, 31 October – 3 November, 2005
18. NASA Document RP-1402, Force Limiting Vibration Testing Monograph
19. Smallwood, D.O.: Methods used to match shock spectra using oscillatory transients. In: Proceedings of the Institute of Environmental Sciences, pp. 490–420 (1974)
20. Heitman, C., Cap, J.S., Murphy, D.: Monte Carlo Optimization of a Single Input Multiple Output (SIMO) input derivation for an oscillatory decaying shock. In: Proceedings of the 87th Shock and Vibration Symposium, New Orleans, LA
21. Cap, J.S., Smallwood, D.O.: Characterization of ignition overpressure using band limited temporal moments. In: Proceedings of the 65th Shock & Vibration Symposium, San Diego, CA, 31 October – 3 November 1994

Jerome S. Cap received his BS in Mechanical Engineering from The Pennsylvania State University in 1981, and his MS in Mechanical Engineering from the same institution in 1982. He has worked for Sandia National Laboratories since 1983 and has worked in the areas of shock, vibration, and acoustic analysis since 1989. Jerry is a Distinguished Member of the Technical Staff.



Chapter 7

Design and Characterization of a Multi-purpose Duffing Oscillator with Flexible Parameter Selection

Markus J. Hochrainer and Anton M. Puhwein

Abstract When studying vibrations theoretically, nonlinear systems are easily generated by extending a linear model by adequate nonlinear expressions. In physical experiments, on the other side, nonlinear effects are frequently observed, but it is rather demanding to design and assemble an oscillator with predefined properties. Since the Duffing oscillator is a well-established nonlinear system, a common task is to study its phenomena experimentally using small scale laboratory models. Although nonlinear forces can be generated by different principles, the proposed oscillator uses magnetic forces to obtain softening/hardening stiffness effects or variable system damping. Furthermore, the design enables an almost independent choice of nonlinear restoring and viscous damping forces. The oscillator consists of a cantilevered beam with a concentrated mass at its end. The excitation is limited to uniaxial ground acceleration using electrodynamic shakers or initial displacements in case of free vibration responses. For measurements, only standard hardware components are required, typically force, displacement or acceleration sensors. The setup is used to demonstrate various important phenomena, including frequency shifts as well as stable and unstable equilibria. The model parameter are determined using analytical, numerical and experimental methods. All results demonstrate an excellent agreement between theoretical predictions and measurements for fundamentals like nonlinear spring and damper characteristics, but also for more advanced results like nonlinear frequency response curves.

Keywords Experimental nonlinear vibrations · Periodic forcing · Duffing oscillator · Magnetic forces · Hysteresis

7.1 Introduction

The study of linear mechanical vibrations is well established, and consequently, engineers are familiar with methods of experimental and theoretical modal analysis. The assumption of linear system behavior has proven adequate for many decades, but when aiming at further system performance expansions, nonlinear effects have to be utilized in real-world applications. The investigation of nonlinear behavior of structural elements with relatively simple geometry is therefore a question of great practical significance. It enables a range of analytical and approximate techniques to be applicable without the need for numerical simulation. One of the most popular nonlinear dynamic systems is the Duffing oscillator, which is in the focus of the present study, because it already exhibits many rich and complex phenomena typical for nonlinear systems.

When considering nonlinear phenomena, investigations and analysis are frequently focused on numerical simulations only. However, if a Duffing oscillator is properly designed and assembled in the laboratory, important nonlinear properties and effects can be studied and analyzed experimentally. The proposed oscillator consists of a linear elastic cantilevered beam with a concentrated mass at its end. The nonlinear restoring forces are provided by a set of permanent magnets attached to the moving mass and the ground. With this minor modification the cantilevered beam becomes nonlinear and it is possible to investigate nonlinear phenomena such as stiffening and hardening of the spring or the emergence of higher harmonic/subharmonic vibrations under steady state excitation. Further effects comprise monostable and bistable behavior, single and multiple dynamic equilibria including jump phenomena as well as chaotic motion. Depending on the system studied, some effects can be observed easily whereas others only occur in a narrow parameter or excitation regime. Although the focus of the current work is on a single degree of freedom system with harmonic excitation, the effects studied will also

M. J. Hochrainer (✉) · A. M. Puhwein
University of Applied Sciences, Wiener Neustadt, Austria
e-mail: markus.hochrainer@fhwn.ac.at; AntonMario.Puhwein2@fhwn.ac.at

be present in systems that are more complex. All phenomena considered occur in both simulations and experiments and can be explained by common solution or approximation methods.

7.2 System Description

When studying vibrations of complex structures with many degrees of freedom, a common approach is to identify critical modes and apply model order reduction techniques to obtain a system with fewer degrees of freedom. In many situations it is possible to approximate the original complex structure by only one dominant mode of vibration, and thus by a single degree of freedom oscillator. If the nonlinear effects can be represented by the nonlinear restoring forces $f_k(x)$, a Taylor series expansion up to the third order directly renders $f_k(x) \approx kx + k_{nl3}x^3$ and the equation of motion becomes

$$m\ddot{x} + c\dot{x} + kx + k_{nl3}x^3 = F \cos \omega t, \quad (7.1)$$

where c , k , x , denote the linear damping, linear stiffness and relative displacement of the oscillator mass m , whereas k_{nl3} describes the cubic nonlinearity of the spring. The excitation is given by a harmonic forcing of amplitude F and frequency ω . In case of ground excitation the forcing amplitude is substituted by $F = -mA_g$, where A_g is the acceleration amplitude of the ground motion. Since the force function is assumed odd, $f_k(x) = -f_k(-x)$, there is no force component proportional to x^2 . Normalizing Eq. (7.1) with respect to the oscillator mass renders the Duffing equation in standard notation

$$\begin{aligned} \ddot{x} + 2\zeta\omega_0\dot{x} + \omega_0^2x + \alpha x^3 &= \gamma \cos \omega t, \\ \omega_0^2 &= k/m, \zeta = c/2m\omega_0, \alpha = k_{nl3}/m, \gamma = F/m \end{aligned} \quad (7.2)$$

with ω_0 , ζ , α and γ denoting the undamped natural frequency of the underlying linear system, its damping ratio, the coefficient of the cubic nonlinearity and the forcing amplitude, respectively. In general, there is no known analytic solution to Eq. (7.1), but several approximate methods work well. The method of harmonic balance [1, 2] renders an approximate solution $\tilde{x}(t)$ by limiting the motion to a single harmonic component $\tilde{x}(t) = A \cos \omega t + B \sin \omega t$. Insertion into the equation of motion (7.2), substitution of $\cos^3 \omega t \approx 3/4 \cos \omega t$ as well as $\sin^3 \omega t \approx 3/4 \sin \omega t$ and collection of sine and cosine terms yields two polynomial equations

$$\begin{aligned} -\omega^2 B - 2\zeta\omega_0\omega A + \omega_0^2 B + \frac{3\alpha}{4} B (A^2 + B^2) &= 0 \\ -\omega^2 A + 2\zeta\omega_0\omega B + \omega_0^2 A + \frac{3\alpha}{4} A (A^2 + B^2) &= \gamma. \end{aligned} \quad (7.3)$$

Adding the squares of both equations and defining the vibrations amplitude $z = \sqrt{A^2 + B^2}$ renders the well-known implicit form of the frequency response function [1, 2].

$$\left(\left(\frac{3\alpha}{4} z^2 + \omega_0^2 - \omega^2 \right)^2 + (2\zeta\omega_0\omega)^2 \right) z^2 = \gamma^2 \quad (7.4)$$

Figure 7.1 shows a typical response amplification function, for both increasing and decreasing frequencies at a constant excitation level. For $\alpha > 0$ the resonance peak is distorted towards higher frequencies and contains stable and unstable solutions, setting $\alpha = 0$ the response amplification function of a linear SDOF system is obtained [3]. Because real physical systems can only follow the stable solutions, two jump phenomena occur. They are responsible for a different system behavior for increasing and decreasing excitation frequencies. This behavior is commonly denoted hysteretic and occurs at the endpoints of the unstable branch [4].

For larger vibration amplitudes, the third order approximation of $f_k(x)$ can become inaccurate and a fifth order approximation might be required. Consequently, the Duffing Eq. (7.2) extends to

$$\ddot{x} + 2\zeta\omega_0\dot{x} + \omega_0^2x + \alpha x^3 + \beta x^5 = \gamma \cos \omega t, \quad (7.5)$$

with $\beta = k_{5nl}/m$ denoting the coefficient of the quintic nonlinearity. Again, the solution can be approximated by the single frequency harmonic $\tilde{x}(t) = A \cos \omega t + B \sin \omega t$. Substitution into the extended equation of motion (7.5) and application of the method of harmonic balance renders a fifth order polynomial equation for z^2 .

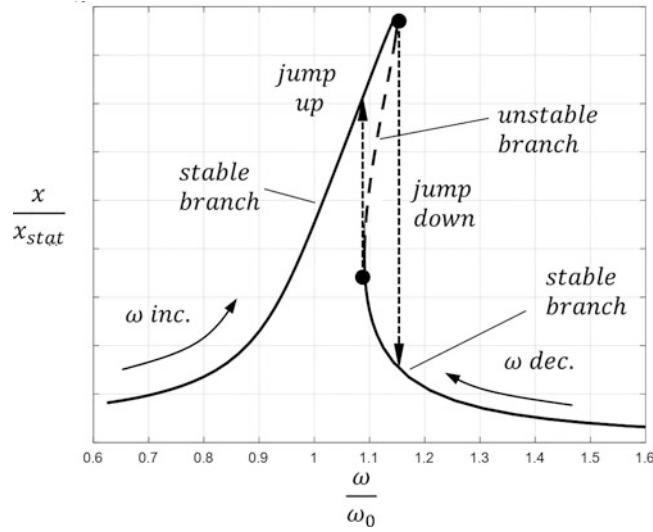


Fig. 7.1 Nonlinear resonance with hysteresis for the Duffing oscillator at a moderate excitation level with hardening spring characteristics, $\alpha > 0$

$$\left(\left(\frac{5\beta}{8}z^4 + \frac{3\alpha}{4}z^2 + \omega_0^2 - \omega^2 \right)^2 + (2\zeta\omega_0\omega)^2 \right) z^2 = \gamma^2, \quad (7.6)$$

when approximating $\cos^5\omega t \approx 5/8 \cos \omega t$ and $\sin^5\omega t \approx 5/8 \sin \omega t$. Consequently, the response curve is able to represent even more evolved effects with up to five equilibria, multiple bending of the resonance and several jumps between stable and unstable branches.

7.3 Experimental Setup

Beam type structures with additional masses have been used successfully to investigate single degree of freedom oscillators in laboratory experiments. Due to the additional mass their fundamental mode of vibration is separated well from the higher order modes, thus the single degree of freedom assumption is valid for a wide operating range. Beams are typically used in a clamped free configuration and respond linearly in relatively wide displacement and frequency range. To obtain a desired nonlinearity, there are two common approaches. The first is a modification of the effective beam length at larger displacements by applying displacement dependent boundary conditions or other additional elements (e.g. hard stops), see Fig. 7.2a. This approach is often used to create multi-linear stiffness elements, but it can hardly model smooth stiffness changes. This drawback is eliminated by the second method, where the desired displacement dependent restoring forces are generated by permanent magnets. Depending on the orientation of the magnets, hardening or softening nonlinearities can be created. The application of magnets for creating nonlinear effects is widespread and many different configurations have been tested, see e.g [1, 2, 5, 6]. The proposed experimental setup is given in Fig. 7.2b, it allows the application of a strong (heavy) permanent magnet at the base, a smaller magnet is attached to the moving mass m .

First measurements have clearly demonstrated the desired spring hardening/softening effect, but for a proper determination and optimization of the magnetic force, a mathematical description is required. The forces acting between two magnets can be derived from electrical and magnetic principles. Magnetic fields can result either from current carrying conductors or from atomic loops in permanent magnets. Experience shows, that the external magnetic field of a permanent magnet is identical to that of a geometrical equivalent conductor with constant outer loop current i [7–9].

If a single particle of charge dq is moving with velocity \mathbf{v} in the magnetic field described by the flux density \mathbf{B} , it will experience the Lorentz force $d\mathbf{F} = dq \mathbf{v} \times \mathbf{B}$. Inside a finite conductor element of length $|\Delta\mathbf{L}|$ and direction \mathbf{L} the flow of charges ΔQ can be replaced by $\Delta Q \mathbf{v} = i \Delta\mathbf{L}$, with i describing the current inside the conductor. With these assumptions the force on the conductor element becomes

$$\Delta\mathbf{F} = i \Delta\mathbf{L} \times \mathbf{B}, \quad (7.7)$$

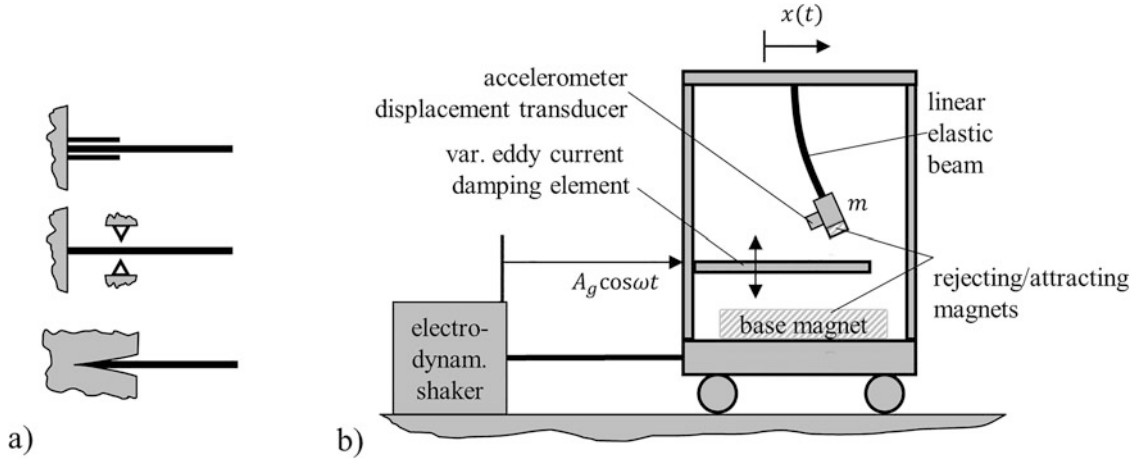


Fig. 7.2 (a) generation of nonlinear behaviour by modification of the effective beam length (b) schematics of base excited Duffing oscillator with nonlinear restoring forces generated by a pair of rejecting/attracting permanent magnets

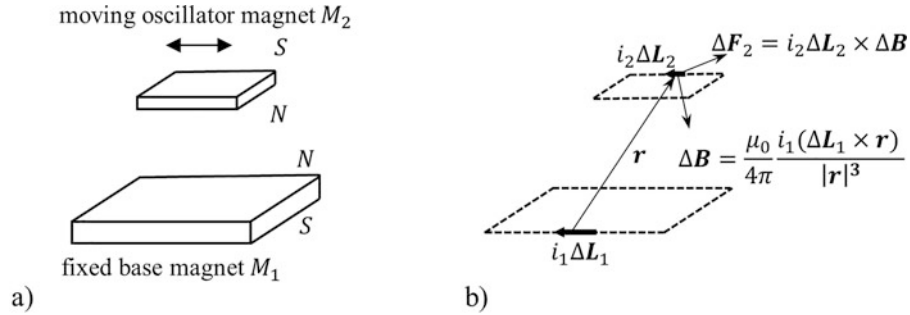


Fig. 7.3 Determination of magnetic forces (a) physical configuration of two permanent magnets M_1 and M_2 (b) equivalent electric diagram

and only the loop current i and its orientation defines the force on a small element of the magnet for a given magnetic flux \mathbf{B} , see Fig. 7.3. On the other side, the same current will produce a magnetic flux density contribution $\Delta \mathbf{B}$ which is known from the law of Biot-Savart

$$\Delta \mathbf{B}(\mathbf{r}) = \frac{\mu}{4\pi} \frac{i \Delta \mathbf{L} \times \mathbf{r}}{|\mathbf{r}|^3}. \quad (7.8)$$

The position vector \mathbf{r} describes the magnetic flux with respect to $\Delta \mathbf{L}$ and the permeability of air is denoted $\mu \approx \mu_0 = 4\pi \cdot 10^{-7}$. At any point, \mathbf{B} is obtained by adding up all individual contributions, $\mathbf{B}(\mathbf{r}) = \mu_0/4\pi \sum (i \Delta \mathbf{L} \times \mathbf{r})/|\mathbf{r}|^3$. Inserting into Eq. (7.7) renders the force acting the conductor $\Delta \mathbf{L}$ by $\Delta \mathbf{F} = \mu_0/4\pi i \Delta \mathbf{L} \times \sum (i \Delta \mathbf{L} \times \mathbf{r})/|\mathbf{r}|^3$.

Since the permanent magnet is represented by a current loop along its circumference, all individual force components $\Delta \mathbf{F}$ must be added to obtain the total force acting on the magnet

$$\mathbf{F} = \frac{\mu_0}{4\pi} \sum \left(i \Delta \mathbf{L} \times \sum \frac{i \Delta \mathbf{L} \times \mathbf{r}}{|\mathbf{r}|^3} \right). \quad (7.9)$$

When evaluating Eq. (7.9) it must be noted, that moving charges cannot exert a force on themselves. Consequently, the force calculation can be further simplified because magnets also cannot produce a resulting rigid body force acting on themselves. In order to determine the magnetic force \mathbf{F}_2 on the moving magnet M_2 , it is sufficient to consider the magnetic flux density resulting from M_1 only,

$$\mathbf{F}_2 = \frac{\mu_0}{4\pi} i_1 i_2 \sum_{M_2} \left(\Delta \mathbf{L}_2 \times \sum_{M_1} \frac{\Delta \mathbf{L}_1 \times \mathbf{r}}{|\mathbf{r}|^3} \right). \quad (7.10)$$

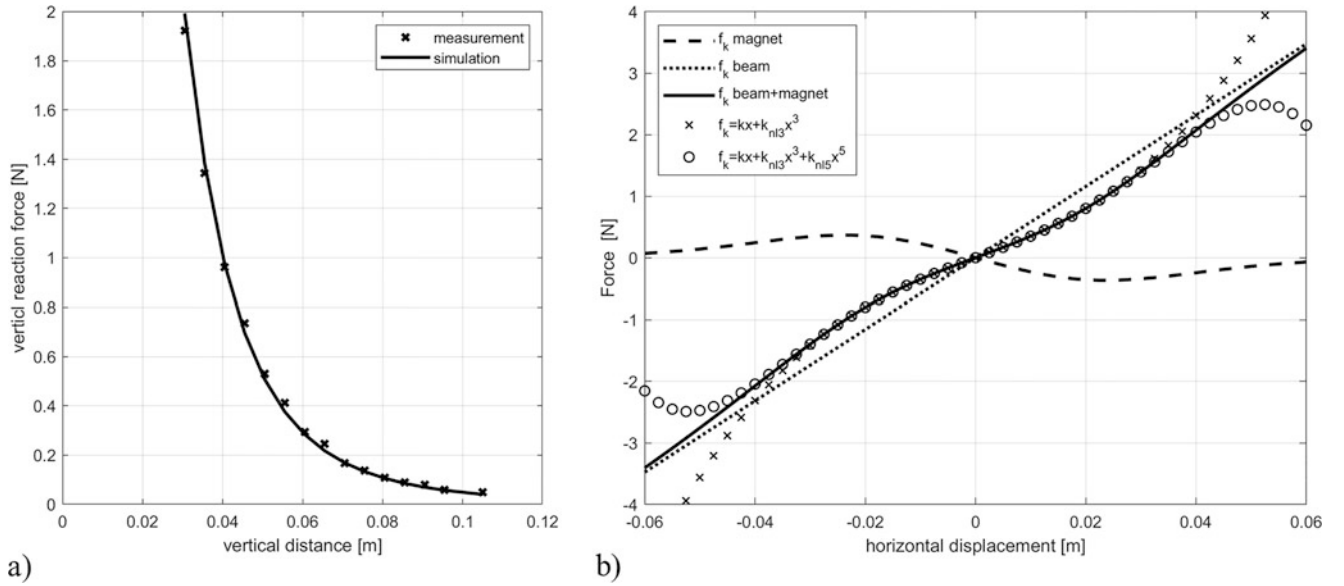


Fig. 7.4 Effects of rejecting magnets (a) comparison of measured and calculated magnetic forces (vertical component only) (b) comparison between the calculated and approximated stiffness function at a vertical distance of 45 mm

When compared to finite element methods, the advantage of the presented method is its excellent performance with respect to calculation speed and accuracy. In particular, the three dimensional geometry of the magnets and their relative position is fully captured and correctly incorporated. Furthermore, the effect of different magnets with respect to material and size is included in the constant factor $i_1 i_2 \mu_0 / 4\pi$. For the proposed setup, see Fig. 7.2b, the vertical force component has been calculated using Eq. (7.10) and measured with a digital scale. Both results show an excellent agreement, see Fig. 7.4a, and the nonlinear, almost inverse proportional dependence on the vertical displacement between the magnets becomes apparent. Figure 7.4b displays the distribution of the magnetic reaction forces as a function of horizontal displacements, and obviously, there again is a strong nonlinear displacement dependence. Similarly, there is a variation in the vertical force component, but in the remainder of the work, only the horizontal contribution is considered. The shape of the resulting magnetic force function is solely dependent on the geometry, position, polarity and strength of the magnets M_1 and M_2 . To obtain a desired nonlinear stiffness it is necessary, to investigate the effect of several different magnets in multiple combinations. For such an optimization process, the efficient computation of F_2 by Eq. (7.10) is again advantageous when compared to finite element methods. Concerning the SDOF oscillator, the nonlinear spring $f_k(x)$ can be described by superimposing the individual contributions of the restoring force of beam and magnet. Obviously, polynomials up to the third and fifth order are required to describe the stiffness function for moderate displacements, see Fig. 7.4b, which displays the comparison between the analytic force calculation and optimal stiffness polynomials for displacements in the range of $-0.03 < x < 0.03$ m. Because there is a strong dependence on the vertical distance between the magnets, the stiffness coefficients must be updated whenever the vertical position is changed. This dependence reveals another important property of the system.

As depicted in Fig. 7.2b an eddy current damping plate is inserted in the magnetic field. The material of the plate is paramagnetic so it does rarely influence the nonlinear forces. However, since it is electrically conducting any motion of magnet M_2 will induce eddy currents, which depend on the distance between the plate and magnet M_2 . If the gap is kept constant, however, the effective damping force is almost proportional to the vibration velocity, and the eddy current damping plate creates the effect of a viscous damper.

Accordingly, it can be summarized, that the experimental setup offers the possibility to individually adapt all essential parameters of the Duffing oscillator. The natural frequency of the linear system is defined by the beam properties and the additional point mass. The nonlinear stiffness variations are determined by the strength, shape and relative position of the permanent magnets, and the viscous system damping is determined by the location of the eddy current damping plate.

7.4 Results and Characterization of the Nonlinear Oscillator

The system described in this work has been tested extensively in the laboratory. The structure has a beam length of 0.133 m , an effective mass of $m = 82 \cdot 10^{-3}\text{ kg}$ and without the base magnet it responds linearly at a natural circular frequency of $\omega_0 = 26.62\text{ rad/s}$ and a damping ratio of $\zeta = 1.28\%$. The forcing is provided by an electrodynamic shaker (LDS V406) with the matching amplifier (LDS P100E), acceleration is measured by IEPE transducers (BK4507) with proper signal conditioning and all displacement are captured by a LDS1607–100 laser optical transducer (Micro-Epsilon). For perfect reference signal tracking without delay and steady state error, an iterative learning control algorithm is added to the system [10]. The nonlinear stiffness is obtained from the interaction of a strong neodym base magnet (length 40 mm , width 40 mm , height 9 mm) and a smaller moving magnet (length 25 mm , width 10 mm , height 2 mm). The base excitation is purely harmonic with acceleration amplitudes between $0.5 < A_g < 2\text{ m/s}^2$ at frequencies near the system's resonance peak.

Typical response curves of a hardening stiffness configuration are shown in Fig. 7.5 for two different damping coefficients and various amplitudes. The same results are displayed in Fig. 7.6 for a softening stiffness configuration. The deformation of the resonance peak is clearly visible, even for the measurements with smaller excitation amplitudes. Similarly, the effect of the viscos damping coefficient ζ on the response amplification function is apparent. For comparison, the experiments are analyzed with the theoretical model, Eq. (7.5), using the harmonic balance approximation of fifth order, Eq. (7.6). For best agreement, the oscillator parameter are determined from a least squares curve fitting optimization of the frequency response function. The inspection of the amplification in Fig. 7.5 indicates a spring softening behavior at higher amplitudes (where no real measurements are available). This however, is not physically motivated, and therefore not correct. It is a result of the stiffness approximation by a polynomial, see Fig. 7.4b. The polynomial approximation is only valid in the displacement regime used for the fitting of the coefficients. An extrapolation is not meaningful because the stiffness function becomes unacceptable high/low. In the contrary, the magnetic forces of the real setup become less important at larger vibration amplitudes, and the system will behave almost like the beam mass system without magnets. Since the method of harmonic balance is only valid for a certain displacement range, a path following algorithm [11] is applied to estimate the system response at various amplitudes. However, path following algorithms are purely numeric, and there is no analytical approximation any longer. Figure 7.7a shows the simulated frequency response for the setup studied in this work. As expected, the system responds linearly for small excitation amplitudes, but the nonlinear effects become dominant if the excitation is increased. A typical stiffening effect is occurs until, at fairly high amplitudes, the resonance peak stabilizes and does not bend or shift any more. Using measurements, the effect of the eddy current damping is also analyzed systematically, see Fig. 7.7b, where the effective damping coefficient ζ is given as a function of the vertical distance to the moving magnet. Again, there is a strong dependence on the vertical position which is in accordance with Fig. 7.4a, since the eddy current damping forces are almost proportional to the magnetic flux density.

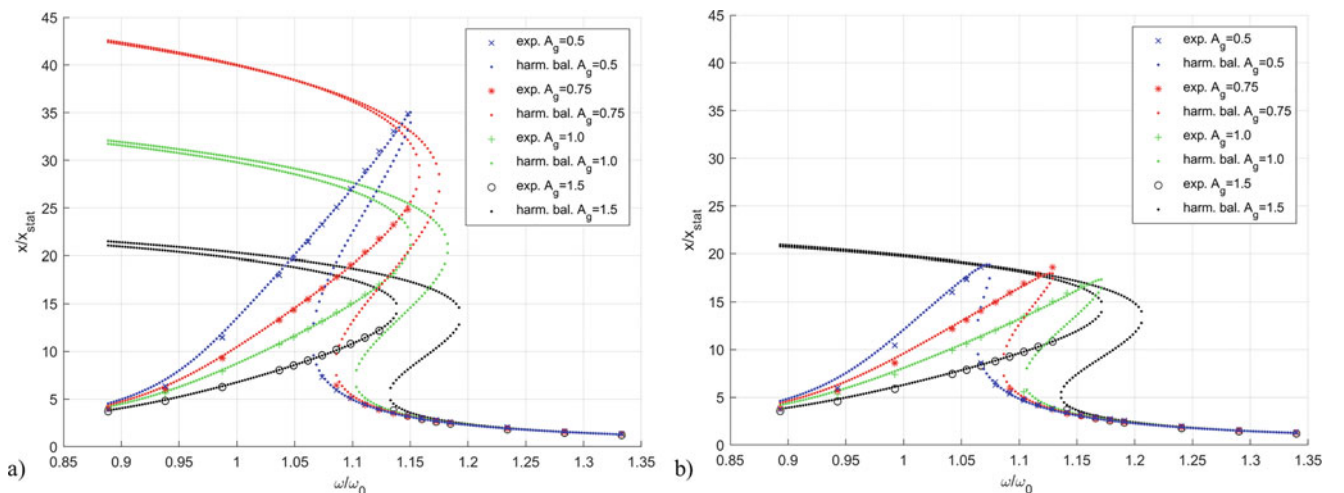


Fig. 7.5 Response amplification function of the physical system with hardening stiffness at various excitation amplitudes A_g , $x_{stat} = A_g/\omega_0^2$ (a) lightly damped oscillator $\zeta = 1.28\%$ (b) moderately damped oscillator $\zeta = 2.5\%$

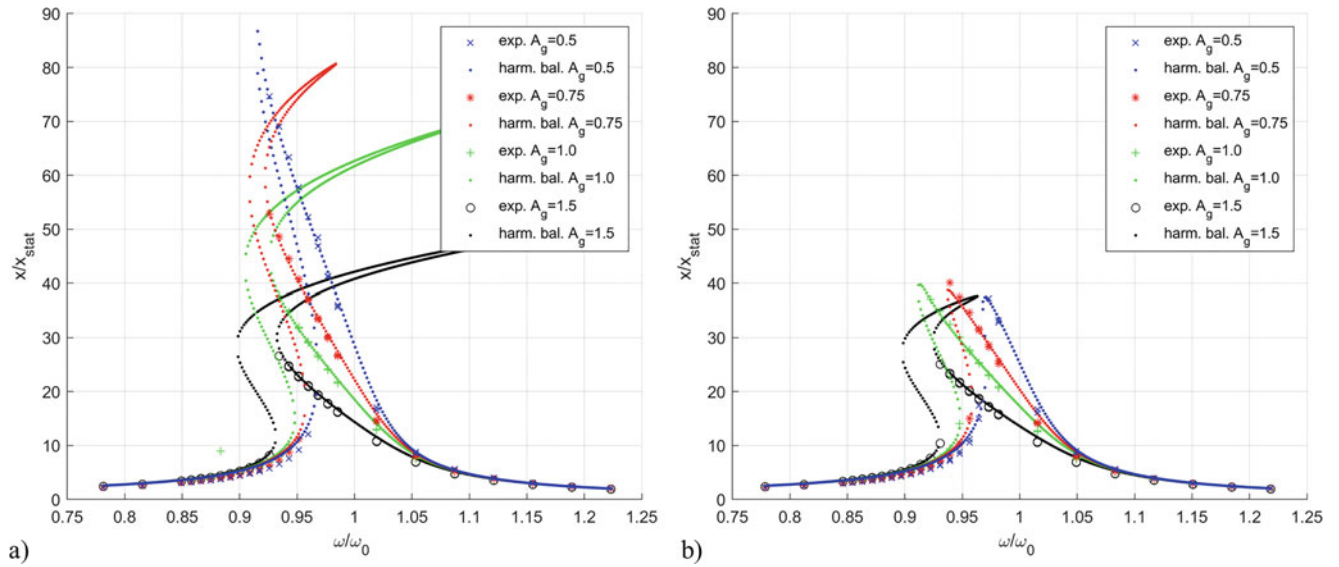


Fig. 7.6 Response amplification function of the physical system with softening stiffness at various excitation amplitudes A_g , $x_{stat} = A_g/\omega_0^2$ (a) lightly damped oscillator $\zeta = 0.6\%$ (b) moderately damped oscillator $\zeta = 1.38\%$

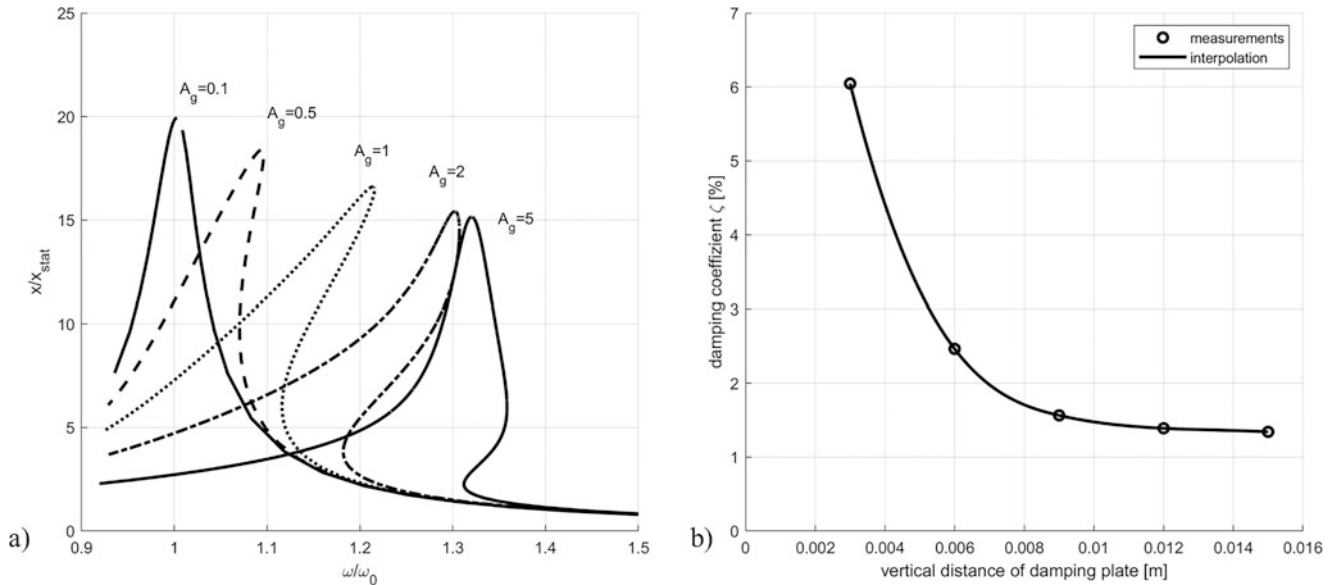


Fig. 7.7 (a) simulated frequency response function of nonlinear oscillator at various amplitudes of A_g , $x_{stat} = A_g/\omega_0^2$, $\zeta = 2.5\%$ using a numerical path following algorithm (b) effective damping coefficient ζ for different positions of eddy current damping plate

7.5 Summary and Conclusion

In this work, the development and design of a multi-purpose Duffing oscillator with flexible parameter selection is presented. The system consists of a linear elastic cantilevered beam with a rigid end mass and two permanent magnets to obtain a desired nonlinear behavior. Accordingly, the recommended setup offers the possibility to adapt all essential parameters of the Duffing oscillator. The natural frequency of the linear system is defined by the beam properties and the additional point mass. The nonlinear stiffness variations are determined by the strength, shape, polarity and relative position of the permanent magnets, and viscous system damping can be added and adapted by insertion of an additional the eddy current damping plate.

Starting from electric principles, the magnetic force contribution is given in an analytic form and therefore the nonlinear effects can be calculated fast and reliable. Using the method presented, the nonlinearity can be modified and trimmed by

exploring the influence of different combinations and locations of permanent magnets. Because the magnetic forces decrease with increasing distance, the nonlinearity reduces for large vibration amplitudes. This effect is known from experiments and must be considered for proper design. The experimental results include measured response amplification functions and corresponding dynamic simulations obtained from harmonic balance approximations.

The proposed system is built and tested in the dynamics laboratory with standard testing components, typically force, displacement or acceleration sensors, and an electrodynamic shaker. Various important nonlinear phenomena are demonstrated for steady state vibrations, including frequency shifts as well as stable and unstable equilibria. All results demonstrate an excellent agreement between theoretical predictions and measurements for fundamentals like nonlinear spring and eddy current damper characteristics, but also for more advanced results like nonlinear frequency response curves.

References

1. Nayfeh, A.H., Mook, D.T.: Nonlinear Oscillations. Wiley (1995)
2. Wagg, D., Neild, S.: Nonlinear Vibrations with Control, 2nd edn. Springer (2015)
3. Brandt, A.: Noise and Vibration Analysis. Wiley (2011)
4. Virgin, L.N.: Introduction to Experimental Nonlinear Dynamics. Cambridge University Press (2000)
5. Perkins, E.: Effects of noise on the frequency response of the monostable Duffing oscillator. *Phys. Lett. A*. **381**, 1009–1013 (2017)
6. Moon, F.C.: Chaotic and Fractal Dynamics. Wiley, New York (1992)
7. Hofmann, H.: Das elektromagnetische Feld Springer (1974, in German)
8. Kraus, J.D.: Electromagnetics. McGrawHill (1991)
9. Ziemann, V.: Hands-On Accelerator Physics Using Matlab. CRC Press (2019)
10. Hochrainer, M., Puhwein, A.: Investigation of nonlinear dynamic phenomena applying real-time hybrid simulation. In: Nonlinear Structures and Systems Conference Proceedings of the Society for Experimental Mechanics Series, vol. 1, (2019). https://doi.org/10.1007/978-3-030-12391-8_16
11. Kerschen, G. (ed.): Modal Analysis of Nonlinear Mechanical Systems CISM International Centre for Mechanical Sciences, vol. 555. Springer (2014)

Markus J. Hochrainer, born 03/081973, received the Ph.D. in 2001 from the Vienna University of Technology, Austria, the M.S. in 1997 from Loughborough Univ., UK, and a M.S. in 1996 from the Johannes Kepler University Linz, Austria. His main research interests include active and passive control of vibrations, system simulation and identification, theoretical and experimental modal analysis, hardware in the loop simulations, acoustics and sound emission. He is the author or co-author of more than 40 papers. From 2001 to 2006 he was project engineer at a civil engineering office focused on sound and vibration emissions from railway/underground projects. In 2006 he joined the Univ. Appl. Sc. where he is currently head of the dynamics laboratory.

Chapter 8

Modeling Viscoelastic Behavior in Transient Analyses



Paul Blelloch and Eric Austin

Abstract Viscoelastic materials are used extensively for vibration isolation of aerospace systems. These materials' time/frequency dependence leads to isolators with complex stiffness—and while the frequency dependence is tractable in a frequency-domain analysis, many critical simulations must be done in the time domain, where the material's time dependence is difficult to represent. The simplest approach is to assign constant isolator properties based on a single key frequency, but doing so diminishes the accuracy of the predictions over a broad frequency range.

It is possible to create a phenomenological model of the viscoelastic behavior by fitting a Maxwell model (Prony series) to test data from either a “complex stiffness” in the frequency domain or a relaxation response in the time domain. This paper shows how a generalized Maxwell model can be tuned to match complex stiffness test data for a viscoelastic isolator using a small number of parameters and then used to reproduce the frequency-dependent stiffness of the original data. In principle, constants for a Maxwell model determined in the frequency domain will also represent the relaxation behavior in the time domain. Representing general time-dependent stiffness requires one massless degree of freedom (DOF) per term in the Prony series, which requires careful treatment in a modal solution. This paper shows how to implement this technique in Nastran using residual vectors to represent the behavior of the massless DOFs and also investigates the implications of numerical integration algorithms on the accuracy of the representation in the time domain.

Keywords Damping · Viscoelastic Material · Simulation · Time Domain · Relaxation

8.1 Introduction

Viscoelastic materials are used extensively for vibration isolation in aerospace systems. One characteristic of these materials is that both the stiffness and damping are frequency dependent, so single spring/damper models are valid at only a single frequency. This becomes problematic when analysis across a broad frequency range is required. One method to address this limitation is to use frequency-dependent properties, although these can only be applied in the frequency domain and are not readily applicable in the time domain. An alternative approach is to use a simple network of linear springs and dampers, sometimes called a generalized Maxwell model, that can be tuned to match the frequency-dependent behavior of the viscoelastic isolator. These models work equally well in the frequency and time domains. We will show how a generalized Maxwell model can be tuned to match complex stiffness test data for a viscoelastic isolator using a small number of parameters and then used for time-domain analysis. Topics covered in this paper include treatment of these models in a modal analysis where retention of residual vectors and selection of an appropriate integration algorithm are critical for correctly characterizing the isolated structure behavior.

P. Blelloch (✉)
ATA Engineering Inc., San Diego, CA, USA
e-mail: paul.blelloch@ata-e.com

E. Austin
Moog CSA, Albuquerque, NM, USA
e-mail: eaustin2@moog.com

8.2 Phenomenological Modeling of a Viscoelastelastic Material

Viscoelastelastic materials are used in many aerospace applications to introduce damping into a system. As the name implies, these materials exhibit a combination of viscous and elastic responses. Creep and relaxation are two physical examples of viscoelastelastic behavior. Figure 8.1 shows the nature of creep, the time-dependent displacement due to a constant force f_o , and relaxation, the time-dependent force needed to enforce a constant displacement u_o . This behavior is characteristic of a “viscoelastelastic solid” containing elastic (k_e) in parallel with elements containing viscous stiffness k_v . Many of the explanations that follow use viscoelastelastic stiffness for simplicity, but all of the argument hold for a viscoelastelastic elastic (or shear) modulus as well.

The time dependence in creep and relaxation is due to a time-dependent stiffness, but we cannot simply relate time-dependent force and displacement by a time-dependent stiffness. However, these quantities can be related in the transform (frequency) domain via the elastic-viscoelastelastic correspondence principle [1]. Figure 8.2 shows the basic flow of the correspondence principle. We start in the upper left with the solution to a boundary-value problem in the time domain, ignoring the time dependence of the stiffness. Continuing clockwise, this solution is ported to the transform domain and the stiffness is then replaced with a Laplace transform of the time-dependent stiffness. This transformed stiffness is what engineers often refer to as frequency-dependent material properties. Taken a step further, the response of a viscoelastelastic material will have both in- and out-of-phase components of displacement with respect to a force excitation. This is the origin of the term “complex modulus” for a viscoelastelastic material. In theory, we could get the time response by doing the inverse Laplace transform of this solution. In practice, this is difficult and we are often satisfied with frequency response functions that capture the time-dependent viscoelastelastic properties.

The time-dependent responses in Fig. 8.1 are due to “creep compliance” and “relaxation stiffness.” The math presented in this section describes the time-dependent force that results from a time-dependent displacement, even though engineers generally predict the opposite. Creep compliance and relaxation stiffness are related [2], so subsequent discussions refer to only the more familiar concept of stiffness.

In a phenomenological sense, the relaxation stiffness shown in Fig. 8.1 is represented by Eq. (8.1):

$$\hat{k}(t) = k_e + k_v e^{-t/\tau} \tag{8.1}$$

where k_e is time independent and k_e and τ characterize the exponential decay. The simple expression yields an “instantaneous” stiffness of $k_e + k_v$ at time = 0+ and an “equilibrium” stiffness of k_e as time gets large. For realistic materials, this would have to be generalized into a Prony series:

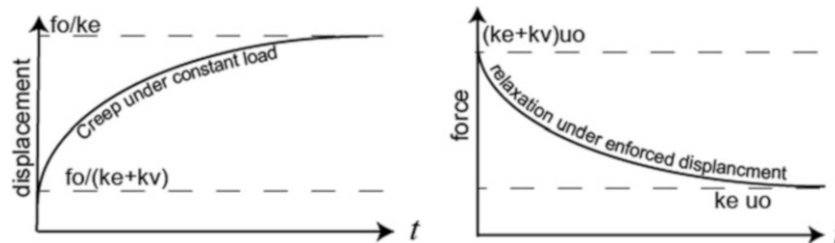


Fig. 8.1 Creep and relaxation phenomena

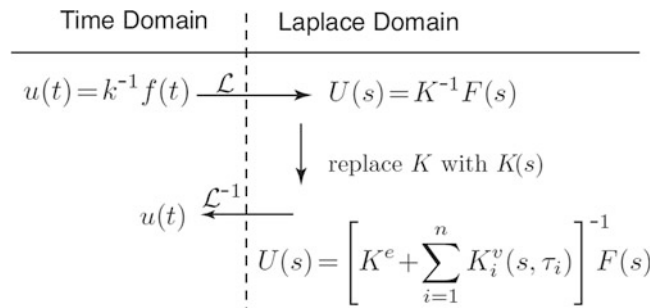


Fig. 8.2 Basic flow of the elastic-viscoelastelastic correspondence principle

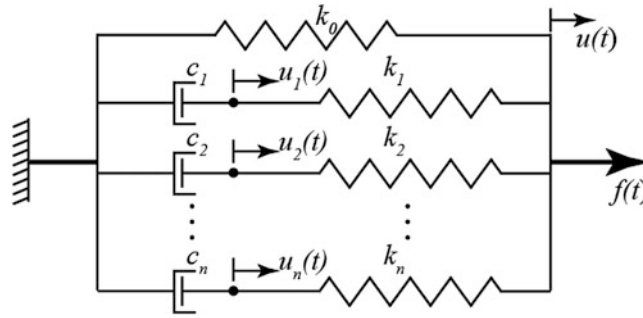


Fig. 8.3 Generalized Maxwell model for viscoelastic behavior

$$\hat{k}(t) = k_o + \sum_{i=1}^n k_i e^{-t/\tau_i} \quad (8.2)$$

We relate the relaxation stiffness to the actual time-dependent stiffness via the Boltzmann superposition principle [2, 3], which states that the force relaxation under an arbitrarily prescribed displacement is

$$f(t) = \int_0^t \hat{k}(t - \alpha) \frac{\partial u(\alpha)}{\partial \alpha} d\alpha \quad (8.3)$$

where $\hat{k}(t)$ is the relaxation stiffness. Taking the Laplace transform of Eq. (8.3) yields

$$F(s) = [\hat{K}(s)] [s U(s)] = [s \hat{K}(s)] [U(s)] = K(s)U(s) \quad (8.4)$$

Taking the Laplace transform of Eq. (8.2) and substituting into Eq. (8.4) yields

$$K(s) = s \hat{K}(s) = s \left(\frac{k_o}{s} + \sum_{i=1}^n \frac{k_i}{s + \frac{1}{\tau_i}} \right) = k_o + \sum_{i=1}^n \frac{s \tau_i k_i}{1 + s \tau_i} \quad (8.5)$$

where k_o now denotes the elastic term, and an arbitrary number of (k_i, τ_i) terms can be used to fit actual relaxation data.

The generalized Maxwell model shown in Fig. 8.3 is a common way to model relaxation behavior in viscoelastic materials. The model has n internal DOFs that phenomenologically capture the time dependence of the material. Summing forces in the Laplace domain and eliminating the internal DOFs leads to the stiffness $K(s)$ shown in Eq. (8.5) after relaxation time constants are defined as $\tau_i = c_i/k_i$.

Restate Eq. (8.5) in the frequency domain by replacing the Laplace variable s with $j\omega$, and break it into its real and imaginary components:

$$\begin{aligned} K(\omega) &= K(s)|_{s \rightarrow j\omega} = k_o + \sum_{i=1}^n \frac{j\omega \tau_i k_i}{1 + j\omega \tau_i} \\ K(\omega) &= k_o + \sum_{i=1}^n \frac{\omega^2 \tau_i^2 k_i}{1 + \omega^2 \tau_i^2} + j \sum_{i=1}^n \frac{\omega \tau_i k_i}{1 + \omega^2 \tau_i^2} = K'(\omega) + j K''(\omega) \end{aligned} \quad (8.6)$$

where K' and K'' are, respectively, the real and imaginary portions of the viscoelastic stiffness.

8.3 Converting Structural to Viscous Damping

Often the frequency-dependent behavior mild enough that the material can be approximated by a single modulus and loss factor. However, this is still problematic for time-domain integration because representing the loss factor as an imaginary stiffness matrix is not an option unless noncausal time-domain integration is considered. The relationship between structural

and viscous damping can be observed by writing the imaginary part of the stiffness for a single-DOF oscillator in the frequency domain:

$$jK'' = jC\omega \text{ or } C = K''/\omega \quad (8.7)$$

A viscous damper can therefore be made equivalent to a structural damper at one frequency only. Typically, the resonant frequency is chosen for this purpose. The problem with this approach is that most practical structures have many frequencies. The traditional approach in Nastran has been to choose a single frequency (PARAM W3 or W4 depending on how the structural damping is defined) and make the equivalence at that frequency. However, the equivalent loss factor g will vary proportionally with frequency so that all modes below the chosen frequency will have lower damping and all modes above will have higher damping. An alternative approach that is available for a modally reduced system is to make the equivalence at each resonant frequency. This is done as follows:

$$[\hat{C}] = \left[\frac{1}{\sqrt{\omega_i}} \right] [\hat{K}''] \left[\frac{1}{\sqrt{\omega_i}} \right] \quad (8.8)$$

Where $\left[\frac{1}{\sqrt{\omega_i}} \right]$ is the diagonal matrix of the inverse square root of the modal frequencies ω_i , $[\hat{K}'']$ is the modally reduced imaginary stiffness matrix, and $[\hat{C}]$ is the equivalent modally reduced viscous damping matrix. Note that the diagonal elements of $[\hat{C}]$ are given as follows:

$$[\hat{C}]_{ii} = [\hat{K}'']_{ii} / \omega_i \quad (8.9)$$

So the diagonal viscous damping terms for every mode match the structural damping of that mode at the resonant frequency. This approach is only available for modal analysis and is implemented in Simcenter Nastran as PARAM, WMODAL, YES. It has proven to accurately capture structural damping when equivalent viscous damping is used, whenever modal density is sufficient high that the response is governed by resonant response.

8.4 Fitting Viscoelastic Models

While converting structural damping to viscous damping using the approach outlined in the previous section does allow for time-domain simulation of isolators modeled as lossy springs, it does nothing to capture the frequency sensitivity of the viscoelastic materials. As shown previously, viscoelasticity can be treated in either the time or frequency domain, and experimental data can also be gathered either through relaxation tests or through direct stiffness characterization in the frequency domain. The time-domain behavior is typically represented by a “master curve,” which plots the relaxation modulus against a reduced time, as illustrated in Fig. 8.4 [4]. The reduced time scales to actual time based on temperature.

The equivalent in the frequency domain is a nomogram, which plots the dynamic modulus (real part of the stiffness) and loss factor (imaginary part of stiffness divided by real part) against a reduced frequency, which is again a function of temperature. A typical nomogram for a viscoelastic material is plotted in Fig. 8.5, from Lima de Sousa et al. [5].

A generalized Maxwell model can be fit to either time or frequency domain using standard numerical optimization techniques. The optimization variables are the parameters, stiffness and damping, of the generalized Maxwell model. Chae et al. [1] directly fit the time-domain relaxation data, whereas Lima de Sousa et al. [5] match the frequency-domain nomogram data. In both cases, the variables in the optimization problem are the parameters of the generalized Maxwell model (spring stiffnesses and viscous damper constants), and the objective function is a curve fit to either the time- or frequency-domain data. Note that the optimization problem is not necessarily convex, and Lima de Sousa et al. [5] use a hybrid optimization technique that first applies a genetic algorithm to find a “good” solution and then a gradient algorithm to optimize the solution. Nomogram fits for eight- and sixteen-parameter Prony terms are plotted in Fig. 8.6.

Note that nomograms are typically plotted over many orders of magnitude in frequency. Figure 8.5, for example, plots results over eleven orders of magnitude. In practice, it is typically only necessary to characterize an isolator over one to two orders of magnitude. In addition, many practical viscoelastic material isolators require metallic components to carry significant loads. These two effects result in behavior that varies less over the frequency range of interest and is easier to fit than a full nomogram.

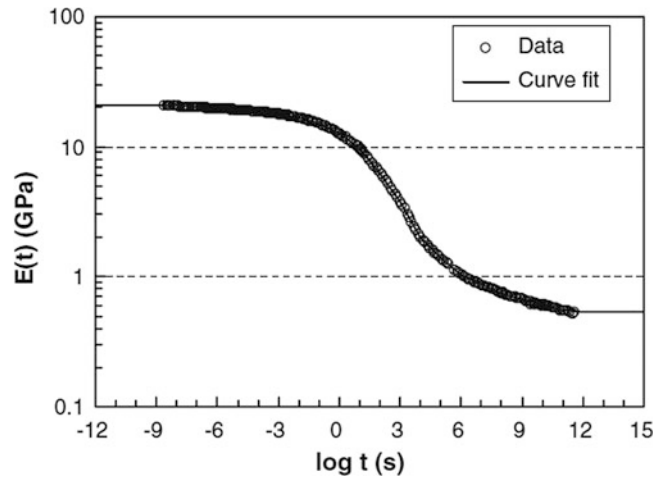


Fig. 8.4 Typical master curve for a viscoelastic material

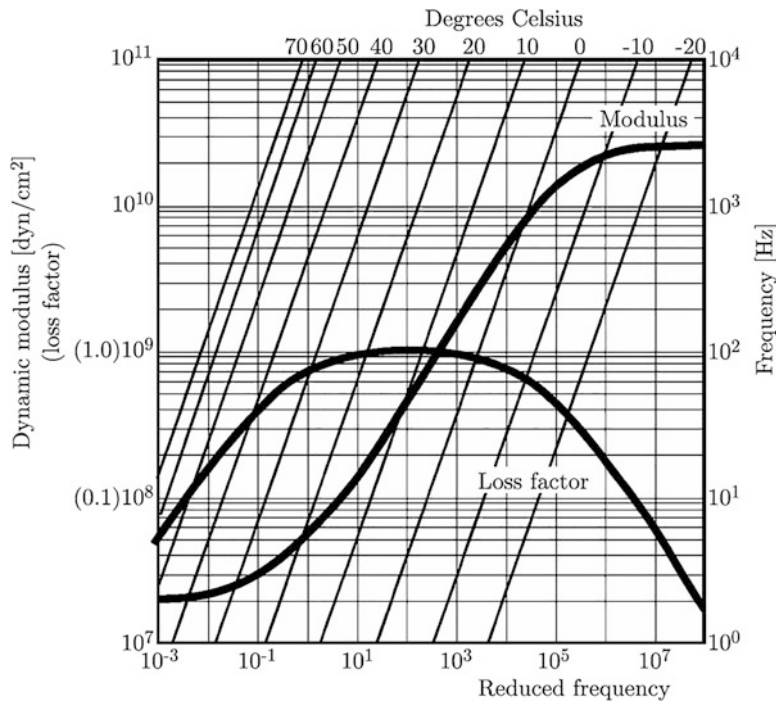


Fig. 8.5 Nomogram for EAR® C1002 [5]

8.4.1 Integrating Equations of Motion

While it is fairly straightforward to fit a generalized Maxwell model to the frequency-dependent stiffness and damping behavior of a viscoelastic material isolator, some care needs to be taken in integrating the equations of motion. This is because it is essential to accurately capture the behavior of the pseudo-DOFs to get the correct behavior. A very simple example can be used to illustrate this point. In this case, the material is EAR C-1002, described by the nomogram in Chae et al. [4]. Assuming a temperature of roughly 14 °C, the reduced frequency and actual frequency are equal. The nomogram data was digitized and a log-polynomial fit was made to get the frequency-dependent data illustrated in Fig. 8.7.

An isolator is to be designed to operate from 1 Hz to 100 Hz, which is the region denoted by the box in Fig. 8.7. A simple three-parameter Maxwell model (two springs and one damper) was fit to the data from 1 Hz to 100 Hz. The corresponding best-fit stiffness values were 7.1367E7 and 5.1641E8, and the best fit damper was 2.4022E6. The resulting fit to the modulus

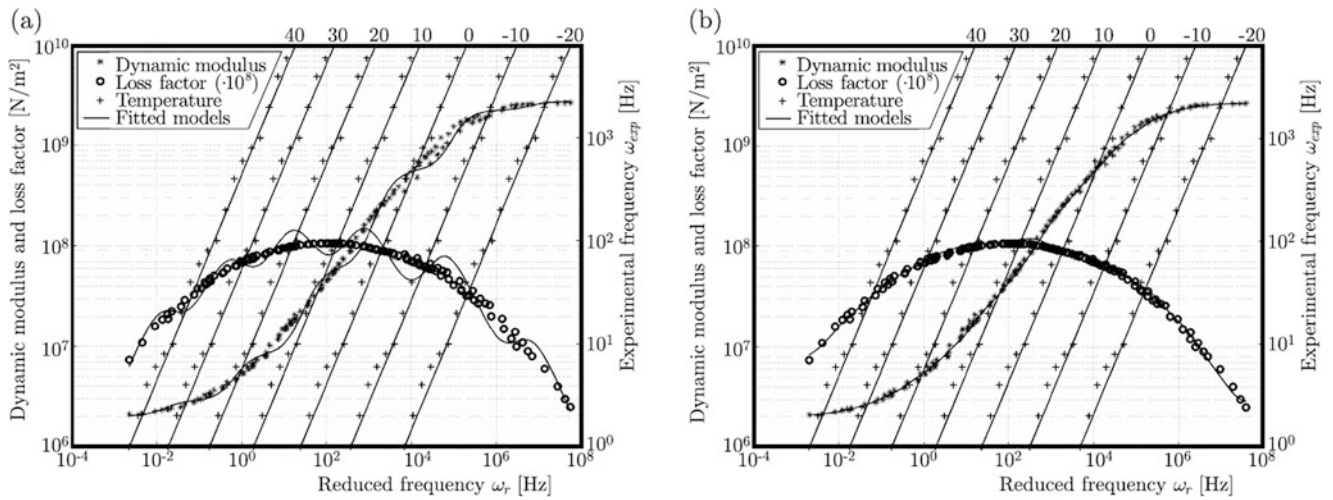


Fig. 8.6 Fits to EAR® C1002 nomogram data using 8 or 16 Prony terms [5]

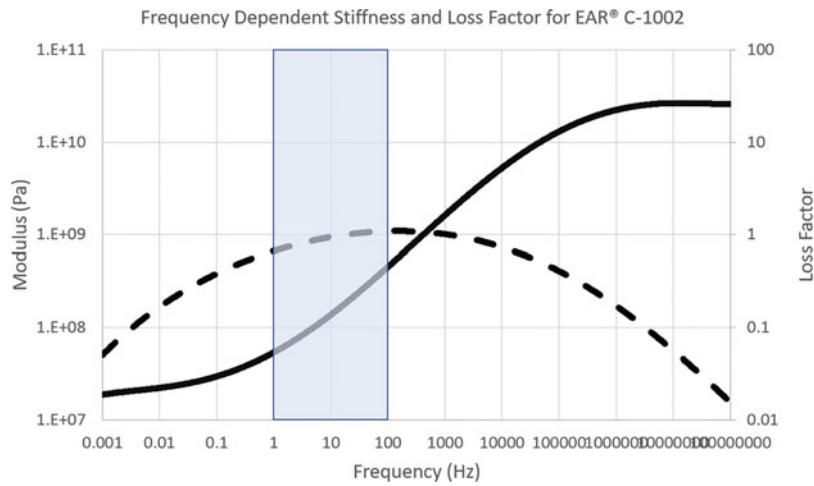


Fig. 8.7 Frequency-dependent stiffness and loss factor for EAR C-1002 at 14 °C

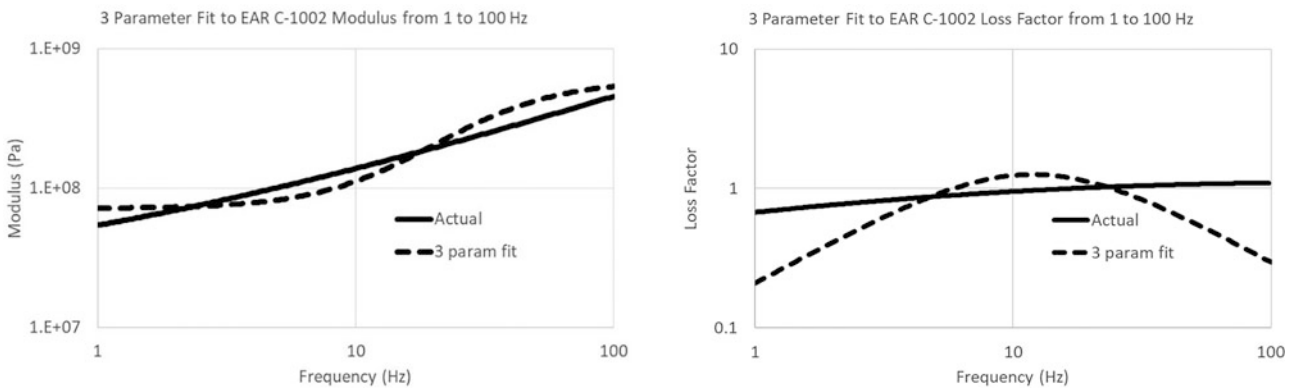


Fig. 8.8 Three-parameter fit from 1 Hz to 100 Hz

and loss factor is illustrated in Fig. 8.8. Note that the fit, particularly in loss factor, is not particularly good; however, it is sufficient for the purposes of this example.

For the purposes of this example, the stiffness and damping values were scaled down by a factor of 1E4 and a mass of 2.8352 kg was added to achieve an isolator frequency of 10 Hz. A corresponding single lossy spring model of the isolator

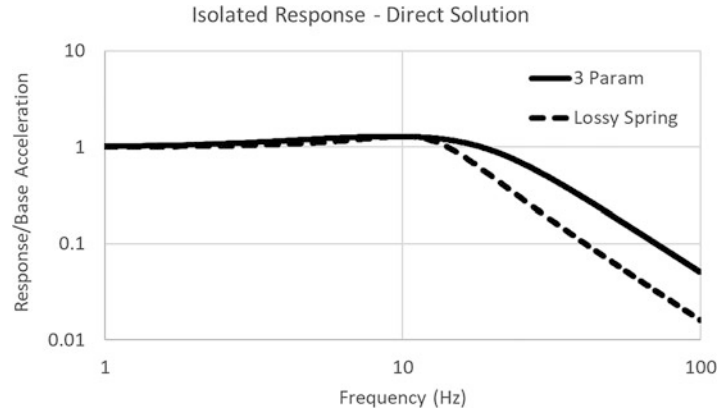


Fig. 8.9 Isolated response with three-parameter model and single lossy spring

can be calculated by looking up the stiffness and loss factor at 10 Hz. These are $1.1193E4$ N/m and 1.24, respectively. Figure 8.9 illustrates the isolated acceleration of the mass for unit acceleration of the base for both the three-parameter model and the lossy spring.

Note that the lossy spring captures the resonant behavior of the isolator very accurately, but it overpredicts the isolation at 100 Hz by approximately a factor of 3. This would result in a significant error in the behavior of the isolator for an input at 100 Hz. The results in Fig. 8.9 were calculated using a direct frequency response (SEDFREQ) in Nastran, which does not require that any mass be added to the internal DOF. However, any approach based on real modes requires that a mass be added to the internal DOF such that the corresponding residual vector has a finite frequency. A mass of $1E-5$ was added, corresponding to a residual mode at 11,238 Hz.¹ With this mass, the modal and direct frequency response solutions are identical in the frequency range of 1–100 Hz.

The following are the equations of motion in physical coordinates for base motion $\{x_3\}$:

$$\begin{bmatrix} 2.8352 & 0 \\ 0 & 1E-5 \end{bmatrix} \begin{Bmatrix} \ddot{x}_1 \\ \ddot{x}_2 \end{Bmatrix} + \begin{bmatrix} 241.74 & -241.74 \\ -241.74 & 241.74 \end{bmatrix} \begin{Bmatrix} \dot{x}_1 \\ \dot{x}_2 \end{Bmatrix} + \begin{bmatrix} 6,959.3 & 0 \\ 0 & 49,859 \end{bmatrix} \begin{Bmatrix} x_1 \\ x_2 \end{Bmatrix} = \begin{Bmatrix} 6,959.3 \\ 49,859 \end{Bmatrix} \{x_3\}$$

The corresponding equations of motion in modal coordinates, using the constraint mode formulation are

$$\begin{bmatrix} 1 & 0 \\ 0 & 1 \end{bmatrix} \begin{Bmatrix} \ddot{q}_1 \\ \ddot{q}_2 \end{Bmatrix} + \begin{bmatrix} 85.2638 & -45,400 \\ -45,400 & 2.4174E7 \end{bmatrix} \begin{Bmatrix} \dot{q}_1 \\ \dot{q}_2 \end{Bmatrix} + \begin{bmatrix} 2,454.6 & 0 \\ 0 & 4.9859E9 \end{bmatrix} \begin{Bmatrix} q_1 \\ q_2 \end{Bmatrix} = \begin{Bmatrix} -1.6838 \\ -.00316 \end{Bmatrix} \{\ddot{x}_3\}$$

$$\begin{Bmatrix} x_1 \\ x_2 \end{Bmatrix} = \begin{bmatrix} 1 & 0.59389 & 0 \\ 1 & 0 & 316.23 \end{bmatrix} \begin{Bmatrix} x_3 \\ q_1 \\ q_2 \end{Bmatrix}$$

The challenge is now to integrate the equations with two strongly coupled, highly damped modes: one at 7.89 Hz and one at 11,238 Hz. Three different methods are considered in the following section, but first it should be noted that the coupling between the two modes is essential to capturing the behavior. The second point to note is that because of the very-high-frequency mode associated with the internal mass, any explicit integrator such as Runge-Kutta will require extremely small time steps and will therefore be very inefficient. The goal is to find an integrator that will be both stable and reasonably accurate for a model of this type. Three different integrators are considered. The first is the coupled integration algorithm implemented in Nastran, which is a variation of the implicit Newmark-beta algorithm. The second is a variation of the uncoupled integration implemented in Nastran, which puts the off-diagonal terms of the damping matrix on the right-hand side of the equations [6]. The third is a complex mode integrator, which first reduces the system to a set of uncoupled complex modes and then integrates those modes independently.

¹In this case, a much larger internal mass could be added without significantly modifying the low-frequency dynamics, but the lower mass was chosen to provide a challenging case for time integration.

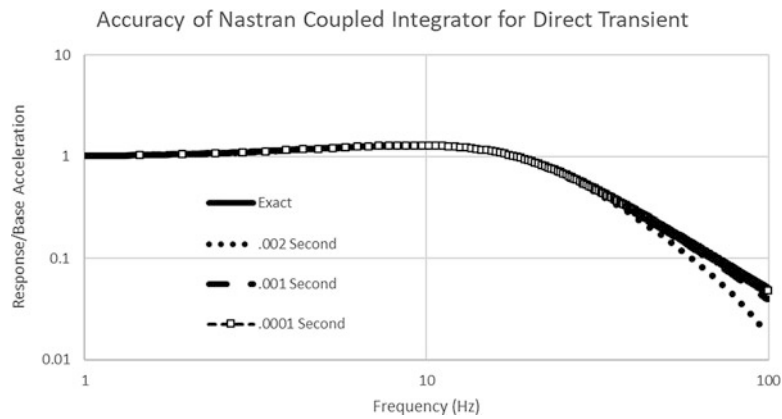


Fig. 8.10 Accuracy of Nastran coupled direct integrator for various time steps

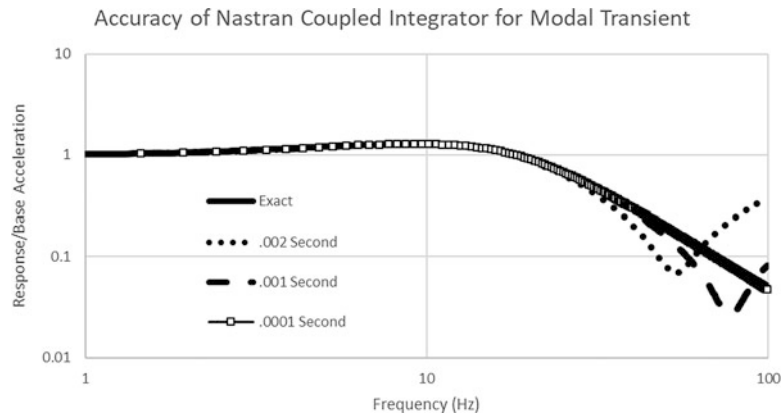


Fig. 8.11 Accuracy of Nastran coupled modal integrator for various time steps

To evaluate these algorithms, a time-domain simulation was performed for a linear sine-sweep excitation from 1 Hz to 100 Hz over a 100 s period. The data was then consistently interpolated to a 0.001 s time step, and the transfer function from input to output was then calculated using Welch’s method with a Hann window, a block size of 2048 (2.048 s), and 90% overlap. The transfer functions were then compared with the “exact” three-parameter frequency domain illustrated in Fig. 8.9.

First, consider the standard Nastran coupled integrator applied without any modal reduction, with various time steps. Time steps of 0.002, 0.001 and 0.0001 s were chosen, and the results are compared with the exact solution in Fig. 8.10. The solution in this case is fairly accurate with either a time step of 0.001 s (ten time steps per highest frequency) or 0.0001 s (100 time steps per highest frequency). Accuracy falls off significantly with a time step of 0.002 s (five time steps per highest frequency).

Next, consider the accuracy of the Nastran coupled integrator applied to the modal equations of motion. The results for the same time step sizes are illustrated in Fig. 8.11. In this case, the solution with a 0.0001 s time step is still accurate, but the solutions with time steps of either 0.001 s or 0.002 s have significant errors at the higher end of the frequency range.

Next, consider the integration algorithm based on the uncoupled solution, with the off-diagonal damping elements on the right-hand side of the equations, referred to here as the Chapman algorithm [6]. The results for all three time steps for the modal solution are plotted in Fig. 8.12. In this case there is no loss of accuracy, even with the coarsest time step.

The complex mode integrator was not completed in time for this paper, although other authors have implemented this approach. It should be noted, however, that the complex roots for this set of equations are at $-3.6605E1$, $-8.4823E1 \pm 8.1459E1j$, and $-2.4174E7$. The root at $-2.4174E7$ is very fast and can almost certainly be ignored, but the real root at $-3.6605E1$ and the complex conjugate pair at $8.4823E1 \pm 8.1459E1j$ can almost certainly not be ignored. The application of a complex mode integrator to this problem would require handling of both real and complex conjugate roots and will not be able to assume that all roots come as complex conjugate pairs.

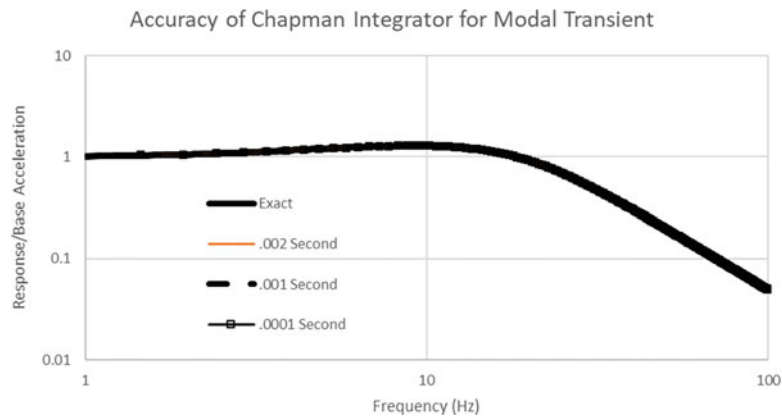


Fig. 8.12 Accuracy of Chapman modal integrator for various time steps

8.5 Summary

A method has been presented that enables simple modeling of viscoelastic isolators in the time domain. For most practical applications, a relatively small number of terms suffices and provides an excellent representation of the frequency-dependent stiffness and damping behavior. This method, however, can prove challenging with time integration of the modal equations of motion because those equations contain very high-frequency terms that must be coupled with the low-frequency modes to capture the correct isolator behavior. Explicit integrators such as Runge-Kutta are poor choices because they require very small time steps. The coupled integrator in Nastran works fairly well but should be checked for convergence with respect to time step, since results can be inaccurate even with relatively small time steps. A variation of the Nastran uncoupled integrator that puts the off-diagonal terms on the right-hand side of the equations is much more robust and gives accurate results with even relatively large time steps.

References

1. Lee, E.H.: Viscoelastic stress analysis. In: Proceedings of the First Symposium on Naval Structural Mechanics, pp. 456–482 (1960)
2. Tschoegl, N.W.: The Phenomenological Theory of Linear Viscoelastic Behavior: An Introduction. Springer-Verlag (1985)
3. Findley, W.N., Lai, J.S., Onaran, K.: Creep and Relaxation of Nonlinear Viscoelastic Materials With an Introduction to Linear Viscoelasticity. Dover (1989)
4. Chae, S.-H., Zhao, J.-H., Edwards, D.R., Ho, P.S.: Characterization of viscoelasticity of molding compounds in the time domain. *J. Electron. Mater.* **39**(4), (2010)
5. Lima de Sousa, T., Kanke, F., Pereira, J.T., Bavastri, C.A.: Property identification of viscoelastic solid materials in nomograms using optimization techniques. *J. Theor. Appl. Mech.* **55**, 1285–1297., Warsaw (2017)
6. Chapman, J.M.: Incorporating a full damping matrix in the transient analyses of nonlinear structures. In: Proceedings of Damping'93, San Francisco (1993)



Chapter 9

Extensions to NIFO and CRP to Estimate Frequency-Independent Nonlinear Parameters

Michael Kwarta and Matthew S. Allen

Abstract The Nonlinear Identification through Feedback of the Output (NIFO) and Conditioned Reverse Path (CRP) methods are a popular family of approaches for nonlinear system identification. They estimate the underlying linear Frequency Response Function (FRF) as well as the parameters describing the mechanical system's nonlinearities. However, one troubling aspect is that the parameters obtained are complex numbers and typically are found to vary with frequency, so post-processing must be employed to obtain physically reasonable parameters and an accurate estimate of the underlying FRFs. This work proposes two methods (based on the \mathbf{H}_1 and \mathbf{H}_2 algorithms) which can be used in the estimation of the linear FRF as well as frequency-independent nonlinear parameters. This paper evaluates the methods numerically using a single degree of freedom system and exploring various methods for determining which nonlinear parameters to include in the model.

Keywords NIFO methods · NIXO methods · Nonlinear system identification · Black-box methods · Nonlinear parameters estimation

9.1 Introduction

The Nonlinear Identification through Feedback of the Output (NIFO) method and Conditioned Reverse Path (CRP) are popular approaches for nonlinear system identification. They estimate the underlying linear Frequency Response Function (FRF) as well as the parameters describing the mechanical system's nonlinearities. The \mathbf{H}_1 -based NIFO method was first proposed in [1], while its twin algorithm, based on the \mathbf{H}_2 estimator, in [2]. Both NIFO algorithms have been successfully used in the estimation of the linear frequency response together with the parameters describing system's nonlinearity. However, one troubling aspect is that the parameters obtained are complex numbers and typically are found to vary with frequency, so post-processing must be employed to obtain physically reasonable parameters [3, 4].

This work proposes two methods (based on the \mathbf{H}_1 and \mathbf{H}_2 algorithms) which can be used in the estimation of the linear FRF as well as frequency-independent nonlinear parameters. Since these two new methods allow for system identification via augmenting the number of outputs, we call them *NIXO methods* – for *Nonlinear Identification through eXtended Outputs*. The methods are first evaluated numerically using a single degree of freedom system. Moreover, a strategy for utilizing the NIXO approaches in the black-box identification of a single degree of freedom mechanical system is presented.

In a future work, both NIXO methods will be employed experimentally to identify the physical parameters describing the nonlinearity of a 3D printed beams for oscillations near their first resonance frequencies. The results will be then used to compute the NNM backbone curve and compared to the solution obtained by another estimation algorithm and data collected using the well-established testing approach.

M. Kwarta (✉)

Department of Engineering Mechanics, University of Wisconsin-Madison, Madison, WI, USA
e-mail: kwarta@wisc.edu

M. S. Allen

Department of Engineering Physics, University of Wisconsin-Madison, Madison, WI, USA
e-mail: matt.allen@wisc.edu

9.2 Derivation of NIFO and NIXO Methods

In this section, the theory behind the three different nonlinear system identification algorithms is presented. These three algorithms are:

- \mathbf{H}_1 - and \mathbf{H}_2 -based NIFO methods that were previously proposed by Adams et al. [1, 2] (also known as the modified \mathbf{H}_1 and \mathbf{H}_2 algorithms),
- Two new \mathbf{H}_1 - and \mathbf{H}_2 -based algorithms dubbed Nonlinear Identification through eXtended Outputs (\mathbf{H}_1 -NIXO and \mathbf{H}_2 -NIXO) and
- Two new \mathbf{H}_1 - and \mathbf{H}_2 -based algorithms dubbed Nonlinear Identification through eXtended Outputs with Linear Data Provided (\mathbf{H}_1 -NIXO-LDP and \mathbf{H}_2 -NIXO-LDP).

The derivations start with steps common for all the algorithms, then they fork and focus on each method separately. For simplicity, we consider a single degree of freedom (SDOF) mechanical system described with equations of motion (EOM) defined in Eqs. (9.1) or (9.2), yet we believe that the algorithms can be generalized to MDOF systems.

$$m\ddot{x} + c\dot{x} + kx + c_2\dot{x}|\dot{x}| + k_3x^3 = f(t), \quad (9.1)$$

$$m\ddot{x} + c\dot{x} + kx + c_2\dot{x}^2 + k_3x^3 = f(t), \quad (9.2)$$

where m , c , k , c_2 and k_3 are *real* and *constant* parameters, $x(t)$ is the response of the system excited for certain initial conditions with a forcing function $f(t)$. If the individual time functions are expressed as in (9.3), then Eqs. (9.1) or (9.2) become equivalent to Eq. (9.4) with $D(\Omega) = k - m\Omega^2 + ic\Omega$ and *frequency-independent* c_2 and k_3 . Equation (9.4) is true for every individual frequency Ω , where $\Omega \in \{\Omega_1, 2\Omega_1, \dots, n\Omega_1\}$, n is the number of frequency samples and Ω_1 is the lowest of the frequencies considered.

$$\begin{aligned} x(t) &= \operatorname{Re}\left\{\sum_{k=1}^n X^k e^{ik\Omega_1 t}\right\} & f(t) &= \operatorname{Re}\left\{\sum_{k=1}^n F^k e^{ik\Omega_1 t}\right\} \\ \dot{x}(t)|\dot{x}(t)| &= \operatorname{Re}\left\{\sum_{k=1}^n dY_2^k e^{ik\Omega_1 t}\right\} & \dot{x}^2(t) &= \operatorname{Re}\left\{\sum_{k=1}^n dY_2^k e^{ik\Omega_1 t}\right\} \\ x(t)|x^2(t)| &= \operatorname{Re}\left\{\sum_{k=1}^n Y_3^k e^{ik\Omega_1 t}\right\} & x^3(t) &= \operatorname{Re}\left\{\sum_{k=1}^n Y_3^k e^{ik\Omega_1 t}\right\} \end{aligned} \quad (9.3)$$

$$D(\Omega) X(\Omega) + c_2 dY_2(\Omega) + k_3 Y_3(\Omega) = F(\Omega), \quad (9.4)$$

Using N_{avg} spectral averages (obtained using e.g. a Hanning window) of signals $x(t)$, $f(t)$ and higher powers of $x(t)$ and $\dot{x}(t)$, Eq. (9.4) can be written in the form shown in Eqs. (9.5) and (9.6). For SDOF systems, matrices \mathbf{X} , $d\mathbf{Y}_2$, \mathbf{Y}_3 and \mathbf{F} have size of $1 \times N_{avg}$. Moreover, Eqs. (9.5) and (9.6) are valid for every individual k -th frequency sample, $k \in \{1, \dots, n\}$.

$$D(k\Omega_1) [X_1, \dots, X_{N_{avg}}] + c_2 [dY_{2,1}, \dots, dY_{2,N_{avg}}] + k_3 [Y_{3,1}, \dots, Y_{3,N_{avg}}] = [F_1, \dots, F_{N_{avg}}] \quad (9.5)$$

$$D(\Omega) \mathbf{X}(\Omega) + c_2 d\mathbf{Y}_2(\Omega) + k_3 \mathbf{Y}_3(\Omega) = \mathbf{F}(\Omega) \quad (9.6)$$

9.2.1 NIFO Algorithms

\mathbf{H}_1 -Based NIFO Method (Modified \mathbf{H}_1 Algorithm)

The original NIFO estimator was first proposed in [1]. It can be obtained by rearranging Eq. (9.6) into the form presented in Eq. (9.7), where the quantity H is a Frequency Response Function ($H(\Omega) = D^{-1}(\Omega)$). The modified \mathbf{H}_1 algorithm is based on Eq. (9.8), which is obtained by right-multiplying Eq. (9.7) by the matrix $[\mathbf{F}^H \ -d\mathbf{Y}_2^H \ -\mathbf{Y}_3^H]$. Note that an equation in the form of Eq. (9.8) can be written for every individual frequency.

$$\mathbf{X} = \begin{bmatrix} H & c_2 H & k_3 H \end{bmatrix} \begin{bmatrix} \mathbf{F} \\ -d\mathbf{Y}_2 \\ -\mathbf{Y}_3 \end{bmatrix} \quad (9.7)$$

$$\mathbf{X} [\mathbf{F}^H \quad -d\mathbf{Y}_2^H \quad -\mathbf{Y}_3^H] = \begin{bmatrix} H & c_2 H & k_3 H \end{bmatrix} \begin{bmatrix} \mathbf{F} \\ -d\mathbf{Y}_2 \\ -\mathbf{Y}_3 \end{bmatrix} [\mathbf{F}^H \quad -d\mathbf{Y}_2^H \quad -\mathbf{Y}_3^H] \quad (9.8)$$

$$\underbrace{\begin{bmatrix} S_{XF} & -S_{XdY_2} & -S_{XdY_3} \end{bmatrix}}_{\mathbf{b}} = \underbrace{\begin{bmatrix} H & c_2 H & k_3 H \end{bmatrix}}_{\hat{\mathbf{x}}} \underbrace{\begin{bmatrix} S_{FF} & -S_{FdY_2} & -S_{FY_3} \\ S_{dY_2dY_2} & S_{dY_2Y_3} \\ \text{Herm. Mtrx} & S_{Y_3Y_3} \end{bmatrix}}_{\mathbf{A}}$$

The \mathbf{H}_1 -based NIFO algorithm results in multiple systems of linear equations of the form $\mathbf{b} = \hat{\mathbf{x}}\mathbf{A}$ (each system corresponds to a different frequency sample). Matrix \mathbf{A} is square and for problems of our interest it is usually non-singular, thus it might be possible to accurately estimate the frequency response function $H(\Omega)$ and parameters c_2 and k_3 through solving Eq. (9.8).

Note that the nonlinear parameters c_2 and k_3 were introduced in Eqs. (9.1) or (9.2) as *real* and *constant* numbers. However, they are computed as *complex* and possibly *frequency-dependent*, since some of the parameters in Eq. (9.8) are complex (as already mentioned above) and the system of equations is solved for each frequency sample separately.

\mathbf{H}_2 -Based NIFO Method (Modified \mathbf{H}_2 Algorithm)

The \mathbf{H}_2 -based NIFO algorithm was first presented in [2]. It is derived by adding additional pseudo-outputs to Eq. (9.7). These additional outputs, $\mathbf{X}_{nl,1}$ and $\mathbf{X}_{nl,2}$, correspond to the nonlinear terms in the EOM, as shown in Eq. (9.9). The modified \mathbf{H}_2 algorithm is based on the formula presented in Eq. (9.10). It can be obtained through right-multiplying Eq. (9.9) by matrix $\begin{bmatrix} \mathbf{X}^H & \mathbf{X}_{nl,1}^H & \mathbf{X}_{nl,2}^H \end{bmatrix}$. As shown in Eq. (9.10), the modification proposed in Eq. (9.9) is needed to overcome the issue of inverting a rectangular matrix. Moreover, due to the cubic stiffness and quadratic damping nonlinearities, we can write: $\mathbf{X}_{nl,1} = d\mathbf{Y}_2$ and $\mathbf{X}_{nl,2} = \mathbf{Y}_3$ and bring Eq. (9.10) to a form of Eq. (9.11). Detailed derivation of the modified \mathbf{H}_2 method is presented in [2].

$$\begin{bmatrix} \mathbf{X} \\ \mathbf{X}_{nl,1} \\ \mathbf{X}_{nl,2} \end{bmatrix} = \begin{bmatrix} H & c_2 H & k_3 H \\ & -1 & \\ & & -1 \end{bmatrix} \begin{bmatrix} \mathbf{F} \\ -d\mathbf{Y}_2 \\ -\mathbf{Y}_3 \end{bmatrix} \quad (9.9)$$

$$\begin{bmatrix} \mathbf{X} \\ \mathbf{X}_{nl,1} \\ \mathbf{X}_{nl,2} \end{bmatrix} \begin{bmatrix} \mathbf{X}^H & \mathbf{X}_{nl,1}^H & \mathbf{X}_{nl,2}^H \end{bmatrix} = \begin{bmatrix} H & c_2 H & k_3 H \\ & -1 & \\ & & -1 \end{bmatrix} \begin{bmatrix} \mathbf{F} \\ -d\mathbf{Y}_2 \\ -\mathbf{Y}_3 \end{bmatrix} \begin{bmatrix} \mathbf{X}^H & \mathbf{X}_{nl,1}^H & \mathbf{X}_{nl,2}^H \end{bmatrix}$$

$$\underbrace{\begin{bmatrix} S_{XX} & S_{XXnl,1} & S_{XXnl,2} \\ S_{Xnl,1Xnl,1} & S_{Xnl,1Xnl,2} \\ \text{Herm. Mtrx} & S_{Xnl,2Xnl,2} \end{bmatrix}}_{\mathbf{U}} = \begin{bmatrix} H & c_2 H & k_3 H \\ & -1 & \\ & & -1 \end{bmatrix} \begin{bmatrix} S_{FX} & S_{FXnl,1} & S_{FXnl,2} \\ -S_{dY_2X} & -S_{dY_2Xnl,1} & -S_{dY_2Xnl,2} \\ -S_{Y_3X} & -S_{Y_3Xnl,1} & -S_{Y_3Xnl,2} \end{bmatrix} \quad (9.10)$$

$$\underbrace{\begin{bmatrix} S_{XX} & S_{XdX_2} & S_{XX_3} \\ S_{dX_2dX_2} & S_{dX_2X_3} \\ \text{Herm. Mtrx} & S_{X_3X_3} \end{bmatrix}}_{\mathbf{U}} = \begin{bmatrix} H & c_2 H & k_3 H \\ & -1 & \\ & & -1 \end{bmatrix} \begin{bmatrix} S_{FX} & S_{FdX_2} & S_{FX_3} \\ -S_{dY_2X} & -S_{dY_2dX_2} & -S_{dY_2X_3} \\ -S_{Y_3X} & \boxed{-S_{Y_3X_3}} \end{bmatrix} \quad (9.11)$$

Hermitian Sub-matrix

Summary of the modified \mathbf{H}_2 algorithm derivation is analogous to the one presented in section on its twin algorithm – \mathbf{H}_1 –based NIXO. Nevertheless, one additional comment might be worth noting. Namely, the rows of matrices \mathbf{B} and \mathbf{U} (ranging from the 2nd to the last) are almost the same. The rows of matrix \mathbf{B} are rows of \mathbf{U} , but multiplied by -1 . This simple observation can be used to save time spent on algorithm implementation. Using MATLAB notation we could write:

$$\mathbf{B}(2:\text{end}, :) = -\mathbf{U}(2:\text{end},);$$

9.2.2 Nonlinear Identification Through eXtended Outputs Algorithms

\mathbf{H}_1 -Based NIXO method

The NIXO methods seek to form a larger linear system in which frequency independent parameters can be enforced. We begin by right-multiplying Eq. (9.6) by \mathbf{F}^H to obtain Eq. (9.12), which is valid for every individual frequency line. Hence, it is possible to express each of these equations the matrix form shown in Eq. (9.13). Note that the frequency sample number is indicated in the quantities' sub- or superscripts, e.g. $S_{XF}(\Omega_i) = S_{XF}^i$ or $D(\Omega_i) = D_i$.

$$\begin{aligned} D(\Omega) \mathbf{X}\mathbf{F}^H + c_2 d\mathbf{Y}_2\mathbf{F}^H + k_3 \mathbf{Y}_3\mathbf{F}^H &= \mathbf{F}\mathbf{F}^H \\ D(\Omega) S_{XF} + c_2 S_{dY_2F} + k_3 S_{Y_3F} &= S_{FF} \end{aligned} \quad (9.12)$$

$$\underbrace{\begin{bmatrix} S_{XF}^1 & & S_{dY_2F}^1 & S_{Y_3F}^1 \\ & \ddots & \vdots & \vdots \\ & & S_{XF}^n & S_{dY_2F}^n & S_{Y_3F}^n \end{bmatrix}}_{\mathbf{S}_{XF}^{H1}} \begin{bmatrix} D_1 \\ \vdots \\ D_n \\ c_2 \\ k_3 \end{bmatrix} = \underbrace{\begin{bmatrix} S_{FF}^1 \\ \vdots \\ S_{FF}^n \end{bmatrix}}_{\mathbf{S}_{FF}^{H1}}, \quad (9.13)$$

where n stands for the number of frequency samples.

Unfortunately, Eq. (9.13) cannot simply be solved by inverting the matrix on the left because there are more unknowns than equations. To be more precise we obtained $2n$ equations and $2n + p_{damp} + p_{stiff}$ unknowns, since some of the parameters in Eq. (9.13) are complex numbers in general. Naturally, p_{damp} and p_{stiff} represent herein the number of the nonlinear damping and stiffness terms in the equation of motion (9.1) or (9.2). In this particular example $p_{damp} = 1$ and $p_{stiff} = 1$.

If the solution of the underdetermined system of equations exists – it is not unique. This can lead to inaccuracies in the parameter estimation. The main concept behind the new \mathbf{H}_1 Nonlinear Identification through eXtended Outputs (\mathbf{H}_1 -NIXO) estimator is to overcome this indeterminacy by providing input and output data sets collected in vibration tests where the system oscillates at multiple different amplitudes. Such data can be used to increase the number of equations in Eq. (9.13) while keeping the number of unknowns fixed. The idea originates from two observations:

1. Parameters from Eqs. (9.1, 9.2), namely m, c, k as well as c_2 and k_3 , define the mechanical system regardless of the excitation type
2. Nonlinear response of the system occurs when it oscillates at large enough amplitudes. Hence, if the set of equations (9.13) is put together, *separately*, for mechanical system oscillating at, say, *two* different amplitudes – it might be possible (due to the nonlinearity) that these $4n$ *real* equations will be linearly independent. Since the number of *real* unknowns ($2n + p_{damp} + p_{stiff}$) is kept constant - then this new (stacked) system of equations becomes overdetermined and thus will typically have a unique solution.¹

To define the algorithm mathematically, consider the same mechanical system subjected, separately, to multiple forcing functions. This forcing functions have to be chosen such that they cause a response at multiple different displacement magnitudes (e.g. they could be chosen as multiple swept sines of different forcing levels), see Eq. (9.14).

¹ One cannot guarantee that the new equations will be linearly independent of those already provided, but if the nonlinearities are amplitude dependent and sufficiently different amplitudes are used then this is likely to be the case.

$$\begin{cases} m\ddot{x} + c\dot{x} + kx + c_2\dot{x}|\dot{x}| + k_3x^3 = f_I(t) \\ m\ddot{x} + c\dot{x} + kx + c_2\dot{x}|\dot{x}| + k_3x^3 = f_{II}(t) \\ \vdots \\ m\ddot{x} + c\dot{x} + kx + c_2\dot{x}|\dot{x}| + k_3x^3 = f_r(t) \end{cases}, \quad (9.14)$$

where r is the number of different forcing functions used to excite the mechanical system.

If we repeat the derivation presented above in this section we end up with r -times the number of equations presented in Eq. (9.13) and an unchanged number of unknowns, with the final form given in Eq. (9.15).

$$\begin{bmatrix} \mathbf{S}_{XF,I}^{H1} \\ \mathbf{S}_{XF,II}^{H1} \\ \vdots \\ \mathbf{S}_{XF,r}^{H1} \end{bmatrix} \begin{bmatrix} D_1 \\ \vdots \\ D_n \\ c_2 \\ k_3 \end{bmatrix} = \begin{bmatrix} \mathbf{S}_{FF,I}^{H1} \\ \mathbf{S}_{FF,II}^{H1} \\ \vdots \\ \mathbf{S}_{FF,r}^{H1} \end{bmatrix} \quad (9.15)$$

Since some of the parameters in Eq. (9.15) are complex, the estimates of c_2 and k_3 are not guaranteed to be real numbers. To overcome this issue, the real and imaginary parts of the unknowns should be estimated separately so that one can force the nonlinear parameter values to be real. To do so, Eq. (9.15) should be brought to its equivalent form presented in Eq. (9.16). The system of derived equations (9.16) is now overdetermined and the unknown parameters can be estimated by solving a linear least squares problem.

$$\begin{bmatrix} \begin{matrix} Re\{S_{XF,I}^1\} & -Im\{S_{XF,I}^1\} \\ Im\{S_{XF,I}^1\} & Re\{S_{XF,I}^1\} \end{matrix} & \begin{matrix} Re\{S_{dY_2F,I}^1\} & Re\{S_{Y_3F,I}^1\} \\ Im\{S_{dY_2F,I}^1\} & Im\{S_{Y_3F,I}^1\} \end{matrix} \\ \vdots & \vdots \\ \begin{matrix} Re\{S_{XF,I}^n\} & -Im\{S_{XF,I}^n\} \\ Im\{S_{XF,I}^n\} & Re\{S_{XF,I}^n\} \end{matrix} & \begin{matrix} Re\{S_{dY_2F,I}^n\} & Re\{S_{Y_3F,I}^n\} \\ Im\{S_{dY_2F,I}^n\} & Im\{S_{Y_3F,I}^n\} \end{matrix} \\ \vdots & \vdots \\ \begin{matrix} Re\{S_{XF,II}^1\} & -Im\{S_{XF,II}^1\} \\ Im\{S_{XF,II}^1\} & Re\{S_{XF,II}^1\} \end{matrix} & \begin{matrix} Re\{S_{dY_2F,II}^1\} & Re\{S_{Y_3F,II}^1\} \\ Im\{S_{dY_2F,II}^1\} & Im\{S_{Y_3F,II}^1\} \end{matrix} \\ \vdots & \vdots \\ \begin{matrix} Re\{S_{XF,II}^n\} & -Im\{S_{XF,II}^n\} \\ Im\{S_{XF,II}^n\} & Re\{S_{XF,II}^n\} \end{matrix} & \begin{matrix} Re\{S_{dY_2F,II}^n\} & Re\{S_{Y_3F,II}^n\} \\ Im\{S_{dY_2F,II}^n\} & Im\{S_{Y_3F,II}^n\} \end{matrix} \\ \vdots & \vdots \\ \begin{matrix} Re\{S_{XF,r}^1\} & -Im\{S_{XF,r}^1\} \\ Im\{S_{XF,r}^1\} & Re\{S_{XF,r}^1\} \end{matrix} & \begin{matrix} Re\{S_{dY_2F,r}^1\} & Re\{S_{Y_3F,r}^1\} \\ Im\{S_{dY_2F,r}^1\} & Im\{S_{Y_3F,r}^1\} \end{matrix} \\ \vdots & \vdots \\ \begin{matrix} Re\{S_{XF,r}^n\} & -Im\{S_{XF,r}^n\} \\ Im\{S_{XF,r}^n\} & Re\{S_{XF,r}^n\} \end{matrix} & \begin{matrix} Re\{S_{dY_2F,r}^n\} & Re\{S_{Y_3F,r}^n\} \\ Im\{S_{dY_2F,r}^n\} & Im\{S_{Y_3F,r}^n\} \end{matrix} \end{bmatrix} \begin{bmatrix} Re\{D_1\} \\ Im\{D_1\} \\ \vdots \\ Re\{D_n\} \\ Im\{D_n\} \\ c_2 \\ k_3 \end{bmatrix} = \begin{bmatrix} Re\{S_{FF,I}^1\} \\ Im\{S_{FF,I}^1\} \\ \vdots \\ Re\{S_{FF,I}^n\} \\ Im\{S_{FF,I}^n\} \\ \vdots \\ Re\{S_{FF,II}^1\} \\ Im\{S_{FF,II}^1\} \\ \vdots \\ Re\{S_{FF,II}^n\} \\ Im\{S_{FF,II}^n\} \\ \vdots \\ Re\{S_{FF,r}^1\} \\ Im\{S_{FF,r}^1\} \\ \vdots \\ Re\{S_{FF,r}^n\} \\ Im\{S_{FF,r}^n\} \end{bmatrix} \quad (9.16)$$

H₂-Based NIXO Method

To identify the nonlinear mechanical system using the new **H₂ Nonlinear Identification through eXtended Outputs (H₂-NIXO)** estimator, bring Eq. (9.6) to a form of Eq. (9.17) and right-multiply it by matrix $[\mathbf{X}^H \ d\mathbf{Y}_2^H \ \mathbf{Y}_3^H]$.

Equation (9.18) is valid for every individual frequency sample. Thus, it is possible to express each of these equations in a matrix form shown in Eq. (9.19). As before the frequency sample number is indicated in the quantities' sub- or superscripts, e.g. $S_{XX}(\Omega_i) = S_{XX}^i$ or $D(\Omega_i) = D_i$.

$$[D(\Omega) \ c_2 \ k_3] \begin{bmatrix} \mathbf{X} \\ d\mathbf{Y}_2 \\ \mathbf{Y}_3 \end{bmatrix} = \mathbf{F} \quad (9.17)$$

$$[D(\Omega) \ c_2 \ k_3] \begin{bmatrix} \mathbf{X} \\ d\mathbf{Y}_2 \\ \mathbf{Y}_3 \end{bmatrix} [\mathbf{X}^H \ d\mathbf{Y}_2^H \ \mathbf{Y}_3^H] = \mathbf{F} [\mathbf{X}^H \ d\mathbf{Y}_2^H \ \mathbf{Y}_3^H]$$

$$[D(\Omega) \ c_2 \ k_3] \begin{bmatrix} S_{XX} & S_{XdY_2} & S_{XY_3} \\ \text{Herm. Mtrx} & S_{dY_2dY_2} & S_{dY_2Y_3} \\ & & S_{Y_3Y_3} \end{bmatrix} = [S_{FX} \ S_{FdY_2} \ S_{FY_3}] \Big| \Big|^H \implies$$

$$\implies \begin{bmatrix} S_{XX} & S_{XdY_2} & S_{XY_3} \\ \text{Herm. Mtrx} & S_{dY_2dY_2} & S_{dY_2Y_3} \\ & & S_{Y_3Y_3} \end{bmatrix} \begin{bmatrix} D^H(\Omega) \\ c_2 \\ k_3 \end{bmatrix} = \begin{bmatrix} S_{XF} \\ S_{dY_2F} \\ S_{Y_3F} \end{bmatrix} \quad (9.18)$$

$$\begin{bmatrix} S_{XX}^1 & & S_{XdY_2}^1 & S_{XY_3}^1 \\ & \ddots & \vdots & \vdots \\ & & S_{XX}^n & S_{XdY_2}^n & S_{XY_3}^n \\ S_{dY_2X}^1 & & S_{dY_2dY_2}^1 & S_{dY_2Y_3}^1 \\ & \ddots & \vdots & \vdots \\ & & S_{dY_2X}^n & S_{dY_2dY_2}^n & S_{dY_2Y_3}^n \\ S_{Y_3X}^1 & & S_{Y_3dY_2}^1 & S_{Y_3Y_3}^1 \\ & \ddots & \vdots & \vdots \\ & & S_{Y_3X}^n & S_{Y_3dY_2}^n & S_{Y_3Y_3}^n \end{bmatrix} \begin{bmatrix} D_1^H \\ \vdots \\ D_n^H \\ c_2 \\ k_3 \end{bmatrix} = \begin{bmatrix} S_{XF}^1 \\ \vdots \\ S_{XF}^n \\ S_{dY_2F}^1 \\ \vdots \\ S_{dY_2F}^n \\ S_{Y_3F}^1 \\ \vdots \\ S_{Y_3F}^n \end{bmatrix} \quad (9.19)$$

To assure that the nonlinear parameters c_2 and k_3 are estimated as real numbers, the problem stated in Eq. (9.19) should be separated into real and imaginary parts, as illustrated in the previous section. As with the prior algorithm, with **H₂-NIXO** we then obtain a linear least squares problem to solve to estimate the nonlinear system parameters.

9.2.3 Nonlinear Identification Through eXtended Outputs Algorithms with Linear Data Provided

Two new nonlinear estimators are presented in the previous section. In addition to finding the values of the parameters describing the nonlinearities, the algorithms also return estimates of the linear Frequency Response Function (FRF). Since

linear experimental vibration analysis can be considered today as well-established, the linear FRF values could possibly be treated as known (i.e. they could be obtained in a separate test where the structure vibrates at low enough amplitude). With this assumption, we could modify the final equations obtained in the previous sections by bringing the FRF terms to the RHS vector of known values. This simple observation reduces the number of unknowns – now the only unknown parameters are c_2 and k_3 . This also significantly reduces sizes of matrices in Eqs. (9.15), (9.16) and (9.19), which makes the algorithms more efficient from the computational viewpoint. This is elaborated below.

H₁-NIXO with Linear Data Provided

If the linear Frequency Response Function is known then Eq. (9.15) can be brought to the form shown in Eq. (9.20) where quantities corresponding to D_j 's are now placed in the RHS vector of known values. Note also that collecting data from multiple vibration tests is no longer needed. The system of equations (9.20) is most likely overdetermined, since the number of frequency samples ($n \sim 1000$) is usually larger than the number of unknown polynomial terms ($p_{dapmp}, p_{stiff} \sim 10$). In case of $p_{dapmp} + p_{stiff} > n$ (which is possible but unlikely), then the number of equations can be populated by providing data collected in vibration tests where the mechanical system oscillates at multiple different amplitudes (as explained in one of the previous sections).

$$\underbrace{\begin{bmatrix} S_{dY_2F}^1 & S_{Y_3F}^1 \\ \vdots & \vdots \\ S_{dY_2F}^n & S_{Y_3F}^n \end{bmatrix}}_{\mathbf{A}_1} \begin{bmatrix} c_2 \\ k_3 \end{bmatrix} = \underbrace{\begin{bmatrix} S_{FF}^1 - S_{XF}^1 D_1 \\ \vdots \\ S_{FF}^n - S_{XF}^n D_n \end{bmatrix}}_{\mathbf{b}_1} \quad (9.20)$$

To enforce the algorithm to estimate the nonlinear parameters c_2 and k_3 as real numbers, Eq. (9.20) should be brought to its equivalent real form shown in Eq. (9.21), where matrix \mathbf{A}_1 and vector \mathbf{b}_1 are defined in Eq. (9.20).

$$\begin{bmatrix} Re\{\mathbf{A}_1\} \\ Im\{\mathbf{A}_1\} \end{bmatrix} \begin{bmatrix} c_2 \\ k_3 \end{bmatrix} = \begin{bmatrix} Re\{\mathbf{b}_1\} \\ Im\{\mathbf{b}_1\} \end{bmatrix} \quad (9.21)$$

H₂-NIXO with Linear Data Provided

The derivation for this algorithm is analogous to that in the previous section. If the linear Frequency Response Function is known then Eq. (9.19) can be brought to the form shown in Eq. (9.22) where quantities corresponding to D_j 's are now placed in the vector on the RHS. The system of equations (9.22) is always overdetermined.

$$\underbrace{\begin{bmatrix} S_{XdY_2}^1 & S_{XY_3}^1 \\ \vdots & \vdots \\ S_{XdY_2}^n & S_{XY_3}^n \\ S_{dY_2dY_2}^1 & S_{dY_2Y_3}^1 \\ \vdots & \vdots \\ S_{dY_2dY_2}^n & S_{dY_2Y_3}^n \\ S_{Y_3dY_2}^1 & S_{Y_3Y_3}^1 \\ \vdots & \vdots \\ S_{Y_3dY_2}^n & S_{Y_3Y_3}^n \end{bmatrix}}_{\mathbf{A}_2} \begin{bmatrix} c_2 \\ k_3 \end{bmatrix} = \underbrace{\begin{bmatrix} S_{XF}^1 - S_{XX}^1 D_1^H \\ \vdots \\ S_{XF}^n - S_{XX}^n D_n^H \\ S_{dY_2F}^1 - S_{dY_2X}^1 D_1^H \\ \vdots \\ S_{dY_2F}^n - S_{dY_2X}^n D_n^H \\ S_{Y_3F}^1 - S_{Y_3X}^1 D_1^H \\ \vdots \\ S_{Y_3F}^n - S_{Y_3X}^n D_n^H \end{bmatrix}}_{\mathbf{b}_2} \quad (9.22)$$

To enforce the algorithm to estimate the nonlinear parameters c_2 and k_3 as real numbers, Eq. (9.22) should be brought to its equivalent form presented in Eq. (9.21), where \mathbf{A}_1 and \mathbf{b}_1 are obviously replaced with \mathbf{A}_2 and \mathbf{b}_2 , respectively. Matrix \mathbf{A}_2 and vector \mathbf{b}_2 are defined in Eq. (9.22).

9.3 Case Study

9.3.1 Mechanical System Description

The algorithms are evaluated using input and output signals collected during simulated experiments of a mechanical system described by the Duffing equation (9.23). Values for the parameters were proposed in [1] and are given in Table 9.1. Auto- and cross-spectra in every case study presented are obtained by applying 25-second-long Hanning windows with 51% of overlap.

$$m\ddot{x} + c\dot{x} + kx + k_3x^3 = f(t) \quad (9.23)$$

9.3.2 Forcing Signals Description

Input and output signals are generated by exciting the structure with two types of forcing functions:

Swept Cosine Forcing Signal

$$f(t) = F \cos(\Omega(t) t) \quad \Omega(t) = \Omega_{st} + \frac{\Omega_{end} - \Omega_{st}}{t_{end} - t_{st}}(t - t_{st}) \quad t \in [t_{st}, t_{end}] \quad (9.24)$$

Broad-Band Burst Random Forcing Signal

$$f(t) = F \text{BurstRand}(t) \quad t \in [t_{st}, t_{end}] \quad (9.25)$$

9.3.3 Case Study 1: System Identification with Model Function Known À Priori

The NIXO and NIFO methods are first used to identify the mechanical system (9.23) with the model function known beforehand. Forcing signals (both swept cosine and burst random) are defined in Tables 9.2 and 9.3. The results obtained are presented in Tables 9.4, 9.5, 9.6, and 9.7 and discussed briefly at the end of this subsection.

9.3.4 Comments to Case Study 1

1. In the case studies explored here, the NIFO methods failed to estimate the linear frequency response function when the input signal was swept cosine. However, if the system was excited with a burst random signal then NIFO estimated the FRF of the underlying linear system to a satisfactory extent. The NIXO methods, on the other hand, succeed in finding accurate enough estimates of the linear FRF regardless of the excitation type.

Table 9.1 Parameters describing SDOF mechanical system with cubic stiffness nonlinearity

m [kg]	c [$\frac{\text{Ns}}{\text{m}}$]	k [$\frac{\text{N}}{\text{m}}$]	k_3 [$\frac{\text{N}}{\text{m}^3}$]
1	4	10^3	10^5

Table 9.2 Values of parameters characteristic to swept cosine and burst random forcing functions

Swept Cosine:	Ω_{st} [Hz]	Ω_{end} [Hz]	t_{st} [s]	t_{end} [s]
	0.01	15	0	1500
Burst Random:	t_{st} [s]	t_{end} [s]	Δt [s]	Burst Start Burst End
	0	512.5	0.01	0% 100%

Table 9.3 Values of parameters shared by swept cosine and burst random forcing functions. Force amplitudes expressed in newtons, frequencies expressed in hertz

Signal Type	F_I or F	F_{II}	DF	FO	Ω_1^{filt}	Ω_2^{filt}	Ω_1^{spect}	Ω_2^{spect}	I/O Signals	Results
Swept Cosine	5.0	0.1	–	–	–	–	0.3	15	Table 9.4	Table 9.5
Burst Random	10.0	0.1	2	8	0.3	15	0.3	15	Table 9.6	Table 9.7

DF – Decimation Factor

FO – Butterworth Filter Order

Ω^{filt} – cut-off frequency; Ω_1^{filt} and Ω_2^{filt} are lower and upper cut-off frequencies, respectively

Ω^{spect} – auto- and cross-spectra are computed for frequency range (Ω_1^{spect} , Ω_2^{spect})

2. The NIFO algorithms returned accurate k_3 values away from the resonant frequency, while in the vicinity of the linear resonance their estimations were wildly erroneous. The NIXO methods return cubic stiffness parameter as a single *frequency-independent* value. Every NIXO algorithm succeeded in estimating k_3 to a satisfactory extent except for \mathbf{H}_1 -NIXO-LDP. However, the accuracy of that method can be increased if data for higher excitation amplitudes is included (as shown in [5]).
3. It is worth noting that (for the NIXO and NIXO-LDP algorithms) the real part of k_3 found as a complex number matches the value of the cubic nonlinear parameter estimated as a real number. Moreover, the real part of k_3 is usually an accurate estimate when the imaginary part is found as a much smaller number. For example, the results obtained with the NIFO algorithms (with swept cosine used as the excitation) show that for off-resonant frequencies $Im\{k_3\}$ was much smaller than $Re\{k_3\}$. Thus, when an accurate parameter was found it typically was predominantly real. Additionally, this observations can be used as one of the decision criteria in the black-box system identification.

9.3.5 Case Study 2(a): Black-Box System Identification – Impact of the Polynomial Degree

In this section, we propose a strategy to utilize the NIXO approaches to identify a single degree of freedom mechanical system of unknown nonlinearity. The algorithms are tested to estimate the parameters of Eq. (9.23) presented in Table 9.1. The model function used in the estimation process is given in Eq. (9.26).

Multiple tests, with different values of polynomial degree p and unknown k_i parameters ($i \in \{2, \dots, p\}$), were conducted. A swept cosine forcing function, defined in Tables 9.2, 9.3 and presented in Table 9.4, was used as the input signal. The results obtained for the case where $p = 6$ are presented in Table 9.8.

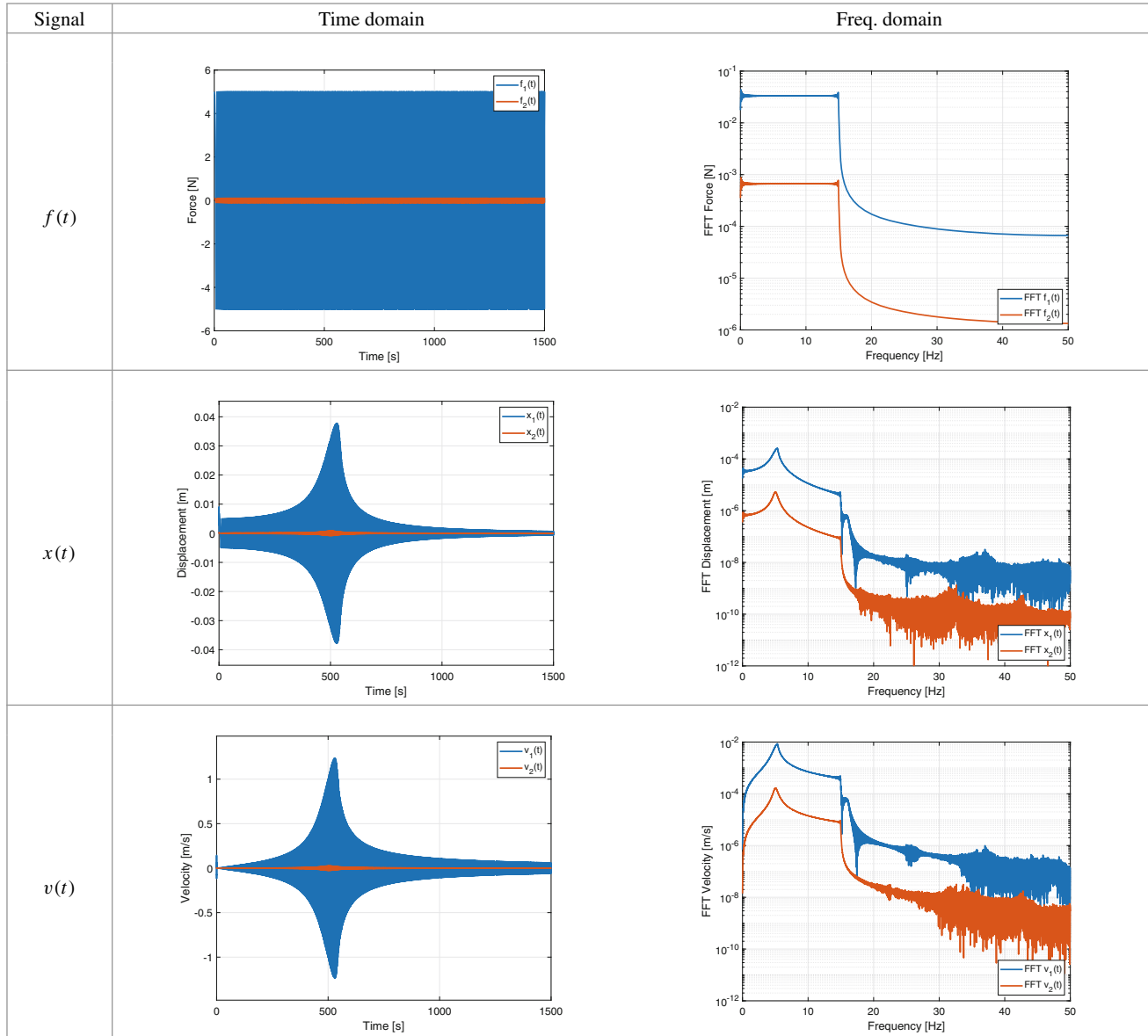
$$m\ddot{x} + c\dot{x} + kx + k_2x|x| + k_3x^3 + \dots + k_px|x|^{p-1} = f(t) \quad (9.26)$$

The outcomes from this case study, obtained using NIXO methods, show that the cubic nonlinearity is most likely dominant in the mechanical system's response. Note that the cubic nonlinear stiffness term turned out to be the most significant for the identification with a polynomial of sixth degree (see e.g. the last column in Table 9.8). The results obtained with NIFO seem to be inconclusive.

Black-box system identification conducted for the remaining values of p ($p \in \{2, 3, \dots, 9\}/\{6\}$) is presented in [6]. It shows similar outcomes for the identification with a polynomial of up to a sixth degree. The analyses conducted for polynomials of degree higher than 6 gave unclear results for both NIXO and NIFO algorithms. Hence, this approach would be limited to smaller numbers of polynomial terms. To explore this further, a second analysis was conducted. This time, the model function consisted of a cubic term and one additional nonlinear stiffness term only. The description and results obtained in this case study are presented in the next subsection.

Table 9.4 Case study with Swept Cosine used as a forcing function. Input/Output Signals

Signal Type	F_I or F	F_{II}	DF	FO	Ω_1^{filt}	Ω_2^{filt}	Ω_1^{spect}	Ω_2^{spect}
Swept Cosine	5.000	0.100	–	–	–	–	0.3	15



9.3.6 Case Study 2(b): Black-box System Identification – Impact of the Additional Polynomial Term

In the previous section, the results obtained correctly revealed that the stiffness nonlinearity in the mechanical system was most likely cubic. That term was dominant when the model function was a polynomial of up to sixth degree. However, when the model function (9.26) was assumed to be a polynomial of higher degree, the results did not give any insight into which nonlinear terms were dominant and which terms could be eliminated from the model function (for details see [6]).

In this section, the results obtained using Eq. (9.27) as a model function are presented. This function assumes that the nonlinearity in the system consists of a cubic term and one additional term only.

$$m\ddot{x} + c\dot{x} + kx + k_3x^3 + k_r x|x|^{p-1} = f(t) \tag{9.27}$$

Table 9.5 Case study with Swept Cosine used as a forcing function. Results

Signal Type	F_I or F	F_{II}	DF	FO	Ω_1^{filt}	Ω_2^{filt}	Ω_1^{spect}	Ω_2^{spect}
Swept Cosine	5.000	0.100	—	—	—	—	0.3	15

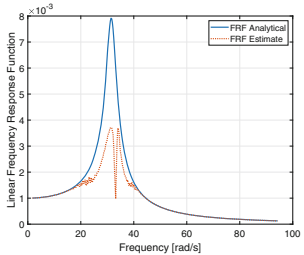
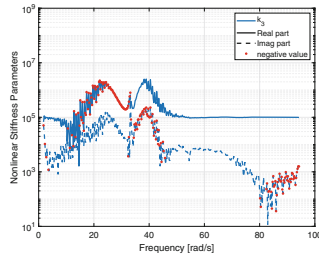
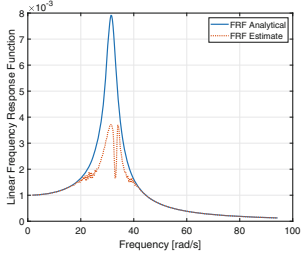
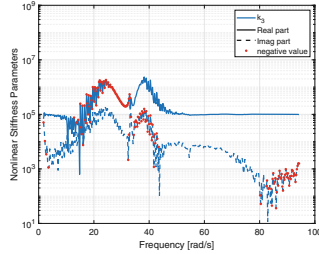
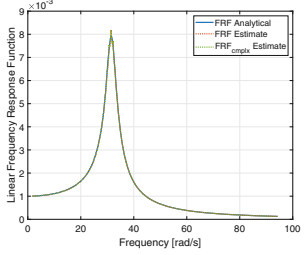
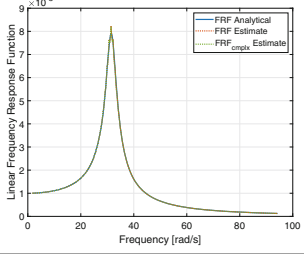
Method	Linear FRF estimate	Nonlin. param. estimates (rel. error)
H_1 -NIFO		
H_2 -NIFO		
H_1 -NIXO		$k_3 = 9.917e + 04$ (0.83%) $k_{3,complex} = 9.917e + 04 - i2.893e + 02$
H_2 -NIXO		$k_3 = 1.040e + 05$ (4.01%) $k_{3,complex} = 1.040e + 05 - i5.453e + 02$
H_1 -NIXO with lin. data provided	×	$k_3 = 9.991e + 04$ (0.09%) $k_{3,complex} = 9.991e + 04 + i5.840e + 02$
H_2 -NIXO with lin. data provided	×	$k_3 = 9.981e + 04$ (0.19%) $k_{3,complex} = 9.981e + 04 - i4.633e + 01$

Table 9.6 Case study with Burst Random forcing function. Input/Output Signals

Signal Type	F_I or F	F_{II}	DF	FO	Ω_1^{filt}	Ω_2^{filt}	Ω_1^{spect}	Ω_2^{spect}
Burst Random	5.000	0.100	2	8	0.3	15	0.3	15

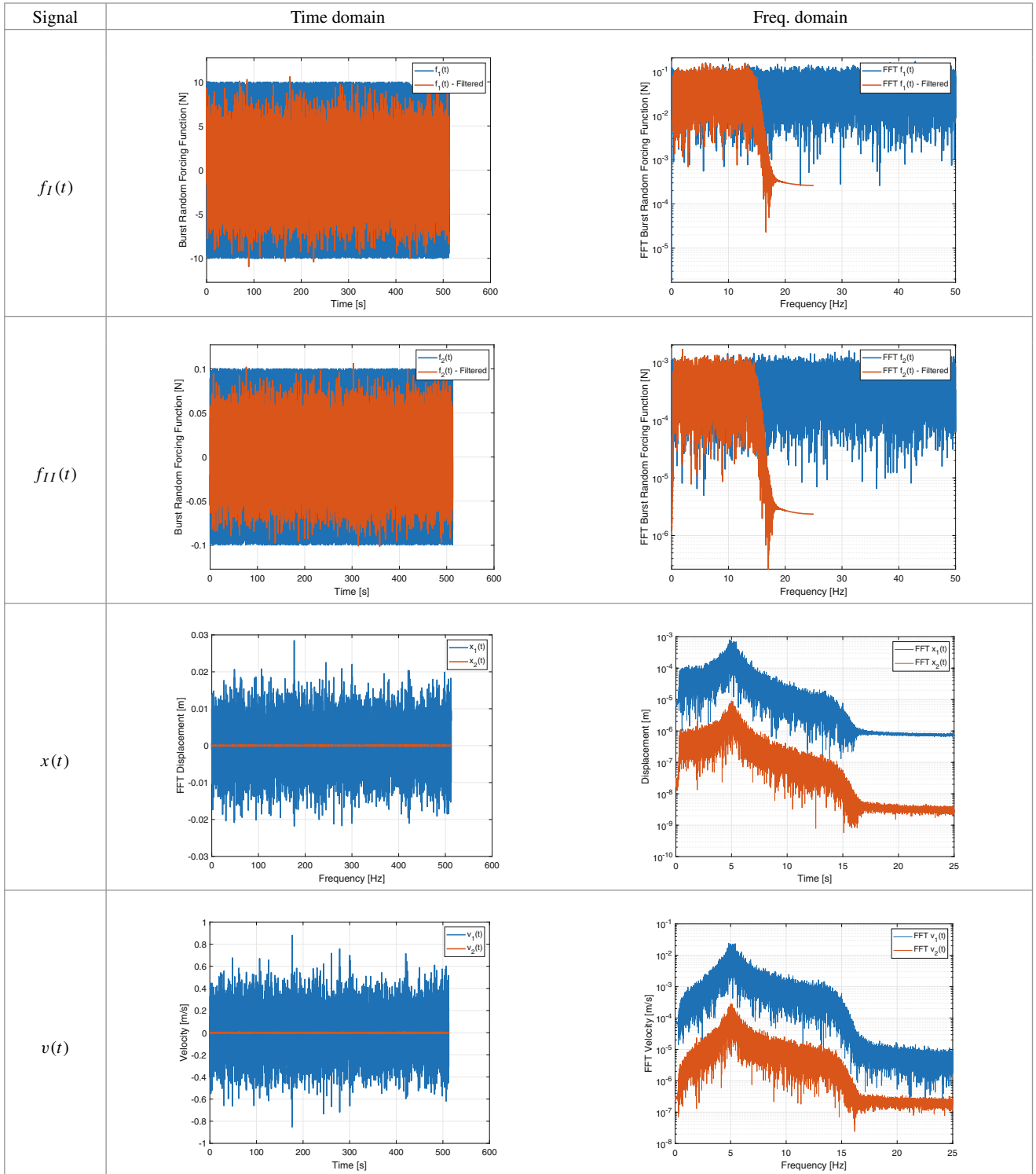
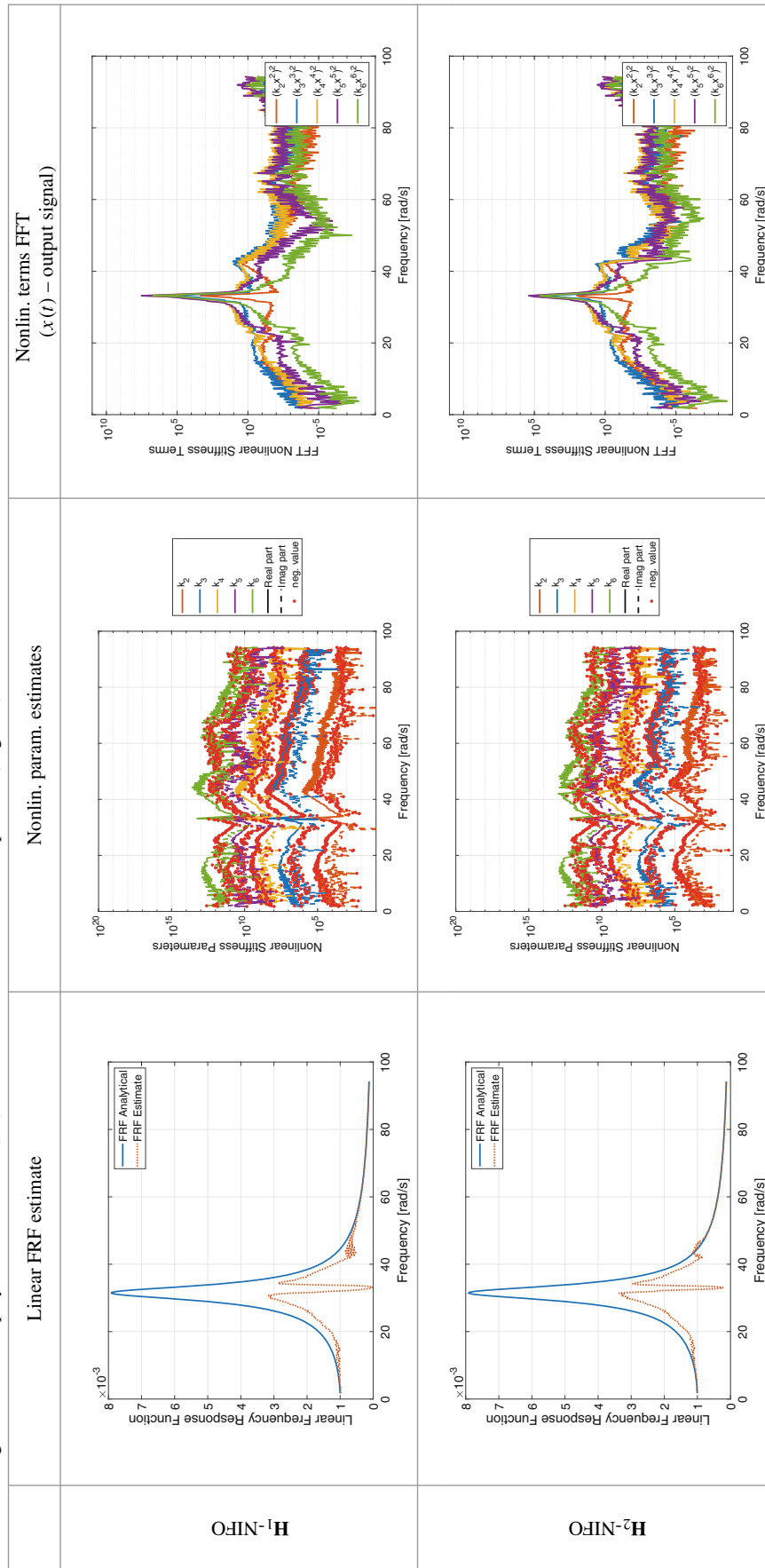


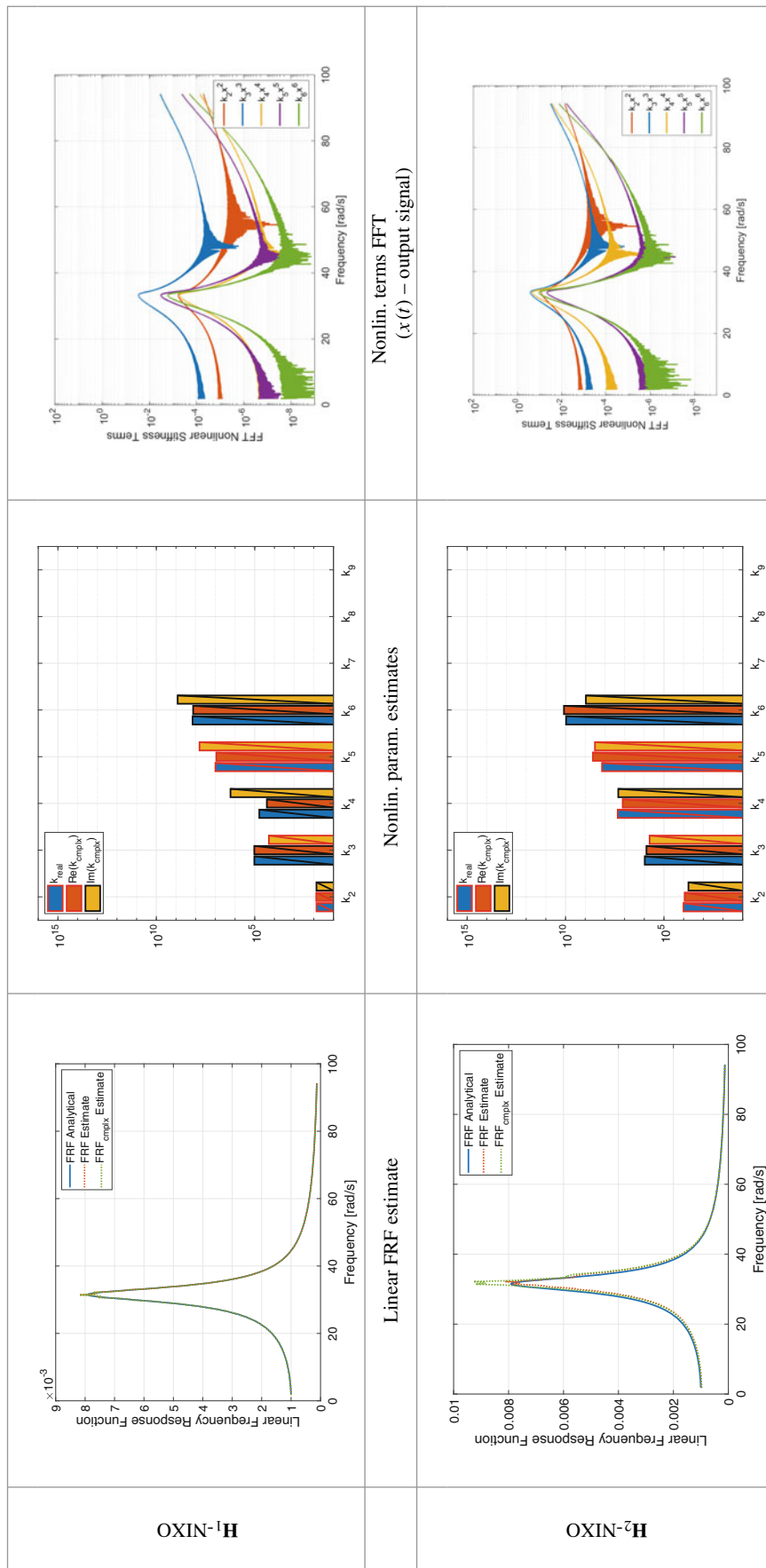
Table 9.7 Case study with Burst Random forcing function. Results

Signal Type	F_I or F	F_{II}	DF	FO	Ω_1^{filt}	Ω_2^{filt}	Ω_1^{spect}	Ω_2^{spect}
Burst Random	5.000	0.100	2	8	0.3	15	0.3	15

Method	Linear FRF estimate	Nonlin. param. estimates (rel. error)
H_1 -NIFO		
H_2 -NIFO		
H_1 -NIXO		$k_3 = 9.914e + 04$ (0.86%) $k_{3,cmplx} = 9.914e + 04 + i1.813e + 03$
H_2 -NIXO		$k_3 = 1.047e + 05$ (4.73%) $k_{3,cmplx} = 1.047e + 05 + i5.614e + 03$
H_1 -NIXO with lin. data provided	×	$k_3 = 4.681e + 04$ (53.19%) $k_{3,cmplx} = 4.681e + 04 + i4.682e + 04$
H_2 -NIXO with lin. data provided	×	$k_3 = 9.880e + 04$ (1.20%) $k_{3,cmplx} = 9.880e + 04 + i4.117e + 04$

Table 9.8 Degree of stiffness polynomial: 2. Black (red) border around the bars indicates positive (negative) value





(continued)

Table 9.8 (continued)

H_1 -NIXO WLDP	×		
H_2 -NIXO WLDP	×		

The mechanical system is again subjected to the swept cosine excitation defined previously. Table 9.9 shows the outcomes from the analysis for additional term power $p = 9$. Results obtained for the remaining powers, namely $p \in \{7, 8\}$ can be found in [6].

9.3.7 Comments to Case Study 2

A strategy to identify an SDOF mechanical system with unknown nonlinearity using NIXO methods was presented in this section. A few comments on the results obtained are enumerated below.

1. In the first stage of the system identification process, NIXO methods using Eq. (9.26) as a model function were used. The outcomes from this stage showed that a cubic nonlinear stiffness was present in the mechanical system. Additionally, the nonlinear stiffness terms of powers lower than or equal to 6 were discovered to be less significant in the system's response.
2. In the second stage of the proposed strategy, NIXO methods used the model function presented in Eq. (9.27). The results from this stage showed that the cubic nonlinearity was also dominant over nonlinearities of higher powers.
3. NIFO methods did not work well when the mechanical system was excited with a swept cosine function. However, this type of forcing can be used as an input signal for the system identification based on the NIXO algorithms. Time did not allow exploring the use of broadband random forcing with NIFO, although the examples in the previous section showed that NIFO was more satisfactory in that case, typically similar to the NIXO method.

9.4 Conclusion and Future Work

This paper presented several new methods that can be successfully used in the estimation of the linear FRF as well as frequency-independent nonlinear parameters of a nonlinear system. The methods were first used in the system identification of a single degree of freedom system with the nonlinearity known a priori. Additionally, a black-box identification scheme utilizing the NIXO approaches was presented. Results were compared to those obtained using NIFO methods, which are popular approaches for nonlinear system identification.

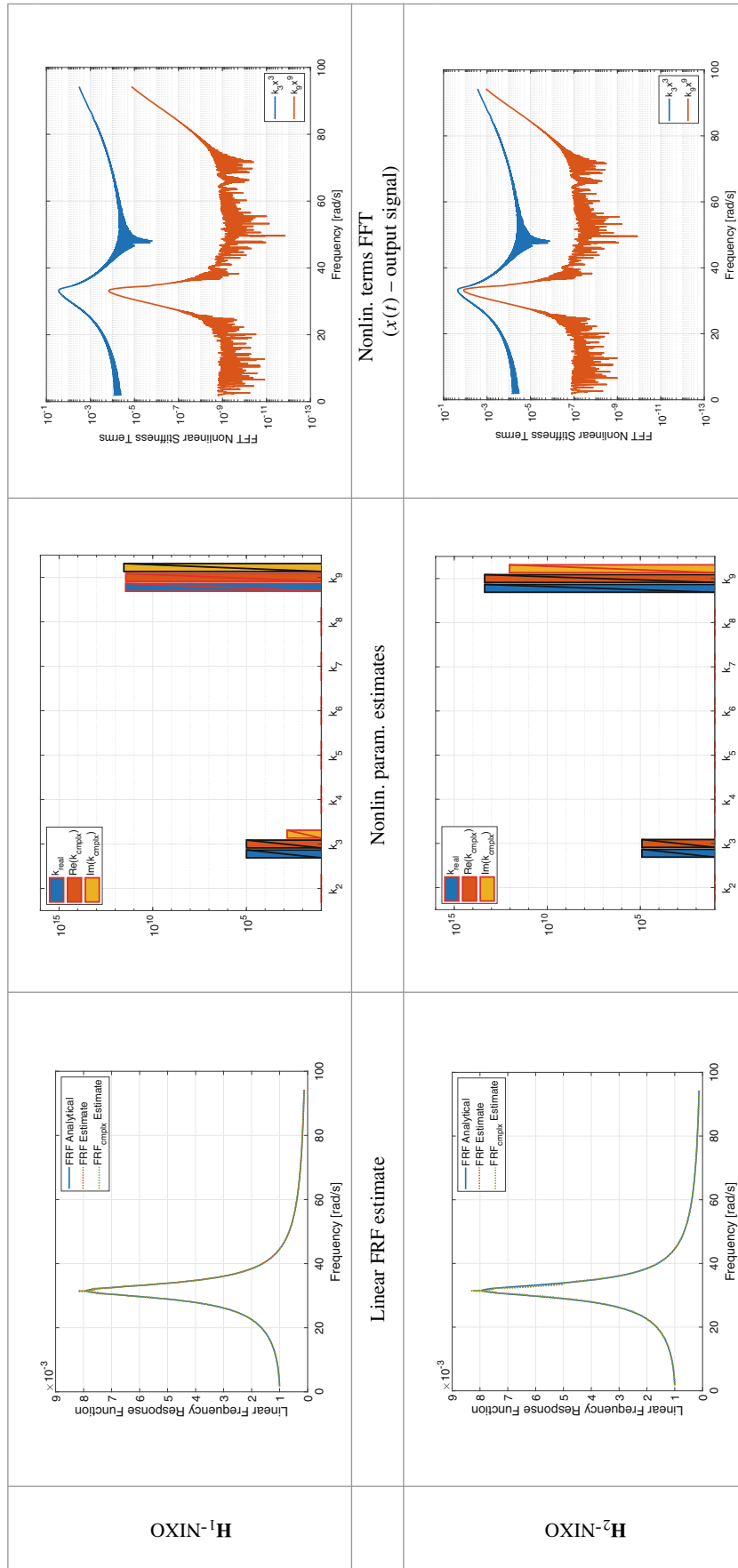
Based on the outcomes presented in this work, it can be said that the NIXO algorithms show certain advantages over the NIFO approaches. First of all, the NIXO-based methods are not input-signal-sensitive. In the case studies used here, the NIFO algorithms required the mechanical system to be excited with a random forcing function. Furthermore, when considering black-box identification, NIXO methods turned out to be more effective than NIFO. The results returned by the former family of methods clearly showed that the cubic nonlinearity was dominant in the system response. The outcomes from the NIFO black-box identification did not show which nonlinear stiffness term was dominant in the system's response. Hence, they did not allow for making a confident decision on which of the nonlinear stiffness terms could be eliminated from the model function.

In a future work, both NIXO methods will be employed experimentally to identify the physical parameters describing the nonlinearity of a 3D printed beams for oscillations near their first vibration modes. The results will be then used to compute the NNM backbone curve and compared to the solution obtained by another estimation algorithm and data collected using the well-established testing approach.

Acknowledgments This work was supported by the Air Force Office of Scientific Research, Award # FA9550-17-1-0009, under the Multi-Scale Structural Mechanics and Prognosis program managed by Dr. Jaimie Tiley. The authors would also like to thank Joseph Hollkamp from the Air Force Research Laboratory's Structural Sciences Center, for his insightful comments and suggesting several improvements to this work.

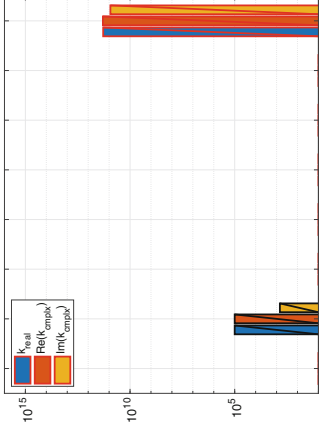
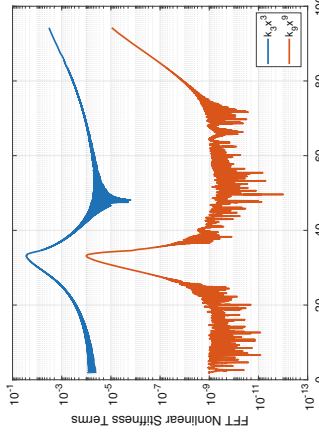
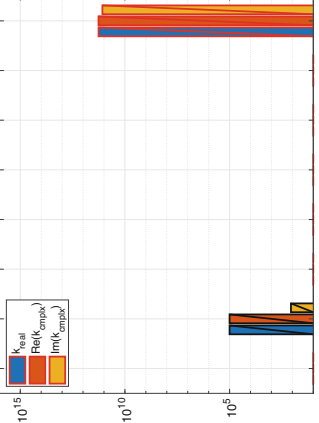
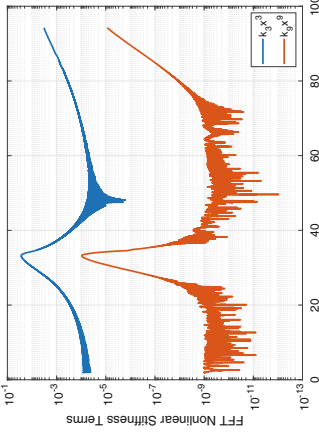
Table 9.9 Additional nonlinear term degree: $r = 2$. Black (red) border around the bars indicates positive (negative) value

	Linear FRF estimate	Nonlin. param. estimates	Nonlin. terms FFT ($x(t) - \text{output signal}$)
H_1 -NIFO			
H_2 -NIFO			



(continued)

Table 9.9 (continued)

<p>H_1-NIXO WLPD</p>	<p>×</p>		
<p>H_2-NIXO WLPD</p>	<p>×</p>		

References

1. Adams, D., Allemang, R.: A frequency domain method for estimating the parameters of a non-linear structural dynamic model through feedback. *Mech. Syst. Signal Process.* **14**(4), 637–656 (2000)
2. Haroon, M., Adams, D.E.: A modified H_2 algorithm for improved frequency response function and nonlinear parameter estimation. *J. Sound Vib.* **320**(3), 822–837 (2009)
3. Kerschen, G., Lenaerts, V., Golinval, J.-C.: Identification of a continuous structure with a geometrical non-linearity. Part I: conditioned reverse path method. *J. Sound Vib.* **262**(4), 889–906 (2003)
4. Noël, J., Kerschen, G.: Nonlinear system identification in structural dynamics: 10 more years of progress. *Mech. Syst. Signal Process.* **83**, 2–35 (2017)
5. Kwarta, M., Allen, M.S.: Derivation, Validation and Comparison of the NIFO and NIXO Algorithms for SDOF Systems. Available at https://sd.engr.wisc.edu/wp-content/uploads/sites/709/2019/10/NIXO_report_01_b.pdf (unpublished). Tech. rep. (2019)
6. Kwarta, M., Allen, M.S.: NIFO and NIXO Estimators for SDOF Systems: Impact of the Output Terms Choice on the Results. Available at https://sd.engr.wisc.edu/wp-content/uploads/sites/709/2019/10/NIXO_report_02.pdf (unpublished). Tech. rep. (2019)

Biography

Michael Kwarta is a graduate student in Mechanical Engineering at the University of Wisconsin – Madison. His recent research focuses on proposing new or improving existing methods used in nonlinear system identification.



Chapter 10

System Characterization and Design Using Mechanical Impedance Representations

Alexandra C. Karlicek, Brandon J. Dilworth, and J. Gregory McDaniel

Abstract Vibration testing is a critical aspect in the qualification of fieldable hardware as dynamic environments are typically design drivers, especially in the case of airborne and space-borne systems. However, when testing components or small subassemblies, it is challenging to match the boundary conditions presented by the true installation interface, which can greatly influence the outcome and inferences of a vibration test campaign. Strategically designed test fixtures, which emulate the impedance of the next level of assembly, can more effectively emulate the boundary conditions present in the fielded system. The objective of this paper is to present an approach to impedance matched fixture design, which requires matching both the transfer and output impedances of the true system. The analyses presented within this paper focus on techniques for matching the drive point impedance, which requires correct solutions for both the transfer and output impedances. The impedance matching approach will utilize undamped lumped parameter systems and highlight the advantages of characterizing the high and low frequency behavior. Additionally, closed form representations of these high and low frequency characteristics will be presented for easily realizable 1D lumped parameter systems.

Keywords Vibration testing · Impedance-matching · Mechanical impedance · Fixture design · System realizability

10.1 Introduction

Component level vibration qualification testing is typically conducted in three mutually orthogonal axes on a vibration shaker table. The input environment is normally specified as base driven input whose amplitudes are derived based on various dynamic excitation sources that are applicable to the environment in which the unit under test will operate. Common test practices dictate that the component test fixture shall provide a rigid boundary condition, and thus should not possess dynamics within the frequency bandwidth that will be tested. Although this design approach may minimize the potential for modal coupling between the test fixture and unit under test, it ultimately presents an unrealistic dynamic interface. An illustration comparing the system environment and the laboratory excitation environment is shown in Fig. 10.1. The image on the far left represents the true dynamic environment, where velocity at the base (v_1) is not equal to the velocity at the interface (v_2). On the contrary, in the test configuration $v_1 \approx v_2$ due to the aforementioned practice of designing rigid fixtures.

The issues encountered as a result of this unrealistic boundary condition include the potential for both under-testing and over-testing across the excitation bandwidth. This phenomenon has been widely recognized in the environmental testing community and is often referred to as the “impedance mismatch problem.” Various strategies for mitigating these issues have been proposed which include testing techniques as well as fixture design. Test techniques include Scharton’s force limited vibration testing [1] and Impedance Matched Multi-Axis Testing (IMMAT), as introduced by Daborn et al. [2]. Concepts for fixture design include Scharton’s [3] multimodal design approach as well as the “N + 1” style test fixtures as investigated by Edwards [4] and Hall [5].

A. C. Karlicek (✉) · B. J. Dilworth
MIT Lincoln Laboratory, Lexington, MA, USA
e-mail: alexandra.karlicek@ll.mit.edu; brandon.dilworth@ll.mit.edu

J. G. McDaniel
Department of Mechanical Engineering, Boston University, Boston, MA, USA
e-mail: jgm@bu.edu

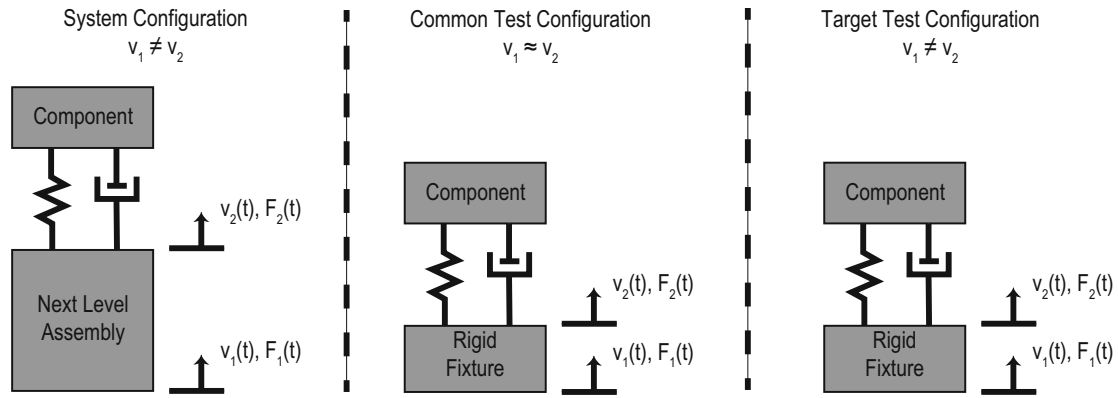


Fig. 10.1 Illustration of system and component test configurations detailing relevant interfaces

10.2 Statement

DISTRIBUTION STATEMENT A. Approved for public release. Distribution is unlimited.

This material is based upon work supported under Air Force Contract No. FA8702-15-D-0001. Any opinions, findings, conclusions or recommendations expressed in this material are those of the author(s) and do not necessarily reflect the views of the U.S. Air Force.

10.3 Background

Generically speaking, mechanical impedance refers to the ratio of the excitation force to the velocity response. An expression for the impedance of a system can be derived from the spatial model of the equation of motion for a viscously damped system, which is described by Eq. (10.1) below, where $[M]$, $[C]$, and $[K]$ are $N \times N$ mass, damping, and stiffness matrices, respectively [6].

$$[M] \{\ddot{x}\} + [C] \{\dot{x}\} + [K] \{x\} = \{F(t)\} \quad (10.1)$$

Note that here N refers to the number of system equations, or number of degrees of freedom, of the system. Additionally, $\{\ddot{x}\}$, $\{\dot{x}\}$, and $\{x\}$ are $N \times 1$ vectors of time variant acceleration, velocity, and displacement responses while $\{F\}$ is an $N \times 1$ vector of time varying external excitation forces [6]. If $\{F(t)\} = \{\tilde{F}\} e^{i\omega t}$, then the particular solution to (10.1) can be represented by a solution of the form $\{x(t)\} = \{\tilde{x}\} e^{i\omega t}$, where \tilde{x} and \tilde{F} represent complex amplitudes [6].

$$\left[(i\omega)^2 [M] + i\omega [C] + [K] \right] \{\tilde{x}\} e^{i\omega t} = \{\tilde{F}\} e^{i\omega t} \quad (10.2)$$

This result can be rewritten in terms of the complex valued dynamic stiffness matrix, $[D(\omega)]$, which is equivalent to the ratio of force to displacement.

$$[D(\omega)] \{\tilde{x}(\omega)\} = \{\tilde{F}(\omega)\} \quad (10.3)$$

When the left hand side of (10.3) is rewritten in terms of velocity, the impedance matrix $[Z(\omega)]$ is found to be $[D(\omega)]/(i\omega)$.

$$\frac{[D(\omega)]}{i\omega} i\omega \{\tilde{x}(\omega)\} = \{\tilde{F}(\omega)\} \equiv [Z(\omega)] \{\tilde{V}(\omega)\} = \{\tilde{F}(\omega)\} \quad (10.4)$$

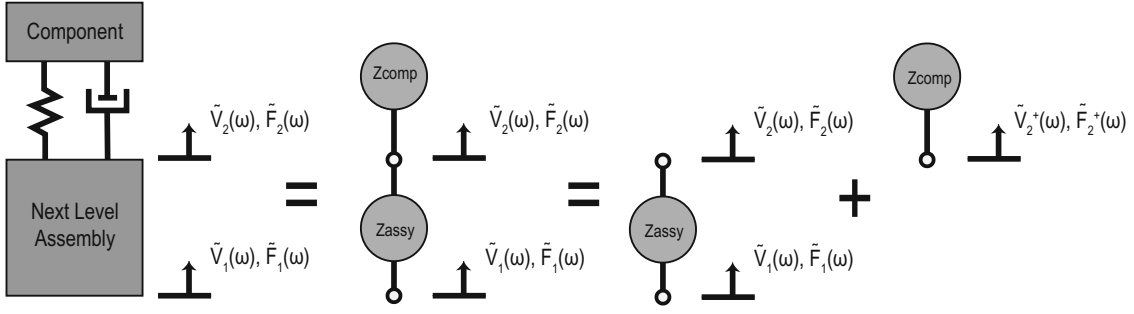


Fig. 10.2 Illustration of system configuration for impedance derivations

As the stated objective is to better emulate the true dynamic environment, then a methodology must be developed such that relative velocities v_2/v_1 presented by the system configuration, illustrated in the leftmost sketch of Fig. 10.1, match those resulting from the impedance equivalent fixture depicted in the rightmost sketch of Fig. 10.1.

First, the system is broken into lumped element representations of the assembly and component, which includes the mounting elements. This representation of the system is depicted in Fig. 10.2, where the assembly is denoted by Z_{assy} and the component is denoted by Z_{comp} . Here the assembly can be thought of as a two port mechanical system where the input, output, and transfer impedances must be considered while the component has just one impedance to be considered.

For the assembly, Z_{11} is the input impedance with \tilde{V}_2 set to zero and Z_{22} is the output impedance with \tilde{V}_1 set to zero. The reverse transfer impedance Z_{12} is \tilde{F}_1/\tilde{V}_2 , where the input is clamped and \tilde{F}_1 is the force required to maintain \tilde{V}_1 equal to zero. Similarly, Z_{21} is the forward transfer impedance \tilde{F}_2/\tilde{V}_1 and \tilde{F}_2 is the force required to clamp the output. These relationships can be represented in matrix format as shown in (10.5).

$$\begin{Bmatrix} \tilde{F}_1 \\ \tilde{F}_2 \end{Bmatrix} = \begin{bmatrix} Z_{11} & Z_{12} \\ Z_{21} & Z_{22} \end{bmatrix} \begin{Bmatrix} \tilde{V}_1 \\ \tilde{V}_2 \end{Bmatrix} \quad (10.5)$$

The impedance of the component, as depicted in the rightmost sketch of Fig. 10.2 is simply $\tilde{F}_2^+/\tilde{V}_2^+$. When the component is connected to the next level assembly there is no external forcing applied at the interface and thus $\tilde{F}_2 = -\tilde{F}_2^+$ and $\tilde{V}_2 = \tilde{V}_2^+$. These relationships result in the system Z_{22} being replaced by $Z_{22} + Z_2$ in (10.5). Again, due to continuity at the interface between the component and assembly the ratio of \tilde{V}_2/\tilde{V}_1 is represented by the ratio in (10.6).

$$\frac{\tilde{V}_2}{\tilde{V}_1} = \frac{Z_{21}}{Z_{22} + Z_2} \quad (10.6)$$

Thus, in order to satisfy the condition that the dynamic behavior of the fixture match that of the higher level assembly both the output impedance Z_{22} and the transfer impedance Z_{21} must be matched. The focus of this paper will be on matching the drive point impedance, Z_d , of the system, as this solution requires all four elements of the impedance matrix in Eq. (10.5) to be properly identified.

Assuming that the force is applied at a single point, $\{\tilde{F}(\omega)\}$ has only one non-zero element. In other words $\{\tilde{F}(\omega)\} = \tilde{F}_d(\omega)\{e_n\}$, where $\{e_n\}$ is a vector whose only non-zero element represents the n th degree of freedom at which the driving force is applied. When this is substituted into (10.4) the n th element of the velocity vector $\{\tilde{V}(\omega)\}_n$ is the drive point velocity, \tilde{V}_d , and can be written as indicated in (10.7).

$$\{\tilde{V}(\omega)\}_n \equiv \tilde{V}_d(\omega) = \left([Z(\omega)]^{-1}\right)_{nn} \tilde{F}_d(\omega) \quad (10.7)$$

From (10.7) the drive point impedance can be expressed as shown in (10.8).

$$Z_d(\omega) \equiv \frac{1}{([Z(\omega)]^{-1})_{nn}} = \frac{\tilde{F}_d(\omega)}{\tilde{V}_d(\omega)} \quad (10.8)$$

Assuming that $[Z]$ is invertible, its inverse can be found by dividing the adjugate of $[Z]$ by the determinant of $[Z]$. Combining this property with (10.8), an equation for the drive point impedance in terms of basic matrix operations can be written as shown in (10.9). It is clear from this representation that all four elements of (10.5) are required in order to evaluate the drive point impedance, as the determinant of the $[Z]$ is required.

$$Z_d(\omega) = \frac{\det[Z]}{adj[Z]_{nn}} \quad (10.9)$$

As the objective of the stated impedance matching problem is to design a test fixture that provides a more realistic dynamic boundary condition, the system that satisfies the desired impedance relationship must be interpretable as a physically buildable structure.

The conversion of a desired input-output relationship into a system of interconnected mechanical elements is known as the mechanical realization problem [7]. Such an input-output relationship for a second order system is presented in Eq. (10.10), where x is an $n \times 1$ vector of displacements, u is an $m \times 1$ vector of inputs, such as external forces, and F is the $n \times m$ input influence matrix. The $p \times 1$ output vector y can be written in terms of the output influence matrices of acceleration, H_a , velocity, H_v , and displacement, H_d [7].

$$\begin{aligned} [M]\{\ddot{x}\} + [C]\{\dot{x}\} + [K]\{x\} &= [F]\{u(t)\} \\ \{y\} &= [H_a]\{\ddot{x}\} + [H_v]\{\dot{x}\} + [H_d]\{x\} \end{aligned} \quad (10.10)$$

Techniques for resolving the mechanical realization problem for undamped or proportionally damped systems are well documented in the literature. These solution approaches, as detailed by Falk [8], O'Hara and Cunniff [9], and Garvey et al. [10, 11], employ transformations of the mass, stiffness, and damping matrices to satisfy the mechanically realizable constraint while preserving the desired input-output relationship.

Although the approach presented above offers a methodical process by which a mechanically realizable system with a specified behavior can be derived, it assumes initial knowledge of the target system mass, stiffness, and damping matrices. A similar body of work, known as inverse problems in vibration, utilizes specified frequency response (FRF) data to reconstruct system matrices [12]. While this generalized class of problems is more applicable to the outlined drive point impedance problem, it also relies heavily on evaluation of the system in terms of matrices, which can be computationally exhaustive.

As an alternative to matrix representations, closed form expressions for mechanical impedance can be derived using analogies to electrical circuits. Under this framework the mechanical impedance of lumped elements representing mass (m), stiffness (k), and damping (c) can be expressed as detailed in Eqs. (10.11), (10.12) and (10.13), as presented by Hixson [13].

$$Z_{mass}(\omega) = i\omega m \quad (10.11)$$

$$Z_{spring}(\omega) = \frac{k}{i\omega} \quad (10.12)$$

$$Z_{dashpot} = c \quad (10.13)$$

The equivalent drive point impedance of a network can be expressed by evaluating the connectivity of individual elements and appropriately summing their effects. The equivalent impedance of mechanical elements deemed to be in parallel (Z_p), i.e. having the same relative velocities between their connections, is simply a sum of the individual impedances. For mechanical elements in series (Z_s), i.e. having different relative velocities between their connections, the equivalent mechanical impedance is the reciprocal of the summed reciprocal impedance of individual elements [13].

$$Z_p(\omega) = \sum_{n=1}^N Z_n(\omega) \quad (10.14)$$

$$\frac{1}{Z_s(\omega)} = \sum_{n=1}^N \frac{1}{Z_n(\omega)} \quad (10.15)$$

Utilization of the rational form of the drive point impedance in order to perform system characterization is studied within the electrical community. This field of study is known as electrical network synthesis, and utilizes the rational expression of impedance or admittance, with fully defined polynomial coefficients, to determine system realizability and derive representative electrical circuit architecture [14].

10.4 Analysis

The objective of this study is to develop a methodology for designing a test fixture that matches the dynamic behavior of the next level of assembly in order to more accurately emulate the true boundary condition. As shown in the background section, this requires matching the frequency dependent output and transfer impedances. This paper will focus on the drive point impedance, as this metric encapsulates both aforementioned impedances.

The test fixture within this analysis will be represented by a lumped parameter, or discretized, model that could be used as a basis for design. To derive this lumped parameter emulator, it is assumed that the frequency dependent drive point impedance of the system of interest is available and that the low frequency, quasi-static behavior is captured. The magnitude of this impedance data then becomes the target function, where the objective is to minimize the overall Root Mean Squared Error (RMSE) between the target behavior and the analytically derived system behavior. This error minimization will be accomplished through evaluation of the topological features of the drive point impedance curve, which includes behavior at the extremes of the frequency band as well as maxima and minima.

The analysis approach to be explored within this paper focuses on undamped systems, as this solution will provide matched resonances, anti-resonances and overall frequency dependent behavior. Results from undamped systems can be extended to lightly damped systems, where a variety of damping models and can be explored to best fit the target drive point impedance signature.

For a system with N modes there are a variety of N -DOF system architectures that can provide the appropriate number of resonances. An array of architectures are considered as various configurations have the potential to provide a low error impedance match. The simplest architecture is a 1D chain, in which the initial spring-mass system is connected to ground and each subsequent spring-mass pair is connected to the $N-1$ spring mass pair. Other architectures include systems where each mass is connected to all other masses as well as ground via spring elements (all connections), systems where each mass in the chain is connected back to ground via spring elements (all grounded), and systems where some but not all masses in the chain are connected to non-adjacent masses or ground using spring elements (partial connections). An example illustration of the various architectures is provided in Fig. 10.3 for a three DOF system, where multiple partial connection systems are shown to demonstrate the variety of manners in which this architecture can be achieved.

The expression for impedance of any N degree of freedom (N -DOF) mass-spring system can be written in fractional form, using either Eq. (10.9) or Eqs. (10.11), (10.12), (10.13), (10.14) and (10.15), where the form of the polynomial expressions in the numerator and denominator can be readily predicted. The generic form of this rational expression can be most readily derived from consideration of (10.9), where each element of $[Z]$ has the form $i\omega m + k/i\omega$, as indicated by (10.2) and (10.4). Thus, the determinant of $[Z]$ has even powers in ω , with the highest power of ω equal to $2N$ and the adjugate of $[Z]$ has odd powers in ω , with the highest power of ω equal to $2N-1$. Substitution of this result into (10.9) yields the general expression represented by Eq. (10.16), where the various coefficients are represented as generically as possible. Again, this result can also be realized from utilization of Eqs. (10.11), (10.12), (10.13), (10.14) and (10.15), where matrix operations are not required and thus computational advantages can be realized for large values of N .

$$|Z_d(\omega)| = \frac{\sum_{n=0}^N a_n \omega^{2n}}{\sum_{n=0}^{N-1} b_n \omega^{2n+1}} \quad (10.16)$$

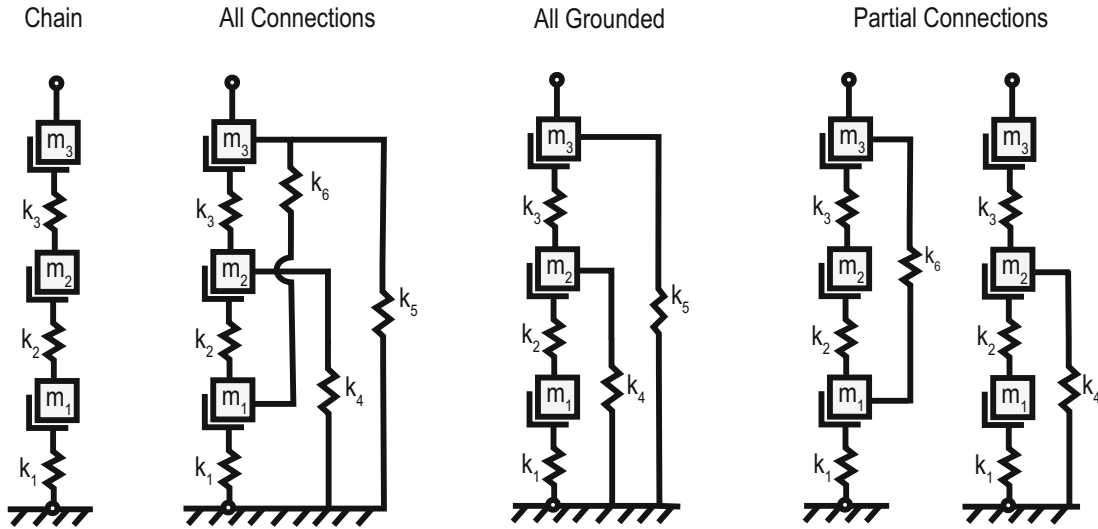


Fig. 10.3 Sample illustration of system architectures shown using 3DOF system

When expanded, Eq. (10.16) can be rewritten for MDOF systems as shown in (17), where the highest and lowest powers in both the numerator and denominator have been separated as their coefficients are of particular importance. For all of the configurations presented in Fig. 10.3, the coefficients of the highest powers in both the numerator and denominator possess only mass terms while the coefficients of the lowest powers possess only stiffness terms. The coefficients of the intermediate powers, a_n and b_n , are mixed coefficients containing combinations of both mass and stiffness elements.

$$|Z_d(\omega)| = \begin{cases} \frac{a_0\omega^{2N} + \sum_{n=1}^{N-1} a_n\omega^{2n} + a_N\omega^0}{b_0\omega^{2N-1} + b_{N-1}\omega^1} & \text{for } N \equiv 2 \\ \frac{a_0\omega^{2N} + \sum_{n=1}^{N-1} a_n\omega^{2n} + a_N\omega^0}{b_0\omega^{2N-1} + \sum_{n=1}^{N-2} b_n\omega^{2n+1} + b_{N-1}\omega^1} & \text{for } N \geq 3 \end{cases} \quad (10.17)$$

As stated above, the high frequency behavior is mass dominated while the low frequency behavior is stiffness dominated, which is expressed mathematically as $a_0/b_0 = f(\{m\})$ and $a_N/b_{N-1} = f(\{k\})$. Utilizing these ratios as approximations for impedance magnitude at the extremes of the frequency domain will yield equivalency expressions in terms of target impedance modulus, frequency, and stiffness or mass, as shown in (10.18) and (10.19).

$$\alpha = |Z_{target}(\omega_{min})| * \omega_{min} \cong \frac{a_N}{b_{N-1}} \cong f(\{k\}) \quad (10.18)$$

$$\beta = \frac{|Z_{target}(\omega_{max})|}{\omega_{max}} \cong \frac{a_0}{b_0} \cong f(\{m\}) \quad (10.19)$$

The expressions above, which are valid for any N -DOF lumped system, can be further refined for the 1D chain architecture shown in the leftmost sketch of Fig. 10.3. This class of system is of particular interest as they are quite easily constructed and thus lend themselves to be readily leveraged for fixture design. The more specific form of (10.17) for 1D chain architectures is presented in (10.20). As indicated the a_0 and b_0 coefficients are products of the m_n discrete masses while the a_N coefficient is a product of the k_n stiffnesses. The b_{N-1} coefficient is slightly more complicated as it involves evaluation of all the possible $N-1$ combinations. For example, when the expression for b_{N-1} is evaluated for the 3DOF chain illustrated in Fig. 10.3 the result is $k_1k_2 + k_1k_3 + k_2k_3$.

$$|Z_{d_{chain}}(\omega)| = \begin{cases} \frac{\prod_{n=1}^N m_n \omega^{2N} + \sum_{n=1}^{N-1} \eta_n \omega^{2n} + \prod_{n=1}^N k_n}{\prod_{n=1}^{N-1} m_n \omega^{2N-1} + \omega^1 \sum_{n=1}^N \prod_{n=1}^N k_n} \text{ for } N \equiv 2 \\ n = 1 \\ n \neq N \\ \frac{\prod_{n=1}^N m_n \omega^{2N} + \sum_{n=1}^{N-1} \eta_n \omega^{2n} + \prod_{n=1}^N k_n}{\prod_{n=1}^{N-1} m_n \omega^{2N-1} + \sum_{n=1}^{N-2} H_n \omega^{2n+1} + \omega^1 \sum_{n=1}^N \prod_{n=1}^N k_n} \text{ for } N \geq 3 \\ n = 1 \\ n \neq N \end{cases} \quad (10.20)$$

This result allows closed form representations of (10.18) and (10.19) to be written, where (10.21) holds exclusively for 1D chain architectures, and (10.22) is applicable to any of the topologies illustrated in Fig. 10.3.

$$\alpha = |Z_{target}(\omega_{min})| * \omega_{min} \cong \frac{\prod_{n=1}^N k_n}{\sum_{n=1}^N \prod_{n=1}^N k_n} \quad n \neq N \quad (10.21)$$

$$\beta = \frac{|Z_{target}(\omega_{max})|}{\omega_{max}} \cong m_N \quad (10.22)$$

In addition to assessing behavior at the extremes of the frequency band, the resonances and anti-resonances can be obtained from the target dataset. There are a variety of approaches to obtaining these frequency values, however it is recommended that established single-input-single-output (SISO) frequency domain modal fitting algorithms be utilized. Application of these algorithms to the impedance modulus will yield anti-resonant frequencies while application of these algorithms to the modulus of mobility, or $1/|Z|$, will yield resonant frequencies. The number of identified resonant frequencies corresponds to the number of degrees of freedom, or lumped masses, that the emulator architecture will possess.

The resonant and anti-resonant frequencies correspond to the roots of the numerator and denominator, respectively, of Eq. (10.16). The knowledge of the roots and zeros, combined with the outputs of Eqs. (10.21) and (10.22) yields a set p equations with p unknowns, for 1D chain architectures only. For polynomials up to order four, analytic expressions for the roots can be found, and thus there are sufficient conditions by which closed form solutions can be found. This polynomial order corresponds to a 4DOF system where the substitution $\omega^2 = \lambda$ is made, such that the highest order in the numerator of (10.20) is λ^4 . As analytic solutions for the roots of a polynomial with order 5 or higher do not exist, this analytic solution approach for system identification of 1D chains fails.

It is desired to evaluate 1D chains that possess more than 4DOF as well as systems of various architectures, thus a numerical solution approach is required. The most obvious approach is to conduct an exhaustive search of the various combinations of individual parameters where the impedance is calculated using Eq. (10.16) for the applicable system architecture under evaluation. The objective of this exhaustive search would be to find the combination of parameters that yields the lowest Weighted Root Mean Squared Error (WRMSE) between the target and calculated impedance modulus, where the RMSE is weighted to reflect the fact that the low amplitude values corresponding to resonances are more critical to match than the high amplitude values near anti-resonances.

Although this approach is very straightforward, it is rather limited, as large allocations of memory are required to compute the output from the various combinations of parameters. For example, a 3DOF chain architecture system with six searchable parameters would have 10^{12} possible combinations if 100 values were evaluated for each parameter. Each of these 10^{12} combinations must be computed at hundreds or thousands of frequency points, resulting in up to 10^{15} computations. Each additional degree of freedom would result in an increase in the number of computations by a power of four, assuming 100 values are investigated for each element. Another shortcoming of exhaustive search is that magnitude of the WRMSE decreases as the discretization of the parameters increases, thus driving the number of required combinations even higher if the true minimum WRMSE is desired.

In order to reduce the number of computations for an exhaustive search it is proposed that Eq. (10.18) be leveraged to determine the best combination of stiffness values to match the low frequency impedance behavior. Although this expression is presented in generality, once a specific architecture is evaluated the coefficients a_0 and b_0 can be found, or for the case of the 1D chain a closed form expression can be readily transcribed using (10.21).

As the ratio of these variables has no mass or frequency dependence (i.e. scalar), the computational expense of this calculation is quite low. The combination of stiffness values that yields the lowest WRMSE between the target and computed α values are selected and the values for the lumped masses can then be found. The value of the N th mass can be solved for using Eq. (10.22) while the values of the remaining masses can be numerically solved for using a variety of analyses including: (1) minimizing the error between the result of Eq. (10.16) and the target impedance modulus, (2) pole and zero fitting of Eq. (10.16) or (3) solutions to the eigenvalue problem.

Although the numerical solution approaches call for exhaustive searching of the mass parameters, the utilization of stiffness dominated low frequency behavior has decoupled the stiffness parameters from this search. As a result the number of computations that are now required to minimize the error between the target and derived drive point impedances is reduced by the length of the frequency vector, $\mathcal{L}(\{\omega\})$, times the length of the mass vector, $\mathcal{L}(\{m\})$, times the length of the stiffness vector, $\mathcal{L}(\{k\})$, raised to the power of the number of springs, q . The reduction in the parameter search space by $\mathcal{L}(\{k\})^q * \mathcal{L}(\{m\}) * \mathcal{L}(\{\omega\})$ will more efficiently yield low WRMSE impedance matches for multiple system architectures, thus offering a more broad design space from which fixtures can be created.

10.5 Conclusion

A methodology for matching the drive point impedance has been proposed that leverages topological features of the impedance curve, including maxima, minima, and behavior near extremes of the frequency band. This approach offers distinct computational advantages as it decouples frequency dependence and mass parameters from the solution of the system stiffness values. Additionally, a formulation has been proposed that allows for a rational expression to be readily transcribed for both the high and low frequency behavior of easily constructed 1D chain systems. The computational advantages offered by these formulations, particularly when utilized in conjunction with the non-matrix based derivation of the drive point impedance, allows for an efficient assessment of multiple system architectures from which a broad design space for fixture design is posed.

References

1. Scharton, T.D.: Force Limited Vibration Testing Monograph. NASA RP-1403, May 1997
2. Daborn, P.M., Roberts, C., Ind, P.R. Next-generation random vibration tests. In: IMAC XXXII, the 32nd International Modal Analysis Conference, Orlando, FL, 2014
3. Scharton, T.D.: Impedance simulation vibration test fixtures for spacecraft tests. Shock Vib. Bull. **40**, (1969)
4. Edwards, T.S.: Improving boundary conditions in component-level shock and vibration tests. [Online]. Available: www.osti.gov/biblio/1146729 (2007). Accessed 23 Sept 2019
5. Hall, T.M.: Analytically investigating impedance-matching test fixtures. In: IMAC in IMAC XXXVII, the 37th International Modal Analysis Conference, Orlando, FL, 2019
6. Maia, N.M.M.: Theoretical and Experimental Modal Analysis. Research Studies Press, Baldock (1998)
7. Chen, W., Dupont, P.E.: Realization of mechanical systems from second-order models. J. Acoust. Soc. Am. **118**(2), 762–773 (2005). <https://doi.org/10.1121/1.1953227>
8. Falk, S.: Die Abbildung eines allgemeine schwingungssystems auf eine einfacheSchwingerkette. Ing. Arch. **23**, 312–328 (1955)
9. O'Hara, G.J., and Cunniff, P.F., "Elements of Normal Mode Theory." Naval Research Laboratory Report, 1963
10. Garvey, S.D., Friswell, M.I., Prells, U.: Coordinate transformations for second order systems. I. General transformations. J. Sound Vib. **258**(5), 885–909 (2002)
11. Garvey, S.D., Friswell, M.I., Prells, U.: Coordinate transformations for second order systems. II. Elementary structure-preserving transformations. J. Sound Vib. **258**(5), 911–930 (2002)
12. Gladwell, G.M.L.: Inverse Problems in Vibration. Kluwer Academic Publishers, Dordrecht (2004)
13. Hixson, E.L.: Mechanical impedance. In: Harris, C.M. (ed.) Shock and Vibration Handbook, pp. 10-1–10-46. McGraw-Hill, New York (1988)
14. Baher, H.: Synthesis of Electrical Networks. Wiley, Chichester (1984)

Chapter 11

Analysis of Full-Field Response from a Multi-Shaker Test



Dagny Beale, Brian Owens, and Ryan Schultz

Abstract Multi-shaker testing is used to represent the response of a structure to a complex operational load in a laboratory setting. One promising method of multi-shaker testing is Impedance Matched Multi-Axis Testing (IMMAT). IMMAT targets responses at discrete measurement points to control the multiple shaker input excitations, resulting in a laboratory response representative of the expected operational response at the controlled measurement points. However, the relationship between full-field operational responses and the full-field IMMAT response has not been thoroughly explored. Poorly chosen excitation positions may match operational responses at the control points, but over or under excite uncontrolled regions of the structure. Additionally, the effectiveness of the IMMAT method on the whole test structure could depend on the type of operational excitation. Spatially distributed excitations, such as acoustic loading, may be difficult to reproduce over the whole test structure in a lab setting using the point force IMMAT excitations. This work will simulate operational and IMMAT responses of a lab-scale structure to analyze the accuracy of IMMAT at uncontrolled regions of the structure. Determination of the effect of control locations and operational locations on the IMMAT method will lead to better test design and improved predictive capabilities.

Keywords IMMAT · MIMO · Test methods · Model methods · Modal

11.1 Background

One major challenge in structural dynamics experimental methods is the ability to recreate a structure's response to a complex, real-world loading (the “environmental” response) in a laboratory setting (the “laboratory” response). One multi-shaker method that has shown significant promise in recreating environmental responses is the Impedance Matched Multi-Axis Testing (IMMAT) method, and is the focus of this work. IMMAT, first proposed by Daborn et al. [1], uses experimental measurements at reference points and the structure's frequency response function (FRF) matrix to calculate the required input force at chosen excitation locations to recreate the environmental response. This method has been shown to successfully recreate environmental responses in a laboratory setting at the reference points chosen [2]. This work has also been extended to show that additional points of the structure not included in the reference response set also respond similarly to the environmental response [3]. However, most previous research on IMMAT used experimental data for the environmental and laboratory responses, and therefore were limited to the analysis of a few discrete points.

Before IMMAT can become a substitute for more traditional laboratory measurement techniques, the robustness of the technique must be understood. A full-field analysis of the differences between the environmental and laboratory responses is needed to help identify sensitivities in the method to the chosen measurement locations, the chosen number of laboratory forces, and the environmental excitation characteristics, among other variables. To study the full-field response of a structure, a finite element (FE) model is needed. This work builds a FE model to simulate the full-field response of a structure to forces

Sandia National Laboratories is a multimission laboratory managed and operated by National Technology and Engineering Solutions of Sandia, LLC., a wholly owned subsidiary of Honeywell International, Inc., for the U.S. Department of Energy's National Nuclear Security Administration under contract DE-NA0003525.

D. Beale (✉) · B. Owens · R. Schultz
Structural Dynamics, Sandia National Laboratories, Albuquerque, NM, USA
e-mail: djoffre@sandia.gov; bcowens@sandia.gov; rschult@sandia.gov

calculated using IMMAT. The visual full-field differences between the simulated environmental response and the simulated laboratory response can be used to better understand the extent to which IMMAT can simulate environmental responses.

11.2 Theory

In practice, IMMAT uses the measured environmental structural response cross power spectral density (CPSD), S_{xx_0} , at measurement points p to calculate the laboratory input force spectra, S_{ff_1} , at chosen forcing locations, q_1 , to reproduce the response. When IMMAT is used with a FE model, the environmental response spectra must first be calculated. Let S_{ff_0} be the environmental force spectra due to forces at points q_0 , which in practice is unknown, but is selected for the simulation. The response to the environmental force is calculated using Eq. 11.1, where H_{pq_0} is the frequency response function (FRF) matrix of the system, and the “H” superscript indicates the conjugate transpose. The required laboratory force to replicate the environmental response spectra is then calculated using Eq. 11.2, in which the “+” superscript indicates the matrix inverse. For this paper’s calculation, the pseudoinverse was used. The success of the input force calculation can be analyzed by calculating the laboratory response to the new force, S_{ff_1} at points q_1 , using Eq. 11.3, and comparing with the original environmental response.

$$S_{xx_0} = H_{pq_0} S_{ff_0} H_{pq_0}^H \quad (11.1)$$

$$S_{ff_1} = H_{pq_1}^+ S_{xx_0} H_{pq_1}^{+H} \quad (11.2)$$

$$S_{xx_1} = H_{pq_1} S_{ff_1} H_{pq_1}^H \quad (11.3)$$

11.3 Method and Results

A FE model of a three-tiered structure dubbed the “wedding cake” was used for this paper’s analysis, as shown in Fig. 11.1. Also shown as blue points are a sub-set of measurement points that match previous experimental testing. The environmental input force was chosen to be three points (17, 51, and 91), with each point excited in the X, Y, and Z directions (respectively),

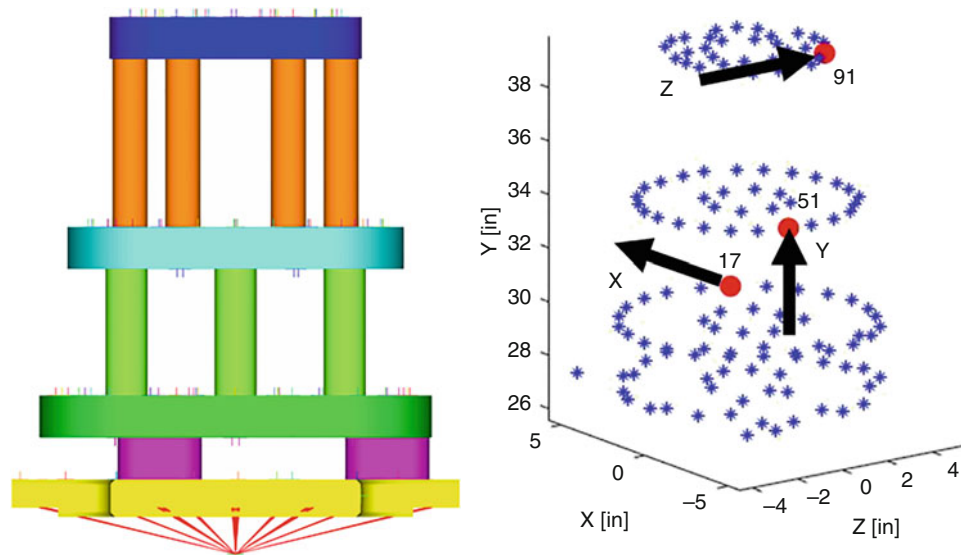


Fig. 11.1 Simulation wedding cake structure (left) and the sample response points (shown in blue) with the forcing points and direction shown as red dots (right)

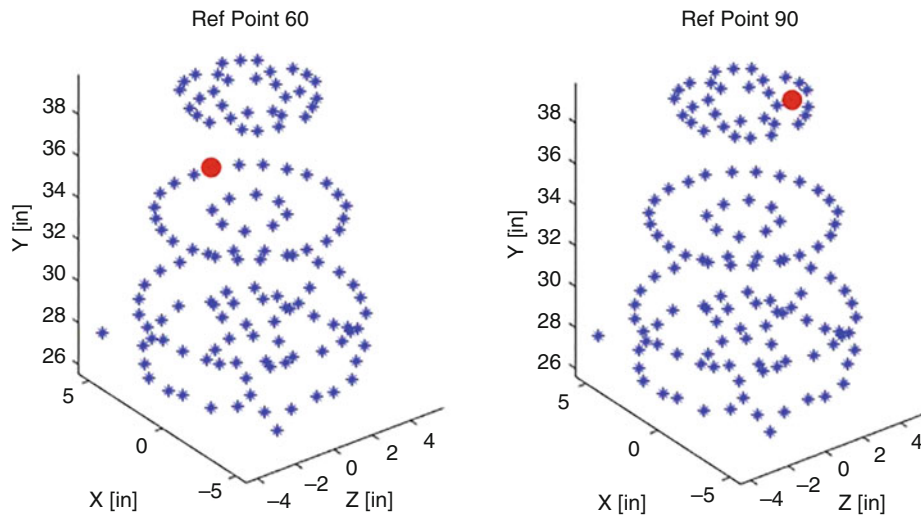


Fig. 11.2 Example point 60 (left) and example point 90 (right)

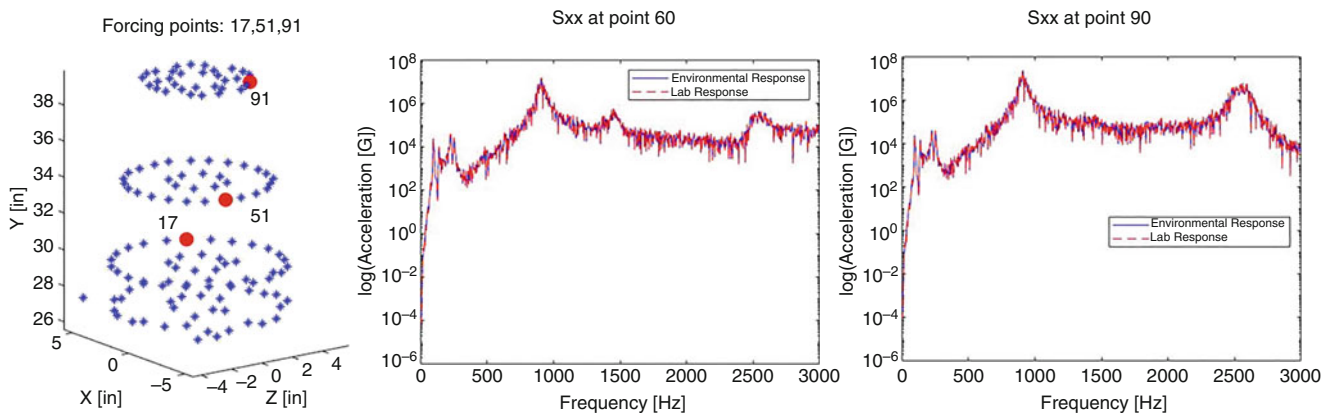


Fig. 11.3 Environmental and laboratory response PSD for the same forcing points (points 17, 51, and 91)

as indicated in the figure. The excitation points were chosen to be distributed around the radius of the structure and among the tiers to better excite the modes.

To verify the force calculation method, the laboratory force locations, q_1 , were chosen to be the same as the environmental force locations, q_0 . The chosen excitation points were points 17, 51, and 91, as shown in Fig. 11.1. The response power spectral densities (PSDs) were calculated at example points 60 and 90 (given in Fig. 11.2) for a simple comparison. The example points were chosen because their response was representative of the overall response comparisons. The response PSD comparison given in Fig. 11.3 shows that the environmental response and the laboratory response are the same.

Next, three different laboratory force locations were chosen to only excite the bottom two tiers. Not including a response on the top tier helps demonstrate how neglecting to excite a sub-component makes the response recreation in the laboratory case more difficult. The laboratory response PSD at example points 60 and 90 are no longer exactly the same as the experimental response PSD, although the two responses are very similar (Fig. 11.4).

Finally, only two of the previous laboratory force locations were chosen, and no forcing points were included on the top two tiers of the wedding cake. This represents the most challenging case for response recreation in the laboratory case. The laboratory response PSD at example points 60 and 90 now significantly differ from the environmental response, especially at lower frequencies (Fig. 11.5).

The simulations of the wedding cake show that forcing location and number is important to the success of laboratory recreation of an environmental response. However, comparing the responses at each point is difficult to analyze. Now that a FE model has been built, the full field differences between the environmental response and the laboratory response can be studied more efficiently by animating the FE responses at all points to both the environmental and the laboratory forces. Images and discussion of the full field responses and comparisons will be included in the presentation.

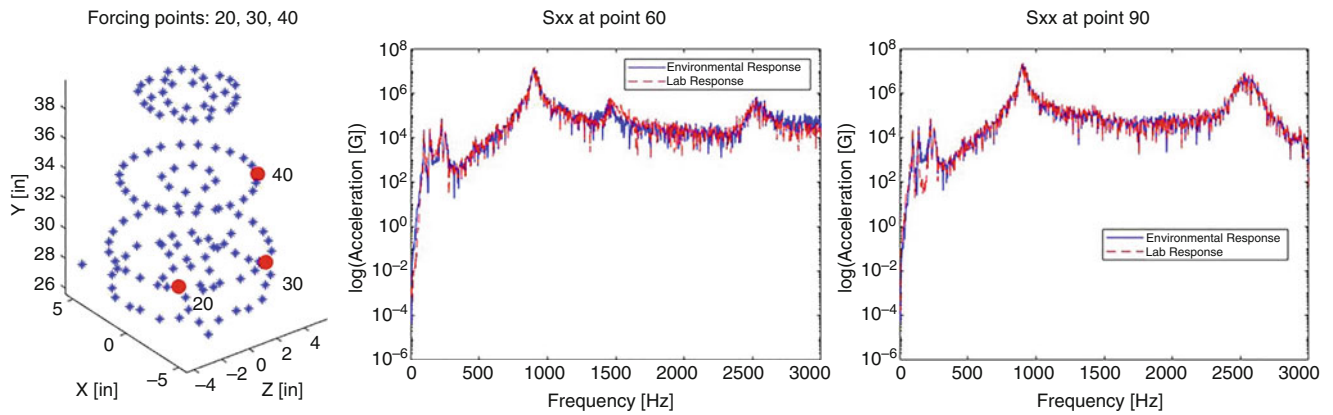


Fig. 11.4 Environmental and laboratory response PSD for laboratory forcing points 20, 30, and 40

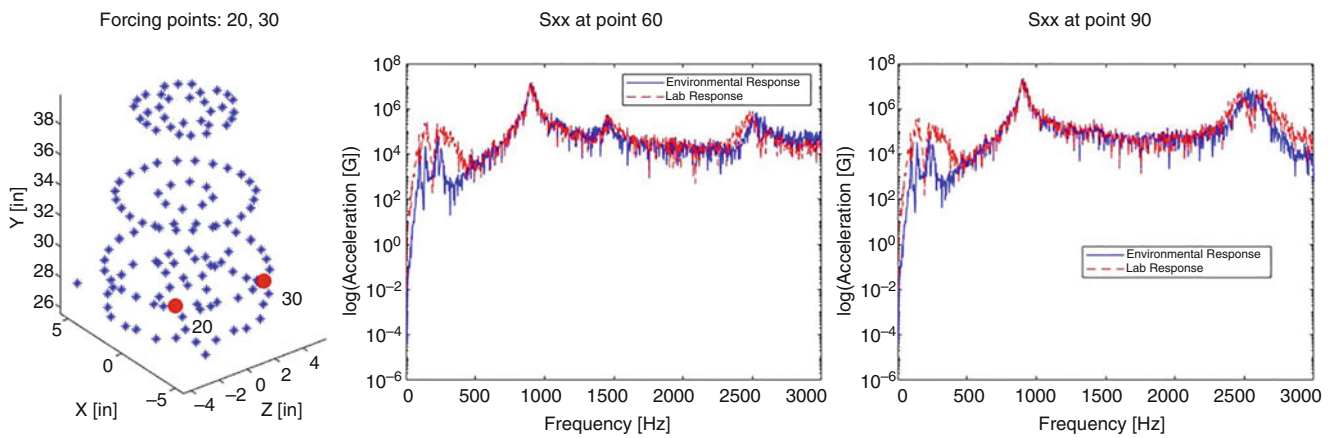


Fig. 11.5 Environmental and laboratory response PSD for laboratory forcing points 20, 30, and 40

References

1. Daborn, P.M., Ind, P.R., Ewins, D.J.: Replicating aerodynamic excitation in the laboratory. In: Topics in Modal Analysis, vol. 7, pp. 259–272. Springer, New York (2014)
2. Mayes, R.L., Rohe, D.P.: Physical vibration simulation of an acoustic environment with six shakers on an industrial structure. In: Proceedings of the 34th International Modal Analysis Conference, Orlando (2016). paper 122
3. Daborn, P.M., et al.: Next-generation random vibration tests. In: Topics in Modal Analysis II, vol. 8, pp. 397–410. Springer, Cham (2014)

Dagny is currently an R&D engineer at Sandia National Laboratories. Previous to working at the Labs, she obtained her masters and PhD from the University of Massachusetts – Lowell, and her bachelors from Michigan Technological University.

Chapter 12

Calibration of Shaker Electro-mechanical Models



Ryan Schultz

Abstract Simple electro-mechanical models of electrodynamic shakers are useful for predicting shaker electrical requirements in vibration testing. A lumped parameter, multiple degree-of-freedom model can sufficiently capture most of the shaker electrical and mechanical features of interest. While several model parameters can be measured directly or obtained from a specifications sheet, others must be inferred from an electrical impedance measurement. Here, shaker model parameters are determined from electrical impedance measurements of a shaker driving a mass. Then, parameter sensitivity is explored to determine a model calibration procedure where model parameters are determined using manual and automated selection methods. The model predictions are then compared to test measurements. The model calibration procedure described in this work provides a simple, practical approach to developing predictive shaker electromechanical models which can then be used in test design and assessment simulations.

Keywords Electro-mechanical model · Electrodynamic shaker · Model calibration

12.1 Introduction

An electrodynamic shaker can be approximated as a coupled electro-mechanical multiple degree-of-freedom (MDOF) system [1]. A simplified MDOF model of an electrodynamic shaker can be used to assess the effects of connecting a shaker to a structure or to estimate the voltage and current requirements to excite a structure. The MDOF model of the shaker includes mechanical parts (springs, masses, and dampers) and electrical parts (inductors and resistors). There is also a coupling part, sometimes called a gyrator, which links or couples the mechanical dynamic system to the electrical dynamic system. This coupling is the electro-magnetic force. The current in the electrical circuit produces a field which reacts with the magnet in the shaker body, generating a force which drives the mechanical system (and vice versa).

Some of the model parameters can be directly measured or obtained from a specification sheet, although some cannot and must be inferred from a dynamic measurement of the electrical impedance. With the measured electrical impedance, unknown model parameters can be tuned to calibrate the shaker model. This tuning process can be done manually by first examining the sensitivity of the electrical impedance to each parameter and then making appropriate changes to affect the impedance in particular frequency ranges. Alternatively, the model parameters can be tuned using a parameter search algorithm. This paper shows model calibration done manually and also with a simple Monte Carlo parameter search.

Sandia National Laboratories is a multimission laboratory managed and operated by National Technology and Engineering Solutions of Sandia, LLC., a wholly owned subsidiary of Honeywell International, Inc., for the U.S. Department of Energy's National Nuclear Security Administration under contract DE-NA0003525

R. Schultz (✉)
Structural Dynamics, Department Sandia National Laboratories, Albuquerque, NM, USA
e-mail: rschult@sandia.gov

12.2 Shaker Electro-mechanical Model

Shaker electro-mechanical models have been derived by various authors over the years using various techniques. Tiwari et al. presents a lumped parameter model of a shaker and provides detailed methods for obtaining various unknown parameters using measurements with specific shaker configurations and reduced expressions for the model applicable to specific frequency ranges [1]. Lang also provides several different test conditions to isolate particular behavior to extract shaker parameters [2]. Smallwood used a two-port impedance model method to represent a shaker, with the entries in the impedance matrix coming from measurements of specific frequency response functions (FRFs) or impedances [3]. Varoto and Oliveira present analytical expressions for a lumped parameter model that also includes terms which account for an amplifier operating in current mode or voltage mode [4]. The approach used here is similar to that given by Lang and Snyder, which presents a matrix form of the lumped parameter model [5]. Mayes et al. used a similar approach with the lumped parameter model equations put in matrix form and then cast in a component mode synthesis problem to connect the shaker model to a model of a system [6]. The set of equations of motion is formed as a matrix equation which can then be solved, giving the shaker response per input FRFs. As there are no external forces, the input is the applied voltage and the response of interest is the shaker head response.

Development of the shaker model begins by examining a typical electrodynamic shaker. Here, the focus is on modal shakers, though similar methods could be used to model large, vibration test shakers as well [3]. A cutaway of a modal shaker is shown in Fig. 12.1. The body of the shaker contains some stationary magnets. A lightweight armature attaches to the body with several flexures which are springs that allow the armature to translate primarily along the axis of the shaker body. The armature is surrounded by a coil through which current flows, generating the transient field which interacts with the magnets to provide the motive force on the armature. A stinger connects the armature to the device under test (DUT).

Figure 12.2 shows the components of the MDOF system used in this work. The mechanical component, shown on the left, has three masses connected by springs and dampers. Mass M_1 is the armature, mass M_2 is the shaker body, and mass

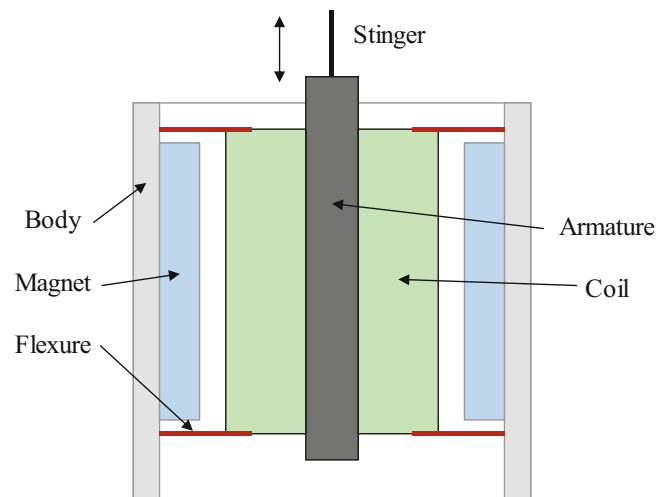


Fig. 12.1 Shaker components

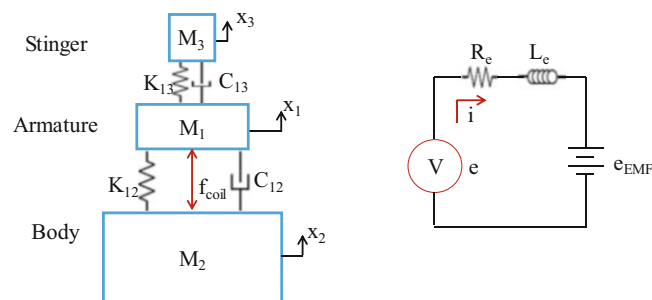


Fig. 12.2 Elements of the shaker mechanical (left) and electrical (right) models

M_3 is the stinger. The stinger mass can represent the mass loading of an attached DUT. The flexures are represented by spring K_{12} and the stinger stiffness is represented by spring K_{13} . If the shaker armature had additional dynamics of interest, or if there was a table or shaker head, additional springs and masses could be added to M_1 to represent these features. This model form with three masses works well for a typical modal shaker in a typical frequency range (i.e. around 1500 Hz). The mechanical component is driven by a force between the body and armature, which is the electromotive force (EMF) of the coil in the magnetic field. The electrical component, shown on the right, has a voltage source which is provided by the amplifier, in series with a resistor and inductor with represent the coil. Then, there is a voltage source which represents the back electromotive force; this is the coupling of the mechanical component back into the electrical component. That is, motion of the mechanical component introduces a voltage in the electrical component through this back EMF source. This coupling is represented in the model by the force factor, BL , which links the current in the electrical domain to the force and relative velocity in the mechanical domain.

12.2.1 Equations of Motion

With the mechanical and electrical component models formed and their parts defined, the equations of motion can be written. There is an equation of motion for each mechanical DOF (each mass), and one equation of motion for the electrical circuit. These four equations can be put in matrix form in the typical mass, damping, and stiffness matrix form as shown below:

$$[M_{\text{shk}}] = \begin{bmatrix} M_1 & 0 & 0 & 0 \\ 0 & M_2 & 0 & 0 \\ 0 & 0 & M_3 & 0 \\ 0 & 0 & 0 & 0 \end{bmatrix}, \quad (12.1)$$

$$[C_{\text{shk}}] = \begin{bmatrix} (C_{12} + C_{13}) & -C_{12} & -C_{13} & 0 \\ -C_{12} & C_{12} & 0 & 0 \\ -C_{13} & 0 & C_{13} & 0 \\ BL & -BL & 0 & L_e \end{bmatrix}, \quad (12.2)$$

$$[K_{\text{shk}}] = \begin{bmatrix} (K_{12} + K_{13}) & -K_{12} & -K_{13} & -BL \\ -K_{12} & K_{12} & 0 & BL \\ -K_{13} & 0 & K_{13} & 0 \\ 0 & 0 & 0 & R_e \end{bmatrix}, \quad (12.3)$$

This system of equations has inputs of force on each mass and voltage on the circuit and outputs of displacement of each mass and current in the circuit. Thus, the system of equations can be written as:

$$[M_{\text{shk}}] \begin{Bmatrix} \ddot{x}_1 \\ \ddot{x}_2 \\ \ddot{x}_3 \\ \dot{i} \end{Bmatrix} + [C_{\text{shk}}] \begin{Bmatrix} \dot{x}_1 \\ \dot{x}_2 \\ \dot{x}_3 \\ i \end{Bmatrix} + [K_{\text{shk}}] \begin{Bmatrix} x_1 \\ x_2 \\ x_3 \\ i \end{Bmatrix} = \begin{Bmatrix} f_1 \\ f_2 \\ f_3 \\ e \end{Bmatrix} \quad (12.4)$$

Direct frequency response can then be used to solve this matrix equation and give the output/input FRFs for all outputs and all inputs.

$$[H] = \left[-\omega^2 [M_{\text{shk}}] + j\omega [C_{\text{shk}}] + [K_{\text{shk}}] \right]^{-1}. \quad (12.5)$$

However, as there are no external forces, $f_1 = f_2 = f_3 = 0$, so the only FRF of interest is with the voltage input, e , which is the fourth column of $[H]$. The result is a four output, one input FRF matrix which is evaluated at each frequency line of interest. This FRF matrix is essentially an impedance model of the coupled electro-mechanical shaker system.

12.2.2 Shaker Force from the Stinger Spring

The force applied by the shaker to the DUT is the force in the spring between masses M_1 and M_3 . This force does not come directly out of this model but can be determined given the displacement of those two masses, x_1 and x_3 , and the stiffness of the stinger spring, k_{13} . The stinger force/input voltage FRF, $H_{f_s e}$, can be obtained using the two displacement/voltage FRFs, $H_{x_1 e}$, $H_{x_3 e}$:

$$H_{f_s e} = K_{13} (H_{x_3 e} - H_{x_1 e}) . \quad (12.6)$$

Note that this is nothing more than Hooke's law, $f = k\Delta x$, written in terms of FRFs.

12.2.3 Features of the Impedance and FRF Curves

The electrical impedance is the ratio of the voltage and current: $Z_{ei} = e/i$. The coupled electro-mechanical shaker system has some interesting features in the impedance, as shown in Fig. 12.3. There are two peaks in the impedance, one at the suspension mode (low frequency) and one at the stinger mode (high frequency). The suspension mode is the mass of the

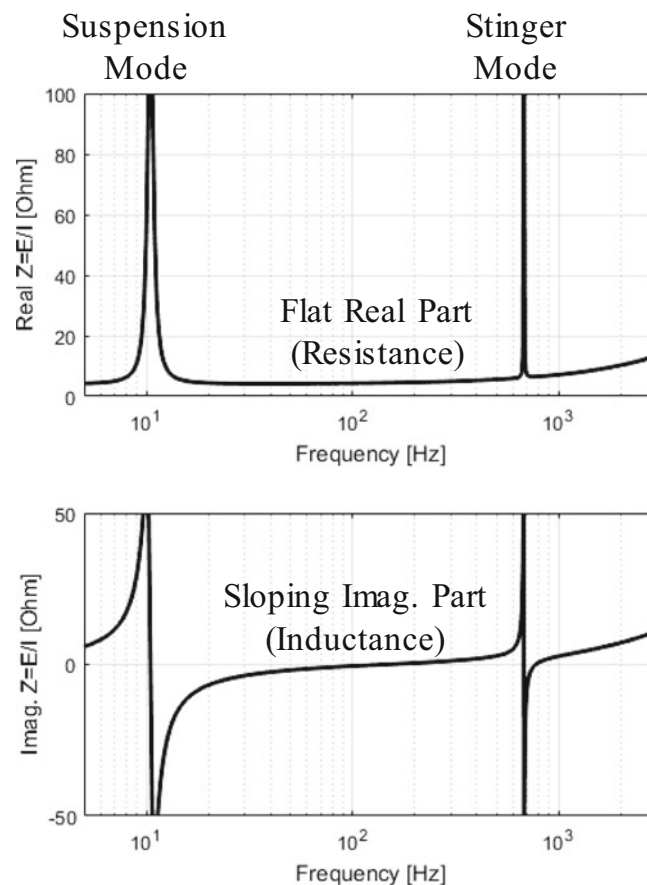


Fig. 12.3 Example electrical impedance from the shaker model. Top: Real part. Bottom: Imaginary part

Table 12.1 Nominal model parameter values

Parameter	Value	Unit
M_1	0.44	kg
M_2	15	kg
M_3	2.6	kg
K_{12}	1.10E+04	N/m
K_{13}	1.46E+07	N/m
C_{12}	17	N/(m/s)
C_{13}	10	N/(m/s)
R_e	4	Ohm
L_e	6.00E-04	Henry
BL	35	N/Amp

armature and stinger moving opposite the shaker body through the flexure springs. The stinger mode is the mass of the stinger moving opposite the armature through the stinger spring. The frequency of these peaks is dependent on the mass and stiffness and the width of the peaks is affected by the damping. Between the two peaks, the real part is dominated by the resistor in the electrical component and the imaginary part is dominated by the inductor. The resistance only affects the real part and is constant with frequency whereas the inductance only affects the imaginary part and the effect is proportional to frequency.

12.2.4 Model Parameter Sensitivity

To tune the model, it is useful to understand how the various model parameters affect the impedance. The figures below show how each parameter affects the impedance by plotting impedance with each parameter at nominal, lower, and higher values. For all parameters except the inductance, lower is one half the nominal value and higher is twice the nominal value. For the inductance lower is one fifth and higher is five times the nominal value. Nominal model parameters are given in Table 12.1.

Note that the stinger mass is large, 2.6 kg, representing a large mass at the end of the shaker, which is representative of the experiment described in the next section.

Increasing the armature mass (M_1) shifts the modes lower in frequency, Fig. 12.4. In this case because the stinger has a large mass attached, changing the armature mass changes the stinger mode frequency more than the suspension mode frequency. Similarly, increasing the stinger mass (M_3) decreases the mode frequencies. The amplitudes of the peaks are not affected, nor is the impedance between the peaks. Increasing the flexure or stinger stiffness increases the mode frequencies, as expected, as seen in Fig. 12.5. The flexure stiffness only affects the suspension mode and the stinger stiffness only affects the stinger mode. The damping C_{12} and C_{13} affect the amplitude and width of the peaks near the suspension and stinger modes, respectively (Fig. 12.6).

The resistance (R_e) only affects the real part of the impedance as it is a constant over all frequencies as seen in Fig. 12.7. The inductance (L_e) only affects the imaginary part and is proportional to frequency. Increasing the resistance increases the real part of the impedance over the entire bandwidth and increasing the inductance increases the imaginary part of the impedance, particularly at high frequency. The force factor (BL) affects both the real and imaginary parts of the impedance over the entire bandwidth and has effects similar the damping in that it affects the amplitude and width of the peaks, see Fig. 12.8. Effects of all the model parameters on the impedance is summarized in Table 12.2.

12.3 Experiment to Determine Shaker Properties

The specification sheet and some basic mass measurements provided estimates of the masses, and the coil resistance could be measured with a multimeter, but many of the model parameters had to be inferred from a measurement of the electrical impedance so an experiment was devised. The objective of this experiment was to drive the shaker with a voltage from an amplifier and measure the response and force at the stinger and the current and voltage supplied to the shaker from the amplifier. In this way, the electrical impedance can be obtained and used to calibrate the model parameters.

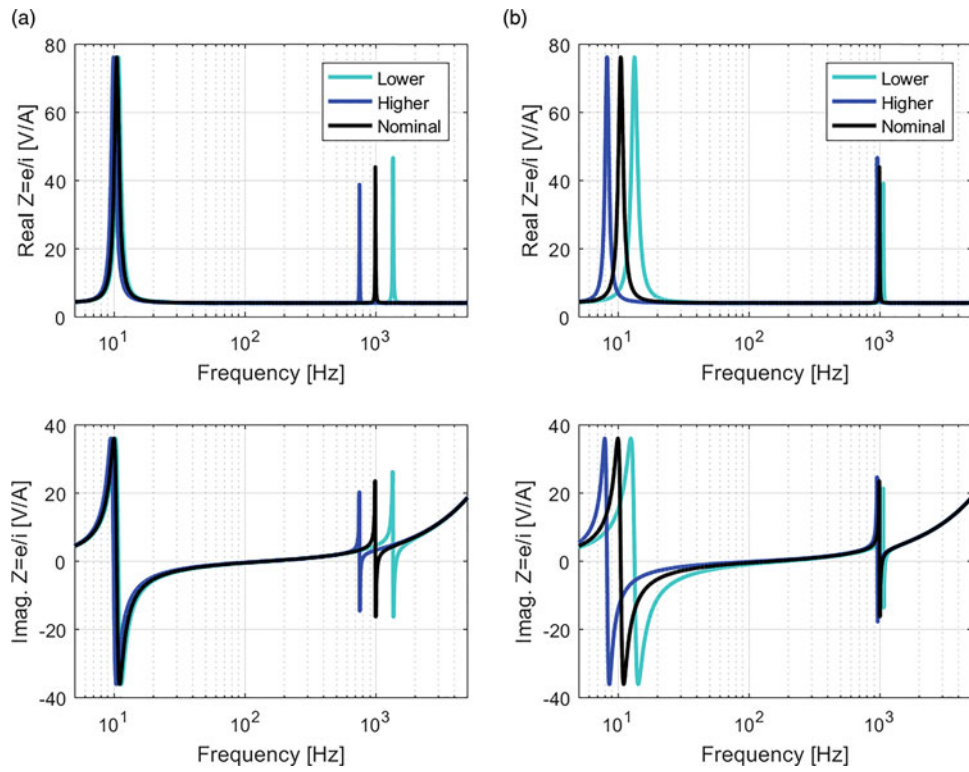


Fig. 12.4 Model impedance sensitivity to M_1 mass (left) and M_3 mass (right). Top: Real part. Bottom: Imaginary part

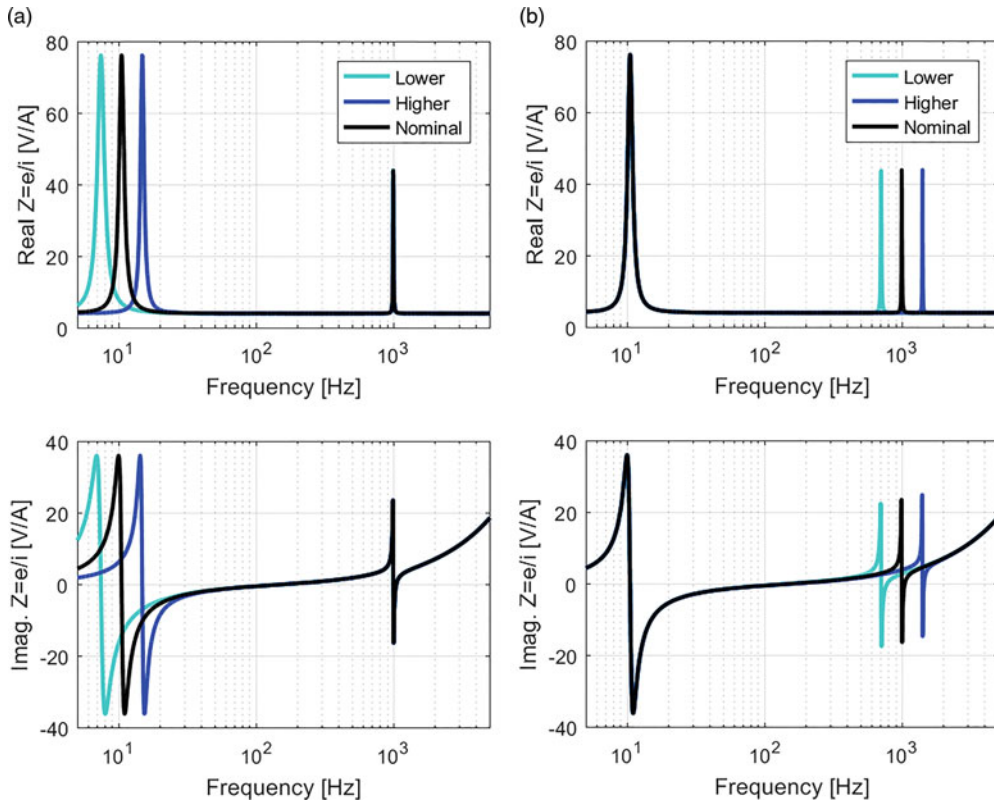


Fig. 12.5 Model impedance sensitivity to K_{12} spring (left) and K_{13} spring (right) values. Top: Real part. Bottom: Imaginary part

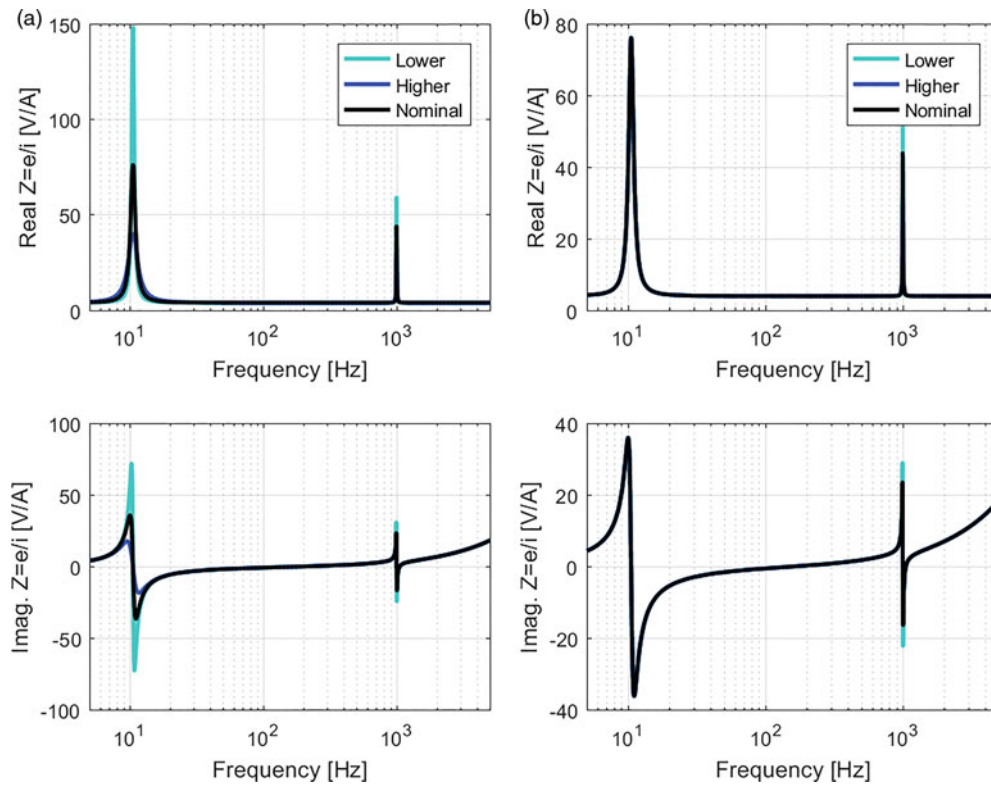


Fig. 12.6 Model impedance sensitivity to C_{12} damper (left) and C_{13} damper (right) values. Top: Real part. Bottom: Imaginary part

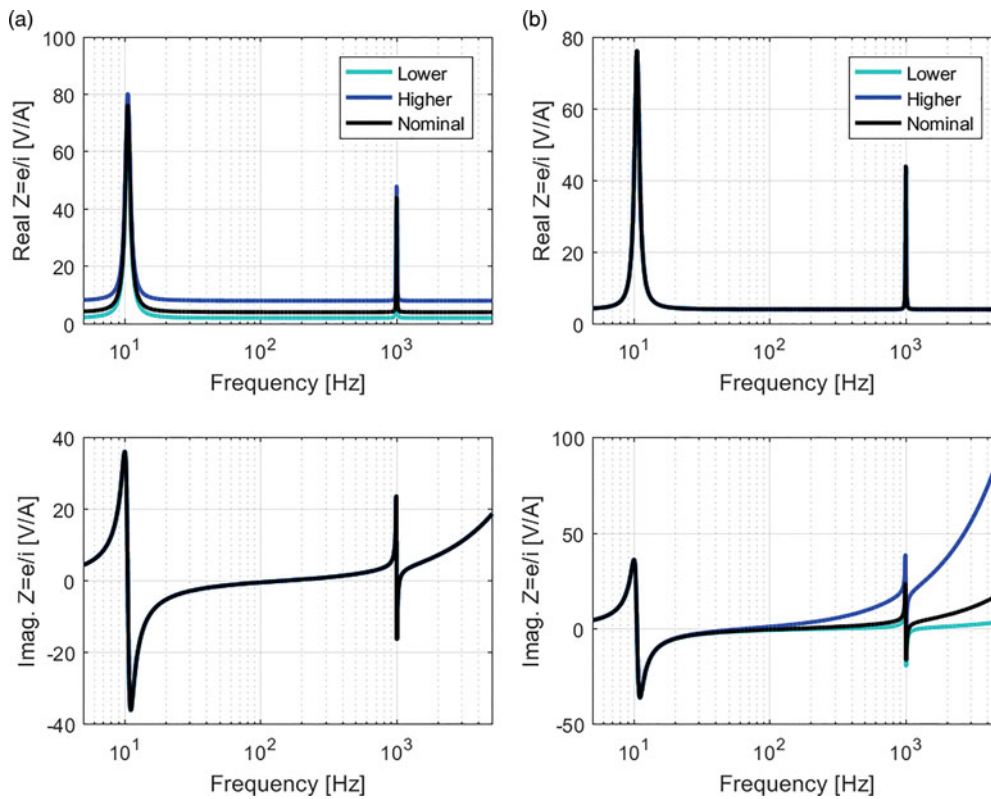


Fig. 12.7 Model impedance sensitivity to resistor R_e (left) and inductor L_e (right) values. Top: Real part. Bottom: Imaginary part

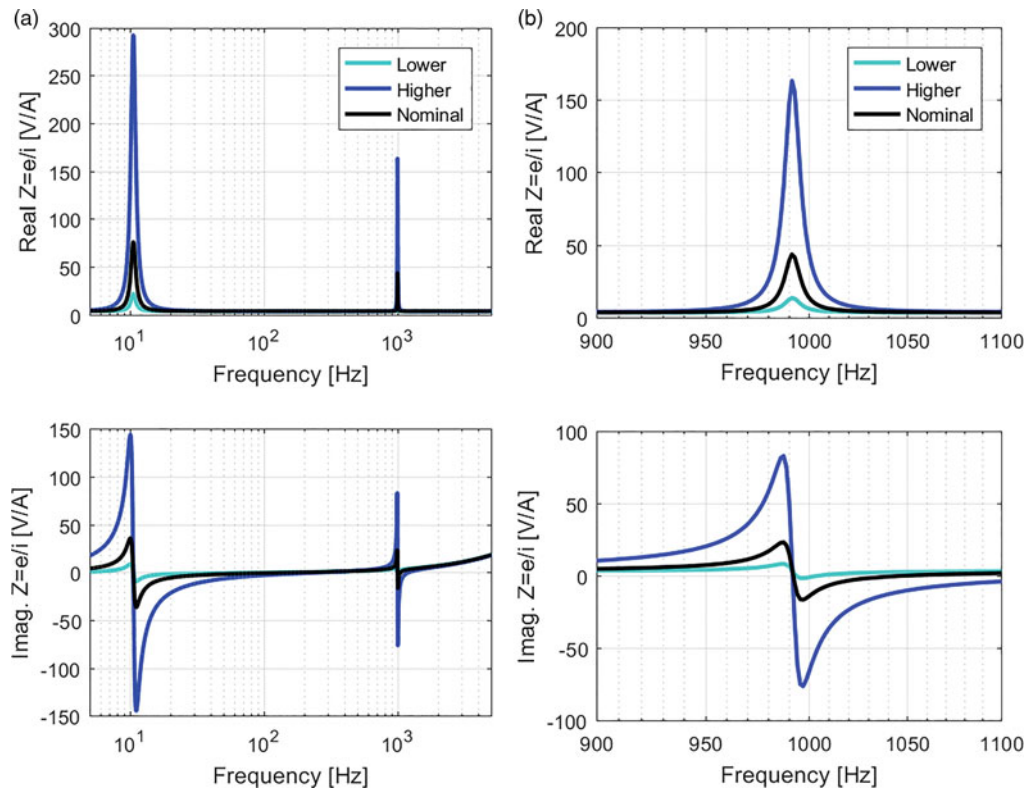


Fig. 12.8 Model impedance sensitivity to BL, left full frequency range, right: zoomed to high frequency range. Top: Real part. Bottom: Imaginary part

Table 12.2 Summary of parameter effects on the electrical impedance

Parameter	Effect of increasing parameter on impedance
M_1	Decreases frequency of suspension and stinger modes
M_2	Decreases frequency of suspension mode
M_3	Decreases frequency of suspension and stinger modes
K_{12}	Increases frequency of suspension mode
K_{13}	Increases frequency of stinger mode
C_{12}	Reduces amplitude at suspension mode
C_{13}	Reduces amplitude at stinger mode
R_e	Increases real part, constant with frequency
L_e	Increases imaginary part, proportional with frequency
BL	Increases amplitude and peak width at suspension and stinger modes

12.3.1 Test Setup

The test setup consisted of a 100 pound-force Modal Shop shaker set horizontally with a 1.5 mm steel wire stinger connecting the shaker armature to a 2.6 kg mass. The mass shifts the stinger mode frequency down to a sufficiently low frequency where it can be easily measured and also is representative of stinger mode frequencies encountered in typical modal tests. This mass was suspended from strings splayed out at an angle to try and keep the mass centered and moving in just one direction. A load cell and accelerometer on the mass measure the applied force and the acceleration of the mass. A photo of the test setup is shown in Fig. 12.9.

In addition to the mechanical measurements, the current and voltage to the shaker was also measured. This was done using a 20:1 voltage divider and a Hall effect clamp on the cable at the output of the amplifier supplying the shaker. A diagram of the electrical measurement equipment is shown in Fig. 12.10.

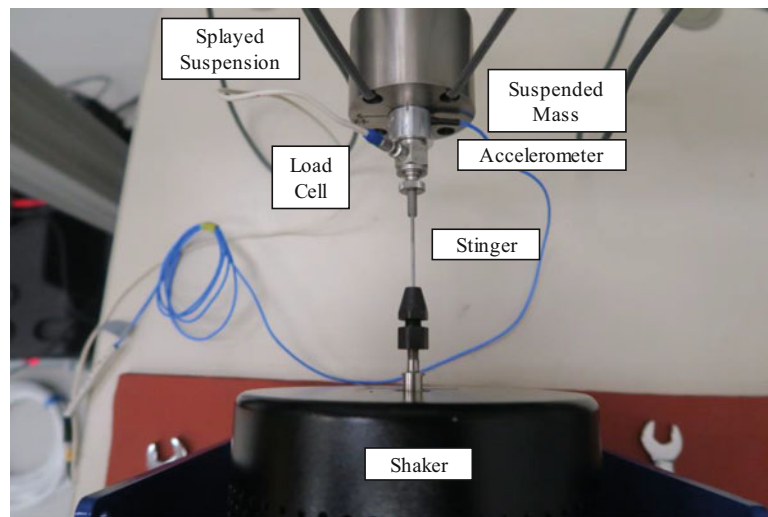


Fig. 12.9 Shaker characterization test setup

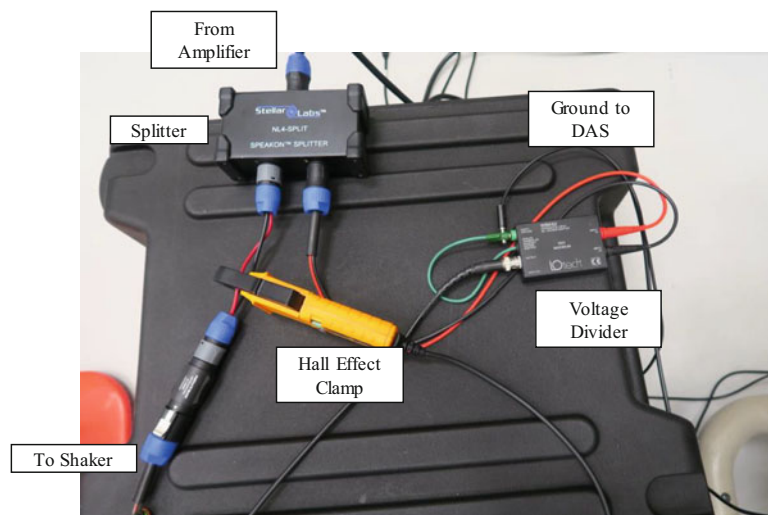


Fig. 12.10 Electrical measurements coming out of the amplifier to the shaker

12.3.2 Model Calibration Process

As previously shown, the different model parameters affect the impedance in different ways. As such, the model parameters can be tuned based on the measurements in a systematic way. Also, some parameters are known or can be measured in different ways, for example the masses can be determined with a scale and the resistance can be measured with a multimeter.

Here is the best approach to calibrating the shaker electro-mechanical model:

- Measure or obtain from specification sheet the shaker armature and body mass and measure the stinger hardware, force gauge, and test mass
- Measure the resistance with a multimeter
- Guess all other values
- Tune the suspension stiffness, K_{12} , based on the frequency of the low-frequency mode
- Tune the stinger stiffness, K_{13} , based on the frequency of the high-frequency mode
- Tune the inductance, L_e , based on the slope of the imaginary part of the impedance
- Tune C_{12} , C_{13} , and BL to match the amplitude of the impedance

12.3.3 *Manual Tuning*

The first step was approximate manual tuning or calibrating of the model parameters based on the impedance measurement. This was quite effective and brought the model impedance very near the measured impedance. Understanding how each parameter affects the model impedance made the manual tuning process possible and quick. Only the damping and force factor terms were difficult to tune because their effects are largely similar; changing the damping may yield similar results to changing the force factor, so it is difficult to determine which is the proper value of each parameter.

12.3.4 *Fine Tuning with a Parameter Search*

To refine the calibration process, a parameter search was used to rapidly implement many combinations of parameter values and compare the model impedance to the test impedance. In this way, model parameters were determined which provide a very good match to the measured impedance, with a minor exception. It was observed that the real part of the impedance was proportional to frequency, much like the effect the inductor has on the imaginary part. The cause of this is not known, but similar effects were seen in the work by Mayes et al. [6]. There, they used a complex inductance value to account for the frequency-dependent real part. The same approach was used here and this greatly improved the real part of the model impedance.

The parameter search used here was implemented as a simple Monte Carlo search wherein multiple parameters could vary over a range from the nominal value. For example, the BL parameter could have seven allowable values, three lower than the nominal and three higher than the nominal. Then, all combinations of all parameters were put in a list where each set of parameters represents a different model configuration. Of course, with many parameters and many possible values for each parameter, this list is too long to evaluate each combination of parameters. Instead, a random subset of the configurations was selected for evaluation. A more sophisticated search algorithm could be used, but this was easy to implement and effective at fine tuning the parameter values after the manual tuning got the model close. The results of each configuration were compared against the test and the best was selected. Defining best is difficult here as the impedance is complex valued and broadband. For this work, an L_2 norm of the error in the real and imaginary parts of the impedance was used. Then, the L_2 norms of the real and imaginary parts were averaged to form a single, scalar error metric and select the best set of parameters to match the test measured impedance. Figure 12.11 shows the model predictions compared with the test measurement using baseline parameters, parameters from a manual tuning, and parameters further refined using the Monte Carlo parameter search method. Table 12.3 provides the parameters for each data set. Even a manual tuning resulted in a very good match to the test measurement, with the parameter search only slightly refining some parameters. The baseline values, particularly the stiffnesses, needed changing to get the model close. Thus, a simple experiment can be very effective in providing model calibration data to dramatically improve the shaker electro-mechanical model.

12.3.5 *Changing Model Parameters When Test Conditions Change*

Ideally, the shaker model should be robust to minor changes in test setup. However, small changes can have a large effect on the shaker response. Also, it is desirable to have a shaker electro-mechanical model which can be used for a range of tests. Most parameters will not change test-to-test since they are inherent properties of the shaker, such as the armature mass or flexure stiffness. However, the stinger stiffness can change significantly depending on the stinger length or diameter. If the stinger is changed, the only model parameters that should change are the stinger stiffness (K_{13}) and damper (C_{13}). To demonstrate effects of stinger length on the impedance, three stinger lengths were used to measure the impedance. Figure 12.12 shows that the impedance is largely the same except for the frequency and amplitude at the stinger mode. Next, the model was changed to try to match the “long” stinger case, changing just K_{13} and C_{13} and leaving all other parameters at the values which were tuned to the “medium” stinger case. As seen in Fig. 12.12, simply changing the stinger parameters still results in a fairly good match to the measured impedance.

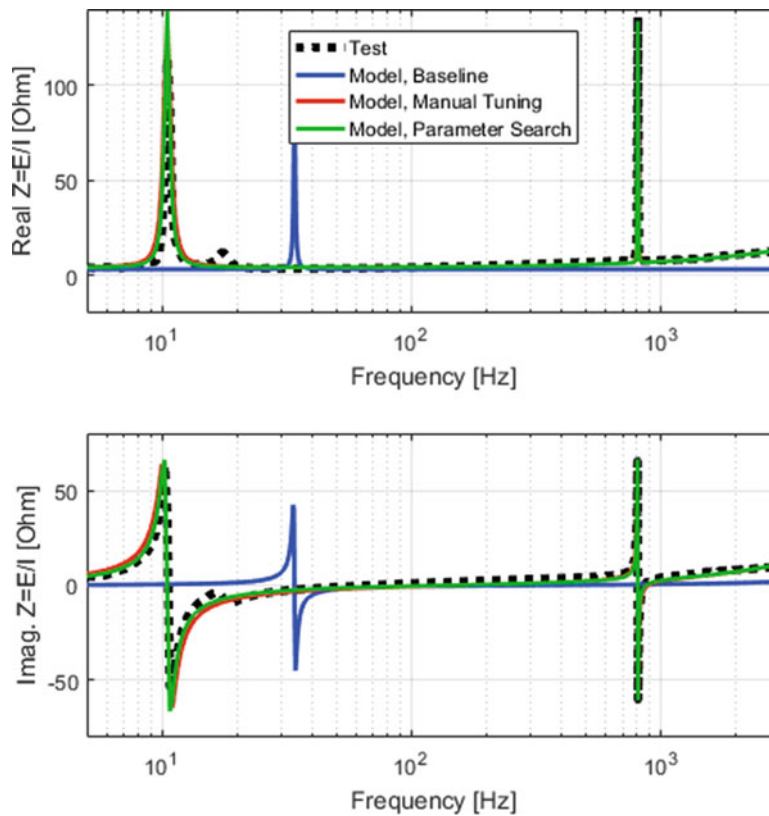


Fig. 12.11 Model predictions compared with test measurements using different parameter values before and resulting from model calibration

Table 12.3 Parameter values before and resulting from model calibration

Parameter	Baseline	Manual	Search	Unit
M_1	0.44	0.44	0.44	kg
M_2	15	15	15	kg
M_3	2.6	2.6	2.6	kg
K_{12}	1.15E+05	1.10E+05	1.10E+05	N/m
K_{13}	2.50E+08	9.63E+06	9.63E+06	N/m
C_{12}	10	12	9.6	N/(m/s)
C_{13}	10	0.5	0.42	N/(m/s)
R_e	3.1	4	4	Ohm
L_e	1.00E-04	6e-4 -j5e-4	6e-4 -j5e-4	Henry
BL	30	40	36	–

12.4 Conclusions

A simple lumped parameter model can capture the coupled electro-mechanical dynamics of typical modal shakers. Such a model could then be used to estimate the effects of the shaker on DUT dynamics or to predict the current and voltage required to achieve some DUT response. While some of the shaker electro-mechanical model parameters can be obtained from a specifications sheet or otherwise measured directly, some parameters such as the force factor and damping have to be inferred from a measurement of the shaker. Here, shaker model parameters were determined from measurements of the electrical impedance. It was found that unknown model parameters can be easily tuned using a manual tuning process and knowledge of the model's sensitivity to the various parameters. The model was found to be reasonably robust to changing test configurations, such as changing the stinger length.

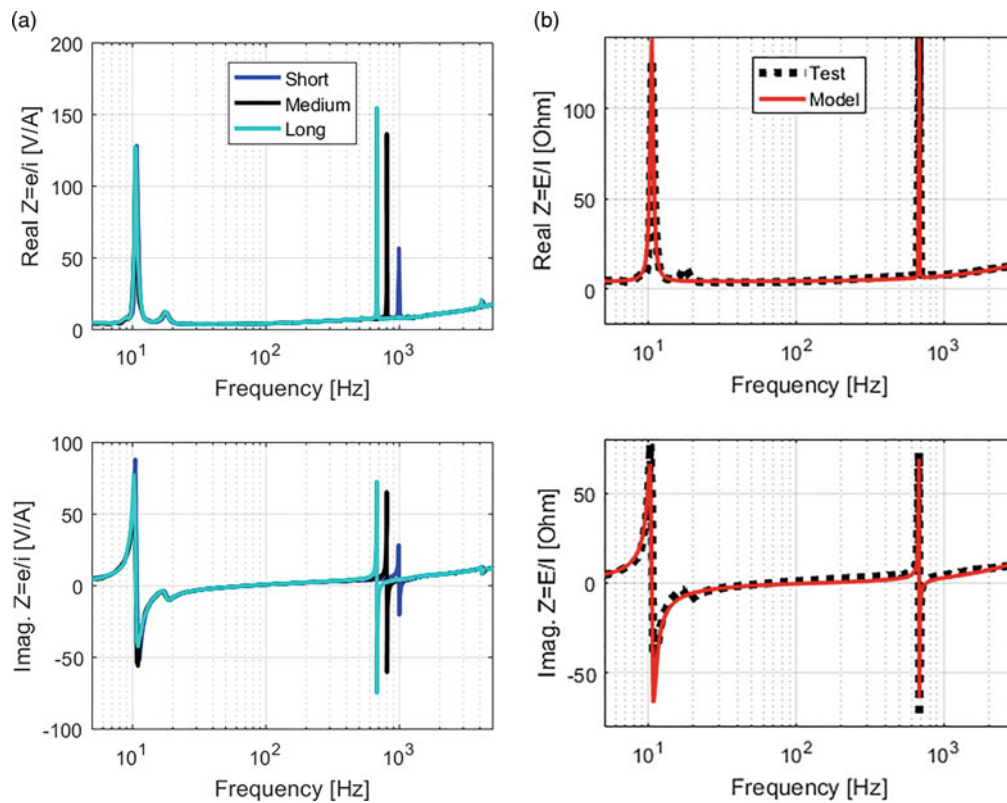


Fig. 12.12 Left: Test-measured impedance using a shorter and longer stinger. Right: Model prediction compared to test results for the long stinger case

References

1. Tiwari, N., Puri, A., Saraswat, A.: Lumped parameter modeling and methodology for extraction of model parameters for an electrodynamic shaker. *J. Low Freq. Noise Vib. Act. Control.* **36**(2), 99–115 (2017)
2. Lang, G.F.: *Electrodynamic shaker fundamentals*. Sound and Vibration, April 1997
3. Smallwood, D.O.: Characterizing electrodynamic shakers. In: *Proceedings of IES, the Institute of Environmental Sciences*, 1997
4. Varoto, P.S., Oliveira, L.P.R.d.: Interaction between a vibration exciter and the structure under test. *Sound and Vibration*, October 2002
5. Lang, G.F., Snyder, D.: Understanding the physics of electrodynamic shaker performance. *Sound and Vibration*, pp. 2–10, October 2001
6. Mayes, R.L., Ankers, L., Daborn, P.M., Moulder, T., Ind, P.: Optimization of shaker locations for multiple shaker environmental testing. In: *Proceedings of IMAC XXXVII, the 37th International Modal Analysis Conference*, 2019

Ryan Schultz is a research and development engineer in the Structural Dynamics department at Sandia National Laboratories.

Sandia National Laboratories is a multimission laboratory managed and operated by National Technology and Engineering Solutions of Sandia, LLC., a wholly owned subsidiary of Honeywell International, Inc., for the U.S. Department of Energy's National Nuclear Security Administration under contract DE-NA0003525.

Chapter 13

A Low-Cost Excitation System for Operational Modal Analysis (OMA)



Max Gille, Johannes Maierhofer, and Daniel J. Rixen

Abstract We introduce a low-cost excitation system for application in operational modal analysis (OMA) working with vibration motors as they can be found in mobile phones. In contrast to experimental modal analysis (EMA), OMA makes an impulse hammer with a force sensor obsolete. If, furthermore, the structural response is measured with a camera instead of multiple accelerometers, this setup does not require an expensive data acquisition system, because no signals need to be recorded synchronously. The excitation of the structure is carried out through vibration motors from mobile phones that can be freely distributed across the structure and which are controlled by a microcontroller. The excitation through many distributed light-weight motors, in contrast to usual methods like manually tapping on the structure, enables long measurements without interfering with the optical measurement. Camera based modal analysis makes very high spatial resolution possible without the need for many accelerometers or a scanning vibrometer.

The setup is tested on two example structures and its potentials are evaluated.

Keywords OMA · Modal analysis · Gradient-based optical flow · Non-contact displacement measurement · Photogrammetry · Random excitation

13.1 Introduction

The use of a digital camera as a displacement sensor for dynamic structural mechanics has been a new development over the past few years. In contrast to the widely-used piezo-electric accelerometers, camera-based displacement identification offers the possibility of full-field measurements instead of having to choose few measurement points. There exist different algorithms to determine the displacements of a captured structure between two frames of a video [1], one very prominent technique is Digital Image Correlation (DIC) [2]. Computationally less demanding algorithms that are applicable for very small displacements are based on the optical flow equation [3]. These optical flow techniques rely on a continuous bright source of light.

Operational modal analysis (OMA) is a way to determine the modal parameters of a structure without the measurement of the excitation forces. Historically, the method originated in the field of civil engineering, where large structures (buildings, bridges) can not be moved to a lab and excited with a force hammer. Instead, the forces acting on these structures due to wind or traffic are considered to be broad band and random. Under this assumption, eigenfrequencies, mode shapes and modal damping can still be extracted from a measurement of displacements, velocities or accelerations on the structure [4].

Operational measurements are also a useful tool in the lab for quick troubleshooting or to investigate non-linearities that are activated by putting much energy into structures. Furthermore, the investigation of different OMA techniques is best performed in a lab to enable reproducible basic conditions. Applying OMA in a lab, though, brings up the question how to excite a structure such that the assumption of a broad band, randomly distributed force still holds true. Commonly, engineers tap on structures with their fingers or excite them manually in another way [5]. From our experience this can be quite inconvenient as for slowly moving structures the measurement duration can be over a minute and one often produces an overload on the sensors. A system that would excite (pseudo-)randomly, but in a well defined range, the structure would remedy both the inconvenience and the danger of many failed measurements due to overloads. Moreover, as we want to research the

M. Gille (✉) · J. Maierhofer · D. J. Rixen

Chair of Applied Mechanics, Faculty of Mechanical Engineering, Technical University of Munich, Garching, Germany
e-mail: max.gille@tum.de; j.maierhofer@tum.de; rixen@tum.de

applicability of camera measurements using gradient-based optical flow methods, an automatic system has the big advantage that it does not change the lighting conditions during the measurements as e. g. hands throwing shadows would do.

13.2 Excitation System

The main idea in this project was to develop a system that could excite a structure independently at as many points possible. For the prototype presented in this work, we used vibration motors known from mobile phones as the excitation sources as they are light-weight, cheap and easy to control.

13.2.1 Electrical Setup

The *AM Multishaker* consists of up to ten DC vibration motors that are plugged onto a custom PCB (printed circuit board). A single-board microcontroller¹ supplies freely programmable PWM (pulse width modulation) signals that are amplified via the custom PCB. A standard USB powerbank acts as the power source. All major parts of the system are depicted in Fig. 13.1.

The software to run the motors in a desired fashion can quite simply be programmed in the *Arduino IDE*.² In our case, the motors are supplied with varying voltages between 0 and 3.3 V. The PWM signal linearly increases and decreases segment-wise with voltages in the higher half of the range being passed three times as fast as the lower half to distribute the excitation energy more equally across the range (see next section). Different motors run up and down in different speeds and start at different initial values such that the ensemble of motors excites the structure in an uncorrelated way. The described voltage supply to the motors is illustrated in Fig. 13.2 for the first few seconds.

13.2.2 Estimation of Excitation Level

The vibrating effect of the motors results from a unbalanced rotating disc inside the motors's housing on which the coils are located. As the center of mass (COM) of this rotating part is only roughly 1.5 mm away from the axis of rotation and its weight being less than one gram, we can expect the force amplitude produced by the motors to be quite low. With the

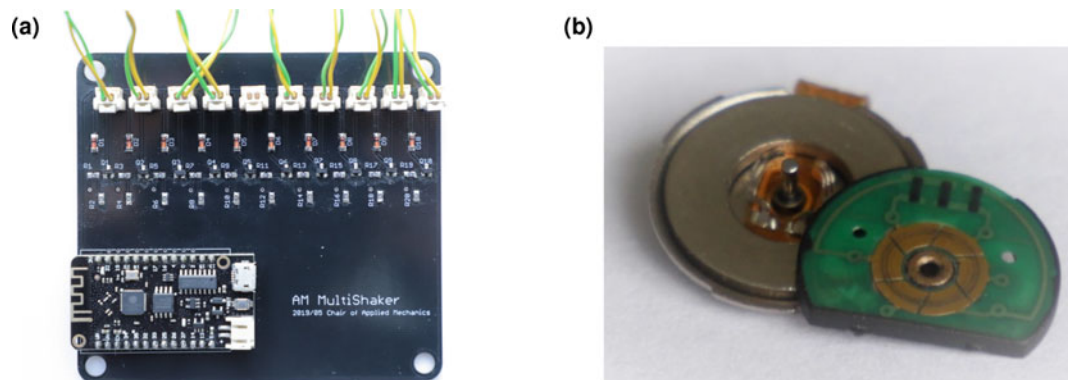


Fig. 13.1 The hardware of the proposed excitation system. (a) The *AM Multishaker* with the microcontroller (bottom left) on top of the custom PCB equipped with SMD (surface mounted device) components that amplify the PWM signals coming out of the microcontroller to drive ten motors connected at the top edge. (b) The interior parts of the vibration motors. Inside the housing (\varnothing 10 mm), a magnet ring and the imbalanced rotor with a small circuit for commutation and the coils underneath can be found

¹Wemos Lolin32 Lite https://wiki.wemos.cc/products:lolin32:lolin32_lite

²<https://www.arduino.cc/en/main/software>

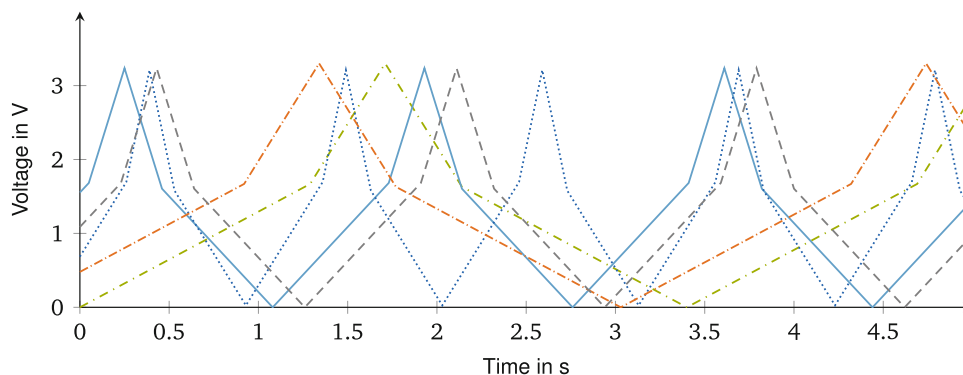


Fig. 13.2 Voltage supply to five of the maximum ten motors plugged into the *AM Multishaker* for the first seconds after switching the microcontroller on. Through different sweep velocities and initial voltages, the structure is exposed to different vibration frequencies across different positions during the measurements

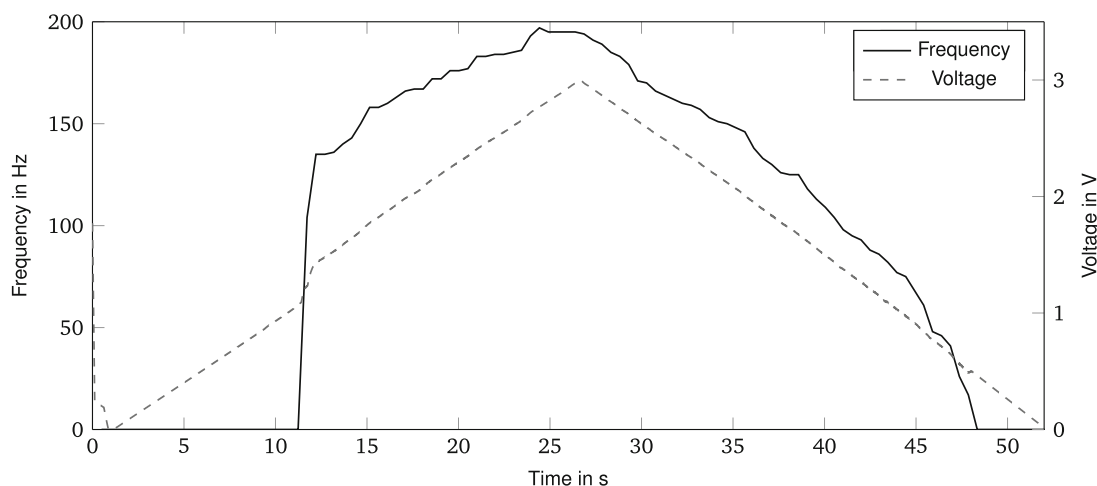


Fig. 13.3 Rotational frequency of the motor and effective voltage during the measurement cycle of slowly increasing and decreasing the motor’s voltage

centripetal force F_c being dependent on the rotation frequency f , the mass m and the distance between COM and rotation axis r as follows:

$$F_c = m(2\pi f)^2 r, \tag{13.1}$$

the resulting force for one motor will be under 1 N at its nominal speed of 12,000 rpm at full voltage. Because of the quadratic nature of Eq. (13.1), this force gets drastically smaller for lower desired excitation frequencies, especially for those frequencies in the observable range for a standard camera well below 50 Hz. At a tenth of the nominal rotational speed ($f = 20$ Hz), the force is lowered to one hundredth its maximum value.

To assess how the rotation frequency of the motors behaves depending on the voltage supply, a linearly increasing and then decreasing PWM signal was given to the one motor such that the whole cycle took just over 50 s. The spinning frequency of the unbalance in the motor was measured by applying an accelerometer on the motor and letting this setup hang freely during the measurement. Frequency and voltage during the described cycle are depicted in Fig. 13.3. Starting at zero voltage, we see that the motor doesn’t spin at all until the voltage roughly reaches 1 V. Above, a constant rise in frequency is observable and the nominal speed at full voltage is verified to be 200 Hz or 12 000 rpm. Once the unbalance is rotating, also voltages below 1 V are enough to overcome internal friction, but it is clearly visible, that frequencies below 50 Hz will be only very marginally excited by the *AM Multishaker*.

13.3 Gradient-Based Optical Flow

To work with camera images as the source of displacement calculation, one has to recap that a grayscale image is nothing but a matrix of brightness values, typically between 0 (black) and 255 (white) for an 8-bit image. Let's consider a certain pattern of different gray values applied to a mechanical structure whose movement will be observed. A certain small part of that pattern is mapped to a single pixel (coordinates x_i, y_i) on the sensor plane and represented by a characteristic brightness or gray value $I(x_i, y_i)$. The basic assumption is the following: if the structure – and thus the pattern – moves, the gray value associated to that part of the pattern doesn't change, it just moves to a different position on the image sensor [6]:

$$I(x_i, y_i, t) = I(x_i + \Delta x, y_i + \Delta y, t + \Delta t) \quad (13.2)$$

The right side of (13.2), approximated with a Taylor series, is

$$I(x_i + \Delta x, y_i + \Delta y, t + \Delta t) = I(x_i, y_i, t) + \underbrace{\frac{\partial I(x_i, y_i, t)}{\partial x}}_{I_x} \cdot \Delta x + \underbrace{\frac{\partial I(x_i, y_i, t)}{\partial y}}_{I_y} \cdot \Delta y + \underbrace{\frac{\partial I(x_i, y_i, t)}{\partial t}}_{I_t} \cdot \Delta t + \dots \quad (13.3)$$

For small displacements the higher order terms in Eq. (13.3) are negligible. Combining both Eqs. (13.2), (13.3), one obtains the basic equation of gradient-based optical flow [7]:

$$I_x \cdot \Delta x + I_y \cdot \Delta y + I_t \cdot \Delta t = 0 \quad (13.4)$$

$$\underbrace{\begin{bmatrix} I_x & I_y \end{bmatrix}}_{\text{grad } I^T} \cdot \begin{bmatrix} \Delta x \\ \Delta y \end{bmatrix} = -I_t \cdot \Delta t \quad (13.5)$$

While the right side of the equation (13.5) is the measurable difference in intensity between two frames at a certain pixel and the gradient vector $\text{grad } I$ can be calculated for a given reference frame, the displacements Δx and Δy are both unknown and cannot both be calculated when considering only equation (13.5).

13.3.1 Simplified Optical Flow

The problem of the two unknowns in Eq. (13.5) can be solved by also taking into account pixels in a small neighbourhood with slightly different spacial gradient vectors and then solve an over-determined system of equations [8]. Another approach is to accept that not both directions of the displacement can be determined and instead compute only the component along the brightness gradient vector [9]. This displacement Δs between a reference and another frame in a video can then be calculated based on the brightness difference ΔI as follows:

$$\Delta s = -\frac{\Delta I}{|\text{grad } I|}, \quad |\text{grad } I| = \sqrt{I_x^2 + I_y^2} \quad (13.6)$$

The fact that only one certain displacement direction can be found from analysing one pixel can be illustrated easily on an example pattern as in Fig. 13.4, a diagonal black/white transition with a white spot as a reference to see the actual displacement between the two frames is depicted: As the pattern moves, in this case straightly upwards, the brightness of the observed pixel decreases. But, it is only possible to determine the displacement along the brightness gradient vector whereas any movement perpendicular to it is not observable. In the case pictured below, this means that even though the pattern has moved upwards (see white reference spot in the lower right corner), we can only calculate the component u_{\perp} in the direction of the gradient $\text{grad } I$ based on the gray value of the observed pixel and the gradient information. Moving the pattern along a direction of constant brightness (perpendicular to the gradient), would obviously not change the pixel's gray value at all and be thus not measurable.

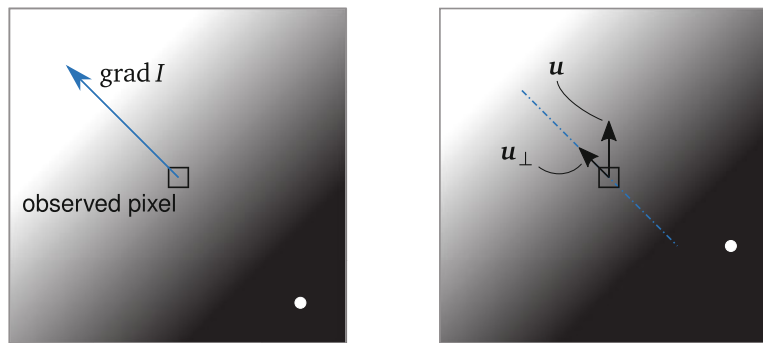


Fig. 13.4 The depicted black/white transition was moved upwards by the vector u from the left image to the right. As it does so, the brightness of the observed pixel changes. Gradient-based optical flow algorithms enable the calculation of movement solely based on the brightness and gradient information of a pixel

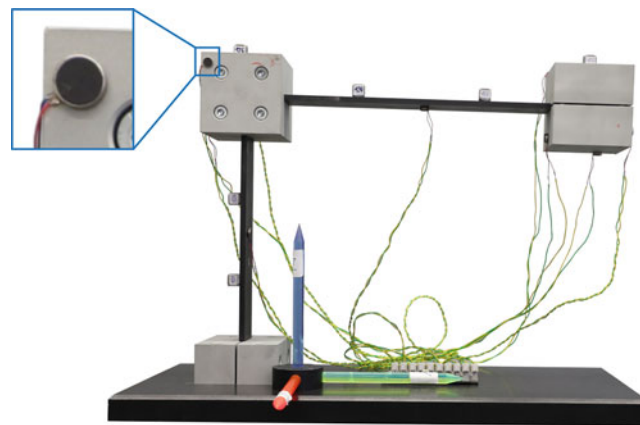


Fig. 13.5 Simple beam-mass structure equipped with the *AM Multishaker* and accelerometers attached. The zoom part shows one of the motors

13.4 Experimental Tests

In this section we evaluate how well the *AM Multishaker* performs and which drawbacks it has, based on two different structures the device was tested on.

13.4.1 Simple Beam-Mass Structure

For a first evaluation, a simple academic construction consisting of a base and two cubes connected to it and each other via steel beams was used. The structure was chosen as its first two eigenfrequencies are below 20 Hz and thus observable by a standard DSLR camera³ taking video footage at 50 fps. Figure 13.5 shows the experimental setup consisting of the structure described above and equipped with the *AM Multishaker* fixed to it via bits of wax. The vibration motors were attached on all parts of the structure and on differently oriented surfaces, such that the excitation would not only act in one plane, which would leave the third physical direction unaffected.

³Canon EOS 6D II

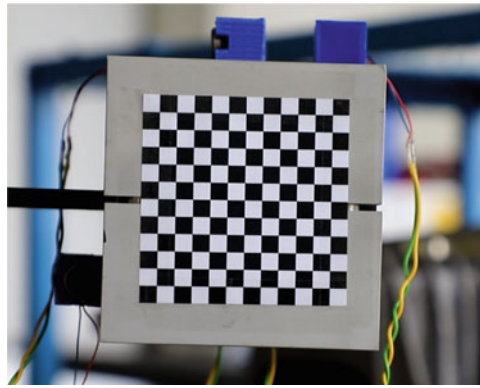


Fig. 13.6 One frame of the video footage of the structure's upper right cube with a checkerboard pattern applied to allow for displacements measurements in both horizontal and vertical direction

Acceleration Measurement

First, the setup was examined using accelerometers⁴ at six positions (see Fig. 13.5). The analysis was performed via LMS Test.Lab using the Operational PolyMAX algorithm, a frequency domain technique. As already mentioned above, the high dependency of the excitation level on the frequency brings some problems with it. A reference measurement with manual tapping as excitation revealed the first eigenfrequencies of the structure to be at $f_1 = 6.5$ Hz, $f_2 = 10.2$ Hz, $f_3 = 21.7$ Hz, a range where one can expect that the excitation coming from the new device is minimal. Still, these eigenfrequencies can be found using the above mentioned frequency domain identification algorithm PolyMAX. The next step, the identification of mode shapes, on the other hand yields no useful results.

Optical Measurement

For this experiment, we taped a printout of a checkerboard pattern to the front facing side of the upper right cube in Fig. 13.5. A standard DSLR camera was placed right in front of the setup on a tripod a video footage was taken while the *AM Multishaker* excited the structure. Figure 13.6 shows one example of the used video footage with the checkerboard pattern applied. The vertical (horizontal) displacements can be calculated from the gray value changes of pixels at horizontal (vertical) edges. Theoretically, the first two eigenfrequencies of the structure are within the scope of the camera's maximum frame rate of 50 fps (Nyquist frequency $f_N = 25$ Hz). But, as mentioned in the previous section, this frequency range suffers from a very low excitation level due to the quadratic relation between rotational speed and centripetal force for a rotating mass. To evaluate, which eigenfrequencies of the structure were excited strongly enough to be measured using the simplified optical flow algorithm, the transient spectrum of the identified vertical displacement is analysed after low-pass filtering the signal such that aliasing is avoided. The blue line in Fig. 13.7 shows this spectrum of the structure's response when it is excited as illustrated in Fig. 13.2. Here, a clear peak at around 6.5 Hz (i.e. the first eigenfrequency) is visible. Above, there is only noise. This result might surprise after the earlier discussion on excitation levels for low frequencies. Indeed, a second measurement, where the *AM Multishaker* was not switched on and thus no (planned) excitation was acting on the structure yields a very similar spectrum (black dashed line in Fig. 13.7) indicating that also in the first measurement only some unknown ambient excitation did activate the first mode.

13.4.2 Wind Turbine Blade

In a second test, we applied the motors on a model-sized wind turbine blade. For such a flat structure whose main dynamics take place in the out-of-plane direction, the motors were first placed in 3D-printed cubes, such that the imbalance would act not only in the plane of the wing, see Fig. 13.8.

⁴Kistler 50 g piezoelectric triaxial sensor

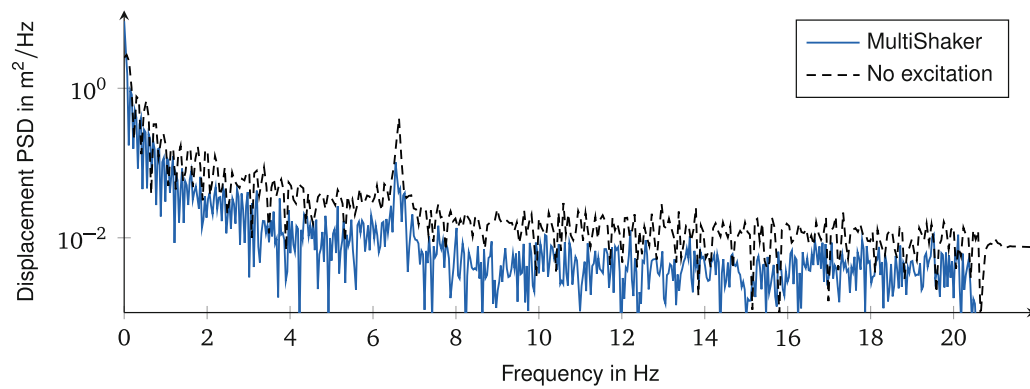


Fig. 13.7 Spectra (power spectral densities, PSD) of the optically identified vertical displacement of the upper right cube from Fig. 13.5 for an excitation with the *AM Multishaker* and no excitation at all

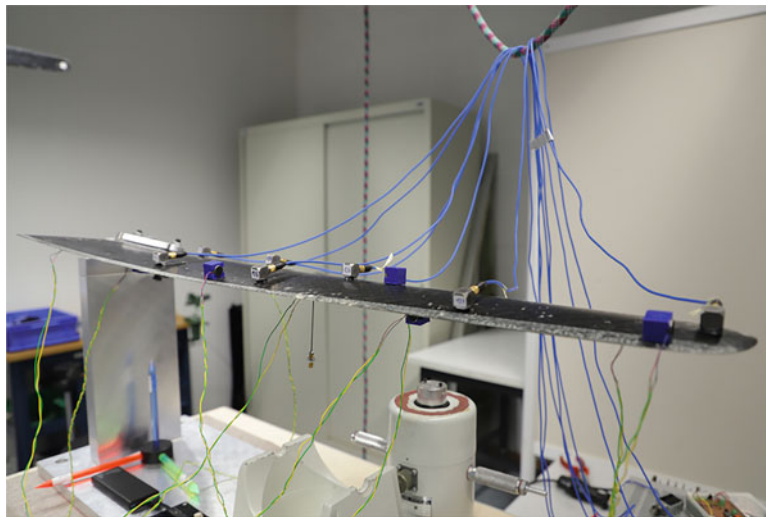


Fig. 13.8 Model of a wind turbine blade. The blade is clamped horizontally at its root and there are seven tri-axial accelerometers attached, as well as the *AM Multishaker*. Some of the motors are mounted at the sides of small cubes to guarantee excitation in all directions

From an earlier experimental modal analysis (EMA) the eigenfrequencies and mode shapes of this structure are well known. The first four eigenfrequencies are within the range of the maximum rotational frequency of the motors (200 Hz). On this structure, the PolyMAX algorithm is able to find all poles that are expected, yet both mode shapes corresponding to eigenfrequencies in the lower band (17 and 63 Hz) are very poorly identified. In the higher frequency regions of above 150 Hz where the other two poles under 200 Hz are located, also the mode shape identification yields plausible results, that match earlier investigations of this structure.

To summarize the results from the experimental tests, it has to be said that the motors exciting the structures appear to be too small and too weak to effectively excite the example structures in the low frequency range. Thus, the usable range with this prototype is quite limited.

13.5 Conclusion

A simple prototype of an excitation system capable of producing uncorrelated harmonic forces at many different structure points in a certain frequency range was designed, built and tested. The aim in developing the setup was to enable optical measurements without influencing the lighting conditions and to facilitate longer measurements by eliminating the need for manual excitation. Future work should evaluate other actuators than the ones used in this paper (DC vibration motors) to

eliminate the big flaw of not being able to effectively work in a low frequency range well below the nominal speed of the motors. If well-suited actuator can be found, the basic idea of the *AM Multishaker* can be re-applied as it is a flexible device that can be simply reprogrammed to apply different excitation patterns.

References

1. Baqersad, J., Poozesh, P., Niezrecki, C., Avitabile, P.: Photogrammetry and optical methods in structural dynamics – a review. *Mech. Syst. Signal Process.* **86**, 17–34 (2017). <https://doi.org/10.1016/j.ymssp.2016.02.011>
2. Chu, T.C., Ranson, W.F., Sutton, M.A.: Applications of digital-image-correlation techniques to experimental mechanics. *Exp. Mech.* **25**(3), 232–244 (1985). <https://doi.org/10.1007/bf02325092>
3. Brandt, J.W.: Improved accuracy in gradient-based optical flow estimation. *Int. J. Comput. Vis.* **25**(1), 5–22 (1997). <https://doi.org/10.1023/a:1007987001439>
4. Brincker, R., Ventura, C.E.: *Introduction to Operational Modal Analysis*. John Wiley & Sons, Ltd (2015). <https://doi.org/10.1002/9781118535141>
5. Batel, M.: Operational modal analysis-another way of doing modal testing. *Sound Vib.* **36**(8), 22–27 (2002)
6. Barron, J.L., Fleet, D.J., Beauchemin, S.S.: Performance of optical flow techniques. *Int. J. Comput. Vis.* **12**(1), 43–77 (1994)
7. Horn, B.K.P., Schunck, B.G.: Determining optical flow. *Artif. Intell.* **17**(1–3), 185–203 (1981). [https://doi.org/10.1016/0004-3702\(81\)90024-2](https://doi.org/10.1016/0004-3702(81)90024-2)
8. Lucas, B.D., Kanade, T.: An iterative image registration technique with an application to stereo vision. In: *Proceedings of the International Joint Conference on Artificial Intelligence*, pp. 674–679 (1981)
9. Javh, J., Slavič, J., Boltežar, M.: The subpixel resolution of optical-flow-based modal analysis. *Mech. Syst. Signal Process.* **88**, 89–99 (2017). <https://doi.org/10.1016/j.ymssp.2016.11.009>

Biography

Max Gille B.Sc. in Mechanical Engineering at TUM in 2015
M.Sc. in Mechanical Engineering at TUM in 2017
Research Assistant at the Chair of Applied Mechanics at TUM since 11/2017

Chapter 14

Reconciling the Difference Between Test and Real Environments: Improving Fixture Design Based on Modal Strain



Scott A. Smith and Matthew R.W. Brake

Abstract With the recent push to make automobiles, aircraft, and other vehicles more fuel-efficient, the redesign of many components are currently underway to reduce the conservativeness of the design with an intent to reduce weight. Laboratory tests are performed to speed up the design qualification process. However, the fixtures used are typically rigid, which provides insight into how a component responds and fails in a “fixed” base manner. Laboratory tests need to be able to reproduce the same stresses and strains experienced to represent real environments. This work proposes that a fixture mimicking the local stiffness and dynamics is required to emulate the actual environmental conditions. This work postulates that the local modal displacements and strains need to match these local dynamics, and the best way to achieve this is through a truncated system.

Keywords Boundary conditions · BARC · Fixture design · Dynamic matching · Component testing

14.1 Approach

To investigate this theory, a simple Euler-Bernoulli beam model is truncated and spring-mass systems are attached at the boundaries. Parameters for the spring-masses are optimized to match the first bending mode dynamics of the truncated and full beams. The full beam is assumed to be the actual environment and is given as the analytical expression of a free-free Euler-Bernoulli Beam of length $5L$, given in Eq. 14.1 and shown in Fig. 14.1a. A truncated beam of length L with attached spring-mass systems (Fig. 14.1b) is utilized as the representative system. For this system Eqs. 14.1a and 14.1b with the appropriate length of L are the same, and Eq. 14.1c is modified to those given in Eq. 14.2. The beams are taken to have the following properties: Modulus of Elasticity of 69 GPa, Density of 2700 kg/m³, and a 2 cm square cross-section.

$$\frac{\partial^2}{\partial x^2} \left(-EI \frac{\partial^2 w(x, t)}{\partial x^2} \right) = \rho A \frac{\partial^2 w(x, t)}{\partial t^2}, \quad x \in [0, 5L] \quad (14.1a)$$

$$\frac{\partial^2 w(x, t)}{\partial x^2} = 0, \quad x \in \{0, 5L\} \quad (14.1b)$$

$$\frac{\partial^3 w(x, t)}{\partial x^3} = 0, \quad x \in \{0, 5L\} \quad (14.1c)$$

$$-EI \frac{\partial^3 w(0, t)}{\partial x^3} = F_1 = kz_0(t) \quad (14.2a)$$

$$-EI \frac{\partial^3 w(L, t)}{\partial x^3} = -F_2 = -kz_L(t) \quad (14.2b)$$

S. A. Smith (✉) · M. R. W. Brake
William Marsh Rice University, Houston, TX, USA
e-mail: scott.a.smith@rice.edu; brake@rice.edu

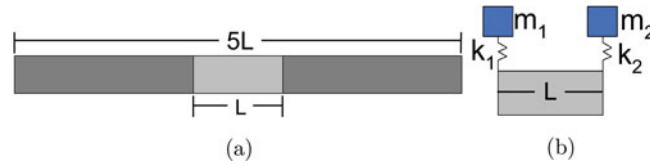


Fig. 14.1 Euler-Bernoulli beams studied; (a) full length and (b) truncated with spring-masses attached at the boundaries

F_1 and F_2 are solved by performing force balance at the boundaries in Fig. 14.1b. The equation of motion for the boundary condition is given as:

$$M \frac{d^2 z_x}{dt^2} = k (\Theta(x) - z_x) \quad (14.3)$$

Using Eqs. 14.3 and 14.2, and applying separation of variables, the steady state boundary becomes

$$-EI \frac{d^3 \Theta(0)}{dx^3} = \frac{\omega^2 M_1 k_1 \Theta(0)}{M_1 \omega^2 - k_1} \quad (14.4a)$$

$$-EI \frac{d^3 \Theta(L)}{dx^3} = -\frac{\omega^2 M_2 k_2 \Theta(L)}{M_2 \omega^2 - k_2} \quad (14.4b)$$

Using Eqs. 14.1a, 14.1b, and 14.4 the natural frequencies and mode shapes can be found as:

$$2 \cos \beta L \cosh \beta L - 2K_1 \cos \beta L \sinh \beta L + 2K_1 \sin \beta L \cosh \beta L - 2K_2 \cos \beta L \sinh \beta L + 2K_2 \sin \beta L \cosh \beta L - 4K_1 K_2 \sin \beta L \sinh \beta L = 0 \quad (14.5a)$$

$$\beta^4 = \omega^2 \frac{\rho A}{EI} \quad (14.5b)$$

$$\Theta_L(x) = A \left[\sin(\beta x) + \frac{1 - \Psi}{2K_1} \cos(\beta x) + \Psi \sinh(\beta x) + \frac{1 - \Psi}{2K_1} \cosh(\beta x) \right] \quad (14.5c)$$

$$\Psi = \frac{\cos(\beta L) + K_2 \sin(\beta L) - \frac{\sigma}{2K_1}}{\cosh(\beta L) - K_2 \sinh(\beta L) - \frac{\sigma}{2K_1}} \quad (14.5d)$$

$$\sigma = \sin(\beta L) - K_2 \cos(\beta L) + \sinh(\beta L) - K_2 \cosh(\beta L) \quad (14.5e)$$

$$K_1 = \frac{\beta m_1}{\rho A \left(\frac{m_1}{k_1} \beta^4 \frac{EI}{\rho A} - 1 \right)} \quad (14.5f)$$

$$K_2 = \frac{\beta m_2}{\rho A \left(\frac{m_2}{k_2} \beta^4 \frac{EI}{\rho A} - 1 \right)} \quad (14.5g)$$

14.2 Simulations

To optimize the springs and masses, an implementation of NSGA-II in Matlab's global optimization toolbox is utilized. The program is used to optimize the scaled mode shape (Eq. 14.6) or strain mode shape (Eq. 14.7) using the Modal Assurance Criterion (MAC), Eq. 14.8, or Modal Strain Assurance Criterion (MSAC) when strain mode shape is used; and the relative error between the frequency of the truncated beam to full length beam.

$$\Theta_s = \frac{\Theta - \min(\Theta)}{\max(\Theta) - \min(\Theta)} \quad (14.6)$$

$$\Psi = \frac{d\Theta}{dx} \quad (14.7)$$

$$MAC = \frac{|\Theta'_L \Theta_{5L}|^2}{(\Theta'_L \Theta_L) (\Theta'_{5L} \Theta_{5L}^*)} \quad (14.8)$$

Two cases are analyzed, symmetric (SSM) and asymmetric (ASM) spring-masses. The symmetric case is studied because the truncated beam is assumed to be centered in the whole beam. The Pareto fronts from using the two different shapes are shown in Fig. 14.2a, b. The asymmetric case allows for the springs and masses to vary independently, the Pareto fronts are shown in Fig. 14.2c, d. As ASM did not converge to a reasonable error for frequency (minimum achieved was 120%) the results from the symmetric cases were used to seed the first generation, the results are shown in Fig. 14.2e, f.

14.3 Conclusions

The conclusion of this study is that there is a possibility to truncate boundary conditions such that the dynamics seen by a component can be matched. However, the use of optimization techniques need to be surveyed in more detail. Furthermore, the applicability of other techniques such as transmission simulator or effective mass need to be assessed. These methods, though, tend to return non-physical masses and stiffness matrices. Since, the overall goal is to make a fixture for testing, the parameters need to have physical representatives. The method must be expanded to a 3D finite element model of a beam, so that it may be applied to more complex structures such as the Box Assembly with Removable Component.

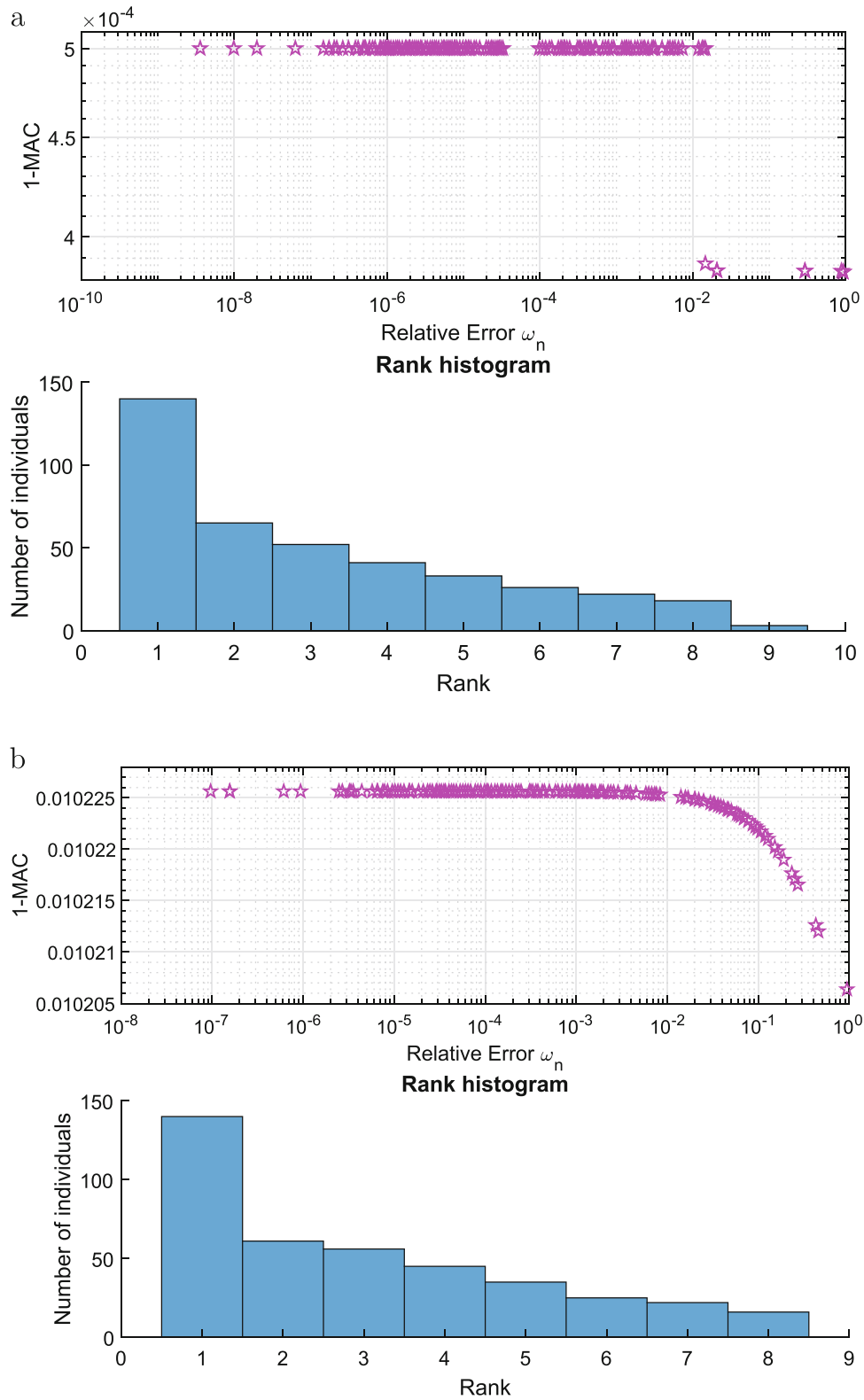


Fig. 14.2 Pareto front and rank histograms of SSM (a) scaled and (b) strain mode shapes, ASM for (c) scaled and (d) strain mode shapes, and ASM seeded with SSM for (e) scaled and (f) strain mode shapes

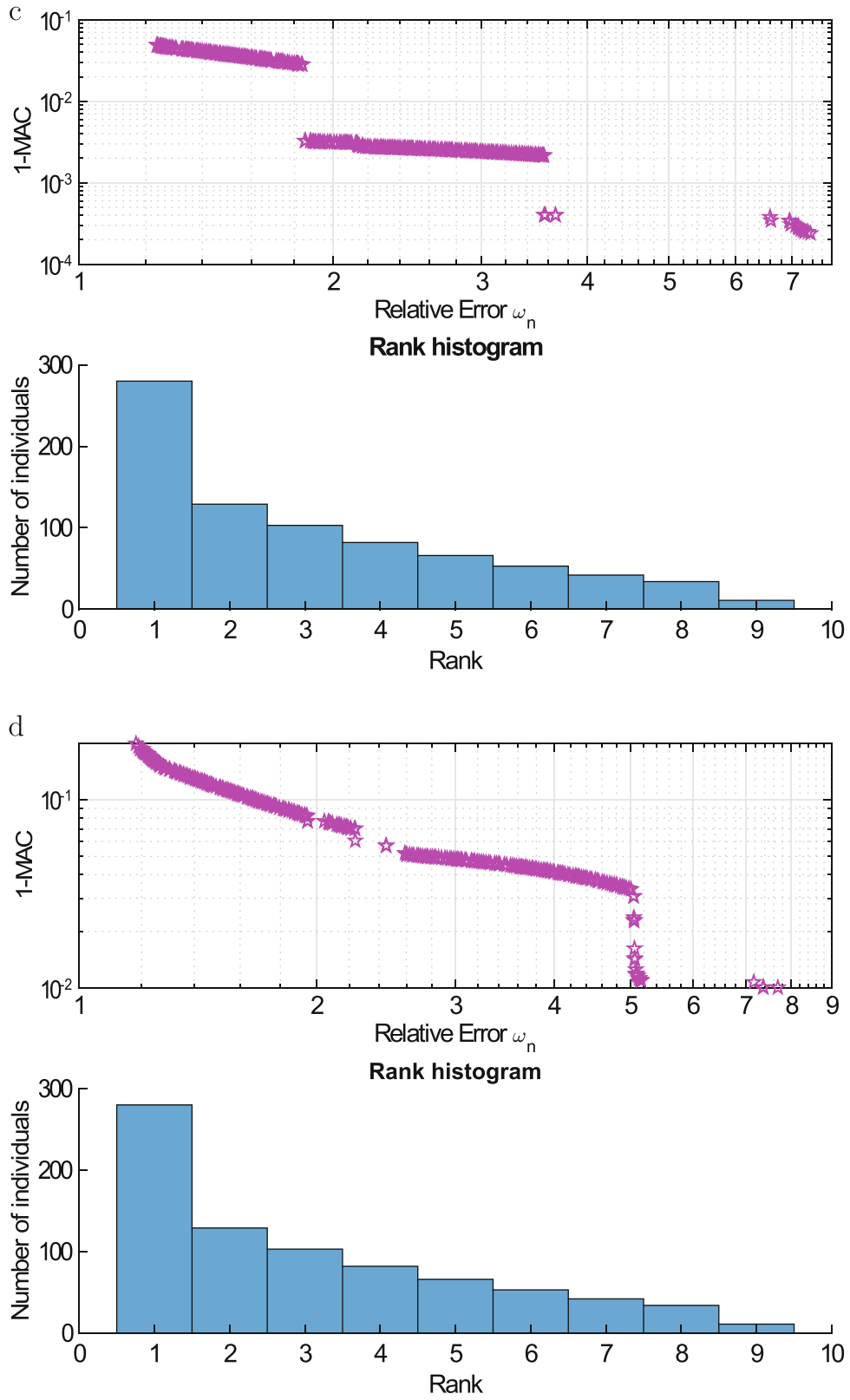


Fig. 14.2 (continued)

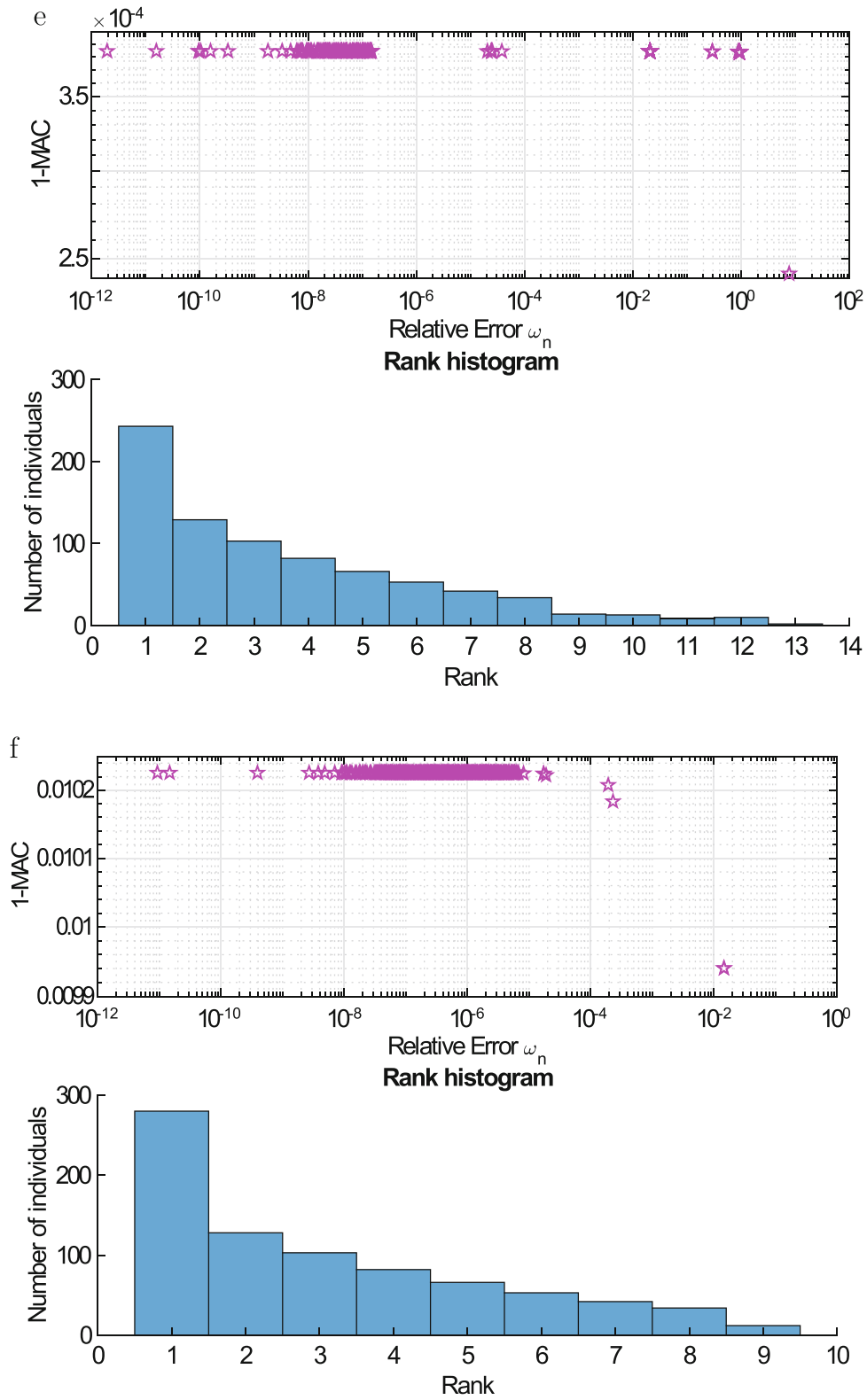


Fig. 14.2 (continued)

References

1. Soine, D.E., Jones, R.J. Jr., Harvie, J.M., Skousen, T.J., Schoenherr, T.F.: Designing hardware for the boundary condition round robin challenge. In: 36th International Modal Analysis Conference (IMAC XXXVI), Orlando (2018)
2. Schoenherr, T.F.: Derivation of six degree of freedom shaker inputs using sub-structuring techniques (2018)
3. Dilworth, B.J., Karlicek, A., Thibault, L.: An approach to component testing: an analytical study (2019)
4. Ristow, J., Gray, J.: Comparing fixed-base and shaker table model correlation methods using JIM beam (2019)
5. Rohe, D.P., Schultz, R.A., Schoenherr, T.F., Skousen, T.J., Jones, R.J.: Comparison of multi-axis testing of the barc structure with varying boundary conditions (2019)
6. Schoenherr, T.F., Coffin, P., Clark, B.: Use of topology optimization to design shock and vibration test fixtures (2019)
7. Hall, T.M.: Analytically investigating impedance-matching test fixtures (2019)
8. Zwink, B., Avitable, P., Tipton, D.G.: Modal projection matching (2019)
9. Devine, T.A., Malladi, V.S., Tarazaga, P.A.: Replicating responses: a virtual environmental test of unknown boundary conditions (2019)
10. Mayes, R., Andkers, L., Daborn, P.: Predicting system response at unmeasured locations (2019)
11. Mayes, R., Andkers, L., Daborn, P., Moulder, T., Ind, P.: Optimization of shaker locations for multiple shaker environmental testing (2019)
12. Harvie, J.M., van der Seijs, M.: Application of transfer path analysis techniques to the boundary condition challenge problem (2019)
13. Schultz, R.: A demonstration of force estimation and regularization methods for multi-shaker testing (2019)
14. Rohe, D.P., Nelson, G.D., Schultz, R.A.: Strategies for shaker placement for impedance-matched multi-axis testing (2019)
15. Musella, U., Blanco, M.A., Mastrodicasa, D., Monco, G., Lorenzo, E.D., Manzato, S., Peeters, B., Mucchi, E., Guillaume, P.: Combining test and simulation to tackle the challenges derived from boundary conditions mismatches in environmental testing (2019)
16. Devine, T.A., Malladi, V.S., Tarazaga, P.A.: Electromechanical impedance method for applications in boundary condition replication (2019)
17. Reyes, J.M., Avitable, P., Jones, R., Soine, D.: Fixture neutralization method – adjustment of vibration response to account for fixture-test article dynamic coupling effects using measured frequency response functions (2019)
18. Reyes, J.M., Avitable, P.: Implementation of the fixture neutralization methodology using data physics vibration controller (2019)

Chapter 15

A Video-Based Course on Random Vibrations



Pernille Lysgaard and Rune Brincker

Abstract Structures vibrate – this is known from structural dynamics courses and applied in design of structures. However, once the structure is there, the observable vibrations do not follow the well-defined shapes considered in modal analysis, the response of a structure is a random combination of those modal shapes. However, the random response contains all the information needed to evaluate on the dynamics of the structure. This course therefore deals with the analysis and interpretation of the random response of linear systems, such as a structure, through the principles of correlation and spectral densities. Furthermore, this course is a 100% e-learning course with video-based lectures and weekly webinars for questions and discussion. A first of its kind at the faculty of Civil Engineering at the Technical University of Denmark. The idea is that this will broaden the availability of an otherwise niche course. At the same time the format allows for the course to be run at three different levels, attempting to make the same course relevant for multiple levels, all the way from MSc to PhD and other interested researchers.

Keywords Random vibrations · Spectral density · Correlation function · e-learning · Self-paced

15.1 Introduction

The course is focusing on the classical problem of random vibration. Consider a measured random response from any structure. This response will be recorded in a number of measurement points, and thus the response will be a vector as a function of time.

The classical problem is that this response – in its raw visualisation – seems chaotic and difficult to interpret. It is preferable to plot the responses in a way where the properties of the system are more visible. The classical ways to do this is to plot correlation functions and spectral density functions. Thus, this course focus on these basic tools to visualise the system property content in random responses. Of course, this has to be understood well also in the case of several responses, i.e. cases where correlation functions and spectral densities turn into matrices.

The aim of the course is thus, to help the students to understand why correlation functions and spectral densities are estimates, how these quantities are estimated, and what they reveal about the properties of the system.

15.2 Structure

The course is run as a 100% self-paced e-learning course where all the content is available to the students from the beginning. This course material consist of video recordings, lecture slides, exercises, notes and readings for ten lectures at three different levels, A, B, and C. It is encouraged that the students orient themselves in the reading material, then watch the video or videos for the lecture with the slides readily available for note taking, move on to the exercises and on this basis prepare questions for the weekly webinar. With this, the students should be ready to complete all exercises and eventually compile their findings and takeaways in a portfolio that is the basis for evaluation of the student on a pass or fail basis.

P. Lysgaard (✉) · R. Brincker
Technical University of Denmark, Kgs. Lyngby, Denmark
e-mail: pelan@byg.dtu.dk; runeb@byg.dtu.dk



Fig. 15.1 Snapshot from the introduction lecture to illustrate the format of the video lectures

For the reading material two books are used, the primary is the textbook *An Introduction to Random Vibrations, Spectral & Wavelet Analysis* by D.E. Newland [1] for theoretical understanding. This is supported by the textbook *Introduction to Operational Modal Analysis* by R. Brincker and C. Ventura [2] for more application uses and examples.

For the videos, they are recorded lectures by coauthor of this article Rune Brincker, see Fig. 15.1 for an idea of the format. There are 31 videos in total. An introduction video used to introduce the concept and content of the course followed by the ten lectures at the three different levels. Level A aims at the participant who wants to understand the basic concepts of random vibrations without too much technicality and application. Level B aims at the participant who wants to be able to understand what is going on in each topic introduced by the course. Level C aims at research participants who wish to challenge the boundaries of the curriculum and experience the possibilities of the methods. For each lecture and each level there are a number of corresponding exercises for the participant to solve and get familiar with the content.

For evaluation of the course the participants are asked to submit a written portfolio of no more than 30 pages. This portfolio encourage a free format where the participant can present exactly what he or she has learned from the course. Within this the participant should have takeaways representing the learning objectives for the course

A student who has met the objectives of the course will be able to:

- Define and estimate probabilistic quantities like mean values and variances from response data
- Define correlation and explain how the concept can be used to extract physical information
- Define auto-correlation and cross-correlation functions and explain how they can be used to extract physical information
- Use numerical methods to estimate auto-correlation and cross-correlation functions
- Explain classical Fourier transforms and use digital Fourier transforms to process response data in MATLAB [3]
- Define spectral density functions and explain how they can be used to extract physical information
- Use numerical methods to estimate spectral density functions
- Outline and describe the concept of linear systems and use MATLAB to perform simple response simulations

15.3 Vision

The main idea with this course is not only to teach the course content to the students of the Technical University of Denmark and guest students but also to make it available to as many as possible, which is why the video format was chosen. Furthermore the split level, e-learning, and self-paced format should allow for all types of participants whether it is MSC students, PhD students, continued education students or anything else.

15.4 Realisation

The course was run for the first time in the fall semester of 2019, starting in September and finishing off in December. Prior to the course it was announced to an international audience as well as internally at the university. However, it is well known that getting participants for a course running for the first time can be troublesome, and thus this proved also the case for this course. By the last day of registration, the course had two participants enrolled. Fortunately, the free format of the course allowed for latecomers and thus, especially the international participants joined over the first couple of weeks. At the time of writing this article the course is half way through and has a team of 11 active participants whereas approximately half are from elsewhere than the Technical University of Denmark.

The course is run on the new teaching platform of the university called DTU Learn [4] from where the participants has access to the webinar platform Adobe Connect [5]. For the purpose of this course the webinar room is set up such that the lecturers have camera and microphone active at all times, while participants can simply listen. There is then an option to raise a hand, which will lead to the lecturers give microphone and video rights, this way the questions are given in a way where a small discussion can arise. However, this format has proven to provide more distance between the lecturers and the participants than first expected and so at the time of writing this article, it is currently a work in progress to obtain feedback from the participants on how the discussion can be more liberate between the participants as well as with the lecturers.

15.5 Conclusion

In conclusion this course is showing good potential to cover geographical distance in order to spread the knowledge of processing random vibration data. However, there are some obstacles related to maintaining the good discussion known from a classic classroom setting that needs to be overcome to make the course satisfactory. Furthermore, there is a wish to expand the knowledge of this course so that the next team participating can be much larger and more people can come to realise the potential of this topic.

References

1. Newland, D.E.: An Introduction to Random Vibrations, Spectral & Wavelet Analysis. Courier Corporation, North Chelmsford (2012)
2. Brincker, R., Ventura, C.: Introduction to Operational Modal Analysis. John Wiley & Sons, Chichester (2015)
3. MATLAB: Version 9.4.0.813654 (R2018a). The MathWorks Inc., Natick (2018)
4. D2L Brightspace: DTU Learn. D2L Corporation, Kitchener (2019)
5. Adobe: Adobe Connect version 10.5. Adobe Inc., San Jose (2019)

Pernille Lysgaard is PhD student at the Dept. of Civil Engineering of the Technical University of Denmark. Her research interests are focused on structural dynamics, operational modal analysis and structural monitoring with damage detection.

Rune Brincker is Professor in Structural Dynamics at the Dept. of Civil Engineering of the Technical University of Denmark. His research interests are focused on operational modal analysis and structural health monitoring.



Chapter 16

Vibration-Based Non-Destructive Techniques for a 3-Level Characterization of Damages in Cables

Abdou Dia, Lamine Dieng, and Laurent Gaillet

Abstract For the characterization of damages of cables, tests have been performed on a safe seven-wire strand which is equipped with eight contactless laser sensors recording the transverse displacements. After this first phase, the same experiments are done on the same cable but with one broken wire, out of the seven. The data (dynamic parameters) from a safe and damaged cable are then compared. For a full damage characterization, the main aim is being able to detect (level 1), locate (level 2), quantify the damage severity (level 3) and predict remaining service lifetime (level 4) of the structure. However vibration-based methods are well known in the literature to provide levels 1 and 2 (detection and location) of damage identification but it seems challenging to go further using only these methods. In this paper, using modal analysis in the frequency domain, detection and location of damage are made. Then a second and a third damages are made in the cable gradually in order to increase the damage severity. Based on the natural frequencies that are less affected by experimental errors and simple to determine, a parameter to estimate the damage severity is provided at the end. Consequently, that allows attaining the level 3 in damage characterization.

Keywords Cables · Damages severity · Modal analysis · Natural frequencies · C_i parameter

16.1 Introduction

Cables are of the critical structural parts of cable-stayed bridges and suspension bridges. These cables are, through their structural life, submitted to different types of solicitations: mechanical loads, thermal loads and chemical attacks. Such actions generate two main pathologies that are corrosion and another one known as fretting-fatigue [1, 2]. Fretting-fatigue is a combination of fatigue solicitations and friction between wires constituting the cable [3]. These pathologies, when not detected early enough and cured, can lead to severe damages not excluding collapse. Thereby, it demonstrates the necessity of monitoring the health of such structures for users' safety. Hence, many non-destructive techniques (NDT) have been developed all along the years to come over these issues. Of these NDT, we have the eddy current inspection, magnetic fields-based inspection, radiographic testing, acoustic emission (AE), vibration-based methods, etc. A review of some of these NDT is given in [4]. In this current work, vibration-based techniques are used in order to evaluate the structural health of cables. In other words, the objectives are, at first to give to practitioners a mean to detect and evaluate damage (wire breaks) severity in cables and then to locate the damage so it can be repaired if necessary.

Therefore, for this work, tests have been performed on a safe seven-wire strand equipped with eight contactless laser sensors recording the transverse displacements where the excitations are made by hammer impacts. After this first phase, the same experiments are carried out on the same cable but with one broken wire, out of the seven. This will allow comparing data (dynamic parameters) from a safe and damaged cable. For a full damage characterization, four levels are defined: the detection, the location, the quantification of the damage severity and the prediction of the remaining service lifetime of the structure [5]. In [6], authors emphasize that vibration-based methods provide levels 1 and 2 (detection and location) but not further; this is also noticed by Le Petit [7]. In this paper, using modal analysis in the frequency domain, detection and location of damage in cable are made. Then a second and a third damages are introduced in the cable gradually in order to increase the damage severity. Based on the natural frequencies that are less affected by experimental errors and simple to determine,

A. Dia (✉) · L. Dieng · L. Gaillet

Materials and Structures Department (MAST), Metallic Structures and Cables Laboratory (SMC), IFSTTAR, Bouguenais Cedex, France
e-mail: abdou.dia@ifsttar.fr; lamine.dieng@ifsttar.fr; laurent.gaillet@ifsttar.fr

a parameter enabling to estimate the damage severity is provided at the end. Consequently, that allows attaining the level 3 in damage characterization that is the damage severity quantification.

16.2 Background

For the analysis of the vibration data, we have used methods based on experimental modal analysis (EMA) since the impact hammer used gives the excitation force. The modal analysis is the extraction of modal parameters (natural frequencies, damping ratios and mode shapes) of a structure from measured (experimental) or simulated (finite elements modelling) vibration data [8]. This modal analysis can be done either in frequency, time or time-frequency domains. When working in the frequency domain, in our case, the determination of the frequency response functions (FRFs) is a required step for the determination of the dynamic parameters. The FRFs are defined as the output to input ratio; the output being the displacements in this case and the input is the force. After determining these FRFs, through mathematical and numerical tools of curve fitting, the dynamic parameters can be extracted, highlighting the need of accurate and less noisy FRFs data. Among these tools of curve fitting used to extract dynamic parameters from FRFs data, there are the well-known and simplest peak-picking method, the circle-fitting method, the global rational fraction polynomial (GRFP) [9], etc. A review of these modal analysis methods can be found at [6, 10].

In this paper, the circle-fitting method is applied to extract dynamic parameters from FRFs as it shows accurate results for a large number of situations [10, 11] and is easily implemented. This method requires also minimum computer resources, it gives better results than other methods such the peak-picking one and is not as sensitive to effects from adjacent modes [12]. This method is based on the fact that the Nyquist plot of the imaginary part vs the real part of an FRF in the vicinity of one resonance (hence its classification in SDoF-Single Degree of Freedom methods) gives a circle-like graph. The fitting of this circle-like graph gives the dynamic parameters [13, 14]. The main drawback of this method is that, even though it can give satisfactory results, it is very time-consuming when one has many FRFs to analyze.

16.3 Experimental Setup

As stated above, a seven-wire strand has been used; a seven meters long specimen of which is mounted on a load test rig as shown in Fig. 16.1a.

Anchor wedges, at both ends, fix the cable to the load test rig. Transient impulses are applied to the cable using an impact hammer equipped with a force transducer (Fig. 16.1c). The tension of the cable is applied using a hydraulic cylinder on which there is a force gauge to measure the force (Fig. 16.1b).

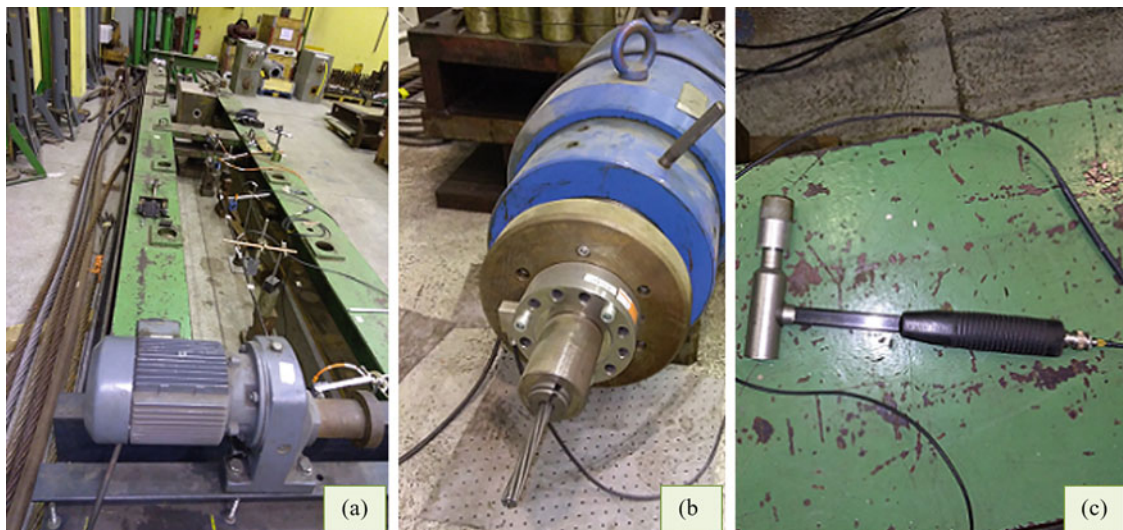


Fig. 16.1 Testing means – (a): load test rig with seven-wire strand and sensors, (b): anchor and hydraulic cylinder, (c): impact hammer

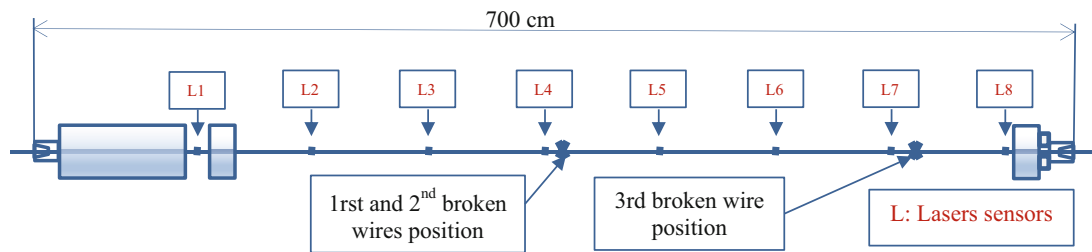


Fig. 16.2 Tests layout

For the data acquisition and storage, laser sensors have been used. The laser sensors give the cable's displacements that are used for the determination of its dynamic characteristics. These lasers are coupled with Quantums MX 1615B and 1610 data acquisition systems. The CATMAN software is used for the visualization of the data. A temperature probe is also used to monitor temperatures variations all along the tests.

Baring in mind that the aim of the tests is to characterize damages in the seven-wire strand, the tests are done on a safe cable and a damaged one with different levels of damages. The damages are introduced in the strand by cutting one, two and three wires gradually. The positions of these damages are represented on Fig. 16.2 that shows also the laser sensors layout. The tests procedure can then be summarized in these seven steps:

1. Tensioning of the cable: the seven-wire strand is taut at 30% of its breaking load
2. Mounting the lasers and the data acquisition systems. To ensure the functionality of these devices some preliminary tests are done. The lasers are placed so that those with the larger measuring ranges are placed in the middle and the others to the ends in order to record all the displacements during the vibration of the cable
3. Excitation of the cable by hammer impact. Near each laser position, the impact is repeated seven times in order to measure data repeatability. The data (cable displacements) given by laser sensors are stored at the sampling rate of 300 Hz during 45 s
4. First wire break: the position is indicated on Fig. 16.2. After this first damage, there is a loss of tensile strength and the cable is not retaut at its first tension value but left as is
5. We repeat steps 2 and 3
6. Introduction of second wire break at the same place than the previous one and we repeat the same tests
7. Introduction of the third wire break near to the anchorage and repeat of the same tests.

16.4 Results Analysis

16.4.1 Damage Detection and Location

To detect and locate damage, vibration-based comparison between cables of different states of safety is done through their dynamic characteristics (natural frequencies, damping ratios and mode shapes). The comparison between safe strand and the strand with one broken wire is then done. To determine the dynamic characteristics, one calculate at first the FRFs since both input and output data are available by using the hammer impact. In Fig. 16.3, the Bode diagrams (phase and amplitude vs frequency) of receptance are plotted. The name 'receptance' is used for FRFs when the output is the displacements. Are only presented in Fig. 16.3, the FRFs obtained with impact at position L1 (see Fig. 16.2) and response at the same position. To lighten the text, the Bode diagrams of the others FRFs are not presented, but they are similar to the one plotted.

An analysis of both FRFs of safe and damaged cables shows that, even though the changes in phases are not very clear (due to the fact that they are very sensitive to noise) [8], the first three resonance peaks, corresponding to location of natural frequencies, are well separated. From the fourth resonance, the peaks are less clear and the level of noise become important. Up to this point of the analysis, the only difference noticed between the two graphs is that the peaks resonances of the damaged cable happen at lower frequency values. Thus, for a more complete comparison between the two states of the cable, one have to determine the dynamic parameters.

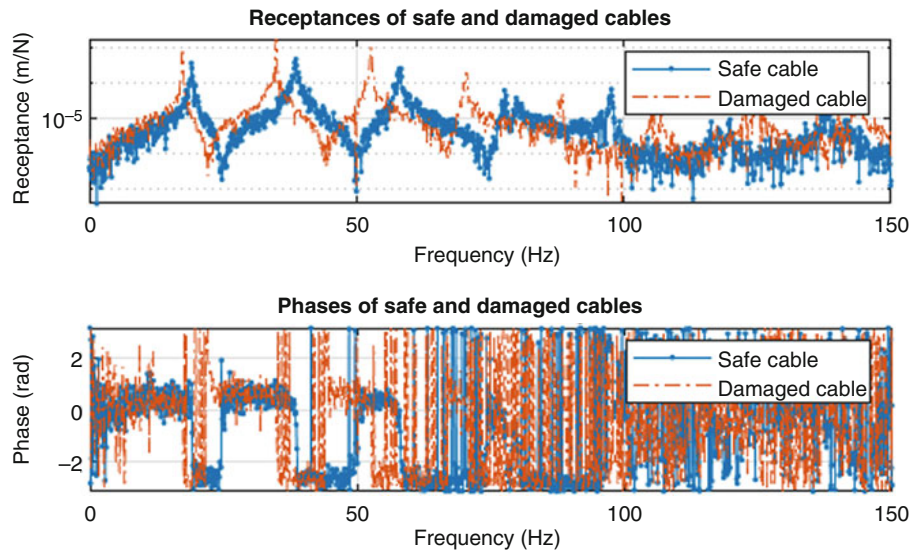


Fig. 16.3 Bode diagrams of safe and damaged cables

Table 16.1 Comparison of safe and damaged cables natural frequencies.

Modes	Safe cable		Damaged cable		
	f_n^s (Hz)	CV^s (%)	f_n^d (Hz)	CV^d (%)	C_i (%)
1	19.16	0.42	17.47	0.18	8.84
2	38.65	0.14	34.68	1.47	10.27
3	58.08	0.18	52.65	0.26	9.35
4	78.06	1.08	70.46	0.13	9.74
5	97.60	0.08	88.39	0.15	9.44

Based on these FRFs curves, the cables dynamic parameters calculation is done. This step is carried out using the circle-fitting method. Natural frequencies and mode shapes are then calculated and used to detect, locate and estimate damage severity in the cable.

Detection

For each hammer impact, the natural frequencies for the two cables are calculated; the mean values with the coefficients of variation are given in Table 16.1. The coefficient of variation is obtained by dividing the standard deviation (std) by the average (mean):

$$CV (\%) = 100 * \frac{std (f_n)}{mean (f_n)} \quad (16.1)$$

The analysis of this Table 16.1 shows that the natural frequencies have decreased for all modes. Since natural frequencies are easily determined, in fact they can be determined directly through FRFs or Fourier transforms plots given by one sensor, and are less affected by experimental errors [15], they are used for the damage detection. To do so, the percentage of changes in natural frequencies, C_i (%) [16, 17], is calculated and the values are included in Table 16.1. This damage indicator is calculated as:

$$C_i (\%) = \frac{f_n^s - f_n^d}{f_n^s} \quad (16.2)$$

Where f_n^s and f_n^d are natural frequencies of respectively safe and damaged cables.

It can be noticed that all the values of C_i are higher than 8%. Taking into account that the errors in natural frequencies values for both states (safe and damaged) are very low ($CV < 1.5\%$ for all of them) compared to those of C_i , one can conclude that the values of $C_i > 8\%$ indicate that there is a damage in the structure, i.e. the cable. Moreover, these values of

the C_i parameter are superior to 5%, the threshold above which one can attribute changes in natural frequencies to damage in structures [18]. Interestingly enough, this parameter is only based on natural frequencies that can be obtained through the data given by only one sensor. Thus in a practical case, there is no need of a “sophisticated” instrumentation to show that there is defect, hidden or not, in structures. However, to further the analysis, it shall be interesting to indicate the location of the defect in the cable. Based only on the C_i parameter, this goal comes out unfulfilled since it does not include a spatial parameter in its expression to locate the damage. For this reason, the MCD (Modal Curvatures Differences) [19] parameter is used for the purpose.

Location

The MCD parameter is based on the curvature mode shapes (ϕ'') which are given from the mode shapes displacement (ϕ) by using central difference approximation [20]:

$$\phi''_{q,i} = \frac{\phi_{q,i-1} - 2*\phi_{q,i} + \phi_{q,i+1}}{h^2} \quad (16.3)$$

Where q is a degree of freedom (DoF), $\phi_{q,i}$ is the displacement mode shape of the mode i at DoF q and h is the mean distance between DoFs (sensors). For the determination of ϕ'' at first and last DoFs (the end points), respectively the first and last addends of the numerator are considered zero values. Consequently, this can introduce some inaccuracies in these values of ϕ'' at end points.

The MCD factor is then calculated by the absolute difference of the curvature mode shapes (ϕ'') between safe and damaged cables:

$$MCD_{q,i} = \left| \left(\phi_{q,i}^s \right)'' - \left(\phi_{q,i}^d \right)'' \right| \quad (16.4)$$

This damage indicator should have a maximum value at the position of a damage. Thus, for the impact next to L1 (laser 1) (see Fig. 16.2 for the position), the MCD values for the first mode are plotted at the Fig. 16.4 below.

In this Fig. 16.4, it can be noticed that the damage is located near to its exact position shown by the asterisk. In fact, using MCD values, the less accurate location is lower than one meter. These results show that the MCD values obtained with the curvature mode shapes of mode 1 are a good mean to localize the damage in the cable. The maximum values noticed at DoF 1 for the impact at L2 (laser n°2) and L5 (laser n°5) can be explained by the fact that the calculation of curvature mode shapes (ϕ'') is not always exact at end points, as noticed earlier.

16.4.2 Estimation of Damage Severity

In the previous section, the damage characterized by one broken wire is detected and located by using C_i and MCD factors. To give a factor estimating the damage severity, one has to consider also the cable with different levels of damage. This is achieved in our case by two and three broken wires in the seven-wire cable. As the C_i factor is based on natural frequencies which can be *easily* determined and are less effected with experimental errors, a mean of estimation of damage severity based on it comes out interesting for fast evaluation of structures safety.

Thus, the natural frequencies of the cable with respectively two and three broken wires are calculated. The calculation of the natural frequencies is based only on the peak of Fourier transforms (FTs) of displacements. To show the relevance of using FTs, the natural frequencies of safe cable are recalculated based on FTs peaks and compared with those given in Table 16.1 that are obtained using circle-fitting method on FRFs. The result is given in Table 16.2 and show the almost equivalence of the two methods *in finding natural frequencies* as the differences are very low (inferior to 0.2%).

Thus, the determined natural frequencies of cable with two and three broken wires are given in Table 16.3.

The results in this Table 16.3 show that by increasing the level of the damage (number of broken wires), the values of natural frequencies decrease. This decrease in natural frequencies results in an increase in the C_i factor. The percentages of change in natural frequencies (C_i) are calculated for the cable with two and three broken wires and the values are compared with those of one broken wire, see Fig. 16.5. For one state of the cable (one specific level of damage), the C_i parameter is almost constant regardless of the chosen mode. Given the fact that, for the location of the damage with MCD factor, the

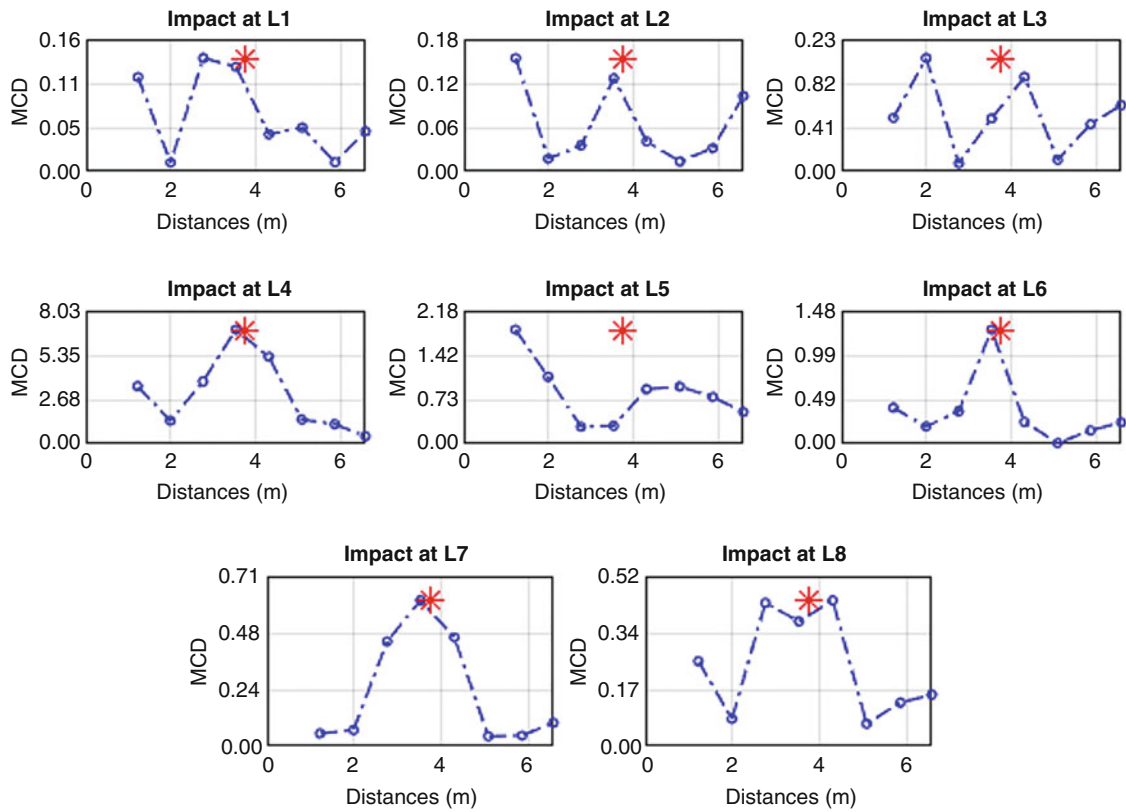


Fig. 16.4 MCD values based on the curvature mode shapes of mode 1

Table 16.2 Natural frequencies of safe cable obtained with TFs and FRFs.

Modes	f_n^s (Hz) with FRFs	f_n^s (Hz) with TFs	Difference (%)
1	19.16	19.19	0.16
2	38.65	38.64	0.03
3	58.08	58.14	0.10
4	78.06	77.95	0.14
5	97.60	97.48	0.12

Table 16.3 Natural frequencies of cables with 2 and 3 broken wires

Modes	Cable with 2 broken wires			Cable with 3 broken wires		
	f_n^{d2} (Hz)	CV_i^{d2} (%)	C_i^{d2} (%)	f_n^{d3} (Hz)	CV_i^{d3} (%)	CV_i^{d3} (%)
1	14.56	0.18	24.14	11.49	0.16	40.13
2	29.08	4.03	24.74	23.03	0.12	40.39
3	43.99	0.16	24.34	34.65	0.26	40.40
4	58.55	2.38	24.89	45.96	3.69	41.03
5	73.28	2.78	24.82	56.51	6.44	42.03

results obtained with the mode 1 best locate the defect, for the damage severity, the C_i parameters calculated with the first natural frequencies will be used.

The C_i values (for the first natural frequency) for the three levels of damage are respectively 9.08%, 24.14% and 40.13%. For comparison, the mean values based on the five natural frequencies are 9.56%, 24.59% and 40.8% respectively.

The damage severity can be expressed directly as the percentage of broken wires over the total wires of the cable. Thus, we define the factor DS (Damage Severity) as:

$$DS (\%) = 100 * \frac{\text{Number of broken wires}}{\text{Total of wires}} \tag{16.5}$$

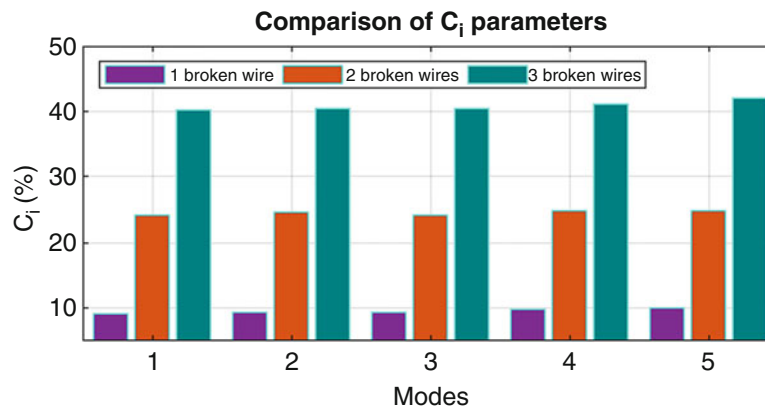


Fig. 16.5 Comparison of C_i parameters for the three levels of damages in the cable

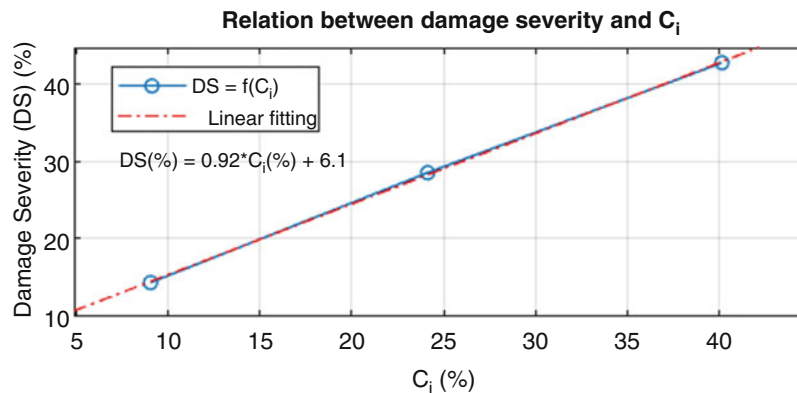


Fig. 16.6 Estimation of damage severity with C_i parameter

In this current study, the values of DS are then 14.29%, 28.57% and 42.86% for respectively one broken wire, two broken wires and three broken wires.

To establish a relation between the C_i parameter and the damage severity, in the Fig. 16.6 one has the DS parameter as a function of C_i parameter. It can be noticed that there is, for these three levels of damage, a linear relation between the C_i parameter and the damage severity (DS) as $DS(\%) = 0.92C_i(\%) + 6.1$. Thus, this relation gives an easy and fast way to estimate the damage severity in cables. This relation also defines a detection threshold of 6.1%; i.e. the damage severity is detectable when the C_i parameter is greater than 6.1%, which agrees with the result found for the cable with one broken wire.

16.5 Conclusion

Using a hammer impact excitation, the detection, location and damage severity estimation on a seven-wire strand have been done. As the hammer with a force transducer gives the input force and laser sensors the displacements of the strand, the FRFs (Frequency Response Functions) are used to calculate the cable's dynamic characteristics by the mean of circle-fitting algorithm. Through the changes in natural frequencies, the C_i parameter constitutes an efficient way to detect damage in cables. Since it cannot give the position of the damage, it is combined with the MCD parameter that locates the damage with more accurate results when it is based on the first curvature mode shapes. Hence, the damage severity estimation is developed based on the first natural frequencies variation for three different levels of damage in the cable. This way of determining the damage severity through the C_i parameter, based only on the variations of first natural frequencies, constitutes an easy, though robust, way to characterize *safety of cables*.

Thus, practically, only one sensor can be used to determine natural frequencies in order to evaluate structures (cables) safety by the mean of the DS parameter. According to a fixed threshold of the DS parameter, the investigation can be furthered using a given number of sensors to locate the damage (through the MCD parameter) and repair it if necessary when

this threshold is exceeded. Therefore, practitioners or project owners can use simple and light means to monitor structures and know when to intervene and take out reparative action.

To validate this approach of characterizing damages in cables, further steps can be taken. At first, the detection of the damage by the MCD parameter should be tested when the damage is near the anchors (for example the third damage introduced in the strand). In addition, the calculation of the DS parameter by the C_i parameter is to be validated with multilayer cables where a broad range of damage severity can be tested by cutting many wires gradually.

References

1. Dieng, L., Périer, V., Gaillet, L., Tessier, C.: Mécanismes de dégradation et moyens de protection des câbles du génie civil. *Mécanique Ind.* **10**(1), 33–42 (2009)
2. Gaillet, L.: Les câbles dans le génie civil: De l'importance de comprendre et connaître leurs états de dégradation, de les protéger. IFSTTAR, 2013
3. Brevet, P.: Pathologie des haubans et câbles: fatigue-Corrosion. In: *Laboatoire Cent. des Ponts Chaussées* (2005)
4. Dwivedi, S.K., Vishwakarma, M., Soni, P.A.: Advances and researches on non destructive testing: a review. *Mater. Today Proc.* **5**(2), 3690–3698 (2018)
5. Rytter, A.: *Vibrational Based Inspection of Civil Engineering Structures*. Department of Building Technology and Structural Engineering, Aalborg University, 1993
6. Doebling, S.W., Farrar, C.R., Prime, M.B.: A summary review of vibration-based damage identification methods. *Shock Vib. Dig.* **30**(2), 91–105 (1998)
7. Le Petit, T.T.H.: Contribution à la détection, à la localisation d'endommagements par des méthodes d'analyse dynamique des modifications structurales d'une poutre avec tension: application au suivi des câbles du génie civil. Université Paris-Est (2014)
8. He, J., Fu, Z.-F., He, J., Fu, Z.-F.: Modal analysis methods – frequency domain. *Modal Anal.* 159–179 (2001)
9. Formenti, D.L., Richardson, M.H.: Global curve fitting of frequency response measurements using the rational fraction polynomial method. In: *IMAC*, pp. 390–397 (1985)
10. Maia, N.M.M.: *Extraction of Valid Modal Properties from Measured Data in Structural Vibrations*. Imperial College (1988)
11. Brownjohn, J.M.W., Raby, A., Bassitt, J., Antonini, A., Hudson, E., Dobson, P.: Experimental modal analysis of British rock lighthouses. *Mar. Struct.* **62**, 1–22 (Nov. 2018)
12. Reynolds, G.: *The Fundamentals of Modal Testing Application Note 243–3*, 2000
13. Ewins, D.J.: *Modal Testing: Theory, Practice, and Application*, 2nd edn. Research Studies Press (2000)
14. He, J., Fu, Z.-F., He, J., Fu, Z.-F.: 7 – Frequency response function measurement. *Modal Anal.* 140–158 (2001)
15. Morassi, A.: Damage detection and generalized Fourier coefficients. *J. Sound Vib.* **302**(1–2), 229–259 (2007)
16. Lee, Y.S., Chung, M.J.: Study on crack detection using eigenfrequency test data. *Comput. Struct.* **77**(3), 327–342 (2000)
17. Sinou, J.-J., Lees, A.W.: The influence of cracks in rotating shafts. *J. Sound Vib.* **285**(4–5), 1015–1037 (2005)
18. Creed, S.G.: Assessment of large engineering structures using data collected during in-service loading. In: Garas, F.K., Clarke, J.L., Armer, G.S.T. (eds.) *Structural Assessment*. Butterworths, London (1987)
19. Dawari, V.B., Vesmawala, G.R.: Modal curvature and modal flexibility methods for honeycomb damage identification in reinforced concrete beams. *Proc. Eng.* **51**, 119–124 (2013)
20. Pandey, A.K., Biswas, M., Samman, M.M.: Damage detection from changes in curvature mode shapes. *J. Sound Vib.* **145**(2), 321–332 (1991)

Abdou DIA, third year Phd Student at the Metallic Structures and Cables Laboratory (SMC) of IFSTTAR (French Institute of Science and Technology for Transport, Development and Networks). Civil Engineer of the graduate school of engineering of the university of Nantes (Polytech Nantes) since 2017. Fields of interest: Vibration of structures, HSM, NDT, FEM.

Chapter 17

Power Grid Time Synchronization for Phase-Sensitive Vibration Measurements



Ferrill T. Rushton, Eugene H. Lin, Jessica Y. Chan, Adam J. Wachtor, Eric B. Flynn, and Nick Lieven

Abstract Phase-sensitive vibration measurements, such as those used for modal analysis, require precise time synchronization between sensors. However, current time synchronization approaches often require specialized hardware and may be impractical to use in certain environments. For example, global positioning system (GPS) synchronization requires GPS receivers and line of sight to GPS satellites, making it difficult to implement such systems underground or indoors.

This paper proposes a new solution for time synchronization that takes advantage of the frequency fluctuations in the power grid. The United States (US) power grid operates at a nominal frequency of 60 Hz and is comprised of three interconnections. However, the actual frequency varies by tens of millihertz over the course of a minute. If measured simultaneously with sensors of interest, this variation provides a basis for signal-based synchronization. These fluctuations are simultaneously observed at any point within an interconnection, allowing the time delay estimation to compare signals from different sensors.

This paper compares the accuracy of the power grid time synchronization to traditional synchronization methods using a free-free beam test performed with accelerometers connected to different data acquisition devices (DAQs), which in turn were connected to the power grid. The raw data was time synchronized using various synchronization approaches and the first three operating deflection shapes of the beam were compared. Results show that power grid time synchronization is able to determine operating deflection shapes as accurately as other traditional synchronization methods. As a result, power grid time synchronization is a viable solution for synchronizing sensors for phase-sensitive vibration measurements where other synchronization methods are infeasible or too expensive.

Keywords Phase-sensitive vibration measurements · Modal analysis · Time synchronization · Power grid · Time delay estimation

17.1 Introduction

Time sensitive vibration experiments, such as those involved in structural health monitoring [1], modal analysis, and wave propagation, are vital to monitoring structures and their structural properties. However, depending on the type of structure and operational environment, difficulties may arise in associating the correct times to the respective measurements accurately. In localized vibration measurements, sensors can be connected to the same DAQ unit, thus inherently providing time synchronization. However, if the sensors are distributed over a large spatial domain, connecting them to the same DAQ

This work was performed during the 2019 Los Alamos Dynamics Summer School at Los Alamos National Laboratory.

F. T. Rushton · E. H. Lin · J. Y. Chan
University of California, San Diego/La Jolla, CA, USA
e-mail: frushton@ucsd.edu; ehlin@ucsd.edu; jyc125@ucsd.edu

A. J. Wachtor (✉) · E. B. Flynn
Los Alamos National Laboratory, Los Alamos, NM, USA
e-mail: ajw@lanl.gov; eflynn@lanl.gov

N. Lieven
University of Bristol, Bristol, UK
e-mail: Nick.Lieven@bristol.ac.uk

is sometimes not practical and often infeasible. As a result, different time synchronization approaches must be applied between DAQs. However, time synchronization approaches are not as accurate as a direct shared connection, and different applications have requirements which are not always possible [2]. For example, in the case of GPS synchronization [3], GPS receivers need line of sight to GPS satellites, which often greatly increases experimental complexity when trying to implement systems underground or within buildings. As another example, wired networks may not be possible when physical barriers exist between sensors. In an attempt to provide an alternative approach, this study explores the use of unique fluctuations of the US power grid's nominal frequency to time-synchronize sensors on spatially distributed DAQs that are designed for vibrational measurements.

There are several considerations which are relevant to time synchronization of sensors via the power grid which include:

1. Understanding why the power grid frequency fluctuates from the nominal frequency of 60 Hz;
2. Which time-delay estimation techniques should be used to align out-of-phase signals from different sensors;
3. Resolving misalignment of clocks on different DAQs; and
4. Verifying that power grid synchronization provides the accuracy needed for phase sensitive vibration measurements by comparing power grid time synchronization experimental results with the results acquired from traditional time synchronization techniques.

17.2 Background

17.2.1 Power Infrastructure

The US power grid is separated into three different interconnections, Eastern, Western, and Texas, each of which consists of one or more balance authorities (BAs). The BAs are responsible for predicting power demands based on a combination of historical data, seasonal demand, and weather forecasts. Depending on the demand, one BA will coordinate with another BA to intentionally create a power imbalance between the two BAs by increasing power generation at the first BA relative to the second BA to facilitate the transfer of electricity between the two BAs. The transfer of electricity will change the supply in the power grid. In addition to the supply changing within the power grid, the demand also changes throughout the day.

The combination of continuous changes in supply and demand throughout the day creates changes in the nominal 60 Hz frequency of the US power grid. When supply is greater than demand, the frequency is greater than 60 Hz. Likewise when demand is greater than supply, the frequency is less than 60 Hz [4, 5]. The variation from the nominal power grid frequency of 60 Hz provides a unique time signature that can be used for time synchronization between two or more spatially distributed sensors [6]. Furthermore, for power to be delivered efficiently across the country, the phase difference between any two points should be approximately constant, so the power grid is phase-coherent [7].

17.2.2 Modal Analysis

Modal analysis is one method of measuring a structure's properties using vibration measurements. Modal analysis is the study of a structure's characteristics or dynamic properties which includes natural frequencies, damping ratios, and mode shapes. Generally, a structure has multiple modes in different amplitudes, and the combination of these amplitudes of frequencies create a general frequency response function (FRF) that will be analyzed [8]. A structure's state can be assessed using modal analysis and then controlled using the assessment [9].

Modal analysis captures the linear input-output relationship between points on a structure. Mode shapes and operating deflection shapes (ODS), which represent the spatial distribution, are derived from measures of the relative phase at each point. As a result, modal analysis is a phase-sensitive vibration measurement technique and thus requires accurate time synchronization in order to produce meaningful results.

Experimental modal tests are generally conducted with either an impact test, or a shaker test. Impact testing involves tapping the structure with a hammer at prescribed locations, while shaker testing involves shaking the structure on a test table at a set of frequencies. Impact testing is easy and portable, while shaker testing allows for a more controllable excitation of the tested structure [8].

In order to determine the accuracy of the mode shapes extracted, the modal assurance criterion (MAC) is used. The MAC is a vector correlation tool developed to check the similarity between two different modal vectors. When MAC diagonal

values are closer to one, it means the two corresponding modal vectors are correlated. When MAC diagonal values are closer to zero, it means the two vectors are uncorrelated [8].

17.2.3 Time Synchronization

Time synchronization is vital to an accurate phase-sensitive vibration experiment. Time synchronization allows the data from one sensor to be collected at the same time and rate as that from another, which in turn makes it possible to pinpoint which data points correspond to which events. This involves reference clocks and sample clocks. Reference clocks are generated to be referenced by other clocks. Sample clocks are used to dictate the timing of the recording of samples from a signal. Reference clocks are generated so that a sample clock can record data between devices synchronously. Of the several issues that arise in an experiment that requires time synchronization, the two main issues are clock drift and clock skew. Clock skew is where clocks start at different times, which results in misaligned timing information. Clock drift is where clock sampling frequencies begin to drift apart due to inaccuracies in each of their clocks [10]. Both of these issues are tackled in different ways in various time synchronization approaches mentioned in the next section.

17.2.4 Time Synchronization Approaches

There are many approaches to the problem of time synchronization, with a number of unique solutions developed in recent years. These approaches fall generally under two categories, time-based synchronization and signal-based synchronization. In time-based synchronization, DAQ units align their clocks to a common time source. In signal-based synchronization, the clocks and trigger signals are shared between two DAQ units [11].

One of the most popular approaches uses the GPS. This is a time-based synchronization approach where DAQ units reference a GPS time source. Synchronizations within 100 ns of UTC can be readily achieved if delays of equipment are accounted for (i.e. receiver, antenna, antenna cable, etc). The cost of implementing a GPS time synchronization system varies greatly depending on the accuracy needed [12], but all such systems require specialized equipment. Furthermore, all GPS receivers must have a clear line-of-sight to reliably measure signals from the satellites, making a GPS-based time synchronization system ill-suited for underground, indoors, and obstructed-view environments [13].

In recent years, work has been done to time synchronize systems using other external sources. Li et al., 2011, took advantage of periodic pulses in FM broadcasts by utilizing FM receiver hardware integrated with ROCS (RDS-assisted cLock Calibration for SensorNet) for time-synchronization [14]. Hao et al., 2014, use an 802.15.4 sensor to detect and synchronize to the periodic beacons broadcasted by Wi-Fi access points with an average synchronization error of 0.12 ms over a period of 10 days [7, 15]. Li et al., 2012, also indirectly exploit the power grid by measuring the intensity changes of fluorescent lights, which form a stable period equal to half that of the power grid's [16]. The last work we discuss in this paper comes from Viswanathan et al., 2016. Viswanathan et al. take advantage of the fluctuations of the power grid from its nominal frequency (i.e. 60 Hz in the United States and 50 Hz in Europe) by using specialized hardware (MCU with sampling rate of 4.2 MHz) to find zero-point crossings to estimate AC cycle lengths. They show that the fluctuations in the nominal frequency of the power grid ensure that, given a sufficient length of time, a unique "Time Fingerprint" (TiF) can be acquired. A TiF from one node, along with its timestamp, can be compared to the "history" of another node to find the time offset between the two nodes' clocks [6].

These approaches all have certain drawbacks. A number of them [6, 7, 14] require specialized hardware, increasing the difficulty and cost of implementing such a time-synchronization approach. Hao et al., 2014, requires the use of an 802.15.4 sensor [15], and Li et al., 2012, require the use of a light sensor [16]. This equipment may not already be implemented in a system. There are other specific drawbacks, such as the susceptibility of equipment to interference from electromagnetic radiation [7]. As another example, the flickering fluorescent light approach requires fluorescent lighting, so is ill-suited for dark environments or outside applications. Lastly, in general, these approaches do not readily allow for retroactive time synchronization of data from a generic data acquisition environment. The method proposed in this paper utilizes pre-existing acquisition equipment typically associated with vibration measurements.

17.2.5 Time-Delay Estimation (TDE) Techniques

In order to synchronize the clock skew between DAQ units, time delay estimation must be performed to align signals. An abundance of TDE techniques exist in published literature. The factors that need to be considered when selecting a TDE technique to implement are as follows [17]:

- Signal to Noise Ratio (SNR)
- Type of input signal (i.e. input step signal)
- Estimation accuracy required
- The size of the sampling period in comparison to the time-delay length

One of the simplest TDE techniques is cross-correlation. Mathematically, the cross-correlation is defined as the following (Eq. 17.1) [18]:

$$w(t) = u(t) \otimes v(t) \triangleq \int_{-\infty}^{\infty} u^*(\tau) v(\tau + t) d\tau \quad (17.1)$$

Where the symbol \otimes represents the cross-correlation operator, $u(t)$ and $v(t)$ are two signals, and $w(t)$ can provide a measure of the “lag” between $u(t)$ and $v(t)$. The maximum value of $w(t)$ is the most likely time-delay between the two signals, i.e. at the time-delay where the signals best match up, the value of the integral is maximized. As illustrated in Fig. 17.1, if the maximum value of $w(t)$ is 450 ms, then the value of $u(\tau)$ is the same as the value of $v(\tau + 450)$ [18].

17.2.6 Time Synchronization Requirements for Vibration Measurements

Time Synchronization is vital to a well conducted vibration measurement. Without time synchronization, data is misaligned and the coherence is lowered, reducing the accuracy of the experiment. Time synchronization is dependent on the sampling frequency of the experiment. The lower the sampling frequency, the lower the need for precise time synchronization. For example, when a vibration experiment on a laboratory floor was sampled at 100 Hz, the modes were correctly identified when using low precision synchronization methods [19]. However, if the vibration experiment is interested in higher frequencies, a higher sampling frequency is necessary, requiring more precision.

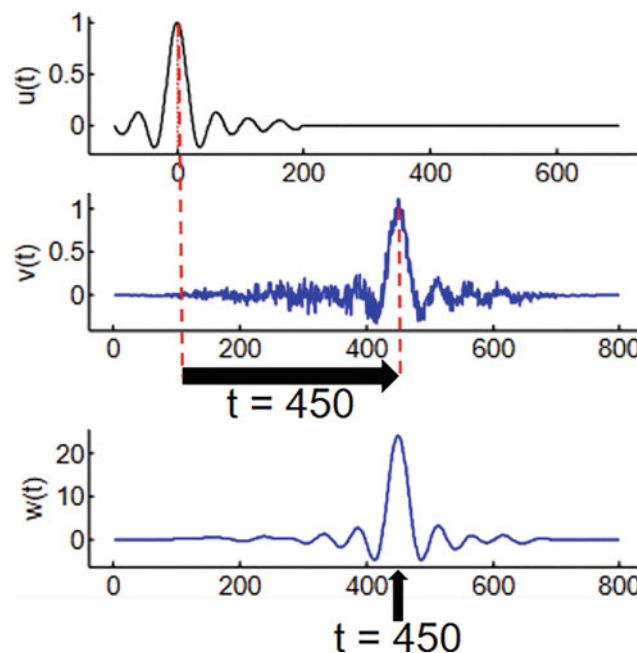


Fig. 17.1 Cross-correlation between $u(t)$ and $v(t)$ [18]

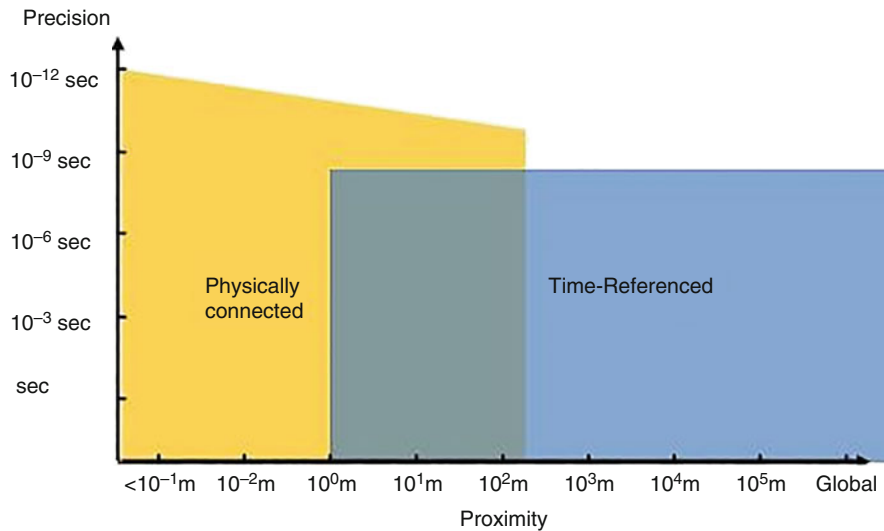


Fig. 17.2 Precision vs proximity of sensors with GPS time referencing [20]

The distance between sensors also affect the accuracy of such measurements. For physically connected systems, the proximity of the connection can increase the precision of the time measurement [20]. However, physical connections have their limits, and thus time-referenced synchronization approaches must be taken instead. However, various time synchronization methods result in different precision, and will be less accurate compared to when the sensors are physically connected (Fig. 17.2).

To summarize, factors to consider when time synchronization is attempted for vibration measurements include:

- Distance of sensors
- Frequency of interest
- Sampling rate of DAQ
- Amount of precision desired

17.3 Synchronization Algorithm

17.3.1 Theoretical Background – Analytic Signal and Real-Time Frequency

The Hilbert Transform $h(t)$ for a one-dimensional signal $x(t)$ is defined by the following integral:

$$h(t) = \frac{1}{\pi} \int_{-\infty}^{\infty} \frac{x(\tau)}{t - \tau} d\tau$$

The integral is improper and is evaluated as a Cauchy principal value. However, the transform may also be represented as a convolution:

$$h(t) = x(t) * y(t)$$

$$y(t) = \frac{1}{\pi t}$$

Performing a Fourier Transform on the above, the following is obtained:

$$H(\omega) = X(\omega) Y(\omega)$$

$$Y(\omega) = -i \operatorname{sgn}(\omega)$$

$$\text{sgn}(\omega) = \begin{cases} 1, & \omega > 0 \\ 0, & \omega = 0 \\ -1, & \omega < 0 \end{cases}$$

An Analytic Signal $x_a(t)$ of the signal $x(t)$ may be constructed using the Hilbert Transform:

$$x_a(t) = x(t) + ih(t)$$

After performing a Fourier Transform:

$$X_a(\omega) = X(\omega) + \text{sgn}(\omega) X(\omega)$$

This causes all the negative frequency components of $X(\omega)$ to cancel out, meaning $X_a(\omega)$ consists of solely the positive frequency components of $X(\omega)$. As a simple example, consider the following (note that A , ω , and ϕ are all functions of t , but the notation is omitted to limit clutter):

$$u(t) = A \cos(\omega t + \phi) = \frac{1}{2} \left(A e^{-i(\omega t + \phi)} + A e^{i(\omega t + \phi)} \right)$$

$$h_u(t) = \frac{1}{2} \left(i A e^{-i(\omega t + \phi)} - i A e^{i(\omega t + \phi)} \right)$$

$$u_a(t) = \frac{1}{2} \left(A e^{-i(\omega t + \phi)} + A e^{i(\omega t + \phi)} \right) + \frac{1}{2} i \left(A e^{-i(\omega t + \phi)} - i A e^{i(\omega t + \phi)} \right) = A e^{i(\omega t + \phi)}$$

Now, the phase of the analytic signal $u_a(t)$ can be extracted by taking its argument, which returns $\omega(t) \cdot t + \phi(t)$. If $\phi(t)$ varies slowly with time, then taking the derivative of the phase with respect to time will approximately give the Real-Time Frequency, which can easily be converted to Hz by dividing by 2π :

$$\frac{d[\omega(t)t + \phi(t)]}{dt} \approx \omega(t); f(t) = \frac{1}{2\pi} \omega(t)$$

The Real-Time Frequency obtained here is the main tool used to time synchronize separate readings of the voltage waveform from the power grid. This is discussed and explained in the next subsection. For a more in-depth discussion of the Hilbert Transform and the Analytic signal, see [21].

17.3.2 Outline of Algorithm

The algorithm developed as part of this study for time-synchronizing raw voltage waveform data from the power grid has multiple steps:

1. Compute the Real-Time Frequency (RTF) of the voltage waveforms
2. Split the first signal into several equally sized sub-sections
3. Calculate an initial time delay estimate (TDE) for each subsection of the first signal
4. Take the average of all the initial TDE's to obtain refined TDE
5. Apply correction due to phase offset between the signals

For ease of discussion, all data is assumed to be stored in column vectors. The subsample of the first signal will be referred to as sig1, its RTF referred to as rtf1, and its raw voltage waveform referred to as volt1. Likewise, for the second signal (i.e. sig2, rtf2, volt2). The associated time vector for sig1 will be referred to as time1, and time2 for sig2. Also, note that all the data collected was done so at 20,000 samples per second. The sampling frequency (20,000 samples/sec) will be referred to as f_s . sig1 is assumed to be completely contained within sig2 (that is, the data collection producing sig2 began before sig1, and the end of sig1 occurs before the end of sig2). Lastly, the algorithm discussed here assumes the raw voltage waveforms were measured under the same transformer (but perhaps on different phases). Other scenarios will be discussed at the end of this section.

17.3.3 Compute the Real-Time Frequency (RTF) of the Voltage Waveforms

The RTF's of sig1 and sig2 are computed by using the Hilbert Transform to obtain the Analytic Signal (see subsection A above). The Analytic Signals will be referred to as sig1A and sig2A, for sig1 and sig2 respectively. The Analytic Signal is of the form:

$$Ae^{i(\omega t + \phi)}$$

Where A is the amplitude, ω is the frequency in radians per second, and ϕ is some phase offset, which is assumed to vary slowly with respect to the period of the signal. The phase of the Analytic Signal, θ , is extracted from sig1A and sig2A, giving $\theta_1 = \omega_1 t + \phi_1$ for sig1A and $\theta_2 = \omega_2 t + \phi_2$ for sig2A. The derivative with respect to time of the phase is then computed to find the RTF (recall it is assumed ϕ varies slowly, so it can be treated as approximately constant), which is then divided by 2π to convert to Hertz:

$$f_1 = \frac{d\theta_1}{dt} * \frac{1}{2\pi} \approx \frac{\omega_1}{2\pi}$$

Note that to avoid discontinuous jumps caused by the phase, the unwrap function in MATLAB is used.

17.3.4 Split the First Signal into Several Equally Sized Sub-Sections

The length of the subsections should be at least 1 min long. As the frequency fluctuates, peaks and valleys are formed in the RTF plots. The algorithm uses these peaks and valleys to home in on regions that potentially correspond with the correct TDE (if this was not done, the runtime would be far larger). Testing revealed that sections of a minute or greater contain at least one peak or valley, but usually more.

17.3.5 Calculate an Initial Time Delay Estimate (TDE) for Each Subsection of the First Signal

“Magnitude of the Difference” (MoD) is next used to determine how well a particular shift of sig1 aligns with the corresponding portion of sig2 that has the same length as sig1, referred to as subSig2. The MoD was achieved by:

$$\text{abs} \left(\text{prctile} \left((\text{subSig2} - \text{sig1})^2, 15 \right) \right)$$

Where prctile() is a function in MATLAB. The first argument is a vector, in this case the square of the difference between subSig2 and sig1, and the second argument is the percentile to be returned. In this case, it was set to 15 (testing was done with several different percentiles, but the 15th percentile consistently provided a better result). The absolute value of this is then taken, as a smaller magnitude corresponds with two vectors being more alike. Taking the 15th percentile instead of the mean is beneficial, as this helps avoid outliers causing a bad result.

This operation can be used to test every possible shift of sig1; however, this is very inefficient, and often simply takes too long for larger datasets. To minimize the potential shifts investigated, the peaks and valleys of sig1 and sig2 are exploited. First, the two signals have their bias approximately removed, and then the magnitude is taken so that the valleys are now peaks as well:

$$\text{sig1M} = |\text{sig1} - \text{mean}(\text{sig1})| \text{ ssM}$$

$$\text{sig2M} = |\text{sig2} - \text{mean}(\text{sig1})|$$

The height of the first peak from sig1M is then used to find all peaks from sig2M that are within some threshold. A predetermined window is then used around these peaks, corresponding with all the shifts that the MoD should be calculated on. The smallest window that consistently gives good results is 1000 (indices) on either side of the peaks. The shift that corresponds with the MoD closest to zero is then taken to be the initial TDE.

17.3.6 Take the Average of All the Initial TDE's to Obtain Refined TDE

This is a straightforward step in the algorithm. A vector containing all initial TDE's from the previous step is formed, outliers are removed, and the mean is calculated. The implementation of removing outliers arose from test data occasionally having the end of sig1 end later than the end of sig2, causing there to not be a respective match for the last sub section of sig1. In the future, the algorithm should be made more robust to this, so it can recognize when there is no matching portion in sig2.

17.3.7 Apply Correction Due to Phase Offset Between the Signals

As stated previously, the raw voltage waveforms were assumed to be measured under the same transformer, but perhaps on different phases. Each phase of the power grid is 120° (a third of a period) off of the other two. This means to know the phase of one waveform relevant to another, the TDE acquired from the previous step must be within ~ 2.78 ms of the actual time delay (this corresponds with half of a third of a period). With this accuracy achieved, the TDE estimate can be corrected a great deal in this step, and the final TDE lies within two sample lengths of the true time delay (in the case of $f_s = 20,000\text{Hz}$). This translates to an uncertainty of ± 0.1 ms.

17.3.8 Other Scenarios

If the raw voltage waveforms were measured under the same transformer and on the same phase, then the algorithm above can be used to provide a TDE. If the raw voltage waveforms were measured in the same building, but different transformers, the algorithm outlined above will not provide a better estimate than part 4 can provide. When under different transformers, the relative phase offset between two waveforms may be any integer multiple of 30° , which would require an accuracy of ~ 0.7 ms. As of now, the algorithm is simply not accurate enough to resolve this, but research into improving and optimizing the algorithm may prove beneficial. The last scenario to discuss is raw voltage waveforms being taken over some long distance. In this case, the relative phase offset between the two signals could be anything, and so the accuracy here is limited by the accuracy of part 4 of the algorithm.

17.4 Methods

Modal analysis on a free-free beam test using the developed algorithm was performed to investigate the accuracy of the developed algorithm in different synchronization scenarios.

17.4.1 Free-Free Beam Modal Analysis

In this experiment, modal analysis is performed on a free-free aluminum beam using several different synchronization techniques. The first three operating deflection shapes (ODS) are extracted and compared with the theoretical Euler-Bernoulli beam model using MAC. By calculating the determinant of these MAC matrices, we can compare the accuracy of each synchronization method. This experiment was performed in the case of when the devices are on the same phase of the same transformer and when the devices are on different phases of the same transformer.

17.4.2 Experimental Setup

For the free-free beam setup, a 6061 Aluminum beam with dimensions 35.2 cm x 5.58 cm x 65024 cm was used. The beam tested was hung from two strings located at a fourth of the total length of the beam as measured from the left and right side of the beam. There were seven accelerometers on the beam, spaced equally from each other with an accelerometer at either

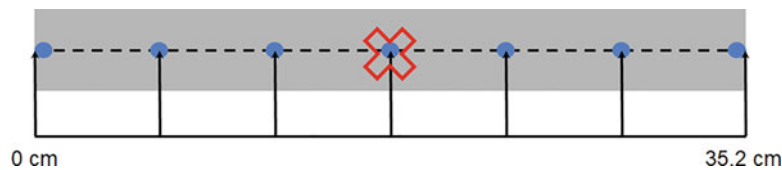


Fig. 17.3 Free-free beam setup

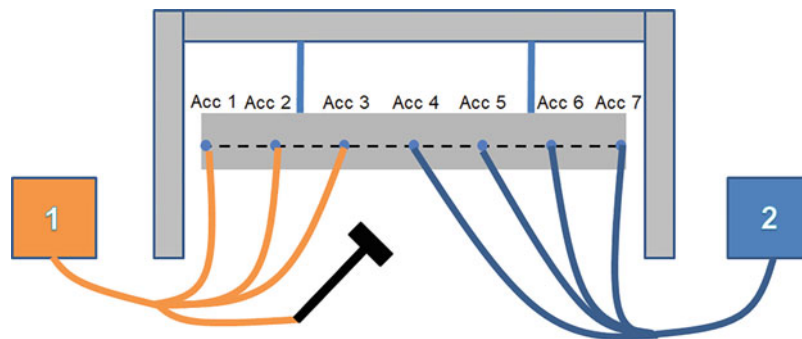


Fig. 17.4 General setup including DAQ cards

end of the beam. A modal testing hammer, Model 086C03 from PCB Piezotronics, was used to hit the center of the beam as indicated in Fig. 17.3 by the red 'X'. The numbers used to reference the accelerometers in the following section are labeled in Fig. 17.4.

For a general setup of the data acquisition hardware, two National Instruments PXI 1033 Chassis were used, each containing a National Instruments PXI 6683 Timing and Synchronization Module and several National Instruments PXI 4462 Sound and Vibration Modules. Based on the type of synchronization used, one or two DAQs would be used. The clocks used to time the sampling frequency would be based off of the PXI 6683 units, overriding the backplane clock of the PXI 1033 chassis. Data acquisition of the acceleration of the accelerometers and force of the hammer would then be acquired by LABVIEW.

17.4.3 Synchronization Testing Scenarios

The various synchronization techniques used which will be described later include:

1. No Synchronization
2. Pure Synchronization
3. Cable Synchronization
4. GPS Synchronization
5. Power Synchronization

In each synchronization scenario, the DAQ units were connected to the testing beam in different ways. The hammer, and the first three accelerometers were connected to one 4462 card (Card 1) while the other four accelerometers were connected to another 4462 card (Card 2). These were shifted around in accordance with various synchronization scenarios.

In addition, these experiments were run such that clock drift would be negligible with the exception of the No Synchronization scenario. This is done differently in each method which are described below.

In the first test scenario, No Synchronization, there was no synchronization between the two DAQ chassis. In this scenario, Card 1 and Card 2 are put on separate chassis, each individually timed by its own 6683 timing module. The free running 10 MHz temperature compensated crystal oscillators (TXCO) are used for the clock in each chassis. Then, during data acquisition, the two DAQs are turned on to acquire data in rapid succession by hand. This setup is a baseline case of where no attempt at robust synchronization is being done. This setup is seen in part a of Fig. 17.5.

In the second test scenario, Pure Synchronization, the two cards are connected to the same chassis, achieving the closest possible synchronization achievable with the equipment. In this scenario, both Card 1 and Card 2 are on the same chassis,

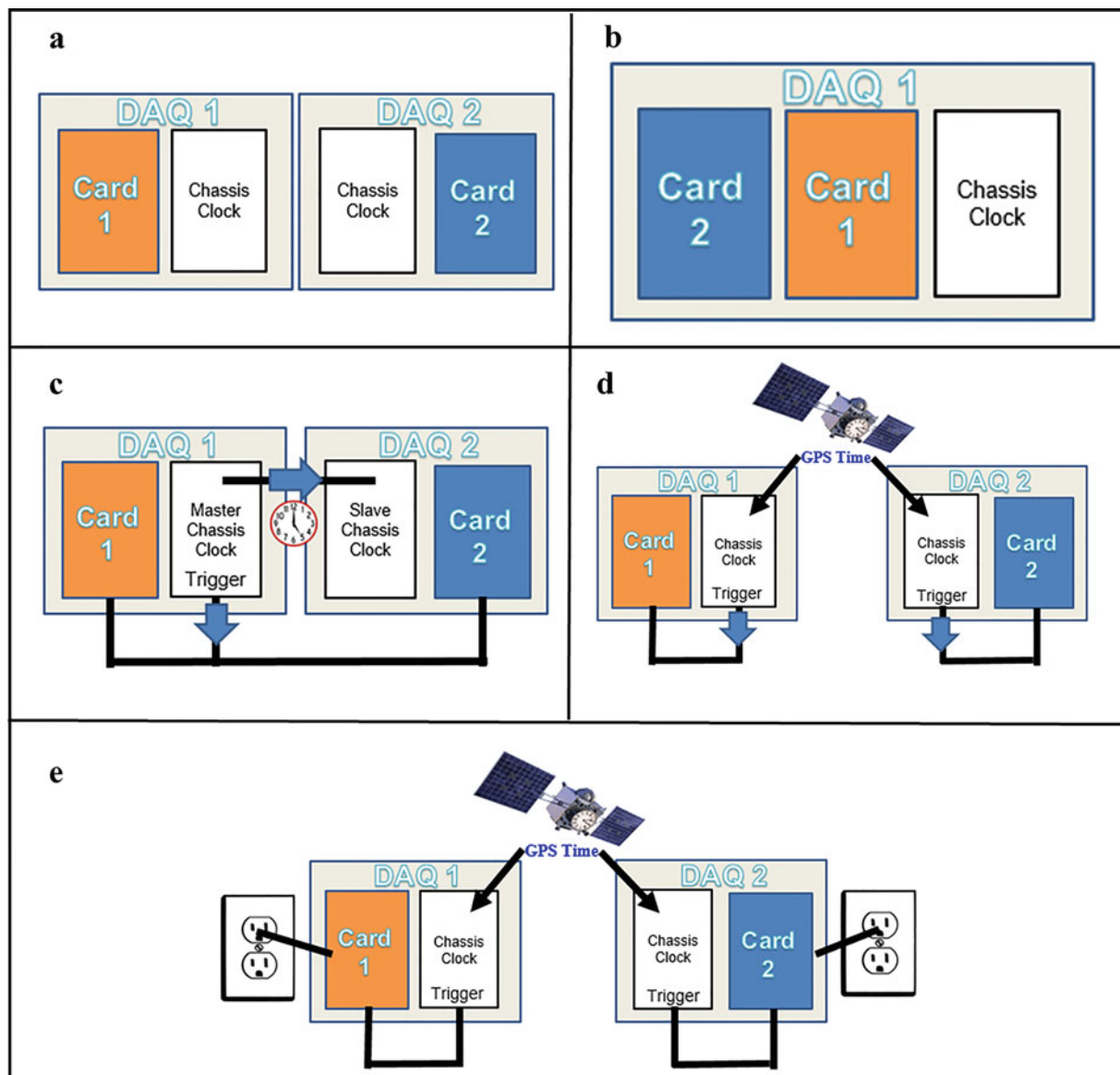


Fig. 17.5 Basic setup of all testing scenarios: a-No Synchronization, b-Pure Synchronization, c-Cable Synchronization, d-GPS Synchronization, e-Power Synchronization

which is timed by one of the modules. The 6683 module is using the TXCO, and since its clock is sent synchronously to both cards, both cards are synchronized with each other, with both cards having no clock skew or clock drift. During data acquisition, the chassis would be turned on to acquire data for both cards at the same time. This setup is seen in part b of Fig. 17.5.

In the third test scenario, Cable Synchronization, the two cards are on two separate DAQ chassis. In this scenario, the clocks of each 6683 card on each chassis is connected through a synchronization cable. The master chassis with Card 1 has a master clock that sends its clock over to the slave clock in the chassis with Card 2. There is also a trigger on the chassis with Card 1 that is sent to both DAQ units, causing them to start at the same time when the trigger is sent. As a result, the data acquisition is synchronized and started at the same time when one chassis is turned on. This results in no clock drift or clock skew. This setup is seen in part c of Fig. 17.5.

The fourth test scenario, GPS Synchronization, also has the two cards on two separate chassis. However in this scenario, the clocks of each 6683 card on each chassis are disciplined to a GPS clock. This is done by connecting a Trimble Bullet GPS Antenna to the 6683 chassis, ensuring that the antenna has a clear line of sight to the sky. The 6683 modules send a trigger to the 4462 acquisition cards at a set time, resulting in synchronous activation and allowing both DAQs to be synchronized

to the GPS clock. The clocks are sampling their frequencies according to the GPS clock, thereby resulting in no clock drift. This setup is seen in part d of Fig. 17.5.

The fifth test scenario, Power Synchronization, is the synchronization method this paper is comparing to the other synchronization methods. In this case the two cards are on two separate chassis. In addition to recording the sensors on the cards, the chassis are also recording the power of the grid by a LeCroy AP031 Differential Probe. This power grid data will be used to acquire the correct time delay using the algorithm mentioned in sect. III. To start the two DAQs, these DAQ units are connected to the GPS clock, which triggers each DAQ at separate times. The DAQs are still connected to the GPS clock to prevent clock drift. This is also done so that when the algorithm is used, there can be a comparison between the time delay the algorithm calculates and the time delay calculated by the GPS clock. The actual power synchronization algorithm does not use the GPS clock for time skew. This setup is seen in part e of Fig. 17.5.

This test scenario is done twice, once where the devices are connected to the same phase of the power grid, and different phases of the power grid, resulting in a total of 6 test scenarios:

1. No Synchronization
2. Pure Synchronization
3. Cable Synchronization
4. GPS Synchronization
5. Power Synchronization (Same Phase)
6. Power Synchronization (Different Phase)

17.4.4 Experiment Procedure

To acquire the ODS of the beam with the various synchronization techniques, 3 trial runs of 6 continuous hits on the beam were performed with the modal hammer. These were taken each at 10 second intervals. However, for Power Synchronization, since more time is required to align the power signals, there was a wait period after beam tests where the DAQ acquires voltage data. This was 5 minutes in the case of same phase, and 20 minutes long in the case of different phase.

17.5 Data Analysis

In order to convert the collected vibrational data from the accelerometers to interpretable ODS, a MATLAB code was used to analyze the accelerometer data.

The FRF was created from dividing the Fourier transform of the output (accelerometer data) over the input (force sensor on hammer data). The peaks of the FRF were then identified to find the resonant frequencies. The ODS were found at the corresponding resonant frequencies. These were then compared to the analytical mode shapes by using a MAC matrix. The analytical mode shapes were calculated using the free vibration equation for a free-free Euler-Bernoulli beam.

To compare the MAC matrices from several trials of each time-synchronization technique, the determinant, along with its mean and standard deviation, was calculated for each MAC matrix (Fig. 17.6).

17.6 Results

In order to compare the accuracies of each synchronization method, and how well each one would fare in a real vibration test, a MAC matrix was used to compare the analytical results derived from the Euler-Bernoulli beam equation to the ODS extracted from the experiment using the various synchronization methods. This was done for all six synchronization scenarios tested, Table 17.1.

According to the calculations derived from the Euler-Bernoulli beam equations, the modes were calculated to be 287.3, 791.9, and 1552.5 Hz. The FRF from the pure synchronization experiment is shown in Fig. 17.7 and the values agree within 10% of the analytically calculate resonant frequencies.

In order to condense this information, the determinants of the MAC matrices were graphed as a bar chart (Fig. 17.8):

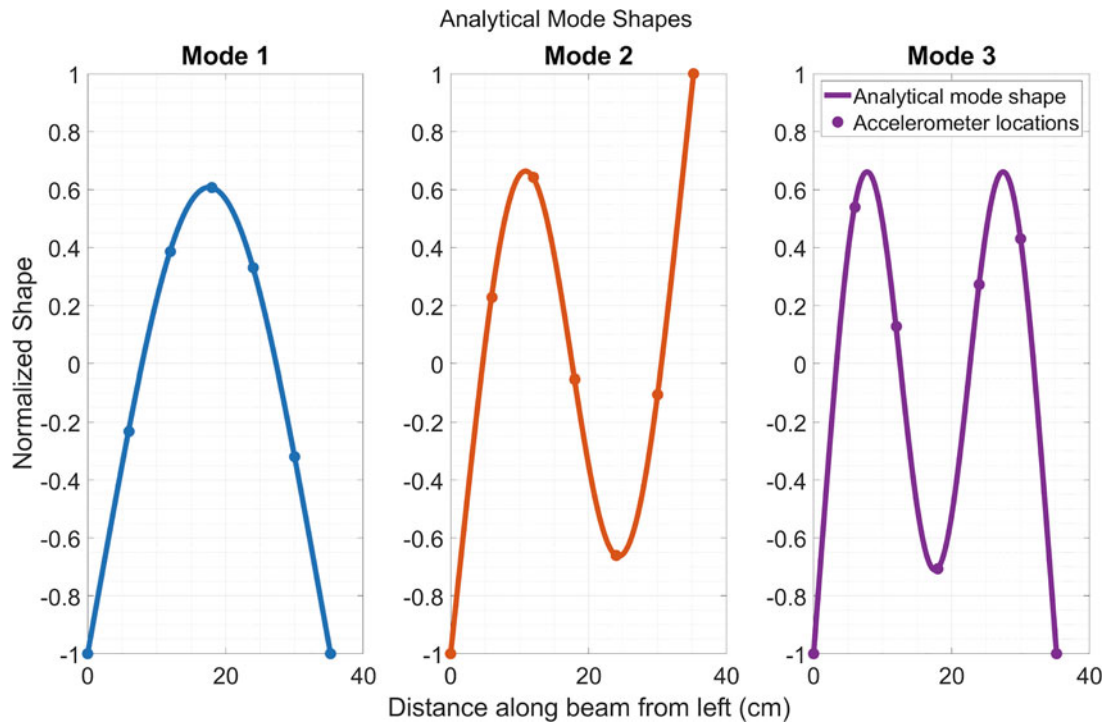


Fig. 17.6 Analytical mode shapes

Table 17.1 MAC matrix determinant values of each synchronization method

Sync method	MAC matrix determinant	Uncertainty (2 standard deviations)
No synchronization	-0.0003967	0.00206
Pure synchronization	0.9316	0.002945
Cable	0.9341	0.0007062
GPS	0.9294	0.0005945
Power (same phase)	0.9202	0.0042525
Power (different phase)	0.9193	0.05051

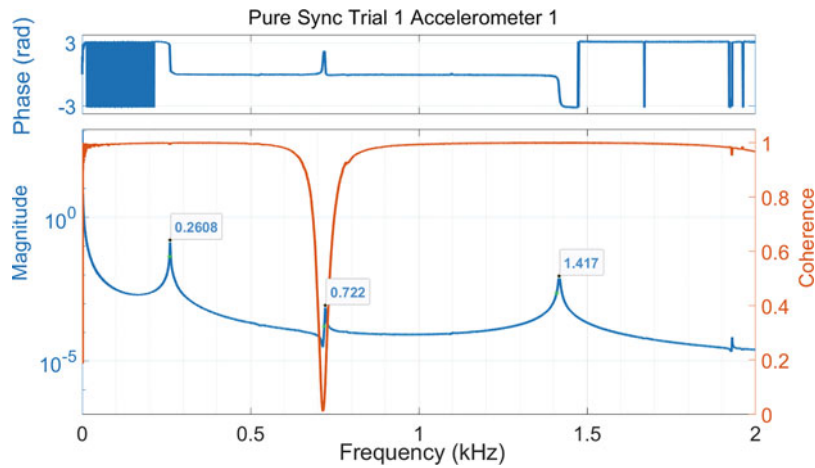


Fig. 17.7 Experimental resonant frequencies in FRF from Pure Synchronization Trial 1

All the resulting MAC matrices, other than No Synchronization, have diagonals that are closely related to 1. In order to compare the MACs with each other, the determinant of each matrix was taken. If the determinants were 1, the vectors would be correlated. If the determinants were 0, the vectors would be uncorrelated.

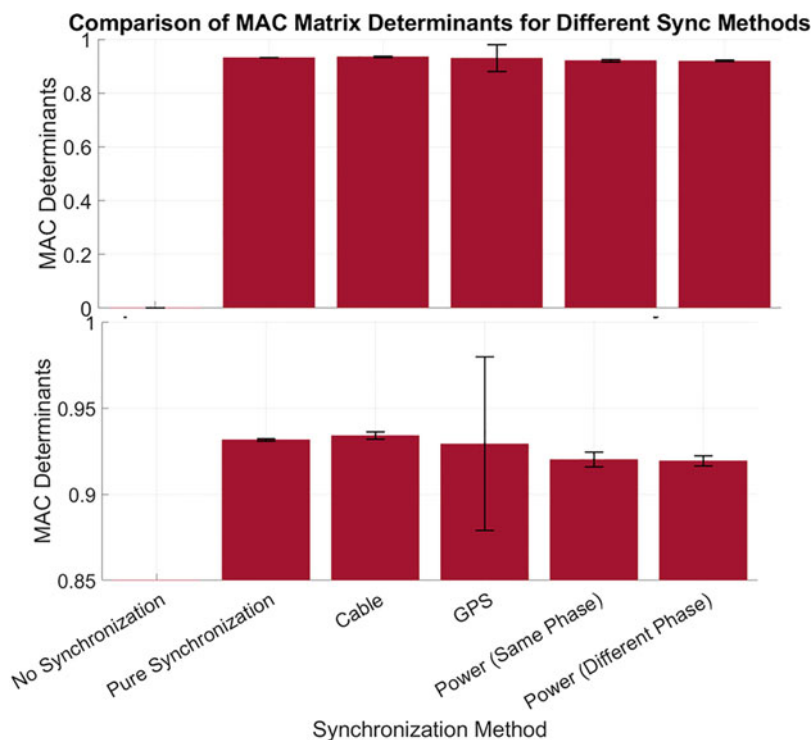


Fig. 17.8 MAC Matrix Comparison Bar Graph (Top shows full graph, bottom zooms into upper portion of graph)

As seen above, the Power Sync MAC matrices have determinants that are very close to 1 alongside with the MAC matrices of traditional synchronization techniques. This shows that for this test case, power synchronization is comparable to traditional synchronization methods with this algorithm when the devices are connected to the same phase and different phases.

This can also be seen by comparing the ODS directly to the analytical solution. The analytical modes are compared to the ODS acquired from power synchronization in Figs. 17.9 and 17.10. As seen in those figures, the shapes agree closely.

17.7 Conclusions

This paper presents a novel form of synchronization through power grid measurements. This new approach expands on the ease of access of synchronization without specialized equipment and with less restrictions on the environment of synchronization. This synchronization method is compared to other traditional synchronization methods by comparing MAC matrices gathered on a free-free beam modal analysis experiment.

The algorithm developed in this paper was shown to perform accurately alongside with traditional forms of synchronization under cases of same phase and different phase on the same transformer network. The power synchronization algorithm was able to produce comparatively similar MACs to traditional synchronization methods alongside the theoretical modes of the beam. The ODS acquired for the power synchronization method, just like when gathered from traditional synchronization methods, are very similar to theoretical mode shapes derived from Euler Bernoulli beam theory.

This experiment is under the assumption that the power grid is consistent and provides continuous power and is resilient to failures. There are anomalies such as swell, undervoltage, sag, and interruptions. More studies need to be performed under the case where power grid voltage data is not always consistently there.

In addition, this experiment was conducted when all clocks were sampling at exactly the same frequency. Because clock drift always occurs when clocks are not connected to a common clock, further investigation needs to be done on how the power synchronization algorithm fare when clock drift is introduced.

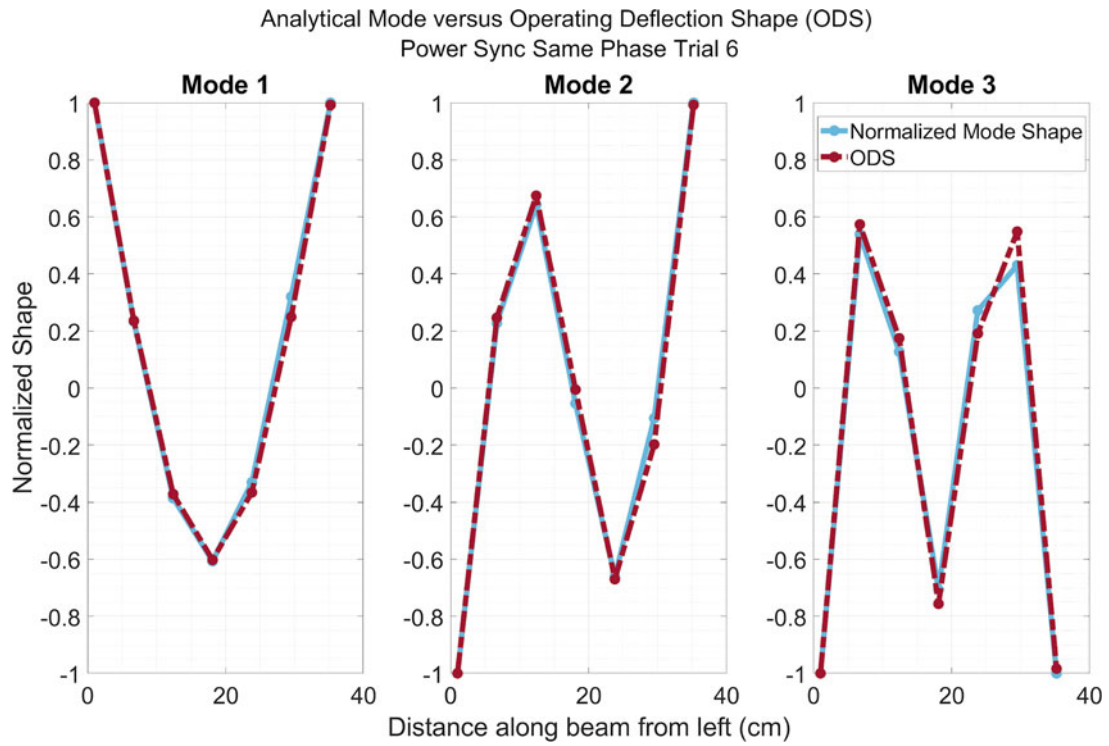


Fig. 17.9 Analytical mode versus ODS in Power Sync Same Phase Trial 6

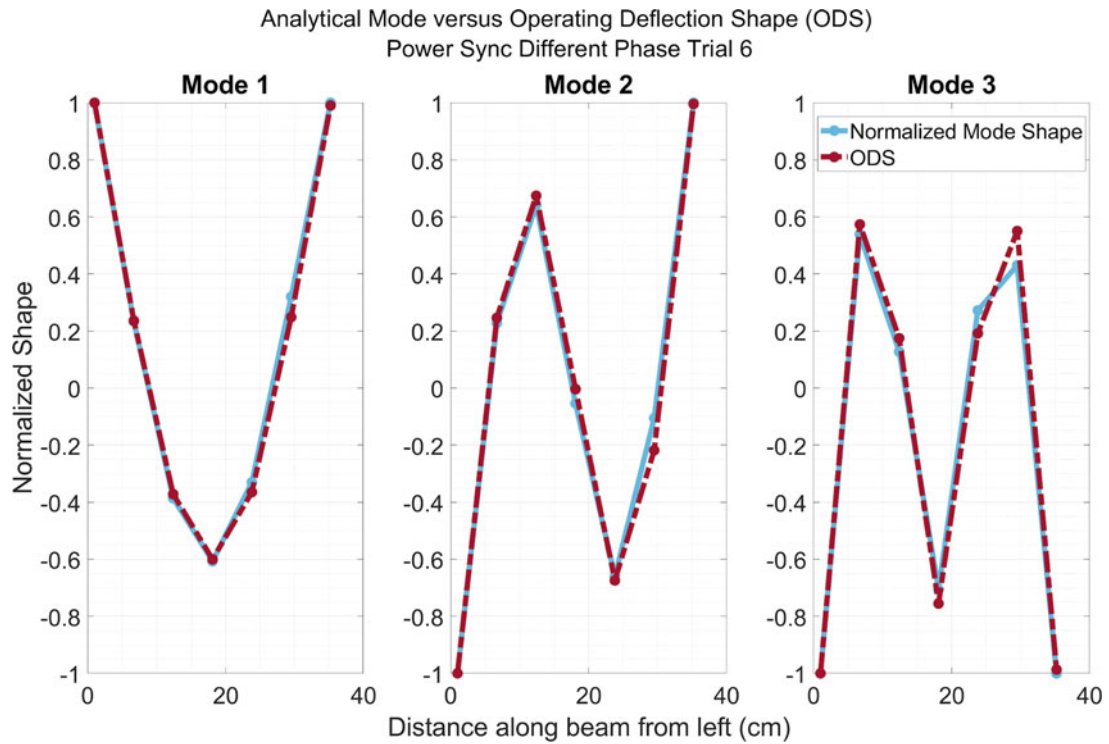


Fig. 17.10 Analytical mode versus ODS in Power Sync Different Phase Trial 6

Appendix

Table 17.2 Pure synchronization modal assurance criterion matrix

Theoretical	Analytical mode shapes		
	1	2	3
1	0.9973 ± 0.0000	0.0005 ± 0.000	0.2583 ± 0.0002
2	0.00015 ± 0.0002	0.9942 ± 0.003	0.001217 ± 0.0020
3	0.2061 ± 0.0002	0.0012 ± 0.000	0.9929 ± 0.0000

Table 17.3 No synchronization modal assurance criterion matrix

Theoretical	Analytical mode shapes		
	1	2	3
1	0.01727 ± 0.02	0.1446 ± 0.2	0.1684 ± 0.2
2	0.02135 ± 0.04	0.0259 ± 0.05	0.08115 ± 0.2
3	0.02633 ± 0.06	0.05478 ± 0.04	0.1881 ± 0.2

Table 17.4 Cable synchronization modal assurance criterion matrix

Theoretical	Analytical mode shapes		
	1	2	3
1	0.9978 ± 0.0001	0.0002667 ± 0.0001	0.2532 ± 0.0007
2	0.0007833 ± 0.0004	0.9942 ± 0.0004	0.00008333 ± 0.0002
3	0.199 ± 0.001	0.002067 ± 0.001	0.992 ± 0.0004

Table 17.5 GPS synchronization modal assurance criterion matrix

Theoretical	Analytical mode shapes		
	1	2	3
1	0.9973 ± 0.0000	0.0004833 ± 0.00008	0.2664 ± 0.0003
2	0.0008167 ± 0.0010	0.9943 ± 0.00070	0.0001333 ± 0.0002
3	0.2081 ± 0.0002	0.001967 ± 0.00020	0.9928 ± 0.0001

Table 17.6 Power synchronization (same phase) modal assurance criterion matrix

Theoretical	Analytical mode shapes		
	1	2	3
1	0.9976 ± 0.0002	0.0002 ± 0.0002	0.2628 ± 0.002
2	0.0003833 ± 0.001	0.9948 ± 0.001	0.0003 ± 0.0005
3	0.2089 ± 0.008	0.004067 ± 0.003	0.9914 ± 0.001

Table 17.7 Power synchronization (different phase) modal assurance criterion matrix

Theoretical	Analytical mode shapes		
	1	2	3
1	0.9975 ± 0.0005	0.0001833 ± 0.0003	0.2626 ± 0.004
2	0.0005 ± 0.0007	0.9947 ± 0.0004	0.00015 ± 0.0003
3	0.2154 ± 0.04	0.01065 ± 0.04	0.9832 ± 0.04

References

1. Balageas, D.: Introduction to structural health monitoring. (2006)
2. Xiong, C., et al.: Operational modal analysis of bridge structures with data from GNSS/accelerometer measurements. *Sensors*. **17**, 436 (2017). <https://doi.org/10.3390/s17030436>
3. Kim, R., Nagayama, T., Jo, H., & Spencer, B.: Preliminary study of low-cost GPS receivers for time synchronization of wireless sensors. *Proceedings of SPIE – The International Society for Optical Engineering*. 31. (2012). <https://doi.org/10.1117/12.915394>
4. The U.S. electric system: A complex, interdependent network. Retrieved from https://www.eia.gov/realtime_grid/#/summary/about?end=20190403&start=20190327
5. Fonville, B., Matsakis, D., & Hardis, J.: Time and frequency from electrical power lines. (2017). <https://doi.org/10.33012/2017.14996>
6. Viswanathan, S., Tan, R., & Yau, D. K. Y.: Exploiting power grid for accurate and secure clock synchronization in industrial IoT. (2016). <https://doi.org/10.1109/RTSS.2016.023>
7. Rowe, A., Gupta, V. & Rajkumar, R.: Low-power clock synchronization using electromagnetic energy radiating from AC power lines. *Proceedings of the 7th ACM Conference on Embedded Networked Sensor Systems, SenSys 2009*. pp. 211–224. (2009). <https://doi.org/10.1145/1644038.1644060>
8. Avitabile, P.: Modal testing. (2018)
9. Chandravanshi, M & Mukhopadhyay, A: Modal Analysis of Structural Vibration. (2013). <https://doi.org/10.1115/IMECE2013-62533>
10. Synchronization Basics. (n.d.). Retrieved from <https://www.ni.com/en-us/innovations/white-papers/12/synchronization-basics.html>
11. Comparing Signal-Based and Time-Based Synchronization. (n.d.). Retrieved from <http://zone.ni.com/reference/en-XX/help/373629D-01/nisync/v/compare-signal-vs-time-programming/>
12. Young Koo, K., Hester, D., Kim, S.: Time synchronization for wireless sensors using low-cost GPS module and Arduino. *Front. Built Environ.* **4**, (2019). <https://doi.org/10.3389/fbuil.2018.00082>
13. Lombardi, M., Nelson, L.M., Novick, A.N., Zhang, V.: Time and frequency measurements using the global positioning system. *Cal Lab Int. J. Metrol.* **8**, 26–33 (2001)
14. Li, L. et al.: Exploiting FM radio data system for adaptive clock calibration in sensor networks. *MobiSys*, (2011)
15. Hao, T., Zhou, R., Xing, G., Mutka, M.W.: WizSync: exploiting Wi-fi infrastructure for clock synchronization in wireless sensor networks. *IEEE Trans. Mobile Comput.* **13**, 149–158 (2011). <https://doi.org/10.1109/RTSS.2011.21>
16. Li, Zhenjiang, Chen, Wenwei, Li, Cheng, Li, Mo, Li, Xiang-Yang & Liu, Yunhao. FLIGHT: clock calibration using fluorescent lighting. (2012) <https://doi.org/10.1145/2348543.2348584>
17. Björklund, S., Le, G. & Nik, R.: A survey and comparison of time-delay estimation methods in linear systems. (2019)
18. Correlation. Retrieved from http://www.ee.ic.ac.uk/hp/staff/dmb/courses/E1Fourier/00800_Correlation.pdf
19. Bocca, M., Eriksson, L., Mahmood, A., Jantti, R., Kullaa, J.: A synchronized wireless sensor network for experimental modal analysis in structural health monitoring. *Comp. Aided Civil Infrastruct. Eng.* **26**, 483–499 (2011). <https://doi.org/10.1111/j.1467-8667.2011.00718.x>
20. Timing and Synchronization Systems. (2019). Retrieved from <http://www.ni.com/product-documentation/9882/en/>
21. Hahn, S.L.: Chapter 7: Hilbert transforms. In: Poularakis, A. (ed.) *The Transforms and Applications Handbook*. CRC Press, Boca Raton (1996)

Chapter 18

Transmission Simulator Based MIMO Response Reconstruction for Vehicle Subcomponents



Christopher A. Schumann, Matthew S. Allen, Washington J. DeLima, and Eric Dodgen

Abstract This report summarizes the work performed at the University of Wisconsin-Madison in evaluating a new testing methodology for recreating the response of a component that is connected at multiple points to another structure. The goal is to account for both the change in impedance when the component is mounted to the shaker, and on faithfully reproducing the environment. The change in impedance will be matched by using the transmission simulator method, which is a process for experimental to analytical substructuring. The environment will then be replicated by using MIMO multi-axis testing. Results from applying this methodology to a two-dimensional Frame on C-beam setup achieved respectable accuracy in recreating the environmental response of a subcomponent.

Keywords MIMO · Environmental testing · Reconstruction · Random vibration · Transmission simulator

18.1 Introduction

Traditionally, vibration environments are measured at key points on the vehicle, which are then used to perform closed-loop single axis shaker tests on the whole assembly. If the environment includes multiple axes, each is typically reproduced separately, often without attention to off-axis motion; in many cases the off-axis motion thus obtained is inaccurate and either over or under predicts the survivability of the components. Full-scale vehicle tests can also be costly in both time and money, making it difficult to perform them often enough to verify the survivability of subcomponents after iterative design changes are made. A new methodology for reconstructing the response of a vehicle subcomponent is proposed, and which focuses on two aspects: the change in impedance, and faithfully reproducing the environment.

To achieve a match in impedance, a substructuring strategy known as the Transmission Simulator (TS) method from [1] will be used, which attaches a fixture called the transmission simulator to a body of interest to create a better experimental model of the body. The transmission simulator method involves using a set of shapes of the transmission simulator, typically its free-free modes, that tell us how many shakers need to be used and how many responses need to be tracked to ensure that we match all the relevant motion. The design of the transmission simulator also mimics the connection geometry which the body of interest experiences in its operational environment and can even be the actual part to which the body is normally joined to. By maintaining the same connection geometry, the impedance of the interface is maintained.

The Department of Energy's Kansas City National Security Campus is operated and managed by Honeywell Federal Manufacturing & Technologies, LLC under contract number DE-NA0002839.

C. A. Schumann (✉)
University of Wisconsin-Madison, Madison, WI, USA
e-mail: caschumann@wisc.edu

M. S. Allen
Department of Engineering Physics, University of Wisconsin-Madison, Madison, WI, USA
e-mail: matt.allen@wisc.edu

W. J. DeLima · E. Dodgen
Honeywell Federal Manufacturing & Technologies, Kansas City, MO, USA
e-mail: wdelima@kcncs.doe.gov; edodgen@kcncs.doe.gov

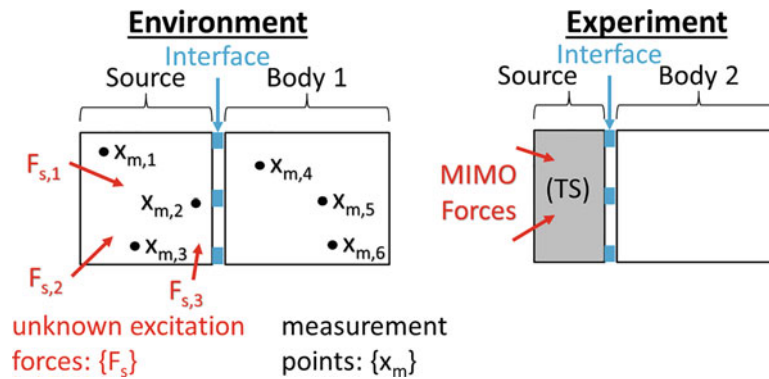


Fig. 18.1 Problem of interest. Record motion of the source and body during environmental loading, then using MIMO inputs on a transmission simulator to replicate the motion going into the body of interest

To reproduce the environment, the transmission simulator and MIMO multi axis testing will be used. It's been shown in [2, 3] that a MIMO setup with small shakers was more effective at reproducing a vibration environment than a large shaker. The transmission simulator can also be characterized by correlating modal test results to a finite element model, allowing it to define a basis set for the motion going into the subcomponent. The combination of these two things will allow the motion of the transmission simulator to be accurately reconstructed in the laboratory. As long as the connection geometry remains the same, the motion of the subcomponent should then match the motion experienced during the operational environment, regardless of the rest of the geometry of the body of interest.

18.2 Methodology

Our goal is to reconstruct the response of a subcomponent that rides on a larger vehicle. Previous work has shown that it is possible to use many small shakers and MIMO multiaxis control to effectively recreate a random environment on a large structure [2]. However, our work is focusing on smaller components so that iterative design changes can be made faster with testing. We will consider the structure that the body of interest rides on as the source in Fig. 18.1. The forces going into the assembly are unknown, and so the environment that the body of interest experiences is also unknown. If there are no external forces on the body of interest, all motion must be transmitted from the source to the body of interest through a specific interface. We will treat part of the source as a transmission simulator, the modes of which will define a basis that can be used to define the motion of the source that affects the component of interest.

In the simplest case, it could include only the rigid body modes of the transmission simulator. In general, we expect to have relatively few modes of the transmission simulator to consider. Then there are two steps to reconstruct the response on the TS and on any body attached to it. The first is to estimate the motion of the TS. We will do this by placing sensors such that the TS mode shape matrix Φ_m^{TS} is full rank and can be inverted, and then using that information to find the modal coordinates Q_m^{TS} . The next step is to reconstruct the motion of the TS using a multiaxis MIMO setup, with shakers placed such that modal forces for all important modes are nonzero and thus the system is fully controllable. Then, with the motion of the transmission simulator recreated, the component of interest is attached, using the same interface as it would have on the full assembly. The response of the component should then match its response from the environment.

18.3 Modal Testing

The assembly of interest was a hollow square cross section bolted onto a C-beam, shown in Fig. 18.2 below. The square cross section, also called the frame, was built from a 2" deep aluminum 6063 hollow square with an outer dimension of 6", an inner dimension of 5.75", and a uniform thickness of 0.125". The middle 2" of a side was cut out to create two "feet"

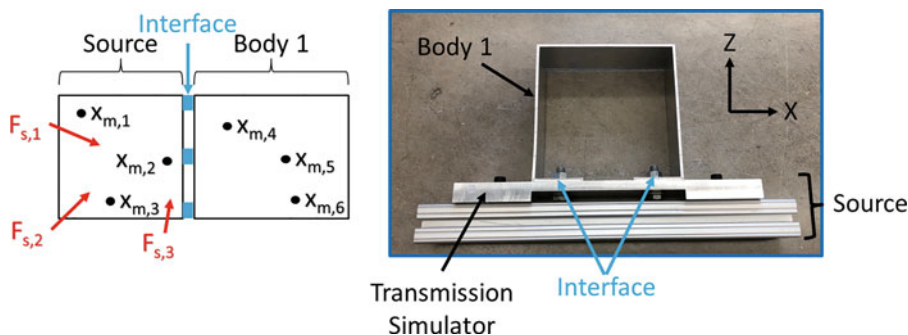


Fig. 18.2 Diagram of Frame on C-beam assembly

Table 18.1 Frame modal analysis results from experiment and FEM

Mode No	Frequency [Hz]		Error %
	Experiment	FEM	
1	43.9	43.9	0.1%
2	97.6	96.7	-0.9%
3	102.3	102.1	-0.3%
4	305.8	306.2	0.1%
5	336.7	335.8	-0.3%
6	393.2	392.7	-0.1%

Table 18.2 C-beam modal analysis results from experiment and FEM

Mode No	Frequency [Hz]		Error %
	Experiment	FEM	
1	465.7	459.6	-1.3%
2	1425.4	1427.2	0.1%
3	1452.9	1439.8	-0.9%
4	2238.7	2214.7	-1.1%
5	3280.6	3247.0	-1.0%
6	4006.1	4187.8	4.3%

for the frame. A .386" through hole was then put through the center of each foot to allow the frame to be bolted onto the C-beam. The C-beam was built from a 12" by 2" by 0.75" stock bar of aluminum 2024. Half the thickness was milled off from the middle 6" of the beam, and two .386" through holes were placed along the center line and 2" from the center for the bolts from the frame. Two more .386" through holes were made 1.5" from the ends to allow the C-beam to bolt onto a piece of 80/20. When assembled, the two parts were connected using two 3/8" grade 8 bolts.

Finite element models were created for both parts. The frame was meshed with 1105 S4R linear shell reduced integration elements, with 7398 physical DOF. The C-beam was meshed with 38,255 C3D20R quadratic brick reduced integration elements, with 522, 327 physical DOF. Roving hammer modal tests were performed on the individual parts to update their respective finite element models. For the frame, a bandwidth of 1600 Hz and acquisition time of 10.24 s was used for two averages at 100 hammer hit locations. The test found 14 modes in the frequency range. The FEM found a similar number of modes but had a large frequency error between them. The wall thicknesses of the frame were measured with a caliper and found to all be less than 0.125". The FEM was updated to match the physical geometry and then analyzed again. The results agreed very well with the experimental data, having an average absolute error of 0.98%. The frequencies for the first six elastic modes are listed in Table 18.1.

A similar modal test was performed for the C-beam. A bandwidth of 4200 Hz and acquisition time of 4.0 s was used for two averages at 33 hammer hit locations. Six elastic modes were found in this range, which matched the number of modes predicted by the FEM. The model was updated to better match the physical geometry, resulting in an average absolute error of 1.46% on the first six elastic modes, shown in Table 18.2.

Table 18.3 Assembly modal analysis results from experiment and FEM

Mode No	Frequency [Hz]		Error %
	Experiment	FEM	
1	112.34	117.8	4.6%
2	262.23	334.4	21.6%
3	369.5	394.0	6.2%
4	446.8	458.7	2.6%
5	594.74	619.9	4.1%
6	699.58	723.9	3.4%

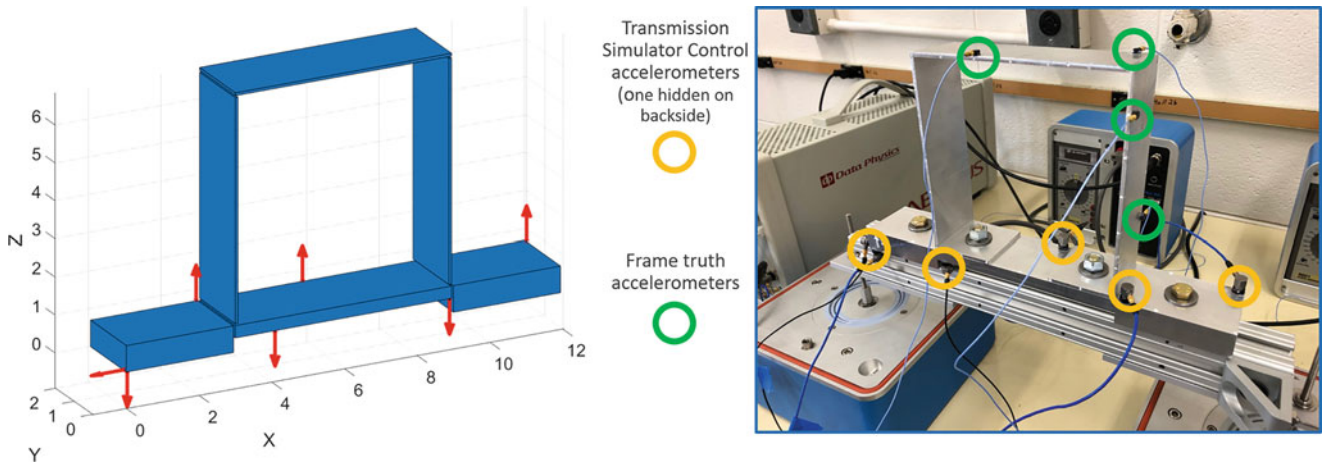


Fig. 18.3 Condition number script used to define best locations for sensors on TS. (a) Matlab sensor location plot. (b) Test sensor locations

The two parts were then assembled by torquing two bolts to 33 lbf-ft. The roving hammer test on assembly found 13 elastic modes found under 1638 Hz, and all but two were bending in the X/Z plane or torsion about the X/Z axes. The X/Z plane is defined in Fig. 18.2. Beam elements were used to approximate the bolts, with rigid constraint elements used to tie the ends to the bolts to the washer imprint locations on the parts. Average absolute frequency error between the experiment and the FEM was 3.0% for in-plane modes, with the first six shown in Table 18.3. The second FEM mode is an out-of-plane mode with a FEM frequency that is highly dependent on the connection method between the parts. Since it shouldn't be active in the X/Z plane it was considered unimportant to replicating the motion in those directions and was not used moving forward.

18.4 MIMO Response Reconstruction

Our method required the mode shape matrix of the transmission simulator $\Phi_m^T S$ to be full rank and invertible so that the modal forces applied by the shakers were nonzero. This requirement allowed the shakers to be placed such that the entire transmission simulator was controllable, and thus the environment could be reproduced well. Accelerometers were placed bases on an algorithm that minimized the condition number of the sensor locations, which was used in [4] to be very effective in placing sensors. The full mode shape matrix was taken from the assembly FEM which had the six rigid body modes replaced by three rigid body modes corresponding to translation in the X and Z directions and rotation about the Y axis, thus keeping all the motion in the X/Z plane. Two DOF at a corner of the transmission simulator, one in the X and one in the Z direction, were selected to be part of the initial sensor set. A set of potential DOF, containing all accessible locations on X or Z faces of the transmission simulator, was loaded into the algorithm, then each potential DOF was added to the sensor set and the condition number of that set was checked. The DOF that made the lowest condition number was added to the set, and the process was repeated, adding one DOF location at a time until the number of desired sensor locations was found. Seven total sensor locations were required to distinguish between the seven modes of the transmission simulator that were in the frequency range of interest. The results of the algorithm from MATLAB are shown in Fig. 18.3a, while the corresponding locations during the test are displayed in Fig. 18.3b.

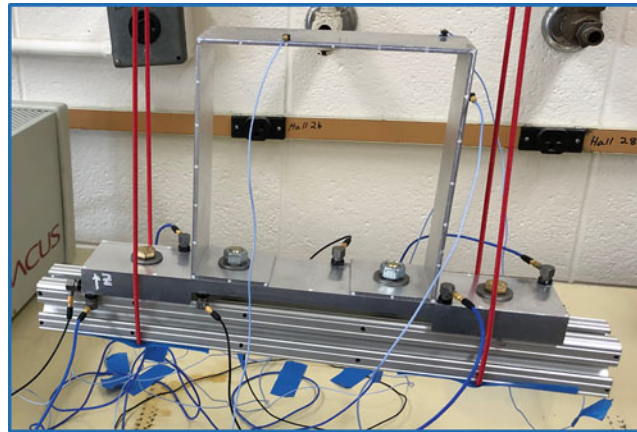


Fig. 18.4 Environmental testing setup

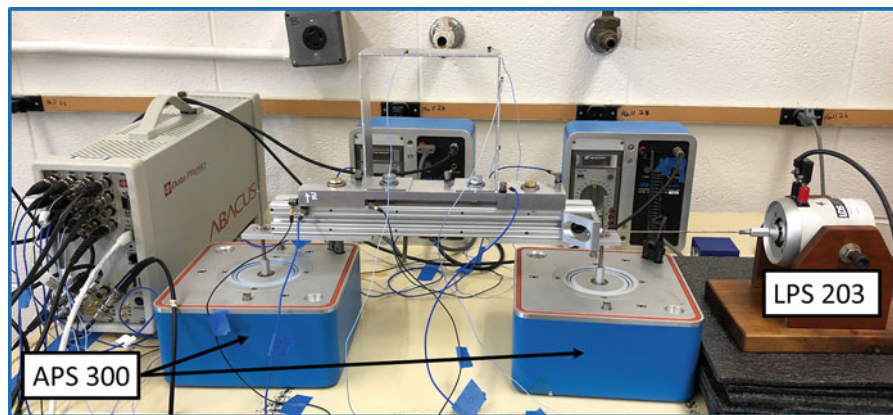


Fig. 18.5 MIMO testing setup with two APS 300 shakers in Z direction and one LPS 203 shaker in x direction

The operational environment of the assembly was created in a laboratory by suspending the full assembly with bungee cords and then using a modal hammer to impact random locations on the 80/20 bar. The hits were all located in the X & Z planes to keep the motion two dimensional. The test ran for a total of 2 min, after which PSDs were extracted for each accelerometer location on both the transmission simulator and the frame (Fig. 18.4).

Three shakers were used to recreate the response of the environment. Two 5 lbf APS 300 shakers were used to control motion in the Z direction, and one 4 lbf LPS 203 shaker was used to control the X direction. Longer stingers were found to give worse control profiles, and so the stingers were kept as short as possible. A 16 channel ABAQUS data acquisition system was used to both control the shakers and record the data from the 11 accelerometers. The output voltages were also split and fed back into the system to make sure the voltage levels never exceeded the specifications of the amplifiers. The whole setup is shown in Fig. 18.5.

The seven accelerometers on the transmission simulator were used to control the shakers, using the only auto PSDs from the environmental testing, which was shown in [5] to be adequate to achieve good control. The abort settings relating to the control quality were disabled, allowing the test to continue running even if the control channels were not being replicated well. The abort settings on the limits to the shakers were still active though, to prevent overloading them. The resulting PSDs of the control accelerometers during the test did not perfectly match the control profiles given to them, as shown in Fig. 18.6, but they were a fair approximation over much of the frequency range.

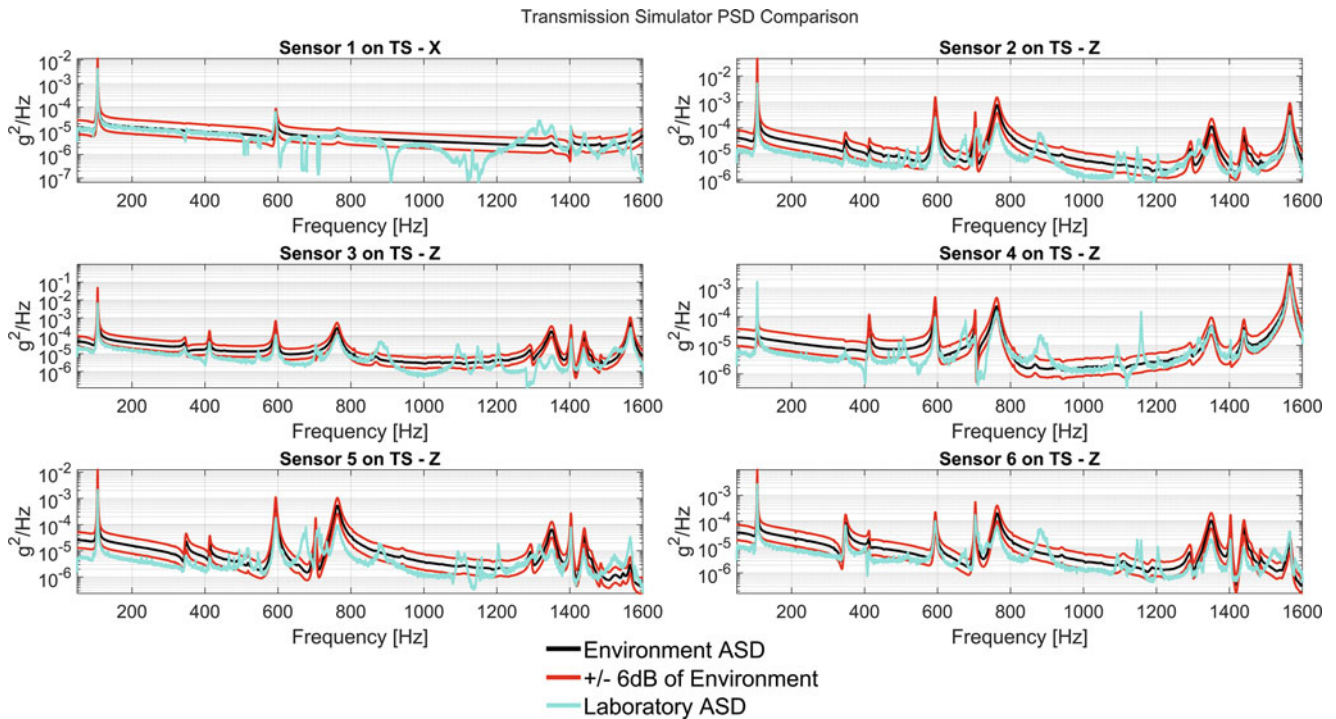


Fig. 18.6 Control PSD's and control profiles during environmental reconstruction

The accelerometers on the frame were not being used as controls, so their responses were only dependent on the inputs to the transmission simulator. The frame accelerometer response PSDs and the environmental truth PSDs have their best correlation below 800 Hz, as shown in Fig. 18.7. There are spurious peaks that appeared during the test that were not present in the environmental, that may be caused by the test setup. However, many of the peaks from the environmental PSDs are matched well, suggesting that there is promise with the method moving forward.

18.5 Conclusions and Continuing Work

This report outlined a new methodology for subcomponent testing using the transmission simulator and multi-axis MIMO testing. We were able to achieve moderate accuracy in replicating an environment onto a square frame by only controlling and exciting the C-beam transmission simulator which it was attached to.

To continue with this research, a new three-dimensional experiment will be conducted by examining a benchmark stool-on-plate structure, shown in Fig. 18.8. A more realistic operational environment, compared to our laboratory environment from last experiment, has already been collected by instrumenting the assembly and participating in a sounding rocket flight. The vibration environment will again be recreated by using MIMO testing, but this time by applying shakers directly to the transmission simulator instead of an intermediate part. The forcing will also be in all three directions for this experiment, instead of limiting it to just in-plane motion. Additionally, new Q-source shakers from Siemens will be used, which give us the capability to apply excitations at nearly any location on our assembly.

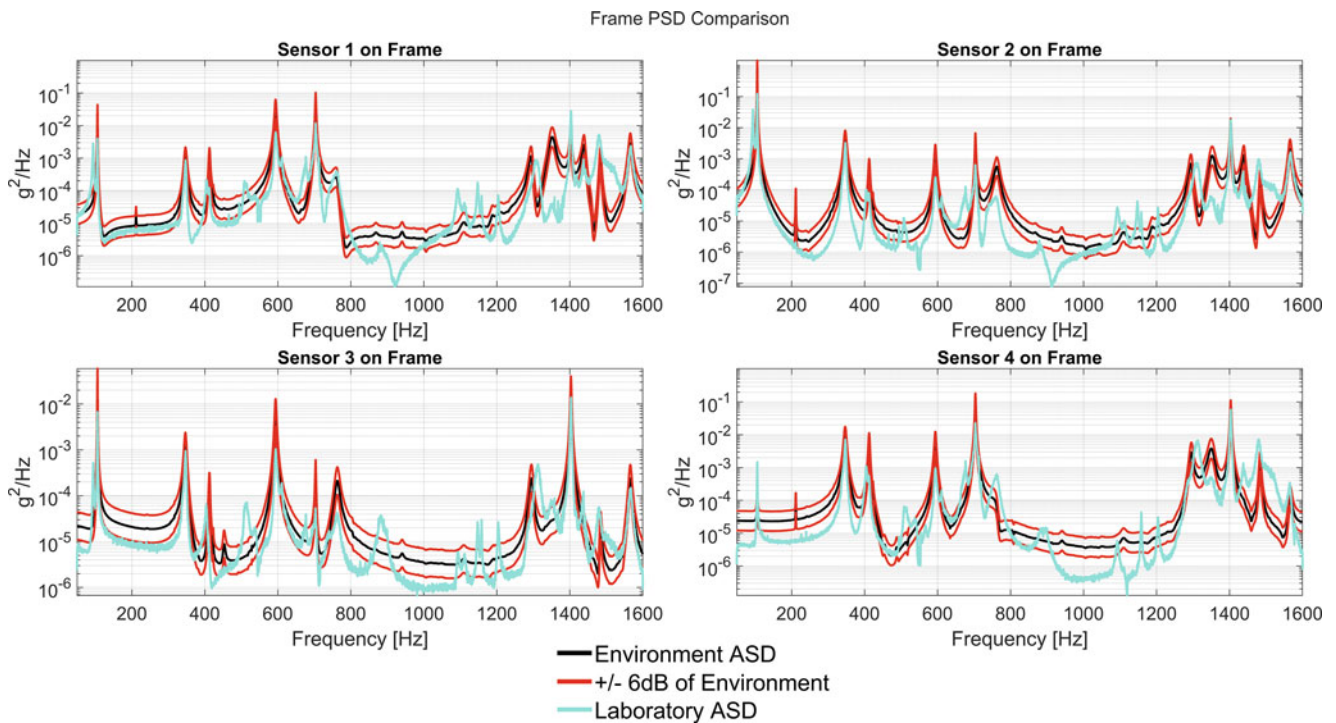
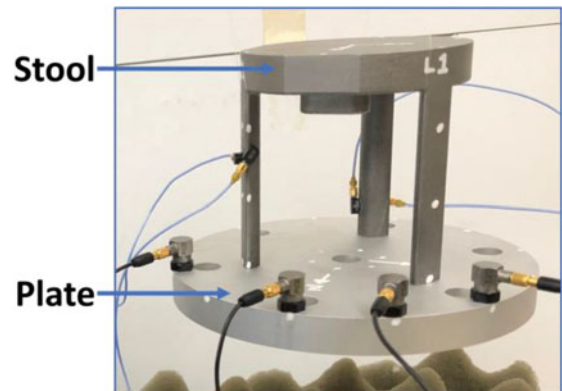


Fig. 18.7 Frame environment and reconstruction PSD's

Fig. 18.8 Stool-on-Plate assembly to be used during the next phase of testing



Acknowledgments The authors gratefully acknowledge the Department of Energy's Kansas City National Security Campus, operated by Honeywell Federal Manufacturing & Technologies LLC, for funding this work under contract number DE-NA0002839.

References

- Allen, M.S., Mayes, R.L., Bergman, E.J.: Experimental modal substructuring to couple and uncouple substructures with flexible fixtures and multi-point connections. *J. Sound Vib.* **329**, 4891–4906 (2010)
- Roberts, C., Ewins, D.: Multi-axis vibration testing of an aerodynamically excited structure. *JVC J. Vib. Control.* **24**(2), 427–437 (2018)
- Daborn, P.M., Roberts, C., Ewins, D.J., Ind, P.R.: Next-generation random vibration tests. In: Presented at the 32nd IMAC Conference and Exposition on Structural Dynamics, 3 February 2014 – 6 February 2014, 2014, vol. 8, pp. 397–410
- Bergman, E.J., Allen, M.S., Kammer, D.C., Mayes, R.L.: Probabilistic investigation of sensitivities of advanced test-analysis model correlation methods. *J. Sound Vib.* **329**, 2516–2531 (2010)
- Mayes, R.L., Rohe, D.P.: Physical Vibration Simulation of an Acoustic Environment with Six Shakers on an Industrial Structure, *Shock & Vibration, Aircraft/Aerospace, Energy Harvesting, Acoustics & Optics*, vol. 9, pp. 29–41. United States. National Nuclear Security Administration, Washington, DC (2016)

Christopher A. Schumann is a second-year masters student at the University of Wisconsin – Madison, working with Professor Matthew Allen.

Chapter 19

Exploring Uncertainties in Multi-Input-Multi-Output (MIMO) Testing



James Woodall, Maimuna Hossain, Arup Maji, John Pott, and Fernando Moreu

Abstract Multi-Input-Multi-Output (MIMO) testing enables more realistic replication of true environment in dynamic testing of structures. MIMO infers inputs from the desired responses at multiple locations on the test article of interest. Errors in the estimation of inputs include but are not limited to: output measurement errors and errors in the Transfer Function (TRF) matrix that captures the input-output relationship. A systematic study involving the measurement of acceleration, control system and system response were undertaken to investigate MIMO actuation of a fixed-end cantilever beam. The response of the beam was also modeled using closed-form equations and finite element method. Various actuation schemes were used to explore the effect of location of actuators in the context of the modal response of the beam. The MIMO input derivation was modeled using the Moore-Penrose Pseudo-Inverse of a rectangular Transfer Function matrix. The results of this study quantify the sources of uncertainty in MIMO vibration testing, specifically the errors due to equipment, sensor calibration, and actuator effects on the beam. The conclusions obtained from the cantilever beam used on this study can be extrapolated to more complex geometries.

Keywords MIMO · Multi-Input · Vibration · Testing · Uncertainty · Acceleration · Structural dynamics

19.1 Introduction

Multiple Input- Multiple Output (MIMO) testing is a critical aspect of modern vibration analysis and research in many engineering fields. MIMO can use field response data and solve for the test inputs [1]. This is useful since in most aerospace scenarios, researchers can easily collect data by attaching sensors, but do not have a way of using that data to determine which forces are acting on the structure. It is common that researchers use a simple beam to conduct MIMO analysis [2]. The analysis of dynamic response can be done using different methods including Finite Elements [3]. This field of research still poses questions regarding signals processing and the inversion of matrices [4]. Another topic of research in MIMO is the examination of what errors are likely in these tests, and how they propagate through the steps performed in both forward (derivation of responses from inputs) and backward MIMO (derivation of inputs from responses).

This paper studies these contemporary MIMO techniques and aims to investigate the errors present in a representative beam experiment, and how these errors impact the ability to accurately deduce unknowns in the test. A series of simple

Sandia National Laboratories is a multimission laboratory managed and operated by National Technology & Engineering Solutions of Sandia, LLC, a wholly owned subsidiary of Honeywell International Inc., for the U.S. Department of Energy's National Nuclear Security Administration under contract DE-NA0003525. This paper describes objective technical results and analysis. Any subjective views or opinions that might be expressed in the paper do not necessarily represent the views of the U.S. Department of Energy or the United States Government.

J. Woodall · F. Moreu (✉)

Department of Civil, Construction, and Environmental Engineering, University of New Mexico, Albuquerque, NM, USA
e-mail: jameswoodall@unm.edu; fmoreu@unm.edu

M. Hossain

Department of Mechanical Engineering, University of New Mexico, Albuquerque, NM, USA
e-mail: hossainm@unm.edu

A. Maji · J. Pott

Sandia National Laboratories, Albuquerque, NM, USA
e-mail: amaji@sandia.gov; jpott@unm.edu

Multiple Input- Single Output (MISO) tests is performed on a cantilever beam, with two inputs. These tests follow examples from past efforts in MIMO to obtain transfer functions of the beam [5]. Strategic locations were chosen along the beam similar to the experiments in Thite (2012) [6]. Two actuators excited the beam and the experimental output data was collected from the tip of the beam. The estimated output was calculated from the input signals and the previously established transfer functions. The measured output was then compared to the estimated output to find a comprehensive measurement of approximate error. Analytical transfer functions for a similar beam were computed and used to find an analytical output given similar inputs to those for the experiment, using methods mentioned in Smallwood (2005) and Trudnowski (2009) [7, 8]. The calculated error representing sensor uncertainty was then added to the analytical output [9]. From these erroneous outputs, a MIMO inversion process was run to deduce the inputs and examine the error and its relation to that in the output. This virtual experiment was performed so different sources of error such as sensor calibration error could be isolated from the others without the uncertainties from coupling or distortion from the input signal. Key observations are made about sources of error from test-taking and post-processing steps.

19.2 Quantifying Uncertainties in Instrumentations

The Linear Voltage Differential Transducer (LVDT) is a displacement sensor used for measuring dynamic properties. This sensor measures displacement in a rod by inducing a voltage that is proportional to the displacement. The ratio that represents this proportionality between output voltage and input displacement is known as the sensitivity of an LVDT. This section summarizes the accuracy of this sensitivity. For each LVDT, the manufacturer provided a sensitivity value. As part of this project, the value was measured in the lab by connecting two LVDTs, one by one, to a voltmeter and collecting the voltage generated for a range of displacement. Figure 19.1 shows the experimental sensitivity calculation for two LVDTs for the full range of displacement.

According to these graphs, the measured sensitivities of LVDT 1 and 2 are 64.32 and 63.74 mV/mm respectively. The manufacturer's specifications are 65.42 and 65.21 respectively. Thus, in both LVDTs there is a flat 1% disagreement when comparing manufacturer-given properties to lab measurements. This generalized disagreement is combined with the error from the tip response and added to the analytical output.

Here, the calibration instrument used to measure displacement has a precision of 0.001 mm and the voltmeter used has a precision of 0.01 V. Thus, the maximum error possible in these calculations is 0.01 V/10 V or 0.1%. Since the error found in Figs. 19.1 and 19.2 show a 1% deviation from manufacturer values and the max error of the calculation itself is only 0.1%, it can be concluded that the sensitivities determined by this calculation are significantly different from the manufacturer and it was decided to account for them in experimental testing.

It is important to note that the slope of the line of best fit are not consistent throughout the displacement range. Additional measures were taken to calculate sensitivities for a smaller range of displacement across the entire range. The results are summarized in Table 19.1. The results show that the best ranges of displacements to use are: 15–150 mm for LVDT 1 and 7.5–150 mm for LVDT 2. Based on these results, experimental work avoided using the first 15 mm of the rod's displacement from the neutral position of the rod.

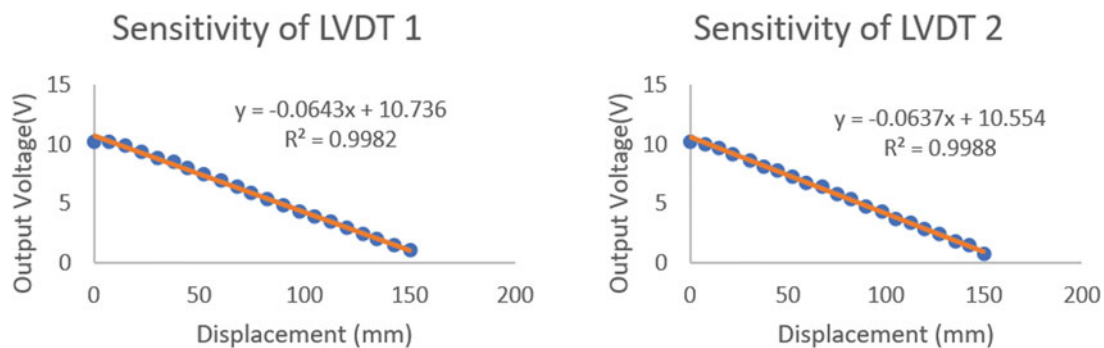


Fig. 19.1 LVDT sensitivity

Fig. 19.2 Analytical model setup

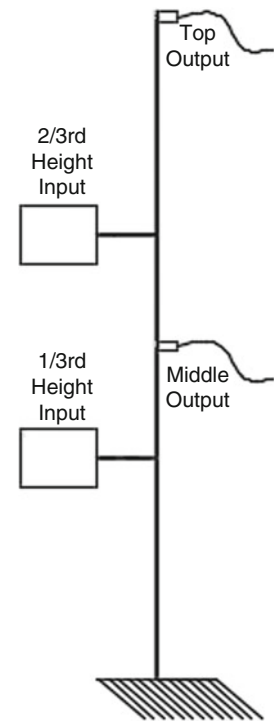


Table 19.1 Summary of correlations for different ranges of displacement

Range of displacement (mm)	Linear correlation LVDT 1	Linear correlation LVDT 2
0–50	0.9646	0.9786
7.5–57.5	0.9964	0.9995
15–65	0.9982	0.9998
22.5–72.5	0.9982	0.9990
30–80	0.9983	0.9987
37.5–87.5	0.9986	0.9988
45–95	0.9986	0.9985
52.7–102.5	0.9987	0.9985
60–110	0.9991	0.9977
67.5–117.5	0.9990	0.9978
75–125	0.9990	0.9981
82.5–132.5	0.9990	0.9977
90–140	0.9993	0.9977
97.5–147.5	0.9993	0.9978
105–150	0.9993	0.9977

19.3 Instrumentation Uncertainties in Analytical MIMO System

The results of examining the LVDT error is used as a general error for any sensor in testing. To isolate the error due to a miscalibration in sensors, a Finite Element Model representing a cantilever beam with assumed Euler Bernoulli Properties was built to represent a simple experiment. This analytical model assumed two inputs and two outputs, as shown in Fig. 19.2. Two outputs were used to ensure that any error is due to the factor being examined, rather than a procedural error from the inherent inaccuracies of using a MISO rather than a MIMO system. This is due to the fact that every point in the frequency domain has an infinite number of solutions when solving a MISO problem, due to having more variables to solve for than equations. Band-limited white noise was generated as the input and was multiplied by the analytical transfer functions to produce an analytical output at the tip and the middle of the beam.

This output was multiplied by a factor of 1.01 and 0.99 to simulate a 1% deviation in sensor calibration for a high estimation and low estimation respectively, replicating a percentile deviation as investigated in Sect. 19.2. While not

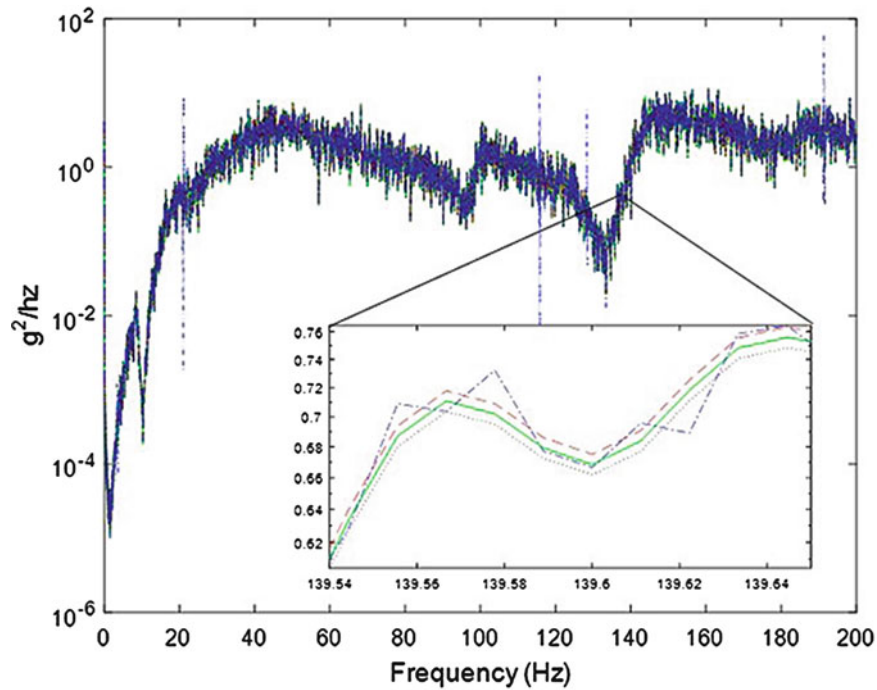


Fig. 19.3 Calculated inputs for 1/3rd height

descriptive of the type of error investigated in Sect. 19.2, the analytical output was additionally perturbed by adding or deducting up to 1% of the measured signal at every point, creating a random alteration of the data to represent noise and small-scale non-linearities. The inversion process was then performed with the modified outputs as described by Eq. 19.1.

$$In = TF^+ Out \quad (19.1)$$

where In = Input Signal Matrix,
 TF = Transfer Function Matrix,
 Out = Output Signal Matrix,
 And $^+$ denotes the Moore-Penrose Pseudo-Inverse of a matrix

The inverse process was also performed with an unadulterated output signal to use as a standard control. A sample of these results are shown in Fig. 19.3, which depicts the ASD of the 1/3rd height input for each miscalibration case, with an arbitrary frequency range zoomed in for closer examination. The pattern observed is consistent across the frequency spectrum and between the two input signals. The flat percentile deviations each lead to an expected consistent miscalculation of the original signal, with an overestimated output resulting in too high of an input, and too low of a signal resulting in a too low of an estimated input. Even though the maximum value of change added to the output for the random perturbations never exceeded the level of the flat deviations, the input signal estimated from it commonly jumps beyond the bounds of those estimated from the flat rates. However, all of them remain close enough to the original signal that they are nearly indistinguishable from an overall view.

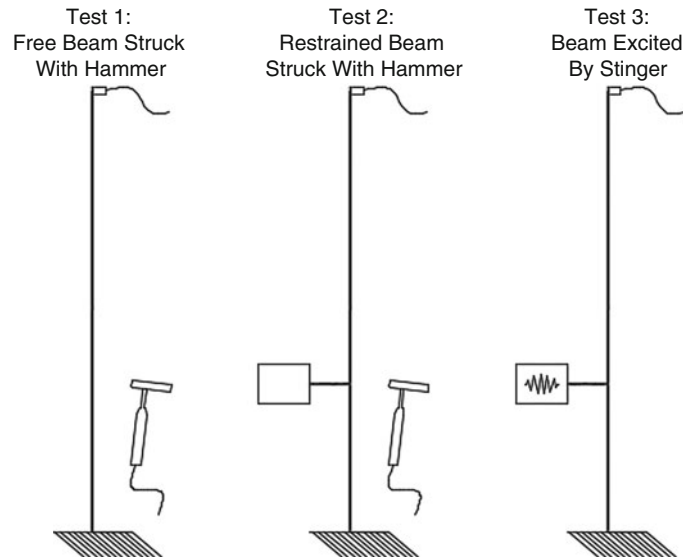
The Error across the frequency range of 0–200 Hz is summarized for each signal alteration by taking the average absolute log of the ratio between the erroneous signal and the measured, as described by Eq. 19.2.

$$Error = \log \left(\frac{Estimated\ Signal}{Measured\ Signal} \right) \quad (19.2)$$

The results for each case are tabulated in Table 19.2. This table shows that the error for a flat error in sensor calibration is very small, and nearly identical for either direction of misestimation. The random noise creates more than three times the error, even though the magnitude of the noise was at most equal to that of the flat error. The reference input calculated from the unaltered analytical output had an error of effectively zero, which is as would be expected.

Table 19.2 Error- average absolute log of ratio

	1/3rd height input	2/3rd height input
Sensor underestimates	0.0044	0.0044
Sensor overestimates	0.0043	0.0043
Sensor randomly perturbed	0.0135	0.0142

**Fig. 19.4** Test setups for stinger effects

19.4 Actuator Attachment Uncertainties in Experimental MIMO System

Noting the resistance to displacement of the stinger, experiments were performed which quantified a source of error in the use of The SmartShaker actuators to excite the beam. It was found that the application of the Stingers caused substantial changes in the natural frequencies of the beam. These tests focused on the addition of the exciter at the 1/3rd height mark, recognizing that the farther up the beam it was located, the more it would restrain the natural response of the beam and alter the Transfer Function. The test setups are depicted in Fig. 19.4.

The experiments were performed by applying a series of impulses with an impact hammer at the location of interest, the 1/3rd height node, both with and without a Stinger attached at the same location. Transfer Functions were then generated from this data for the acceleration at the tip with respect to input force. Another test was run in which the dynamic impedance of the exciter was observed, as it was used to actuate the beam at a variety of frequencies, and the response of the tip with respect to the input acceleration was noted. By necessity of testing structure with two different type of inputs (hammer vs. Stinger), the format of data is different for this test from the previous two, leading to an offset in magnitude. However, the location of peak resonances still offers valuable insight into the impact of how the testing equipment works, and how it can affect the results of tests depending on the assumptions used. A summary of the three Transfer Functions calculated are depicted in Fig. 19.5. As seen, both the attachment and the state of operation of the Stingers make a significant difference in the dynamic properties of the structure for small-scale testing such as the cantilever beam used. Larger test specimens would have lesser impact, but the difference in dynamic response must be accounted for when dealing with relatively light or flimsy objects. While it is not demonstrated in this paper, it is easy to see how this deviation will be exacerbated as the device is moved higher up the beam and closer to the top, as more of its motion is restrained and the increasing moment arm amplifies the effects of the resistance.

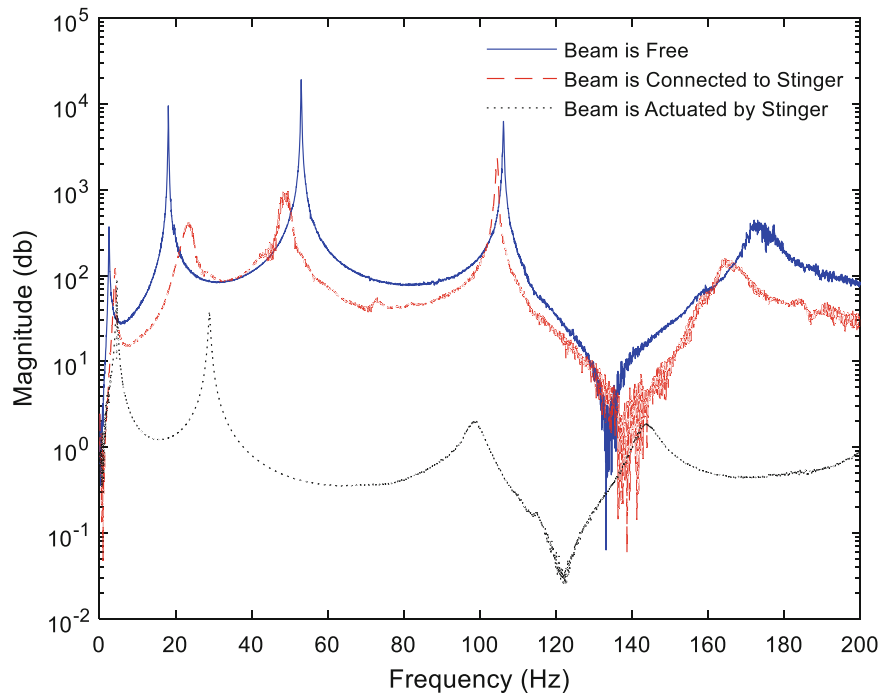


Fig. 19.5 Compared transfer functions of beam tip with respect to 1/3 HEIGHT INPUT

19.5 Ongoing Work

The primary experiments discussed were performed as a precursor to current research, examining potential sources of error in MIMO tests and how to best avoid them. Research is currently being performed on a cantilever aluminum beam of known properties with two TMS SmartShaker exciters attached at 1/3rd and 2/3rd the length of the height respectively, via stingers. Three accelerometers are also attached, one at the tip to collect the output response, and one at each input location to measure the input vibration. This setup can be seen in Fig. 19.6. Each stinger is individually excited with band-limited white noise ranging from 1 to 200 Hz to establish the transfer function for the tip with respect to each input location. For this process, both exciters were left attached, even if only one was being run, to ensure consistent dynamic properties of the beam response. The shifting of Transfer Functions due to dynamic impedance provided a clear source of error for the simple test performed, as simply leaving both Stingers attached while only running one to define the patterns of beam response did not accurately define the dynamic properties of the system once both lines of input are active. Using the conclusions reached in this paper to help ensure accuracy, patterns of error inherent in the MIMO process and how it correlates with the magnitude of relevant Transfer Functions are being performed. Future research includes quantifying the different causes of uncertainty and examining how each one respectively propagates within MIMO analysis for various systems.

19.6 Conclusions

This paper investigates causes and influences of uncertainties in MIMO testing due to equipment use, and the nature of errors found with different tests and with different equipment will vary accordingly. This paper investigated two potential equipment-related sources of error in MIMO testing for a simply supported beam. The error due to flat rate deviation in sensors was found to be small and of consistent nature per the original deviation, while random error had more significant impact. However, even this random error was ultimately small in comparison to the scale of the original signal. It was also found that the exciters used to actuate the beam had a significant impact on the dynamic response of the system, which changed depending on if the exciter (stinger) was running or just attached. There are many other potential sources of uncertainty in MIMO testing which are independent of the equipment used, and will be studied in the future.

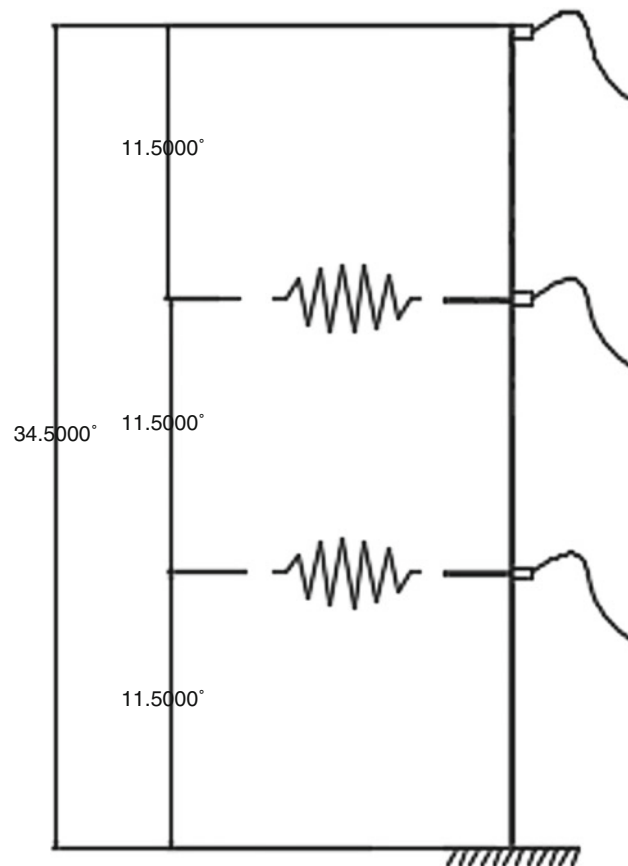


Fig. 19.6 Experiment setup

References

1. Gombi, S.L., Ramakrishna, D.S.: Identification of impact force acting on a cantilever beam using inverse technique. Third international conference on smart materials and nanotechnology in engineering (2012). <https://doi.org/10.1117/12.921380>
2. Ratnam, C.: Dynamic response of a multiple cracked cantilever beam. *Int. J. Res. Eng. Technol.* **4**(12), 195–198 (2015). <https://doi.org/10.15623/ijret.2015.0412038>
3. Palazzolo, A.B.: Beam finite elements for vibration analysis. In: *Vibration Theory and Applications with Finite Elements and Active Vibration Control*, pp. 637–750 (2016). <https://doi.org/10.1002/9781118403921.ch9>
4. Papanicolaou, V.G., Kravvaritis, D.: An inverse spectral problem for the Euler – Bernoulli equation for the vibrating beam. *Inverse Prob.* **13**(4), 1083–1092 (1997). <https://doi.org/10.1088/0266-5611/13/4/013>
5. Nestorović, T., Durrani, N., Trajkov, M.: Experimental model identification and vibration control of a smart cantilever beam using piezoelectric actuators and sensors. *J. Electroceram.* **29**(1), 42–55 (2012). <https://doi.org/10.1007/s10832-012-9736-1>
6. Thite, A., Thompson, D.: Selection of response measurement locations to improve inverse force determination. *Appl. Acoust.* **67**(8), 797–818 (2006). <https://doi.org/10.1016/j.apacoust.2006.01.001>
7. Smallwood, D.O.: Extreme inputs/outputs for multiple input multiple output linear systems (2005). <https://doi.org/10.2172/875611>
8. Trudnowski, D., Pierre, J.: Signal processing methods for estimating small-signal dynamic properties from measured responses. In: *Inter-Area Oscillations in Power Systems*, pp. 1–36 (2009). https://doi.org/10.1007/978-0-387-89530-7_1
9. Wang, L., Wang, X., Li, X.: Inverse system method for dynamic loads identification via noisy measured dynamic responses. *Eng. Comput.* **33**(4), 1070–1094 (2016). <https://doi.org/10.1108/ec-04-2015-0103>

James Woodall is a graduate research assistant in the Department of Civil, Construction and Environmental Engineering of the University of New Mexico, pursuing a MS in structural engineering. His BS is from the University of New Mexico in the Department of Civil, Construction and Environmental Engineering (2018).

Maimuna Hossain is a graduate research assistant in the Department of Mechanical Engineering of the University of New Mexico, pursuing a PhD in structural engineering. Her BS is from the University of Columbia in the Department of Mechanical Engineering (2017).

Arup Maji is a Research Scientist in Sandia National Laboratories. His PhD is from the University of Northwestern in Structural Engineering (1988).

John Pott is a Senior Manager in Sandia National Laboratories. His PhD is from the University of Illinois at Urbana-Champaign in the Department of Theoretical and Applied Mechanics (1984).

Fernando Moreu is an Assistant Professor in the Department of Civil, Construction and Environmental Engineering of the University of New Mexico, with courtesy appointments in the Department of Mechanical Engineering and the Department of Electrical and Computing Engineering. His PhD is from the University of Illinois at Urbana-Champaign in Structural Engineering (2015).

Chapter 20

Experimental Evaluation of the Inertia Properties of Large Diesel Engines



Mohammad Afzal, Kari Saine, Claus Paro, and Eddy Dascotte

Abstract Inertia properties of several medium speed large diesel engines are evaluated using the Inertia Restrain Method (IRM). This method requires measuring frequency response functions (FRFs) at several well-chosen locations and under dynamic loading in different directions that stimulate rigid body movements. The mass line values of the measured FRFs are then evaluated and, together with the sensor locations, are used by IRM to determine center of gravity, mass and mass moments of inertia.

The aim of the study is to investigate the accuracy and robustness of the IRM for extracting the inertia properties of complex structures. Therefore, several line- and V-engines were measured. The experimental results are compared with finite element models and result obtained from weighing tests. Different types of excitation source such as hammer and shaker are used to excite the structure. The result obtained from two excitation sources are compared and discussed. The effect of measurement point locations and driving point accelerometers on the FRFs and inertia properties are investigated.

The extracted inertia properties in all cases are considered sufficiently accurate. This indicates that the IRM is a robust tool for identifying the inertia properties of large and complex structures and can be employed at an industrial level.

Keywords Inertia restrain method · Mass line · Diesel engine · Inertia properties · Frequency response functions

20.1 Introduction

Accurate prediction of the rigid body modes is essential for medium speed large diesel engines to avoid a large displacement at low frequencies. Due to a variation in the dynamic stiffness of engine mounts and partially known inertia properties, this becomes a challenging task. Accurate values of the inertia properties are often unknown since an accurate finite element (FE) model of the full engine is seldom available due to the complex nature of the engine components. A weighing test is used at Wärtsilä Finland Oy to determine the mass of engines and center of gravity in the longitudinal and transversal directions. However, the moment of inertias and the center of gravity in the vertical direction cannot be determined by the weighing test.

As all ten inertia properties of a complex structure cannot be easily determined, this has led to the development of several experimental based methods in last decades [1–4]. Among the developed method, the inertia restrain method (IRM) is known to be relatively insensitive to the measurement noises [5, 6]. The IRM uses the frequency response function (FRF) mass-line values to compute the inertia properties as presented by many researchers [7, 8]. Different variants of the IRM are proposed in the literature [2, 4, 9, 10]. The method presented in Ref. [4] is implemented in the FEMtools commercial software [11] that was used in this study. The advantage of this method is that the procedure is non-iterative and inertia properties are obtained through a direct solution of two linear problems.

The objective of this study is to apply the IRM tool as implemented in the Rigid Body Property Extractor module (RBPE) of FEMtools on heavy and complex structures such as medium speed large diesel engines and investigate the robustness

M. Afzal

KTH Royal Institute of Technology, The Marcus Wallenberg Laboratory for Sound and Vibration Research (MWL), Stockholm, Sweden

K. Saine · C. Paro

Wärtsilä Finland Oy, Research and Development, WSSC, Vaasa, Finland

e-mail: kari.saine@wartsila.com; claus.paro@wartsila.com

E. Dascotte (✉)

Dynamic Design Solutions (DDS) NV, Leuven, Belgium

e-mail: eddy.dascotte@dds.be

of the tool for the industrial application. Several line and V-engines are measured to achieve the goal. The accuracy of the IRM depends on the selection of measurement and excitation points and directions since the linear problems require several inversions. In order to minimize these errors, the recommendations outlined in Refs. [5, 11] are taken into consideration. The obtained inertia properties are compared with finite element data if available and weighing test results. The effect of the measurement and excitation points on the FRFs and inertia properties are analysed experimentally. The obtained results are discussed in detail.

20.2 Theoretical Background

The IRM procedure requires the mass-line values as input, obtained from measured FRFs, see [4]. Precise values of the mass-line are required for a good estimate of the inertia properties. To compute the inertia properties, kinematics and dynamics equations are solved separately. To derive the required equations, consider the structure illustrated in Fig. 20.1 with its origin at o and centre of gravity (COG) at point c defined by the coordinates (x_c, y_c, z_c) .

The kinematic relationship between the acceleration at a general point, i and the origin is

$$\begin{bmatrix} \ddot{x}_i \\ \ddot{y}_i \\ \ddot{z}_i \end{bmatrix} = \begin{bmatrix} \ddot{x}_o \\ \ddot{y}_o \\ \ddot{z}_o \end{bmatrix} + \begin{bmatrix} 0 & z_i & -y_i \\ -z_i & 0 & x_i \\ y_i & -x_i & 0 \end{bmatrix} \begin{bmatrix} \ddot{y}_x \\ \ddot{\theta}_y \\ \ddot{\theta}_z \end{bmatrix}, \quad (20.1)$$

where $(\ddot{x}_o, \ddot{y}_o, \ddot{z}_o, \ddot{\theta}_x, \ddot{\theta}_y, \ddot{\theta}_z)$ are the rigid body acceleration at origin and $(\ddot{x}_c, \ddot{y}_c, \ddot{z}_c)$ denotes the acceleration at a general point i . To obtain the angular acceleration at origin without measuring the translational acceleration at the origin, Eq. (20.1) is re-arranged as

$$\begin{bmatrix} \ddot{x}_i/F \\ \ddot{y}_i/F \\ \ddot{z}_i/F \end{bmatrix} = \underbrace{\begin{bmatrix} 1 & 0 & 0 & 0 & z_i & -y_i \\ 0 & 1 & 0 & -z_i & 0 & x_i \\ 0 & 0 & 1 & y_i & -x_i & 0 \end{bmatrix}}_{\Psi} \begin{bmatrix} \ddot{x}_o/F \\ \ddot{y}_o/F \\ \ddot{z}_o/F \\ \ddot{\theta}_x/F \\ \ddot{\theta}_y/F \\ \ddot{\theta}_z/F \end{bmatrix}, \quad (20.2)$$

where F is an applied force at any co-ordinates' directions. Now, the massline values can be directly substituted to Eq. (20.2). To solve the equation, minimum 6 response directions and one excitation direction are required, thus two sets of Eq. (20.2). However, the equation is solved in a least-squares sense using all available massline values. Moreover, the solution requires the pseudo-inverse of matrix Ψ . It means that the rank of matrix Ψ must be equal to 6. This leads to some constraints in the

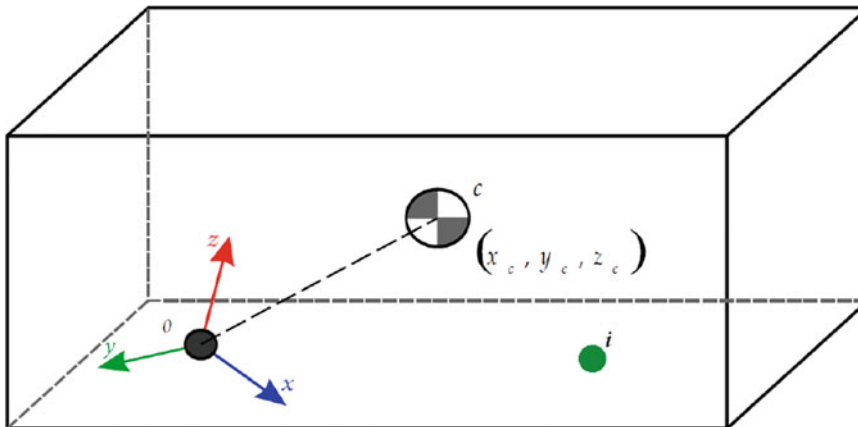


Fig. 20.1 Center of gravity, origin and a general point i

selection of measurement and excitation directions, such as that the acceleration measured at one point cannot be used for more than two directions (using a tri-axial accelerometer). More details are described in Refs. [5, 11].

If the structure is considered as perfectly rigid and unconstrained, then the linearized dynamic equation of motion with respect to COG is given by

$$\begin{bmatrix} m & 0 & 0 & 0 & 0 & 0 \\ 0 & m & 0 & 0 & 0 & 0 \\ 0 & 0 & m & 0 & 0 & 0 \\ 0 & 0 & 0 & J_{xx} & -J_{xy} & -J_{xz} \\ 0 & 0 & 0 & -J_{yx} & J_{yy} & -J_{yz} \\ 0 & 0 & 0 & -J_{zx} & -J_{zy} & J_{zz} \end{bmatrix} \begin{bmatrix} \ddot{x}_c \\ \ddot{y}_c \\ \ddot{z}_c \\ \ddot{\theta}_x \\ \ddot{\theta}_y \\ \ddot{\theta}_z \end{bmatrix} = \begin{bmatrix} f_x \\ f_y \\ f_z \\ t_x \\ t_y \\ t_z \end{bmatrix}_c, \quad (20.3)$$

Where $(f_x, f_y, f_z, t_x, t_y, t_z)$ is the force vector at the COG and ten unknown inertia properties $m, x_c, y_c, z_c, J_{xx}, J_{yy}, J_{zz}, J_{xy}, J_{yz}$ and J_{zx} are to be determined from Eq. (20.3). To compute the required properties, moments (t_x, t_y, t_z) and acceleration of the COG $(\ddot{x}_c, \ddot{y}_c, \ddot{z}_c)$ must be eliminated from the equation and coordinates of COG x_c, y_c and z_c be introduced. The following equations are used for this purpose.

A relation between the force and moments at COG reads as

$$\begin{bmatrix} t_x \\ t_y \\ t_z \end{bmatrix}_c = \begin{bmatrix} 0 & z_i - z_c & -(y_i - y_c) \\ -(z_i - z_c) & 0 & x_i - x_c \\ y_i - y_c & -(x_i - x_c) & 0 \end{bmatrix} \begin{bmatrix} f_x \\ f_y \\ f_z \end{bmatrix}_c, \quad (20.4)$$

and to eliminate the COG acceleration, the following relationship is used in addition to Eq. (20.1).

$$\begin{bmatrix} \ddot{x}_i \\ \ddot{y}_i \\ \ddot{z}_i \end{bmatrix} = \begin{bmatrix} \ddot{x}_c \\ \ddot{y}_c \\ \ddot{z}_c \end{bmatrix} + \begin{bmatrix} 0 & z_i - z_c & -(y_i - y_c) \\ -(z_i - z_c) & 0 & x_i - x_c \\ y_i - y_c & -(x_i - x_c) & 0 \end{bmatrix} \begin{bmatrix} \ddot{\theta}_x \\ \ddot{\theta}_y \\ \ddot{\theta}_z \end{bmatrix}. \quad (20.5)$$

Using Eqs. (20.1), (20.4) and (20.5), the linearized dynamic equation of motion (20.3) may be rearranged to construct the system shown below where the coefficient matrix contains the known acceleration responses obtained from Eq. (20.2). The resulting equations are

$$\begin{bmatrix} 0 & -m \ddot{\theta}_z & m \ddot{\theta}_y & 0 & 0 & 0 & 0 & 0 & 0 \\ m \ddot{\theta}_z & 0 & -m \ddot{\theta}_x & 0 & 0 & 0 & 0 & 0 & 0 \\ -m \ddot{\theta}_y & m \ddot{\theta}_z & 0 & 0 & 0 & 0 & 0 & 0 & 0 \\ 0 & F_z & -F_y & \ddot{\theta}_x & 0 & 0 & -\ddot{\theta}_y & 0 & -\ddot{\theta}_z \\ -F_z & 0 & F_x & 0 & \ddot{\theta}_y & 0 & -\ddot{\theta}_x & -\ddot{\theta}_z & 0 \\ F_y & -F_x & 0 & 0 & 0 & \ddot{\theta}_z & 0 & -\ddot{\theta}_y & -\ddot{\theta}_x \end{bmatrix} \begin{bmatrix} x_c \\ y_c \\ z_c \\ J_{xx} \\ J_{yy} \\ J_{zz} \\ J_{xy} \\ J_{yz} \\ J_{zx} \end{bmatrix} = \begin{bmatrix} F_x - m \ddot{x}_o \\ F_y - m \ddot{y}_o \\ F_z - m \ddot{z}_o \\ y_i F_z - z_i F_y \\ z_i F_x - x_i F_z \\ x_i F_y - y_i F_x \end{bmatrix}, \quad (20.6)$$

in which the first 3 equations are uncoupled from the others. Therefore, Eq. (20.6) is solved in two steps. Moving the mass term to the left side, the first set of the equation is written as

$$\begin{bmatrix} \ddot{x}_o & 0 & -\ddot{\theta}_z & \ddot{\theta}_y \\ \ddot{y}_o & \ddot{\theta}_z & 0 & -\ddot{\theta}_x \\ \ddot{z}_o & -\ddot{\theta}_y & \ddot{\theta}_x & 0 \end{bmatrix} \begin{bmatrix} m \\ mx_c \\ my_c \\ mz_c \end{bmatrix} = \begin{bmatrix} F_x \\ F_y \\ F_z \end{bmatrix}. \quad (20.7)$$

The mass and COG values are determined using Eq. (20.7). In the next step, the inertia values are computed by using the second set of Eq. (20.6) after adding the previously computed mass and COG contributions. In practice, only one load case (say F_x) is used at a time to solve Eq. (20.7) and therefore, the actual equation is

$$\begin{bmatrix} \ddot{x}_o/F_x & 0 & -\ddot{\theta}_z/F_x & \ddot{\theta}_y/F_x \\ \ddot{y}_o/F_x & \ddot{\theta}_z/F_x & 0 & -\ddot{\theta}_x/F_x \\ \ddot{z}_o/F_x & -\ddot{\theta}_y/F_x & \ddot{\theta}_x/F_x & 0 \end{bmatrix} \begin{bmatrix} m \\ mx_c \\ my_c \\ mz_c \end{bmatrix} = \begin{bmatrix} 1 \\ 0 \\ 0 \end{bmatrix}, \quad (20.8)$$

in which mass-line values can be directly substituted. Note that with this formulation, 3 load cases are required to identify all rigid body mass property terms. However, with 2 load cases, it is possible to identify the mass and COG terms using the first step described above. Furthermore, the above formulation can be easily adapted to the case of an imposed mass, m .

20.3 Experimental Results

To validate the robustness of RBPE module developed by Dynamic Design Solutions (DDS) as an add-on module to FEMtools, several Wärtsilä engines are measured. The engines are mounted on soft steel springs to minimize the effect of rigid body modes on the mass-line. Eight measurement points and four load cases are often measured to collect the sufficient number of FRFs data for extracting the inertia properties. The guideline presented in Ref. [5] is considered for choosing the measurement and excitation directions. Three examples are presented in this section and obtained results are discussed in detail.

Example 1 In this example, a W16V32E engine block that weighs ~20 ton is measured and inertia properties are compared with the finite element data. W16V32E stands for Wärtsilä 16 cylinders V engine with 320 [mm] bore diameter. The engine block is chosen because an accurate FE model is available. The measurement setup and FE model of the engine block are depicted in Fig. 20.2. Hammer excitation is given in four directions (at points 1 and 2 in the transversal and vertical directions) and four response locations (1, 2, 7 and 8) are chosen to capture the required FRFs. The initial plan was to measure only the bare engine block. However, during the actual measurement, the engine block was assembled with cylinder liners as shown in Fig. 20.2. The cylinder liners add both mass and stiffness to the structure. Nevertheless, it does not affect the compared results as it is done for the same configuration.

The obtained results are shown in Table 20.1. The result shows a close agreement with the calculation and deviation in the absolute values are within 5% in most of the cases. In some cases, the error percentage is high, however the deviation in

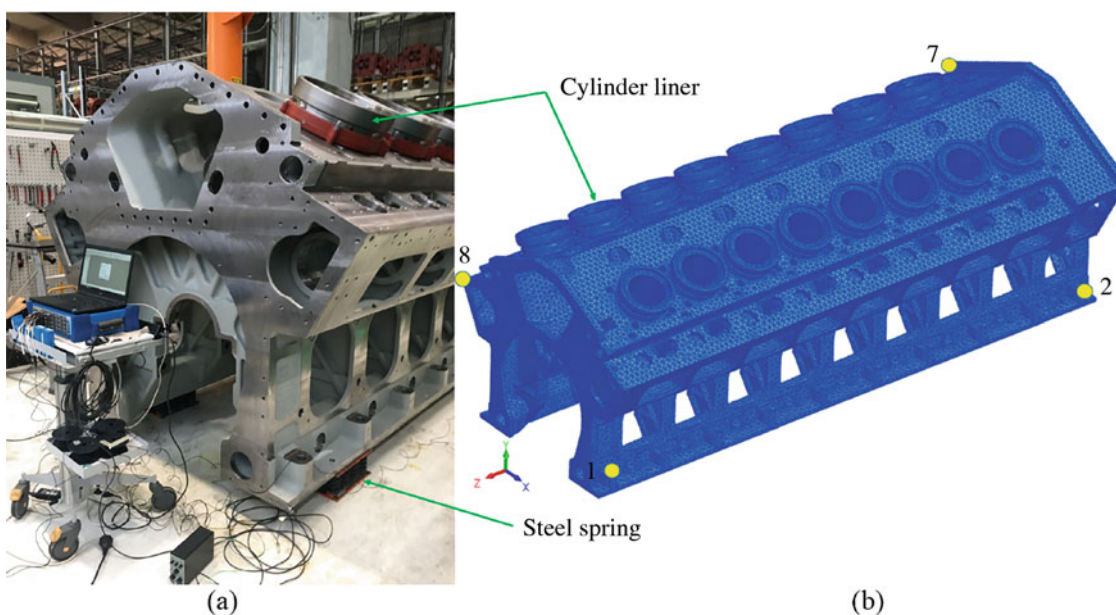
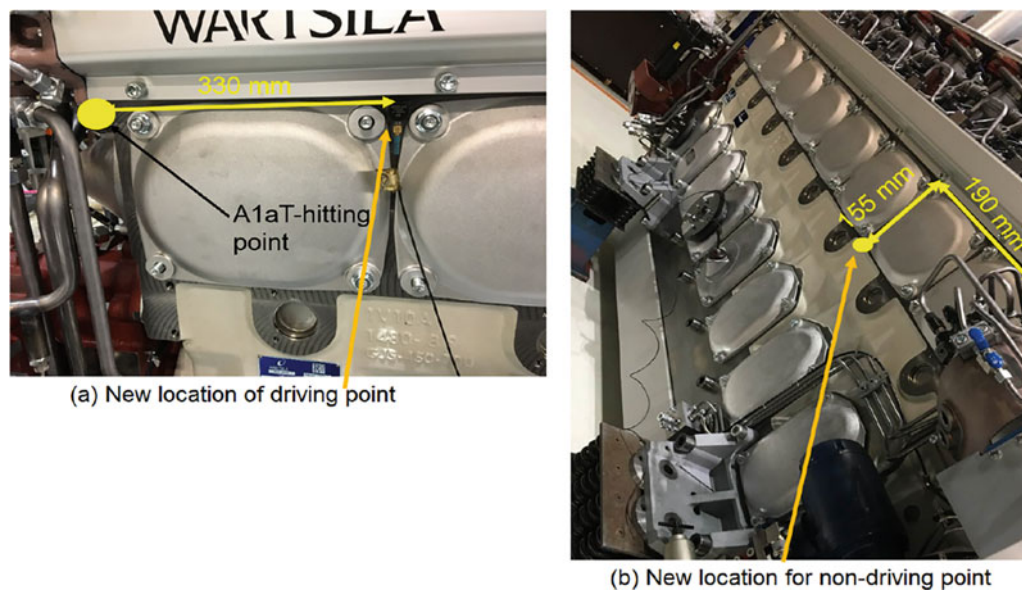


Fig. 20.2 (a) Measurement setup and (b) finite element model of a W16V32E engine block with the cylinder liner. Measurement points are numbered 1, 2, 7 and 8 and excitations are given at points 1 and 2 in the transversal and vertical directions

Table 20.1 Inertia properties of the W16V32E engine block and its comparison with finite element values

Inertia properties	FE values	Extracted values	Error	With enforced mass	Error
Mass [tn]	21.4	20.8	2.8%	21.4	0%
x_c [mm]	-0.2	-1.0	400%	-1.0	-500%
y_c [mm]	500.7	526.0	-4.9%	526.0	-4.9%
Z_c [mm]	2583.6	2575.6	0.3%	2575.0	0.3%
J_{xx} [kg.m ²]	56566	53816	4.8%	57037	0.8%
J_{yy} [kg.m ²]	56733	55157	2.8%	58459	-3.0%
J_{zz} [kg.m ²]	12902	11115	13.8%	11780	8.7%
J_{xy} [kg.m ²]	-5	994	-	1053	-
J_{yz} [kg.m ²]	-453	-381	15.9%	-404	10.8%
J_{zx} [kg.m ²]	92	131	-44.5%	139	-51%

**Fig. 20.3** New locations for the driving point and non-driving points

terms of the magnitude is within the acceptable limit. The error in the cross moment of inertia is rather high. Nevertheless, the magnitude of these inertia terms is small and therefore it will have a little effect on the calculation of rigid body modes.

In FEMtools RBPE, the mass of the structure, which is often known from the weighing test, can be enforced. The mass enforcement resulted in a better agreement between the inertia values. Therefore, it is recommended, if available from a weighing test, to use the mass of the structure in the RBPE tool. However, this does not improve the computation of COG locations.

Example 2 Frequency response functions measurement of a complete W8L20DF engine is performed in this example. A hammer (tip mass = 2.57 kg) is used to excite the structure and data is acquired using the NVGate data acquisition system.

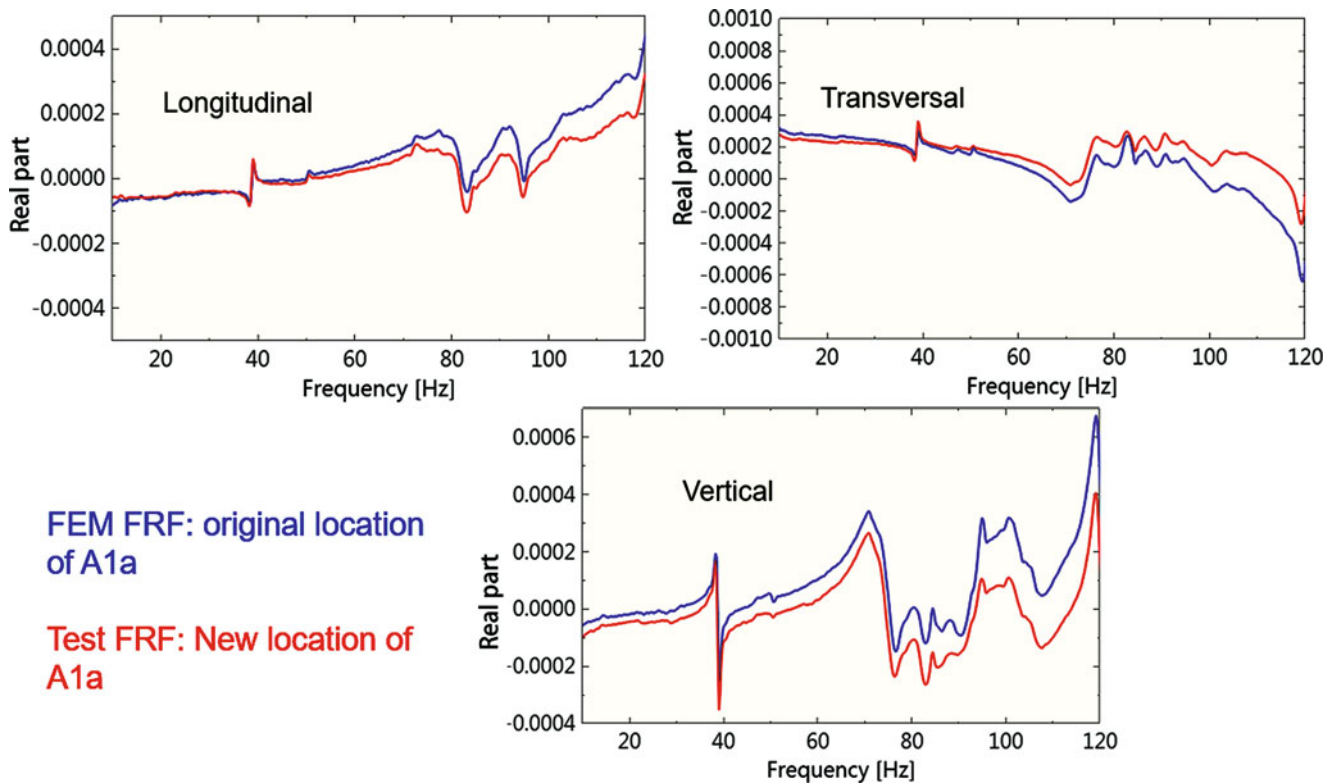
Five excitation directions (four in the feet and one in the top corner of the engine block, see Fig. 20.3a) and 8 corners of the engine block are chosen as the response locations. The corners are selected to avoid the local resonance of the engine components that may contaminate the FRFs data.

A complete set of FRFs are also measured after shifting a driving point and one non-driving point accelerometer (see Fig. 20.3). Theoretically, moving a non-driving point measurement location should not affect the computed values whereas moving a driving point accelerometer could have a significant influence on the FRF and hence on the inertia properties.

It can be difficult to measure the response and excitation at the same location and therefore it is important to study the sensitivity of the driving point FRF. It is also noticed during the measurements that often the quality of driving point FRF is not adequate. Note that the excitation locations are the same in both cases (before and after shifting the response locations).

Table 20.2 Comparison of evaluated inertia properties and weighing test results for W8L20DF engine

Inertia properties	Weighing result	Extracted result	Error	Extracted using shifted points	Error
Mass [tn]	11.78	11.43	-3.1%	11.27	1.4%
x_c [mm]	1364	1367	0.2%	1387	-1.5%
y_c [mm]	82.6	89.2	7.4%	88.1	1.2%
Z_c [mm]	NA	458.1	NA	458.1	NA
J_{xx} [kg.m ²]	NA	3690	NA	3485	NA
J_{yy} [kg.m ²]	NA	15093	NA	15516	NA
J_{zz} [kg.m ²]	NA	12829	NA	10019	NA
J_{xy} [kg.m ²]	NA	-738	NA	-819	NA
J_{yz} [kg.m ²]	NA	-648	NA	-92	NA
J_{zx} [kg.m ²]	NA	-1165	NA	-780	NA

**Fig. 20.4** The effect of shifting the driving point location on the real part of the FRF [Frequency axis is 10–120 Hz]

The obtained results are compared in Table 20.2. They are fairly close to each other, indicating that a shift in the driving point excitation location has a marginal effect on the inertia properties. This result is important for the case where it is not possible to keep the accelerometer and excitation source very close to each other.

The deviation in the moment of inertia is larger compared to the mass value and COG. This corresponds well with the statistical error analysis presented in Ref. [5]. Note that in this case, the distance between driving point response and excitation location is 330 [mm] (15% of the total length) which is fairly large. A similar result is obtained with another engine (W8L34DF) but using a shaker excitation. This is reported in following example 3.

To further investigate the above finding, the real part of the driving point FRFs are compared in Fig. 20.4. The real part of the FRFs is considered here because that is used to extract the inertia properties. The curves show that the mass-line for all three directions are very close although there are some discrepancies at higher frequencies. This corresponds well with the obtained results. Moreover, this also indicates the robustness of the tool. It means that even a large shift in the measurement

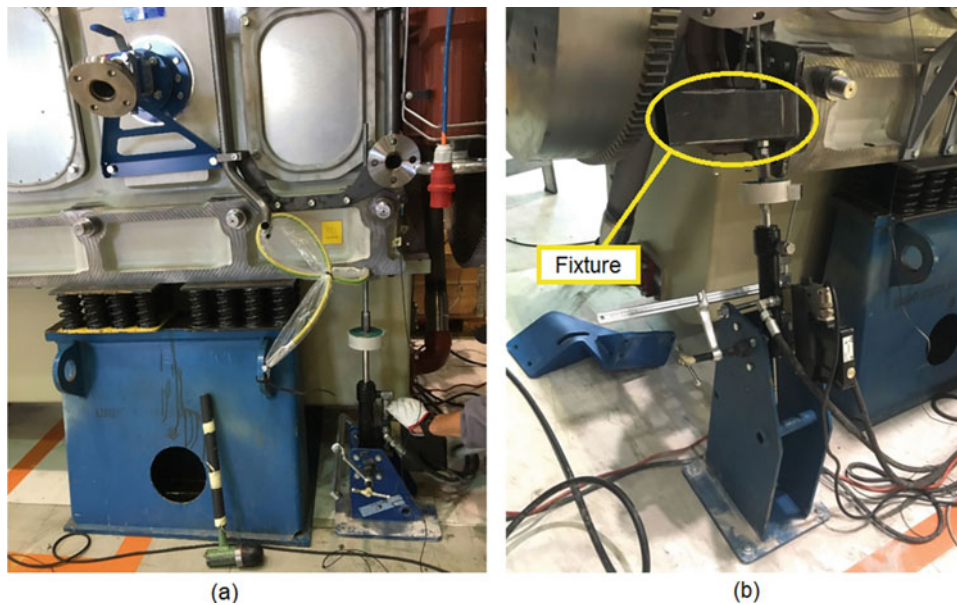


Fig. 20.5 (a) Vertical and (b) angle excitation using the hydraulic shaker

Table 20.3 Comparison of the evaluated inertia properties and weighing test results for W8L34DF engine

Inertia properties	Weighing result	Hammer excitation	Error	Shaker excitation	Error
Mass [tn]	42.76	43.61	-2.0%	41.82	2.1%
x_c [mm]	2197	2240	-1.9%	2206	-0.4%
y_c [mm]	45	31	31%	54	20%
z_c [mm]	NA	681	NA	675	NA
J_{xx} [kg.m ²]	NA	27206	NA	28930	NA
J_{yy} [kg.m ²]	NA	130079	NA	133727	NA
J_{zz} [kg-in ²]	NA	127931	NA	147819	NA
J_{xy} [kg.m ²]	NA	3716	NA	3245	NA
J_{yz} [kg.m ²]	NA	-10578	NA	-6900	NA
J_{zx} [kg.m ²]	NA	9217	NA	12888	NA

location has a marginal effect on the inertia properties. At least, this is true for a large and heavy structure like investigated in this paper. In practice, the driving response point has a smaller shift compared to the present case.

Example 3 The frequency response functions measurement is performed on a rather heavy W8L34DF engine (~40 ton), using both hammer and shaker excitations.

Two sources of excitation are employed as it was uncertain that the hammer will be able to excite the low frequency mass-line region. The shaker excitation is applied using a hydraulic shaker as shown in Fig. 20.5. Using a shaker, it is rather difficult to impart the excitation in the transversal and horizontal directions. Whereas, to extract all the inertia properties, all excitations (minimum 3) must not be in the same direction. To circumvent the problem, a fixture is designed to provide the excitation at an angle of 20 degrees from the vertical direction as shown in Fig. 20.5b.

Five excitation directions are chosen with a hammer and four excitation directions (two in vertical and two at an angle) are employed in the shaker test. In both cases, 8 response points are measured on the corners of the engine block.

The obtained results are presented in Table 20.3. The mass and the COG in the x-direction are very close to the weighing results, but some deviation is seen in the transversal direction. However, the deviation in terms of the magnitude is within the acceptable limit.

The comparison between hammer and shaker results reveal small discrepancies that may be due to a better signal-to-noise ratio in the case of shaker excitation. However, it is hard to say that the shaker result is more accurate compared to the hammer test without good reference data.

The main conclusion of the analysis is that both the hammer and shaker excitations can be used to extract the inertia properties of a W32 line engine as the results are very close to each other. However, a shaker excitation must be used in the

case of a W32 V-engine which is twice heavier than the line engines. On the other hand, hammer excitation is sufficient in the case of a W20 engine and it is much faster compared to a shaker excitation measurement setup.

A complete set of FRFs is also measured after shifting a driving point location in the vertical excitation. The extracted inertia properties are exactly the same in this case that indicates that the small shift in the driving point measurement location has no or marginal (see, example 2) effect on the inertia properties. Note that the excitation point is the same in both cases. The real part of the driving point FRFs shows that the mass line for all three directions are very close even though there are some discrepancies at higher frequencies. This corresponds well with the obtained results.

20.4 Remarks and Practical Suggestions on the Measurement Procedures

The IRM uses the measured FRFs to extract the inertia properties implying that FRFs with high signal-to-noise ratio will lead to an accurate result. Nevertheless, based on our experience with testing the diesel engines, a few additional guidelines must be considered while performing these measurements as stated below:

- The coordinates of the excitation and response locations should be marked as accurate as possible.
- Minimum three excitation directions are required to extract the inertia properties. However, it is recommended to use 4–5 excitation directions if possible. Furthermore, the excitation location must be stiff and flat.
- Only a few response directions (6–8) are required, however the same response locations must be measured for each excitation direction.
- Only one coordinate system can be used at one point (local or global). It means that if an excitation is given in the vertical direction at one point then another excitation cannot not be at an angle at the same point. A workaround is to duplicate the point with different coordinate system.
- It is essential to measure driving point FRFs for each excitation direction in the same coordinate system.
- Rigid body natural frequencies are not of interest for these measurements. However, they should be kept as low as possible such that the lowest elastic mode is at least twice of the highest rigid body mode.
- The structure should be mounted on flexible springs. Hanging the engine with soft connections has not yielded a satisfactory result to the authors.

20.5 Conclusion

In this study, the rigid body inertia properties of several Wärtsilä engines are extracted using the inertia restrain method, available as an add-on specialist tool (RBPE) in the FEMtools software. Experimental results are compared with finite element data and weighing test results.

The obtained results reveal that the evaluated rigid body inertia properties are in close agreement with the weighing test and finite element results. The deviation of the values is within 5%. This is a promising result and indicates that the IRM can be potentially used for the identification of rigid body inertia properties for massive diesel engines. The inertia properties obtained using two different excitation sources (hammer and shaker) are also in good agreement. The selection of the excitation source mainly depends on the weight of the structure.

The effect of shifting the driving and non-driving point accelerometer locations is also investigated. The results show that the IRM predicts the inertia properties quite well and has a marginal effect of shifting (5- 8% of the maximum length) the driving point accelerometer and sometimes it has no effect on the properties. This shows that the IRM is a robust tool for identifying the inertia properties of large and heavy structures.

Acknowledgements This research is funded by Wärtsilä Finland Oy.

References

1. Lamontia, M.A.: On the determination and use of residual flexibilities, inertia restraints and rigid body modes. In: Proceedings of the 1st IMAC, Orlando, FL (1982)
2. Bretl, J., Conti, P.: Rigid body mass properties from test data. In: Proceedings of the 5th IMAC, London (1987)

3. Nuutila, O., Saine, K., Toivola, J.: Experimental methods for determining rigid body inertia properties from frequency response function of medium speed diesel engines. In: Proceedings of the 11th international modal analysis conference, pp. 1121–1125 (1993)
4. Fregolent, A., Sestieri, A.: Identification of rigid body inertia properties from experimental data. *Mech. Syst. Signal Process.* **10**(6), 697–709 (1996)
5. Lee, H., Lee, Y.B., Park, Y.S.: Response and excitation points selection for accurate rigid-body inertia properties identification. *Mech. Syst. Signal Process.* **13**, 571–592 (1999)
6. Toivola, J., Nuutila, O.: Comparison of three methods for determining rigid body inertia properties from frequency response functions. In: Proceedings of the 11th International modal analysis conference, pp. 1126–1132 (1993)
7. Furusawa, M., Tominaga, T.: Rigid body modes enhancement and rdof estimation for experimental modal analysis. In: Proceedings of the 4th IMAC, Los Angeles, CA (1986)
8. Crowley, J., Rockrin, T., Brown, D.: Use of rigid body calculations in tests. In: Proceedings of the 4th IMAC, Los Angeles, CA (1986)
9. Wei, Y.S., Reis, J.: Experimental determination of rigid body inertia properties. In: Proceedings of 6th IMAC, Las Vegas, NV (1989)
10. Furusawa, M.: A method of determining rigid body inertia properties. In: Proceedings of the 6th IMAC, Las Vegas, NV (1989)
11. FEMtools Rigid Body Properties Extractor (RBPE) User Guide: (2019). <https://www.femtools.com>

Eddy Dascotte: General Manager, Dynamic Design Solutions NV, CAE software research and development company, 1994–present. Project Engineer, Dynamic Engineering NV, noise and vibration consultants, Leuven, Belgium, 1987–1993. Research Assistant, University of Brussels, Dpt of Civil Engineering, 1984–87. Master in Civil Engineering, University of Brussels, 1984.



Chapter 21

Dynamic Performance and Uncertainty Analysis of a Piezometaelastic Structure for Vibration Control and Energy Harvesting

Leticia H. Maki, Make S. Valencia, and Paulo S. Varoto

Abstract This paper aims to study the dynamics of a foldable vibration based piezoelectric energy harvesting system for low frequency applications and passive vibration attenuation. Most of up to date reported work has focused on developing new harvesting devices and techniques to power small electronics such as pacemakers and sensor networks for structural health monitoring of machines and structural systems. It falls within the general area of smart structures and uses piezoelectric materials in the mechanical-to-electrical energy conversion process. The electromechanical devices are capable of converting ambient structural vibration signals in electrical energy. The well-known cantilever beam model partially or fully covered by piezoelectric layers is one of the simplest and most exploited models for piezoelectric energy harvesting. The energy harvester consists of a combination of beams forming a foldable structure. The presence of uncertainties in some key parameters can significantly alter the dynamic response of the harvesting device thus affecting its overall performance in the mechanical to electrical energy conversion process. Uncertain parameters are introduced in the dynamic model and numerical simulations are conducted through the well known Monte Carlo Simulation method.

Keywords Piezoelectric energy harvesting · Mechanical vibrations · Uncertainties analysis

21.1 Introduction

Research on vibrations of structures that use intelligent materials, which collect and convert vibrational energy, commonly found in the environment, into useful electrical energy has been targeted and received more attention in recent years. This concept is a process commonly referred to as Piezoelectric Energy Harvesting. There has been a growth in researches in the sustainable energy sector seeking innovative technology solutions for generating renewable and sustainable energy sources that can power small devices in general or store this energy for later use. As technology advances, implantable devices are getting smaller and so as well their batteries. However and inevitably, reduction in size is generally associated to smaller mass and higher stiffness, what causes increases in the resulting natural frequencies of the mechanical device. Most of environmental vibration signals are within low frequencies, that is from 0 to 100 Hz. Therefore, important investigations [2, 3, 8, 18] have currently being carried out in order to overcome this challenge and bringing new configurations for the energy harvester that can properly handle low natural frequencies.

The increasing demand for volume reduction of piezoelectric power generators has required smaller and consequently lighter devices to be available, [4, 7, 27]. An immediate consequence of the reduction in volume and mass is the increase in the harvester natural frequency, especially when it is designed and constructed from beams covered with piezoelectric material. Thus, as the natural frequency increases, the generator may lose efficiency mainly at low frequencies due to its inability to tune to the disturbance signal. Numerous works have recently been published to propose solutions to establish an appropriate relationship between the value of the generator's first natural frequency and its stiffness and mass characteristics. We highlight those that aim to take advantage of nonlinear effects intrinsic to the system [5, 16, 28] and others that use geometric effects to obtain lower natural frequencies [2, 3, 8, 9, 20].

It is well known that items produced on a large scale invariably suffer minor dimensional variations as well as may also be subject to variations in the electrical and material properties. Similarly, computational models formulated to study the dynamic behavior of structures are also subject to errors, due to the simplifying assumptions adopted in the system

L. H. Maki · M. S. Valencia · P. S. Varoto (✉)
University of São Paulo São Carlos Engineering School – EESC-USP, São Carlos, SP, Brasil
e-mail: leticia.maki@usp.br; mervalencia@usp.br; varoto@sc.usp.br

modeling. Such variations cause variations in the errors of the manufacturing process, and such variations in errors are generically called uncertainties in the most diverse areas of contemporary engineering. Regarding the piezoelectric energy harvesting theme, the study of uncertainties is significantly important for several reasons, the main ones are: (i) Power generators usually have higher performance under operating conditions than their natural frequency. The dominant frequency is very close to the dominant frequency of the structural vibration signal from which the energy is collected. Therefore, small dimensional variations or electromechanical properties can cause significant variations in the dominant natural frequency of the piezoelectric generator [15]; (ii) uncertainties in the computational model may provide results that differ from those observed in experimental tests, which may compromise the model validation as well as the energy generator optimization process [14]; (iii) errors and parametric variability in experimental tests may, similar to numerical models, lead to the emergence of uncertainties in experimental results, [1, 23], which may also compromise future optimization processes.

Recently reported researches have focused on studying the dynamic performance and optimization of harvester under parametric uncertainties [1, 13, 14, 17, 22, 23, 25] in linear harvesting devices. This more comprehensive study on the effects of model is needed since the effects of uncertain parameters can influence in different ways the resulting output voltage of the harvester. In this sense, the inclusion of identification, characterization and quantification studies of uncertainties in the modeling is very important, since studies have analyzed the system response with uncertain parameters and showed that the introduction of these uncertainties reveal a variability in the generated voltage [22]. This voltage is sensitive to various parameter sources such as material properties, geometric properties, tolerances and operating conditions [23]. This paper aims to investigate the dynamic performance in terms of frequency bandwidth for a piezoelectric harvesting foldable structure composed of beam elements partially covered by piezoelectric material using electro-mechanical equations and Euler-Bernoulli theory for beams. The analytical work is based on a previously similar investigation [2]. Numerically simulated and experimental results are compared in order to verify the analytical model. Moreover, the effects of uncertain parameters in the system output, that is, electrical voltage and power will be carried out in order to provide important guidelines for the optimum design of such devices.

21.2 Problem Definition

The piezoelectric energy model used in this work is shown in Fig. 21.1. The harvester consists of beams connected by blocks with a tip mass in the last beam, piezoelectric layers are added in just one side of each beam and covering the whole beam forming the unimorph configuration. The model shown in Fig. 21.1 follows the same methodology as developed in [2], except the addition of moment of inertia to the blocks. The challenge in energy harvesting area is to obtain a harvester whose configuration has natural frequencies in low frequencies band, that is from 0-100Hz, so the system will have low mode shapes with a small addition in the weight or volume. The equations derivations are based on Euler-Bernoulli beam theory, resulting in transmissibility frequency response functions (*FRF*), relating the harvester output mechanical displacement and electrical voltage and power due to the base driven motion. Expressions for these transmissibility FRF constitute the harvester electromechanical response model that will be described in the next section. Later, experimental tests are performed in order to validate the analytical model.

Moreover, variations or uncertainties are imposed to parameters as electrical resistance, capacitance, mass of tip mass and piezoelectric layer thickness in order to explore the system sensibility when these parameters are modified. Epistemic model uncertainties is simulated using Monte Carlo method for the model shown in Fig. 21.1.

21.3 Electromechanical Model

This section addresses the development of the electromechanical model equations that describe the dynamic behavior of a foldable energy harvesting structure, as shown in Fig. 21.1. It consists of uniform beams connected by blocks with a tip mass in the last beam. Each beam is assumed to be an Euler-Bernoulli beam whose model neglects the deformation effects of the cross section created by shear force, as well as the rotation inertia of the beam. These mean that small rotation angles and deformations are considered. As previously mentioned, the geometric model shown in Fig. 21.1 follows the same methodology as developed in [2].

Derivation of the electromechanical model employees the well known Euler-Bernoulli beam model [21] and a simple kinematic diagram consisting of two beams connected by an intermediate lumped mass is shown in Fig. 21.2

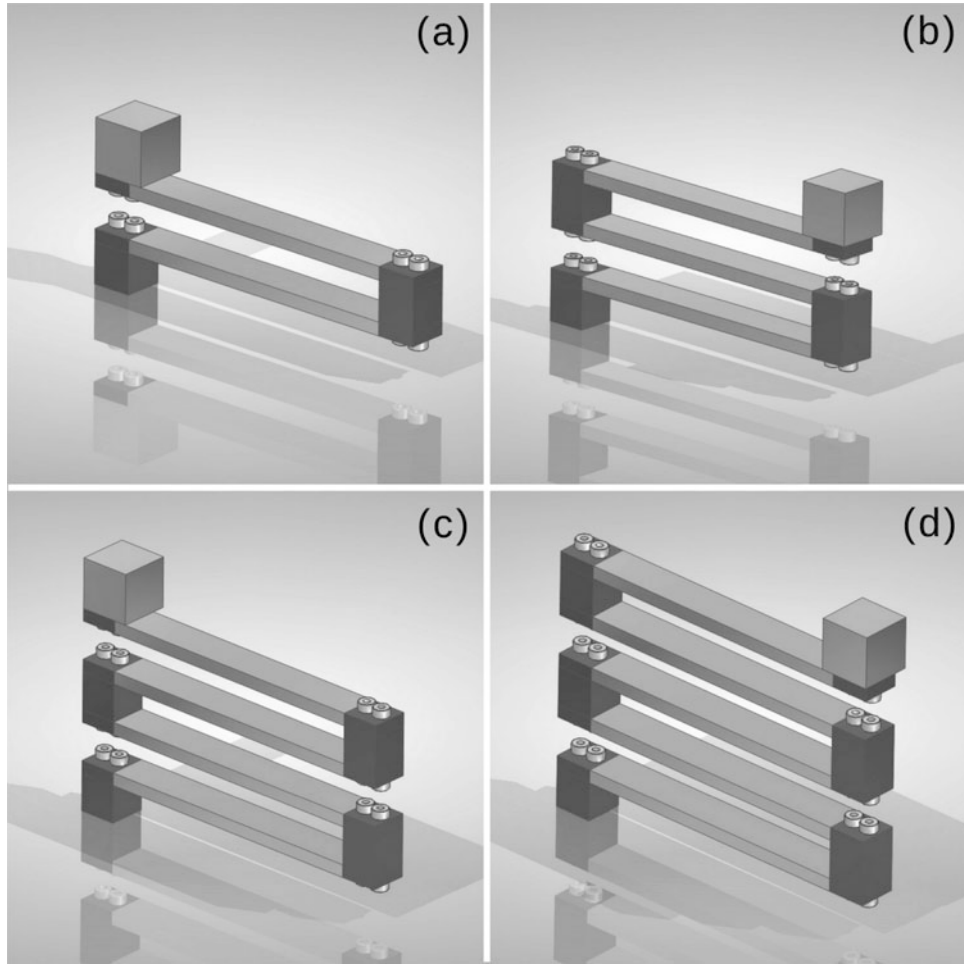


Fig. 21.1 Foldable energy harvesting geometric model with different number of beam segments

The coupled equation of motion in the z direction in terms of the relative displacement $u_r(x, t)$ for a beam with a tip mass considering viscous damping can be stated as [2, 21]:

$$\rho A \frac{\partial^2 u_r(x, t)}{\partial t^2} + C \frac{\partial u_r(x, t)}{\partial t} + EI \frac{\partial^4 u_r(x, t)}{\partial x^4} + \alpha \left[\frac{d\delta(x)}{dx} - \frac{d\delta(x-L)}{dx} \right] v(t) = f(x, t) \quad (21.1)$$

where E is the Young's Modulus and I is the polar moment of inertia of the beam, ρ is the density and A is the cross sectional area of the beam. The right hand side of Eq. (21.1) $f(x, t)$ indicated as a general excitation term contains terms related to the input base driven motion and output voltage from the piezoelectric layer, and is written as:

$$f(x, t) = - \left[\rho A + m_l \delta(x - x^*, i - k) + M_t \delta(x - x_{end}, i - n) \right] \frac{d^2 w_b(t)}{dt^2} \quad (21.2)$$

ρA is the total mass per unit length of the beam. The last two terms from Eq. (21.2) are related to inertia contribution, M_t and m_l are the tip and link masses, respectively. Since the piezoelectric layers are added to the beam, their properties are also considered in the equation:

$$\rho A = b_s (\rho_s t_s + \rho_p t_p) \quad (21.3)$$

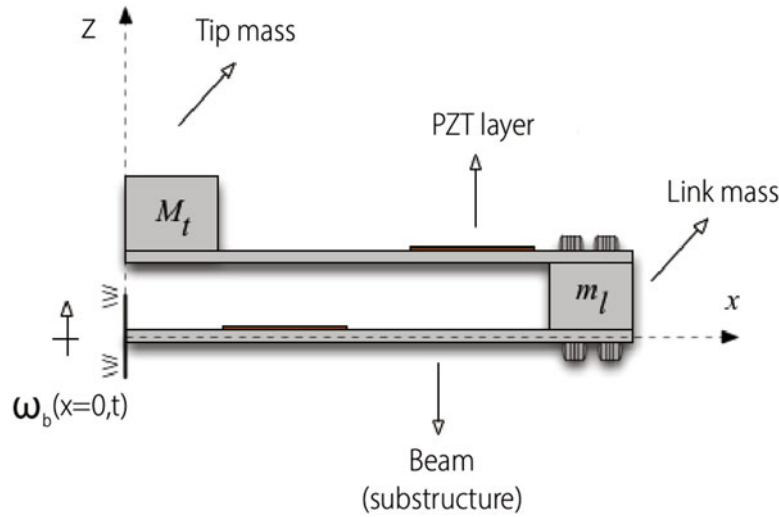


Fig. 21.2 Foldable energy harvesting model with two beams

where b is the width and t the thickness. The subscript s and p refers to, respectively, substructure (beam) and piezoelectric material. The product EI is commonly denoted as bending stiffness [21] and is calculated considering both layers, the beam and the piezoelectric. The unimorph configuration is adopted [10] and the bending stiffness is then written as:

$$EI = b_s \left[\frac{E_s(h_b^3 - h_a^3) + E_p(h_c^3 - h_b^3)}{3} \right] \quad (21.4)$$

with

$$h_a = -h_{sa}; \quad h_b = h_{pa} - h_p; \quad h_c = h_{pa} \quad (21.5)$$

$$h_{pa} = \frac{t_p^2 + \frac{2E_s t_p t_s}{E_p} + \frac{E_s t_s^2}{E_p}}{2 \left(t_p + E_s \frac{t_s}{E_p} \right)} \quad (21.6)$$

$$h_{sa} = \frac{t_p^2 + 2t_p t_s + \frac{E_s t_s^2}{E_p}}{2 \left(t_p + E_s \frac{t_s}{E_p} \right)} \quad (21.7)$$

From Eq. (21.2), α is the coupling term for parallel connection between the piezoelectric layers of adjacent beams and it is given as [11]:

$$\alpha = -2 \int_{\frac{t_s}{2}}^{t_p + \frac{t_s}{2}} e_{31} \frac{b_s}{t_p} z dz = -2b_s e_{31} \frac{(t_p + t_s)}{2} \quad (21.8)$$

where e_{31} is the piezoelectric coefficient.

Determination of the system natural frequencies and eigenfunctions require the solution of the undamped equation of motion for free vibration, that is obtained from Eq. (21.1) and expressed as

$$\rho A \frac{\partial^2 u(x, t)}{\partial t^2} + EI \frac{\partial^4 u(x, t)}{\partial x^4} = 0 \quad (21.9)$$

where in this case Eq. (21.9) is written in terms of the beam's absolute transverse displacement $u(x, t)$. The free vibration solution can be found using the method of separation of variables [21]:

$$u_i(x, t) = \sum_{j=1}^{\infty} \phi_{ij}(x) \eta_j(t) \quad (21.10)$$

The function $\phi_{ij}(x)$ is the j -th eigenfunction of the i -th beam and $\eta_j(t)$ is a time domain function. Considering the following solutions [21]:

$$\eta_j(t) = D_j \cos(\omega_{nj}t) + E_j B \sin(\omega_{nj}t) \quad (21.11)$$

$$\phi_{ij}(x) = A_{ij} \cos(\beta_j x) + B_{ij} \sin(\beta_j x) + C_{ij} \cosh(\beta_j x) + D_{ij} \sinh(\beta_j x) \quad (21.12)$$

where ω_{nj} is the j th undamped natural frequency of the system:

$$\omega_{nj} = \beta_j^2 \sqrt{\frac{EI}{\rho A}} \quad (21.13)$$

The eigenfunction constants for each beam expressed in Eq. (21.12) (A_{ij} , B_{ij} , C_{ij} , D_{ij}) and the eigenvalues β_j depend boundary and continuity conditions. Two boundary conditions are used at each end, and for the clamped end in the first beam of the assemblage they are given as:

$$\begin{cases} \phi_{1j}(x) = 0 \\ \phi'_{1j}(x) = 0 \end{cases} \quad (21.14a)$$

$$\begin{cases} \phi_{1j}(x) = 0 \\ \phi'_{1j}(x) = 0 \end{cases} \quad (21.14b)$$

where x can be L_s (length of the beam) or zero, depending on the configuration of the structure. Similarly, for the last beam where the tip mass is located, the equilibrium conditions are given as:

$$\begin{cases} EI \phi''_{nj}(x) \pm I_t \phi'_{nj}(x) \omega_{nj}^2 = 0 \\ EI \phi'''_{nj}(x) \pm M_t \phi_{nj}(x) \omega_{nj}^2 = 0 \end{cases} \quad (21.15a)$$

$$\begin{cases} EI \phi''_{nj}(x) \pm I_t \phi'_{nj}(x) \omega_{nj}^2 = 0 \\ EI \phi'''_{nj}(x) \pm M_t \phi_{nj}(x) \omega_{nj}^2 = 0 \end{cases} \quad (21.15b)$$

where x assumes the value zero or L depending on the structure configuration while the plus or minus sign is associated with $x = 0$ or $x = L$, respectively. Equations (21.15a) and (21.15b) account for the mass moments of inertia of the link and end masses given by I_l and I_t , respectively. Similarly continuity and equilibrium conditions at the connection between adjacent and consecutive beams can be written as:

$$\begin{cases} \phi_{ij}(x) = \phi_{(i+1)j}(x) \\ \phi'_{ij}(x) = \phi'_{(i+1)j}(x) \\ EI \phi''_{ij}(x) = -EI \phi''_{(i+1)j}(x) \pm I_l \omega_{nj}^2 \phi'_{(i+1)j}(x) \\ EI \phi'''_{ij}(x) = -EI \phi'''_{(i+1)j}(x) \pm M_l \omega_{nj}^2 \phi_{(i+1)j}(x) \end{cases} \quad (21.16a)$$

$$\begin{cases} \phi_{ij}(x) = \phi_{(i+1)j}(x) \\ \phi'_{ij}(x) = \phi'_{(i+1)j}(x) \\ EI \phi''_{ij}(x) = -EI \phi''_{(i+1)j}(x) \pm I_l \omega_{nj}^2 \phi'_{(i+1)j}(x) \\ EI \phi'''_{ij}(x) = -EI \phi'''_{(i+1)j}(x) \pm M_l \omega_{nj}^2 \phi_{(i+1)j}(x) \end{cases} \quad (21.16b)$$

$$\begin{cases} \phi_{ij}(x) = \phi_{(i+1)j}(x) \\ \phi'_{ij}(x) = \phi'_{(i+1)j}(x) \\ EI \phi''_{ij}(x) = -EI \phi''_{(i+1)j}(x) \pm I_l \omega_{nj}^2 \phi'_{(i+1)j}(x) \\ EI \phi'''_{ij}(x) = -EI \phi'''_{(i+1)j}(x) \pm M_l \omega_{nj}^2 \phi_{(i+1)j}(x) \end{cases} \quad (21.16c)$$

$$\begin{cases} \phi_{ij}(x) = \phi_{(i+1)j}(x) \\ \phi'_{ij}(x) = \phi'_{(i+1)j}(x) \\ EI \phi''_{ij}(x) = -EI \phi''_{(i+1)j}(x) \pm I_l \omega_{nj}^2 \phi'_{(i+1)j}(x) \\ EI \phi'''_{ij}(x) = -EI \phi'''_{(i+1)j}(x) \pm M_l \omega_{nj}^2 \phi_{(i+1)j}(x) \end{cases} \quad (21.16d)$$

Application of the above defined boundary conditions (21.14a), (21.14b), (21.15a), (21.15b) in the equation (21.12) leads to a system of equations given as:

$$[V_{ij}] \begin{bmatrix} A_{ij} \\ B_{ij} \\ C_{ij} \\ D_{ij} \end{bmatrix} = 0 \quad [T_{nj}] \begin{bmatrix} A_{nj} \\ B_{nj} \\ C_{nj} \\ D_{nj} \end{bmatrix} = 0 \quad (21.17)$$

$$[V_{ij}] = \begin{bmatrix} \cos(\beta_j x) & \sin(\beta_j x) & \cosh(\beta_j x) & \sinh(\beta_j x) \\ -\beta_j \sin(\beta_j x) & \beta_j \cos(\beta_j x) & \beta_j \sinh(\beta_j x) & \beta_j \cosh(\beta_j x) \end{bmatrix} \quad (21.18)$$

$$[T_{(i+1)j}] =$$

$$\begin{bmatrix} EI\beta_j^2(-\cos(\beta_j x_t)) & EI\beta_j^2(-\sin(\beta_j x_t)) & EI\beta_j^2 \cosh(\beta_j x_t) & EI\beta_j^2 \sinh(\beta_j x_t) \\ \pm(-I_t\beta_j^5 c^2(-\sin(\beta_j x_t))) & \pm(-I_t\beta_j^5 c^2 \cos(\beta_j x_t)) & \pm(-I_t\beta_j^5 c^2 \sinh(\beta_j x_t)) & \pm(-I_t\beta_j^5 c^2 \cosh(\beta_j x_t)) \\ EI\beta_j^3 \sin(\beta_j x_t) & EI\beta_j^3(-\cos(\beta_j x_t)) & EI\beta_j^3 \sinh(\beta_j x_t) & EI\beta_j^3 \cosh(\beta_j x_t) \\ \pm(-M_t\omega_n^2 \cos(\beta_j x_t)) & \pm(-M_t\omega_n^2 \sin(\beta_j x_t)) & \pm(-M_t\omega_n^2 \cosh(\beta_j x_t)) & \pm(-M_t\omega_n^2 \sinh(\beta_j x_t)) \end{bmatrix} \quad (21.19)$$

The value x in the Eq. (21.18) is zero since the clamped part of the beam is always located in the origin of the coordinate system, according to Fig. 21.2. Moreover, applying the boundary conditions (21.16a), (21.16b), (21.16c), (21.16d) for the Eq. (21.12):

$$[L_{ij}] \begin{bmatrix} A_{ij} \\ B_{ij} \\ C_{ij} \\ D_{ij} \end{bmatrix} = [R_{2j}] \begin{bmatrix} A_{(i+1)j} \\ B_{(i+1)j} \\ C_{(i+1)j} \\ D_{(i+1)j} \end{bmatrix} \quad (21.20)$$

$$[L_{(i+1)j}] = \begin{bmatrix} \cos(\beta_j x) & \sin(\beta_j x) & \cosh(\beta_j x) & \sinh(\beta_j x) \\ -\sin(\beta_j x) & \cos(\beta_j x) & \sinh(\beta_j x) & \cosh(\beta_j x) \\ -EI\beta_j^2 \cos(\beta_j x) & -EI\beta_j^2 \sin(\beta_j x) & EI\beta_j^2 \cosh(\beta_j x) & EI\beta_j^2 \sinh(\beta_j x) \\ EI\beta_j^3 \sin(\beta_j x) & -EI\beta_j^3 \cos(\beta_j x) & EI\beta_j^3 \sinh(\beta_j x) & EI\beta_j^3 \cosh(\beta_j x) \end{bmatrix} \quad (21.21)$$

$$[R_{ij}] = \begin{bmatrix} \cos(\beta_j x) & \sin(\beta_j x) & \cosh(\beta_j x) & \sinh(\beta_j x) \\ -\sin(\beta_j x) & \cos(\beta_j x) & \sinh(\beta_j x) & \cosh(\beta_j x) \\ EI\beta_j^2 \cos(\beta_j x) & EI\beta_j^2 \sin(\beta_j x) & -EI\beta_j^2 \cosh(\beta_j x) & -EI\beta_j^2 \sinh(\beta_j x) \\ \pm(-I_L\beta_j^5 c^2(-\sin(\beta_j x))) & \pm(-I_L\beta_j^5 c^5 \cos(\beta_j x)) & \pm(-I_L\beta_j^5 c^5 \cosh(\beta_j x)) & \pm(-I_L\beta_j^5 c^2 \cosh(\beta_j x)) \\ -EI\beta_j^3 \sin(\beta_j x) & EI\beta_j^3 \cos(\beta_j x) & -EI\beta_j^3 \sinh(\beta_j x) & -EI\beta_j^3 \cosh(\beta_j x) \\ \pm(-M_L\omega_n^2 \cos(\beta_j x)) & \pm(-M_L\omega_n^2 \sin(\beta_j x)) & \pm(-M_L\omega_n^2 \cosh(\beta_j x)) & \pm(-M_L\omega_n^2 \sinh(\beta_j x)) \end{bmatrix} \quad (21.22)$$

Writing the equation (21.20) for n beams:

$$\begin{Bmatrix} A_{nj} \\ B_{nj} \\ C_{nj} \\ D_{nj} \end{Bmatrix} = [R_{nj}]^{-1} [L_{(n-1)j}] [R_{(n-1)j}]^{-1} [L_{(n-2)j}] \dots [R_{2j}]^{-1} [L_{1j}] \begin{Bmatrix} A_{1j} \\ B_{1j} \\ C_{1j} \\ D_{1j} \end{Bmatrix} \quad (21.23)$$

after reorganizing Eqs. (21.17) and (21.20) the resulting equation is expressed as a function of the first beam coefficients:

$$[N] \begin{bmatrix} A_{1j} \\ B_{1j} \\ C_{1j} \\ D_{1j} \end{bmatrix} = 0 \quad (21.24)$$

where,

$$[N] = \begin{bmatrix} V_{1j} \\ T_{nj} R_{nj}^{-1} L_{(n-1)j} R_{(n-1)j}^{-1} L_{(n-2)j} \dots R_{2j}^{-1} L_{1j} \end{bmatrix} \quad (21.25)$$

The system of Eq. (21.24) is linear and homogeneous and the nontrivial solution requires that $|N(\beta_j)| = 0$. This leads to the characteristic equation, whose roots are the system's eigenvalues, which in turn give the undamped natural frequencies. For each eigenvalue β_j there exists an infinite number of solutions for the j -th eigenfunction according to Eq. (21.24). A reasonable way to solve for a set of coefficients is to adopt a value for A_{1j} , e.g. unity, and solve for the remaining coefficients in terms of this value [6].

Once all eigenvalues and eigenfunction coefficients are found, solution for the undamped free vibration problem is determined through modal superposition according to Eq. (21.10).

Solution for the forced harmonic problem requires that the a given prescribed base input motion $w_b(x = 0, t)$ be written as

$$w_b(x = 0, t) = w_b(t) = y_b e^{i\omega t} \quad (21.26)$$

where y_b represents the input displacement amplitude. Since Eq. (21.1) requires the input be defined in terms of the base driven acceleration, Eq. (21.26) is transformed according to

$$\ddot{w}_b(t) = a_b e^{i\omega t} \quad (21.27)$$

where $a_b = -\omega^2 y_b$ the amplitude of the system input.

Substitution of Eq. (21.27) into Eq. (21.1) considering that all initial conditions be identically zero, leads to the forced coupled harmonic base driven equation of motion for the i -th beam. Solution is carried out by uncoupling the degrees of freedom into modal space, first substituting Eq. (21.10) into Eq. (21.1), multiplying both sides of the resulting equation by an eigenfunction $\phi_{ij}(x)$ and integrating the resulting equation from 0 to L_s . By using the orthogonality conditions [2, 21], the equation of motion for the j -th eigenfunction is found to be

$$M_j \ddot{\eta}_j(t) + C_j \dot{\eta}_j(t) + K_j \eta_j(t) + \vartheta P_i \left(\phi'_{ij}(L) - \phi'_{ij}(0) \right) v(t) = \quad (21.28)$$

$$- \left(\rho A \int_0^L \phi_{ij}(x) dx + m_l \phi_{ij}(\bar{x}) + M_t \phi_{in}(x_t) \right) \ddot{w}_b(t)$$

where M_j , C_j and K_j are the generalized mass, damping and stiffness coefficients related to the j -th mode eigenfunction, respectively. Rayleigh proportional damping [6] is assumed in this case. Equation (21.29) can be stated in a simple way according to

$$\ddot{\eta}_j + 2\zeta_j \omega_{nj} \dot{\eta}_j + \omega_{nj}^2 \eta_j = -\chi_j v(t) - \gamma_j \ddot{w}_b \quad (21.29)$$

where ζ_j is the modal damping coefficient associated with the j -th mode shape, and:

$$\chi_j = \alpha \sum_{i=1}^n P_i (\phi'_{ij}(L_s) - \phi'_{ij}(0)) \quad (21.30)$$

$$P_i = \text{sign}(\phi'_{ij}(L_s) - \phi'_{ij}(0)) \quad (21.31)$$

$$\gamma_j = M_t \phi_{nj}(x) + \rho A \sum_{i=1}^n \int_0^{L_s} \phi_{ij}(x) dx + \sum_{i=2}^n M_L \phi_{ij}(x) \quad (21.32)$$

where in the equation (21.30) P_i is to adjust the signal assuming the number 1 or -1 [2]. For the electrical model, Kirchhoff law is used for parallel connection and the current $i_i(t)$ is given as [10]:

$$i(t) = \frac{dq(t)}{dt} = - \int_{x=0}^{L_p} d_{31} E_p h_p c b \frac{\partial^3 w(x, t)}{\partial x^2 \partial t} dx - \frac{\epsilon_{33}^e b L}{h_p} \frac{dv(t)}{dt} \quad (21.33)$$

where C_p is the electrical capacitance and R the electrical resistance, therefore the differential equation for electrical circuit can be written as [2, 11]:

$$P_i C_p \dot{v}(t) + i_i(t) = -2b_s d_{31} E_p \frac{t_p + t_s}{2} \sum_{j=1}^{\infty} \frac{dT_j(t)}{dt} [\phi'_{ij}(L_s) - \phi'_{ij}(0)] \quad (21.34)$$

where,

$$C_p = 2\epsilon_{33}^s \frac{L_s b_s}{t_p} \quad (21.35)$$

ϵ_{33}^s is the piezoelectric permittivity at a constant stress and d_{31} is the piezoelectric coupling coefficient. Note that it is assumed the piezoelectric layers cover the whole beam.

Substitution of Eq. (21.27) in Eq. (21.1), the motion transmissibility FRF's relating the motion at the free end of the last beam segment to the input base motion can be determined. Reorganizing equations (21.1) and (21.34) and applying Fourier transformation, the FRF for voltage to base acceleration is obtained:

$$\frac{v(\omega)}{a_b(\omega)} = \frac{\sum_{j=1}^{\infty} \frac{j\omega\chi_j\gamma_j}{\omega_{nj}^2 + 2\zeta\omega_{jn}\omega - \omega^2}}{\frac{1}{R} + j\omega C_p + \sum_{j=1}^{\infty} \frac{j\omega\chi_j^2}{\omega_{nj}^2 + 2\zeta\omega_{nj}j\omega - \omega^2}} \quad (21.36)$$

using the above equation, the power transfer function is:

$$\frac{p(\omega)}{a_b^2(\omega)} = \frac{v^2(\omega)}{R} = \frac{1}{R} \left(\frac{\sum_{j=1}^{\infty} \frac{j\omega\chi_j\gamma_j}{\omega_{nj}^2 + 2\zeta\omega_{jn}\omega - \omega^2}}{\frac{1}{R} + j\omega C_p + \sum_{j=1}^{\infty} \frac{j\omega\chi_j^2}{\omega_{nj}^2 + 2\zeta\omega_{nj}j\omega - \omega^2}} \right)^2 \quad (21.37)$$

Replacing the equation (21.36) in (21.29) and the result in (21.1), the displacement for the tip mass transfer function is calculated as:

$$\frac{u_r(\omega)}{a_b(\omega)} = \left(\sum_{j=1}^{\infty} \frac{-1}{\omega_{nj}^2 + 2\zeta\omega_{nj}j\omega - \omega^2} \right) \left(\chi_j \frac{\sum_{j=1}^{\infty} \frac{j\omega\chi_j\gamma_j}{\omega_{nj}^2 + 2\zeta\omega_{nj}j\omega - \omega^2}}{\sum_{j=1}^{\infty} \frac{j\omega\chi_j^2}{\omega_{nj}^2 + 2\zeta\omega_{nj}j\omega - \omega^2}} + \gamma_j \right) \phi_{nj}(x) \quad (21.38)$$

the variable x depends on where the tip mass is located.

The relative tip mass acceleration to the base acceleration transfer function is determined as:

$$\frac{a_r(\omega)}{a_b(\omega)} = -\omega^2 \frac{u_r(\omega)}{a_b(\omega)} \quad (21.39)$$

and once the relative acceleration transmissibility FRF is found, the corresponding absolute FRF can be easily determined [11]. Equations (21.36), (21.37), (21.38) and (21.39) correspond to the electromechanical frequency domain response model [12, 19] of the energy harvesting system studied and they will be further used in numerical simulations.

21.4 Model Verification

In this section, the validation of the system will be performed through the comparison of theoretical model responses and experimental results. The results are presented through the frequency response functions previously defined. Firstly, properties of the beam, piezoelectric layers, link and tip mass are used in order to write a Matlab[®] to calculate the motion and voltage transmissibility FRF as well as output electrical power for the energy harvesting system formed from a different number of piezoelectric beams. Tables 21.1 and 21.2 exhibit geometric and material properties used in the simulations. Results from numerical simulations will be further compared to experimental results obtained from a prototype.

Notice that the only parameter changed was the number of beams, beams were all kept with the same length, width and thickness, as well as the link and tip mass. The material for the beams, link and tip mass are made of aluminum alloy. The electrical-mechanical system consists of a foldable structure with piezoelectric layers partially covering the top of each beam as shown in the Fig. 21.3.

Once the actual harvester's prototype is built, it is attached to the vibration exciter table through a rigid aluminum beam as shown in Fig. 21.4, that exhibits the four beam version of the foldable harvester with a tip mass attached to the free end of the last beam segment.

Base driven experimental tests are performed on different energy harvesting configurations according to the test setup shown in Fig. 21.4. Miniature tear drop accelerometers 100 mV/g are used to monitor the input base motion as well as the output acceleration in the vertical direction on the tip mass at the free end of the last beam. Since the natural frequencies change with the number of beams on a given assemblage, the frequency range of test was continuously adjusted to gather at least two natural frequencies for each tested harvesting configuration. Broad-band random excitation signal with hanning windows were used in all measurement channels and these were measured by using a Dp Quattro frequency analyzer.

Table 21.1 Geometric parameters

Parameter	Beam	Link mass	Tip mass	PZT
Length (mm)	127.3	12.7	12.7	114.6
Width (mm)	12.7	12.7	25.4	12.7
Thickness (mm)	3.18	12.7	12.7	0.26

Table 21.2 Material and electromechanical properties

Property	Beam	Link mass	Tip mass	PZT
Young Modulus (GPa)	69	69	69	66
Density (kg/m ³)	2700	2700	2700	7800
Permittivity, ϵ (nF/m)	–	–	–	13.3
Resistance (Ω)	–	–	–	500×10^3
Capacitance (nF)	–	–	–	0.48911

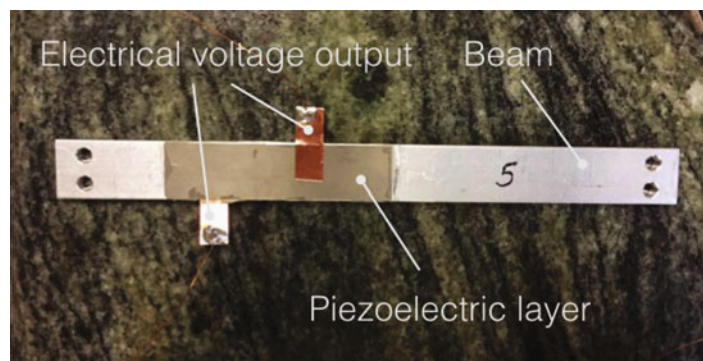


Fig. 21.3 Single beam instrumented with partial monolithic piezoelectric ceramic layer



Fig. 21.4 Foldable harvester on top of vibration exciter table

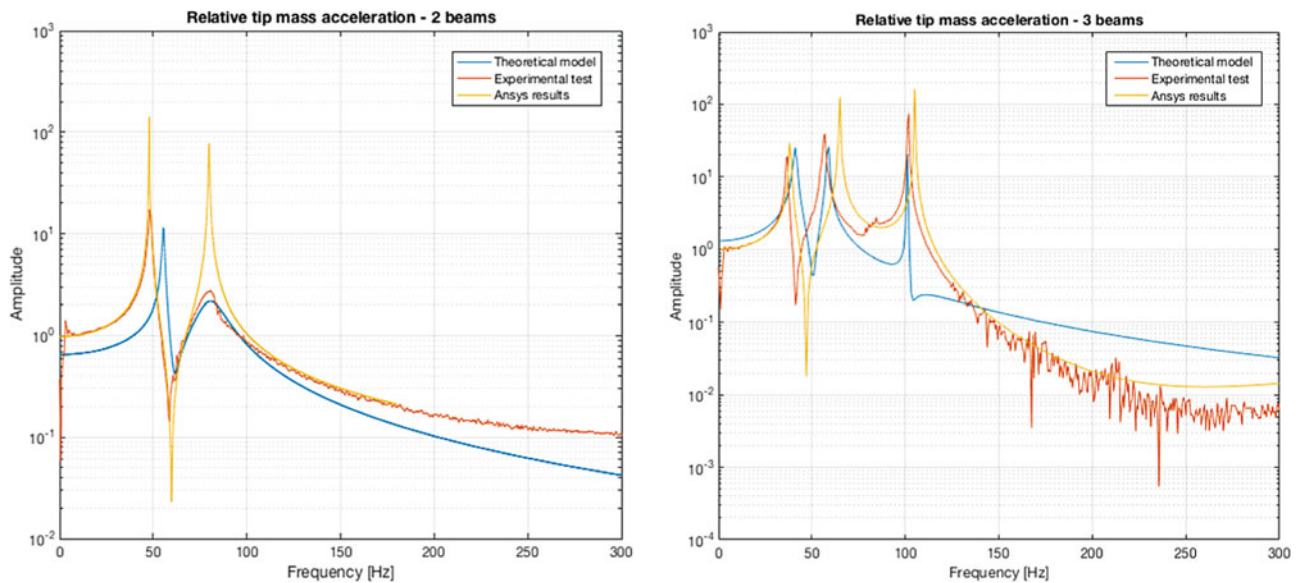


Fig. 21.5 Measured and numerically calculated mechanical transmissibility FRF for foldable 2-beam system

21.4.1 Mechanical Verification

The model verification were divided in two subsections: mechanical and electromechanical validation. The difference between the latter and the former are the inclusion of piezoelectric layers that provide voltage and power as output while mechanical model provides displacement and relative tip mass acceleration. The mechanical model used for this validation consists of a fan-folded structure with two and three beams, and without piezoelectric layers. Moreover, numerical simulations were developed in a Finite Element code and their results are shown in Fig. 21.5.

21.4.2 Eletromechanical Verification

Verification of the electromechanical model is performed in a similar manner as it was previously done for the case of pure mechanical FRFs. In this case, the same broadband signal was applied to the harvester for a different number of beams and the output voltage for the first beam was used to get the voltage transmissibility FRF. Figure 21.6 show experimental and numerically simulated data for a two beam energy harvesting configuration. Tables 21.3 and 21.4 show a comparison of the first and second natural frequency values for the same system.

There is a reasonably good match between theoretical FE and the experimental results while results for the continuous model tend to present larger differences in comparison with the experimentally obtained results. The second most important aspect to notice is the decreased of natural frequencies while the number of beams in the harvester is increased. This addresses the problem description, once it is possible to design an energy harvester in low frequency bands increasing the number of beams but in a small volume, therefore, a structure small enough in volume can be conceived for a different number of applications.

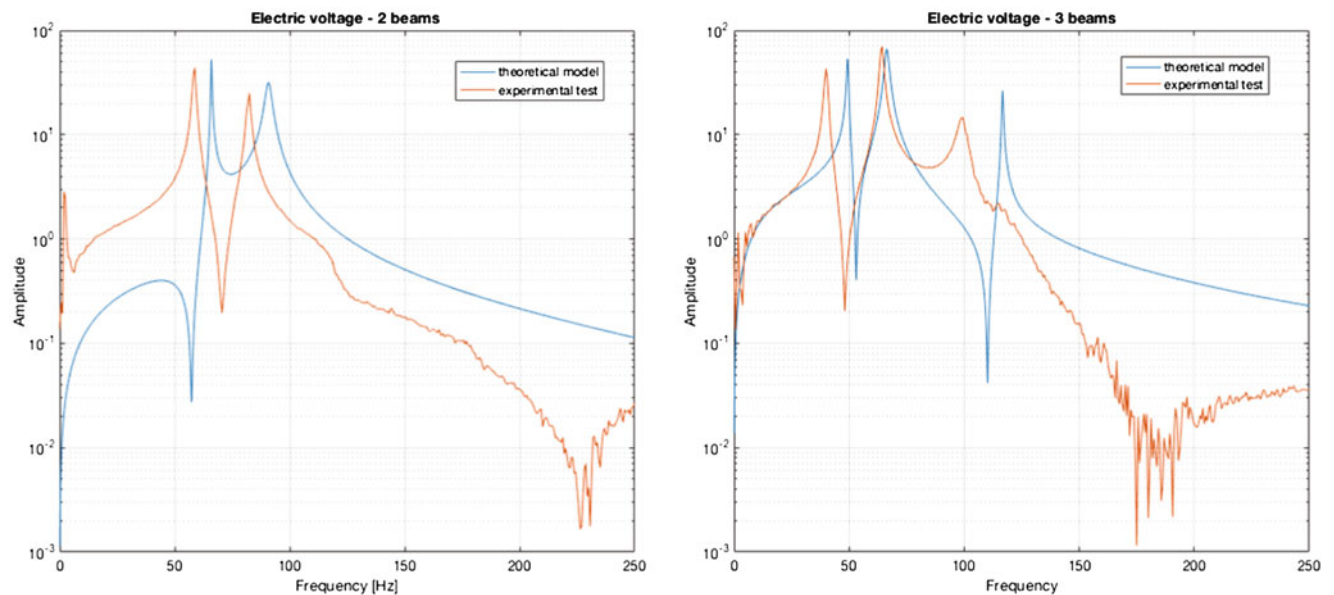


Fig. 21.6 Electromechanical transmissibility comparison for two beam harvester

Table 21.3 Comparison of results for first natural frequency

Number of beams	Theoretical model (Hz)	Experimental test (Hz)	FE results (Hz)
2 beams	65.9	55.75	63.34
3 beams	48.75	40.00	43.57
4 beams	38.05	28.12	33.77
5 beams	33.10	22.72	24.00

Table 21.4 Comparison of results for second natural frequency

Number of beams	Theoretical model (Hz)	Experimental test (Hz)	FE results (Hz)
2 beams	90.80	82.50	93.79
3 beams	65.58	61.38	72.98
4 beams	50.50	49.00	51.90
5 beams	42.91	39.06	41.76

21.5 Sensitivity and Uncertainty Analysis

The sensitivity analysis aims to verify the dynamic response of the fan-folded structure while some parameters are changed. These effects can be determined through the FRF's response in the frequency domain. Changing only one parameter the MATLAB® code is run for each value in the sample, it may or may not modify the natural frequencies of the harvester. Basically, uncertainty analysis follows the same concept and goal but with different methodology and the sample size.

Setting two beams and all the other parameters constant, the value for tip mass and electrical resistance are altered. In the following picture Fig. 21.7 M_t is changed from $M_t = 0$ kg up to $M_t = 1.3 \cdot 10^{-3}$ kg which is equivalent to about 30% of beam mass, and it shows the influence of tip mass in the frequency response, especially the natural frequencies which decrease with the increase the mass of tip mass.

Also, the resistance value is modified according to the range $R = [10, 10^2, 10^3, 10^4, 5 \cdot 10^4, 10^6]\Omega$: where $R = 10\Omega$ is representing a short circuit and $R = 10^6\Omega$ an open circuit. Therefore, we obtain the following result shown in Fig. 21.8.

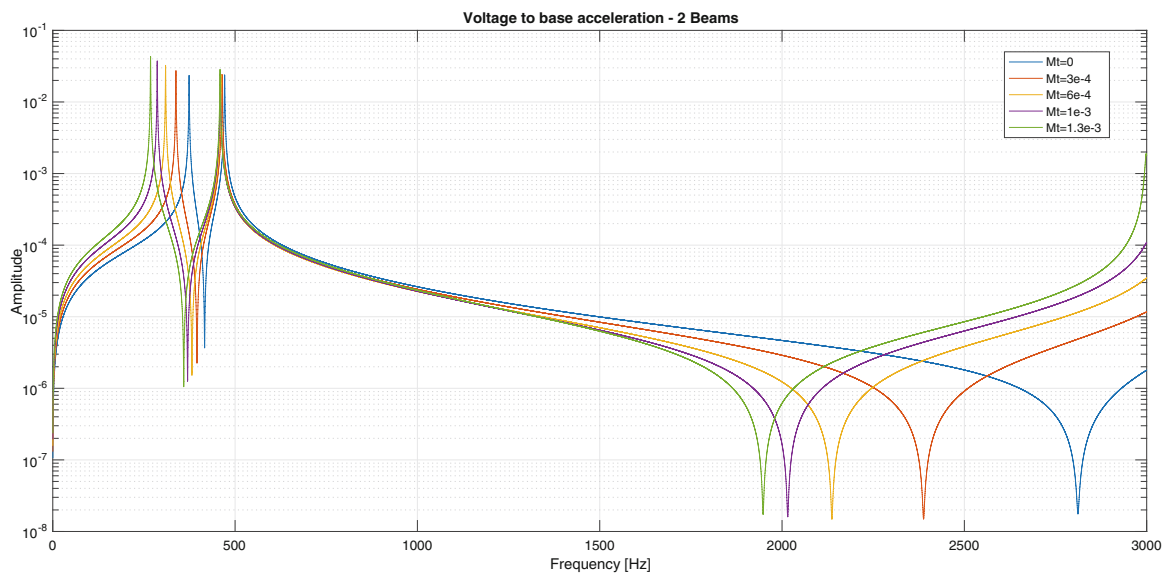


Fig. 21.7 Frequency response of voltage varying tip mass

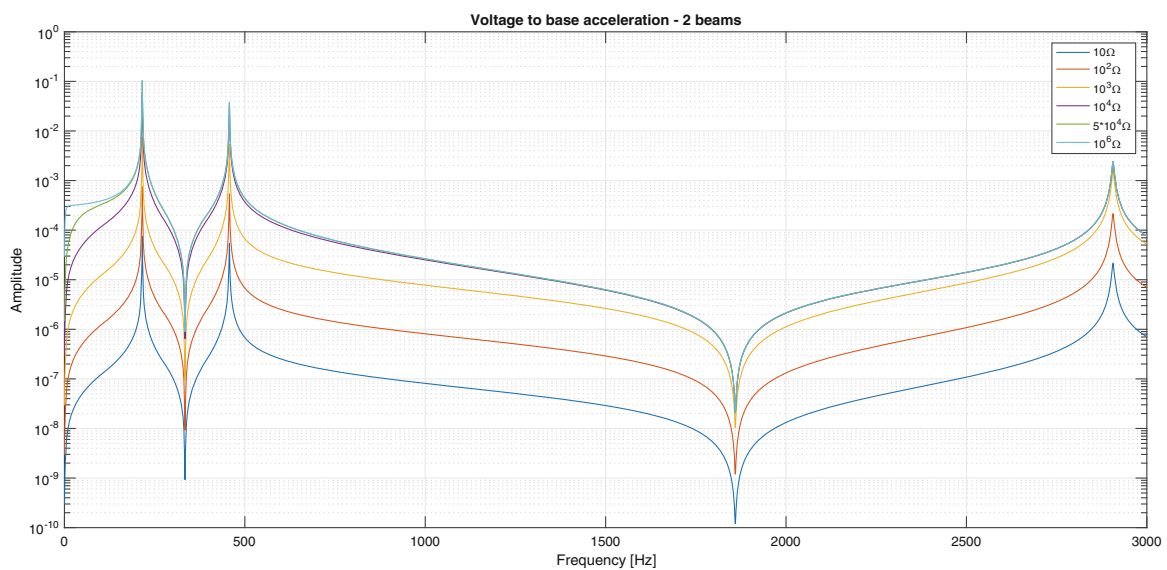
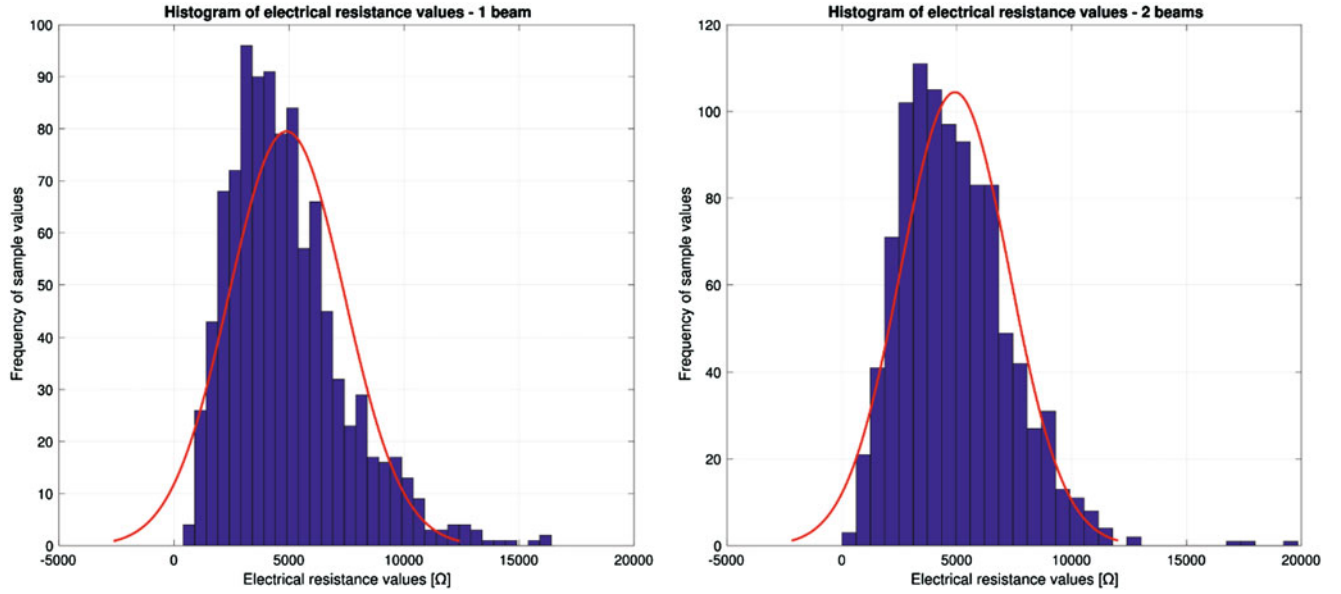


Fig. 21.8 Frequency response of voltage varying resistance

Table 21.5 Relative dispersion parameter for perturbed variables

Parameter	Relative dispersion (δ)
R_l	0.5
C_p	0.5
M_t	0.05
t_p	0.05

**Fig. 21.9** Electrical resistance histogram for 1 and 2 beams

It is seen from Fig. 21.8 that the output voltage is intensified with the increasing values of the load resistance.

As previously pointed out, this work also aims to perform an uncertainty investigation on the energy harvesting system by employing the Monte Carlo Simulation method, [24]. The Monte Carlo Simulation is a statistical method and essentially consists in generating a set of random samples, according to a given statistical distribution for a chosen parameter that will be perturbed. The probabilistic model for each perturbed random parameter is constructed according to the Maximum Entropy Principle, yielding a Gamma probability density function according to [24]

$$p_X(x) = \mathcal{K}_{]0, +\infty[}(x) \frac{(\delta^{-2})^{\frac{1}{\delta^2}}}{\Gamma(\delta^{-2})m_X} \left(\frac{x}{m_X}\right)^{\frac{1}{\delta^2}-1} \exp\left\{-\frac{x}{\delta^2 m_X}\right\} \quad (21.40)$$

Table 21.5 shows the values of the dispersion coefficient δ used to construct the gamma distribution for each perturbed variable.

In the present case, the effects of perturbations are present on the harvester's electromechanical transmissibility frequency response functions and that depend on the harvester's output electrical voltages and power, obtained from the solution of the system's equations in frequency domain. According to [26], once the model is evaluated for all samples in the random interval, confidence intervals can be determined for all parameters. The gamma statistical distributions and corresponding confidence intervals for all perturbed variables are shown in Figs. 21.9, 21.10, 21.11, 21.12, 21.13, and 21.14.

Statistically, confidence intervals contain values for a corresponding parameter that when tested should not be rejected with the same sample. In terms of energy harvesting, depending on the application this variation in voltage or power can have a significant effect on the converted energy that can be used to power small devices.

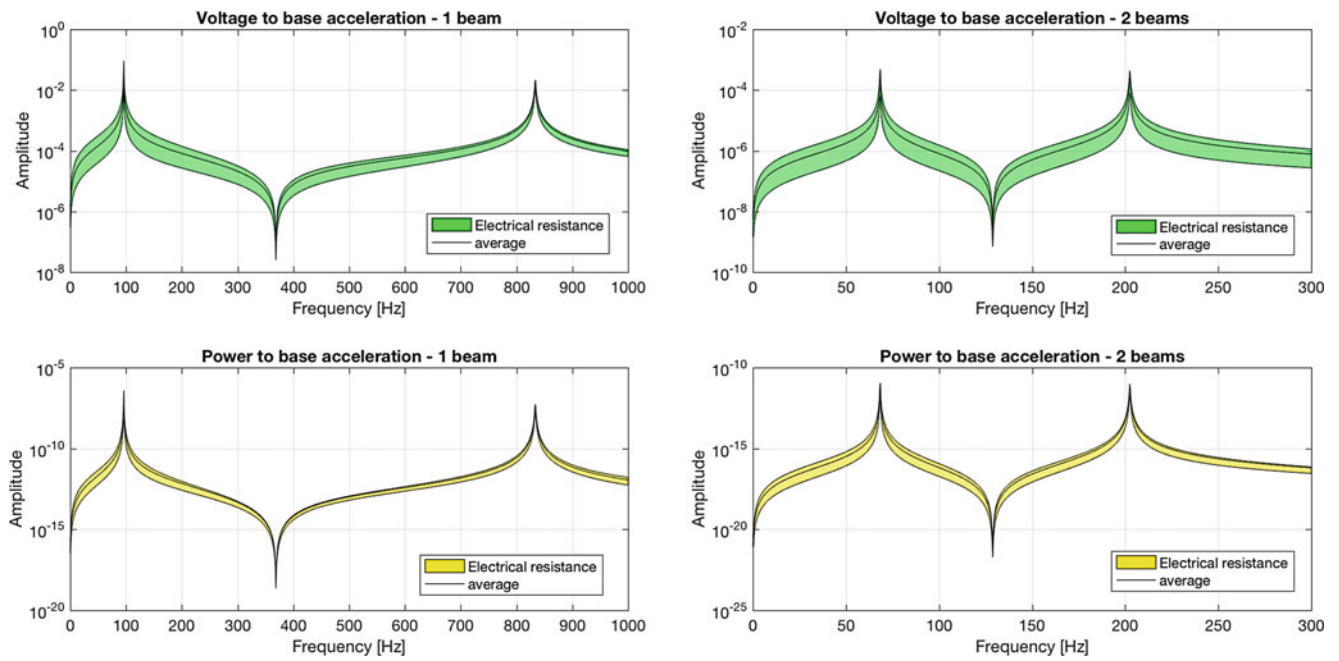


Fig. 21.10 Confidence intervals: load resistance

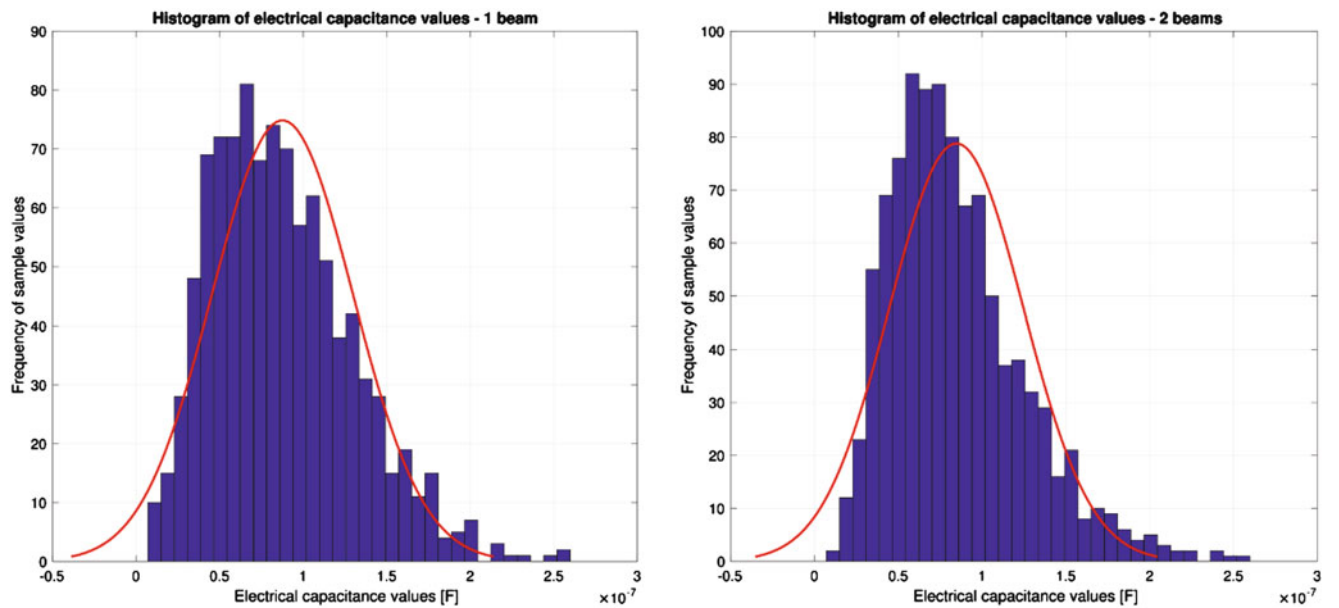


Fig. 21.11 Electrical capacitance histogram for 1 and 2 beams

21.6 Final Remarks

This article aims to model a foldable energy harvester. The equation derivations describe the dynamic behavior of structure and are based on Euler-Bernoulli beam theory. The challenge is to model a system with low vibration modes with a slight increase in the weight or volume of the structure and the results have covered this aspect, once we could verify that natural frequencies decrease with the increase of the number beams. According to the experimental tests, there is a good agreement between experimental and FE results, but the continuous model needs further improvements in order to

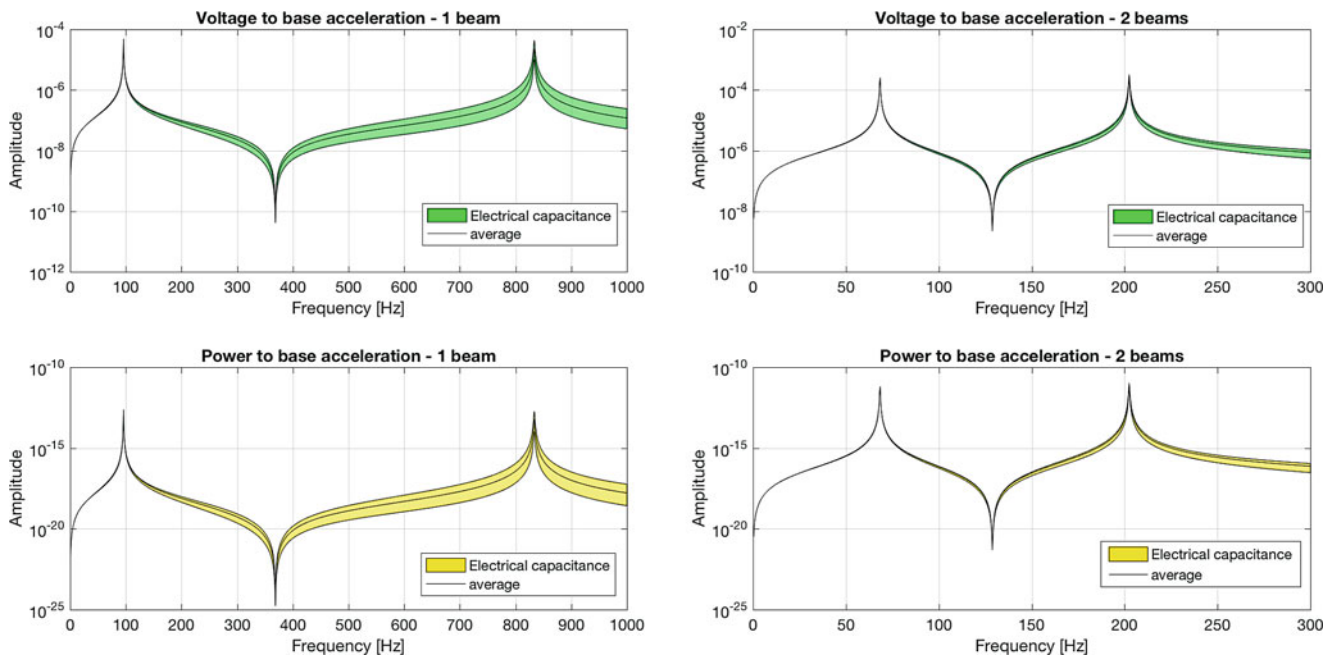


Fig. 21.12 Confidence intervals: piezoelectric internal capacitance

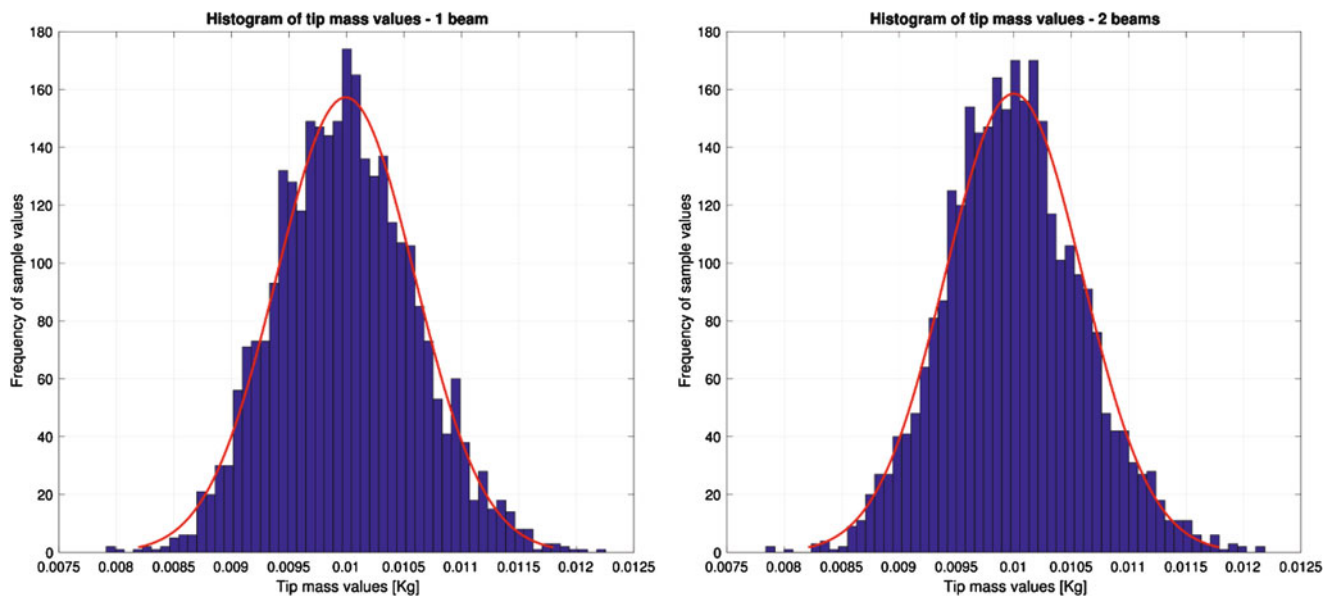


Fig. 21.13 Mass of tip mass histogram for 1 and 2 beams

present a better correlation with the measured results. Moreover, the consideration of uncertainty in design and optimization of mechanical vibration study based on energy harvesting concept has shown the foldable structure sensitivity to some parameters. Perturbation on these parameters can alter significantly the system response, that is, voltage and power generated. Hence, the uncertainty analysis is important to achieve better performance for foldable based cantilever energy harvesting systems

Acknowledgments All the support received from University of São Paulo, Brazil, FAPESP (Official funding agency of the state of São Paulo, grant Nr. 2017/20458-2) and CAPES (Brazilian Federal Funding Agency) is very much appreciated and acknowledged by the authors.

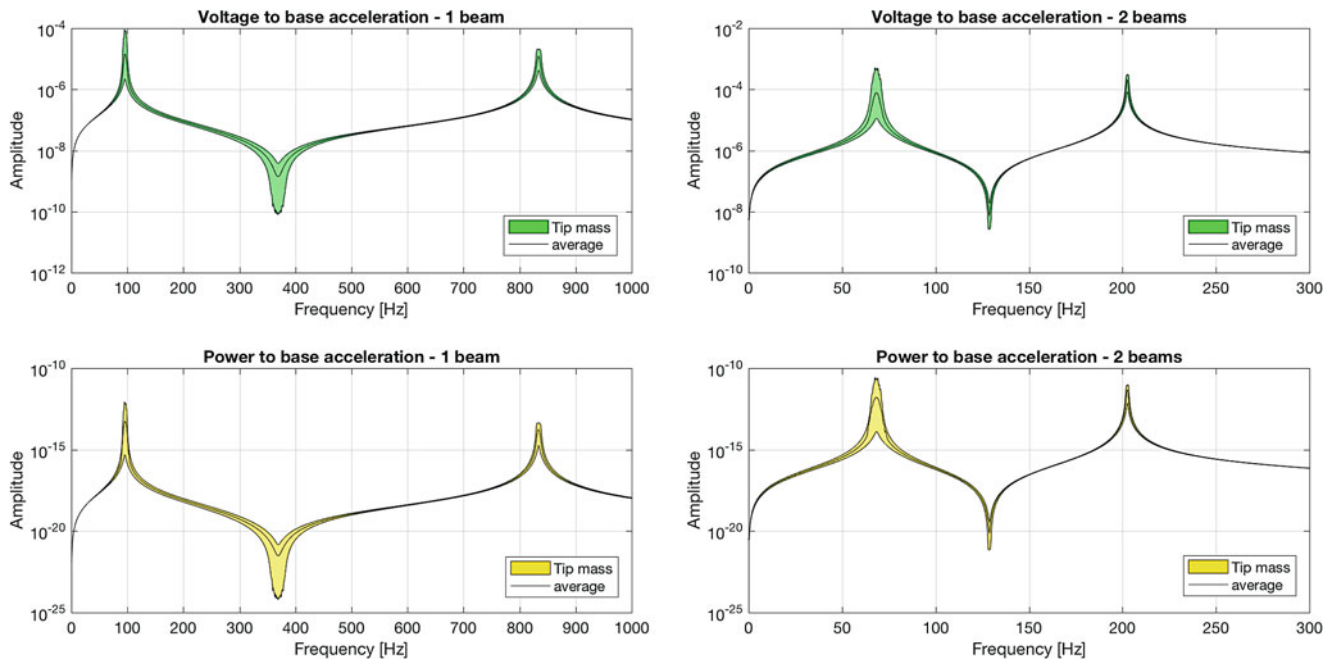


Fig. 21.14 Uncertainty parameter: value of tip mass

References

1. Ali, S., Friswell, M.I., Adhikari, S.: Piezoelectric energy harvesting with parametric uncertainty. *Smart Mater. Struct.* **19**(1), 1–9 (2010)
2. Ansari, M., Karami, M.A.: Modeling and experimental verification of a fan-folded vibration energy harvester for leadless pacemakers. *J. Appl. Phys.* **119**(9), 094506 (2016)
3. Ansari, M., Karami, M.A.: A sub-cc nonlinear piezoelectric energy harvester for powering leadless pacemakers. *J. Intell. Mater. Syst. Struct.* **1**(1), 1–8 (2017)
4. Beeby, S.P., Tudor, M.J., White, N.M.: Energy harvesting vibration sources for microsystems applications. *Meas. Sci. Technol.* **17**(12), 175–195 (2006)
5. Chen, L., Jiang, W.: Internal resonance energy harvesting. *Sound Vib.* **82**(3), 57–66 (2015)
6. Clough, R., Penzien, J.: Dynamics of structures. *Comput. Struct.* **1**, 730 (2003)
7. Cook-Chennault, K.A., Thambi, N., Sastry, A.M.: Powering MEMS portable devices—a review of non-regenerative and regenerative power supply systems with special emphasis on piezoelectric energy harvesting systems. *Smart Mater. Struct.* **17**, 1–33 (2008)
8. Deterre, M., Boutaud, B., Dalmolin, R., Boisseau, S., Chaillout, J.-J., Lefevre, E., Dufour-Gergam, E.: Energy harvesting system for cardiac implant applications. In: 2011 Symposium on Design, Test, Integration and Packaging of MEMS/MOEMS (DTIP), pp. 387–391. IEEE (2011)
9. Deterre, M., Lefevre, E., Zhu, Y., Woytasik, M., Deterre, M., Boutaud, B., Molin, R.D.: Micro blood pressure energy harvester for intracardiac pacemaker. *J. Microelectromech. Syst.* **23**(3), 651–660 (2014)
10. Erturk, A., Inman, D.J.: A distributed parameter electromechanical model for cantilevered piezoelectric energy harvesters. *J. Vib. Acoust.* **130**, 1–15 (2008)
11. Erturk, A., Inman, D.J.: *Piezoelectric Energy Harvesting*, 1st edn. Wiley, NY (2011)
12. Ewins, D.J.: *Modal Testing: Theory, Practice and Applications*, 1st edn. RSP, London (2000)
13. Franco, V., Varoto, P.S.: Parameter uncertainties in the design and optimization of cantilever piezoelectric energy harvesters. *Mech. Syst. Signal Process.* **93**(1), 593–609 (2017)
14. Franco, V.R.: *Optimization Techniques Applied to Piezoelectric Vibration Energy Harvesting Systems*. Ph.D. thesis, Sao Carlos School of Engineering, University of Sao Paulo, Brazil (2013)
15. Franco, V.R., Varoto, P.S.: Parameter uncertainties in the design and optimization of cantilever piezoelectric energy harvesters. *Mech. Syst. Signal Process.* **93**(1), 593–609 (2017)
16. Galbier, A., Karami, M.A.: Using an elastic magnifier to increase power output and performance of heart-beat harvesters. *Smart Mater. Struct.* **26**, 1–16 (2017)
17. Haji Hosseinloo, A., Turitsyn, K.: Design of vibratory energy harvesters under stochastic parametric uncertainty: a new optimization philosophy. *Smart Mater. Struct.* **10** (2016)
18. Karami, M.A., Inman, D.J.: Analytical modeling and experimental verification of the vibrations of the zigzag microstructure for energy harvesting. *J. Vib. Acoust.* **133**(1), 011002 (2011)
19. McConnell, K.G., Varoto, P.S.: *Vibration Testing: Theory and Practice*, 2nd edn. Wiley, NY (2008)
20. Mitcheson, P.D.: Energy harvesting for human wearable and implantable bio-sensors. In: 32nd Annual International Conference of the IEEE EMBS, pp. 3432–3436. IEEE (2010)
21. Rao, S.: *Vibrations of Continuous Systems*. Wiley, NY (2007)

22. Ruiz, R.O., Meruane, V.: Effect of uncertainties in the dynamical behavior of piezoelectric energy harvesters. *Proc. Eng.* **199**(1), 3486–3491 (2017)
23. Seong, S., H. C., Lee, S.: Design under uncertainty for reliable power generation of piezoelectric energy harvester. *J. Intell. Mater. Syst. Struct.* **28**(17), 2437–2449 (2017)
24. Soize, C.: *Uncertainty Quantification*. Springer, Switzerland (2017)
25. Trindade, M.A., Santos, H.G.T.: Effect of bonding layer uncertainties on the performance of surface-mounted piezoelectric sensors and actuators. In: *XIV International Symposium on Dynamic Problems of Mechanics (DINAME)*, pp. 1–8 (2013)
26. Varoto, P.S.: Dynamic behavior and performance analysis of piezoelastic energy harvesters under model and parameter uncertainties. In: *Sensors and Instrumentation, Aircraft/Aerospace and Energy Harvesting*, vol. 8 – Proceedings of the 36th IMAC, A Conference and Exposition on Structural Dynamics. SEM-IMAC (2018)
27. Williams, C.B., Yates, R.B.: Analysis of a micro-electric generator for microsystems. *Sensors Actuators A* **52**(1–3), 8–11 (1996)
28. Yang, W., Towfighian, S.: Internal resonance and low frequency vibration energy harvesting. *Smart Mater. Struct.* **26**, 1–11 (2017)

Biography

Paulo S. Varoto BSc on Mechanical Engineering – University of Sao Paulo-Brazil 1988
MSc on Mechanical Engineering – University of Sao Paulo – Brazil 1991
PhD on Engineering Mechanics – Iowa State University – USA – 1996



Chapter 22

Assessing Predictive Capabilities for Nonlinear Dynamic Structural Responses

Liliana C. Haus, B. Evan Saunders, Jonathan E. Acosta, Thomas E. Allard, Kyle A. Brindley, and Andrew J. Morello

Abstract Complex assemblies subject to engineering environments often contain material, interfacial, or geometric features that produce nonlinear responses. One specific interfacial feature of interest is contact under vibrational loads. Our project expands upon previous work by developing both linear and nonlinear finite element (FE) models of a four degree-of-freedom benchmark testbed, configured for variable states of intermittent contact, using Abaqus/Explicit. The goal of our study is to explore the effects of available contact interaction models on quantitative validation metrics. A better understanding of contact algorithms in FE software would help increase confidence in FE models of complex, nonlinear dynamic systems. The validation metrics of interest include features of the acceleration time series such as basic statistics (peak amplitude, mean, standard deviation, skewness, kurtosis, normal probability plot) – as well as features of the frequency domain including natural frequencies, mode shapes, power spectral density, and frequency response function plots. First, the linear FE model is used for baseline verification and validation purposes. Once it is validated against experimental data to within an acceptable margin of error, the linear model is used as the base for the nonlinear model. The nonlinear simulation explores Abaqus contact algorithms and their effects upon the dynamic response of the structure. In particular, the contact interactions we focus on are “hard” contact and the various types of “softened” contact. Finally, the nonlinear model is validated against data collected from experiments with the physical structure and the effects of the various contact interactions are analyzed.

Keywords Nonlinear dynamic systems · Finite element modeling · Abaqus · Interfacial contact · Contact interactions

22.1 Introduction

22.1.1 Motivation

It has become increasingly common for structural and dynamic analyses of complex structures to be completed within finite element (FE) software, in which a structure is geometrically described, discretized, excited, and analyzed. While linear FE models can be relatively reliably and accurately represented through their governing physical equations, the introduction of nonlinearities to the system can increase the complexity of the model and make it difficult to define a mathematical representation of the system. Despite this, there have been many instances of successfully validated models of extremely complex nonlinear systems [1–3]. However, relatively few studies have been performed to evaluate the various modeling techniques and assumptions that are used during the creation of a FE model. These decisions are of particular importance

L. C. Haus

Department of Mechanical Engineering, University of Texas at Dallas, Richardson, TX, USA
e-mail: Liliana.Haus@utdallas.edu

B. E. Saunders

Department of Mechanical & Aerospace Engineering, New Mexico State University, Las Cruces, NM, USA
e-mail: bsaunders@lanl.gov

J. E. Acosta

Department of Mechanical Engineering, University of Texas at El Paso, El Paso, TX, USA
e-mail: jeacosta@lanl.gov

T. E. Allard · K. A. Brindley (✉) · A. J. Morello

Los Alamos National Laboratory, Los Alamos, NM, USA
e-mail: tea@lanl.gov; kbrindley@lanl.gov; amorello@lanl.gov

to the creation of a nonlinear FE model because nonlinearities introduce significant sources of uncertainties to the model. By developing a better understanding of the effect of these crucial steps in the creation of a FE model, uncertainties in the process of FE model development can be reduced making it easier to pin-point sources of error in a FE model during model validation. In this report, we will focus on the effects of different contact interaction definitions on the system dynamics. The goal of this report is to expand upon the work of previous studies by validating a FE model of a 4 degree-of-freedom structure, which will be described in more detail in the next section. In doing so, we will investigate the effects of available contact interaction models on the dynamics of the modeled structure through the use of quantitative validation metrics in order to develop a simple but well-understood model of the structure. A better understanding of the primary contact algorithms available in the Abaqus FE modeling software would help increase confidence in FE models of complex, nonlinear dynamic systems and would aid in the identification of additional sources of uncertainty arising from FE modeling techniques.

22.1.2 Project Background

This report is concerned with the validation of an Abaqus FE model of a 4 degree-of-freedom impact oscillator structure (hereafter referred to as a four-story structure, or FSS) with nonlinearities due to interfacial interactions (Fig. 22.1). Several studies have been performed using this structure in the past. In 2007, Farrar et al. performed preliminary testing on the FSS and used the resulting data, as well as data from other previously analyzed nonlinear systems, to develop and support the understanding that nonlinearities in systems can be used to detect the presence of damage [4]. In 2009, Figueiredo et al. expanded upon this work and developed an initial numerical, lumped-mass model of the FSS and used it to explore some statistical data analysis techniques for detecting nonlinearities [5]. Most recently, in 2016, Nishio et al. [6] built upon the previous studies and modified the numerical lumped-mass model to better represent the nonlinear behavior of the FSS, in addition to defining and analyzing further data analysis techniques for detecting nonlinearities in the system response. In general, the broad goal of these reports was the development of data analysis methods for feature extraction to detect

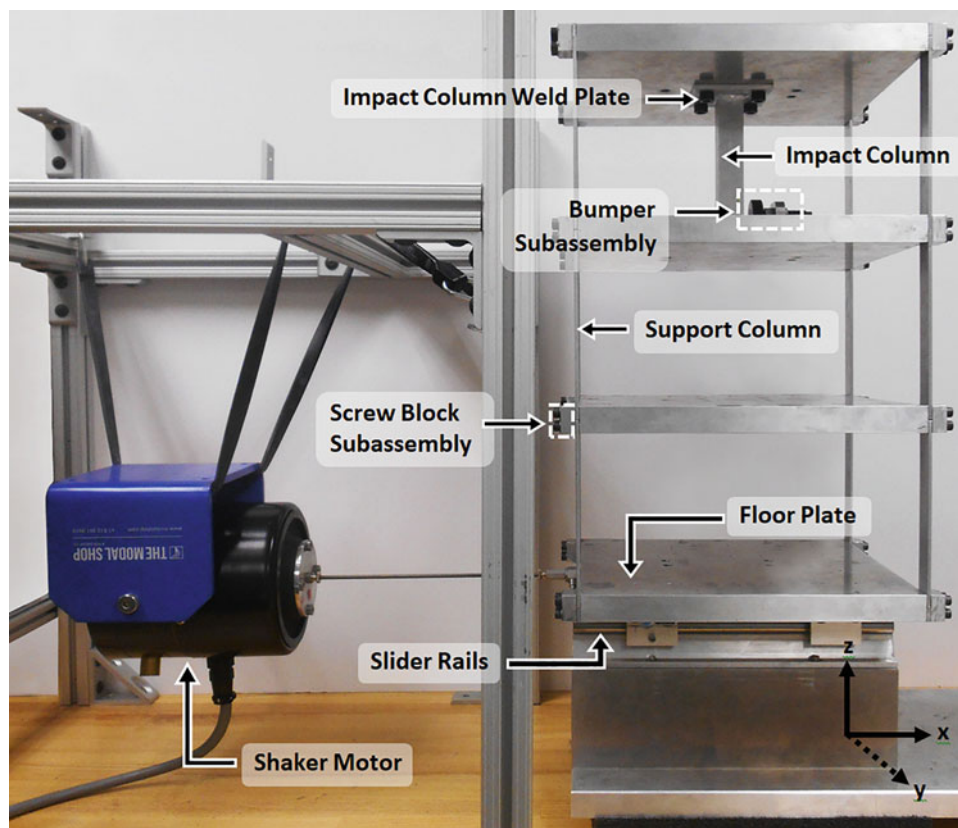


Fig. 22.1 Shaker and shaker tower test-bed setup

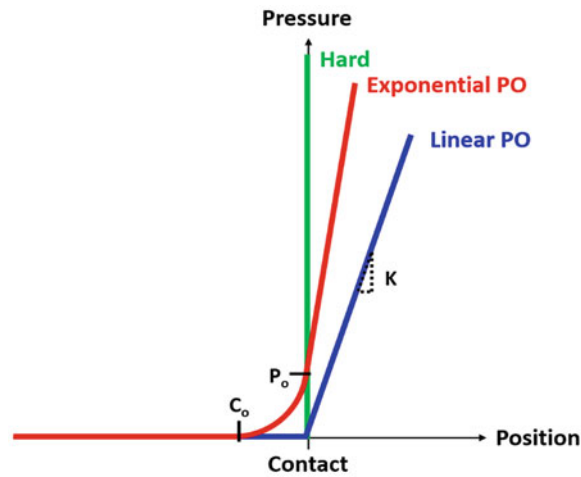


Fig. 22.2 Hard, exponential pressure-overclosure, and linear pressure-overclosure contact interaction pressure application methods

structural damage. A “feature” is defined as any scalar or vector quantity that can be extracted from a set or sets of data for use in system classification and model validation. While the reports discussed features that are useful in the detection of structural damage and nonlinearities, they also found that some features are better for *characterization* of the nonlinear response of a structure.

In these reports, “damage” is defined within the 4-story structure as contact between the tower’s impact column and its corresponding bumper (Fig. 22.1). This sort of interaction is commonly denoted as “interfacial contact,” and it causes the system to respond to excitations in a nonlinear manner. An example of a structure that exhibits this behavior in the real world is a bridge with a crack through it. As the loading on the bridge changes, the crack opens and closes, resulting in further damage and introducing nonlinearities into the dynamic response of the bridge. Because this type of structural damage causes a system to display a nonlinear dynamic response, the features that the aforementioned studies found particularly useful in damage detection can also be used in our study to aid in characterization of our FE model’s dynamic response due to the application of different contact interactions. Contact interactions are a constraint that must be applied within an Abaqus FE model when it is expected that two surfaces will make contact during a simulation. While Abaqus offers numerous types of contact interaction constraints, in this study we are exploring the effects of three of the more common contact interaction definitions: hard contact pressure-overclosure, linear pressure-overclosure (linear PO), and exponential pressure-overclosure (exponential PO).

The difference between these three contact interaction definitions is the manner in which contact pressure is applied between contacting surfaces (Fig. 22.2). The first type of contact interaction is hard contact, in which an instantaneous step of pressure is applied when two surfaces come into contact. The second type is linear pressure-overclosure, in which pressure is applied when two surfaces make contact. The applied contact pressure increases linearly with overclosure distance at a rate that can be specified within Abaqus by modifying a stiffness parameter, K . The third and final type of contact interaction that we are analyzing in this study is exponential pressure-overclosure. This constraint starts taking effect shortly before Abaqus detects that contact will occur and applies a contact pressure that exponentially increases with overclosure distance. Exponential pressure-overclosure contact is defined by two parameters: c_0 (clearance) and p_0 (initial pressure), where c_0 defines the distance between the two contacting surfaces at which the contact pressure is preemptively applied, and p_0 defines the amount of pressure that should be applied at the instant contact occurs.

22.1.3 Theoretical Background

Alongside validating the FE model of the FSS, one of the primary goals of this study is to analyze the effects of these different contact interaction definitions on the dynamic response of the system. To do this, we utilize features extracted both directly from the time domain acceleration response of the system, as well as features that must be obtained through analysis of the data after it has been projected into the frequency domain. The features that we found most useful to our study are described below and are classified based on their usefulness in nonlinearity detection, verification/validation metrics, and signal processing.

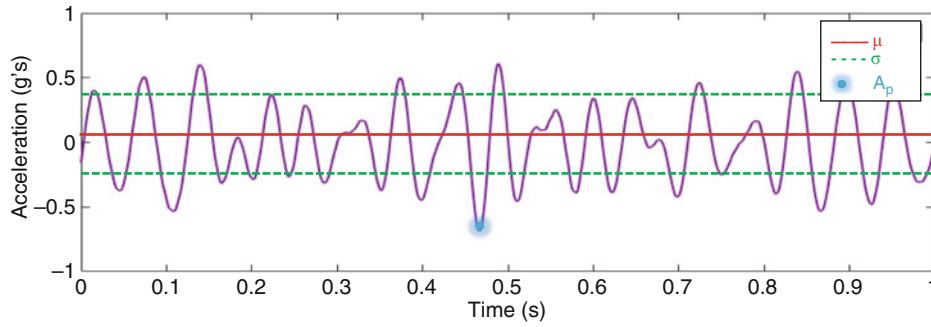


Fig. 22.3 Illustration of mean, standard deviation, and peak amplitude

22.1.3.1 Time Domain Data Analysis

To analyze the time domain data found throughout the course of this study, a number of statistical features were calculated using the raw time domain acceleration data from both the physical FSS and the FE model. If a normally distributed random signal is applied to a linear system, the system's response will also be normally distributed. Thus, statistical values are very useful in detecting nonlinear behavior in a dynamic system response.

- **Mean amplitude (μ)** is defined as the average of a series of time domain data points and can be calculated using the equation shown in Eq. 22.1. In this equation, N is the total number of data points in a data set, i denotes the i th data point as a function of time, and x_i is the value of the i th data point [7] (Fig. 22.3). This metric is useful for model validation and comparison.

$$\mu = \frac{1}{N} \sum_{i=1}^N x_i \quad (22.1)$$

- **Standard deviation (σ)** is used to describe the spread of a set of data in relation to the data set's mean and can be calculated using the equation shown in Eq. 22.2. This metric is useful for model validation and comparison.

$$\sigma = \sqrt{\frac{1}{N} \sum_{i=1}^N (x_i - \mu)^2} \quad (22.2)$$

- **Peak amplitude (A_p)** is determined by finding the absolute maximum value in a set of data (Fig. 22.3). This metric is useful for model validation and comparison. It can also be used in nonlinearity detection if the local peak amplitudes are found across a set of acceleration data because spikes in acceleration can be used to detect interfacial contact occurrences in time [6] (Fig. 22.3).
- **Mean peak amplitude (μ_{Ap})** can be calculated by locating the local peaks in acceleration across a set of acceleration data (Fig. 22.4). When calculating the average peak acceleration, the first quarter of the data is neglected because this time period is the ramp-up period of the simulation (which starts from rest). The magnitude of the acceleration peaks are then averaged. When impact events occur during the excitation of the nonlinear model, acceleration spikes are detected. To understand dynamic response of the nonlinear system under different contact interaction definitions, we determined that it would be useful to gauge the overall trend in acceleration spikes.
- **Skewness (s)**, also known as the third statistical moment, is a measure of how asymmetrical a data set is. For example, if a data set has more high values and only a few low values, the probability distribution would be skewed to the right and the skewness is said to be negative. A skewness of 0 is characteristic of a normal distribution and indicative of a linear system. This statistic is useful for detecting system nonlinearities because the increased acceleration spikes skew the data. The further the skewness is from 0, the more nonlinear the system. Skewness is calculated using Eq. 22.3.

$$s = \frac{\sum_{i=1}^N (x_i - \mu)^3}{(N - 1) \sigma^3} \quad (22.3)$$

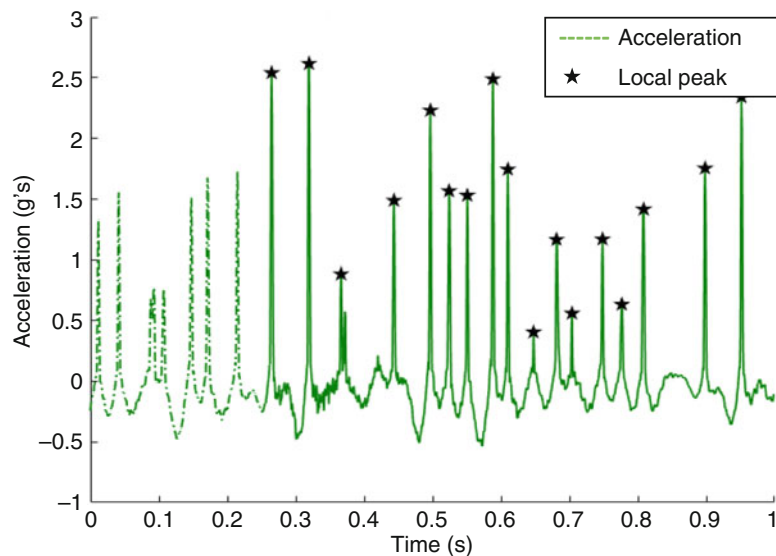


Fig. 22.4 Illustration of method of calculating mean peak amplitude

- **Kurtosis (k)**, also known as the fourth statistical moment, is a measure of the amount of variation in a data set. For example, if the majority of a data set (but for a few data points) is concentrated around one value, then the variation in the data set is caused by extreme deviations from the mean. This causes a tall, “pointed” probability distribution and the kurtosis is considered high. This feature is also a good nonlinearity detector because nonlinear systems will have a high value of kurtosis. A kurtosis value of 3 is characteristic of a normal distribution and indicative of a linear system. The further the kurtosis is from 3, the more nonlinear the system. Kurtosis is calculated using Eq. 22.4.

$$k = \frac{\sum_{i=1}^N (x_i - \mu)^4}{(N - 1) \sigma^4} \quad (22.4)$$

22.1.3.2 Frequency Domain Data Analysis

We also used frequency domain data analysis techniques to validate the model and observe the effects of the different types of contact interactions. Frequency domain analysis is particularly useful for detecting inherent characteristics of the dynamic response of a system.

- **Natural frequency (ω_n)** is defined as the frequency at which a perturbed object or system will oscillate when not driven by some external force. Natural frequencies are a defining characteristic of the linear dynamic response of a structure and are therefore useful in model validation and comparison. We will determine the natural frequencies of our experimental structure and FE model using their respective plots of the frequency response function, as described below.
- **Mode Shapes ($\{\varphi\}$)** are patterns of oscillation that occur at each natural frequency of a system. Just like natural frequency, mode shapes are another defining characteristic of the linear dynamic response of a system. Mode shapes can be expressed as the eigenvectors of a system. As such, they can be analyzed as vectors as well. To determine the degree of similarity between experimental results and simulation results, the mode shapes were compared using Modal Assurance Criteria (MAC), in which the dot product is taken between the two mode shape vectors of interest, $\{\varphi_1\}$ and $\{\varphi_2\}$, as in Eq. 22.5. The superscript T denotes a transpose. If the vectors are identical, the MAC is 1 (100%). If they are perpendicular, the MAC is 0 (0%).

$$\text{MAC} = \frac{|\{\varphi_1\}^T \{\varphi_2\}|^2}{(\{\varphi_1\}^T \{\varphi_1\}) (\{\varphi_2\}^T \{\varphi_2\})} \quad (22.5)$$

- **Power spectral density (PSD)** measures the power of a signal as a function of frequency. A PSD plot can be used to determine a system's natural frequencies; when the system is excited at its natural frequencies, resonance occurs and the power of the signal increases, producing peaks. To calculate the PSDs for our experiments and simulations, we utilized MATLAB's `pwelch` function with a Hann window and 50% overlap to our time-domain acceleration data vectors. Because the PSD plot of a system is indicative of many of its frequency domain characteristics, the PSD is useful in the process of model validation.
- **Frequency response function (FRF)** measures the relationship between a system's input excitation and output response as a function of frequency. For vibration data of a linear system, analysis of its peaks is a good way to determine the natural frequencies and mode shapes. For a nonlinear system, integer multiples of the natural frequencies (super- and sub-harmonics) will also be visible. The FRF is useful in model validation and comparison. To calculate the FRF, we applied a Hann window with 50% overlap to our time-domain input and output data vectors and performed a Fast Fourier Transform on both. This produces frequency-domain input $x(f)$ and output $y(f)$ data that is complex-valued. The auto powers (g_{xx} , g_{yy}) and cross powers (g_{xy} , g_{yx}) of the data can be calculated using Eqs. 6a-d, where $x^*(f)$ and $y^*(f)$ denote the complex conjugates of $x(f)$ and $y(f)$. The frequency response function can then be calculated using Eq. 22.7.

$$g_{xx}(f) = x(f) * x^*(f) \quad g_{yy}(f) = y(f) * y^*(f) \quad (22.6a, b)$$

$$g_{xy}(f) = x(f) * y^*(f) \quad g_{yx}(f) = y(f) * x^*(f) \quad (22.6c, d)$$

$$FRF = \frac{g_{yx}(f)}{g_{xx}(f)} \quad (22.7)$$

- **Coherence (γ^2)** indicates how much of a system's output response is due to the input as a function of frequency [8]. For example, good coherence means the output is perfectly linearly related to the input, the FRF is of good quality, and the results are repeatable. Bad coherence indicates that there is noise, or the output is nonlinearly related to input. Coherence can be expected to take a sharp dip at both natural frequencies/resonances and anti-resonances. Coherence is useful for verifying the quality of our experimental results and can be used to detect nonlinearities. Coherence can be calculated using Eq. 22.8.

$$\gamma^2 = \frac{g_{xy}(f) g_{yx}(f)}{g_{xx}(f) g_{yy}(f)} \quad (22.8)$$

22.2 Physical Structure

22.2.1 Test-Bed Structure Description

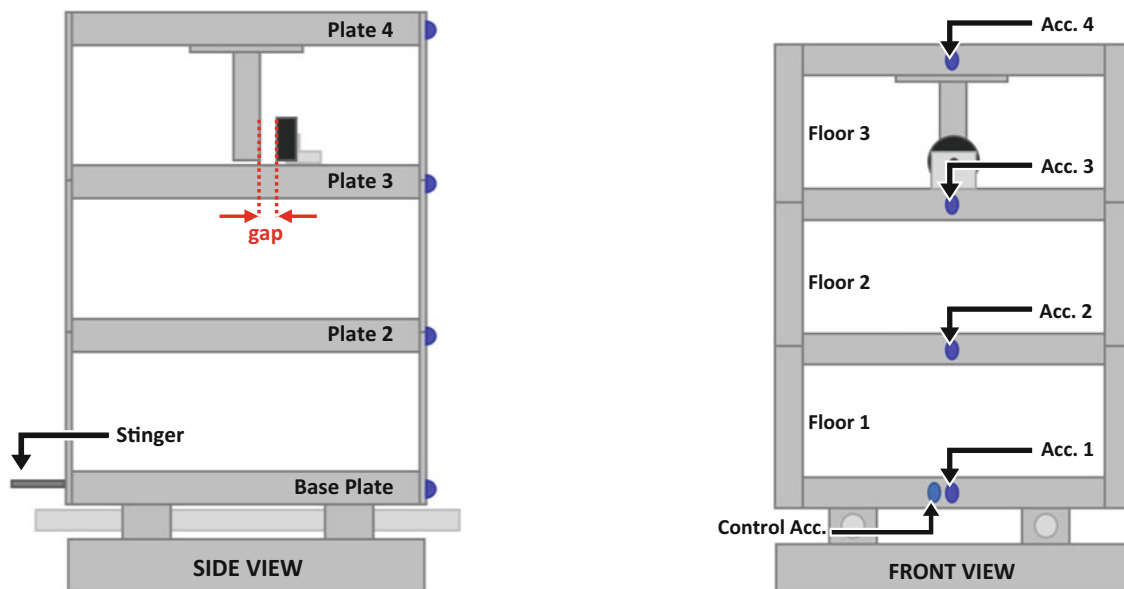
To begin exploring the effects of contact interactions on a nonlinear FE model, it is necessary to have some metric with which to compare simulation results. In this study, we are utilizing a FSS that has been tested extensively in the past (Fig. 22.1) [4–6]. The test structure setup consists of an electrodynamic shaker motor, the FSS, and a pair of slider rails along which the shaker tower moves on a set of bearings to reduce friction. The shaker motor is suspended from an aluminum frame in order to reduce feedback between the shaker and the tower. In previous studies, the shaker had been mounted to the same plate on which the tower and rails are mounted, and it was suspected that this setup resulted in interactions between the shaker and tower. Through a set of preliminary tests, we found the coherence of the system to be higher with the shaker suspended from the aluminum frame than when it is mounted on the same aluminum plate as the tower. As such, we moved forward with the shaker in the suspended configuration. The shaker is connected to the tower by a stinger, which transmits excitations from the shaker to the tower. The tower itself is composed of thin support columns, thick-walled hollow impact columns, floor plates, and bumpers (Fig. 22.1). The dimensions and masses of these components are recorded in Table 22.1. It should be noted that the impact columns are thick-walled shells with a square cross-section, and they are welded to a square rectangular plate. To determine the mass of the impact column, the column, plate to which it is welded, and four mounting bolts were weighed together. The bumper is supported by an L-shaped piece of aluminum, which is bolted to its respective

Table 22.1 Shaker tower component dimensions and masses

Component	x-dim (mm)	y-dim (mm)	z-dim (mm)	Wall thickness (mm)	Mass (g)
Floor plate	304.8	304.8	25.40	–	6401
Support column	3.175	25.40	177.8	–	37.0
Impact columns	25.40	25.40	139.7	3.175	258.1
Impact column weld plate	76.20	76.20	5.207	–	–
Bumper head	11.11	$\phi = 31.75$	$\phi = 31.75$	–	87.6
Bumper subassembly	–	–	–	–	194.4
Screw block subassembly	12.70	25.40	25.40	–	51.1

Table 22.2 Shaker tower material properties

Material	Young's Modulus (Gpa)	Density (tonne/m ³)	Poisson's Ratio
Al 6061	65	2.65	0.331
AISI 1045	200	7.80	0.29

**Fig. 22.5** Labeled schematic of shaker tower (side view). Labeled schematic of shaker tower (front view)

floor plate. The mass of the bumper, bumper support base, and the restraining bolts and nuts were taken together. The floor plates, support columns, impact columns, and bumper support base are assumed to be composed of Al 6061. The bumper material is not known with certainty, but it is assumed to be a medium-grade steel with properties similar to AISI 1045. The assumed properties of the aluminum and the steel can be found in Table 22.2.

We assembled the FSS such that there was an impact column and bumper subassembly on only the third floor (Fig. 22.1). The structure can be set up in either a linear or nonlinear configuration. In the linear configuration, the gap between the bumper and impact column is set to 10 mm (Fig. 22.5). This distance ensures that there will be no contact between the bumper and impact column during testing. To create the nonlinear configuration, the gap distance between the bumper and impact column is adjusted such that there is only a 0.1 mm gap between the bumper face and impact column. In our experiment, a feeler gauge was used to measure this distance (Fig. 22.5).

When in the nonlinear configuration, the FSS can be considered a bilinear system, wherein the tower has one stiffness before the bumper and impact column make contact, and a higher stiffness when the bumper and impact column are in contact. This phenomenon is illustrated in Fig. 22.6, where the stiffness k_1 corresponds to the tower before an impact event occurs, and the stiffness k_2 corresponds to the stiffness of the tower *during* an impact event. However, because it is not possible for a physical system to instantaneously change from one stiffness to another, there must be some smooth transition region between the initial stiffness and the final stiffness that occurs after the point of contact.

Fig. 22.6 Representation of tower's stiffness before and during an impact event

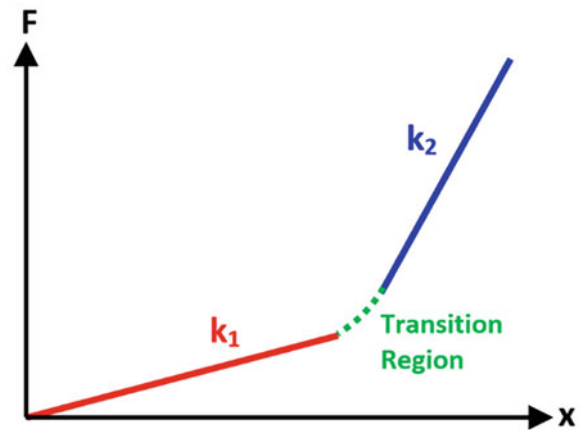


Table 22.3 Test-bed setup components and properties

Component	Description	Sensitivity	Model	DAQ Device	DAQ Channel #
Acc. 1	Uniaxial PCB Piezotronics Acc.	1027 mV/g	355B04	5	0
Acc. 2	Uniaxial PCB Piezotronics Acc.	1029 mV/g	355B04	5	1
Acc. 3	Uniaxial PCB Piezotronics Acc.	1014 mV/g	355B04	5	2
Acc. 4	Uniaxial PCB Piezotronics Acc.	1019 mV/g	355B04	5	3
Control Acc.	Uniaxial PCB Piezotronics Acc.	102.3 mV/g	352A24	8	1
DAQ Chassis	National Instruments PXI Chassis	–	1042Q	–	–
DAQ Devices	NI Sound and Vibration Module	–	4461/4462	–	–
Shaker control	LDS Laser USB Vibration Controller	–	LAS200	–	–
Shaker motor	75lbf Dual-Purpose Electro-dyn. Shaker	–	2075E-HT	–	–
Power amp.	Labworks PA-138 Linear Power Amp.	–	PA-138	–	–

22.2.2 Data Acquisition

For both the linear and nonlinear setups, the FSS was excited with a broadband random signal from 10–200 Hz with a a_{rms} (root mean square acceleration) value of 0.9 g's for a total of 30 seconds per test. A shaker controller software was used to specify the power spectral density (PSD) of the random excitation input and to interface directly with the shaker controller. An accelerometer on the first floor provided feedback to the closed loop control system to maintain the desired input PSD. The shaker motor itself was driven by a linear power amplifier. To collect data from the test-bed for comparison to the FE model, four PCB Piezotronics uniaxial accelerometers (Table 22.3) were mounted on the tower. One accelerometer was placed on the centerline of each floor on the side of the tower opposite the shaker input (Fig. 22.5). The readings from the four uniaxial accelerometers were recorded with a sampling frequency of 1280 Hz with a four-input channel DAQ, and the control accelerometer data was recorded at the same sampling frequency with a two-input two-output channel DAQ. Further details of the excitation and data acquisition equipment are provided in Table 22.3. In the data analysis performed in this report, we drew comparisons based on the data collected by Accelerometer 4, located on the top plate of the tower, because the nonlinearities of the structure are most obvious between plates 3 and 4.

22.3 Finite Element Model

22.3.1 Model Parameters

In this report, the Abaqus finite element (FE) modeling software was used to perform the FE modeling and simulation. The dimensions used in the FE model are defined in Table 22.1. The material properties of the aluminum components were found within the LA-14489 report [6], and the material properties that could not be located within the report were defined using the MatWeb online material database [9]. The material properties of the structure are not known with certainty. However, some

Table 22.4 Assumptions, simplifications, and justifications of finite element model

#	Assumption	Simplification	Justification
01	Torsional motion is negligible, and the structure moves in one dimension.	Abaqus model is two-dimensional, plane strain elements used.	The physical structure was designed to move only in one direction, and preliminary tests indicated insignificant torsional motion.
02	Bolts, screw blocks, and accelerometer masses are negligible.	Only plates, bumpers, bumper components, impact columns, and support columns were modeled.	Preliminary simulations showed minimal variation with these parts included.
03	Nonlinearities in joints are negligible.	Joint nodes were modeled using tie constraints (essentially welded).	Previous studies showed the structure's dynamic response is linear in the linear configuration [6].
04	Friction is accounted for by excitation application.	Friction between the bearings and rails was not modeled.	Applying the experimental acceleration of the base plate as the excitation to the FE model accounts for friction at the rails.
05	Shock effects are negligible; plates move as rigid bodies.	Acceleration data was extracted from a single node on each plate in the Abaqus model.	Stiffness of the floors is much greater than the stiffness of the columns which almost completely restrain the joint rotations such that the structure behaves as a shear-frame [10].
06	Base plate has constant acceleration across its length.	Acceleration data from physical model is applied uniformly across bottom of the base plate.	Plates behave as rigid bodies.
07	Negligible tangential sliding between contact surfaces.	Contact is applied normal to the local surface profile.	It is expected that relative vertical displacements are small between contacting surfaces.
08	Negligible feedback between shaker and tower.	Excitation of the tower is due to only the force application of the shaker.	Coherence between the force input and tower acceleration were found to be reasonable.
09	Isotropic material behavior.	Simple material models were used for aluminum and steel components.	The materials are nominally homogeneous and isotropic at the scale of the simulation.
10	Negligible variation in properties across material families.	Aluminum was modeled as a variation of Al 6061 and steel was modeled as medium-grade carbon steel AISI 1045.	Component material data is not readily available, but preliminary simulations were insensitive to variations in the relevant material properties within the expected range of materials.
11	Environmental conditions are negligible.	No thermal aspects incorporated into Abaqus model.	Experiments are performed in a climate-controlled laboratory.

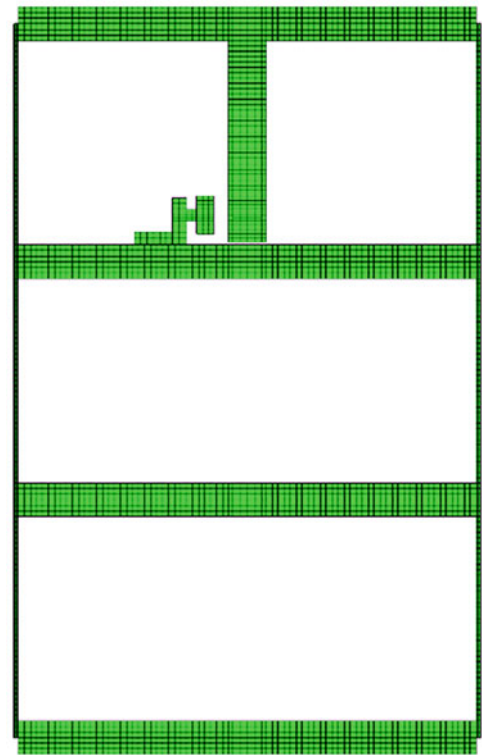
preliminary simulations showed that if the aluminum material properties are varied within the reasonable range of properties reported for Al 6061, the effects on the dynamic response of the system are minimal.

22.3.1.1 Simplifications and Assumptions

To maintain simplicity in the FE model, several simplifications and assumptions were made regarding the structure's geometry, environment, assembly, and methods of excitation. These simplifications, assumptions, and their respective justifications are summarized in Table 22.4. The table pertains primarily to assumptions that were made based on: (1) features of the physical model that we deemed inconsequential to the dynamics of the system, (2) aspects of the physics of the structure that were not known with certainty, and (3) limitations of the available options in Abaqus.

22.3.2 Simulation Descriptions

The Abaqus FE modeling software offers two methods of analysis: Abaqus/Standard and Abaqus/Explicit. For purposes of verification and validation, we defined and analyzed the results of two different Abaqus/Standard studies and one

Fig. 22.7 Meshed FE model

Abaqus/Explicit study. Abaqus/Standard is used primarily for solving static or quasi-static problems using an implicit time integration technique. Abaqus/Explicit, on the other hand, is more suited to dynamic simulations using explicit time integration. Because of the different time integration techniques, Abaqus/Explicit requires a much smaller time step than Abaqus/Standard, so only short simulation periods should be defined to reduce computation time [11]. Figure 22.7 illustrates the complete meshed FE model as modelled in Abaqus. It is worth noting that it is difficult to characterize the damping characteristics of system, which are usually attributed to the material selected. In Abaqus/Explicit analyses, it is recommended that a small amount of bulk viscosity associated with volumetric straining is introduced to the model [11]. For the following simulations Abaqus/Explicit, the default bulk viscosity parameters were used, but no other damping properties were assigned.

22.3.2.1 Modal Frequency Analysis

Modal frequency analysis was performed using Abaqus/Standard. For this analysis, the structure was only permitted to translate in the x-direction to be representative of the physical experiments. To avoid rigid body and high frequency modes, modal frequencies and mode shapes were extracted from 1 to 2000 Hz. However, our data analysis will only consider the first three modes of the structure. This was done for two reasons. First, because of the decidedly unidirectional motion of the physical test-bed structure and the placement of the uniaxial accelerometers, we can only measure modes in the x-direction (the direction of motion). Second, according to the modal participation factor data from the Abaqus modal frequency analysis (Table 22.5), the first three modes in the x-direction are the most influential in the overall motion of the structure.

22.3.2.2 Standard Displacement Analysis

A displacement analysis study was also performed using Abaqus/Standard. In this study, a displacement of 5 mm was applied to the top plate of the structure, and the bottom plate of the structure was held fixed. The purpose of this study was to determine the stiffness properties of the structure and compare them to theoretical calculations of the stiffness of an equivalent lumped spring-mass structure using Euler-Bernoulli beam theory. The process is described in Sect. 22.4 of this report. The stiffness of the structure was determined by recording the reaction force at the point of displacement application

Table 22.5 Participation factors of first 10 x-direction modes

Mode	Participation Factor	% Participation
1	3.68×10^{-9}	73.814%
2	1.20×10^{-9}	24.099%
3	8.31×10^{-11}	1.667%
4	5.71×10^{-12}	0.115%
5	2.23×10^{-12}	0.045%
6	6.23×10^{-12}	0.125%
7	1.15×10^{-12}	0.023%
8	5.97×10^{-13}	0.012%
9	5.03×10^{-13}	0.010%
10	9.04×10^{-14}	0.002%

Table 22.6 Linear PO contact parameters

K (N/mm)	Case
2000	Case 37
700	Case 38
500	Case 39
400	Case 40
300	Case 41
100	Case 42
0.1	Case 43

and calculating the ratio of the maximum reaction force to the final displacement value. This study was performed for the structure in two configurations. The first was the less stiff linear configuration, wherein the bumper was backed off from the impact column as in Fig. 22.7. The second was the stiffer linear configuration, in which the bumper was in full contact (i.e., gap = 0 mm) with the impact column throughout the entire duration of the displacement analysis. With the bumper and impact column in contact, the duo acts as an additional support column with an increased thickness.

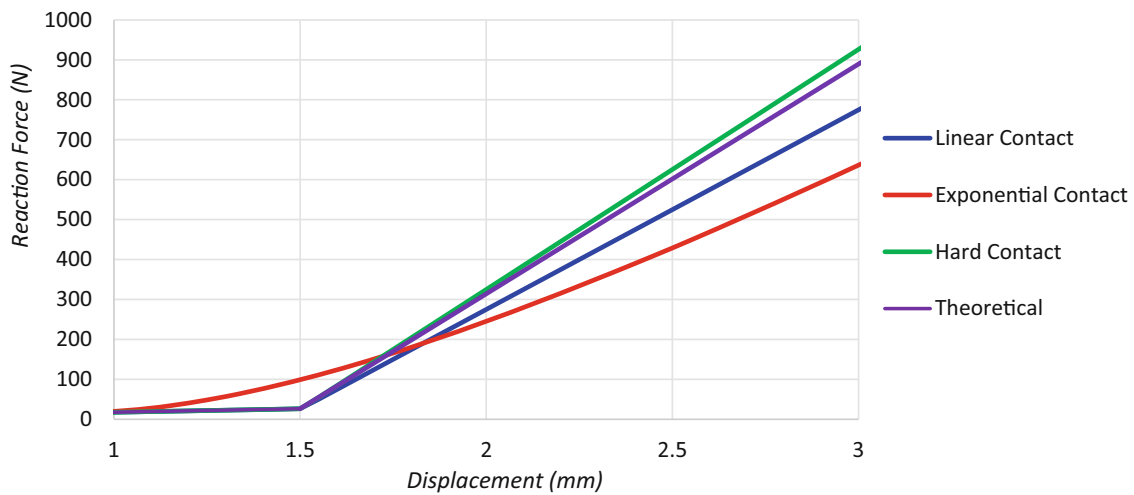
22.3.2.3 Dynamic Explicit Analysis

The final analysis that was performed for this study was a dynamic analysis of the structure using Abaqus/Explicit. This simulation was intended to excite the FE model in the same way that the physical structure was excited during the random excitation testing. To achieve this, we used the time history of acceleration values of Accelerometer 1 (located on the base plate of the physical structure) as the excitation input to the FE model. The acceleration was applied as a time-dependent amplitude at every node on the bottom surface of the base plate in the FE model, and the base plate was not permitted to translate in the vertical direction or rotate about the z-axis. Because applying long time histories in Abaqus/Explicit models is computationally expensive, we were limited to applying one second of acceleration data from the physical model to the FE model. For consistency, we always used the physical model acceleration data from Accelerometer 1 data between $t = 15$ s and $t = 16$ s as the input to the FE model. Because the acceleration response is due to a random excitation, the exact interval of data used to excite the FE model should be inconsequential as long as the time history is sufficiently complete. We verified the 1 second time history's completeness by comparing its FRF and coherence to that of a full 30-second data and found them to agree well. To compare the Abaqus model data to that of the physical structure, we extracted the acceleration from the nodes corresponding to the locations of the accelerometers during the physical experiments.

One of the primary goals of this study is to analyze the effects of different contact interaction definitions on the dynamic response of a system. The dynamic explicit analysis is the most useful of the three aforementioned Abaqus analysis types for observing the effects of different contact interactions. This analysis method was performed on the Abaqus FE model in both the linear and nonlinear configurations. In the linear configuration, contact does not occur between the bumper and impact column, so the contact definitions are irrelevant. However, contact is assured in the nonlinear configuration, so the effects of the different contact definitions can be analyzed in the results of the nonlinear FE model. In this study, we are exploring the effects of three common contact interaction definitions: hard contact, linear PO, and exponential PO. Unlike linear PO and exponential PO, hard contact has no parameters to vary. As such, we called the one trial of hard contact Case 1. In the linear PO contact interaction, the stiffness parameter, K, can be varied. We performed several Abaqus simulation studies with various values of K (Table 22.6). Similarly, exponential PO contact is defined by two parameters: c_0 (clearance) and p_0 (initial pressure). Table 22.7 shows the combinations of p_0 and c_0 that we tested within our study.

Table 22.7 Exponential PO contact parameter combinations

	$p_0 = 3$ MPa	$p_0 = 4$ MPa	$p_0 = 5$ MPa	$p_0 = 6$ MPa	$p_0 = 7$ MPa
$c_0 = 0.01$ mm	Case 2	Case 9	Case 16	Case 23	Case 30
$c_0 = 0.05$ mm	Case 3	Case 10	Case 17	Case 24	Case 31
$c_0 = 0.1$ mm	Case 4	Case 11	Case 18	Case 25	Case 32
$c_0 = 0.2$ mm	Case 5	Case 12	Case 19	Case 26	Case 33
$c_0 = 0.3$ mm	Case 6	Case 13	Case 20	Case 27	Case 34
$c_0 = 0.4$ mm	Case 7	Case 14	Case 21	Case 28	Case 35
$c_0 = 0.5$ mm	Case 8	Case 15	Case 22	Case 29	Case 36

**Fig. 22.8** Force vs displacement of FSS for theoretical, hard, exponential ($c_0 = 0.2$ mm, $p_0 = 5$ MPa), and linear contact ($K = 500$ N/mm)

Initial values for K , c_0 , and p_0 were determined using a quasi-static displacement study and adjusted by comparing the resulting force-displacement plots to the calculated theoretical force-displacement relationship. The parameter (in the case of linear contact) or parameter combination (in the case of exponential contact) that yielded a force-displacement plot in the range of the theoretical force-displacement plot served as the starting parameter or parameter pair in the dynamic explicit analysis. Figure 22.8 shows the force versus displacement plots of the theoretical tower, tower with hard contact, tower with linear pressure-overclosure contact with $K = 500$ N/mm, and the tower with exponential pressure-overclosure contact with $p_0 = 5$ MPa and $c_0 = 0.2$ mm. In the figure, contact can be seen to initiate after approximately 1.5 mm of displacement of the top of the tower. It should be noted that the starting parameter values do not necessarily yield the best match to the tower's stiffness properties. Rather, they provide a starting point to begin looking for the best match to the tower's stiffness properties.

22.3.3 Mesh Convergence Study

The FE model mesh size is based on the number of seeds per the shortest feature edge and the desired area per element. The element size was chosen to ensure that enough seeds are created to describe all model features and to create overlapping nodes at each tie constraint. A mesh convergence study was performed for the linear Abaqus/Standard modal analysis, linear Abaqus/Standard displacement analysis, and nonlinear Abaqus/Explicit dynamic analysis. For both the modal and dynamic analyses, the convergence of the first three natural frequencies was considered. For the displacement analysis, the convergence of the stiffness of the tower was considered. The results of the modal analysis mesh convergence indicated that the mesh converges at approximately 10,000 elements (seed size of ~ 2 mm). The results of the displacement analysis mesh convergence indicated that the mesh converges at approximately 1000 elements (seed size of ~ 10 mm). Finally, the results of the dynamic analysis mesh convergence indicated that the mesh converges at approximately 3000 elements (seed size of ~ 4 mm). Because our primary concern in this study is with the dynamic analysis and because we could not feasibly run an

Abaqus/Explicit model with 10,000 elements within the time constraints of the project, we elected to move forward in our analyses using a mesh with approximately 3000 elements, which corresponds to a seed size of 4 mm in our model.

22.4 Model Verification

To verify that the Abaqus model was implemented correctly, we performed two preliminary analyses. First, we verified that the total equivalent stiffness of the model was in the domain of what it should be analytically using Euler-Bernoulli beam theory. We then performed analysis to ensure that the system displays a linear response in the linear configuration, and a nonlinear response in the nonlinear configuration. These verification studies are described below.

22.4.1 Stiffness Verification

Our first verification study consisted of two static displacement simulations (for the hanging column and bumper both out of contact and in full contact, as described below) in which the bottom floor plate of the Abaqus model was fixed and a known displacement δ was applied to the top floor. We could then solve for the displacement of the middle floors and resultant force at the top floor, and thereby determine the overall stiffness of the tower. The tower was treated as an equivalent Euler-Bernoulli beam model, and its global stiffness matrix was determined analytically. Figure 22.9 illustrates the analytical model of the shaker tower structure. The governing equation of motion of the tower is shown in Eq. 22.9. M_T , C_T , and K_T are the global mass, damping, and stiffness matrices of the tower (T), respectively. X , F , and R are global vectors whose respective components are the displacement, applied force, and reaction force on each floor. The stiffness of the tower depends solely on the support columns and impact columns. The tower was deformed via a quasi-static displacement, so both the acceleration and velocity of the structure are zero.

$$M_T \ddot{X} + C_T \dot{X} + K_T X = F + R \quad (22.9)$$

Fig. 22.9 Analytical model of the 4 DOF tower

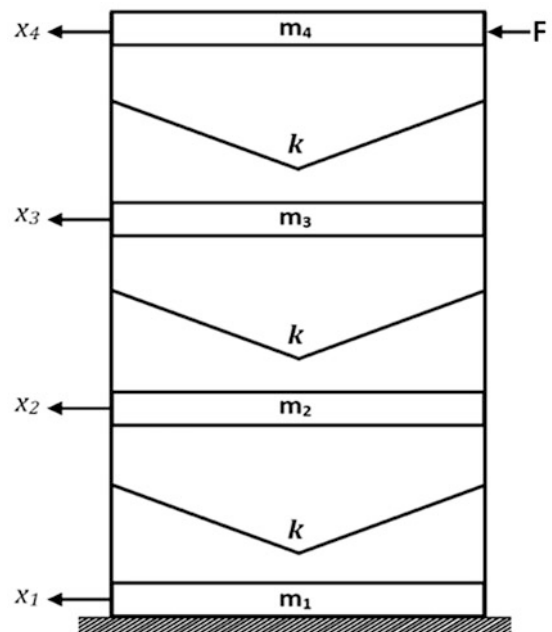


Table 22.8 Model Verification—No-Contact Static Displacement Simulation

Measurement	x_2 (mm)	x_3 (mm)	f_4 (N)	k_{total} (N/mm)
Analytical	1.667	3.333	88.05	17.61
Abaqus	1.665	3.332	87.20	17.44
% Difference	0.100%	0.040%	0.973%	0.973%

22.4.1.1 No-Contact Setup

For the contact-free setup, analytically treating the support columns as fixed-fixed Euler-Bernoulli beams results in a support-column stiffness of $k_s = 12 (E_s I_s / L_s^3)$. E_s is the elastic modulus of the support columns, L_s is the length of the support columns, and I_s is the moment of inertia of the support columns given by $I = bh^3/12$ for width b and thickness h . The stiffness between any two floors is the value of k_s multiplied by 4. The dimensions and properties of the tower used in these calculations are listed in Tables 22.1 and 22.2 of Sect. 22.2, with one exception: the length of the support columns is taken as the distance between the column mounting holes, 6.25 in (158.75 mm). Using these properties, we found a between-floor stiffness of $k = 52.832$ N/mm. Treating the entire structure as a lumped-mass model gives the following system of matrices:

$$K_T = k \begin{bmatrix} 1 & -1 & 0 & 0 \\ -1 & 2 & -1 & 0 \\ 0 & -1 & 2 & -1 \\ 0 & 0 & -1 & 1 \end{bmatrix} \quad X = \begin{bmatrix} x_1 = 0 \\ x_2 = \frac{\delta}{3} \\ x_3 = \frac{2\delta}{3} \\ x_4 = \delta \end{bmatrix} \quad F = \begin{bmatrix} f_1 = 0 \\ f_2 = 0 \\ f_3 = 0 \\ f_4 = \frac{k\delta}{3} \end{bmatrix} \quad R = \begin{bmatrix} r_1 = \frac{-k\delta}{3} \\ r_2 = 0 \\ r_3 = 0 \\ r_4 = 0 \end{bmatrix} \quad (22.10)$$

In these matrices, x , f , and r are the respective displacement, applied force, and reaction force on each floor. Subscripts 1–4 refer to floor number. We then performed an Abaqus/Standard displacement analysis with seed size of 1 mm (a finer mesh size than was deemed required by our mesh convergence study). A displacement of $\delta = 5.0$ mm was applied to the top floor, and we output the maximum force at the location of the displacement application. Table 22.8 compares the displacements of floors 2 and 3, the applied force f_4 , and the equivalent total stiffness of the tower k_{total} due to the combined stiffness of the three floors (calculated as the applied force divided by displacement δ) between the Abaqus model and the analytic frame model under the same displacement. From this table, it can be seen that the differences in displacements, applied force, and stiffness between the analytic model and the Abaqus model were all less than 1%, demonstrating good agreement between the model and theoretical calculations for the no-contact static displacement scenario.

22.4.1.2 Full-Contact Setup

When the hanging column and bumper are in contact, the stiffness of the structure increases. As a result, a plot of force vs. displacement where the tower transitions from zero to full contact will not display a single slope (i.e., stiffness), but will be bilinear for the case without and with contact. When in full contact, the stiffness between floors 3 and 4 becomes $k + k_b$, where k_b is the stiffness of the impact column-bumper subassembly. Modeling the impact column-bumper subassembly as a cantilever Euler-Bernoulli beam, we obtain a stiffness of $k_b = 3 (E_b I_b / L_b^3)$. E_b , L_b , and I_b are the respective elastic modulus, length, and moment of inertia of the impact column-bumper subassembly. Using the hanging-column dimensions and properties from Tables 22.1 and 22.2 to calculate the subassembly's moment of inertia, we obtained a stiffness of $k_b \approx 1696$ N/mm. Defining $\alpha = \frac{k_b}{k}$, the new stiffness, displacement, and applied- and reaction-force matrices are as follows:

$$K_T = k \begin{bmatrix} 1 & -1 & 0 & 0 \\ -1 & 2 & -1 & 0 \\ 0 & -1 & 2 + \alpha & -1 - \alpha \\ 0 & 0 & -1 - \alpha & 1 + \alpha \end{bmatrix} \quad X = \begin{bmatrix} x_1 = 0 \\ x_2 = \delta \frac{1 + \alpha}{3 + 2\alpha} \\ x_3 = 2\delta \frac{1 + \alpha}{3 + 2\alpha} \\ x_4 = \delta \end{bmatrix} \quad F = \begin{bmatrix} f_1 = 0 \\ f_2 = 0 \\ f_3 = 0 \\ f_4 = k\delta \frac{1 + \alpha}{3 + 2\alpha} \end{bmatrix} \quad R = \begin{bmatrix} r_1 = -k\delta \frac{1 + \alpha}{3 + 2\alpha} \\ r_2 = 0 \\ r_3 = 0 \\ r_4 = 0 \end{bmatrix} \quad (22.11)$$

We again performed an Abaqus/Standard displacement analysis with seed size of 1 mm and a displacement of $\delta = 5$ mm at the top floor. Table 22.9 compares the displacements (x_2 , x_3), applied force (f_4), and total tower stiffness (k_{total}) between

Table 22.9 Model verification—full-contact static displacement simulation

Measurement	x_2 (mm)	x_3 (mm)	f^t (N)	k_{total} (N/mm)
Analytical	2.463	4.926	130.1	26.02
Abaqus	2.463	4.929	129.0	25.81
% Difference	0.008%	0.069%	0.829%	0.829%

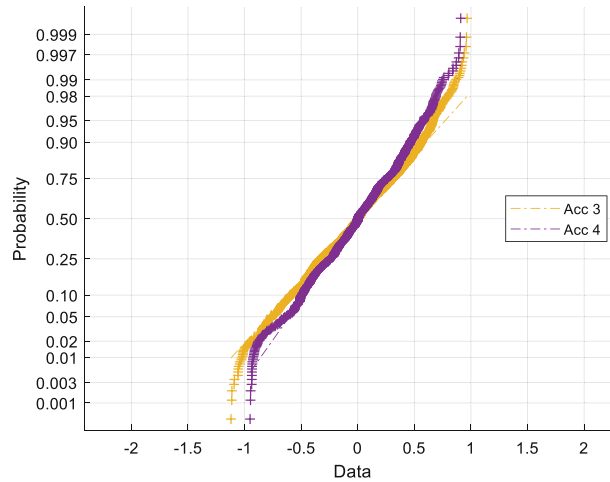


Fig. 22.10 Linear Normal Probability Plot (Abaqus)

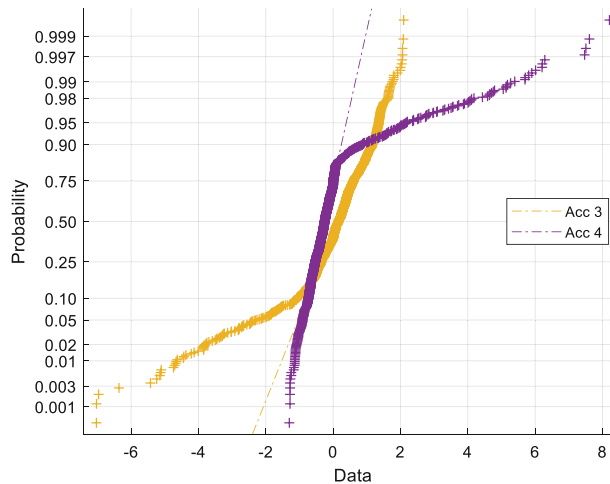


Fig. 22.11 Nonlinear Normal Probability Plot (Abaqus)

the Abaqus model and the analytic frame model. From this table, it can be seen that the differences in all parameters between the analytic model and the Abaqus model were again less than 1%, demonstrating good agreement for this second simulation.

22.4.2 Linearity

If a normally distributed random signal is applied to a linear system, the system’s response will also be normally distributed. However, this does not hold true for nonlinear systems. To ensure the Abaqus model predictions for the linear and nonlinear configurations were indeed linear and nonlinear respectively, we excited the Abaqus model with physical acceleration data obtained from a normally distributed random excitation experiment and compared the normal probability plots (NPPs) of the Abaqus model in both the linear and nonlinear configurations. Figures 22.10 and 22.11 show the NPPs for floors 3 and 4 for linear and nonlinear data. We analyzed the data from these floors because these are the floors that are directly attached to the

impact column and bumper and should therefore demonstrate any nonlinearities most clearly. From Figs. 22.10 and 22.11, it can be seen that the acceleration data from floors 3 and 4 in the linear plot has a highly linear trend, whereas the nonlinear plot has very clearly defined tails. This indicates that nonlinearities are present, such as the bilinear behavior that occurs due to contact between the impact columns and bumper. As such, we concluded that the linear and nonlinear simulations behaved as expected.

In addition to comparing normal probability plots, we also compared basic statistics. In the linear simulation, the skewness is -0.19149 (near 0) and the kurtosis is 2.714 (near 3), which is characteristic of normally distributed data. In the nonlinear simulation, the skewness is 3.4766 and kurtosis is 17.591 , which are significantly farther from 0 and 3. This provides further evidence that the linear and nonlinear simulations behaved as intended.

22.5 Model Validation

In this section of the report, we will present and interpret the results of the Abaqus experiments in the context of the physical experiments. We use two primary methods to quantify the degree of similarity between our model and experiment. When comparing scalar values, such as mean, standard deviation, peak value, skewness, kurtosis, and natural frequency of the time domain acceleration data, the standard percent error is calculated as in Eq. 22.12.

$$\%error = \frac{|a - p|}{a} \cdot 100 \quad (22.12)$$

In this equation, a is the experimental value and p is the simulation value. When comparing vectors of data, such as the power spectral density or the frequency response function, we calculate the root mean square error (RMSE), shown below in Eq. 22.13. In this equation, a_i is the i^{th} experimental value in a vector, p_i is the i^{th} simulation value in a vector, and N is the total number of values in the vector. For both percent error and RMSE, a lower value is desired.

$$RMSE = \sqrt{\frac{1}{N} \sum_i^N (a_i - p_i)^2} \quad (22.13)$$

22.5.1 Linear Model Validation

To validate the linear FE model, we compared the acceleration data from plate 4 of the physical structure (Fig. 22.12) to the acceleration data of the same plate in the FE model (Fig. 22.13). The data was compared in both the time domain and the frequency domain. We first looked at the percent error between the statistics of the acceleration data of the linear physical experiment and the linear simulation in the time domain. The results are displayed in Table 22.10.

Table 22.10 shows that the majority of the time domain statistics are within acceptable agreement. The peak amplitude and skewness metrics are the farthest off of the set of statistical metrics (however, it is worth noting that the values of skewness are still small with respect to the values of skewness that are indicative of nonlinear behavior seen in Sect. 22.4.2). We believe the high margin of error of the peak amplitudes and the skewness between the model and the experiment is because damping was not assigned in the material definition of the FE model. The FE model produced higher peak amplitudes than the experiment across the sample space of simulations. This led to a high percent error between the peak amplitudes of the acceleration data from the experiment and simulation and caused the simulation data to be skewed toward higher accelerations. While this reduces the accuracy of our FE model, it is of little consequence to the effects of different contact interactions on the dynamic response of a system. Thus, by keeping the FE model constant and varying only the contact interactions and parameters, we can effectively detect trends due to the contact interactions and their parameters. In order to achieve a better match between the linear FE model and linear FSS structure, we recommend that damping be included in the FE model in the future.

In addition to the time domain analysis, we also performed analysis of the acceleration data within the frequency domain. We calculated and compared the natural frequencies, FRFs, PSDs, and mode shapes of the experiment and model data. Percent error was used to compare the natural frequencies, RMSE was used to compare the FRFs and PSDs, and the MAC was used to compare the mode shapes. Table 22.11 contains the percent errors between the experiment and the model of the

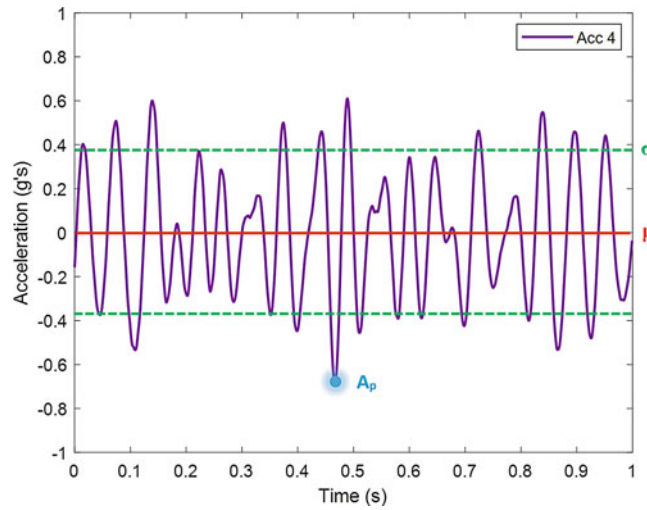


Fig. 22.12 Acceleration data from plate 4 in physical experiment

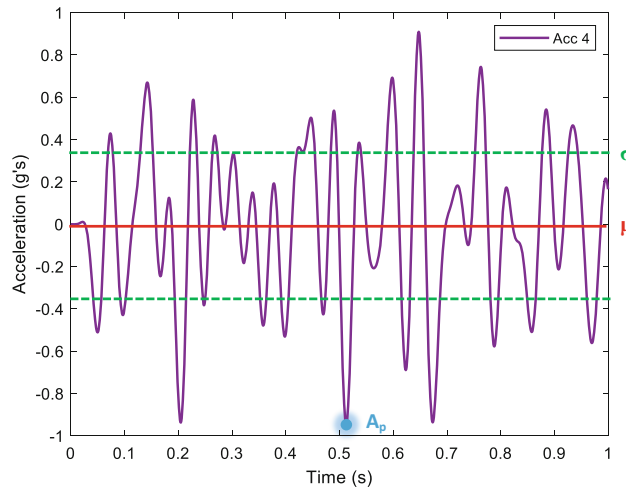


Fig. 22.13 Acceleration data from plate 4 in FE model

Table 22.10 Percent error between model comparison metrics for linear experiment results and simulation predictions

	Experiment	Model	Error (%)
Peak amp. (g's)	-0.6834	-0.9515	39.2
Mean (g's)	-0.0073	-0.0076	7.5
Std. Dev. (g's)	0.3877	0.3710	4.3
Skewness	0.0254	-0.1915	854.9
Kurtosis	2.911	2.714	5.9

first three natural frequencies, as well as the MAC of the first three modes and the RMSE of the respective comparisons of the PSD and FRF magnitude plots. Figure 22.14 shows a direct comparison between the first three normalized mode shapes of the experiment and the model. From Table 22.11, it can be seen that there is less than 10% error on average between the first three natural frequencies, the mode shapes are less than 2% away from being identical, and the RMSE values of the comparisons of the experiment's and model's respective FRFs and PSDs are very near zero. These three facts combined show that the frequency domain characteristics of the linear model match well to those of the physical structure. Because frequency domain characteristics are more representative of the dynamic properties of a system than raw time domain behavior, we conclude that the linear model reasonably captures the relevant properties of the physical structure and can be used as a starting point for the nonlinear model.

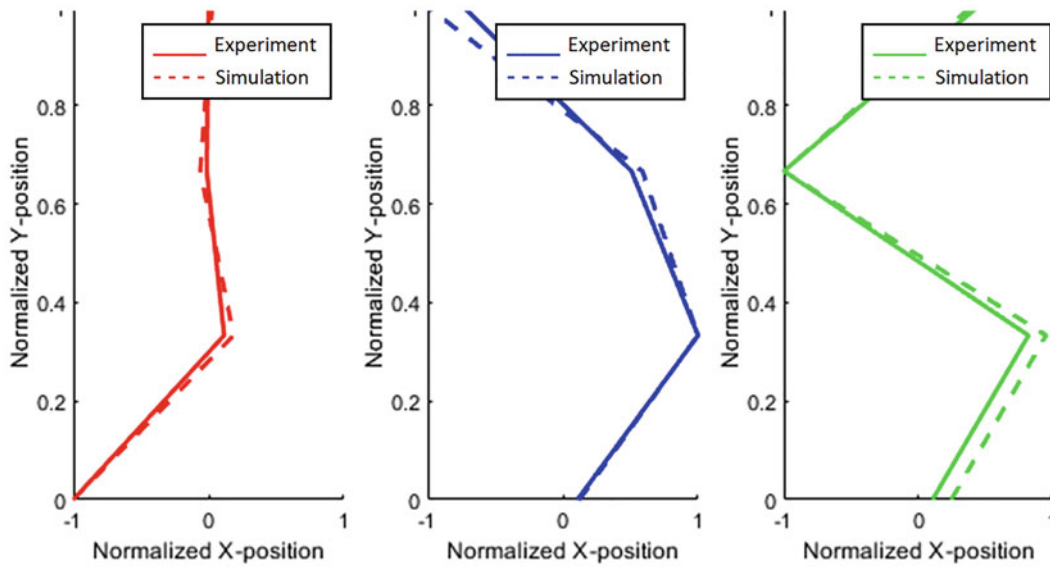


Fig. 22.14 Modes 1–3 (respectively) of the physical experiment and Abaqus model

Table 22.11 Model comparison metrics for linear experiment results and simulation predictions

	Experiment ω_n (Hz)	Model ω_n (Hz)	Error (%)	MAC (%)	RMSE
1st Mode	10.48	11.670	11.35	99.15	–
2nd Mode	19.91	21.612	8.55	98.26	–
3rd Mode	26.54	28.284	6.57	99.54	–
FRF	–	–	–	–	0.1604
PSD	–	–	–	–	0.0018

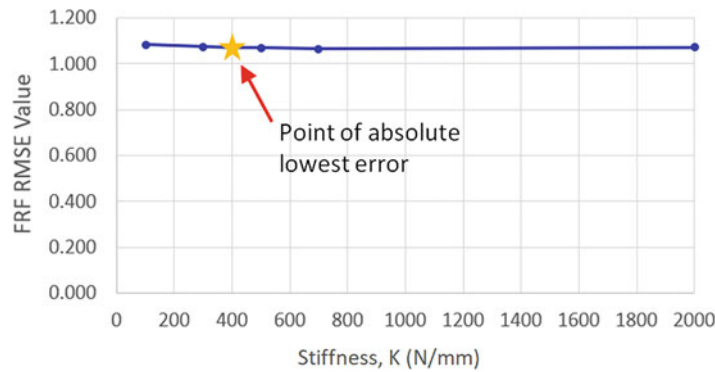


Fig. 22.15 Nonlinear PSD RMSE values, linear PO

22.5.2 Nonlinear Model Validation

Just as in the linear simulations, the acceleration of the base plate of the FSS was used as the input to the Abaqus model. Though in the case of the nonlinear simulations, the base plate acceleration from the nonlinear shaker tests was used. No clear trends were observed in the statistically based validation metrics across the sample space of 6 linear PO contact interaction simulations or across the sample space of 35 exponential PO contact interaction simulations. Thus, conclusions regarding the performance of the different contact interactions and their respective parameter variations were drawn primarily from the trends observed in the RMSEs of the PSD and FRF plots of the acceleration data from the top plate of the FSS. The plots of PSD RMSE value and FRF RMSE value for varying linear PO stiffness K are provided in Figs. 22.15 and 22.16.

From Figs. 22.15 and 22.16, two primary observations can be made. First, the RMSE values are relatively low across the sample space for both the PSD and FRF. Second, and most important, the RMSE values of both the PSD and the FRF remain

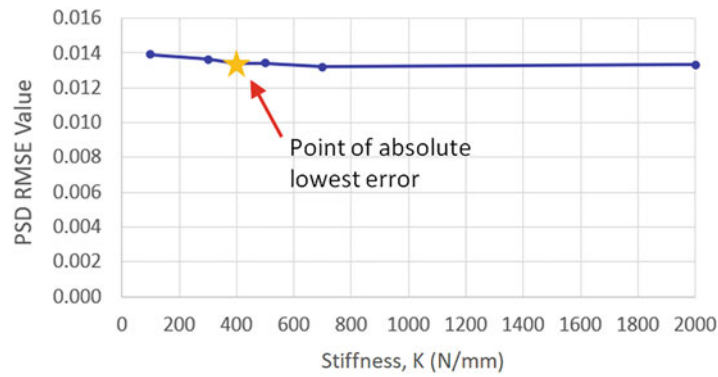
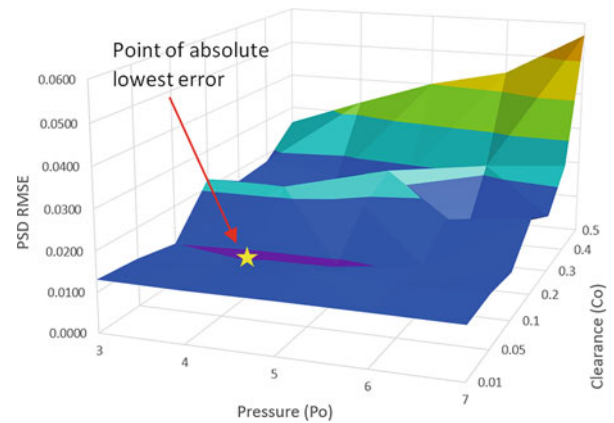


Fig. 22.16 Nonlinear FRF RMSE values, linear PO

Fig. 22.17 Nonlinear PSD RMSE values, exponential PO



relatively constant across the sample space of K values, varying by only 0.001 in the case of the PSD and 0.01 in the case of the FRF. This indicates that the selection of the value of the stiffness parameter K in the linear PO contact definition has minimal effect upon the dynamic response of the system. The point of absolute lowest error occurs at $K = 400$ N/mm in both the case of the PSD and the FRF, and it is marked with a star in Figs. 22.15 and 22.16.

Because the exponential PO contact definition had two parameters to define, it is necessary to plot a 3D surface plot in order to find the trends in data. Figure 22.17 displays the overall trend in the RMSE values of the PSD across the sample space of p_0 and c_0 parameter combinations. In this plot, there are three (p_0, c_0) points of lowest error: $(p_0 = 4, c_0 = 0.1)$, $(p_0 = 4, c_0 = 0.3)$, and $(p_0 = 6, c_0 = 0.3)$. Figure 22.18 shows the overall trend in the RMSE values of the FRF across the sample space of p_0 and c_0 parameter combinations. In this plot, the same three points of lowest error exist. Between the two surface plots, the point of absolute lowest error occurs when $p_0 = 4$ MPa and $c_0 = 0.1$ mm, and it is marked with a star in Figs. 22.17 and 22.18. The fact that both the PSD and FRF display similar trends in error across the sample space of 35 p_0 and c_0 parameter combinations indicates that there does exist a definitive pair of p_0 and c_0 parameters for which the system can be best dynamically represented. For the purpose of discussion, we are taking the point of absolute lowest error as the parameter combination that best represents the dynamics of the system. However, a more refined parametric study centered around this point of lowest error may find a parameter combination that yields even less error than the point found within our relatively coarse sample space.

To determine the performance of the three different contact interactions relative to one another, we compared the PSD RMSE value, FRF RMSE value, and the RMSE of the mean acceleration amplitude peaks of the hard contact interaction to the best exponential PO ($p_0 = 4$ MPa, $c_0 = 0.1$ mm) and best linear PO ($K = 400$ N/mm) cases. The results are shown in Table 22.12. Clearly, the exponential PO contact interaction has the lowest error in all three cases. Also worth noting is that the linear PO contact interaction and the hard contact interaction have extremely similar levels of error for the PSD and FRF, indicating that there is little difference between the system dynamics when either of these two contact interactions are selected. We hypothesize that the larger RMSE in the mean peak acceleration amplitudes is caused by the lack of damping in the FE model.

To explore this hypothesis, the acceleration time series of the best exponential PO, linear PO, and hard contact simulations was analyzed (Fig. 22.19). From this figure, three primary observations can be drawn. First, the acceleration time history of all three simulations show considerably higher acceleration spikes than the acceleration time history produced by the experiment. This provides further evidence in favor of the inclusion of additional damping in the FE model. Secondly, the

Fig. 22.18 Nonlinear FRF RMSE values, exponential PO

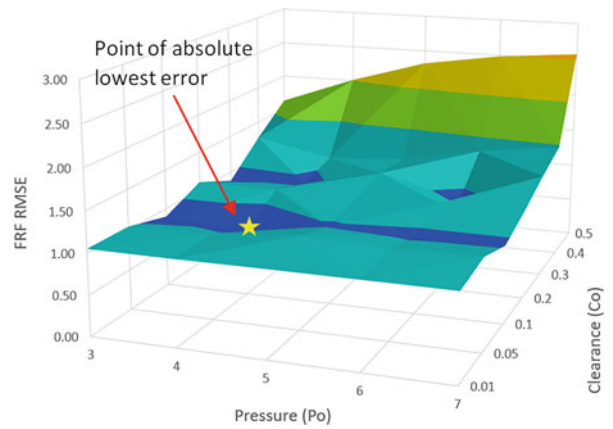


Table 22.12 PSD, FRF, and mean peak amplitude RMSE comparisons for the 3 types of contact interactions

	PSD RMSE	FRF RMSE	Mean Peak Amp. RMSE
Linear PO	0.0133	1.069	4.033
Hard contact	0.0130	1.067	4.037
Exponential PO	0.0087	0.8192	3.855

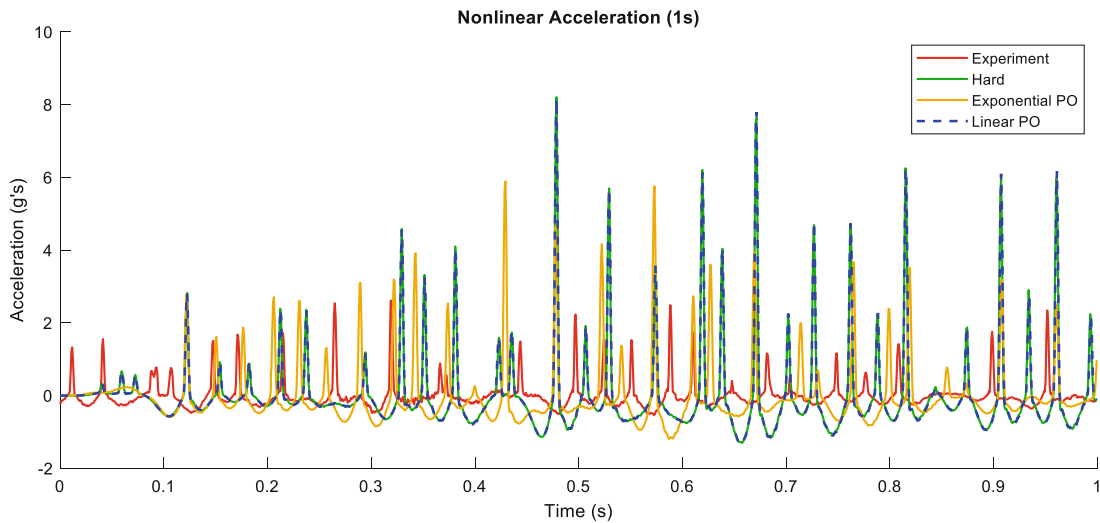


Fig. 22.19 Acc. Time series of nonlinear experiment, hard, exponential ($c_0 = 0.2$ mm, $p_0 = 5$ MPa), and linear contact ($K = 500$ N/mm)

linear PO and hard contact interaction definitions produce very nearly identical acceleration time series. However, the hard contact interaction definition produces slightly higher spikes in acceleration during impact events, which explains the slightly higher error of the hard contact interaction simulation versus the linear PO contact interaction simulation in relation to the experimental results. The final conclusion that can be drawn from Fig. 22.19 is that the exponential PO contact interaction definition produces lower acceleration spikes during impact events in general. While still higher than the peaks produced during the experimental acceleration time series, this provides further evidence that the exponential PO produces the best results.

22.6 Conclusions

Through the completion of this study, it was found that the exponential PO contact interaction produces a dynamic system response that is closer to the target experimental data than did the linear PO contact interaction or the hard contact interaction. We hypothesize that this is because exponential PO contact interaction captures some of the more complicated physics of the

FSS dynamics that the linear PO and hard contact interaction do not. In particular, it is possible that the bilinear behavior of the nonlinear FSS is captured by the exponential PO contact interaction, in which pressure is applied at an exponential rate at some specified distance before contact occurs.

An additional finding of this study is that there appears to be little variation in the dynamic response of the system when the model is designed with linear PO contact interactions versus when the model is designed with hard contact interactions. In other words, linear PO and hard contact interactions yield similar system dynamics. It was also found that the linear PO contact interaction was insensitive to variation in its stiffness parameter in relation to the validation metrics that were observed in this study.

Finally, a secondary goal of this study was to determine whether or not a simple Abaqus model could be used to accurately represent the dynamics of the 4 DOF shaker tower. Based on the relatively low agreement between the experimental data and the simulation data with respect to the selected validation metrics, we conclude that an accurate model of the FSS structure would almost certainly require addressing some of the assumptions and simplifications we made in the modeling process, as will be discussed in the following section.

22.7 Future Work

There are three primary methods by which we propose this study could be improved in the future. The first method is by addressing some of the assumptions and simplifications we made during the modeling process in order to improve the match between the model and the physical experiment. In particular, it is possible that moving from the 2D model to a 3D model would uncover some new aspects of the effects of the different contact interaction definitions (Assumption #01). Finally, and most importantly, we recommend that additional damping be included in future models. In our model, the default bulk viscosity parameters were used, but no other damping properties were assigned. We suspect that the inclusion of additional damping would help reduce the amplitude of the large acceleration spikes that occurred during impact events of the nonlinear simulations and therefore yield a more accurate FE model.

The second method by which this study could be expanded is by including further validation metrics for comparison between the experiment and simulation. In particular, the Hölder exponent, a measure of the consistency of a signal, is useful for detecting the occurrence of impact events in the time domain. We expect this metric to be especially useful in validating the model against the experimental data.

Finally, the third way we propose to extend this work is by performing additional physical experiments with more diverse experimental setups. For example, the arrangement of impact columns and bumpers on the FSS can be rearranged to modify the location and number of nonlinearities. Similarly, the support columns could be exchanged for a set of a different thickness, or masses could be added to the floors to change the inertial properties of the tower. Any of these changes would alter the dynamic behavior of the system and allow for testing of the versatility of the model. Finally, performing experiments with additional types of excitation (such as sinusoidal or impact) could potentially provide further information about the effects of different contact definitions on the dynamic response of a system.

Acknowledgements We would like to thank Thomas Roberts and Brian West of the Los Alamos National Lab Engineering Institute for their help in wrestling our experimental apparatus into working order. We would also like to thank Dr. Peter Avitabile, Dr. Michael Todd, Dr. François Hemez, and Dr. Charles Farrar for their expertise and guidance in the realm of data analysis. Finally, we would also like to thank Dr. Adam Wachtor for his patience and endless willingness to help throughout the duration of this project.

References

1. Maupin, R.D., Hylock, J.E., Rutherford, A.C., Hemez, F.M., Schultze, J.F., Salazar, I.F., Anderson, M.C.: Validation assessment capability for improved fidelity engineering shock response calculations. Technical Report LA-14215 of the Advanced Scientific Computing Verification and Validation Program, Los Alamos National Laboratory, Los Alamos, New Mexico, May 2005. Classified S/RD (2005)
2. Rutherford, M., Maupin, R., Hylock, J., Anderson, M.: Validation of a threaded assembly, part III: Validation. Technical Report LA-UR-05-2500 of the Engineering Sciences and Applications, Los Alamos National Laboratory, Los Alamos, New Mexico, April 2005. Unlimited Public Release (2005)
3. Dar, U.A., Zhang, W., Xu, Y.: FE analysis of dynamic response of aircraft windshield against bird impact. *Int. J. Aerosp. Eng.* **2013**, Article ID 171768, (2013)
4. Farrar, C.R., Worden, K., Todd, M.D., Park, G., Nichols, J., Adams, D. E., Bement, M. T., Farinholt, K.: Nonlinear system identification for damage detection. Technical Report LA-14353-MS, Los Alamos National Laboratory, Los Alamos, New Mexico, November (2007)

5. Figueiredo, E., Park, G., Figueiras, J., Farrer, C., Worden, K.: Structural health monitoring algorithm comparisons using standard data sets. Technical Report LA-14393, Los Alamos National Laboratory, Los Alamos, New Mexico, March (2009)
6. Nishio, M., Hemez, F., Stull, C., Farrar, C., Park, G., Cornwell, P., Figueiredo, E., Luscher, D.J., Worden, K.: Feature extraction for structural dynamics model validation. Technical Report LA-14489, Los Alamos National Laboratory, Los Alamos, New Mexico, May (2016)
7. Butterfield, T.: Descriptive statistics. In: Online Teaching Material. The University of Utah, Utah (2011). <https://www.che.utah.edu/~tony/OTM/Statistics/DescriptiveStatistics/>
8. Thomson, W., Dahleh, M.: Theory of Vibration with Applications, 5th edn, pp. 398–400. Prentice Hall, Upper Saddle River (1998)
9. Matweb.: Overview of materials for medium carbon steel. http://www.matweb.com/search/datasheet_print.aspx?matguid=098700ed63b24b14bd3bfdbec937489f (2019). Last accessed August 2, 2019
10. Chopra, A.: Dynamics of Structures: Theory and Applications to Earthquake Engineering, 5th edn, p. 742. Pearson, Hoboken (2017)
11. Dassault Systèmes Simulia Corp.: SIMULIA User Assistance 2019. Dassault Systèmes (2019). Last accessed June 2019



Chapter 23

Identify Loose Footings of Machines Using Model Updating-Based Method

Shih-Yin Chien, Zhen Wah Chew, and Yum Ji Chan

Abstract In order to improve precision of machines in operation, the actual parameters on a machine, such as stiffness of its footings, can be sought using sensitivity-based model updating methodology. The under-determined model updating problem is avoided by moving a perturbation mass around the machine and creating new sensitivity equations. The positions of the perturbation mass are determined using the singular value decomposition (SVD) analysis of sensitivity matrix. Plate-footings assembly is utilized in both simulation and experiment to demonstrate the feasibility of the model updating of footing stiffness. Results show that this methodology can identify the weak footings, if several constraints are imposed on the relationship among stiffness parameters. Studies carried out on machine tool prototype are described.

Keywords Model updating · Footing stiffness · System perturbation · Singular value decomposition

23.1 Introduction

Modern machines are designed with the aid of computer-aided engineering, and it frequently involves building digital twins for both development and application stages. For example, the mechatronic digital twins of machine tools are also known as “virtual machine tools” [1, 2]. The numerous parameters in a digital twin can be calibrated using model updating approach [3]. However, the parameter discrepancy between the numerical model and the physical system does not always originate from the numerical model. The model updating approach is applied in this study to detect loose footings in machines. The proposed method is demonstrated on (i) a plate-footings assembly (Fig. 23.1a) and (ii) a miniature machine tool (Fig. 23.1b), with results on the latter are discussed.

23.2 Background

In the sensitivity-based model updating methodology, uniqueness of identified parameters requires an overdetermined problem, that is, the number of performance parameters should be more than that of the design parameters. However, in identification of machine footings, the problem is inherently underdetermined: assuming the machine being a rigid body, there are only 6 rigid-body modes while a 19-tonne machine tool can have up to 9 footings, involving 27 stiffness parameters. The problem is under-determined and no unique solution could be found directly.

In the current study, the underdetermined nature of the problem is tackled by adding a perturbation mass and move it around to create more sensitivity equations and transform the problem to an overdetermined one. Such a method has been used in operational modal analysis to seek mass-normalised mode shapes [4], and it is noted that no actual masses needs to be installed in machines with movable components, such as machine tools. The locations of perturbation mass are determined by singular value decomposition (SVD) of the sensitivity matrix. The combination of locations is taken, if a condition-number-like parameter is minimized [5].

S.-Y. Chien · Z. W. Chew · Y. J. Chan (✉)
Department of Mechanical Engineering, National Chung Hsing University, Taichung, Taiwan
e-mail: yjchan@nchu.edu.tw

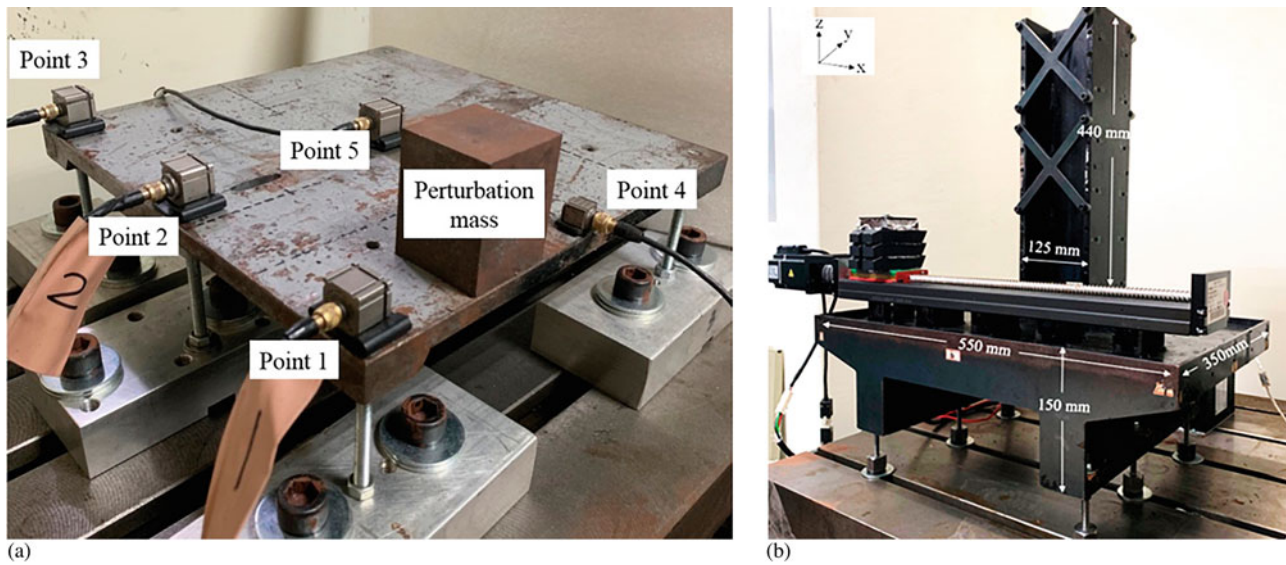


Fig. 23.1 Objects modelled in this study: (a) Plate-footings assembly. (b) Machine tool prototype

23.3 Numerical Demonstration

In this study, a numerical model of a flexible square plate with six footings is built. As each footing can be assumed three springs in the x -, y - and z -directions, 18 stiffness parameters are to be identified, but there are only 6 rigid body mode shapes of plate-footings assembly. A perturbation mass is put on the plate: by carrying out SVD analysis on the sensitivity matrix, the optimal combination of the perturbation mass positions is sought.

To demonstrate the procedure, the horizontal (that is, in the x - and y - directions) and vertical stiffness of a single footing (in this case, Footing 1) are γ times and γ^2 times of their nominal values, respectively, in order to simulate the variation of stiffness upon diameter change. It is found that coupling between the dynamics in the x - and y - directions would lead to ill-conditioned sensitivity matrix in model updating and inaccurate identification. Therefore, model updating is carried out with footing stiffness in both transverse directions assumed to be equal (that is, $k_x = k_y$), thus the parameters to be identified reduced to 12. Figure 23.2 (right) shows that each level of footing stiffness can be identified accurately. To achieve such results, iteration step reduction, inclusion of regularization parameter λ^2 [3] and inclusion of more natural frequencies are desirable, if the stiffness change is significant.

23.4 Experimental Validation

The plate-footings assembly shown in Fig. 23.1a is studied experimentally. One footing is artificially weakened by reducing its diameter. The perturbation mass is moved to three different positions and experimental modal analysis (EMA) is conducted using tap test. Initial identification results are inaccurate because of measurement error. To deal with such an issue, only the vertical footing stiffness are identified, and transverse footings stiffness change is constrained to be proportional to the square of vertical counterpart. The final identification results (Fig. 23.3) agree with the imposed values.

23.5 Conclusion

A method to identify footing stiffness of machines based on sensitivity-based model updating is proposed and demonstrated. The amount of stiffness parameters makes the problem under-determined but it can be solved by moving a perturbation mass around. The optimal combination of the perturbation mass positions can be determined with the help of SVD analysis on the sensitivity matrix. To identify the footings stiffness successfully in experiments, the horizontal stiffness has to be assumed equal and constraint added between horizontal and vertical footings stiffness.

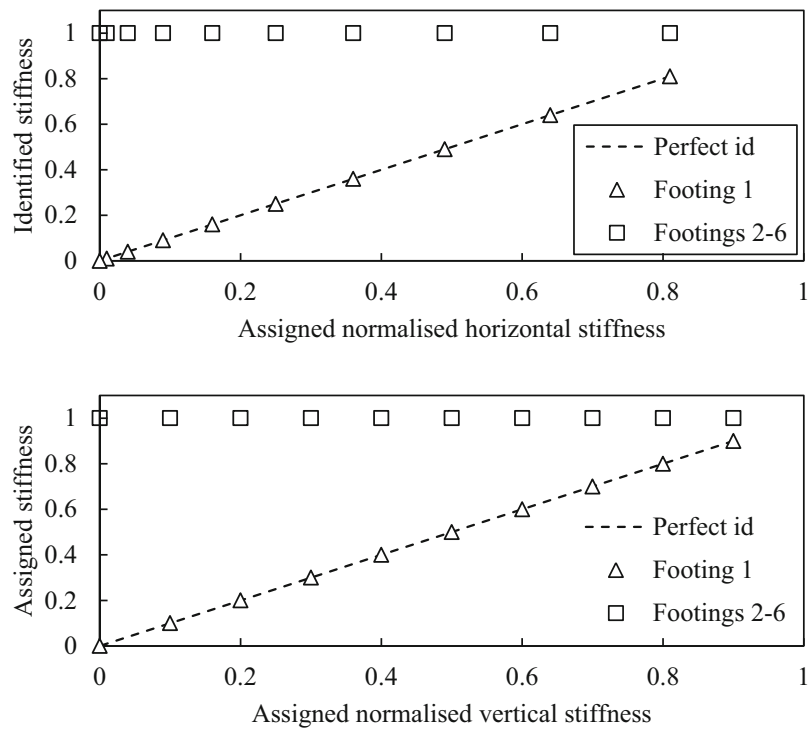


Fig. 23.2 Comparison between assigned and identified footing stiffness

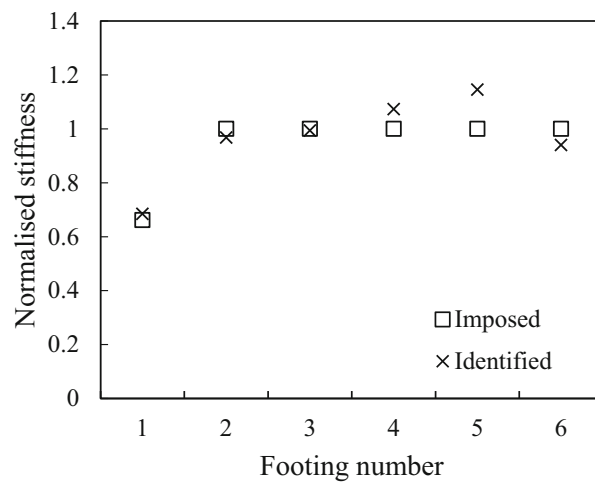


Fig. 23.3 Results of vertical footings stiffness identification based on experiment data

Acknowledgements The research is supported by the Ministry of Science of Technology, Taiwan with Grant number 108-2221-E-005-053.

References

1. Altintas, Y., Brecher, C., Weck, M., Witt, S.: Virtual machine tool. *CIRP Ann. Manuf. Technol.* **54**(2), 115–138 (2005)
2. Zaeh, M., Siedl, D.: A new method for simulation of machining performance by integrating finite element and multi-body simulation for machine tools. *CIRP Ann. Manuf. Technol.* **56**(1), 383–386 (2007)
3. Mottershead, J.E., Link, M., Friswell, M.I.: The sensitivity method in finite element model updating: a tutorial. *Mech. Syst. Signal Process.* **25**(7), 2275–2296 (2011)

4. Martinez, L.B.P., Pelayo, F., García, M., Aenlle, M.L., Ismael, G.: Comparison of different techniques to scale mode shapes in operational modal analysis. In: Proceedings of 6th International Operational Modal Analysis Conference, Gijon, Spain, May 2017
5. Hong, Y.C.: Model Updating of Machine Tool Feet and Sliders. Master thesis, National Chung Hsing University, 2018

Mr Zhen Wah Chew is currently a Master's student at National Chung Hsing University, Taichung, Taiwan. His research interests include structural dynamics and vibration of assembled structures.



Chapter 24

Bayesian Finite Element Model Updating Using a Population Markov Chain Monte Carlo Algorithm

M. Sherri, I. Boulkaibet, T. Marwala, and M. I. Friswell

Abstract Bayesian methods have become very popular in the area of finite element model updating (FEMU) in the last decade, where these methods are considered as powerful tools in quantifying the uncertainties associated with the modelling and the experimental processes. Based on Bayes' theorem, the posterior distribution function can be employed to describe the modelling and the experimental uncertainties while an improved version of the finite element model (FEM) is obtained by solving the posterior formulation. Unfortunately, an analytical solution of the posterior distribution function may not be available due to the complexity of the system as well as the size of the unknown parameters. Alternatively, Markov Chain Monte Carlo (MCMC) methods are very useful stochastic tools that can be employed to solve complex posterior functions and provide approximate solutions. The Metropolis-Hastings (M-H) method is the most common MCMC approach that has been frequently used to approximate distribution functions, where the M-H approach gained its simplicity from using random walk steps to define new candidates. Unfortunately, the performance of the M-H method decreases with the complexity of the modelled systems as well as the number of the uncertain parameters. Several techniques have been proposed to improve the performance of the M-H method such as introducing an adaptation procedure to improve the candidates. In this paper, an evolutionary approach, known as the Population Markov Chain Monte Carlo (Pop-MCMC) method, is adopted to improve the performance of the MCMC algorithms. In this approach, multiple chains are run in parallel and information exchange among these parallel chains are incorporated for the exploration of the search space, while a Metropolis-Hastings criterion is used to accept or reject the candidates for each chain. In this paper, the Pop-MCMC method is presented in detail while the performance of this method is investigated by updating two structural examples.

Keywords Bayesian method · Finite element model updating · Population Markov chain Monte Carlo · Evolutionary algorithm · Posterior distribution function

24.1 Introduction

The Finite Element method (FEM) is considered as one of the most common modelling approaches used for structural design and analysis. This approach is mainly a computational technique that can be used to simplify the numerical evaluation of structural systems, and modelling these systems as a combination of discrete finite elements [1, 2]. Usually, FEMs are able to accurately approximate the behavior of simple structures. However, dealing with more complex systems may reduce the FEMs' accuracy, especially when uncertainties are present in both the modelling and experimental measurements. Thus, a mismatch between the FEM results and the experimental measurements are highly likely.

M. Sherri (✉)

Department of Mechanical Engineering Science, University of Johannesburg, Auckland Park, South Africa

I. Boulkaibet

College of Engineering and Technology, American University of the Middle East, Egaila, Kuwait

e-mail: ilyes.boulkaibet@aum.edu.kw

T. Marwala

Institute for Intelligent Systems, University of Johannesburg, Auckland Park, South Africa

e-mail: tmarwala@uj.ac.za

M. I. Friswell

College of Engineering, Swansea University, Bay Campus, Swansea, UK

e-mail: m.i.friswell@swansea.ac.uk

To alleviate the mismatch between the modelling and the measurement results, FEMs need to be updated in order to improve their modelling accuracy [3, 4]. Generally, the main purpose of finite element model updating (FEMU) is to minimize the difference between measured data and the modelling results. The FEMU procedures can be directly achieved by equating the experimental data and the FEM outputs, and this can be attained by constraining the updating process to the system matrices (mass & stiffness) of the FEM. The results of the direct methods often appear impractical since the values of the updating parameters may not have physical meaning. On the other hand, performing iterative optimizations to update FEMs is more effective and the obtained results have physical meaning. In iterative approaches, also known as indirect approaches, an objective function that aims to reduce the errors between the numerical and experimental results is defined and iteratively minimized, while the final results of the updating parameters, obtained at the end of the iterative mechanisms, are more realistic and can be used to obtain an improved version of the finite element model (FEM).

Generally, certain uncertainties, such as errors related to mathematical simplifications, are associated with the modelling procedure and can easily affect the FEMs' accuracy. Furthermore, experimental results are also contaminated with noise that may have significant impacts on the updating results. To deal with modelling and experimental uncertainties, uncertainty quantification approaches, such as the Bayesian approach, are implemented to update FEMs and to quantify uncertainties associated with the updating parameters. In Bayesian approaches, the unknown parameters are defined as a random vector with multi-variable probability density function (PDF), and these unknown parameters and their related uncertainties are obtained by solving the Bayesian formulations. Generally, FEMU for complex systems are nonlinear and a multidimensional optimization problems, and the Bayesian formulations related to complex systems are very difficult and cannot be solved analytically. In this case, sampling techniques are the most practical options to solve the Bayesian formulations, and to obtain the unknown parameters along with their uncertainties. Markov Chain Monte Carlo (MCMC) algorithms [5, 6] are the most recognized sampling approaches used to solve complex distributions functions (Posterior PDF). In MCMC algorithms, samples are obtained as elements of randomness and controlled by the updated values of the posterior PDF, while the new samples are accepted or rejected according to the Metropolis-Hastings (M-H) criterion [7–12]. Unfortunately, classical MCMC approaches may become trapped in local optimal (or near-optimal) solutions when applied to solve posterior PDFs of large complex systems with large unknown parameters.

In this paper, a hybrid algorithm called the Population Markov Chain Monte Carlo (Pop-MCMC) is used to solve the FEMU problem for complex structural systems [13–15]. The Pop-MCMC algorithm is a combination of the Metropolis-Hastings approach and an Evolutionary Algorithm (EA), where independent multi-chains are generated and used for the sampling procedure while information is exchanged between these chains at each time step. As a hybrid method, statistical information associated with the evolutionary population of the Markov chains are used to improve the candidate solutions by altering the tuning parameters, and this will drive the algorithm in terms of ergodicity and convergence. In this paper, the efficiency and the limitation of the Pop-MCMC algorithm are tested by updating two structural systems. The paper is organized as follows: Sect. 24.2 introduces the Bayesian approach. Section 24.3 describes the Pop-MCMC algorithm, while Sect. 24.4 presents the results when a simple mass-spring structure is updated using Pop-MCMC. In Sect. 24.5, the updating results of an unsymmetrical H-shaped structure are presented. Finally, the paper is concluded in Sect. 24.6.

24.2 The Bayesian Model

In this paper, FEMU problems are solved using Bayesian theory [9, 16, 17]. The main concern of the approach is to determine the posterior PDF, and the updating parameters of the FEM are obtained when the posterior PDF is solved. The posterior function is computed as:

$$P(\boldsymbol{\theta} | \mathcal{D}, \mathcal{M}) \propto P(\mathcal{D} | \boldsymbol{\theta}, \mathcal{M}) P(\boldsymbol{\theta} | \mathcal{M}) \quad (24.1)$$

The probability distribution of the posterior function is presented by $P(\boldsymbol{\theta} | \mathcal{D}, \mathcal{M})$, while \mathcal{M} describes the model class for the target system, each model class \mathcal{M} is defined by certain updating parameter $\boldsymbol{\theta} \in \Theta \subset \mathcal{R}^Q$. The model class \mathcal{M} is only included when several classes of model updating are involved, and model selection is required to select the best model. In this paper, only one model class is considered and the term of \mathcal{M} is removed to simplify the Bayesian formulation. \mathcal{D} represents the experimental measurements which are used to improve the predictions of the FEM. In this paper, \mathcal{D} contains natural frequencies f_i^m and mode shapes $\boldsymbol{\phi}_i^m$. The likelihood function $P(\mathcal{D} | \boldsymbol{\theta}, \mathcal{M})$ describes the differences between the measured data and the FE model outputs. $P(\boldsymbol{\theta})$ is the prior probability distribution function that introduces the initial knowledge of the uncertain parameters for a specific model class \mathcal{M} and in the absence of \mathcal{D} . The likelihood function is given by:

$$P(\mathcal{D}|\boldsymbol{\theta}) = \frac{1}{\left(\frac{2\pi}{\beta_c}\right)^{N_m/2} \prod_{i=1}^{N_m} f_i^m} \exp\left(-\frac{\beta_c}{2} \sum_i^{N_m} \left(\frac{f_i^m - f_i}{f_i^m}\right)^2\right) \quad (24.2)$$

N_m is the number of measured modes, f_i^m and f_i are the i th analytical and measured natural frequencies, and β_c is a constant. The initial knowledge of the updating parameters, the prior PDF, is defined by the following Gaussian distribution function:

$$P(\boldsymbol{\theta}) = \frac{1}{(2\pi)^{Q/2} \prod_{i=1}^Q \frac{1}{\sqrt{\alpha_i}}} \exp\left(-\sum_i^Q \frac{\alpha_i}{2} \|\theta^i - \theta_0^i\|^2\right) = \frac{1}{(2\pi)^{Q/2} \prod_{i=1}^Q \frac{1}{\sqrt{\alpha_i}}} \exp\left(-\frac{1}{2}(\boldsymbol{\theta} - \boldsymbol{\theta}_0)^T \boldsymbol{\Sigma}^{-1} (\boldsymbol{\theta} - \boldsymbol{\theta}_0)\right) \quad (24.3)$$

Where Q is the number of the uncertain parameters, $\boldsymbol{\theta}_0$ is the mean value of the updating parameters, α_i , $i = (1, \dots, Q)$ is the i th coefficient of the updating parameter, and the notation $\|\cdot\|$ is the Euclidean norm of \cdot .

By substituting the formulas of the likelihood function Eq. (24.2), and the prior function Eq. (24.3) into the Bayesian model Eq. (24.1), the posterior function $P(\boldsymbol{\theta}|\mathcal{D})$ of the unknown parameters $\boldsymbol{\theta}$ given the measured data \mathcal{D} is defined by the following equation:

$$P(\boldsymbol{\theta}|\mathcal{D}) \propto \frac{1}{Z_s(\alpha, \beta_c)} \exp\left(-\frac{\beta_c}{2} \sum_i^{N_m} \left(\frac{f_i^m - f_i}{f_i^m}\right)^2 - \sum_i^Q \frac{\alpha_i}{2} \|\theta^i - \theta_0^i\|^2\right) \quad (24.4)$$

and the constant:

$$Z_s(\alpha, \beta_c) = \left(\frac{2\pi}{\beta_c}\right)^{N_m/2} \prod_{i=1}^{N_m} f_i^m (2\pi)^{Q/2} \prod_{i=1}^Q \frac{1}{\sqrt{\alpha_i}} \quad (24.5)$$

Generally, the complexity of the posterior PDF is proportional to the complexity of the targeted FEM as well as the number of updating parameters involved in the updating process. For certain relatively complex structures, the solution of the posterior PDF cannot be obtained analytically, especially when the search space is relatively large, and a significant number of updating parameters are involved in the updating procedure. Therefore, the use of sampling techniques is the only practical approach to approximate the posterior PDF solutions. Basically, the main objective of sampling methods is to generate a number N_s of vectors for the updating parameters $\{\boldsymbol{\theta}_1, \boldsymbol{\theta}_2, \dots, \boldsymbol{\theta}_{N_s}\}$, and these samples are then used to approximate the solutions of the posterior PDF. The Markov Chain Monte Carlo (MCMC) algorithms are common sampling techniques used to draw samples from complex distribution functions, posterior PDF, and most of these MCMC approaches are based on the Metropolis-Hastings (M-H) acceptance-rejection criterion. In this paper, a combination of the evolutionary algorithm and the Metropolis-Hastings criterion is used to generate samples from the posterior PDF. The next section will present the Pop-MCMC algorithm.

24.3 Population Markov Chain Monte Carlo (Pop-MCMC) Algorithm

The Pop-MCMC algorithm is a population-based stochastic search algorithm adopted for optimization and learning problems. The main concept of this algorithm is to improve the sampling procedure by merging the evolutionary optimization steps with the Metropolis-Hastings (M-H) acceptance-rejection criterion [18–21]. In the last few decades, many suggestions have been proposed to enhance the MCMC sampling abilities at a population level in order to obtain a better mixing in MCMC sampling procedures. This work [22, 23] has shown that improvements in the MCMC accuracy for solving FEMU problems can be achieved when MCMC approaches are operated at a population-based level. In this paper, the population MCMC technique is used to provide samples and approximate the FEMU solution. The Metropolis-Hastings (M-H) algorithm is used to construct Markov chains from a given target probability distribution, and multiple independent chains are run in parallel in order to maintain a balanced prediction, and to satisfy the maximum convergence of the desired stationary distribution.

Generally, evolutionary algorithms are used to extend the searching procedure from one individual to a population, and information is exchanged among the individuals in order to find the overall best solution. In the first step, the algorithm

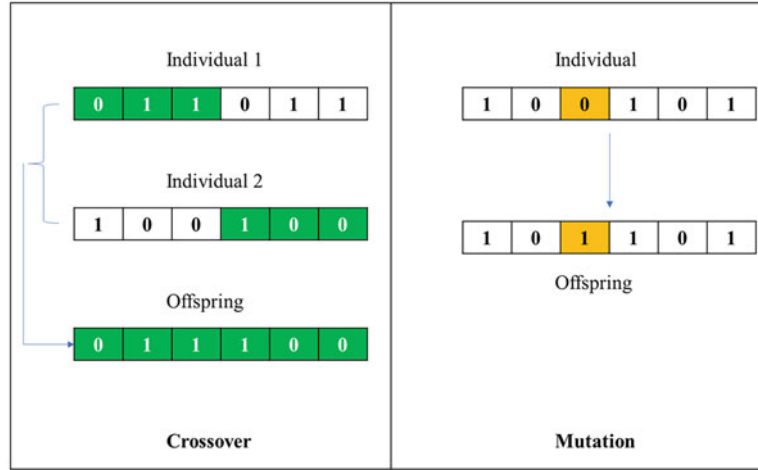


Fig. 24.1 Illustration of the genetic operators

generates an initial population of solutions and then keep altering the values of these populations until the targeted criterion is met. This can be done by selecting individuals based on their performance, in which the individual's performance is defined by the value of the fitness function. The selected individuals are then modified on the basis of the common genetic operators (crossover and mutation). In the crossover procedure, two individuals are randomly selected from the population and set as parents, and then information is exchanged between these parents at a predefined selected point. On the other hand, only a single individual is selected in the mutation procedure, where the value of the selected individual is modified in some way (such as flipping a bit in the individual binary string representation) to maintain diversity from the original state. Then, the improved individual becomes the new algorithm offspring. Figure 24.1 explains the crossover and mutation operators. Finally, the evolutionary algorithm selects the next new generation from the current population (including the offspring), and the new solutions are generated following the same procedure until the targeted criterion is met (minimizing the fitness function or reaching a predefined iteration number).

In this paper, crossover and mutation operators are used to improve candidates and enforce information exchange between the independent chains. The Pop-MCMC algorithm uses a modified version of the genetic operators (crossover and mutation) to propose new generations, and the obtained new candidates are set to be values of the Markov chains since the mutation probability is different than zero, and the population size is constrained. Furthermore, the Markov chains are balanced when the MCMC Metropolis-Hastings acceptance rate is used as a post-selection to determine whether to move to the new state or remain unchanged.

Let $\hat{\theta} = \{\theta_1, \theta_2, \dots, \theta_i, \dots, \theta_N\}$ denotes the population of the updating parameters, where $\theta_i = \{\theta_i^1, \theta_i^2, \dots, \theta_i^Q\}$ is the i th chain, Q is the dimension of the unknown parameters vector (also called the individual), and N is the population size. The Metropolis-Hastings algorithm uses a proposal distribution $F(\theta^* | \theta^k)$ to generate new candidate where θ^k represents the current individual (current solution or state) and θ^* is the newly proposed state. Changing the chain from the current state θ^k to the new generation (or proposal) θ^* is determined by the transition probability $\tau(\theta^* | \theta^k)$, which is also defined by the candidate distribution and the acceptance probability:

$$\tau(\theta^* | \theta^k) = F(\theta^* | \theta^k) A(\theta^* | \theta^k) \quad (24.6)$$

and $A(\theta^* | \theta^k)$ is the acceptance probability:

$$A(\theta^* | \theta^k) = \min \left\{ 1, \frac{P(\theta^* | D) F(\theta^k | \theta^*)}{P(\theta^k | D) F(\theta^* | \theta^k)} \right\} \quad (24.7)$$

For simplification, the candidate distribution is selected to have the following property:

$$F(\theta^* | \theta^k) = F(\theta^k | \theta^*) \quad (24.8)$$

The Pop-MCMC algorithm exploits an adaptive mutation operator to provide candidate solutions, and the new proposed state is based on a simple probabilistic alteration. The mutation in the Pop-MCMC algorithm is a modified version of the mutation in evolutionary algorithms where the new offspring state is determined based on the current population distribution, which includes the contribution of previous generation series. In the Pop-MCMC algorithm, the proposed adaptive mutation uses subspace sampling and outlier chain correction to speed up the convergence towards the target distribution. The subspace sampling is performed by randomly updating selected dimensions of the updating parameter vector θ^i at each step of the generated candidates, while the jump rate $\delta\theta^i$ of the i th chain, $i = \{1, 2, \dots, N\}$ at iteration $t = \{2, \dots, T\}$ is calculated from the chain series $\theta = \{\theta_{t-1}^1, \dots, \theta_{t-1}^N\}$ as follows:

$$\delta\theta_V^i = \zeta_{\tilde{d}} + (1_{\tilde{d}} + \lambda_{\tilde{d}}) \gamma_{(e, \tilde{d})} \sum_{j=1}^e (\theta_V^{a_j} - \theta_V^{b_j}) \quad (24.9)$$

where V is a \tilde{d} -dimensional subset of the updating parameter space, $\mathbb{R}^{\tilde{d}} \subseteq \mathbb{R}^Q$, \tilde{d} -entities are constructed with the help of the crossover operator, as will be discussed later, and $\delta\theta_{\neq V}^i = 0$. The jump rate $\gamma = \frac{2.38}{\sqrt{2ed}}$, and e is the selected number of the chain pairs, and its default value is $e = 3$. The vectors a and b contain e set values and are drawn from $\{1, \dots, i, \dots, N\}$. The values of λ and ζ are sampled independently from the multivariate uniform distribution $\mathcal{U}_{\tilde{d}}(-\mu, \mu)$ and the normal distribution $\mathcal{N}_{\tilde{d}}(0, \bar{\mu})$, respectively. The value of μ is normally taken as the minimal bandwidth distribution $\mu = 0.1$, and $\bar{\mu} = 10^{-6}$ is small compared to the width of the target distribution. The mutation of the candidate sample θ^* of the i th chain becomes:

$$\theta^* = \theta^i + \delta\theta^i \quad (24.10)$$

and the M-H acceptance probability $A(\theta^* | \theta^k = i)$ is used to determine whether to accept this candidate or not. If the candidate point θ^* is accepted then the i th chain moves to the new position, $\theta_t^i = \theta^*$, otherwise $\theta_t^i = \theta_{t-1}^i$ remains.

Another important feature of the Pop-MCMC algorithm is to allow the independent chains to exchange information by employing the crossover operator. The operator is applied before each candidate is created and operates as follows. An initial value of crossover \mathcal{CR} is sampled from a geometric sequence $m_{\mathcal{CR}}$ such that $\mathcal{CR} = \left\{ \frac{1}{m_{\mathcal{CR}}}, \frac{2}{m_{\mathcal{CR}}}, \dots, 1 \right\}$ using the discrete multinomial distribution $\mathcal{M}(\mathcal{CR}, P_{\mathcal{CR}})$, where $P_{\mathcal{CR}}$ is the selection crossover probability. The default value of $m_{\mathcal{CR}}$ is 3. Then, the Q -vector $Z = \{Z_1, \dots, Z_Q\}$ is drawn from the standard multivariate uniform distribution $Z \sim U_Q(0, 1)$. The values of j which satisfy $Z_j \leq \mathcal{CR}$ are stored in the subset V , and this will extend the candidate that used for sampling in Eq. (24.9). If the subset V is zero-length, a one-dimension random sampling $\{1, \dots, Q\}$ is generated to avoid the empty jump vector. The selection crossover probability $P_{\mathcal{CR}}$ is tuned at every iteration by estimating the maximum variation of the N chains and stored in the crossover probability vector $m_{\mathcal{CR}}$. The probabilistic crossover operator improves the search efficiency and continuously introduces new directions in the parameter space while chains can adopt and exchange information to extend their current positions.

The Pop-MCMC algorithm is summarized as follows:

1. Initialize the population by generating N individuals, and calculating their posterior PDFs.
2. Randomly, select two individuals from the population.
3. Choose whether to crossover or mutate:
 - (a) Draw Z from a uniform distribution $Z \sim U_Q(0, 1)$.
 - (b) If $Z > P_{\mathcal{CR}}$, then perform crossover.
 - (c) The individuals selected for crossover are then considered for Metropolis-Hastings acceptance probability as in Eq. (24.7).
4. If the crossover is not selected, the two individuals are then altered separately using adaptive mutation.
5. Accept the new state $\theta^* \rightarrow \theta^k$ with probability $\min\{1, A(\theta^* | \theta^k)\}$, otherwise θ^k unchanged.
6. Repeat the steps of 2–5 until the termination condition is met.

In the next sections, the Pop-MCMC algorithm is tested for FEMU problems where the algorithm is applied to update two structural examples. The first structure is a simple five-degree of freedom mass-spring system, and the second structure is an unsymmetrical H-shaped beam.

24.4 FEMU Problem 1: Mass-Spring System

In this section, the Pop-MCMC algorithm is tested by updating a five-degree of freedom mass-spring system as presented in Fig. 24.2.

The system consists of 5 masses connected by 10 springs. The numerical values of the masses are: $m_1 = 2.7$ kg, $m_2 = 1.7$ kg, $m_3 = 6.1$ kg, $m_4 = 5.3$ kg and $m_5 = 2.9$ kg. The stiffness coefficients of the springs are: $k_3 = 3200$ N/m, $k_5 = 1840$ N/m, $k_7 = 2200$ N/m, $k_9 = 2800$ N/m and $k_{10} = 2000$ N/m. The selected coefficients $k_1, k_2, k_4, k_6,$ and k_8 are set to be the uncertain parameters $\theta = \{\theta_1, \theta_2, \theta_3, \theta_4, \theta_5\} = \{k_1, k_2, k_4, k_6, k_8\}$. The Pop-MCMC algorithm maximum number of iterations is $T = 10000$, the crossover probability is $m_{CR} = 3$, and the selected number of chain pairs is $e = 3$. The updating parameters are bounded by: $\theta_{max} = \{4800, 2600, 2670, 3400, 2750\}$, and $\theta_{min} = \{3200, 1800, 1600, 1800, 2050\}$. The initial vector of the updating parameter θ is set to $\theta_0 = \{4600, 2580, 1680, 3100, 2350\}$. The obtained samples are presented in the scatter plots in Fig. 24.3.

The scatter plot also shows confidence ellipses of the samples, where the regions of the ellipses contain 95% of the obtained samples. As shown in Fig. 24.3, the Pop-MCMC algorithm has found the high probability area of the solutions after few iterations. Table 24.1 presents the updated values of the uncertain parameters, the initial parameters, and the coefficient of variation (c.o.v), which is calculated by dividing the standard deviation σ_i by the updating vector θ_i . The c.o.v values are less than 2.5% which demonstrates that the Pop-MCMC has performed well and identified the high probability area in the search space. Furthermore, the updating parameters are almost identical to the nominal values which indicates the effectiveness the Pop-MCMC algorithm in updating the system.

Table 24.2 shows nominal frequencies, initial frequencies, updating frequencies, errors estimated as $\frac{|f_i^m - f_i|}{f_i^m}$, and the total average error $TAE = \frac{1}{N_m} \sum_{i=1}^{N_m} \frac{|f_i^m - f_i|}{f_i^m}$, $N_m = 5$. Further, the c.o.v values of the obtained natural frequencies are less than 0.2% for all frequencies which indicates that the Pop-MCMC has successfully updated the system.

Furthermore, the Pop-MCMC algorithm has successfully reduced the total average error for natural frequencies to 0.04%. Fig. 24.4 illustrates the evaluation of the total average error where TAE is determined by computing the mean values of the obtained samples at each iteration $\bar{\theta} = E(\theta) \approx \frac{1}{N_s} \sum_{j=1}^i \theta^j$, where i represents the current iteration. Then, the mean value $\bar{\theta}$ is used to calculate the updating frequencies of the FE model. As shown in Fig. 24.4, it is clear that the algorithm converges after the first 2000 iterations.

The correlation between the updating parameters is given in Fig. 24.5. All parameters are correlated since all values are different than zero. Furthermore, the majority of the updating parameters are weakly correlated (correlation value < 0.3) except the pair (θ_1, θ_2) where the correlation value is relatively high (> 0.7).

In the next section, the Pop-MCMC algorithm is used to update a real unsymmetrical H-shaped structure.

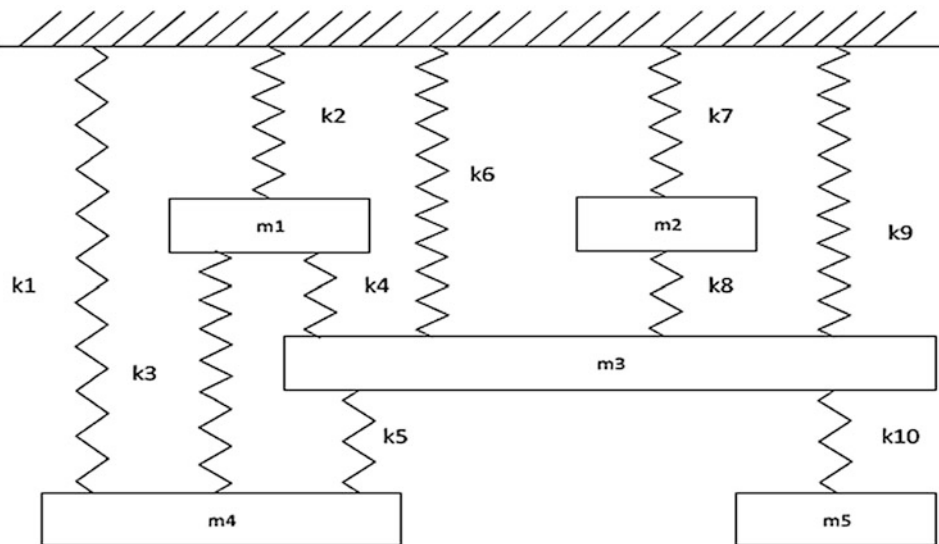


Fig. 24.2 The five degrees of freedom mass-spring system

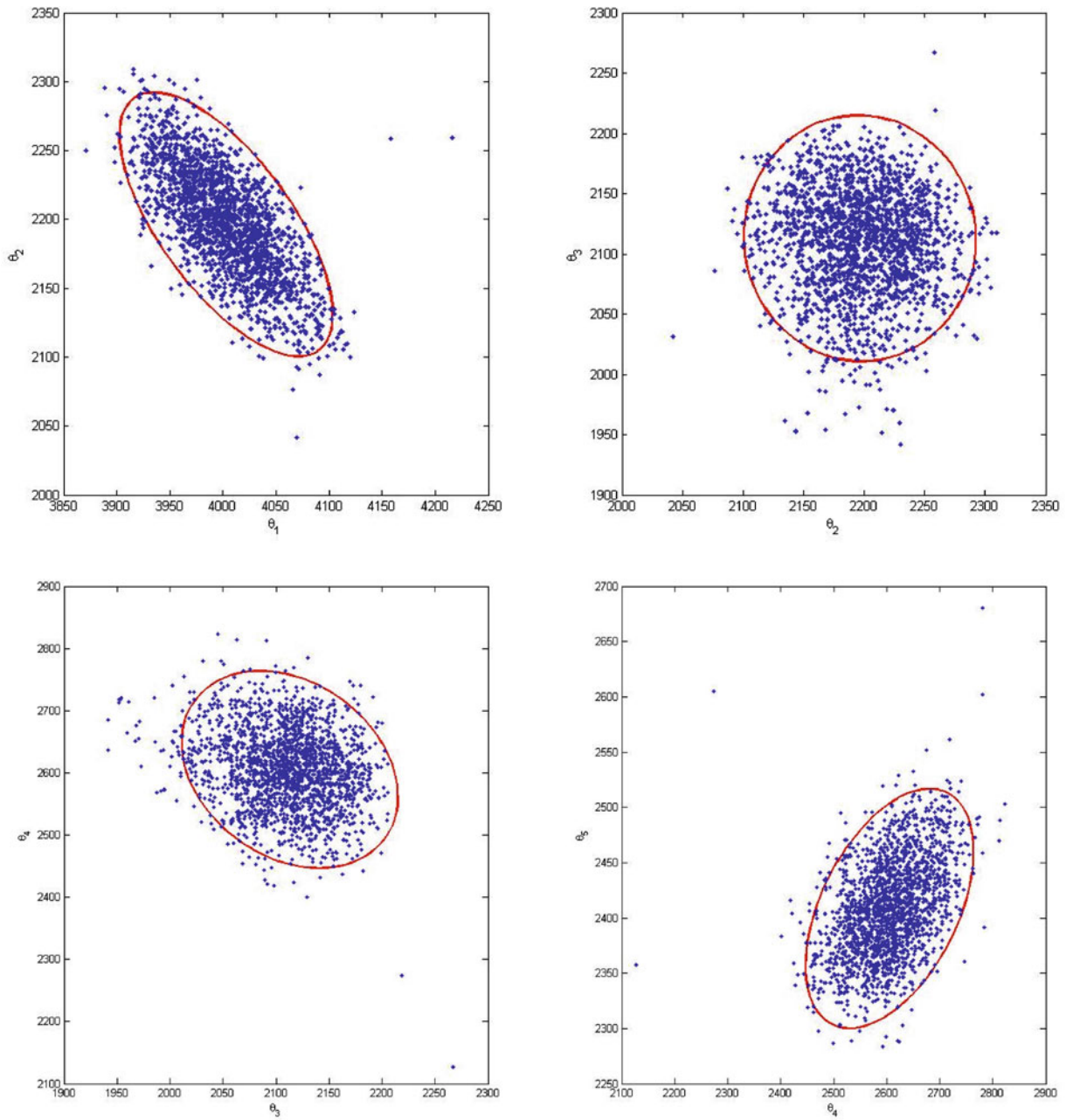


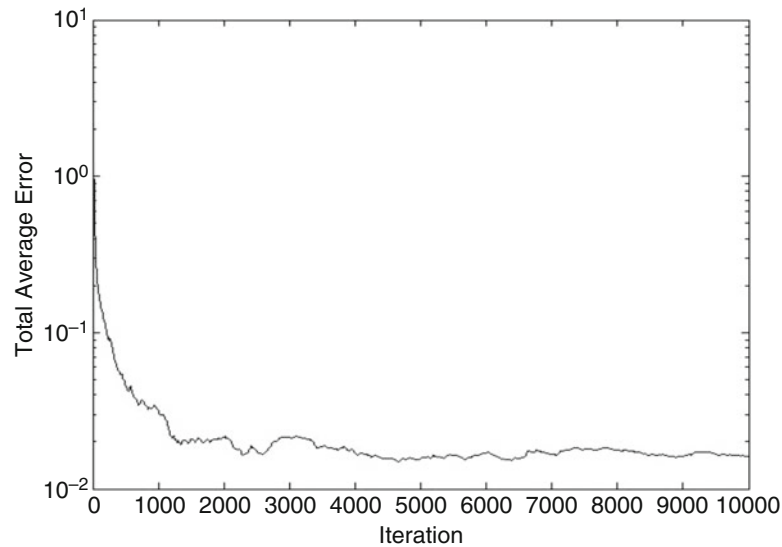
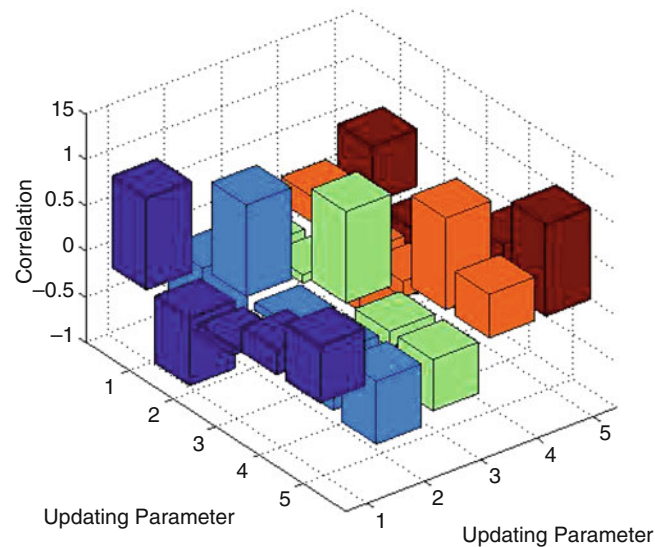
Fig. 24.3 The scatter plots of the samples using the Pop-MCMC algorithm

Table 24.1 The updating parameters obtained by the Pop-MCMC algorithm

Uncertain parameters (N/m)						
	Initial	Nominal values	Error (%)	Pop-MCMC (θ_i)	Error (%)	$\frac{\sigma_i}{\theta_i}$ c.o.v (%)
θ_1	4600	4010	14.71	4003.0	0.17	1.02
θ_2	2580	2210	16.74	2196.3	0.62	1.78
θ_3	1680	2130	21.13	2113.0	0.8	1.97
θ_4	3100	2595	19.46	2605.4	0.4	2.40
θ_5	2350	2398	02.00	2408.5	0.44	2.10

Table 24.2 The updated natural frequencies and the errors obtained by the Pop-MCMC

Modes	Nominal Frequency (Hz)	Initial Frequency (Hz)	Error (%)	Frequency Pop-MCMC (Hz)	c.o.v (%)	Error (%)
1	3.507	3.577	1.97	3.507	0.120	0.01
2	5.149	5.371	4.30	5.149	0.125	0.00
3	7.083	7.239	2.21	7.082	0.115	0.01
4	8.892	9.030	1.56	8.894	0.116	0.02
5	9.426	9.412	0.16	9.426	0.128	0.00
TAE	_____	_____	2.04	_____	_____	0.04

**Fig. 24.4** The evaluation of the Total Average Error (*TAE*) at each iteration using the Pop-MCMC algorithm**Fig. 24.5** The correlation between the updating parameters

24.5 FEMU Problem 2: The Unsymmetrical H-Shaped Structural System

In this section, the performance of the Pop-MCMC method is investigated by updating an unsymmetrical H-shaped structure with real measured data. The FE model of the structure is shown in Fig. 24.6, where the structure is discretized into 12 finite elements, and each element is modelled as an Euler-Bernoulli beam. An electromagnetic exciter is attached at the middle

of the structure as indicated by the double arrow, and the response is measured by an accelerometer. The measured natural frequencies obtained by the modal test are: 53.9, 117.3, 208.4, 254.0, and 445.0 Hz. The cross-sectional area A_{xx} and the moment of inertia I_{xx} are chosen to be the updating parameters, where the selected elements are at left, middle, and right as displayed in Fig. 24.6. The updating vector is then: $\theta = \{I_{x1}, I_{x2}, I_{x3}, A_{x1}, A_{x2}, A_{x3}\}$.

The Young's modulus of the structural beam is set to 7.2×10^{10} N/m², and the density is 2785 kg/m³. The updating vector θ is bounded by: $[4.73 \times 10^{-8}, 4.73 \times 10^{-8}, 4.73 \times 10^{-8}, 5.16 \times 10^{-4}, 5.16 \times 10^{-4}, 5.16 \times 10^{-4}]$ and $[0.73 \times 10^{-8}, 0.73 \times 10^{-8}, 0.73 \times 10^{-8}, 1.16 \times 10^{-4}, 1.16 \times 10^{-4}, 1.16 \times 10^{-4}]$, respectively. The updating boundaries are used to ensure that the parameters obtained are realistic. The number of samples is set to $T = 5000$, the crossover probability is $m_{CR} = 2$, and the selected number of the chain pairs is $e = 3$. The values of $\sigma = [5 \times 10^{-8}, 5 \times 10^{-8}, 5 \times 10^{-8}, 5 \times 10^{-4}, 5 \times 10^{-4}, 5 \times 10^{-4}]$.

The Pop-MCMC results of the updating parameters are given in Table 24.3 along with the results of the M-H algorithm. Clearly, the obtained results for both algorithms are different from the initial parameters, which indicates that both algorithms have successfully updated the structure. The c.o.v values of the updating parameters found by the Pop-MCMC are small (<3.0 %) while c.o.v values obtained by the M-H algorithm are relatively high (>13.0 %). This means that the Pop-MCMC has performed well in identifying the high probability area. Furthermore, the results show that the Pop-MCMC algorithm performed better than the M-H method.

Table 24.4 presents natural frequencies determined by the Pop-MCMC and M-H algorithms, the c.o.v values and the errors. As expected, the natural frequencies found by the Pop-MCMC algorithm are more accurate than the initial and the M-H frequencies. The Pop-MCMC has corrected the FEM and minimized the TAE from 5.37% to 0.81%, while the M-H algorithm was only able to reduce the total error to 3.01%. Furthermore, the c.o.v values for Pop-MCMC are less than 1.6%, while M-H method produced a c.o.v values of 5.0%. In general, the results reveal the advantages of the Pop-MCMC algorithm in updating uncertain models.

The correlations between the updating parameters are shown in Fig. 24.7. As shown, the majority of the parameters are weakly correlated except the pair (θ_1, θ_5) where the correlation for this pair is 0.65.

In Fig. 24.8, the evaluation of the total average error of the generated samples is illustrated where the Pop-MCMC algorithm has started to converge after 500 iterations.

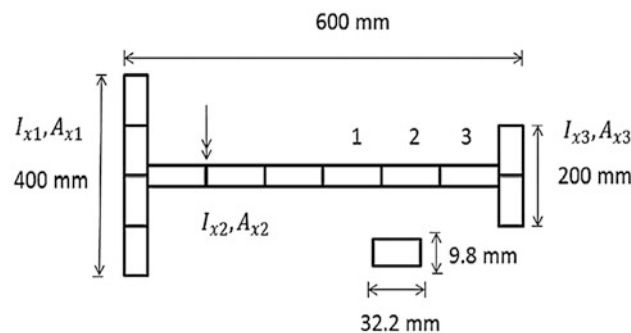


Fig. 24.6 The unsymmetrical H-shaped structure

Table 24.3 The initial and the updating parameters with the c.o.v values using the Pop-MCMC and M-H algorithms

	Initial	Pop-MCMC (θ_i)	$\frac{\sigma_i}{\theta_i}$ (%)	M-H (θ_i)	$\frac{\sigma_i}{\theta_i}$ (%)
θ_1	2.7265×10^{-8}	2.8043×10^{-8}	1.02	2.31×10^{-8}	22.59
θ_2	2.7265×10^{-8}	2.6861×10^{-8}	1.78	2.68×10^{-8}	15.25
θ_3	2.7265×10^{-8}	2.6873×10^{-8}	1.97	2.17×10^{-8}	13.96
θ_4	3.1556×10^{-4}	3.3756×10^{-4}	2.48	2.85×10^{-4}	14.36
θ_5	3.1556×10^{-4}	2.4104×10^{-4}	2.93	2.83×10^{-4}	14.36
θ_6	3.1556×10^{-4}	3.0143×10^{-4}	1.84	2.77×10^{-4}	13.08

Table 24.4 Natural frequencies, c.o.v values and errors for updating parameters using the Pop-MCMC and M-H techniques

Modes	Measured Frequency (Hz)	Initial Frequency (Hz)	Error (%)	Frequency Pop-MCMC (Hz)	c.o.v (%)	Error (%)	Frequency M-H (Hz)	c.o.v (%)	Error (%)
1	53.90	51.04	5.31	52.71	0.89	2.19	53.92	3.96	0.04
2	117.30	115.79	1.29	118.04	0.98	0.62	122.05	4.28	4.05
3	208.40	199.88	4.09	206.44	1.30	0.94	210.93	4.95	1.22
4	254.00	245.76	3.25	254.08	1.23	0.03	258.94	4.81	1.94
5	445.00	387.53	12.92	446.31	1.55	0.29	410.33	4.74	7.79
TAE			5.37			0.81			3.01

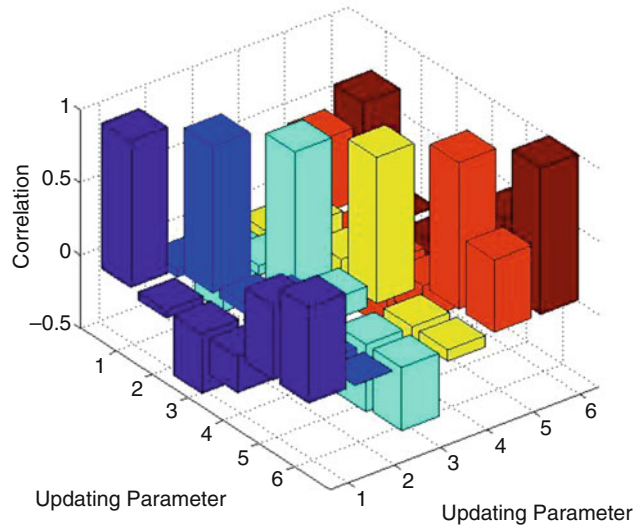


Fig. 24.7 The correlation between the updating parameters obtained by the Pop-MCMC algorithm

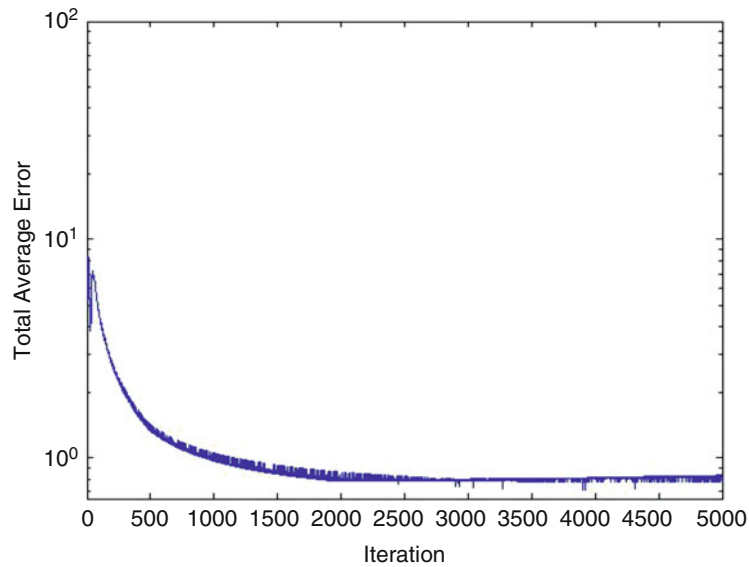


Fig. 24.8 The evaluation of the TAE using the Pop-MCMC method

24.6 Conclusion

In this paper, the Population Markov Chain Monte Carlo algorithm (Pop-MCMC) is used to sample from the posterior distribution function in order to update FEMs. The Pop-MCMC method is a population-based stochastic search algorithm that allows the Markov chains to exchange information between each other at the population level. The algorithm employs improved versions of the genetic operators; probabilistic crossover and adaptive mutation. The performance of the Pop-MCMC in updating FEMs is tested by updating two structural examples. The first structure is a five-degree of freedom mass-spring system, and the algorithm was able to reduce total average error from 2.04% to 0.04%. The second structure is an unsymmetrical H-shaped structure, and the algorithm's results were compared with results obtained by the M-H method. Furthermore, the Pop-MCMC algorithm has delivered more efficient results than the results obtained by the M-H method; the Pop-MCMC algorithm has reduced the total average error of the updated frequencies to 0.81% while the M-H algorithm reduced the total average error to only 3.01%. In future work, more improved versions of the Pop-MCMC algorithm will be introduced and investigated in updating FEMs.

References

1. Dhatt, G., Lefranç, E., Touzot, G.: Finite Element Method. Wiley, London (2012)
2. Bathe, K.J.: Finite element method. In: Wiley Encyclopedia of Computer Science Engineering, pp. 1–12. Wiley, New York (2007)
3. Friswell, M.I., Mottershead, J.E.: Finite Element Model Updating in Structural Dynamics. Springer Science & Business Media, New York (2013)
4. Marwala, T.: Finite Element Model Updating Using Computational Intelligence Techniques: Applications to Structural Dynamics. Springer Science & Business Media, London (2010)
5. Andrieu, C., Doucet, A., Holenstein, R.: Particle Markov Chain Monte Carlo methods. *J. R. Stat. Soc. Ser. B.* **72**(3), 269–342 (2010)
6. Brooks, S., Gelman, A., Jones, G., Meng, X.-L.: Handbook of Markov Chain Monte Carlo. CRC Press, London (2011)
7. Chib, S., Greenberg, E.: Understanding the Metropolis-Hastings algorithm. *Am. Stat.* **49**(4), 327–335 (1995)
8. Chib, S., Jeliazkov, I.: Accept-reject Metropolis-Hastings sampling and marginal likelihood estimation. *Statistica Neerlandica.* **59**(1), 30–44 (2005)
9. Snoek, J., Larochelle, H., Adams, R.P.: Practical Bayesian optimization of machine learning algorithms. In: Advances in Neural Information Processing Systems, pp. 2951–2959. Neural Information Processing Systems, La Jolla (2012)
10. Oh, S., Russell, S., Sastry, S.: Markov Chain Monte Carlo data association for multi-target tracking. *IEEE Trans. Autom. Control.* **54**(3), 481–497 (2009)
11. Boulkaibet, I.: Finite Element Model Updating Using Markov Chain Monte Carlo Techniques. University of Johannesburg, Johannesburg (2014)
12. Boulkaibet, I., Marwala, T., Friswell, M.I., Adhikari, S.: An adaptive Markov Chain Monte Carlo method for Bayesian finite element model updating. In: Special Topics in Structural Dynamics, vol. 6, pp. 55–65. Springer, Cham (2016)
13. Zitzler, E., Laumanns, M., Thiele, L.: SPEA2: Improving the strength Pareto evolutionary algorithm. TIK-report, vol. 103, (2001)
14. Han, K.-H., Kim, J.-H.: Quantum-inspired evolutionary algorithm for a class of combinatorial optimization. *IEEE Trans. Evol. Comput.* **6**(6), 580–593 (2002)
15. Zhang, Q., Li, H.: MOEA/D: a multiobjective evolutionary algorithm based on decomposition. *IEEE Trans. Evol. Comput.* **11**(6), 712–731 (2007)
16. Mockus, J.: Bayesian Approach to Global Optimization: Theory and Applications. Springer Science & Business Media, Dordrecht (2012)
17. Boulkaibet, I., Marwala, T., Mthembu, L., Friswell, M.I., Adhikari, S.: Sampling techniques in Bayesian finite element model updating. In: Topics in Model Validation and Uncertainty Quantification, vol. 4, pp. 75–83. Springer, New York (2012)
18. Laskey, K.B., Myers, J.W.: Population Markov Chain Monte Carlo. *Mach. Learn.* **50**(1–2), 175–196 (2003)
19. Myers, J.W., Laskey, K.B., Levitt, T.: Learning Bayesian networks from incomplete data with stochastic search algorithms. In: Proceedings of the Fifteenth Conference on Uncertainty in Artificial Intelligence, pp. 476–485. Morgan Kaufmann Publishers Inc (1999)
20. Hoyt, P.J.: Discretization and Learning of Bayesian Networks using Stochastic Search, with Application to Base Realignment and Closure (BRAC). PhD Thesis, George Mason University, USA (2008)
21. Myers, J.W.: Stochastic algorithms for learning with incomplete data: an application to Bayesian networks. PhD Thesis, George Mason University, USA (1999)
22. Boulkaibet, I., Mthembu, L., Marwala, T., Friswell, M.I., Adhikari, S.: Finite element model updating using an evolutionary Markov chain Monte Carlo algorithm. In: Dynamics of Civil Structures, vol. 2, pp. 245–253. Springer, Cham (2015)
23. Sherri, M., Boulkaibet, I., Marwala, T., Friswell, M.I.: A differential evolution Markov chain Monte Carlo algorithm for Bayesian model updating. In: Special Topics in Structural Dynamics, vol. 5, pp. 115–125. Springer, Cham (2019)

Marwan Sherri is a PhD candidate in the Department of Mechanical Engineering Science at the University of Johannesburg. His Research focuses on the Finite Element Model Updating Techniques. He has an MSc and BSc of Mechanical Engineering from Jordan.



Chapter 25

Modal Analysis of the Box Assembly with Removable Component in Two Configurations

Levi H. Manring, Brian P. Mann, and John F. Schultze

Abstract To ensure accurate predictions of behavior and life-cycle of components in their real-use environment, it is essential to develop accurate simulation and testing procedures that reflect such an environment. For components on machines that experience a significant dynamic environment (such as airplanes, missiles, and automobiles), creating testing procedures that accurately mimic such a complex and harsh environment is a significant challenge. Often, testing a system by subjecting it to its operating environment is prohibitive due to cost and testing limitations. Thus, the usefulness of bench testing components through a testing procedure that mimics an operating environment is clear. Structural environmental testing is typically performed using a shaker to apply an environment to a component. However, shaker testing is currently limited in its ability to recreate environments because it often involves excitation in only one axis, when the system experiences a six degree of freedom excitation in practice. Additionally, there are many issues in matching boundary conditions in environmental testing.

This paper seeks to explore environmental testing on a simple structure called the “Box Assembly with Removable Component” (BARC). Results from modal testing of the structure will investigate the structures mode shapes, damping, and natural frequencies in a free-free configuration and a fixed-base configuration (mounted to a shaker table). This paper will present a comparison of the mode shapes in these two configurations as well as reciprocities from the modal testing to give further insight into the impedance mismatch between these configurations. Additionally, results from uniaxial shaker excitation of the BARC structure in three axes will be presented. Understanding the differences in dynamics between the two configurations gives insight into how the BARC shaker testing can be understood to more accurately reflect an operational environment.

Keywords Modal analysis · Multiaxial testing · Environmental testing · BARC

25.1 Introduction and Background

In order to qualify components for field use, it is helpful to accurately test them in a laboratory setting. This is particularly important when testing in the field is cost-prohibitive and limited in scope. Mimicking an operating environment in a laboratory is not a trivial objective. Often, the qualification for components is fatigue-based. If fatigue life can be accurately estimated in a cost-effective way, that is extremely useful in predicting the performance of components. Typically, an operating environment involves 6 degree-of-freedom (DOF) excitation. Component vibration testing is typically performed with shakers and there are hardware challenges and costs in creating shakers that can excite components in more than 1DOF at a time. Thus, most laboratory component testing involves single-axis excitation, which has been shown to poorly recreate the stresses and corresponding fatigue in components as compared to more advanced triaxial or multiaxial testing strategies [1, 2]. In [3], the authors compared several techniques for estimating multiaxial vibration fatigue to accurately predict crack location and time-to-failure of a component. Using both experiment and theory, they achieved good results for predicting time-to-failure estimation, but did not have as conclusive results with crack location prediction. Matsubara’s

L. H. Manring (✉) · B. P. Mann

Department of Mechanical Engineering and Materials Science, Pratt School of Engineering, Duke University, Durham, NC, USA
e-mail: levi.manring@duke.edu; brian.mann@duke.edu

J. F. Schultze

Los Alamos National Laboratory, Weapons Test Engineering E-14, Los Alamos, NM, USA
e-mail: schultze@lanl.gov

damage criterion, which relies on crack initiation and crack growth, was used to predict fatigue damage with high accuracy in [4]. Since this method has only been applied for constant amplitude loading, the authors proposed an extension of the criterion to accommodate random vibration excitation with all necessary parameters calculated from the stress power spectral densities (PSD's). One of the most common methods for estimating stress in a component is the equivalent von Mises stress criterion, and in [5] analytical expressions were obtained to estimate the accuracy of this criteria for multiaxial fatigue calculations and intervals of applicability were defined. It is useful to evaluate multiaxial damage criterion in the frequency domain for computational efficiency and in [6], fatigue damage was determined using the Sines multiaxial fatigue damage criterion in the frequency domain, which provided damage information for each element in a finite element model. In [7], seven different frequency-domain methods were compared to determine the accuracy of fatigue life predictions and their resistance to challenging structural testing issues.

While understanding the fatigue performance of a structure is an essential part of laboratory component testing, one of the challenging issues with recreating operating environments in a laboratory is the issue of control. Typically, there is some reference response(s) that defines the operating environment and to recreate the environment on a shaker-table, a control scheme must be devised. In random vibration testing, often the control signal is stationary and Gaussian, but in [8, 9] the authors demonstrated that a non-stationary non-Gaussian random vibration control strategy can produce a different fatigue life, in spite of the fact that these two control reference PSD's are the same. In [10, 11], methods for generating the drive profiles for multiaxial vibration tables were presented, and in [11] a complex fatigue environment of sine on random vibration was presented along with a control strategy to achieve this environment. In an attempt to minimize the physical demands on a multiaxial vibration table, the authors of [12] developed a control procedure to minimize the actuator demands to match the reference PSD's for multi-axis testing. By minimizing the physical demands on the shaker, there was the ability to potentially test a component at a higher level.

The BARC structure was designed as a test case for improving aspects of environmental testing, such as fatigue life estimation accuracy, multiaxial control, and overcoming impedance mismatching from differences in boundary condition configurations between laboratory and operating environment. In [13], the BARC was used to demonstrate that the boundary condition of the removable component is directionally dependent, thus nonlinear, and the principle of superposition does not apply. The use of piezoelectric patches was demonstrated to ensure repeatability in recreating boundary conditions for testing the BARC in [14]. Using electromechanical impedance, the authors sought to identify inconsistencies in testing configurations. Transfer path analysis techniques, which perform well for complex systems with closely spaced modes and high damping, were used in [15] to gain insight into the vibration transmission from the source excitation throughout the BARC structure. Preliminary modal testing of the BARC was performed in [16] along with FEA simulations. An attempt to match the dynamics of a BARC with a modified BARC where the box assembly has been additively manufactured was presented in [17], in which an open loop control scheme and three different boundary conditions were used. The impedance mismatch of different boundary conditions was further studied in [18], where FEA modal parameters were evaluated against experimental modal analysis to determine consistency and further tested with different boundary conditions. A variation of the BARC fixture was examined in [19], in which the box assembly was cut in half and studied with different geometric parameters to match impedances. The BARC has also been used to examine fatigue life. Multiple single-axis tests were used in [20] to estimate the lifetime of the BARC using Miner's rule, and an assessment of over-testing or under-testing the structure demonstrated the possible performance of this accumulated lifetimes estimation technique. A laser-doppler-vibrometer was used in [21] to extract full-field strain estimation from testing of the BARC to understand the fatigue experienced during testing. A thorough study to recreate an operational environment was performed in [22] using data from commercial scooter vibration. The authors used both accelerometer and strain measurements to obtain reference PSD's and performed both uniaxial and tri-axial testing on the BARC structure with good results. Finally, a compilation of modal parameters of the BARC as determined by multiple contributing research organizations was presented in [23], along with corresponding testing methods.

This paper seeks to study the BARC's behavior in two different boundary condition configurations and compare their modal parameters and shapes. These configurations are free-free and fixed-base. This comparison is useful when there are inherent differences between the laboratory test configuration and the operating environment configuration. For instance, it is difficult to controlled-input vibration testing without mounting the component in question to a shaker, but that configuration is inherently different than a free-free configuration. Additionally, results from single-axis shaker testing in the X, Y, and Z directions will be presented.

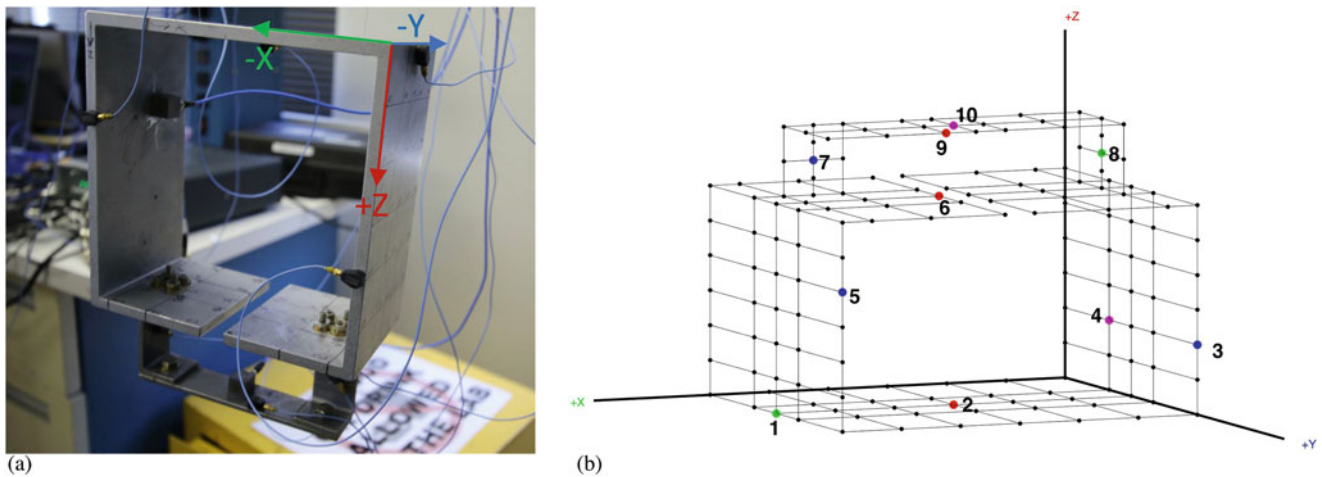


Fig. 25.1 (a) Free-free modal testing configuration. (b) A nodal depiction of the BARC free-free configuration. X, Y, and Z axis accelerometer measurement locations are depicted in green, blue, and red, respectively. Tri-axial accelerometer measurements are depicted in magenta

25.2 Experimental Setup and Procedure

To better understand the structural dynamics of the BARC, the structure was subjected to modal testing in two configurations of free-free and fixed-base. The BARC was suspended upside-down from two loops made of fishing line to approximate a free-free configuration. Fourteen accelerometer channels were measured in different locations and directions on the structure. A picture of the test setup can be seen in Fig. 25.1 and a diagram of the testing locations and directions can be seen in Fig. 25.1b.

The nodal depiction shown in Fig. 25.1b includes 158 nodes. The dynamic response of the system was measured with an impact hammer to provide an impulse force upon the BARC and the response was measured with accelerometers. In each case, the BARC was impacted normal to the surface and all measurements were taken normal to the surface. Considering the fact that nodes on the edges of the BARC can be impacted in two directions and nodes on the corners can be impacted in all three, there were 260 impact tests. Thus, a corresponding 260 frequency response functions (FRF's) were generated. The modal test was completed using an LMS Scadas Mobile 2-card data acquisition system interfacing with Siemen's Simcenter Testlab software.

In fixed-base modal testing, shown in Fig. 25.2, the BARC was attached by four bolts to a shaker table. The table had a 1-inch grid, and the four bolts formed a 3-inch by 1-inch rectangle, slightly off-center from the central X-Z plane, consistent with planned future testing. Each bolt was torqued to 33 inch-pounds. Only twelve accelerometer channels were used in this modal test, with locations 1–6 and 10 in common with the free-free testing. The nodal depiction can be seen in Fig. 25.2b. The fixed-base configuration was tested in a similar manner as the free-free configuration. There were some nodes on the side of the BARC closest to the shaker (see Fig. 25.2) which were unreachable by the impact hammer, but otherwise the testing was the same. For this reason, and the fact that the underside of the base was also unreachable due to its contact with the shaker table, the total number of impact tests was 238.

To further understand the dynamics of the BARC structure, the structure was subjected to single-axis shaker testing in the X, Y, and Z directions. Figure 25.2 depicts the BARC mounted for shaker testing in the X-direction. The Y-directional testing configuration can be seen in Fig. 25.3. The testing in the Z-direction was performed by decoupling the shaker from the table, rotating it 90 degrees, and attaching an expander head for mounting it vertically, shown in Fig. 25.3b.

The same data acquisition setup and software used for modal testing was implemented using a random vibration control strategy. For each directional configuration, two different control locations were used. An accelerometer was placed on the table (or expander head), directly next to the BARC, as one control location. The second control location was the tri-axial accelerometer at location 10 on the removable component (see Figs. 25.1B and 25.2B). As a determination of repeatability, each directional test was completed with at least two different RMS levels and performed three times. An example of the reference control PSD profile and the measured response can be seen in Fig. 25.4.

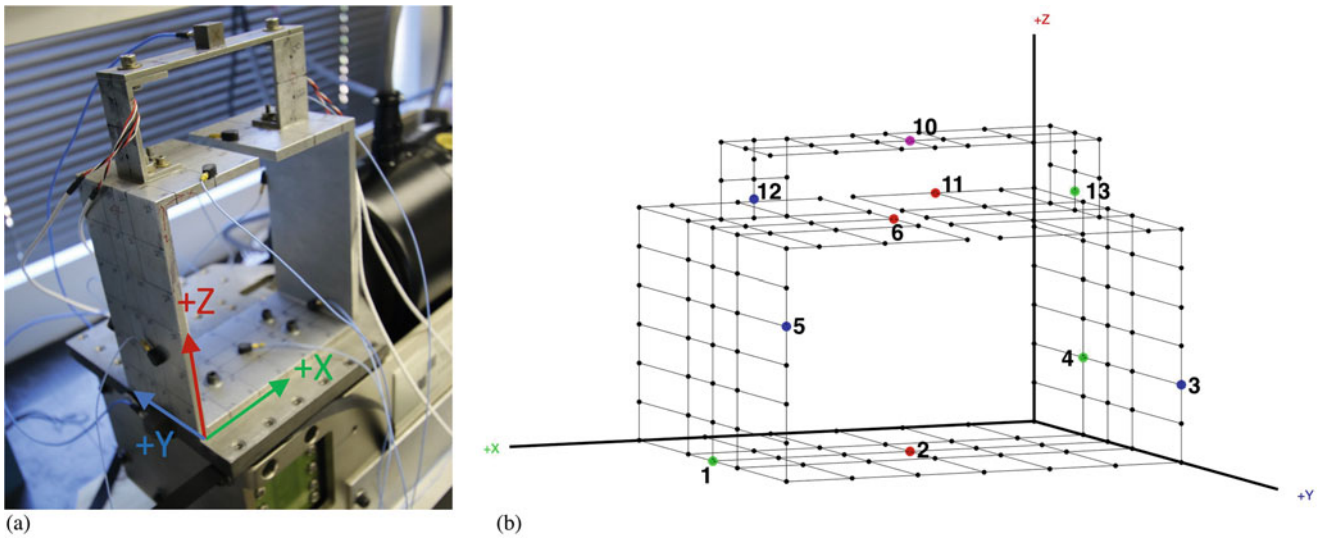


Fig. 25.2 (a) Fixed-base modal testing configuration. (b) A nodal depiction of the BARC fixed-base configuration. X, Y, and Z axis accelerometer measurement locations are depicted in green, blue, and red, respectively. Tri-axial accelerometer measurements are depicted in magenta

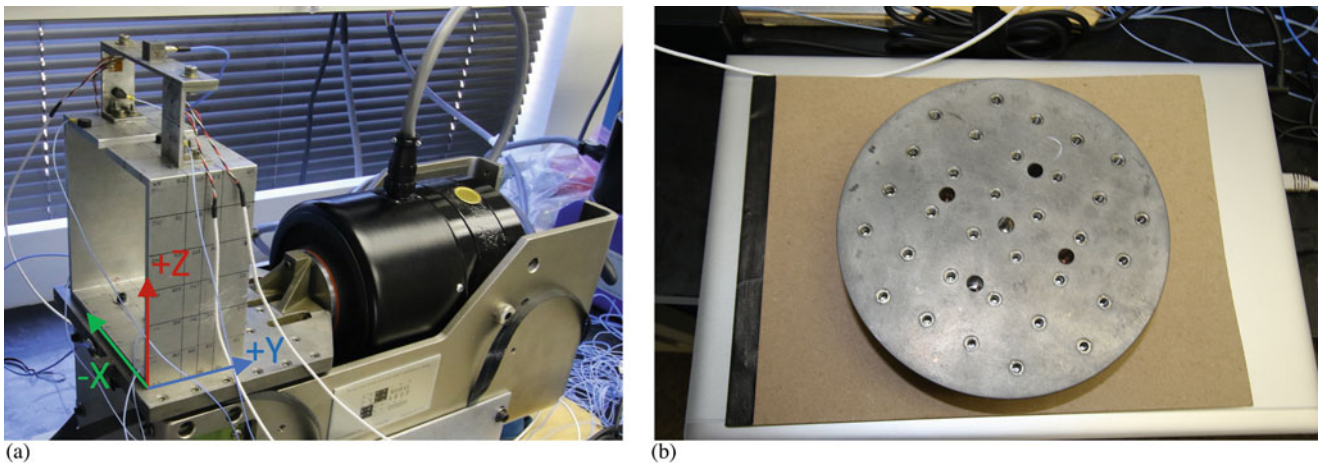


Fig. 25.3 (a) The BARC mounted to the shaker table for single-axis testing in the Y-direction. (b) The expander head used for single-axis testing in the Z-direction

25.3 Modal Results and Comparison

One of the key reasons for performing modal testing in the two configurations of free-free and fixed-base is to examine the key dynamic differences between them. This vibration test, the BARC was mounted in a fixed-base configuration. However, if the BARC is to mimic the environment experienced by a rocket or missile, which has a nearly perfect free-free configuration when it is flying through the air, boundary conditions will be inherently different. Thus, a comparison between the dynamic response in both of these configurations proves useful. From the impact tests of the BARC structure in the free-free and fixed-base configurations, modal parameters of the structure were extracted using Simcenter Testlab to select modes and fit an analytical model to the experimental data. Upon an initial examination of the data, it is clear that the dynamic properties of these two configurations are considerably different. By simply summing the FRF's and then normalizing the result, it can be seen that the frequency response of the BARC changes significantly between these two configurations.

Figure 25.5 shows the fixed-base configuration has modes at lower frequencies. The reason for this is that the shaker table adds some low-frequency modes since it has the ability to move during the modal test. The analytical model matched the experimental data very well for the free-free configuration across the entire frequency bandwidth but a good fit for the fixed-free configuration only was achieved up to ~ 1000 Hz. Table 25.1 shows the complete modal parameters for the first fourteen modes of each configuration.

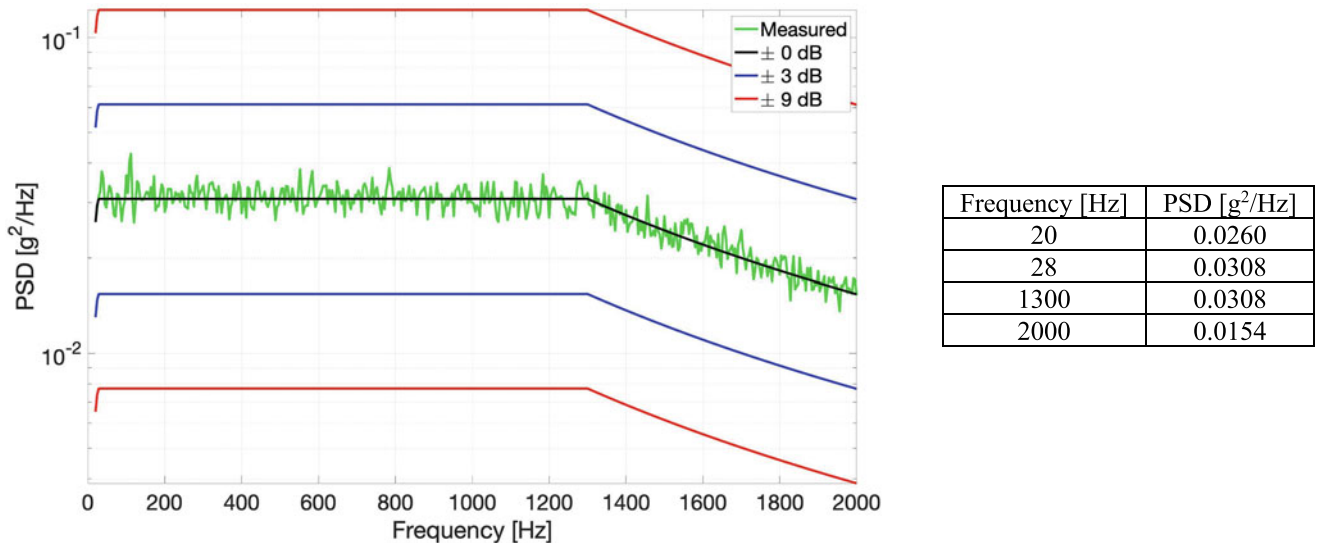


Fig. 25.4 Left: A control reference profile and measured response for shaker testing in the X-direction (RMS of ~0.75). Right: tabular values for the 0 dB profile

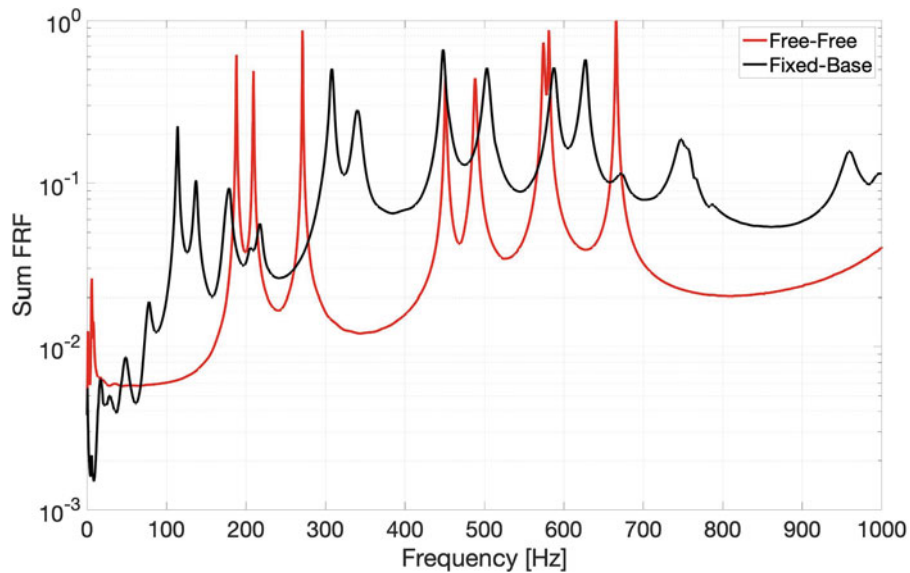


Fig. 25.5 The normalized sum of the FRF's for the free-free and fixed base configurations

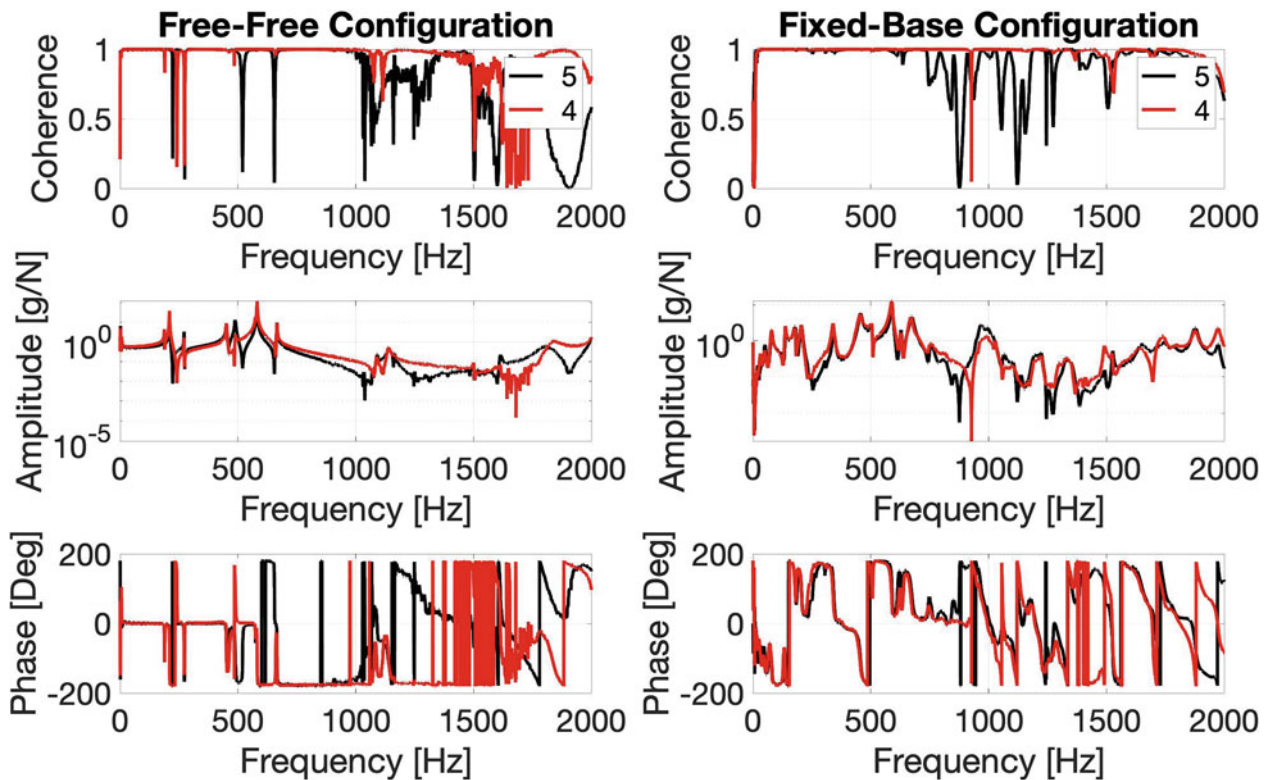
From Table 25.1, it is apparent that the damping of the fixed-base configuration is significantly higher across the board, approximately 5x higher than the free-free configuration. This is to be expected since the BARC is mounted to the shaker table, which allows more energy dissipation from the structure. This is because the shaker table adds damping and mechanical impedance to the response of the system.

Additional insight into the dynamics of the BARC structure can be gained through examining its reciprocity. Reciprocity of a structure is obtained by impacting at location A and measuring at location B, and comparing that FRF to one obtained by impacting at location B and measuring at location A. This gives an understanding for path dependency in energy transfer through the structure in question. Figures 25.6 and 25.7 show reciprocity results between two sets of locations on the BARC.

In Fig. 25.6, one important thing to note is that this reciprocity is for a set of cross-axes measurements, with location 4 measured in the X-direction and location 5 measured in the Y-direction. The Y-axis of the BARC is much stiffer than the other two axes, so motion in that direction is more difficult to capture. That may explain why at higher frequencies the coherence drops off. Overall, it appears that from these two representative reciprocity plots, the BARC does not appear to have significant path dependencies in transfer of energy through the structure. Figure 25.6 shows reciprocity for two measurements

Table 25.1 Modal parameters for the free-free and fixed base configurations

Mode #	Free-Free Configuration		Fixed-Base Configuration	
	Damping (%)	Frequency (Hz)	Damping (%)	Frequency (Hz)
1	0.16	187.8984	0.86	113.8567
2	0.17	209.2959	1.40	136.6946
3	0.07	271.1764	1.62	179.3960
4	0.19	451.0619	2.00	216.8512
5	0.29	488.4713	0.62	307.8149
6	0.21	574.4055	1.48	337.7893
7	0.11	581.1963	0.43	448.0270
8	0.09	665.8117	1.05	501.9830
9	0.31	1089.4229	0.55	587.2299
10	0.48	1138.7169	0.50	626.5261
11	0.13	1500.7744	0.87	674.4678
12	0.17	1614.0525	0.87	747.3193
13	1.14	1837.5115	0.93	756.0956
14	4.05	2008.8539	0.37	764.5404

**Fig. 25.6** Reciprocity between locations 4 and 5

taken in the Z-direction at different locations. The dynamic complexity of the fixed-base configuration compared to the free-free configuration can be seen in Figs. 25.6 and 25.7, particularly in the 0–500 Hz bandwidth.

At this point in our modal analysis study of the BARC, we know that the structure has different modal properties between the two configurations in question and what those modal properties are. It is of interest to know which modes in the free-free configuration correspond to modes in the fixed-base configuration. This would also give insight into knowing which modes in the fixed-base results are the result of shaker table dynamics. To achieve this goal, the Modal Assurance Criterion (MAC) calculation [24] can be performed on the modes obtained from each configuration to determine correlation between mode shapes. The procedure for obtaining mode shape correlation between these configurations is as follows. First, only FRF's in common between the two configurations are used, since measurement locations 1–6 and 10 are in common and

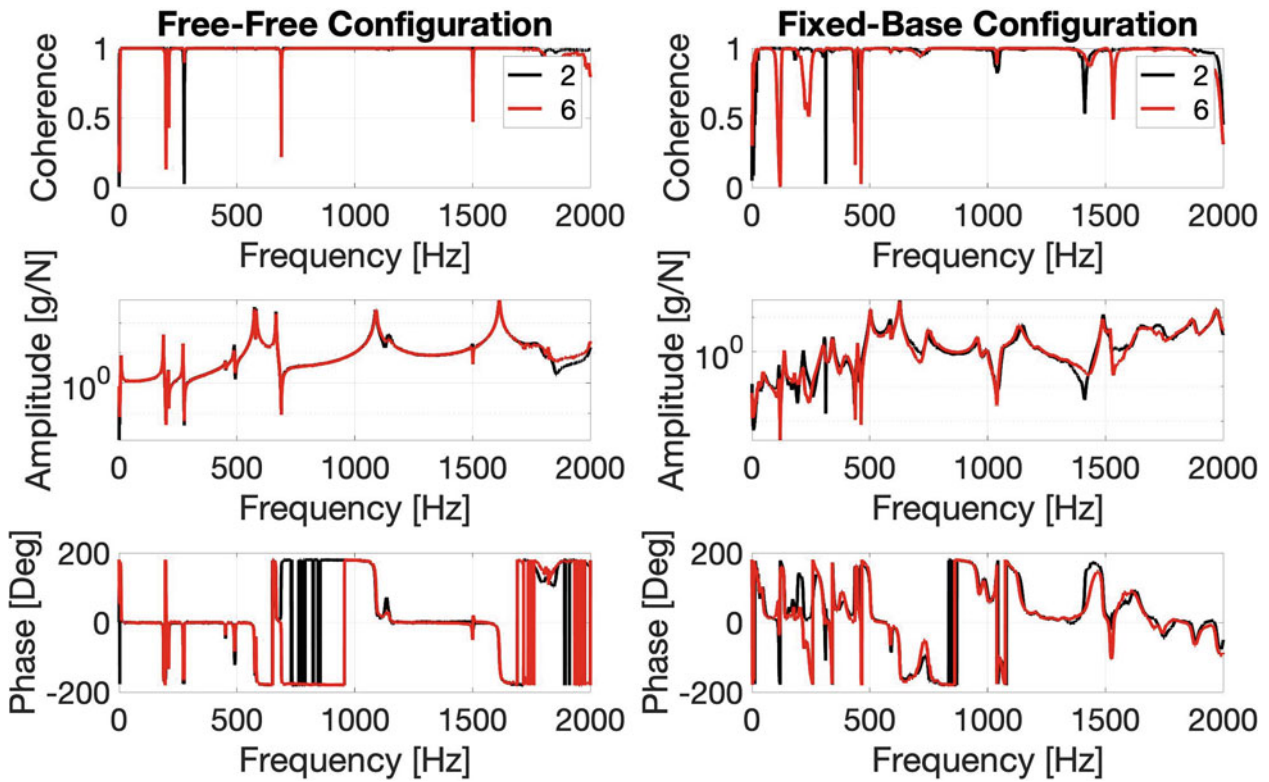


Fig. 25.7 Reciprocity between locations 2 and 6

Table 25.2 Correlated mode shapes between the free-free and fixed-base configurations

Free-Free Mode #	Fixed-Base Mode #
1	4
2	6
3	5
4	7
5	7
6	10
7	9
8	12
8	13
8	14
9	5

certain areas of the fixed-base test were unreachable by an impact hammer. By extracting the imaginary component of the FRF's at each eigen-frequency, a matrix of eigenvectors $M_{configuration}$ can be obtained for each measurement location. This matrix M is of size $m \times n$, where m is the number of common FRF's and n is the number of eigen-frequencies, which is in this case, fourteen. The reason this is performed for each measurement location is that one measurement location may capture aspects of mode shapes that might not be captured by another. For instance, this is true for torsional modes, which would primarily be captured by measurements in the Y-direction at locations 3 and 5. By finding the MAC between $M_{free - free}$ and $M_{fixed - base}$, we can determine which modes are strongly correlated by finding which rows and columns correspond to element of the MAC are greater than some specified correlation criterion value, $c = 0.6$. The resulting correlated mode shapes as determined by this MAC calculation can be seen in Table 25.2.

While Table 25.2 is the resulting mathematical result of a MAC calculation comparing mode shapes from the free-free configuration and the fixed-base configuration, it is useful to validate these findings by visually comparing mode shapes to see if indeed the modes appear to be correlated.

In Figs. 25.8, 25.9 and 25.10, the first 3 mode shape correlations from Table 25.2 are visually compared, confirming the MAC prediction of correlation between free-free and fixed-base modes. The consistent “dimple” in the top of the fixed-

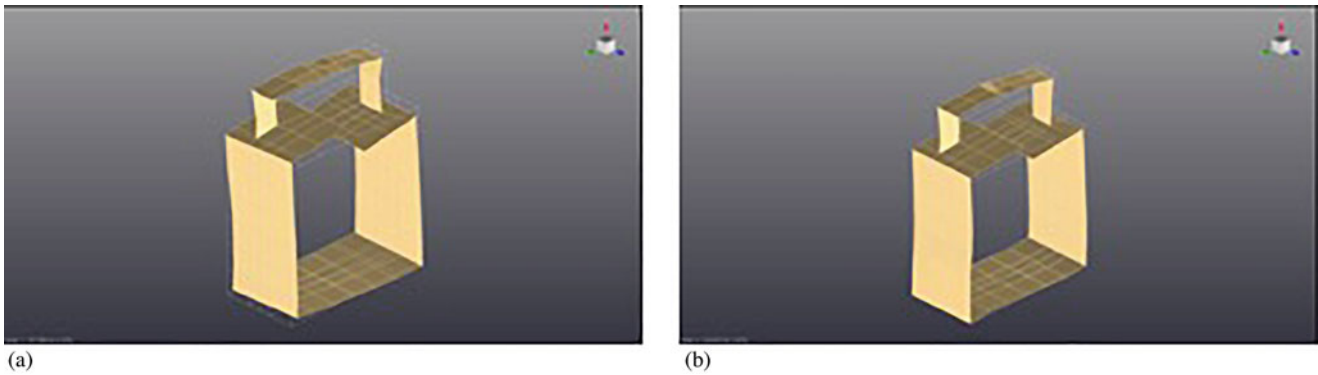


Fig. 25.8 (a) Free-free configuration mode shape 1. (b). Fixed-base configuration mode shape 4

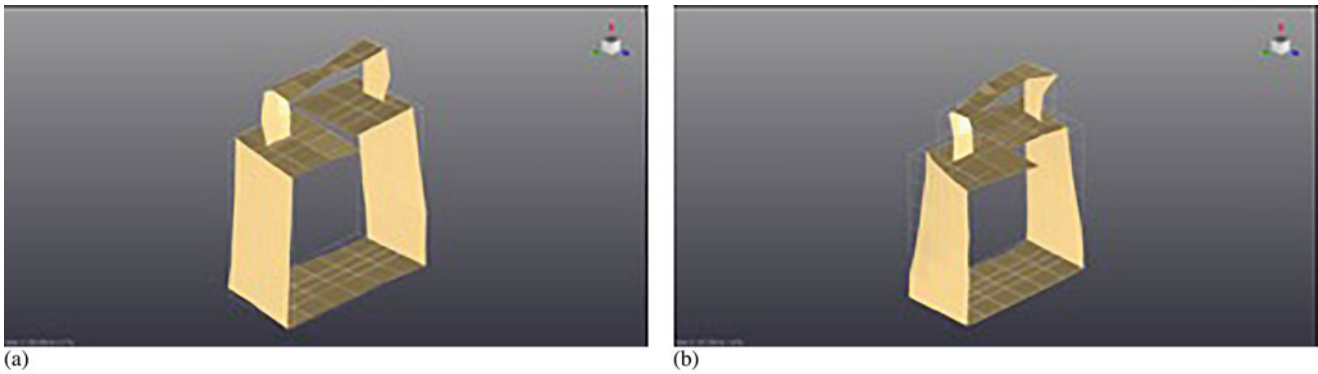


Fig. 25.9 (a) Free-free configuration mode shape 2. (b) Fixed-base configuration mode shape 6

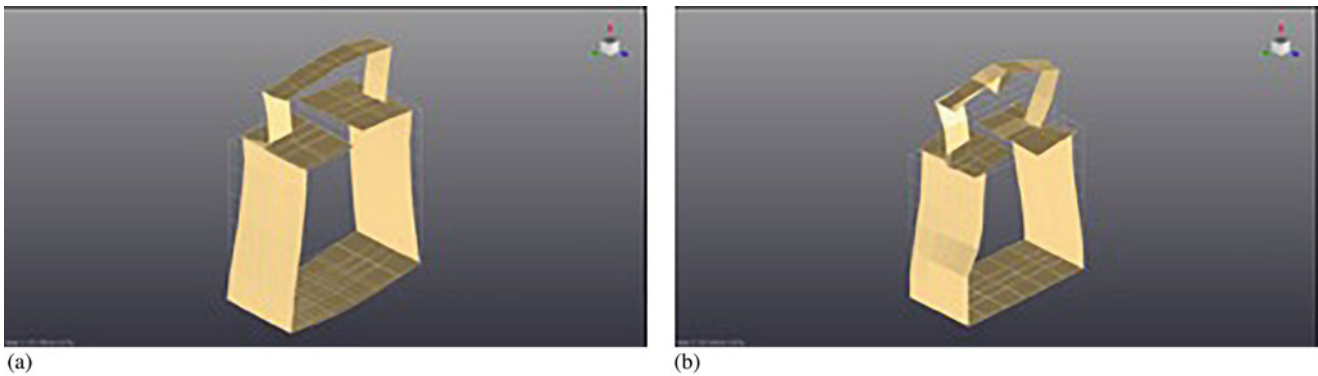


Fig. 25.10 (a) Free-free configuration mode shape 3. (b) Fixed-base configuration mode shape 5

base visualization is the result of not being able to perform an impact test at that node, thus it remains stationary in the visualizations. Figures 25.8 and 25.10 show bending modes in the X-direction that is well represented in both configurations. Figure 25.9 clearly shows a torsional mode. Since the modal correlation starts with mode 4 in the fixed-base configuration, it is likely that the first three modes in the fixed-base configuration are contributed by the shaker table.

25.4 Shaker Test Results

The relative motion between points on the BARC can be understood from shaker testing, in which the BARC was subjected to random excitation in X, Y, and Z axes separately. From the frequency response of the system in each direction, the transmissibility between locations on the BARC can be determined.

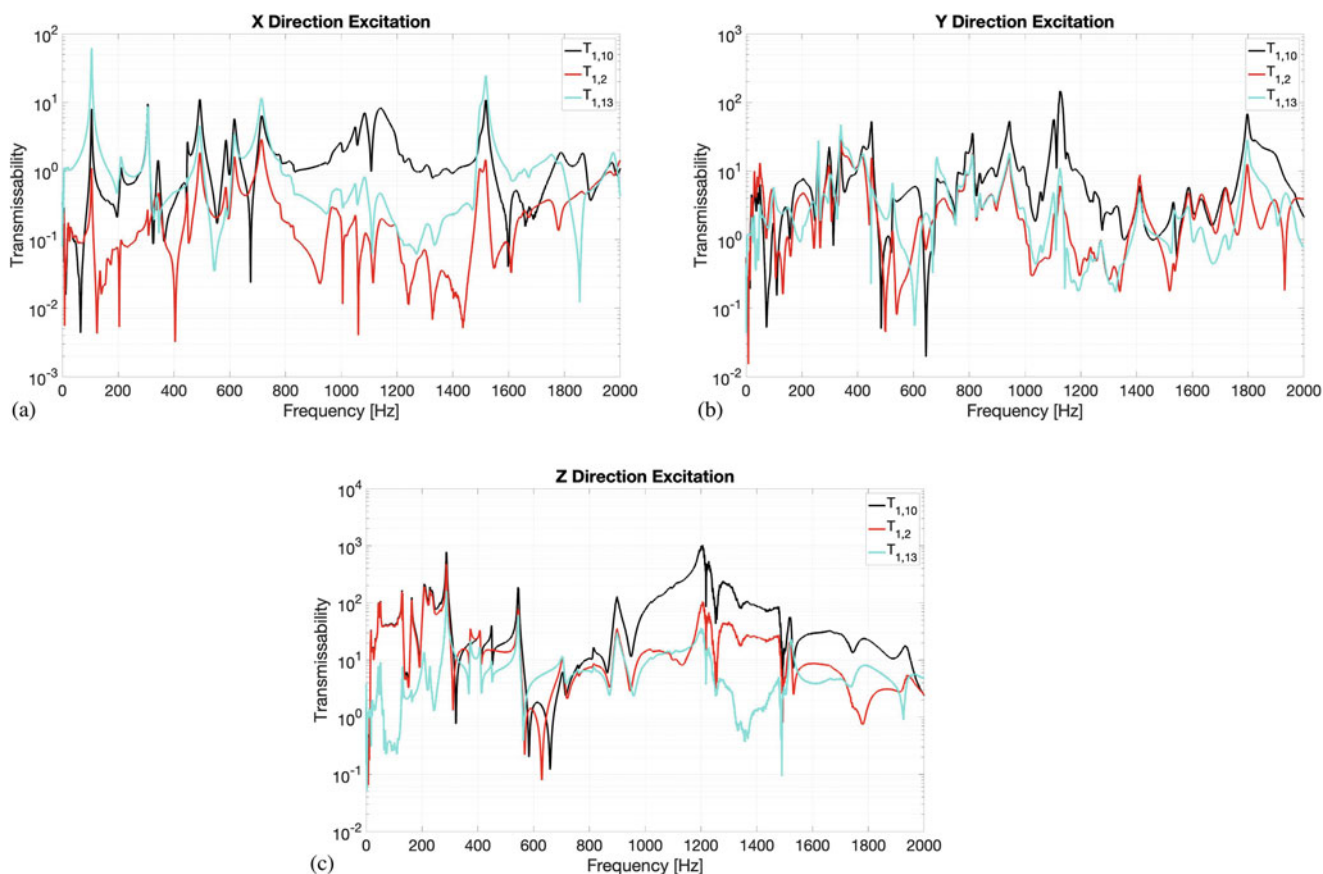


Fig. 25.11 Transmissibility from location 2 to locations 6, 10, and 11 in X, Y, and Z directions

Figure 25.11 shows the transmissibility between location 1 and locations 2, 10, and 13. For location 10, the accelerometer measurement considered is in the Z-direction. With some information about where these references are located, intuition about the dynamics of the structure can be confirmed. For example, locations 1 and 2 are on the base of the structure, which is fixed, so, it is expected that the relative motion between these two points would be very small. The X-direction transmissibility plot in the upper left corner of Fig. 25.11 shows that the relative motion between locations 1 and 2 is small, and between 1 and locations 10 and 13 is larger. This follows from intuition, since the upper part of the BARC is expected to flex much more than the rigid base. These transmissibility plots also show at what frequencies the motion of the BARC changes. In the Y-direction transmissibility plot in the upper right corner of Fig. 25.11, the motion of the BARC changes quite a bit. Unexpectedly there is larger motion between locations 1 and 2. It is possible due to the asymmetry of the mounting holes fixing the BARC to the shaker table that there is some rocking occurring. The motion between 1 and 13 stays relatively small here, most likely due to cross-axes excitation. We do expect location 10 to exhibit the most motion in general relative to the base, and that follows through each excitation direction. Finally, the Z-direction transmissibility plot shows quite substantial motion between locations 1 and 2. This may be due to the fact location 2 is measured in same direction as excitation in this case, thus it would likely have more motion than a measurement in the X-direction, such as location 1. Even though the X and Z directions are fairly coupled in motion on the BARC structure, location 1 is at a joint, which would prove to be quite rigid.

25.5 Conclusions and Future Work

In conclusion, this paper has sought to understand the dynamics of the BARC structure in two configurations: free-free and fixed-base. Modal analysis was used to determine the modal parameters of each configuration and a MAC calculation was used to correlate mode shapes between the two configurations. The result was that several of the first modes of the fixed-

base modal results can be contributed to the shaker, and a visual comparison of the mode shapes agreed with the numerical assessment of correlated modes. Furthermore, the BARC was tested using uniaxial random excitation in the X, Y, and Z directions to understand examine how it behaves in each direction. By examining the transmissibility plots for this testing, the relative motion of the BARC at different locations can be better understood as it depends on directional excitation.

Future endeavors in studying the BARC include recreating an operating environment in a laboratory setting using closed-loop control. This study of the dynamics of the BARC will prove useful in developing such a control loop and understanding its performance and possible weaknesses.

Acknowledgements Many thanks to the Los Alamos National Laboratory for funding this work as well as Siemens representative William Flynn for his assistance with Simcenter Testlab.

References

- Whiteman, W.E., Berman, M.S.: Fatigue failure results for multi-axial versus uniaxial stress screen vibration testing. *Shock. Vib.* **9**(6), 319–328 (2002)
- Aykan, M., Celik, M.: Vibration fatigue analysis and multi-axial effect in testing of aerospace structures. *Mech. Syst. Signal Process.* **23**(3), 897–907 (2009)
- Mršnik, M., Slavič, J., Boltežar, M.: Multiaxial vibration fatigue—a theoretical and experimental comparison. *Mech. Syst. Signal Process.* **76**, 409–423 (2016)
- Yaich, A., El Hami, A.: Multiaxial fatigue damage estimation of structures under random vibrations using Matsubara’s criterion. *Int. J. Fatigue.* **124**, 253–264 (2019)
- Benasciutti, D.: Some analytical expressions to measure the accuracy of the “equivalent von Mises stress” in vibration multiaxial fatigue. *J. Sound Vib.* **333**(18), 4326–4340 (2014)
- Yaich, A., et al.: Local multiaxial fatigue damage estimation for structures under random vibrations. *Finite Elem. Anal. Des.* **132**, 1–7 (2017)
- Mršnik, M., Slavič, J., Boltežar, M.: Frequency-domain methods for a vibration-fatigue-life estimation—application to real data. *Int. J. Fatigue.* **47**, 8–17 (2013)
- Zheng, R., et al.: Multiple-input multiple-output non-stationary non-Gaussian random vibration control by inverse system method. *Mech. Syst. Signal Process.* **124**, 124–141 (2019)
- Palmieri, M., et al.: Non-Gaussianity and non-stationarity in vibration fatigue. *Int. J. Fatigue.* **97**, 9–19 (2017)
- Kim, C.-J., Kang, Y.J., Lee, B.-H.: Generation of driving profile on a multi-axial vibration table for vibration fatigue testing. *Mech. Syst. Signal Process.* **26**, 244–253 (2012)
- Zheng, R., et al.: Generation of sine on random vibrations for multi-axial fatigue tests. *Mech. Syst. Signal Process.* **126**, 649–661 (2019)
- Musella, U., et al.: A minimum drives automatic target definition procedure for multi-axis random control testing. *Mech. Syst. Signal Process.* **107**, 452–468 (2018)
- Smith, S., Brake, M.: Effects of multi-axial versus single-axial excitation of jointed systems. In: *Sensors and Instrumentation, Aircraft/Aerospace, Energy Harvesting & Dynamic Environments Testing*, vol. 7, pp. 45–50. Springer, Cham (2020)
- Devine, T.A., Malladi, V.S., Tarazaga, P.A.: Electromechanical impedance method for applications in boundary condition replication. In: *Sensors and Instrumentation, Aircraft/Aerospace, Energy Harvesting & Dynamic Environments Testing*, vol. 7, pp. 93–96. Springer, Cham (2020)
- Harvie, J.M., van der Seijs, M.: Application of transfer path analysis techniques to the boundary condition challenge problem. In: *Sensors and Instrumentation, Aircraft/Aerospace, Energy Harvesting & Dynamic Environments Testing*, vol. 7, pp. 157–166. Springer, Cham (2020)
- Varoto, P.S.: Issues in laboratory simulation of field vibration data: experimental results on a typical structure. In: *Sensors and Instrumentation, Aircraft/Aerospace, Energy Harvesting & Dynamic Environments Testing*, vol. 7, pp. 347–354. Springer, Cham (2020)
- Rohe, D.P., et al.: Comparison of multi-axis testing of the barc structure with varying boundary conditions. In: *Sensors and Instrumentation, Aircraft/Aerospace, Energy Harvesting & Dynamic Environments Testing*, vol. 7, pp. 179–193. Springer, Cham (2020)
- Dilworth, B.J., Karlicek, A., Thibault, L.: An approach to component testing: an analytical study. In: *Sensors and Instrumentation, Aircraft/Aerospace, Energy Harvesting & Dynamic Environments Testing*, vol. 7, pp. 341–345. Springer, Cham (2020)
- Hall, T.M.: Analytically investigating impedance-matching test fixtures. In: *Sensors and Instrumentation, Aircraft/Aerospace, Energy Harvesting & Dynamic Environments Testing*, vol. 7, pp. 21–31. Springer (2020)
- Bouma, A., et al.: Accumulated lifetimes in single-Axis vibration testing. In: *Sensors and Instrumentation, Aircraft/Aerospace, Energy Harvesting & Dynamic Environments Testing*, vol. 7, pp. 131–146. Springer, Cham (2020)
- Witt, B., Rohe, D., Schoenherr, T.: Full-field strain shape estimation from 3D SLDV. In: *Rotating Machinery, Optical Methods & Scanning LDV Methods*, vol. 6, pp. 31–45. Springer, Cham (2019)

22. Musella, U., et al.: Combining test and simulation to tackle the challenges derived from boundary conditions mismatches in environmental testing. In: *Sensors and Instrumentation, Aircraft/Aerospace, Energy Harvesting & Dynamic Environments Testing*, vol. 7, pp. 259–269. Springer, Cham (2020)
23. Rohe, D.P., et al.: Testing summary for the box assembly with removable component structure. In: *Sensors and Instrumentation, Aircraft/Aerospace, Energy Harvesting & Dynamic Environments Testing*, vol. 7, pp. 167–177. Springer, Cham (2020)
24. Pastor, M., Binda, M., Harčarik, T.: Modal assurance criterion. *Proced. Eng.* **48**, 543–548 (2012)

Levi H. Manning is a third-year PhD student at Duke University studying adaptive dynamic control systems under the advisement of Dr. Brian Mann. He has ongoing work in collaboration with the Los Alamos National Laboratory in this research area and has spent two summers working there.



Chapter 26

Using the SWAT Method for Reconstructing Forces on a Drop Shock Table to Better Inform Finite Element Simulations

Brian A. Ferri, Tyler F. Schoenherr, and Ryan Jennings

Abstract Drop shock machines are commonly used to create a single sided shock pulse that is characterized by an amplitude and a pulse length. While the amplitude of the pulse input is critical in determining a majority of the stresses found in a test article, the pulse length determines the frequency content excited by the shock and can also have an effect on stress. Current simulation methods to model the drop shock machine environment typically use an experimentally measured acceleration on the surface of the drop tower carriage as the input. This measurement assumes that the surface of the drop table is rigid through the shock event, due to a lack of knowledge about the true input force on the drop table during the shock event. The purpose of this work is to test this rigid assumption and reconstruct the input force to better characterize the shock event seen by a test article. Results from laboratory modal and drop tests, force reconstruction using SWAT, and FEM analysis are presented along with a brief background into the drop shock machine environment and the SWAT method.

Keywords Drop tower · SWAT · Boundary condition · Fixture · BARC

26.1 Introduction

In order to repeatedly replicate a scenario where an object falls and is met with a solid surface, such as the ground, an electromechanical shaker or drop shock machine is used in a laboratory environment. This work focuses exclusively on the drop shock machine, also referred to as a drop tower. Drop towers are especially useful in creating high G level shocks that span long time durations. However, the machines are designed such that the amplitude and the length of the pulse delivered can be changed by adjusting the height or by changing the material that the falling object contacts.

A drop tower is comprised of a few basic components starting with the table, also referred to as the carriage. The carriage is a heavy mass with a mounting surface that has tapped, threaded holes for fixturing test articles. The carriage is guided by a rail on either side that ensures that the trajectory of the falling carriage is vertical. Ideally, however, the carriage does not come into contact with the rails during the drop until the brakes are initiated upon the carriage traveling back up after bouncing at the bottom. The base of the tower is a thick and sturdy structure with an impacting surface that undergoes low displacement even during shock events. A “programmer material” is placed on the impact surface in order to prolong the deceleration of the carriage and increase the pulse length of the applied shock profile. Adjusting this lift height allows for control of the amplitude of the applied shock profile. Figure 26.1 displays each of the components for the Lansmont HSX30

Sandia National Laboratories is a multi-mission laboratory managed and operated by National Technology and Engineering Solutions of Sandia, LLC., a wholly owned subsidiary of Honeywell International, Inc., for the U.S. Department of Energy’s National Nuclear Security Administration under contract DE-NA-0003525.

The Department of Energy’s Kansas City National Security Campus is operated and managed by Honeywell Federal Manufacturing & Technologies, LLC under contract number DE-NA0002839.

B. A. Ferri (✉) · T. F. Schoenherr
Sandia National Laboratories, Albuquerque, NM, USA
e-mail: bferris@sandia.gov; sfschoe@sandia.gov

R. Jennings
Kansas City National Security Campus, Kansas City, MO, USA
e-mail: rjennings@kcncs.doe.gov

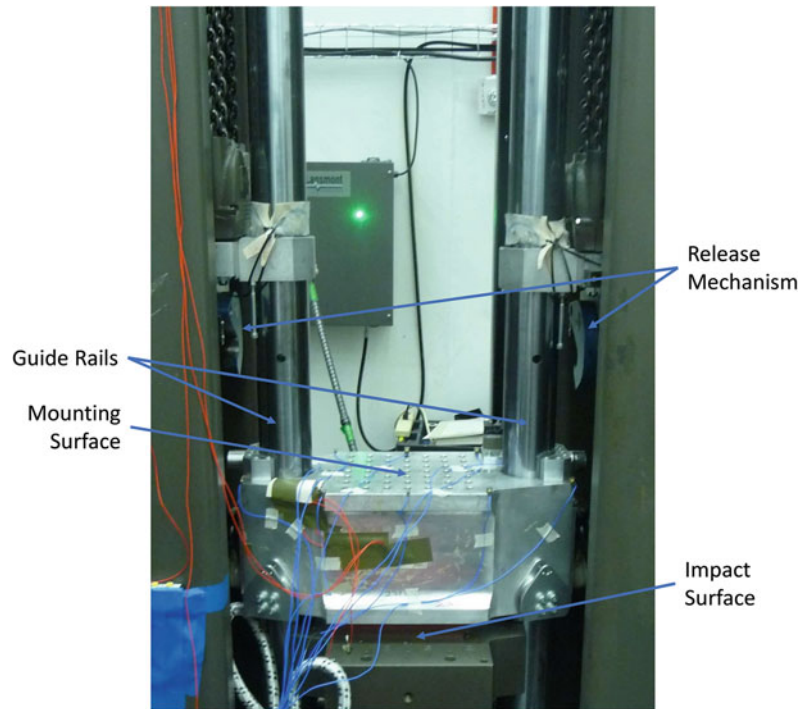


Fig. 26.1 Drop tower components and configuration

drop tower which is located in the dynamic testing lab at the Kansas City National Security Campus. The testing and analysis performed in this work are exclusively based on this specific tower.

Currently, the computational analyses of drop shock tests assume that the table, or carriage, of the drop tower is rigid through a drop event. Rigid is defined as all points within the carriage having no relative motion with respect to any other point on the carriage. To model the response of a test article, the article is fixed to a rigid surface. That surface is forced to move with the same acceleration as is measured during the test.

The rigid assumption breaks down if elastic motion of the carriage is excited during the drop environment. This dynamic response of the carriage is the primary driver for this work. In order to fully understand and characterize the drop tower, a finite element model of the carriage is developed and calibrated to the modes measured in the test performed using a modal impact hammer and 10 tri-axial accelerometers mounted at 10 locations around the top surface of the carriage.

In order to predict the carriage response in the FEM model, an input force is required. Since there is no load cell in existence that can be placed in between the carriage and the reaction mass, an experimental technique known as the Sum of Weighted Accelerations Technique (SWAT) is used. The forces calculated from the response of the carriage during drop environments are used with the calibrated model to predict drop environment response.

26.2 Theory

Shock testing is a standard procedure used when designing and qualifying parts and assemblies exposed to single sided pulse shocks. A drop tower converts potential energy at a given height into a haversine shaped shock pulse that reduces the momentum of the carriage and test article over a given time. The relationship between the potential energy at a specified drop height and the amplitude and duration of a haversine pulse is laid out by Deiters et al [3] and is given by Equation 26.1

$$\sqrt{2gh} = \frac{2A\tau}{\pi} \quad (26.1)$$

where A is the pulse amplitude and τ is the pulse width. From Equation 26.1, there is no way to adjust only the height in order to fully understand the force input. From physics however, if the impacting surface is modelled as a linear spring, then the time it takes to stop a falling object is shown by

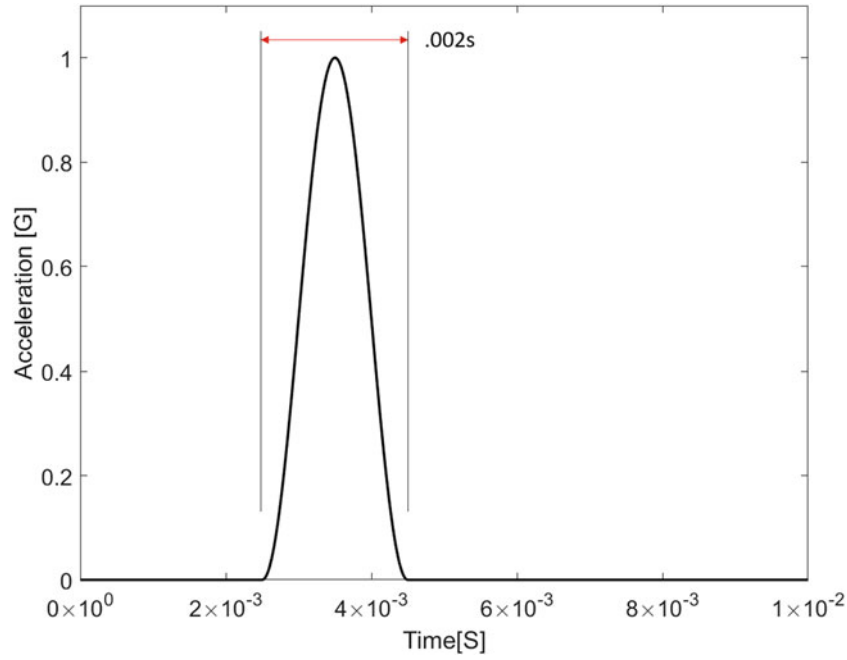


Fig. 26.2 Half-Sine pulse with 2 a millisecond pulse length and 1G amplitude

$$\tau = \frac{\pi}{2} \sqrt{\frac{m}{k}} \quad (26.2)$$

where m is the mass of the carriage and test article. As the mass is constant, changing the stiffness of the programmer, k , inversely affects the change in stopping time, or pulse length. An example haversine with a 2ms pulse length and a 1G amplitude is shown in Fig. 26.2.

A pulse like the one shown in Fig. 26.2 is an ideal waveform. However, in reality, the programmer rarely behaves like a linear spring. Thus, the only way to create an analytical expression for the pulse shape is to characterize the non-linearities of the programmer through the range of motion present in the experiment. This characterization would need to be repeated for each of the programmers and quickly becomes prohibitive.

While the environments for drop shocks are described by their pulse length and amplitude, it is also important to show the frequency content of different pulses as it determines the characteristics of the dynamic response. Figure 26.3 shows the same pulse as was shown in Fig. 26.2 with 2 millisecond pulse length and 1G amplitude. A Fast Fourier Transform operation is performed in MATLAB [4] to transform the signal from the time domain to the frequency domain.

As shown in the figure, the frequencies up to 500 Hz or $1/\tau$ are all equally present in magnitude in the haversine pulse. After 500 Hz, the magnitude of the frequency decays exponentially (or linearly on a log-log plot such as the one in Fig. 26.3). Thus, as the pulse length of the impulse decreases, the range of equally present frequency content that exists will increase to a broadband limit.

Another way that shock profiles are commonly characterized in the mechanical environments community is by their shock response spectrum (SRS) shown in Fig. 26.4.

In order to develop a model of the drop tower environment, an accurate depiction of the input load is needed. The SWAT and SWAT-TEEM algorithms are used as methods to determine the input to the drop tower environment. These algorithms have been used in previous works [1, 5, 6] to calculate external forces acting on the unit of interest in various environments and detailed derivations for both algorithms can be found in the work by Schoenherr [7].

The expressions for SWAT is reproduced here as

$$[M_r \ 0] \phi^+ \ddot{x} = \phi_r^T \bar{F} \quad (26.3)$$

and SWAT-TEEM as

$$[M_r \ 0] \cdot [\phi_r \ \ddot{x}_{fd}] \ddot{x} = \phi_r^T \bar{F}, \quad (26.4)$$

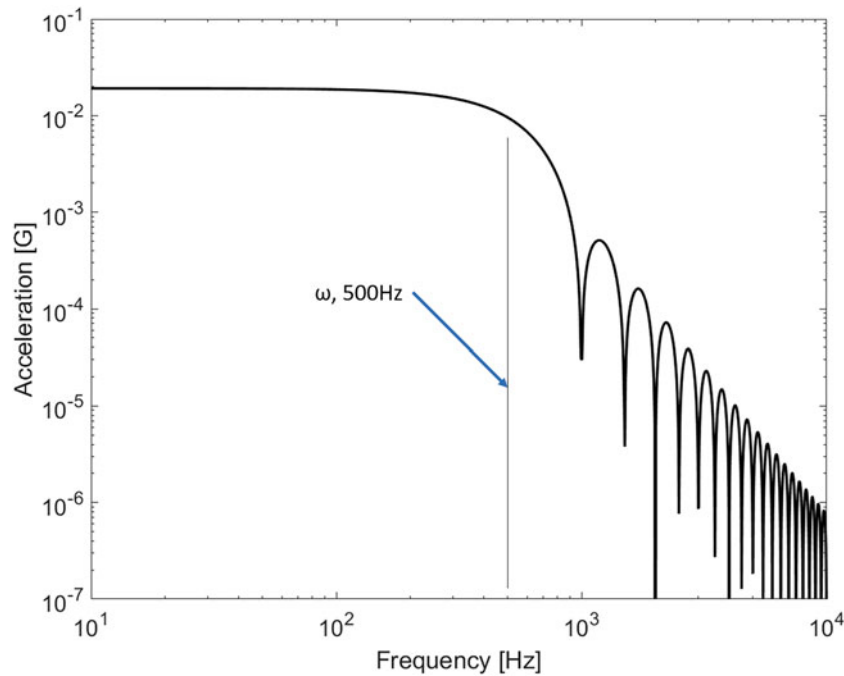


Fig. 26.3 Fast Fourier Transform of haversine impulse

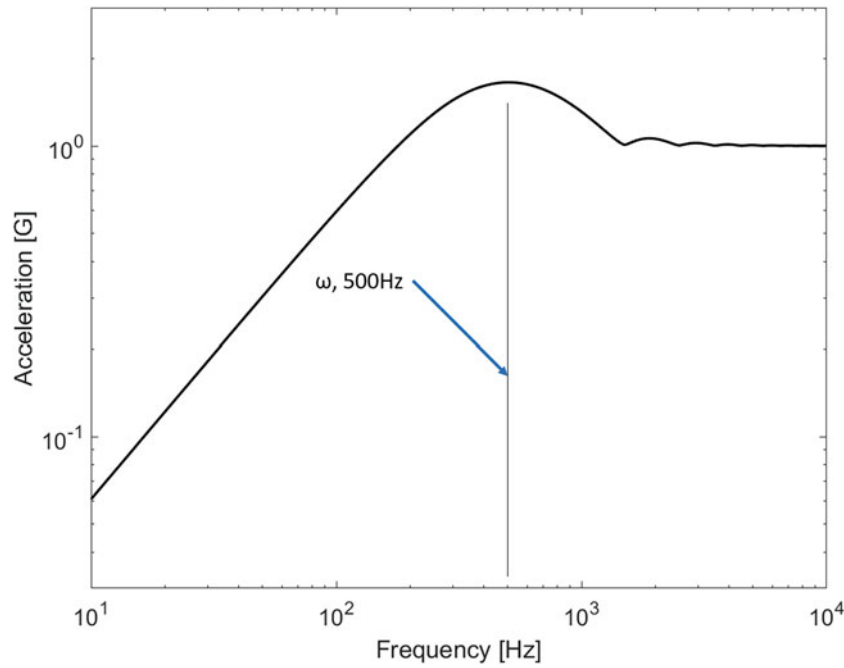


Fig. 26.4 Shock Response Spectrum of haversine impulse

where M_r are the masses and inertias of the test unit, \ddot{x}_{fd} are the accelerations of the test unit undergoing free decay, ϕ is the matrix of mode shapes of the test unit with the subscript r designating rigid body modes, the superscript $+$ is the Moore-Penrose pseudoinverse, \ddot{x} are the accelerations of the test unit during the environment, and \vec{F} is the external forces acting on the test unit.

Equations 26.3 and 26.4 deserve more explanation with respect to their similarities and differences. Both techniques solve for the sum of all the external forces resolved at the test unit's center of gravity designated as $\phi_r^T \vec{F}$. Both techniques also solve for a weighting vector that is premultiplied by the time domain responses of the test unit. The difference between the

two techniques is the weighting vector. The SWAT algorithm uses the mode shapes of the test unit to eliminate the elastic motion from the measured accelerations whereas the SWAT-TEEM algorithm uses the measured accelerations of the test unit after all of the external forces are zero.

For SWAT-TEEM to be applicable, the test unit must experience a period of time where no external forces are acting on it. It is only during this time where the \ddot{x}_{fd} can be extracted from the full measured set of data, \ddot{x} . The benefit of this method over SWAT is that a set of mode shapes do not have to be measured and slight differences in configuration do not degrade the result because the filter is computed based on the configuration used during the actual environment.

26.3 Modal Analysis

26.3.1 Analytical Modal Analysis

A model of the carriage is constructed and is displayed in Fig. 26.5.

The modes for the system were found using Sierra SD [9] on a model that included the carriage plus some of the mechanical hardware. The Sierra SD model is comprised of roughly 400,000 ten node tetrahedral elements. All of the component surfaces are tied together and the bolted joints are not modeled. The primary material is Aluminum 7075 which makes up the carriage and a few of the hardware components. A mesh refinement study is performed and converges with respect to the natural frequencies calculated. The mass of the model is 229.5 lbs compared to 233 lbs measured in the lab.

The model is calibrated to an experimental modal analysis test described in Sect. 26.3.2, and Figs. 26.6, 26.7, 26.8 show the modes of the carriage.

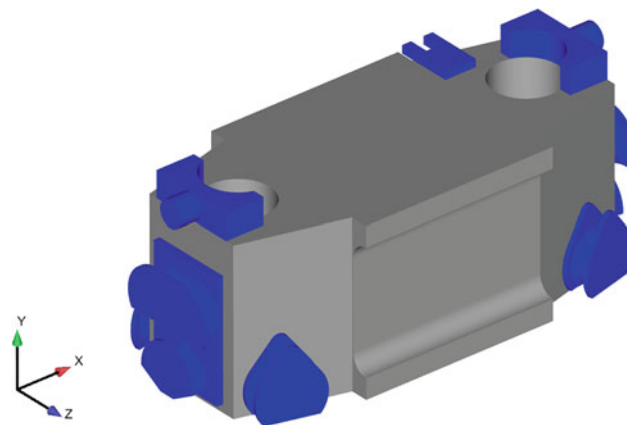


Fig. 26.5 Full model of drop tower carriage with all mechanical hardware attached

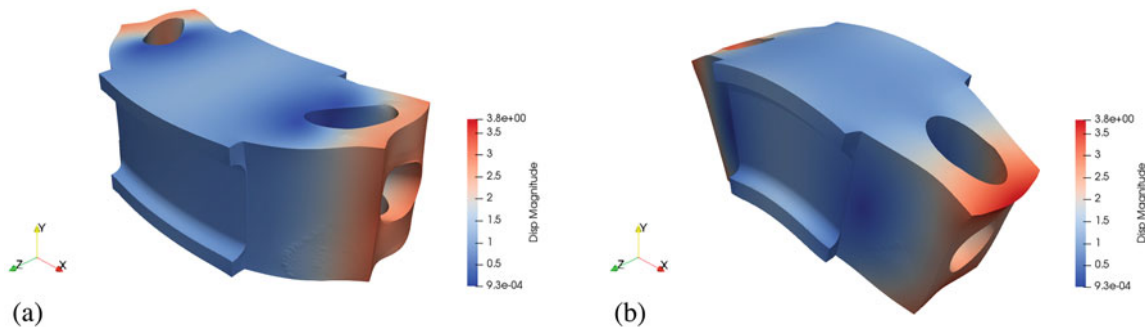


Fig. 26.6 First two elastic modes of the drop tower carriage found with Sierra SD. (a) 1st elastic mode 2177 Hz. (b) 2nd elastic mode 2258 Hz

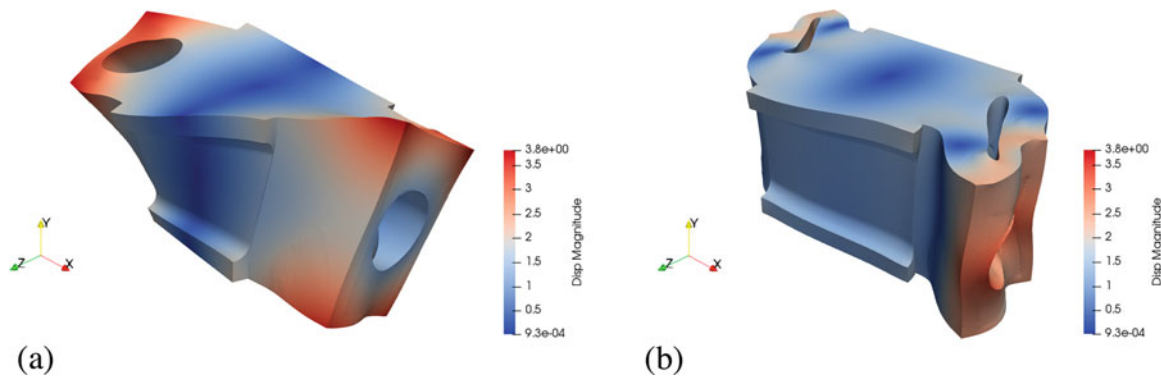


Fig. 26.7 3rd and 4th elastic modes of the drop tower carriage found with Sierra SD. (a) 3rd elastic mode 2291 Hz. (b) 4th elastic mode 3372 Hz

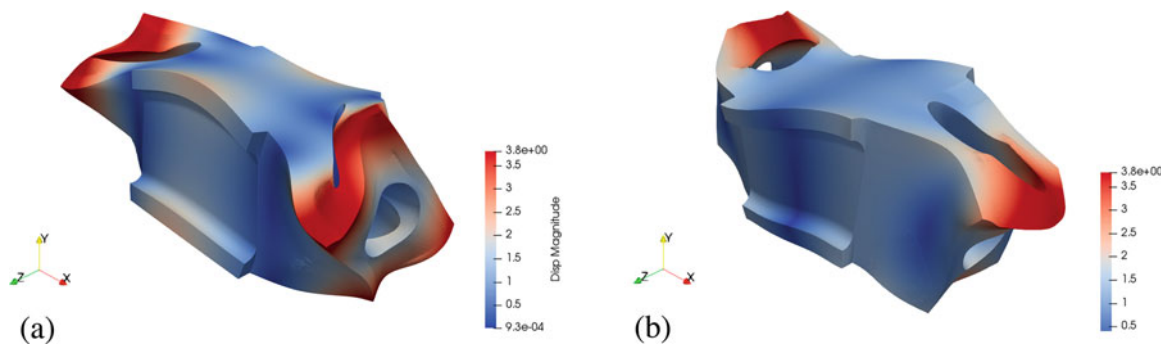


Fig. 26.8 5th and 6th elastic modes of the drop tower carriage found with Sierra SD. (a) 5th elastic mode 3396 Hz. (b) 6th elastic mode 3531 Hz

26.3.2 Experimental Modal Analysis

An experimental modal analysis was performed to validate the results of the analytical modal analysis. The test was performed on the drop shock machine carriage, in a replicated free-free condition by placing foam underneath the carriage and letting the carriage rest on the foam. Ten tri-axial accelerometers were used to measure the response on the top surface of the carriage. The experimental setup can be seen in Fig. 26.9.

A modal impact hammer was used to impact the carriage in various locations, and the hammer and accelerometer responses were captured with a data acquisition system. LMS software [8] was used to determine the mode shapes and frequencies for five of the first six elastic modes. The test setup was not successful in capturing the fourth elastic mode, but that was acceptable because the main concern was capturing the modes with motion in the direction of travel of the carriage.

The mode shapes and frequencies were then compared to the analytical modes of the calibrated model. The comparisons can be seen in Figs. 26.10, 26.11, and 26.12.

The modal assurance criterion (MAC) plot computed using FEM Tools [2] is shown in Fig. 26.13. The experimental analytical mode shape and frequency match very well for the second elastic mode, and reasonably well for the first, third, fifth, and sixth elastic modes. Pretest predictions showed that the 2nd elastic mode was the most important mode with respect to the SWAT technique.

26.4 Drop Tower Force Reconstruction

26.4.1 Experimental Drop Shock Environment

After the conclusion of the modal tests, the carriage is dropped from many different heights onto many different programmer materials. The programmer materials include different size and quantities of felt sheets, and gaskets, as well as differently

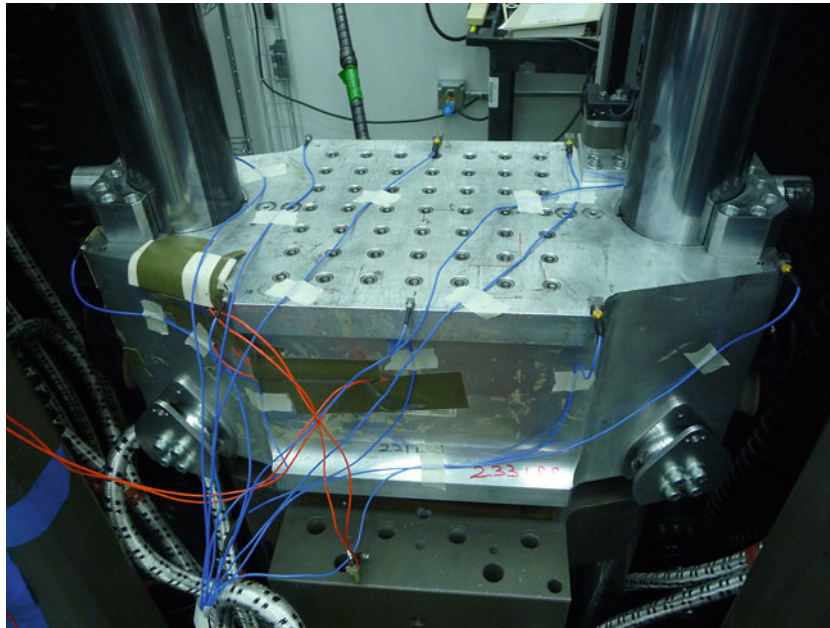


Fig. 26.9 Experimental Modal Analysis Setup

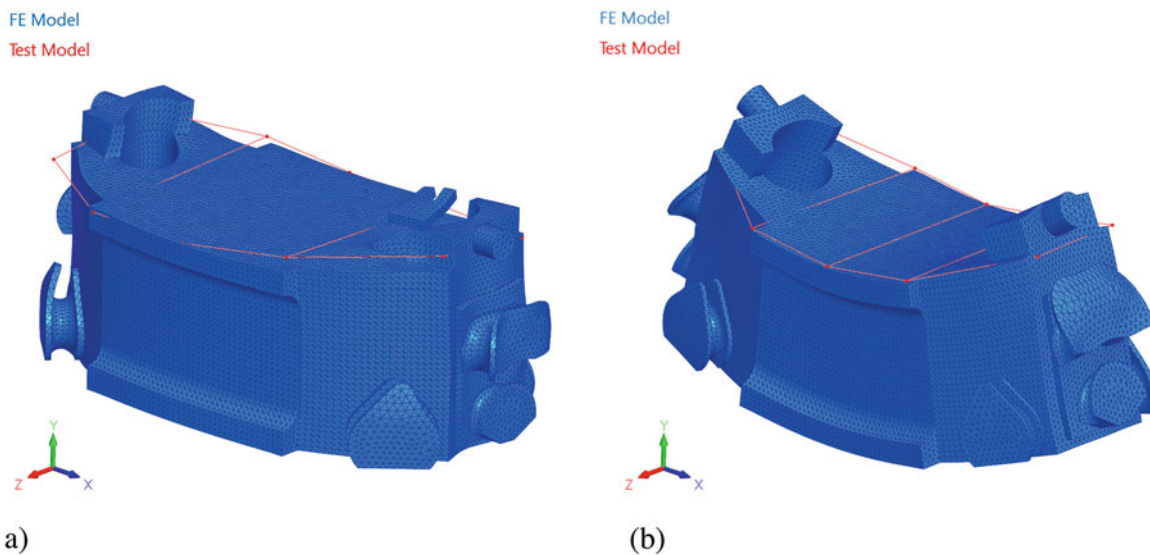


Fig. 26.10 Comparison of first two elastic modes found experimentally vs analytically. (a) 1st elastic mode Analytical: 2177 Hz Experimental: 2202 Hz. (b) 2nd elastic mode Analytical: 2258 Hz Experimental: 2257 Hz

sized and shaped polymeric programmers. Ten tri-axial accelerometers are used to measure the response on the top surface of the carriage in the same locations as the modal tests. The experimental setup is shown in Fig. 26.14.

The force on the carriage is calculated for three of the experimental drops with varying pulse widths. The lift and release mechanism for the HSX30 has a sensor that records the drop height to a 0.5" precision. Parameters for the three drop tests can be seen in Table 26.1.

For the purposes of illustrating the SWAT method in this paper, runs 04, 21, and 25 are shown as examples. Run 04 used a single 1/4 inch piece of felt and two 1/16 inch pieces of felt as programmer. Run 21 used a single 1/8 inch piece of gasket as programmer. Run 25 used a single 1/32 inch piece of gasket as programmer. These programmer materials can be seen in Figs. 26.15, 26.16, and 26.17.

By varying the combination of programming material and drop height in a drop shock test, different pulse lengths and amplitudes for the shock are achieved. The accelerometer responses for those runs are shown in Figs. 26.18, 26.19, and

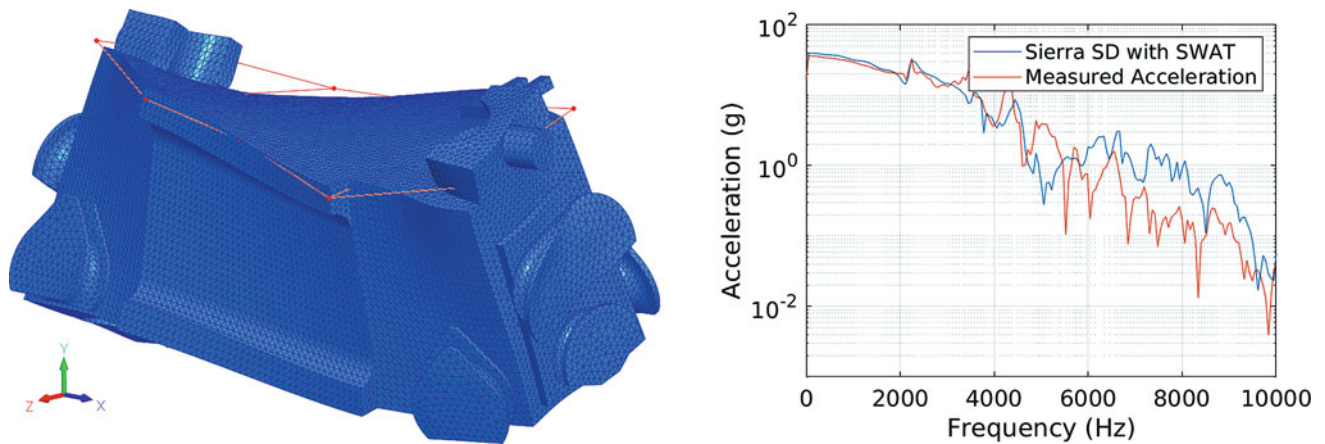


Fig. 26.11 Comparison of the third elastic mode found experimentally vs analytically. (a) 3rd elastic mode Analytical: 2291 Hz Experimental: 2458 Hz. (b) 4th elastic mode not found experimentally

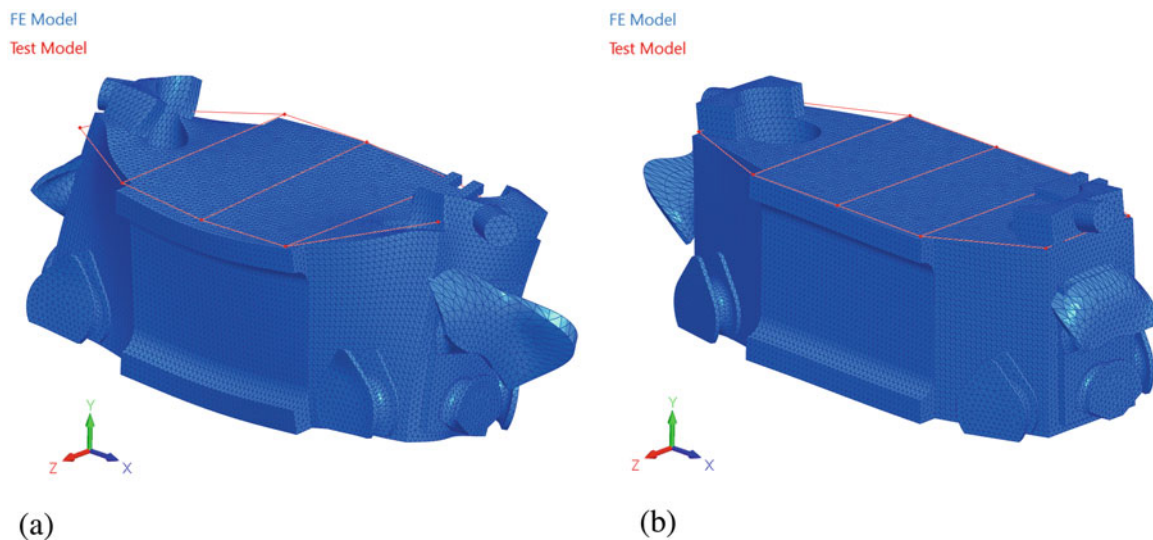


Fig. 26.12 Comparison of the fifth and sixth elastic modes found experimentally vs analytically. (a) 5th elastic mode Analytical: 3396 Hz Experimental: 3296 Hz. (b) 6th elastic mode Analytical: 3531 Hz Experimental: 3584 Hz

26.20. Each run shows that each measurement has a different representation of the impulse as the elastic motion of the carriage affects the response on the top surface of the carriage. The differences increase along with the oscillations the shorter the time duration on the impulse.

26.4.2 SWAT Analysis

The force from the three drops are reconstructed using the SWAT and SWAT-TEEM algorithms. The SWAT algorithm uses the 1st and 2nd bending modes fit from the experimental modal analysis test. In order to compare the reconstructed forces to current force methods, the response from the accelerometer that is closest to the center of the carriage is scaled with the mass to provide a force. This scaled accelerometer force is the same as $F = ma$ where F is the force, m is the system mass, and a is the system acceleration. This force is correct if there is no elastic motion in the carriage and is represented in Figs. 26.21, 26.22, and 26.23 and is designated as “Scaled Accel”. All of the forces compared are low-pass filtered with a cutoff frequency of 7kHz.

Run 04, shown in Fig. 26.21, has the longest impact pulse width of the three examples. The longer pulse width means lower frequency force is input to the carriage. Even though the first natural frequency of the carriage is excited and is

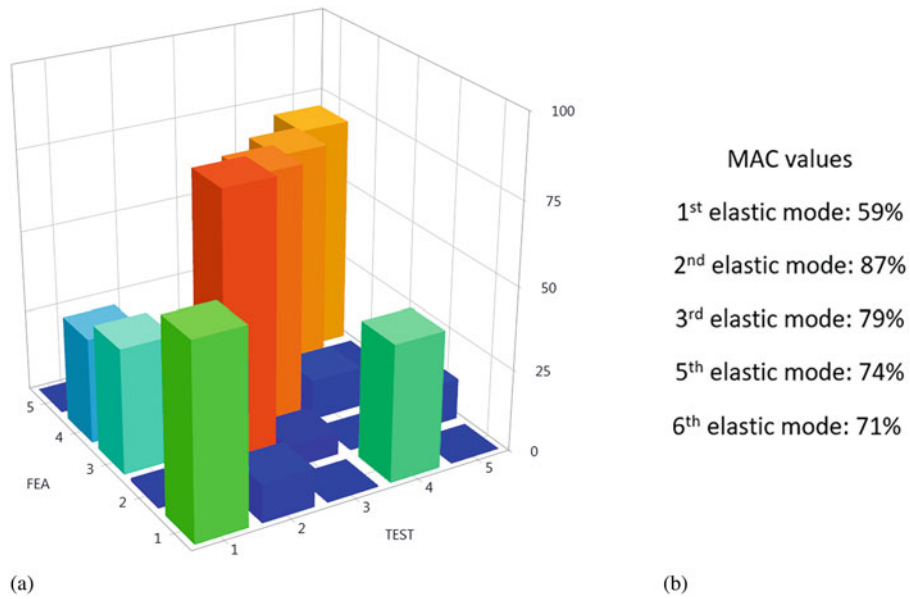


Fig. 26.13 MAC plot of 1st, 2nd, 3rd, 5th, and 6th elastic mode shapes found experimentally vs analytically

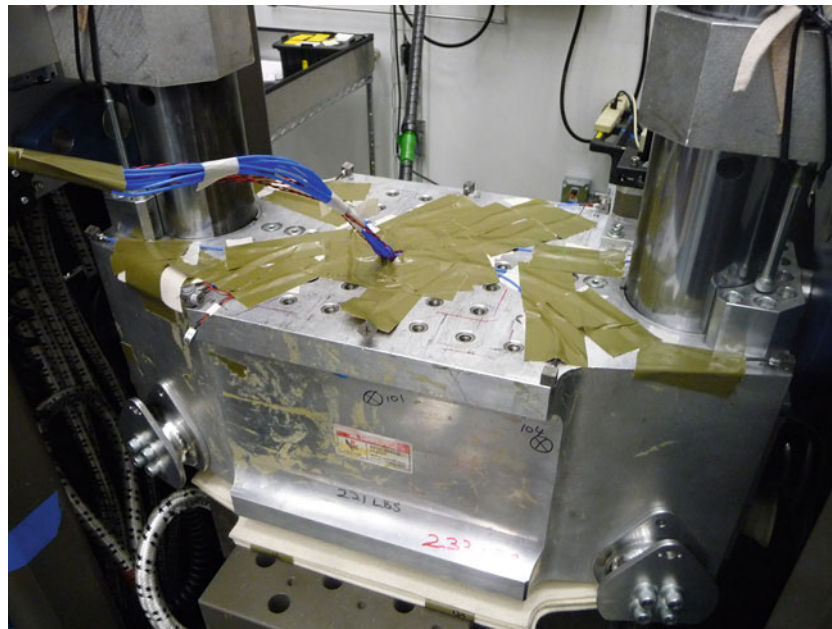


Fig. 26.14 Experimental setup for drop shock tests

Table 26.1 Drop test parameters for tests on which forces are reconstructed

Run #	Drop Height (in)	Pulse Width (ms)	Max Accel (g)
004	34	1.0	1400
021	12	0.3	2000
025	5	0.1	2500

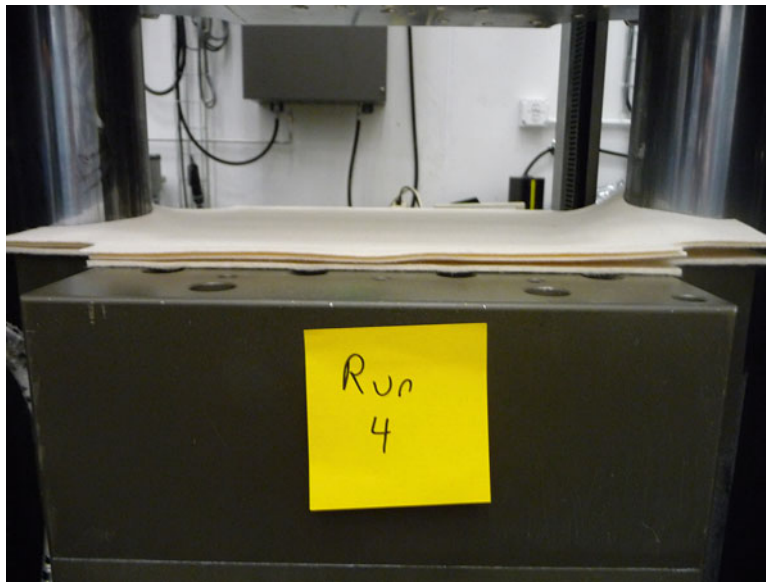


Fig. 26.15 Programming material used in run 04



Fig. 26.16 Programming material used in run 21

measured by the response, most of the pulse is constructed of lower frequency energy. The scaled measured acceleration only has 5% error with respect to its peak value and about an error of 0.2ms with respect to the pulse length due to the carriage having only a little elastic motion.

Run 21, shown in Fig. 26.22, has a shorter input pulse width that excited the first natural frequency of the carriage enough to distort the input pulse. The dynamics measured by the accelerometer make the pulse appear to be a shorter duration and approximately 10% higher amplitude. There is also significant “input” after the pulse which is the motion of the carriage in resonance. The amplitude of the response is dependent on where the motion is measured.

Run 25 has the shortest pulse duration input that excites the dynamics of the carriage to levels comparable to the input pulse as the scaled acceleration input is calculated to be about two times the amplitude and half the width of the actual pulse. This input is also dependent on the measured location. The scaled accelerations from the different locations provide very different input definitions with respect to each other and the reconstructed force in Fig. 26.23. For this environment, the 7 kHz filter was applied to both the scaled accelerometer pseudo force and the SWAT forces. The true force has frequency content



Fig. 26.17 Programming material used in run 25

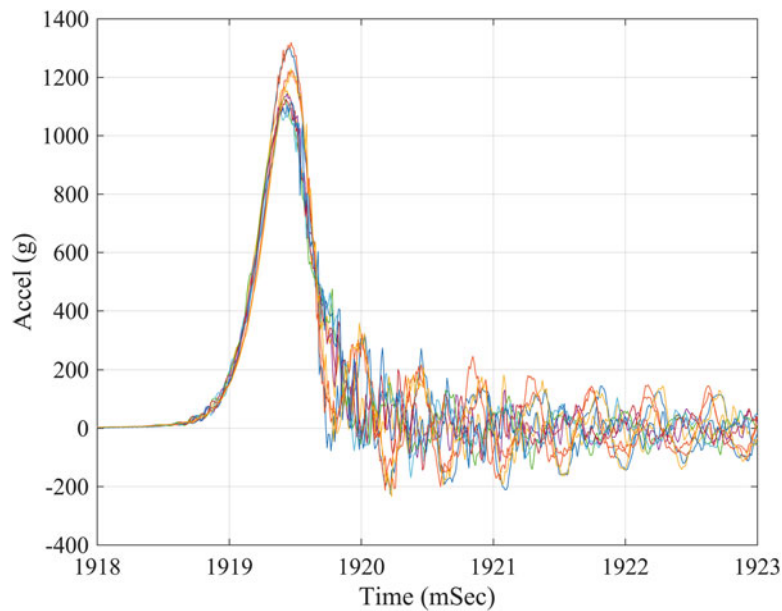


Fig. 26.18 Accelerometer responses during run 04

above 7 kHz. This means that the input is only valid for frequencies less than 7 kHz when examining the system response. In this case, if the failure mode is above 7 kHz, then an alternate method should be used.

26.5 Force and Model Validation

In order to show how the Sierra SD model compares to the experiment, the SWAT input from run21 is used as a pressure input in a Sierra SD simulation. An area of faces on the model that corresponds to the programming material is chosen and a pressure load that is proportional to the SWAT force magnitude is applied in the Y direction over the entire area. The model damping is 3% and the first bending mode in Y has an additional 1% damping applied in a modal transient analysis. Figure 26.24 shows the model setup.

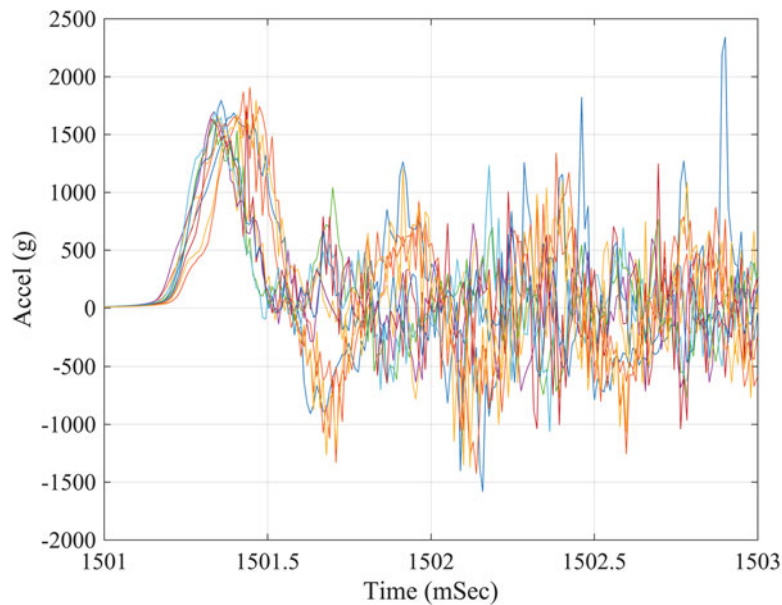


Fig. 26.19 Accelerometer responses during run 21

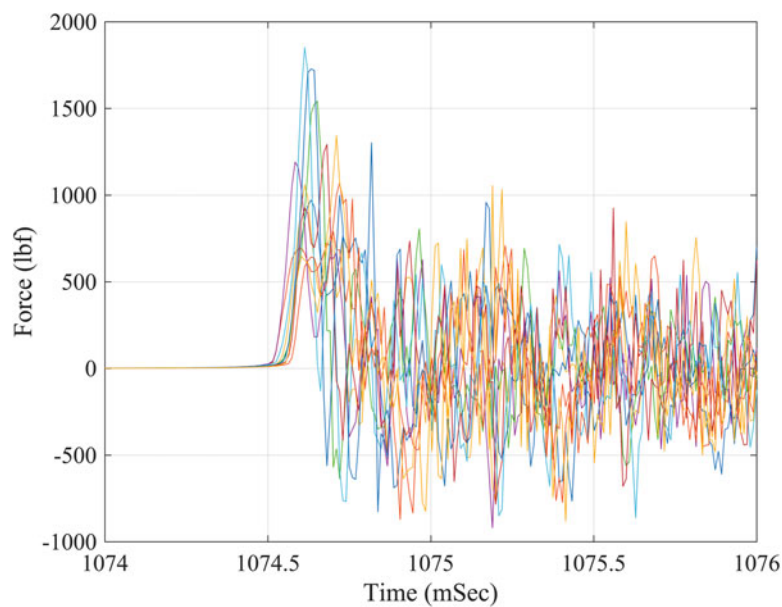


Fig. 26.20 Accelerometer responses during run 25

All of the measured locations are analyzed, but for this paper, the end, corner, and middle locations of interest (shown in Fig. 26.24) are displayed. The time and frequency response for these locations in the Y direction are shown in Figs. 26.25, 26.26, and 26.27.

As seen in Figs. 26.25, 26.26, and 26.27, the magnitude of the initial pulse increases from the end to the middle and the FFT of the signal shows more distinct response from the mode at 2258 Hz corresponding to the first bending mode in the Y direction. In addition to the good agreement in the Y direction at all of the measured locations, Figs. 26.28 and 26.29 show how the model also agrees with the measured X acceleration at the end and the measured Z acceleration respectively.

The response that showed the greatest discrepancy between Sierra SD and the test was the X direction response at the middle of the carriage shown in Fig. 26.30.

Figure 26.30 shows that there were secondary impacts which were most likely metal on metal to induce the high frequency response.

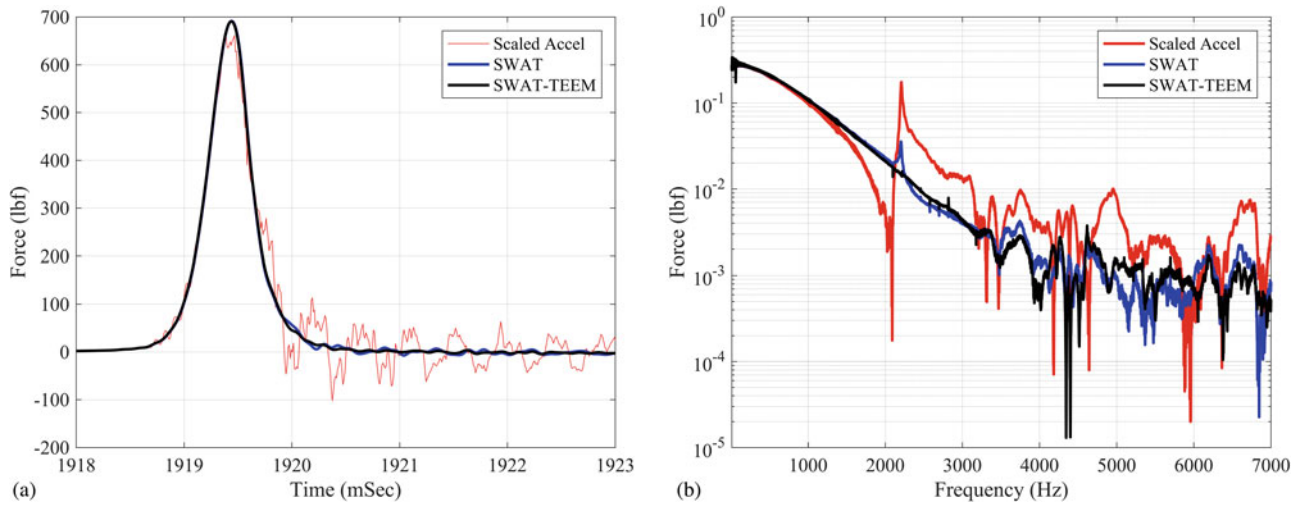


Fig. 26.21 Forces calculated from run04. (a) Time domain. (b) Frequency domain

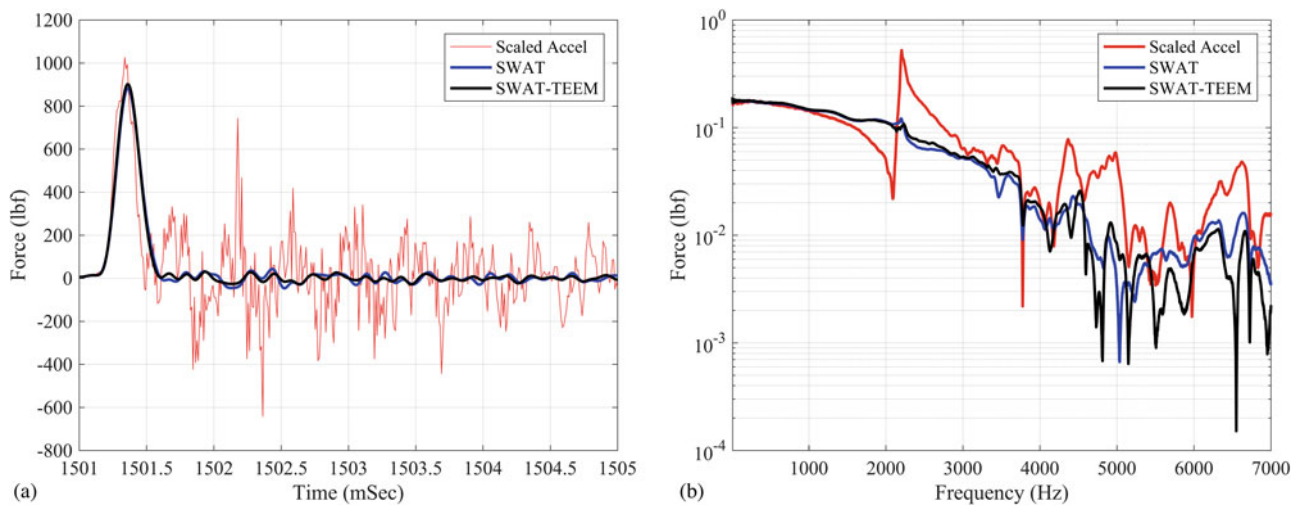


Fig. 26.22 Forces calculated from run21. (a) Time domain. (b) Frequency domain

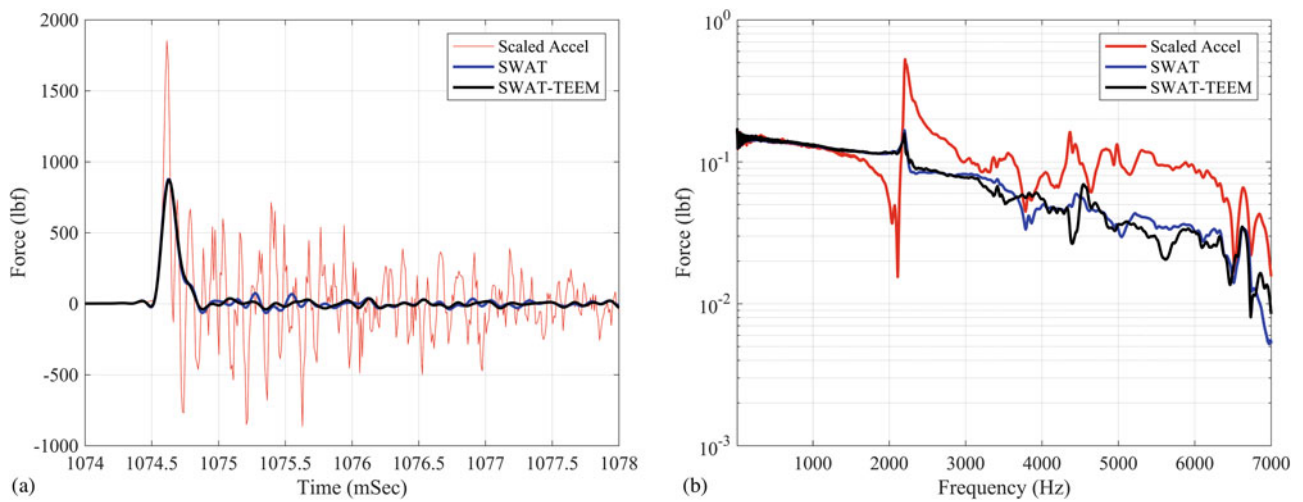


Fig. 26.23 Forces calculated from run25. (a) Time domain. (b) Frequency domain

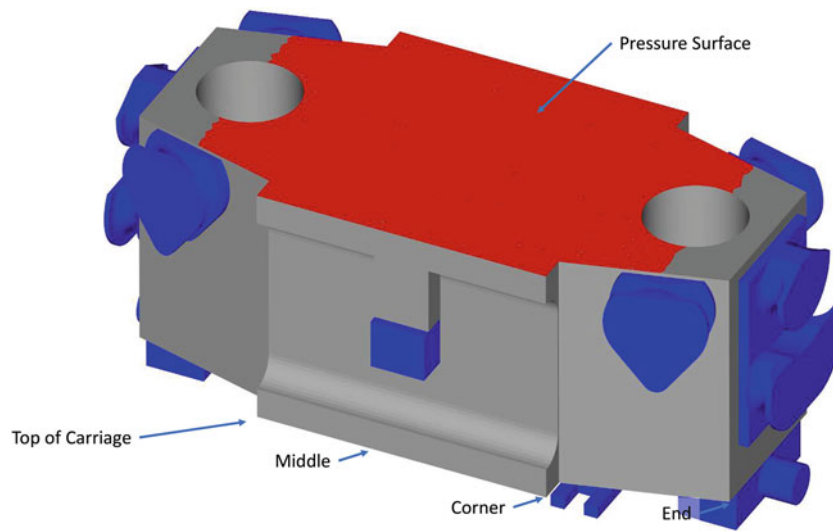


Fig. 26.24 Sierra SD model setup for force validation

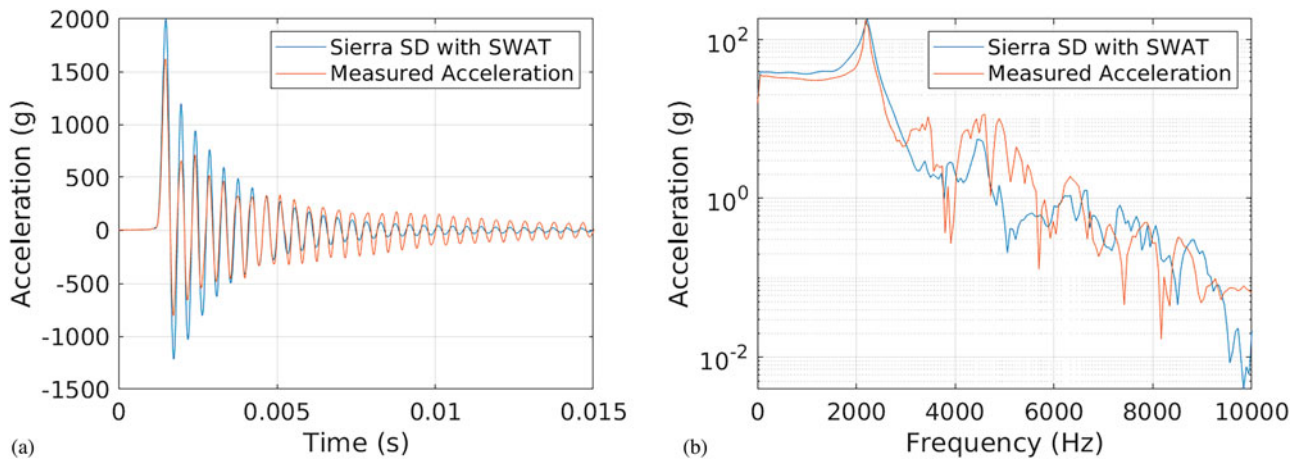


Fig. 26.25 End response from Sierra SD with SWAT input compared to measured in the Y direction. (a) Time response. (b) FFT of time response

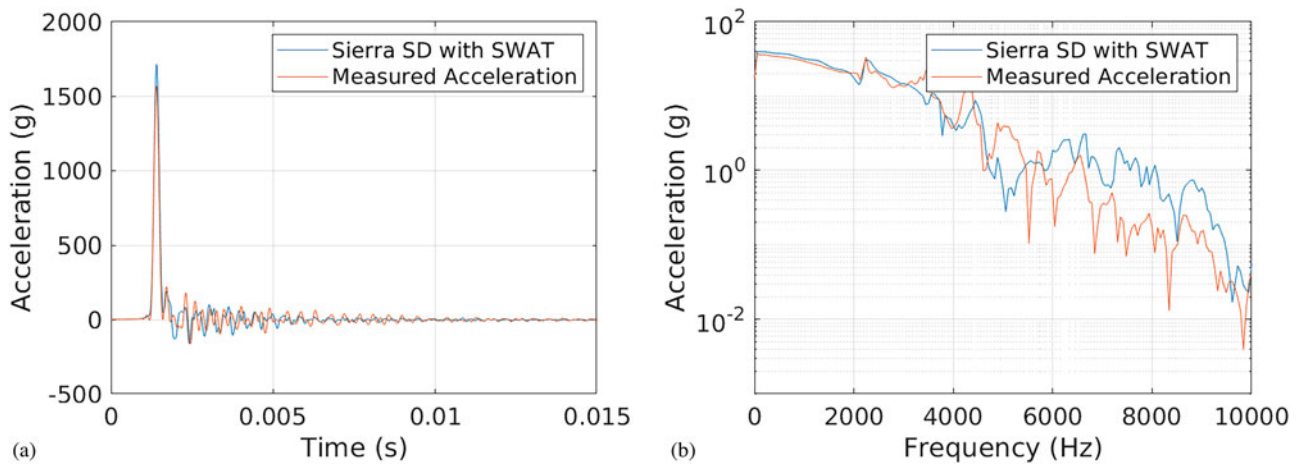


Fig. 26.26 Corner response from Sierra SD with SWAT input compared to measured in the Y direction. (a) Time response. (b) FFT of time response

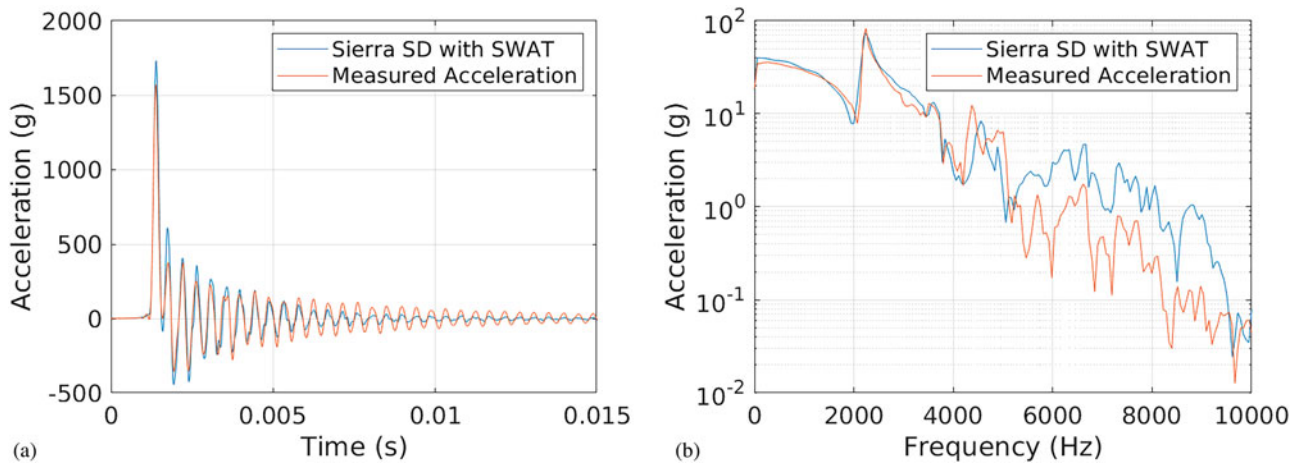


Fig. 26.27 Middle response from Sierra SD with SWAT input compared to measured in the Y direction. (a) Time response. (b) FFT of time response

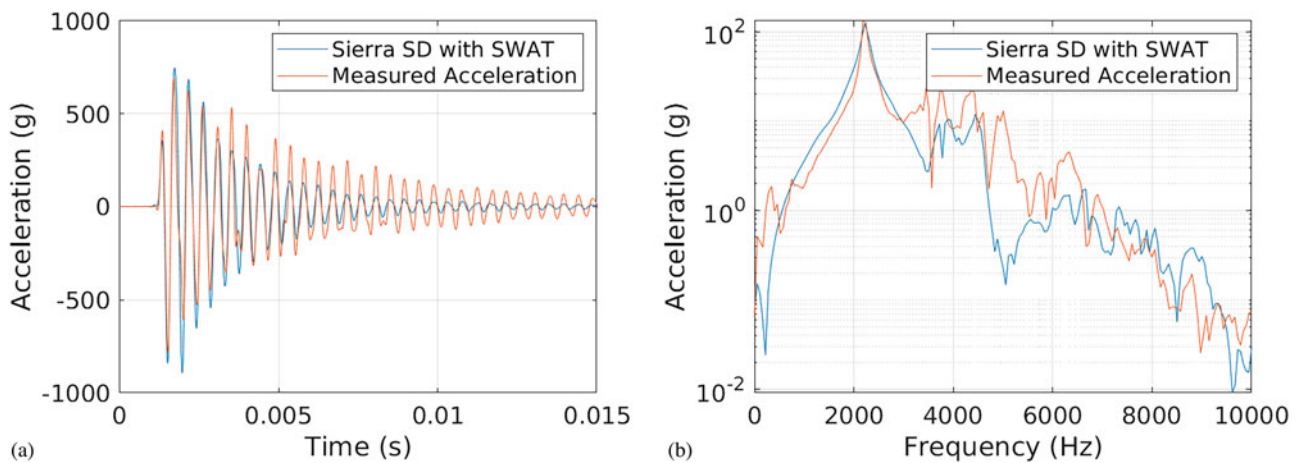


Fig. 26.28 End response from Sierra SD with SWAT input compared to measured in the X direction. (a) Time response. (b) FFT of time response

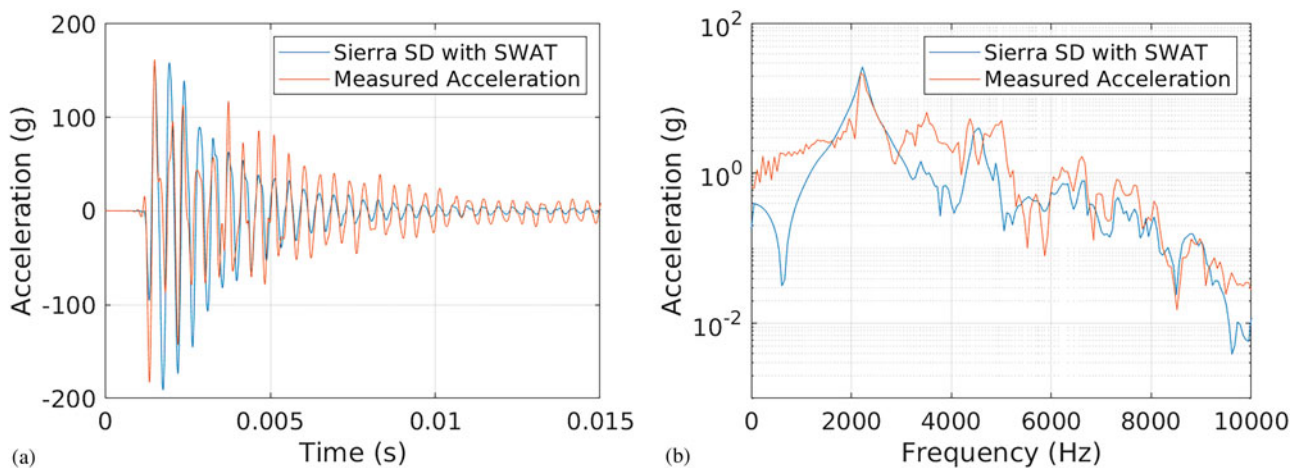


Fig. 26.29 Middle response from Sierra SD with SWAT input compared to measured in the Z direction. (a) Time response. (b) FFT of time response

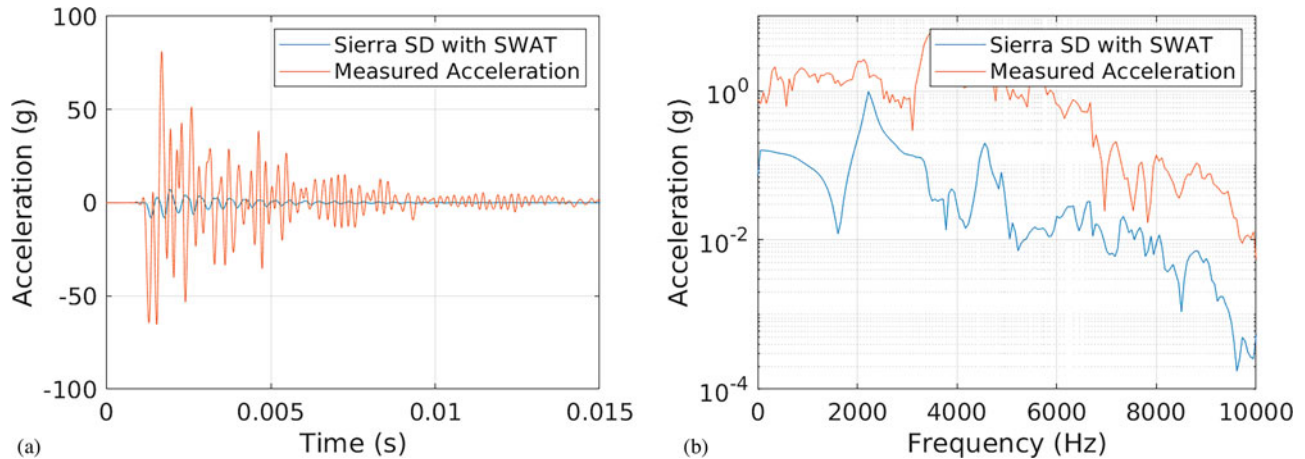


Fig. 26.30 Middle response from Sierra SD with SWAT input compared to measured in the X direction. (a) Time response. (b) FFT of time response

The comparison of the response between the model and the experiment is a concatenation of all of the errors within the process. These errors include model form error, the inability to characterize any intermittent impact or rattling forces acting on the carriage, or errors in SWAT. With respect to the error in SWAT, the error in this case study would be realized as the force showing an oscillating at a specific frequency due to the SWAT theory.

26.6 Conclusion

This work shows how the dynamics of the carriage of a drop shock machine can affect the measured response depending on choices made in instrumentation. Given a single accelerometer on the carriage, an analysis using the measured acceleration as an input to a simulation could give an incomplete response and would disclude the base strain being imparted on the unit under test.

The SWAT technique is able to use the carriage measured response to create a force input. The calculated force input is validated by applying it to a calibrated model as the model showed good agreement to the measured accelerations.

References

1. Carne, T.G., Bateman, V.I., Dohrmann, C.R.: Force reconstruction using the inverse of the mode-shape matrix. Technical Report SAND90-2737, Sandia National Laboratories (1990)
2. Dynamic Design Solutions: Femtools 4.0.1 (2017)
3. Deiters, T.A., Baker, M., Indermuehle, K.C., Engelhardt, C.W.: Using analysis to design for drop or other shock environments. *Sound Vib.* (2000)
4. Mathworks: Matlab r2019a (2019)
5. Mayes, R.L.: Measurement of lateral launch lads on re-entry vehicles using swat. In: Proceedings of the 12th International Modal Analysis Conference, pp. 1063–1068 (1994)
6. Schoenherr, T.F.: Reconstructing forces from continuous connections using swat. In: De Clerck, J. (ed.) *Topics in Modal Analysis I*, vol. 7, pp. 65–75. Springer International Publishing (2014)
7. Schoenherr, T.F.: Calculating the impact force of supersonic hail stones using swat-teem. In: Wicks, A. (ed.) *Shock & Vibration, Aircraft/Aerospace, and Energy Harvesting*, vol. 9, pp. 67–79. Springer International Publishing (2015)
8. Siemens: Testlab 17 (2019)
9. Sierra Structural Dynamics Development Team: Sierra structural dynamics – user’s notes. Technical Report SAND2017-3553, Sandia National Laboratories (2017)

Biography

Brian A. Ferri joined Sandia National Laboratories in 2017 as an analyst performing linear dynamic computational modeling. Prior to joining Sandia, Brian received his bachelors and masters degrees from Georgia Institute of Technology where he completed his graduate thesis on modeling spall in Aluminum for plate-flyer experiments.



Chapter 27

Pointless Grading and Digital Content Delivery as Educational Differentiators: A Case Study for Noise and Vibration Courses

Andrew R. Barnard

Abstract University professors need to be content delivery specialists to compete for students' attention with lots of other content in the digital world. In addition, grading systems, although necessary for student evaluation, are a constant barrier between faculty and student interaction. This paper presents non-traditional ways to deliver content to students and evaluate students, in an effort to break down artificial barriers between faculty and students. The case study involves two courses at Michigan Technological University: Acoustics and Noise Control, and Shock and Vibration. Traffic light grading is discussed as a way to move away from point-based evaluation systems. Coupled with student-led exam debrief sessions, student investment in the new grading system has been high. Flipped classroom examples will also be discussed as a content delivery strategy, allowing more person-to-person interaction during classroom hours. This paper will share teaching strategies through examples of successes and failures of these strategies in teaching noise and vibration courses.

Keywords Education · Grading · Noise control · Flipped classroom · Teaching

27.1 Introduction

Over my years of teaching, I have noticed frustration of both faculty and students when it comes to course content delivery and grading policies. For content delivery, the “death-by-powerpoint” style of lectures has pervaded university education. While it provides a nice set of reference notes for the students, sometimes even negating the need for a course textbook, it is not an effective content delivery method for students in a classroom setting. I have personally noticed this, as I'm sure many other university professors have, with students dozing off about 15–20 min into a viewgraph lecture. New delivery techniques exist using online technology that can dramatically increase student classroom participation, which can increase long term retention of knowledge.

A flipped classroom approach involves short pre-recorded lectures that students watch before class. Then class time is used for interactive learning activities, such as practice problems, demonstrations, coding exercises, and others. This encourages students to be an active participant in their discovery during class time. In this paper, I will discuss a case study where the flipped classroom approach was used in MEEM 4702: Shock and Vibration class at Michigan Technological University.

In terms of grading policies, I have experienced high stress on students due to grades, particularly at the end of the semester. Anyone who has taught a university course can relate to the inevitable student “haggling” that will happen at the end of the semester. The conversation is usually about how one point here or one point there over the course of the semester can bump the student into the next grade level. When using a point-based grading system, even with a rigid rubric, there can be some wiggle-room in assigning grades. Some professors feel obliged to upgrade close grades at the end of the semester, while others hold firm on the semester point accrual. This leads to inconsistent policies from course-to-course that students tend to find unfair. My solution was to get rid of points altogether and make every assignment and pass-fail. This was implemented in MEEM 4704: Acoustics and Noise Control at Michigan Technological University. After the first year, it was obvious that there were problems with this approach as well, so a hybrid system was developed, which I call traffic light grading. Traffic light grading will be discussed in this case study.

A. R. Barnard (✉)

Department of Mechanical Engineering – Engineering Mechanics, College of Engineering at Michigan Technological University, Houghton, MI, USA

e-mail: arbarnar@mtu.edu

27.2 Discussion

27.2.1 Content Delivery

The flipped classroom approach was implemented in about half of the recitation sessions throughout the semester for MEEM 4702: Shock and Vibration. The other half of the sessions were more traditional lecture sessions. Short videos were developed for content delivery prior to class. The videos were no longer than 20 min each and of varied format. Some pre-class videos used powerpoint slides with live markup and narration, some used paper and pen with an overhead projector and narration, some were linked to external YouTube videos, and some were MATLAB programming tutorials. In post course surveys, a majority of the students preferred this method of delivery because they could re-watch videos at any time if they didn't master the material the first time. To ensure students watch the pre-class videos, pop-quizzes were held in class, at the beginning of class, for roughly half of the sessions. The quizzes were one question asking students about the content of the pre-class video, not necessarily to complete a problem. After the first few quizzes, student viewing of the videos prior to class was nearly 100%.

Classroom time for the flipped sessions was used for several purposes. The students did many in-class exercises. For example, in a session discussing machine isolators, students were given a real world piece of equipment (a Generac Generator) and asked to design a mounting system. This forced them to use tools from the pre-class video on sizing mounts as well as consider non-vibration design metrics. Students needed to consider stability (1 mount vs. 5+ mounts), environmental parameters, cost, mounting hole design, and other parameters. Having an entire class to look at one in-depth problem allowed for many discussions beyond just solving the vibration problem.

Many mechanical engineers struggle with programming. Due to more class time for interactive activities, we spent several class sessions doing interactive MATLAB programming. After watching a pre-class video on the convolution integral, we were able to discuss numerical integration in detail in class and have the student program a convolution integral code live in class.

Finally, having more classroom time for one-on-one instruction and group work led to much more participation from students. Student participation was part of the grade for the course and was tracked using a simple sticky-note method. Students all had a pad of sticky-notes and whenever they participated, they turned in one with their name on it for the instructor to count at the end of the semester. Participation included asking good questions, participating in in-class problem solving, putting a solution on the board, sharing programming code in class, and helping others in class.

Overall, the students appreciated the flipped classroom model by the end of the semester. Some were hesitant at first because it seemed like "more work." However, most of those students accepted the method by the end of the semester because they realized that they learned more and retained it better, and had video lectures to review at any time through the course management system. As the instructor, I also found this method more engaging than lecturing to uninterested or sleeping students. Questions from students were thoughtful and more regular and I was able to see where students were struggling in real time during in-class activities. It was more work for the instructor the first year due to making all of the videos. However, the course was much easier to prep for in subsequent years because the recorded lectures could be used again.

27.2.2 Traffic Light Grading

Traffic light grading involved three levels of understanding of assignments and exams: Green = mastery, Yellow = some confusion but concepts understood, Red = little-to-no understanding or effort. These were the only 3 levels of grade that could be achieved on a given assignment, i.e. there was no partial credit. Each assignment was assigned a total of 2–4 points, with points tied to assignment color. For example, an assignment worth 3 points would be 3 points for green, 1.5 points for yellow, and 0 points for red. The total number of points in the class 45 points including assignments, laboratories, exams, and a final project. No partial credit was available. However, students were all given 3 tokens for the class. Tokens could be used for a retry on an assignment, lab report, or exam, where the student could move up one level (yellow to green or red to yellow) with a corrected submission. The solutions were not given to the class until after the retry period was past. The students were allowed to discuss the assignments with one another to help each other, and students could use any resource to try and improve their grade on the retry, including coming to office hours and discussing the assignment with the instructor.

Using tokens for exams was a little different than assignments and lab reports. The exams were done in class, at 3 pm in the afternoon. Then in the evening, usually at 7 pm, a room was scheduled for an exam debrief. This was an optional

session where students could talk to one another to discuss solution methods and exam problems. I attended these sessions as the instructor, but did not give the students any guidance, with the exception of if there was a poorly written question that the students didn't grasp. Students sometimes organized into groups to talk about solution methods and sometimes worked together as a whole class. The most interesting things happened when groups of students had different answers on a problem and both "camps" were convinced they were right. Then they had to really discuss the solution and try to figure out which group was correct. One example of this was a simple rounding difference between two groups that resulted in a 1 dB difference in an answer to a problem. It was fun to watch them have an unprompted significant figures discussion, a topic that I often struggle to have students understand in class lectures.

Final course grading was done using the 45 points available in the class. However, the grade expectations are higher than normal based on the fact that students have 3 tokens to use to improve scores. To receive an A grade, students need to 44 points or more. Each subsequent grade category was 2 points lower than the previous. The students know the point values for all the assignments up front in the class and can easily track their progress and decide how and when to use their tokens to optimize their grades. Since switching to this grading scheme, I have not had a single student complaining about points on any assignments or exams. In addition, grading is extremely efficient because all the instructor needs to do is look through the assignments and group them into three groups. I intentionally didn't write comments on student assignments in an attempt for them to go out and find the correct solution. Only incorrect solutions were indicated to students, without showing where they went wrong. The onus was shifted to the student to find resources to understand where they went wrong.

Based on post course surveys for MEEM 4704: Acoustics and Noise Control, the students appreciated the simplicity of the grading system and the ability to retry some assignments and exams. The exam debrief sessions were specifically pointed out by several students as extremely helpful. In my opinion, the traffic light grading system reduced the stress on students and reduced grading effort on the instructor. It also completely eliminated the grade negotiations and haggling at the end of the semester. I think this reflects a fair grading system with high student buy-in.

27.3 Summary

Methods for content delivery and novel grading systems were presented with examples and case studies from two vibration and acoustics courses at Michigan Technological University. Although these methods were not invented by the author, descriptions and examples of where they can be helpful were discussed. In general, student excitement for new learning techniques at the beginning of the semester was low. However, by the middle of the semester most, if not all, students had bought in to the techniques. By the end of semester course and instructor surveys, students expressed their appreciation for doing something different that helped them better master the material as well as reduce grading stress. I am now spreading these techniques to other courses as the pilot programs have shown great success in improving student learning outcomes and reducing long term instructor effort in both class preparation and grading.

Acknowledgements I would like to acknowledge Dr. William Predebon, Chair of the department of Mechanical Engineering – Engineering Mechanics at Michigan Technological University for supporting me in trying innovative teaching methods. I would also like to thank my Dynamic Systems Lab colleagues, Jason Blough, Chuck Van Karsen, Jim De Clerck, and Darrell Robinette, for acting as a sounding board in the development of these methods.

Andrew R. Barnard is an associate professor of Mechanical Engineering - Engineering Mechanics and the director of the Great Lakes Research Center at Michigan Technological University.

Chapter 28

Toward Extracting Multidimensional Kinematics from SWIFT Experiments



Ethan Billingsley, Robert Billette, Yolnan Chen, Christopher Tilger, Michael Murphy, and Mike Bowden

Abstract The Shock Wave Image Framing Technique (SWIFT) developed at Los Alamos National Laboratory is an implementation of focused shadowgraphy for visualizing the propagation of explosively-driven shock waves within transparent witness media. A SWIFT image depicts the area traversed by the leading shockwave as a distinctly dark area within the media, and allows the projection of axisymmetric, 3-D shock structures into a 2-D plane. This technique has successfully extracted 2-D shock positions utilizing conventional image processing techniques on a 1-D axisymmetric axis about the charge center. To expand SWIFT's capabilities, the development of analysis tools for 2-D kinematic extraction is necessary. These 2-D measurements would allow for enhanced performance characterization of small-scale explosive components and aid design optimization, diagnostics, and explosive shock model development. Complex, three-dimensional, diverging shock waves evolve with time into effectively spherical shapes independent of initial geometry. As time progresses well beyond the detonation event, these smoothed, spherical shapes have averaged out much of the information describing the initial conditions, reaching a location we refer to as the "far field." A lower-order model for shock propagation is developed and compared to high fidelity numerical simulations of similar conditions to actual SWIFT experiments. In order to establish a relevant SWIFT domain, where shock curve shapes remain distinct for the extraction of 2-D kinematics, the lower-order model is optimized with respect to the high-fidelity numerical simulations. For shadowgraphs acquired in early time, the optimization converges to unique solutions of the parameter models. However, the optimization begins to diverge as time progresses, indicating a difficulty in extracting unique, two-dimensional data from the image. With the establishment of the far field, engineers can implement existing shock dynamics on SWIFT images up to this boundary or weight a similar analysis of a multi-image data set appropriately.

Keywords SWIFT · Explosive · Detonator · Shockwave

28.1 Introduction

Over the past decade, the Q-6 Detonation Science and Technology group at Los Alamos National Laboratory (LANL) has developed and refined the shock wave image framing technique (SWIFT) to directly record the two-dimensional evolution of detonator-driven shock waves in polymethyl methacrylate (PMMA) test samples with high precision. Multidimensional effects typically are important for various types of problems in both solid and fluid mechanics. Quantitative performance characterization of small-scale explosive components provides engineers with critical data needed for design optimization.

E. Billingsley

Department of Mechanical & Aerospace Engineering, New Mexico State University, Las Cruces, NM, USA
e-mail: ethan98@nmsu.edu

R. Billette

Department of Electrical Engineering, Michigan State University, East Lansing, MI, USA
e-mail: billett5@msu.edu

Y. Chen

Department of Mechanical Engineering, Rose-Hulman Institute of Technology, Terre Haute, IN, USA
e-mail: cheny15@rose-hulman.edu

C. Tilger (✉) · M. Murphy · M. Bowden

Detonation Science and Technology, Los Alamos National Laboratory, Los Alamos, NM, USA
e-mail: ctilger@lanl.gov; mjmurphy@lanl.gov; bowden@lanl.gov

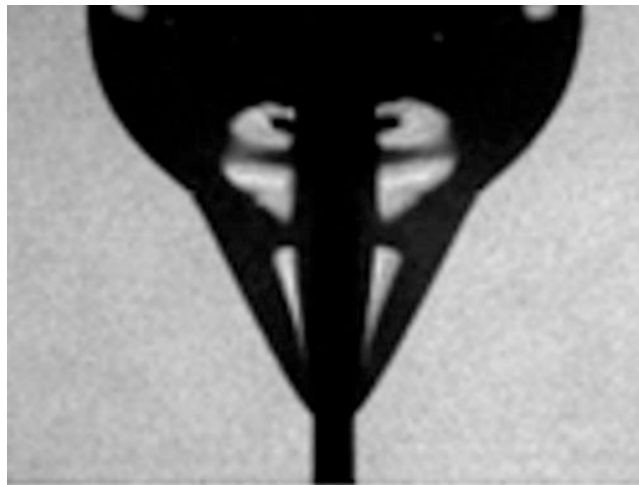


Fig. 28.1 SWIFT image of a shockwave evolving along a column of XTX 8004 within PMMA

In previous work, Murphy describes the use of SWIFT for extracting kinematics in two explosive configurations. One used a detonator to drive a shockwave into a PMMA block observed with SWIFT. The second setup also used a detonator to light off an extrudable explosive (XTX-8004) column placed in the center of the block, which forms shockwaves as the detonation front travels down the column. In order to extract the kinematic solutions for instantaneous shock position, velocity, and pressure; an ODE was proposed, which was numerically solved with a genetic clustering algorithm. The results of this optimization-based data reduction approach were in close agreement to the measurements from an appropriately placed photonic Doppler velocimetry (PDV) probe, a trusted diagnostic for velocity measurements [1]. Characterizing the detonation of high explosive (HE) geometries is difficult with traditional 1-D experimental techniques, generally requiring many 1-D probes across one or more experiments. In another study utilizing SWIFT, charge diameter was varied to examine its effect on the detonation and resultant shock properties [2].

Owing to the rapid temporal evolution in extreme environments, shock waves are difficult to observe with the unaided eye. SWIFT operates on the principles of focused shadowgraphy to enable observation. Shadowgraphy is a method for visualizing index of refraction variations within a medium by observing the deflection of light rays traversing through the material. Often, and as is the case here, these variations are caused by differences in density. The refracted backlight is projected onto a screen or directly imaged by a camera. Since detonating HE material generates shock waves with a jump-discontinuity of increased density at the front and slower decay at the rear, the backlight in SWIFT is significantly refracted at shock interfaces, appearing on the camera as distinct regions and shown in Fig. 28.1. These sharp light-to-dark transitions readily allow for a variety of digital image analysis techniques during post-processing and analysis.

In the experiments considered here, the capacitive discharge of electrical energy into an initiation mechanism causes it to function. Two initiators, commonly deployed for applications requiring precise timing (such as SWIFT), are the exploding bridgewire (EBW) and exploding foil initiator (EFI). The EBW uses high electrical current to vaporize a wire and generate rapidly expanding plasma, which provides enough energy to set off an HE. This type of detonator was invented at LANL by Luis Alvarez during the Manhattan Project [3]. The EFI, or slapper detonator, uses high electrical current to vaporize a foil, which in turn causes plasma to form. The expanding plasma propels a flyer, which impacts an HE and causes it to begin detonating. In 1965, the EFI was invented at Lawrence Livermore National Laboratory by John Stroud [3]. Each of these mechanisms has inherent strengths and weaknesses. However, for the lab studies considered here both perform reliably and effectively initiate the HE.

During detonation, a supersonic chemical reaction stimulates the creation of expanding gas, which arises from both the reaction itself as well as the heat from the energy release. This expanding gas causes an abrupt increase in pressure, and drives a shock wave into the inert material (PMMA) where it is coupled at the HE/inert interface. This shock wave travels at the shock velocity (speed of information), whereas the material behind the shock physically moves at the particle velocity. The shock wave propagates faster than the speed of sound of the media in which it exists. While the medium in front of the shockwave is undisturbed, the medium immediately behind the shockwave is compressed. This discontinuity at the shock front is modeled by the Rankine-Hugoniot jump equations. These equations use Lagrangian coordinates (from the perspective of the shockwave) to model a control volume in front of and behind the shockwave. Three equations of state are derived from the balance of mass, momentum and energy. The variables in these equations are as follows: shock velocity (U),

particle velocity (u), specific volume (v), pressure (P), and energy (e). Three fundamental empirical relationships (U - u , P - v , and P - u) can be formed with the Rankine-Hugoniot jump equations using experimental data to describe the state of a material under shock [4]. With the development of a technique for off-centerline velocity measurements, the P - v Rankine-Hugoniot equation could prove useful for determining 2-D pressures within a SWIFT image.

In order to expand the SWIFT technique, investigation of off-centerline, 2-D kinematic data obtained from SWIFT images as the shock front evolves is necessary. According to Baskar and Prasad, several mathematical methods have been developed for use in extracting kinematic information from 2-D shock fronts, such as shock ray theory, weakly nonlinear ray theory, Whitham's geometrical shock dynamics, and Euler's equations of motion [5]. Additionally, there exists hydrodynamics codes, such as ALE3D, which are very useful for both 2-D and 3-D shock modeling. This is especially useful for characterizing HE geometries during detonation. However, the team chose to create a geometrical model rather than a strictly physics based model in order to simplify the complicated nature of the models discussed by Baskar and Prasad.

Analysis was conducted as a reverse design problem as we attempted to reconstruct conditions that created the shock waves. We attempted to derive these initial conditions at a single point in time by observing existing data at multiple different time intervals. The team searched for a point in time in which precise extraction of initial conditions from the available data becomes difficult/impossible, which we refer to as the "far field." The location of this time would provide an upper bound of a time range where the data that most accurately leads back to the initial conditions could be recorded. A method for determining this reliability metric and providing guidance while establishing the optimal framerate for SWIFT experiments is discussed in this work. To achieve this goal, the team has developed a low-order model that generates shock fronts using specified input parameters. Given a SWIFT image at a certain time, the low-order model will use a genetic algorithm to narrow down a range of input parameters to a set of idealized inputs. This model compares the low-order shock front curve to a curve fitted to idealized, simulated SWIFT images.

28.2 Background

28.2.1 Experimental Setup

PMMA is used as the inert media in the SWIFT experiments for its ease of manufacturability as well as its optical clarity. The shock waves within the PMMA are driven with a PETN-loaded detonator, which is the main component that converts an electrical input signal to explosive energy. PETN is chosen as the high explosive in the detonator because of its ideal detonation wave characteristics. The SWIFT setup uses a SI-LUX640 spoiled-coherence laser backlight that passes through a collimating lens. The light is "spoiled-coherence" in order to avoid the "speckling" effect of conventional lasers. The collimating lens converts the beam into parallel rays that pass through the object plane. These collimated rays pass through a focusing lens and a bandpass filter before converging to a focal point at the cutoff plane. Finally, the light enters the imaging lens and reaches a SIMD16 ultra-high-speed framing camera [6]. Because the shock wave propagates faster than the speed of sound in PMMA, an extremely high frame rate camera is necessary. The camera is carefully calibrated to capture sixteen images of the shock wave propagating through the PMMA test block. A more detailed schematic of the SWIFT setup is shown in Fig. 28.2 below, followed by sixteen ALE3D-simulated images in Fig. 28.3.

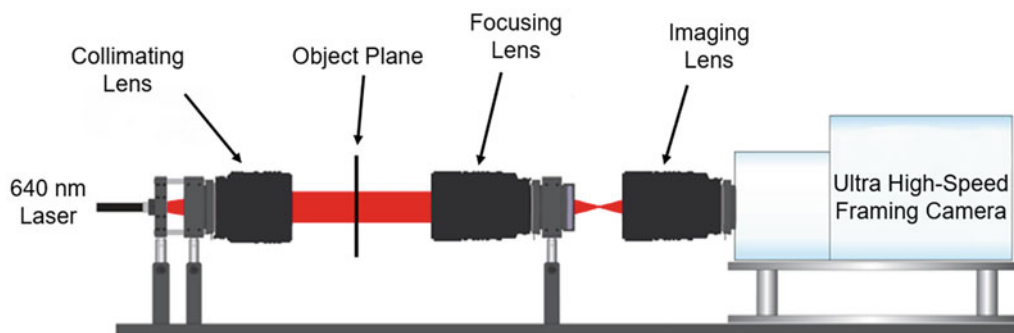


Fig. 28.2 SWIFT setup

28.2.2 General Shock Wave Theory

Throughout the project, the team considered two different shockwaves. Namely, the detonation wave and the shock wave within the PMMA. The detonation wave is created when the PETN within the detonator is initiated. Although PETN performs like an ideal HE, the detonation wave is assumed to have an elliptical shape and constant axial velocity as it propagates within the detonator. This constant velocity is known as the detonation velocity, and is dependent upon the pressing density of the HE. Once the detonation wave reaches the boundary between the detonator and PMMA, a second shock propagates throughout the PMMA with an exponentially decaying velocity, and evolves over time into a spherical wave shape.

28.2.3 Theory Behind the Model

To develop the low-order model, the team calculated the location and time at which the detonation wave intersected the boundaries of the detonator. These spatiotemporal locations are called breakout points, and are defined as the intersection points between the cross-sectional detonator geometry and the detonation wave front. To create these breakout points, the team modeled the detonation wave to start expanding from a radius size of zero at time $t = 0$ for both the semiminor and semimajor axis. The detonation wave expands at a unique detonation velocity for both the semimajor and semiminor axis, and intersects the detonator geometry until there are no remaining surfaces left to intersect. As these breakout points appear, the model generates an expanding circle centered at each breakout point, eventually resulting in the overlap of multiple breakout circles. These breakout circles originate from the breakout points and grow with an exponentially decaying velocity, analogous to how circular waves ripple outward after a pebble is dropped in a pond. When the next set of breakout points are created, the next circles start growing from a radius size of 0 mm. With this pattern, the most recent breakout points always have breakout circles centered about them that are smaller than the previous circles centered at earlier breakout points. The breakout point circles generated in our Ripple Evolution (RipE) Model were set to exhibit the same velocity profile as that obtained from the shock front along the centerline of the detonator. Figure 28.4 below shows an example of how these circles overlap near the end of the ALE3D-generated frame set.

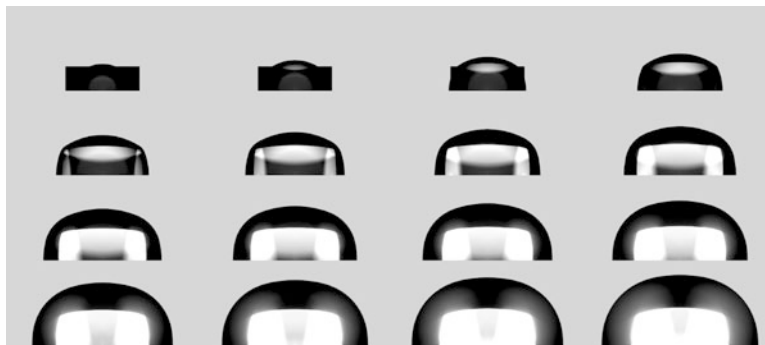


Fig. 28.3 Simulated evolution of a shockwave from a cylindrical detonator. Images progress from left to right and top to bottom

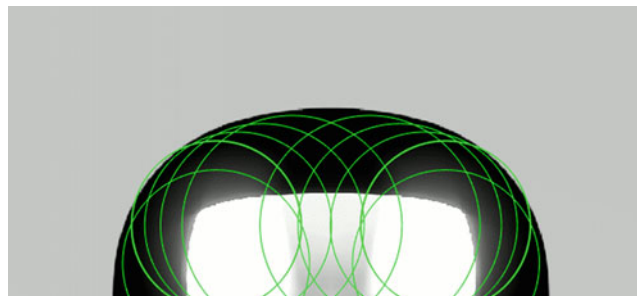


Fig. 28.4 Ripple Evolution Model near the last frame

Using a bisection method while analyzing the x domain, y values may be evaluated and determined to be either within or outside the breakout circles. With this technique, points may be plotted on the edge of the breakout circles to approximate the shock boundary of the model. The team implemented a genetic algorithm to determine an appropriate set of inputs that would match the shock boundary of an ALE3D-generated SWIFT image at any point in time. ALE3D is an arbitrary Lagrangian-Euler numerical simulation used to solve computationally intensive physical problems. The ALE3D shock boundary was found using Canny edge detection, which measures intensity variations within an image to determine the most likely edge. A convolution mask is also applied to the image for edge detection. The zeros of the Laplacian of the shock wave image corresponds to an edge, or a sharp change in contrast in an image. The Laplacian is the second derivative, of which the zeros are the local maximum of the gradient. By highlighting the pixels corresponding to the zeros, and suppressing non-edges, the edges become most prominent [7].

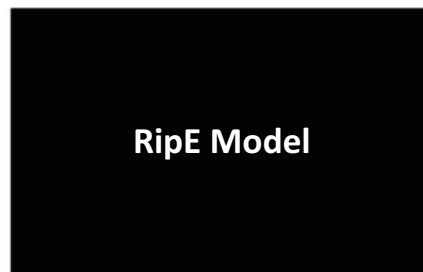
28.3 Analysis

28.3.1 Model Setup

There are several parameters that play an important role in our model when analyzing a cylindrical detonator. These parameters are listed in Table 28.1 below. The team approximated both the maximum and minimum values for the range of each parameter and set a resolution for each. The resolution defines the step size within the range, which allows a random value of the parameter to be generated when implementing the genetic algorithm described below. Comparing the meshed circle boundary of our RipE model to the boundary of the ALE3D image, the fitness of the meshed boundary was evaluated using the inverse of the area between the two curves, and normalized according to the arc length of the ALE3D shock front. Normalization is key to keeping fitness consistent between frames, otherwise a more evolved shock front will have a lower fitness due to its larger domain. The genetic algorithm then improves iteratively upon the fitness until a maximum fitness value is reached as highlighted in Fig. 28.5.

Parameters

A λ a
 b w r
 x y



Modeled Shock Boundary

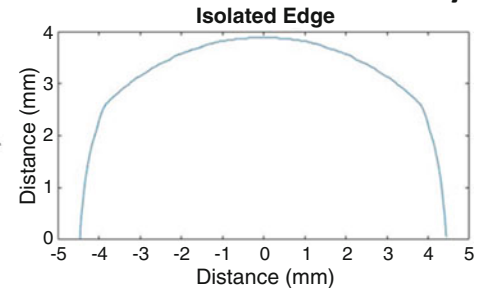


Fig. 28.5 RipE Model as a black box. Input parameters are used to generate a model shock boundary that is compared to the reference image is assigned a fitness value

Table 28.1 Detonation parameter specifications

Detonation parameter	Symbol	Min value	Max value	Resolution
Breakout shock velocity	A	3.4000 km/s	6.4000 km/s	0.0118 km/s
Decay constant	λ	0.1000	0.5000	0.0016
Semimajor axis detonation velocity (horizontal)	a	6.4000 km/s	9.40000 km/s	0.0118 km/s
Semiminor axis detonation velocity (vertical)	b	$a \times 0.85$ km/s	$a \times 0.95$ km/s	0.0137 km/s
Initiation X location	x	-0.0381 mm	0.0381 mm	0.0003 mm
Initiation Y location	y	0.0000 mm	0.0381 mm	0.0003 mm
Height	h	2.0000 mm	3.0000 mm	0.0039 mm
Width	w	7.3800 mm	8.3800 mm	0.0039 mm

28.3.2 Genetic Algorithm

The purpose of the genetic algorithm is to solve for the 8 initial parameters (for a cylindrical detonator) that output the closest curve to the reference curve generated in ALE3D. In order to solve for these 8 parameters, each parameter may first be represented as either a 7-bit or 8-bit section of a binary string. This section of the binary string is referred to as a member. As shown in Table 28.1, a range for each of the initial parameters is created by specifying both a maximum and a minimum value that the parameter could fall between. A resolution is specified using the maximum and minimum values of each range, and is chosen so that Eq. 28.1 below is satisfied.

$$(maximum\ value - minimum\ value) \div resolution = 255\ or\ 127 \tag{28.1}$$

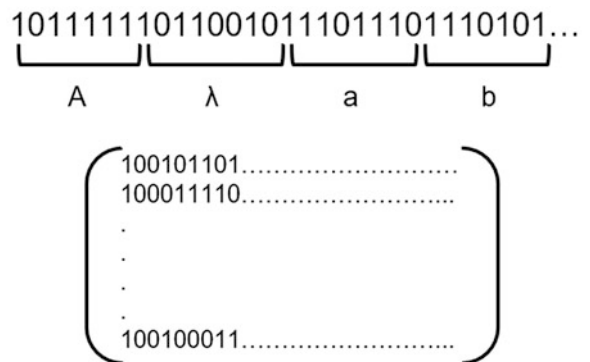
This step is completed to ensure that each one of the 256 numbers represented by the 8-bit segment (or 128 for a 7-bit segment) for describing a parameter of interest is useable. The parameter is described by the following equation:

$$parameter\ value = minimum\ value + resolution * (binary\ segment\ converted\ to\ an\ integer) \tag{28.2}$$

Equation 28.2 provides the ability to represent up to 256 different values that the parameter could possibly be within the range. With this method for representing each parameter, the binary segments are combined into one binary string with a length of 63 bits. The string is specifically 63 bits long because the seventh parameter is represented by only 7 bits, while the rest of the parameters are each represented by 8 bits. An entire population of members, or binary strings, is then created to test for fitness within the genetic algorithm. Figure 28.6 below illustrates how each parameter is combined into a member and inserted into the population matrix.

The first step in this process is to specify a population size of 500, for example, which results in a 500 by 63 binary matrix. The genetic algorithm tests each one of the rows in the matrix by extracting each parameter segment from the row, converting each segment to an integer, inserting those integers in Eq. 28.2 to create decimal values for each parameter, and inserting each parameter value into the lower-order model to generate a shock boundary. This boundary is then compared to an ALE3D boundary at the corresponding time of interest. The inverse of the area between the two boundaries is then taken and divided by the arc length of the reference boundary. This results in a normalized fitness value for each member. This process repeats itself 500 times until the fitness of the entire population has been calculated. Once this process has been completed, each member of the population is placed into a mating pool, with its probability of selection being proportional to its individual fitness. The algorithm then selects a pair of parents, performs crossover between their binary segments, and assigns a 5% probability of mutation to the new offspring. This mating occurs 500 times until an entirely new population has been created. At this point the algorithm returns to the first step and repeats the selection, breeding, and mutation processes for a total of 500 generations. Once the fitness of each member of the population in the final generation has been assigned, the average fitness is used to determine the resulting parameters. The average of each bit of the entire final population is calculated, and rounded to preserve the logical values. The resulting binary string is assumed to encode the detonation parameters which generated the shock wave of interest.

Fig. 28.6 Member and population visualization



28.3.3 Shockwave Boundary Fitting

Figure 28.7 below illustrates how the low-order model converges to a solution. The solid blue line shown in Fig. 28.6 represents the extracted outline of the ALE3D-generated shock front. The green line represents the attempt of the low-order model to fit a line over the reference shock boundary as closely as possible. The solid magenta outline represents the true shape of the detonator, while the dashed black line represents the algorithms closest approximation of the detonator shape.

28.3.4 Detection of First Four Parameters Across All Frames of the Cylindrical Detonator

After implementing the genetic algorithm across all 16 frames on 500 members for 500 generations, results were obtained that demonstrate the consistency of the genetic algorithm, indicating a possible far field bracket estimation. The results illustrated in Fig. 28.8 below were obtained by first setting the initiation location and detonator dimensions to fixed values before applying the algorithm.

The team noticed that four of the parameter values tended to have a higher variance after the algorithm evaluated frame 7. These four parameter values are as follows: major detonation velocity (V Det Major), minor detonation velocity (V Det Minor), breakout shock front velocity (A), and exponential decay coefficient (Lambda). The time corresponding to image 7 is approximately 0.77 μ s after initiation. The deviation was noticed on the cylindrical detonator shape and documented in Table 28.2 below.

28.3.5 Detection of Remaining Four Parameters Across all Frames of the Cylinder Detonator

Next, we determined the remaining four parameters across all frames of the cylindrical detonator set. These remaining four parameter values are as follows: horizontal initiation displacement (X), vertical initiation displacement (Y), the height of

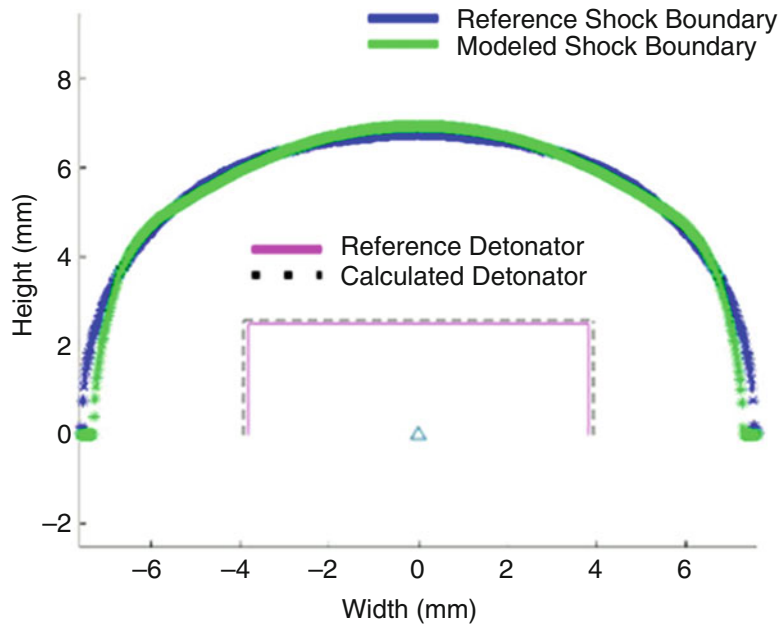


Fig. 28.7 Model convergence compared to reference

Table 28.2 Variance of average parameter values

Frame	Var(A)	Var(\square)	Var(Major)	Var(Minor)
1-7	0.001500	0.011300	0.000190	0.000092
8-16	0.008500	0.221800	0.003300	0.003900

the cylindrical detonator (Height), and the diameter of the cylindrical detonator (Width), which appears as the width of a rectangle when viewing the front cross section. The setup for this analysis involved specifying a population size of 250 members, and allowing a maximum of 250 generations. Figure 28.9 below demonstrates results that are both more accurate and more precise in this set of four parameters than in the previous set of four parameters. Additionally, percent error for each of these four resulting parameters is extremely low when compared with the true values shown in Table 28.3 below.

Compared to the true values, the four parameters, X, Y, Height, and Width, had percent errors ranging from approximately 0.001% to 0.00375%. With parameters of V Det Major, V Det Minor, A, and Lambda fixed, the algorithm is shown to be able to accurately determine the detonator geometry and initiation location of detonation. Height parameter had notably higher percent error compared to X, Y, and Width parameters.

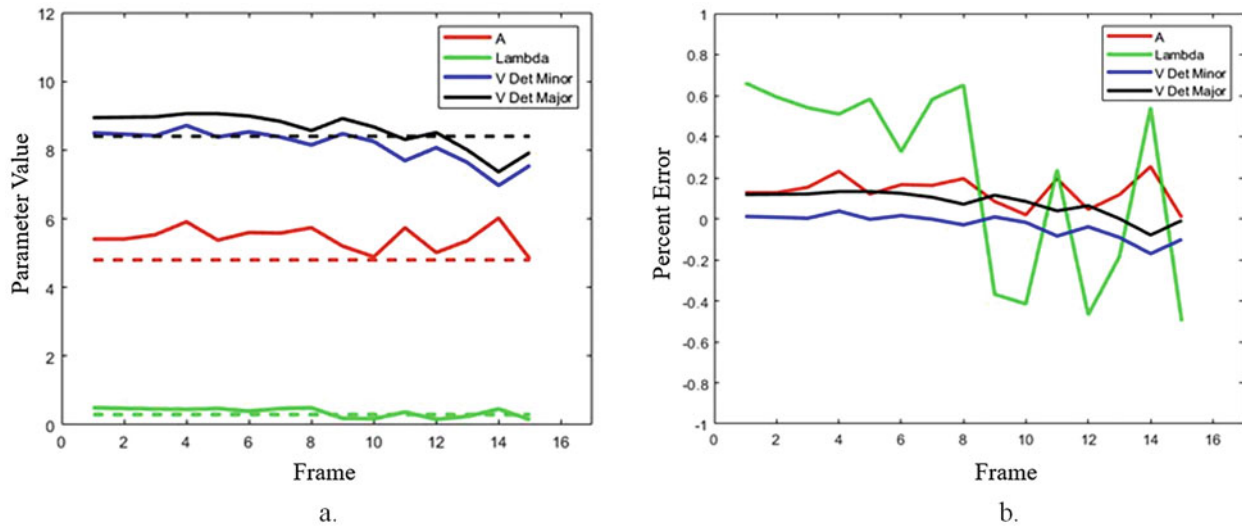


Fig. 28.8 (a) First 4 parameter values across all 16 frames. The trend shows instability in frames later than 7. (b) Percent error of 4 detonation parameters across all 16 frames. Divergence occurs near frame 7

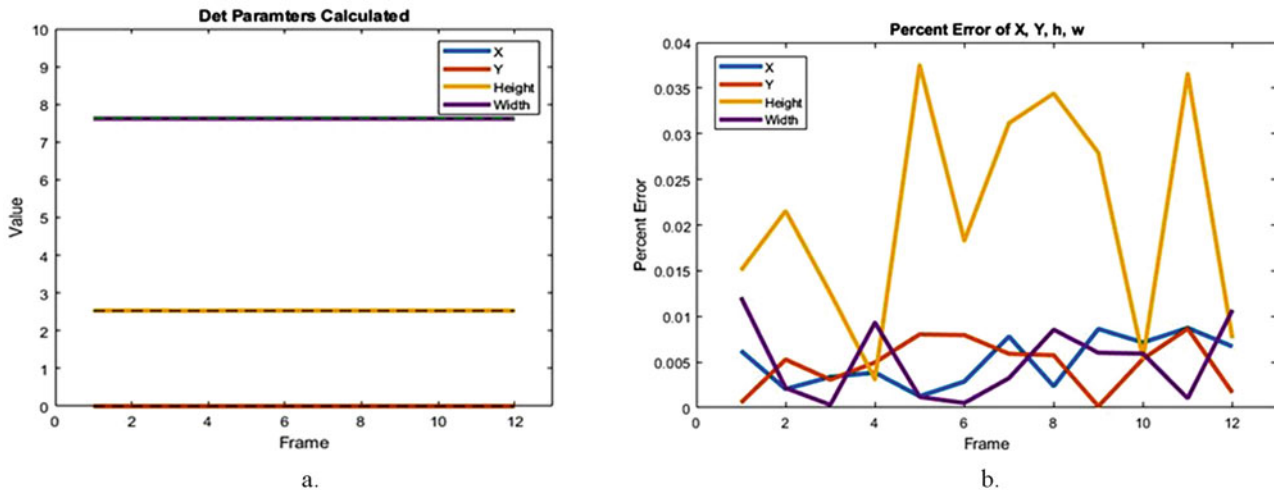


Fig. 28.9 (a) Last 4 parameter values across all 16 frames. The trend demonstrates high accuracy in results. (b) Percent error of detonation parameters across all 16 frames. Height error varies more than the rest

Table 28.3 True parameter values

	X (mm)	Y (mm)	Height (mm)	Width (mm)
True value	0.00	0.00	2.52	7.66

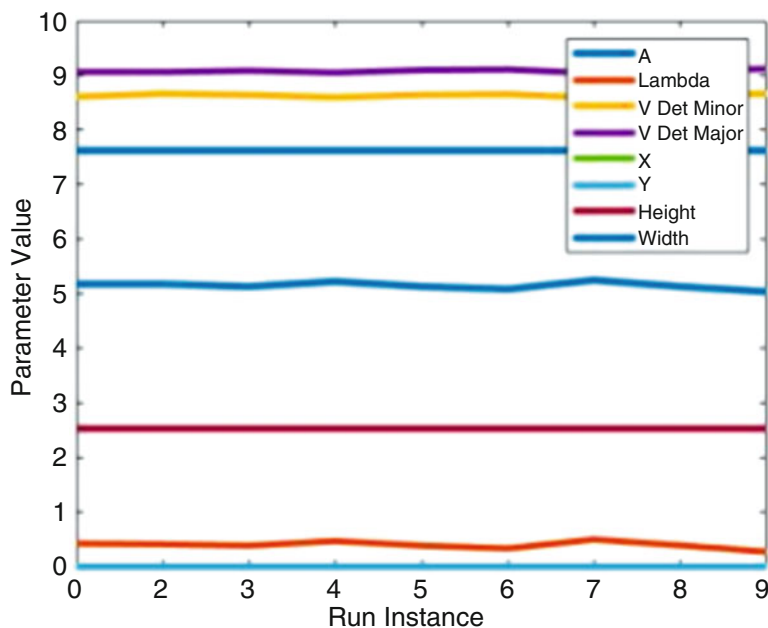


Fig. 28.10 Parameter Variation across 9 Runs of Frame 5

28.3.6 Parameter Detection Across Multiple Runs of Frame 5

In order to demonstrate the consistency of the algorithm's results, we chose to run the algorithm on a single frame from the cylindrical detonator to illustrate the minimal variation in the parameters. We chose frame 5 of the cylindrical set because we hypothesized that frames in the near-field (before frames 7 or 8) would tend to yield reliable results. Additionally, frame 5 is the first frame to show a complete wave front that has no intersection with the detonator geometry, which allows for easier curve fitting. Figure 28.10 above demonstrates the minimal variation of all the parameter values across the 9 runs of frame 5.

With all parameters of the model varied, the algorithm is shown to converge to a set of parameters for a single frame in the hypothesized near field region of the shockwave. The average error between the actual parameters and the calculated parameters is 0.5%. This indicates very high consistency of the genetic algorithm coupled with the low-order model. The genetic algorithm and low-order model are reliable and consistent when implemented on a data set multiple times. Compared to the actual parameters from the ALE3D data, the algorithm determined the model parameters with precision over multiple runs on the same image.

28.4 Conclusion

In summary, the team's goal was to develop a low-order model implementing a genetic algorithm with the capability of calculating initial parameters responsible for generating an ALE3D- simulated shock front at a specified time. With the determination of these initial parameters across all 16 images, the variance values of each parameter across all frames were compared for the case of a cylindrical detonator. The results indicated that there was significantly more fluctuation in the standard deviation of these values around frame 7 or 8, possibly indicating the existence of the far field beginning around the time of frame 7 (0.77 μ s after initiation). Future work would involve the verification of this hypothesis, continued development of the RipE model to determine localized pressure regions within the shock boundary, and use of a wider range of detonation parameters. The genetic algorithm is demonstrated to be consistent when implemented on a data set multiple times, which indicates low sensitivity to initial population and a small bound on the asymptotic fitness of the final population. Knowing this, the team can confidently rely on the genetic algorithm, and attend to adjustments of the low-order geometric model in future work. LA-UR-19-30,683.

Acknowledgements The team would like to thank Mark Lieber for generating the ALE3D simulations necessary for the development and calibration of the low-order model and genetic algorithm.

References

1. Murphy, M. J.: Extracting accurate shock kinematics from SWIFT experiments. In: Proceedings of the 16th international detonation symposium, in press, Chesapeake, MD, July 2018
2. Murphy, M.J., Johnson, C.E.: Preliminary investigations of HE performance characterization using SWIFT. *J. Phys. Conf. Ser.* **500**, 142024-1–142024-6 (2014)
3. Varosh, R.: Electric detonators: EBW and EFI. *Propellants, Explos., Pyrotech.* **21**(3), 150–154 (1996). <https://doi.org/10.1002/prop.19960210308>
4. Cooper, P.W.: *Explosives Engineering*. VCH Publ, New York (1996)
5. Baskar, S., Prasad, P.: Propagation of curved shock fronts using shock ray theory and comparison with other theories. *J. Fluid Mech.* **523**, 171–198 (2005)
6. SIMD – Ultra-High-Speed Framing camera: Adept Turnkey Pty Ltd. (n.d.): Retrieved from http://www.adept.net.au/cameras/spec_image/simD.shtml
7. Shrivakshan, G.T.: A comparison of various edge detection techniques used in image processing. *Int J Comput Sci Issues.* **9**(5), 269–276 (2012)

Chapter 29

An Acceleration-Based Approach to Force Limiting a Random Vibration Test



T. Van Fossen and K. Napolitano

Abstract Random vibration testing often requires limiting the rigid body interface forces between the test article and shake table to protect the test article from overtest. Force limiting is typically performed by limiting the sum of the forces from several load cell measurements to a prescribed force limit curve. While the use of load cells is considered standard practice, this approach often requires a costly fixture design program and adds complexity during pretest analysis and assembly. This paper presents an alternative approach to force limiting, where the rigid body interface forces are estimated from accelerometer measurements and a reduced mass matrix. This acceleration-based approach eliminates the need for interface fixturing and requires only a standard modal pretest analysis and the measurement of several accelerometer degrees of freedom during test, thereby reducing the cost and complexity of the test program. The efficacy of the acceleration-based force limiting approach is demonstrated using test data from a recent random vibration test program, along with the results of a trade study evaluating the sensitivity of modeling inaccuracies on the accuracy of the rigid body interface forces calculated using this approach.

Keywords Random vibration · Force limiting · Rigid body forces · Modal pretest analysis · Flight hardware qualification

Nomenclature

A	measured accelerations (time histories or FRFs)
ASET	set of DOF used to create TAM
C	semi-empirical force-limiting constant
CG	center of gravity
CI	confidence interval
dB	decibel
DOF	degrees of freedom
f	frequency
f_b	break frequency
FEM	finite element model
F_{Lim}	force limit PSD
F_{RB}	rigid body force/moment time histories or FRFs
FRF	frequency response function
FX, FY, FZ	directional rigid body interface forces
IRKE	iterative residual kinetic energy
J_{ii}	elements of the inertia tensor
m	total mass of the test article
M	reduced mass matrix
M_{mod}	reduced mass matrix estimated from $M_{RB, mod}$
M_{RB}	rigid body mass matrix

T. Van Fossen (✉) · K. Napolitano
ATA Engineering, Inc., San Diego, CA, USA
e-mail: tyler.vanfossen@ata-e.com; kevin.napolitano@ata-e.com

$M_{RB, mod}$	modified rigid body mass matrix
n	a constant controlling force limit roll-off slope
N	number of ASET DOF
pinv	pseudo-inverse
POgg	pseudo-orthogonality
PSD	power spectral density
PSD_{IN}	acceleration input PSD
R	rigid body mode shape coefficients
R^T	transposed rigid body mode shape coefficients
TAM	test analysis model
x, y, z	directional CG coordinates

29.1 Introduction

Random vibration testing is often performed to qualify aerospace hardware to the expected vibration environments during flight. However, if left unchecked during testing, the measured rigid body interface forces between the test article and shaker table may exceed the expected flight levels—a concept known as overtest. Overtest may be caused by several factors, but it can usually be attributed to a mismatch in impedance between the test and flight boundary conditions [1]. To ensure that the test environments are representative of the expected flight environments and to protect the test article from overtest, the rigid body interface forces measured during test are limited to prescribed power spectral density (PSD) force limit curves. One force limit PSD is defined for each unique input PSD, such that each independent input axis may have a unique force limit PSD. During test, the acceleration input PSD is notched at all frequencies where the rigid body interface forces exceed the force limit curve. Notching can be either active (i.e., notches are updated after each data frame) or passive (i.e., notches are calculated from low-level runs and built directly into the input PSD). Both on-axis (i.e., aligned with the input axis) and off-axis (i.e., orthogonal to the input axis) forces are often limited to the same force limit specification.

Several methods exist for calculating force limit PSDs; this paper presents the semi-empirical force limiting approach defined in the NASA Technical Handbook [1] and shown in Eq. 29.1a, 29.1b. Using this approach, the force limit PSD for each input axis is calculated as a piecewise function of frequency, such that the magnitude of the force limit PSD is allowed to roll off beyond the break frequency, which is typically defined as the modal frequency with the highest on-axis modal effective mass.

Semi-empirical force limit equation [1]:

$$F_{Lim} = C^2 m^2 \text{PSD}_{IN}, \quad f < f_b \quad (29.1a)$$

$$F_{Lim} = C^2 m^2 (f_b/f)^{2n} \text{PSD}_{IN}, \quad f \geq f_b \quad (29.1b)$$

where:

C is a dimensionless constant (frequency independent), which depends on the configuration

f is frequency

f_b is the break frequency

F_{Lim} is the force limit PSD

m is the total mass of the test article

n is a positive constant controlling roll-off slope

PSD_{IN} is the acceleration input PSD

During testing, the rigid body interface forces are typically measured using summing amplifiers to sum the forces from several load cell measurements in the time domain. While the use of load cells has been considered standard practice for many years, this approach often requires expensive instrumentation and fixture design programs. For the case study presented (described in the next paragraph), the estimated cost of the necessary instrumentation and fixturing is over \$100,000, a significant portion of the overall cost of the test program. In an effort to reduce cost, this paper presents an alternative approach to force limiting, whereas accelerometer measurements and a corresponding test-analysis model (TAM) are used to estimate the rigid body interface forces.

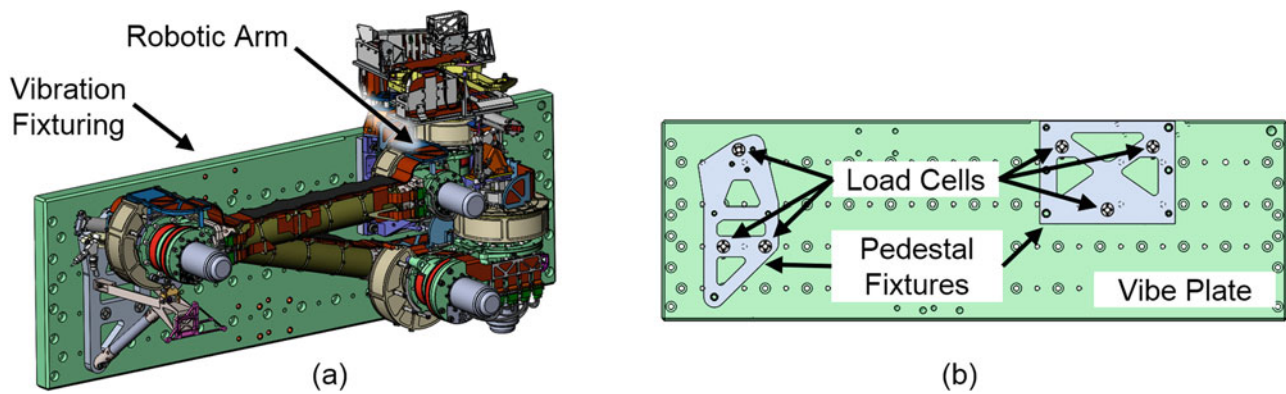


Fig. 29.1 CAD models of the (a) test configuration and (b) vibration fixturing

This paper presents data from the Mars 2020 robotic arm random vibration test program to demonstrate the efficacy of the acceleration-based approach. While this test program used traditional load cell measurements for force limiting, additional accelerometer measurements were acquired for this demonstration. Figure 29.1 shows the test configuration with the robotic arm mounted to vibration fixturing consisting of a vibrate plate, two pedestal fixtures, and six triaxial load cells. Note that the inclusion of the pedestal fixtures and load cells (required for force-based force limiting but not acceleration-based force limiting) changes the boundary conditions of the test article and therefore the modes of the test configuration—an undesirable side effect of the traditional force limiting approach.

29.2 Technical Approach

This section presents an acceleration-based approach for estimating rigid body interface forces and moments from random vibration test data. The approach uses standard modal pretest analysis techniques to select enough test degrees of freedom (DOF) to accurately capture modal mass across the frequency range where force limiting is expected. Guyan reduction [2] is used to generate a TAM consisting of reduced mass and stiffness matrices and a list of test DOF (referred to as the ASET), and rigid body mode shape coefficients are calculated based on geometry. During test, N acceleration DOF are measured (where N corresponds to the number of ASET DOF), and the rigid body interface forces are estimated using Eq. 29.2:

Acceleration-based rigid body force calculation:

$$F_{RB} = R^T M A \quad (29.2)$$

where:

A is an $[N \times 1]$ vector of measured acceleration time histories or frequency response functions (FRFs)

F_{RB} is a $[6 \times 1]$ vector of estimated rigid body force/moment time histories or FRFs

M is the $[N \times N]$ reduced mass matrix

R^T is an $[N \times 6]$ matrix of transposed rigid body mode shape coefficients

Note that while the focus of this paper is on the estimation of rigid body interface forces, Eq. 29.2 also returns the estimated rigid body interface moments. Also note that the measured acceleration data can be in either time history or FRF form, with the resultant from Eq. 29.2 returned in the same form as the acceleration data. When Eq. 29.2 is used with acceleration time histories, the resultant can be converted to PSD form using the same signal processing techniques used with the force-based load cell approach.

29.3 Analytical Validation

A modal pretest analysis was conducted prior to the Mars 2020 robotic arm random vibration test program, and additional accelerometer measurements were acquired during test for the purpose of experimentally validating the acceleration-based

force limiting approach. This section details the modal pretest analysis process and analytically validates the acceleration-based approach by comparing the estimated rigid body interface forces to analytical forces recovered directly from Nastran.

The iterative residual kinetic energy (IRKE) [3] method was used to generate a large pool of candidate ASET DOF, and down-selection was performed using the *downselect_sensors* function within ATA Engineering’s IMAT™ software. This function uses Guyan reduction [2] to remove one candidate DOF at a time and calculates the sensitivity to pseudo-orthogonality (POgg) quality to the removal of each DOF, where POgg quality is measured as the root sum square of the difference between the POgg and identity matrices. Targets were set for both the diagonal (≥ 0.95) and off-diagonal (≤ 0.05) POgg terms to ensure that modal mass was adequately captured across the frequency range where force limiting was expected (< 100 Hz for this test), and the minimum number of ASET DOF was determined by evaluating POgg quality for several incremental TAMs and selecting the TAM with the fewest DOF that meets the POgg targets.

Table 29.1 shows the results from several incremental TAMs (diagonal POgg terms only), suggesting that 33 DOF are required to meet the diagonal target (≥ 0.95). Table 29.2 shows the full POgg matrix for the 33-DOF TAM, confirming that the off-diagonal target (≤ 0.05) is also met using this number of DOF.

Table 29.1 POgg (diagonal terms only) vs. number of ASET DOF

FEM Shape	Freq (Hz)	Number of ASET DOF								
		37	36	35	34	33	32	31	30	29
1	26.6	1.00	1.00	1.00	1.00	0.99	0.99	0.99	0.99	0.99
2	30.9	0.99	0.99	0.99	0.99	0.98	0.98	0.98	0.98	0.98
3	36.0	1.00	1.00	1.00	1.00	0.98	0.98	0.96	0.96	0.96
4	51.1	0.99	0.99	0.99	0.99	0.98	0.98	0.98	0.98	0.98
5	53.0	0.98	0.98	0.98	0.98	0.98	0.98	0.98	0.98	0.98
6	61.8	0.98	0.98	0.98	0.98	0.98	0.98	0.98	0.97	0.97
7	72.1	0.97	0.97	0.97	0.96	0.96	0.96	0.95	0.95	0.94
8	76.5	0.96	0.96	0.96	0.96	0.96	0.93	0.93	0.93	0.92
9	91.1	0.95	0.95	0.95	0.95	0.95	0.95	0.95	0.91	0.85
10	92.1	0.99	0.99	0.99	0.99	0.99	0.98	0.98	0.97	0.97
11	93.9	0.96	0.96	0.96	0.96	0.95	0.95	0.95	0.94	0.94
12	106.3	0.94	0.94	0.94	0.94	0.94	0.94	0.94	0.94	0.92

Table 29.2 POgg matrix using final TAM (33 DOF)

		TARGET FEM Shapes											
		1	2	3	4	5	6	7	8	9	10	11	12
Freq (Hz)		26.6	30.9	36.0	51.1	53.0	61.8	72.1	76.5	91.1	92.1	93.9	106.3
FEM Shapes	1	26.6	0.99	0.00	-0.01	0.00	0.00	0.00	0.00	0.01	0.00	0.00	0.00
	2	30.9	0.00	0.98	0.00	0.00	0.00	0.00	-0.01	-0.01	0.01	0.00	0.02
	3	36.0	-0.01	0.00	0.98	-0.01	0.00	0.00	0.01	0.00	0.01	0.00	0.01
	4	51.1	0.00	0.00	-0.01	0.98	-0.01	0.00	0.00	0.00	0.01	0.01	0.02
	5	53.0	0.00	0.00	0.00	-0.01	0.98	0.00	0.00	0.00	0.00	0.00	0.00
	6	61.8	0.00	0.00	0.00	0.00	0.00	0.98	-0.01	0.00	-0.01	0.00	-0.01
	7	72.1	0.00	-0.01	0.01	0.00	0.00	-0.01	0.96	0.00	-0.01	0.00	0.00
	8	76.5	0.00	-0.01	0.00	0.00	0.00	0.00	0.00	0.96	0.01	0.00	0.00
	9	91.1	0.01	0.01	0.01	0.01	0.00	-0.01	-0.01	0.01	0.95	0.00	-0.02
	10	92.1	0.00	0.00	0.00	0.01	0.00	0.00	0.00	0.00	0.00	0.99	-0.01
	11	93.9	0.00	0.02	0.01	0.02	0.00	-0.01	0.00	0.00	-0.02	-0.01	0.95
	12	106.3	0.00	0.02	-0.01	-0.01	0.00	0.00	0.01	0.01	-0.01	0.00	-0.01

The final ASET (containing 33 DOF) is shown on the finite element model (FEM) in Fig. 29.2. Considering that ten of the ASET DOF were already planned for response limiting, the acceleration-based force limiting approach required just 23 additional acceleration DOF. When compared to the 18 load cell DOF required for traditional force-based force limiting, the acceleration-based approach requires only a marginal increase in the number of measurement DOF and enables the estimation of modal parameters (frequency, damping, and shape coefficients) for the first few modes and the visualization of operating deflection shapes during test.

The acceleration-based approach was validated analytically by recovering acceleration FRFs for the ASET DOF in Nastran, estimating the rigid body interface forces using Eq. 29.2, and comparing these forces to those recovered directly from the sum of the load cell elements in Nastran. Initial comparisons showed that the estimated forces were considerably

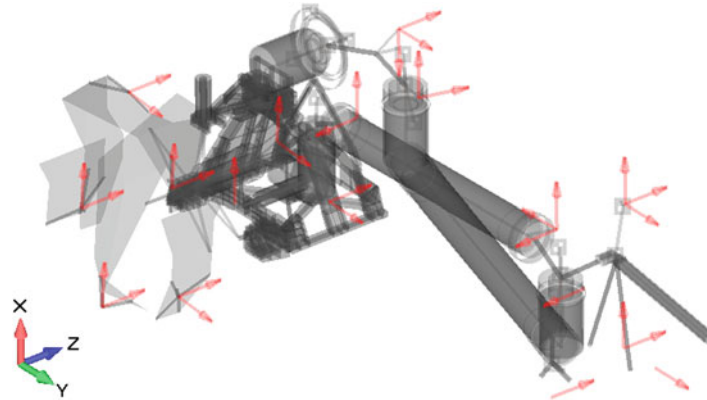


Fig. 29.2 Final ASET (33 DOF) displayed on the FEM

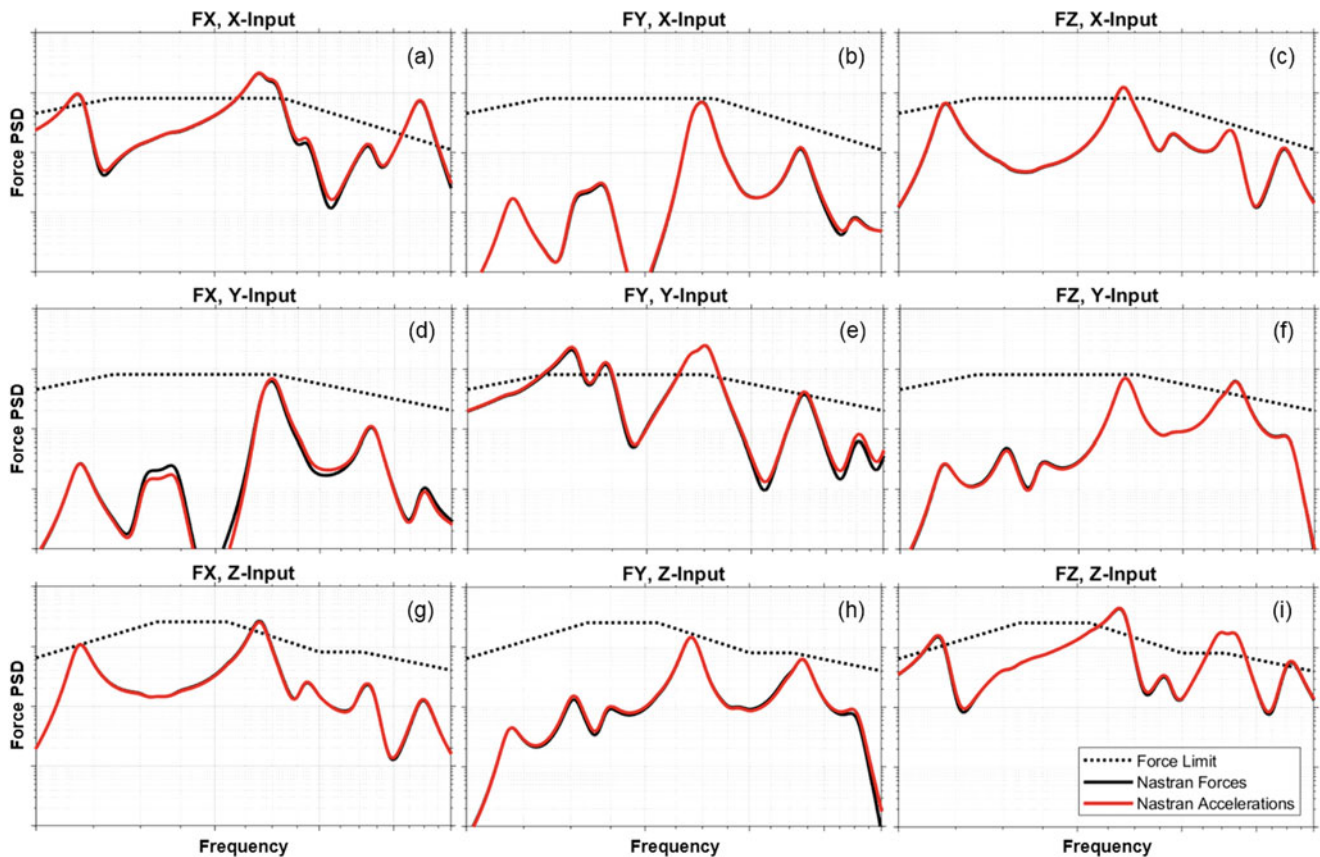


Fig. 29.3 Comparison of analytical rigid body interface forces calculated using both forces and accelerations: (a) FX, x-input (b) FY, x-input (c) FZ, x-input (d) FX, y-input (e) FY, y-input (f) FZ, y-input (g) FX, z-input (h) FY, z-input (i) FZ, z-input

lower in magnitude, suggesting that mass was “leaking” into the fixturing DOF. Thus, the TAM calculations were updated to use the free-free model configuration such that several boundary DOF could be included. The final ASET presented earlier (33 DOF) includes these additional boundary DOF, whereas the POGg data presented earlier was calculated using an equivalent fixed-base TAM with the boundary DOF removed (since the Nastran ASET cannot contain boundary DOF). The analytical comparison between the directional rigid body interface forces (FX, FY, and FZ) calculated using both the force-based and acceleration-based approaches is shown in Fig. 29.3 for each input direction (x, y, and z).

The forces estimated using the acceleration-based approach nearly directly overlay the forces obtained using the force-based approach, providing analytical validation of the acceleration-based force limiting approach. The estimated forces are within 1 dB of the expected forces across the frequency range of interest with considerably less error at higher magnitudes (where force limiting is expected).

29.4 Experimental Validation

Test data from the Mars 2020 robotic arm random vibration test program was used to experimentally validate the acceleration-based force limiting approach. A shaker table was used to excite the test article in three independent, orthogonal input directions—x, y, and z—and force limiting was enforced using the traditional force-based approach by summing the forces from six load cells integrated into the fixturing shown in Fig. 29.1. The ASET DOF (33 acceleration DOF) were also measured for the purpose of experimentally validating the acceleration-based force limiting approach. Figure 29.4 shows the comparisons between measured rigid body interface forces obtained by summing the load cell forces and the forces estimated using the measured acceleration FRFs, rigid body mode shapes, and TAM with Eq. 29.2.

In general, the acceleration-based and force-based forces agree well at higher force magnitudes (within 1 dB), with larger errors at lower force magnitudes. It is worth noting that the test-measured forces were lower in magnitude than the predicted forces from pretest analysis, so no notching was observed during testing. Since the accuracy of the estimated forces generally

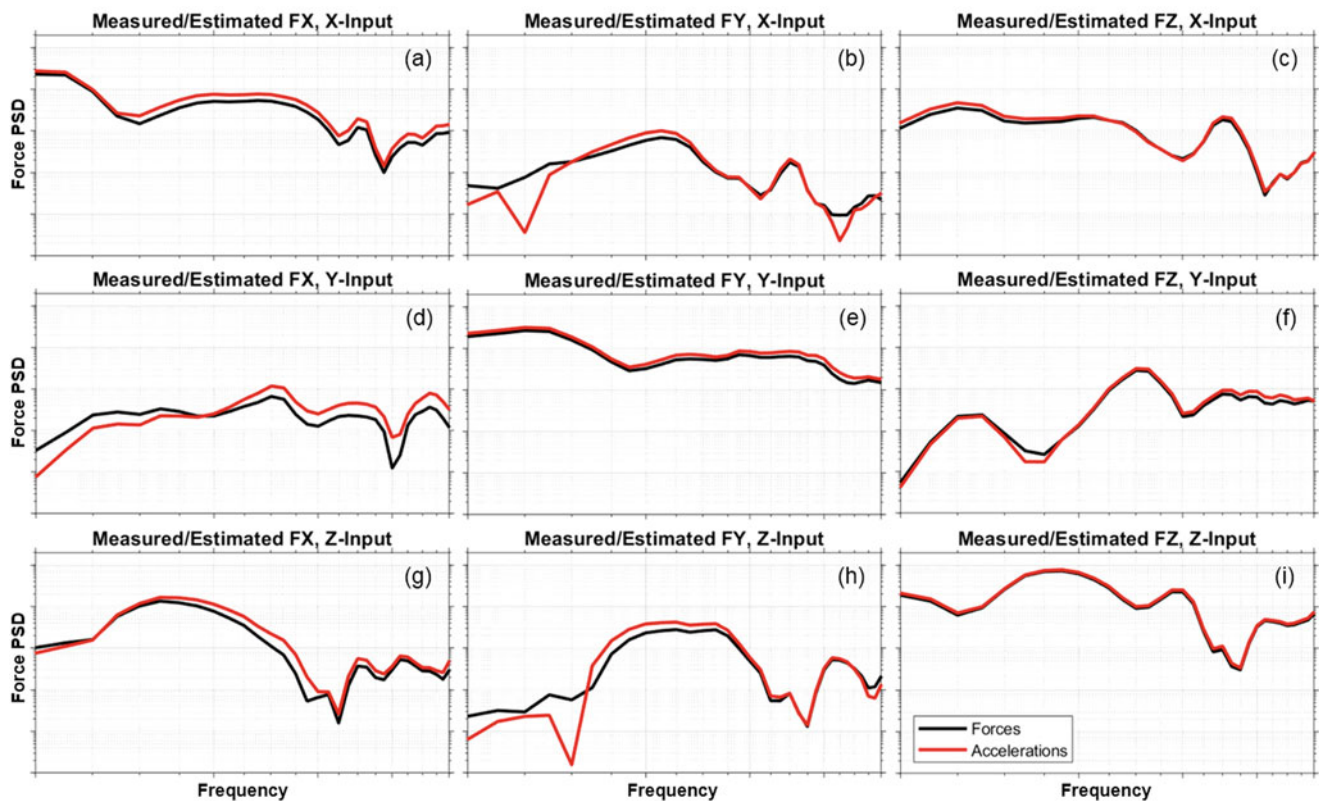


Fig. 29.4 Comparison of rigid body interface forces by approach (force-based and acceleration-based): (a) FX, x-input (b) FY, x-input (c) FZ, x-input (d) FX, y-input (e) FY, y-input (f) FZ, y-input (g) FX, z-input (h) FY, z-input (i) FZ, z-input

improves with magnitude, it is believed that the level of agreement between the estimated and measured forces would have been higher at the notch frequencies had notching been observed.

As with any force and/or response limiting approach, on-site validation is recommended to prevent accidental overtest due to an improperly configured limiting approach. It is recommended that the acceleration-based force limiting approach be verified in the same way as the force-based approach, by inputting a low-level random or sine input and verifying that $F \approx MA$ at low frequencies. In other words, verify that the drive-axis rigid body interface force is approximately equal to the product of the mass of the test article and the magnitude of the input acceleration.

29.5 Sensitivity to Modeling Inaccuracies

Given that the acceleration-based force limiting approach relies on analytically obtained data (reduced mass matrix and rigid body shapes), a trade study was performed to evaluate sensitivity of this approach to various modeling inaccuracies including variations in mass, center of gravity (CG), inertia, and stiffness (which affects modal frequencies). Other than stiffness (which was adjusted by directly editing several Nastran property cards), the trade study was conducted by modifying the rigid body mass matrix and reestimating the reduced mass matrix. The rigid body mass matrix—a 6x6 matrix describing the mass, CG, and inertia of the test article—is calculated from Eq. 29.3 and shown in Eq. 29.4.

Calculation of the rigid body mass matrix:

$$M_{RB} = R^T M R \quad (29.3)$$

where:

M is the [N×N] reduced mass matrix

M_{RB} is the [6×6] rigid body mass matrix

R is an [N×6] matrix of rigid body mode shape coefficients

R^T is an [6×N] matrix of transposed rigid body mode shape coefficients

Rigid body mass matrix:

$$M_{RB} = \begin{bmatrix} m & 0 & 0 & 0 & mz & -my \\ 0 & m & 0 & -mz & 0 & mx \\ 0 & 0 & m & my & -mx & 0 \\ 0 & -mz & my & J_{xx} & -J_{xy} & -J_{xz} \\ mz & 0 & -mx & -J_{yx} & J_{yy} & -J_{yz} \\ -my & mx & 0 & -J_{zx} & -J_{zy} & J_{zz} \end{bmatrix} \quad (29.4)$$

where:

J_{ii} are the inertia tensor elements (i.e., the lower-right [3×3] of the rigid body mass matrix)

m is the total mass of the test article

M_{RB} is the [6×6] rigid body mass matrix

x, y, z are the x-, y-, and z-coordinates of the CG

For the trade study, mass was adjusted by scaling each matrix element in the rigid body mass matrix containing the mass variable m , while leaving each inertia term unchanged. The CG was adjusted by scaling each directional component (x, y, z) separately, while leaving each inertia term unchanged. Inertia was adjusted by uniformly scaling all inertia terms without modifying any of the mass or CG terms. The modified rigid body mass matrix was then used to estimate a modified reduced mass matrix using Eq. 29.5.

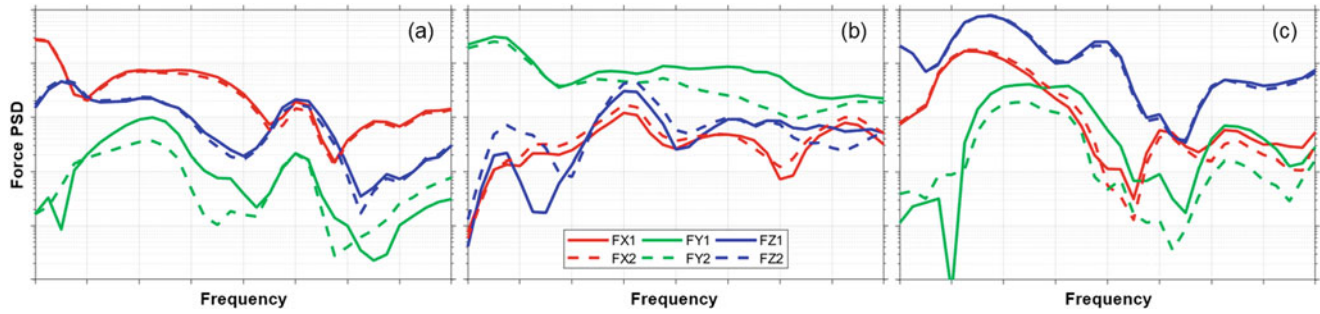


Fig. 29.5 Comparison of estimated rigid body interface forces calculated using both the nominal (solid lines) and round-tripped (dashed lines) mass matrices for (a) x-input (b) y-input (c) z-input

Estimation of TAM mass matrix from rigid body mass matrix:

$$M_{mod} \approx \text{pinv}(R^T) * M_{RB,mod} * \text{pinv}(R) \quad (29.5)$$

where:

M_{mod} is the [N×N] reduced mass matrix estimated from modified rigid body mass matrix

$M_{RB,mod}$ is the [6×6] modified rigid body mass matrix

R is an [N×6] matrix of rigid body mode shape coefficients

R^T is an [6×N] matrix of transposed rigid body mode shape coefficients

Note that R cannot be inverted directly because it is not a square matrix, so the pseudo-inverse matrix operation is used. While this introduces errors in the reduced mass matrix and therefore the estimated rigid body forces, the level of error introduced at the highest magnitudes in the rigid body force PSDs was found to be negligible. Thus, because Eq. 29.5 provides an efficient means to evaluating a large number of model variations, it was used for the trade study, but only the error in the highest magnitude force for each input direction was evaluated. Figure 29.5 compares the rigid body forces calculated using the nominal TAM mass matrix (solid lines) to those calculated using the round-tripped mass matrix obtained from Eq. 29.5 without modifying the rigid body mass matrix to show the level of error introduced by this approach. The level of error within the round-tripped mass matrix generally depends on the magnitude of the force, with minimal error at the highest peaks. Understanding that this method inherently introduces larger errors at lower magnitudes, only the error at the peak magnitude for each input direction was considered for the trade study.

Table 29.3 presents the error in the peak forces relative to the error found using the nominal FEM for various modeling inaccuracies. All errors were calculated using round-tripped mass matrices calculated from Eq. 29.5 with only one variable adjusted at a time. Each variable was allowed modest inaccuracy representing the expected worst case for that variable. Since mass is typically easy to measure, the FEM is expected to capture the true mass within $\pm 10\%$. The CG is a little trickier to measure and is often not measured at all, but since solid models do a reasonable job of estimating CG, each CG term (CGx, CGy, CGz) is expected to be within $\pm 20\%$. Larger errors are expected for the inertia tensor and actuator stiffnesses unless a correlated model is used, so these were allowed to vary by $\pm 50\%$.

The results show that the acceleration-based approach is insensitive to large changes in inertia and stiffness (0 dB), fairly insensitive to modest changes in mass (within 1 dB), and fairly sensitive to modest changes in CG depending on the input direction and affected CG coordinate (as much as 3 dB error). The approach's insensitivity to large changes in stiffness can be explained by the fact that while stiffness affects the flexible mode shapes and stiffness matrix, it does not affect the rigid body mode shapes or mass matrix (at least negligibly). The approach's insensitivity to large changes in inertia can be explained by examining the sizes of the matrices involved in the rigid body force calculation (Eq. 29.2). Substituting the estimated mass matrix from Eq. 29.5 into Eq. 29.2 (Eq. 29.6a), it becomes clear (after simplifying the equation to Eq. 29.6d) that only the first three rows of the rigid body mass matrix affect the calculation of the estimated rigid body forces, since the the product of a 6×6 matrix and a 6×1 vector is a 6×1 vector, and each row of the resultant vector is only affected by the corresponding row of the 6×6 matrix. In other words, each row of the modified rigid body mass matrix affects only the corresponding rigid body force/moment (e.g., row one affects only FX, row two affects only FY, etc.). Since we are only considering the rigid body forces (and not moments) for this trade study, changes to the inertia tensor do not affect the estimated rigid body forces because the inertia tensor is located in the bottom three rows of the rigid body mass matrix.

Substitute Eq. 29.5 into Eq. 29.2 for M and simplify:

Table 29.3 Peak force error (dB) relative to nominal FEM for various modeling inaccuracies

Modeling Inaccuracy	Input Direction		
	X	Y	Z
Mass +10%	0.83	0.83	0.83
Mass -10%	-0.92	-0.92	-0.92
CGx +20%	0.00	0.05	-1.13
CGx -20%	0.00	-0.05	1.08
CGy +20%	-0.02	0.00	0.59
CGy -20%	0.02	0.00	-0.62
CGz +20%	-3.04	-0.54	0.00
CGz -20%	2.46	0.52	0.00
Inertia +50%	0.00	0.00	0.00
Inertia -50%	0.00	0.00	0.00
Stiffness +50%	0.00	0.00	0.00
Stiffness -50%	0.00	0.00	0.00

$$F_{RB} \approx R^T * pinv(R^T) * M_{RB,mod} * pinv(R) * A \quad (29.6a)$$

$$R^T * pinv(R^T) * M_{RB,mod} = M_{RB,mod} \quad (29.6b)$$

$$pinv(R) * A = \{v\} \quad (29.6c)$$

$$F_{RB} \approx M_{RB,mod} * \{v\} \quad (29.6d)$$

where:

A is an [Nx1] vector of measured acceleration time histories or FRFs

F_{RB} is a [6x1] vector of estimated rigid body force/moment time histories or FRFs

$M_{RB,mod}$ is the modified [6x6] rigid body mass matrix

R is an [Nx6] matrix of rigid body mode shape coefficients

$\{v\}$ is the [6x1] column vector product of $pinv(R) * A$

Table 29.3 suggests that changes in mass result in direct scaling of the rigid body interface forces, since the error reported for each input direction is the same. This makes sense, because only the first three rows of the rigid body mass matrix affect the rigid body forces, and all nonzero terms in the rigid body mass matrix (Eq. 29.4) scale linearly with mass. Similarly, Eq. 29.4 shows (confirmed in Table 29.3) that for a given change in CG coordinate, only two of the rigid body forces are affected, since each of the first three rows contains only the two off-axis CG coordinates.

The sensitivity of the error in peak force to a given change in CG coordinate can be explained by rearranging Eq. 29.6a (not presented in this paper) to show that each rigid body force is affected by the product of each off-axis CG coordinate and the rigid body rotational shape about the other off-axis. For example, F_X is affected by the product of CG_y and R_z (rigid body rotation about the z-axis) and the product of CG_z and R_y (rigid body rotation about the y-axis). It can also be shown (not presented in this paper) that the rotational shape coefficients are affected by the two off-axis CG coordinates (e.g., R_y is affected by CG_x and CG_z) due to error in the center of rotation used for the calculation of the shape coefficients. Since the rigid body shape coefficients are multiplied by the measured accelerations (Eq. 29.6c), the level of error introduced by the flawed rotational coefficients is proportional to the magnitude of the measured accelerations and the degree to which the operating deflection shape contains the affected rotational motion. Tying this discussion back to Table 29.3, the largest error occurs for x-input when CG_z is shifted. It is no coincidence that the mode shape corresponding to the highest force peak for this input direction is the robotic arm rocking about the y-axis, since F_X (the directional force PSD containing highest force peak) is known to be affected by CG_z and R_y and CG_z is known to affect the R_y shape coefficients.

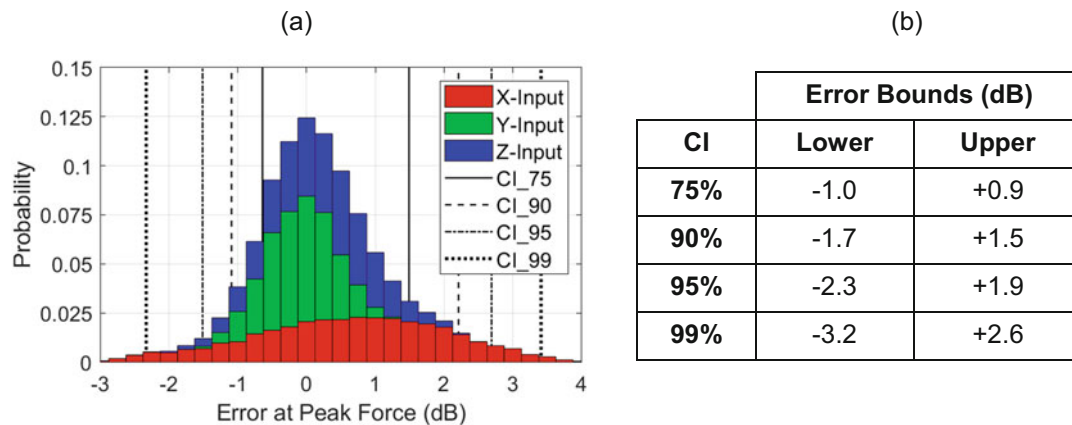


Fig. 29.6 (a) Distribution of peak force error (dB) from 10,000 Monte Carlo iterations and (b) corresponding CI error bounds

To provide insight into the accuracy of the acceleration-based force limiting approach, a Monte Carlo simulation was performed to simulate various modeling inaccuracies using the presented case study data. For each modeling variable presented in Table 29.3, a zero-mean normal distribution was assumed such that the nominal modeling values were the most likely values to be selected and the worst-case values were the least likely. The standard deviation of each distribution was set to be one-half the worst case value, and values outside the worst-case values were clipped to the worst-case values. The resulting distribution of peak force errors is shown in Fig. 29.6 for 10,000 Monte Carlo iterations for each input direction. The lower and upper error bounds for several confidence intervals (CIs) are also shown in Fig. 29.6. For example, 95% of the Monte Carlo iterations were found to produce peak force errors between -2.3 and 1.9 dB. This could be restated to say that with 95% confidence, the acceleration-based force limiting approach is capable of estimating peak forces within 2.3 dB when using a reasonably accurate FEM.

29.6 Conclusion

An acceleration-based force limiting approach was presented and validated both analytically and experimentally. The results indicate that accelerometer measurements can be used in conjunction with rigid body mode shapes and a reduced mass matrix from pretest analysis to estimate rigid body interface forces during test with reasonable accuracy. The number of required accelerometer DOF is determined using standard modal pretest analysis techniques to verify that modal mass is sufficiently captured by the TAM across the frequency range where force limiting is expected. Compared to the traditional force limiting approach, which relies on load cells being integrated into specially-designed fixturing, the acceleration-based approach has the potential to greatly reduce the cost associated with force limiting by eliminating the need for expensive instrumentation and fixturing. For the case study presented, it is estimated that acceleration-based approach could have reduced the cost associated with force limiting by approximately 80% with the ability to estimate the rigid body interface forces with reasonable accuracy (within 1 dB at high force magnitudes). Understanding that the acceleration-based approach relies on the accuracy of the pretest analysis FEM, a trade study was conducted to evaluate the sensitivity of this approach to various modeling inaccuracies. It was found that the acceleration-based force calculation is insensitive to large changes in stiffness and inertia, fairly insensitive to modest changes in mass, but fairly sensitive to modest changes in CG. Using test data from the presented trade study and assuming modest modeling inaccuracies, it is estimated with high confidence (>95%) that the acceleration-based approach is capable of predicting high-magnitude rigid body force magnitudes (i.e., the forces likely to be require force limiting) within ± 3 dB of the actual force magnitudes experienced by the test article during test.

Acknowledgements A special thank you to Motiv Space Systems, Inc., for allowing additional measurements to be made during the Mars 2020 robotic arm random vibration test program and for their approval in sharing these data and other details of the test program within this paper.

References

1. NASA Technical Handbook NASA-HDBK 7004C.: Force Limited Vibration Testing. November 30, 2012
2. Guyan, R.J.: Reduction of stiffness and mass matrices. AIAA J. **3**, (1965)
3. Coppelino, R.N.: Automated response DOF selection for mapping of experimental normal modes. In: 16th international modal analysis conference, Santa Barbara, February 2–5, 1998

Mr. Van Fossen is an alumnus of the University of Wisconsin-Madison and began his career with ATA Engineering in 2013 as a test engineer involved with numerous vibration test programs. He is now working more of an analysis role from ATA's regional office in Denver, Colorado.

Chapter 30

Frequency Based Substructuring on Resonant Plate



Erica M. Jacobson, Jason R. Blough, James P. DeClerck, Charles D. Van Karsen, and David Soine

Abstract Resonant plate pyroshock tests were originally designed to test one component axis at a time, while the qualification pyroshock tests often have multi-axis specifications to meet. Traditionally, one Shock Response Spectrum (SRS) is created for each single axis test record, which is then compared to the specified qualification SRS. There is interest in creating a multi-axis shock test environment using traditional resonant plate test components to save testing time and create a more realistic test environment. As a potential approach to test system design, LaGrange-Multiplier Frequency Based Substructuring (LM-FBS) is used to arrange single-axis resonant plate subsystems in different assembly configurations. LM-FBS uses Frequency Response Functions (FRFs) of the resonant plate parts, virtually assembles the parts, and produces FRFs of the assembly. To estimate potential shock test performance, an inverse Fourier transform is applied to the assembly FRF to get a time domain impulse response, then an SRS is calculated for all three response axes. A least squares regression is used to optimize the SRS produced from different assembly configuration to a multi-axis specification SRS. Preliminary assembly iterations are performed on a finite element model, and the final multi-axis configuration is verified with testing.

Keywords LaGrange-multiplier frequency based substructuring · Shock response Spectrum · Pyroshock · Optimization · Multi-Axis test

30.1 Introduction

Pyroshock events are short-duration, high-amplitude, high-frequency events that can be damaging to small electronics and structures. Examples of pyroshock events are pyrotechnic detonations or metal-on-metal impacts and occur, for example, during the stages of a space vehicle launch. Small structures have to undergo pyroshock qualification testing and meet a provided specification within a certain tolerance. Resonant plates are used to test a structure by impacting one side of the plate with a projectile and measuring the component response on the opposite side. The specifications are in the form of Shock Response Spectra (SRS), provided for each component axis. Since only one component axis is tested at a time, the test must be repeated three times (one for each orthogonal component axis) to complete the qualification tests [1].

Although there is interest in creating a multi-axis pyroshock test environment, the only evidence of doing so is through a “guess and check” method. A small set of multi-axis response locations on the resonant are predetermined by the test engineer, and the in- and off-axis shock response spectra are compared [2].

The motivation for this project is to eliminate the need for “guess and check”, and to find the optimal configuration of resonant plate components to create a multi-axis pyroshock test environment. Frequency based substructuring is used on the resonant plate Finite Element Model (FEM) to create a variety of possible configurations. The component SRS for each

The Department of Energy’s Kansas City National Security Campus is operated and managed by Honeywell Federal Manufacturing & Technologies, LLC under contract number DE-NA0002839

E. M. Jacobson (✉) · J. R. Blough · J. P. DeClerck · C. D. Van Karsen
Department of Mechanical Engineering & Engineering Mechanics, Michigan Technological University, Houghton, MI, USA
e-mail: ejacobso@mtu.edu; jrbough@mtu.edu; jdeclerck@mtu.edu; cdvankar@mtu.edu

D. Soine
Sandia National Laboratories, Albuquerque, NM, USA
e-mail: desoine@sandia.gov

orthogonal axis (+XYZ) is computed. Objective functions are applied to the in- (+Z) and off-axis (+XY) component SRS. The ideal configuration is verified with a physical test, along with two other configurations.

30.2 Background

The Shock Response Spectrum is a calculation that allows a shock event to be represented in the frequency domain. Using a set of predetermined natural frequencies (the x-axis of the SRS plot) and damping ratios, the SRS is computed from the component acceleration. This research uses “maximax” SRS calculations, e.g. the maximum absolute value, and implements David Smallwood’s MATLAB code of ramp invariant recursive time-domain method [3, 4].

Frequency Based Substructuring (FBS) is a method of calculating assembly dynamics from subsystem dynamics, generally in the form of frequency response functions (FRFs). FBS is often used during the early stages of the design process and for troubleshooting applications and eliminates the need to test the entire assembly. For each subsystem, external and interface degrees of freedom (DOFs) are defined. The interface DOFs are the connection points and should have the same geometry between the subsystems. The external DOFs are any other DOFs of interest, such as an input or response location on the assembly (Fig. 30.1). A full matrix of FRFs is necessary for the FBS calculations, meaning the dynamics between each DOF must be calculated. This can be done analytically with a Finite Element Model (FEM), or experimentally through modal analysis [5, 6].

LM-FBS NOTATION:

- u : measured quantity of displacement, velocity, or acceleration (acceleration is used in this research)
- f : external forces of the separate subsystems
- g : interface forces between the subsystems (represented by LaGrange Multipliers)
- F : substructured assembly forces ($f + g$)
- H : subsystem FRFs (u/f)
- \hat{H} : substructured assembly FRFs (u/F)
- Z : inverse of H (f/u)

There are two constraint conditions that must be met to assemble the subsystems together. The first is the coordinate compatibility condition, meaning the interface DOFs between the subsystems have the same displacement and are connected rigidly (infinite stiffness). The second condition is the force equilibrium condition and states that the interface forces between interface DOFs are equal and opposite in magnitude.

$$\text{Coordinate Compatibility : } u_I^a = u_I^b \quad Bu = 0.$$

$$\text{Force Equilibrium : } g_I^a = -g_I^b \quad B^T \lambda = g$$

This research uses LaGrange-Multiplier FBS (LM-FBS). LM-FBS implements the above conditions using a signed Boolean matrix (B) to indicate which interface DOFs are paired together. DOFs to be paired are marked with a “1” and all other DOFs are marked with “0”. One of the DOFs must be marked as “-1” to satisfy the coordinate compatibility condition, and that decision is arbitrary. A LaGrange Multiplier (λ) to represent the interface forces and are not explicitly solved for.

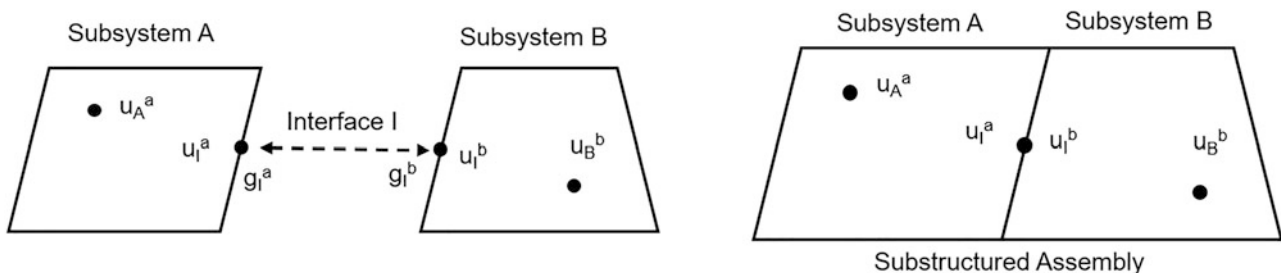


Fig. 30.1 Frequency based substructuring notation on subsystems and substructured assembly

$$\begin{bmatrix} Z & B^T \\ B & 0 \end{bmatrix} \begin{Bmatrix} u \\ \lambda \end{Bmatrix} = \begin{Bmatrix} F \\ 0 \end{Bmatrix}$$

The two conditions are mathematically expressed using block matrices. Solving the expression above satisfies both conditions simultaneously. The top row of the matrix expression consists of the substructured assembly dynamics obtained from the force equilibrium condition, where the total force (F) is the sum of the external (f) and interface (g) forces. The bottom row is the coordinate compatibility condition. This expression can be rearranged into the following:

$$\hat{H} = H - HB^T(BHB^T)^{-1}BH$$

Where the substructured assembly FRFs (\hat{H}) are calculated using the block matrix subsystem FRFs (H) and the signed Boolean matrix (B). The substructured assembly FRFs include all DOFs, some of which are redundant.

30.3 Analysis

The circular resonant plate is separated into two subsystems: subsystem A consists of the impact pad and circular plate, and subsystem B contains the payload. The global input DOF on subsystem A is the center of the impact pad, in-axis (+Z), representing the location of the projectile impact during a resonant plate shock test (Fig. 30.2). The interface DOFs between the subsystems are four bolt holes, representative of the physical assembly, in all three orthogonal directions (+XYZ). The response DOFs on subsystem B are five locations and three orthogonal directions (+XYZ). The interface DOFs must contain all three response directions (+XYZ) to accurately calculate in- and off-axis response of subsystem B.

Assumptions about the finite element model and calculation process are:

1. Measurement noise is low
2. Ignoring rotary DOFs won't affect the FBS calculation results
3. Modal truncation won't affect the FBS calculation results

A finite element model was used for the optimization and collection of FRFs. The model was created by Will Larsen and Chuck Van Karsen and correlated to the physical hardware through modal tests. The model was created in HyperMesh Desktop 2017. The impact pad and payload are made of tetra solid elements, the resonant plate is made from quad shell elements, and the support springs are modeled as bushings. The assembly, considered *model truth*, is modeled with contact surfaces correlated to test data. The interface DOFs are modeled using RBE3 elements: a group of eight nodes surrounding the bolt holes are connected in all six DOFs to an independent node. The independent node is used as the interface location.

For each subsystem, the external and interface DOFs are selected as both the input and response to populate the entire FRF matrix. The FRFs are calculated using a unit impulse frequency response function method, which used modal calculations and *Lanczos* eigenvalue solver. FRFs are calculated over a frequency range of 100 Hz to 10 kHz with a constant damping ratio of 0.5%. In this research, u is nodal acceleration.

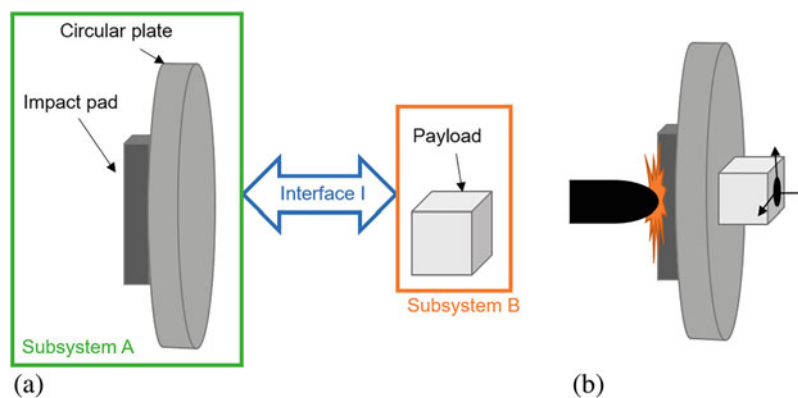


Fig. 30.2 Resonant plate subsystems and assembly

Since the circular resonant plate is symmetrical in geometry and mode shapes, only 1/8th of the plate was selected for optimization. The payload is moved to eleven locations, each with 0-degree and 45-degree orientations. In total, 22 locations are included in the optimization. There are five response locations for each payload location, making a total of 110 possible multi-axis configurations!

The resulting calculations from LM-FBS are FRFs. To calculate the component SRS, first, the impulse response function is calculated from the inverse Fourier transform of the FRFs between the global input (impact pad +Z) and global response (payload node +XYZ). Then, a time domain response is calculated by convolving the impulse response function with a time domain shock pulse previously obtained from test data. Last, time domain response is used to calculate the component shock response spectrum for each axis (+XYZ).

The goal of this research is to find a configuration where the in- and off-axis responses are equal in magnitude. An objective function, defined as the square root of the sum of the squares, was selected to mathematically determine the separation between the in- and off-axis component SRS.

$$RSS(X, Z) + RSS(Y, Z) \text{ where } RSS(x, y) = \sqrt{\frac{1}{m} \sum_{k=1}^m (x_k - y_k)^2}$$

The optimization process consists of arranging the subsystem FRFs into a block matrix, calculating the multi-axis SRS using LM-FBS, setting tolerance bands around the in-axis SRS, and solving a set of objective functions. This is repeated for every configuration. The optimal configuration minimizes the objective functions.

1. Collect payload (or test object) FRFs
2. Use resonant plate FRFs across a set of possible configurations
3. LM-FBS for each configuration:
 - (a) Arrange subsystem FRFs into a block matrix
 - (b) Calculate LM-FBS, obtain substructured assembly FRFs
 - (c) Inverse Fourier transform
 - (d) Convolve with shock pulse (from test data)
 - (e) Shock response spectrum
4. Set tolerance bands around in-axis SRS
5. Calculate objective function, select the optimal configuration

30.4 Results

The configuration that minimizes all objective functions is the 0-degree oriented payload at (−3,3) inches from the center at the response node on the front face towards the edge of the payload (Fig. 30.3). The other two configurations used for validation were “center” (0-degree oriented payload at x = 0 in, y = 0 in) and “bottom” (45-degree oriented payload at x = −5 in, y = 0 in). The same payload response node was used.

FRFs were also collected experimentally on both the assembly and subsystems, for the optimal configuration (Fig. 30.4) and two other configurations (“bottom” and “center”). Triaxial accelerometers and an impact hammer were used to collect input and response dynamics at each DOF of interest. FEM dynamics were used for subsystem B since the payload doesn’t have dynamics in the frequency range of interest – dynamics of the frame used for suspension were contaminating the experimental data.

An “adjusted truth assembly” was created, both experimentally and analytically, to verify what was occurring mathematically during LM-FBS calculations. In the FEM, groupings of nodes surrounding the bolt holes were rigidly constrained together using RBE2 elements. This was replicated in the experimental assembly by using lock washers between the circular plate and payload.

For each configuration, six methods can be compared: truth assembly, adjusted assembly, and substructured assembly experimentally or analytically. A table of the knee frequencies (drum mode frequency) across all six methods and three configurations is below (Table 30.1)

There is an agreement between the substructured assembly and adjusted assembly, indicating the discrepancy between the former and the truth assembly is due to the interface dynamics. It is expected that as the number of interface DOFs

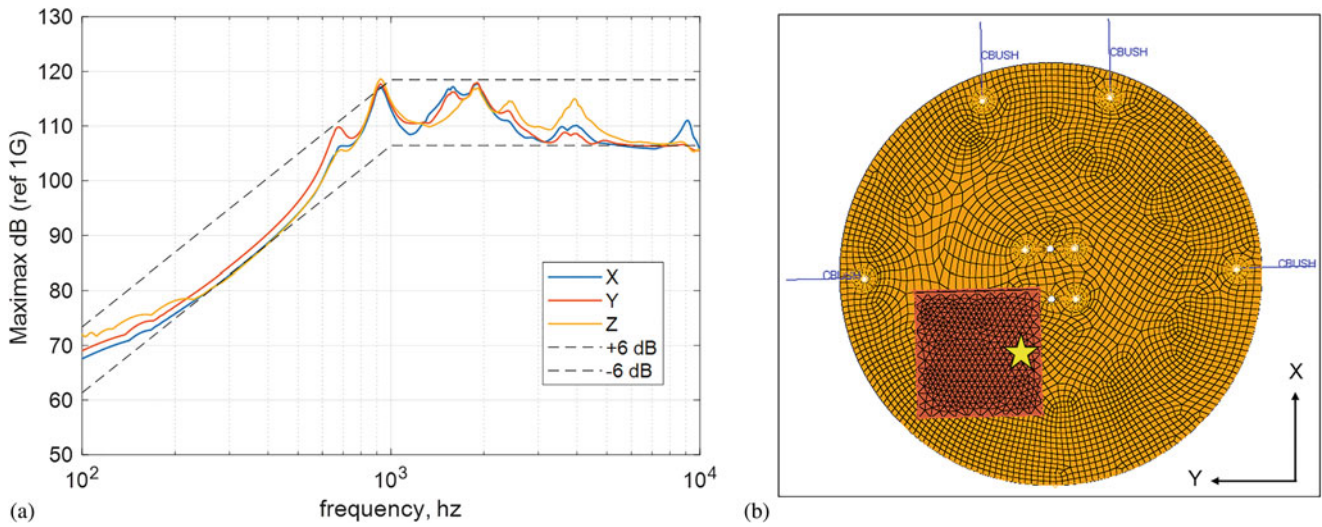


Fig. 30.3 Optimal configuration geometry and multi-axis shock response spectrum

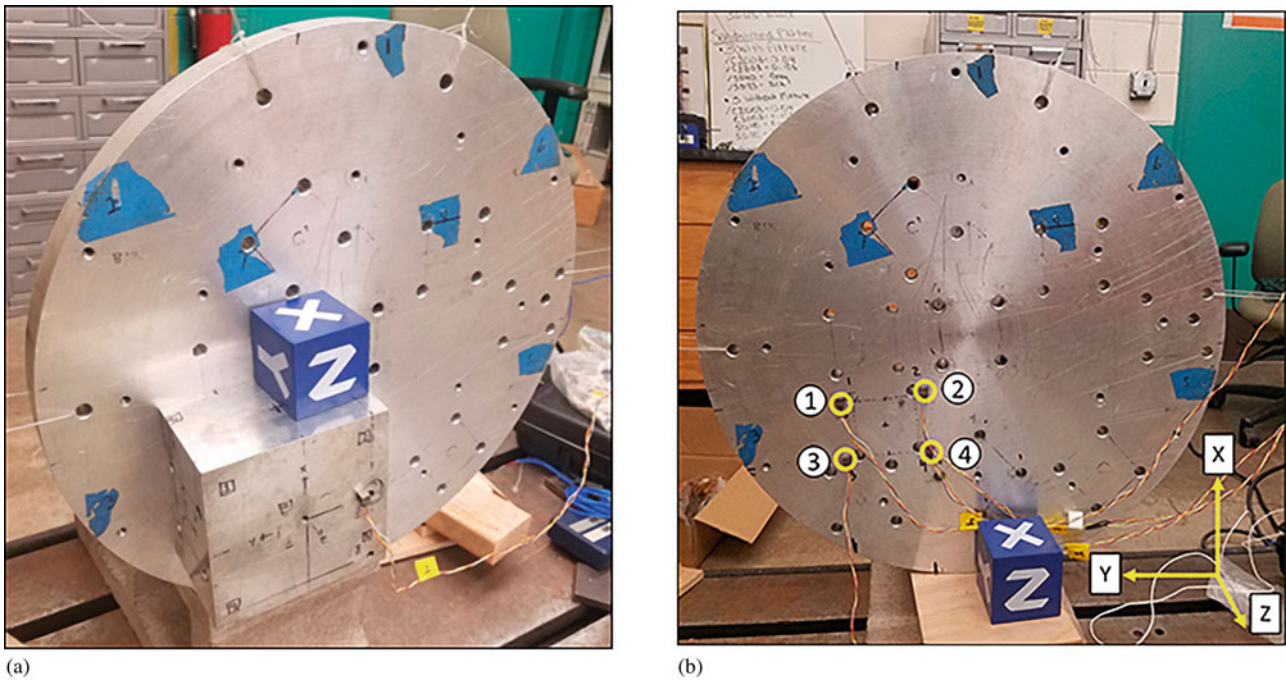


Fig. 30.4 Experimental setup for optimal configuration truth assembly and subsystem A

Table 30.1 Knee frequencies (Hz) for three configurations and six methods

Configuration	Method	FBS	Adjusted assembly	Truth assembly
Center	Model	936	966	1177
	Test	965	950	1209
Bottom	Model	873	922	1103
	Test	921	962	1132
Corner	Model	920	970	1190
	Test	860	924	1057

increase, the interface dynamics will increase in stiffness, and the substructured assembly dynamics will closely match the truth assembly.

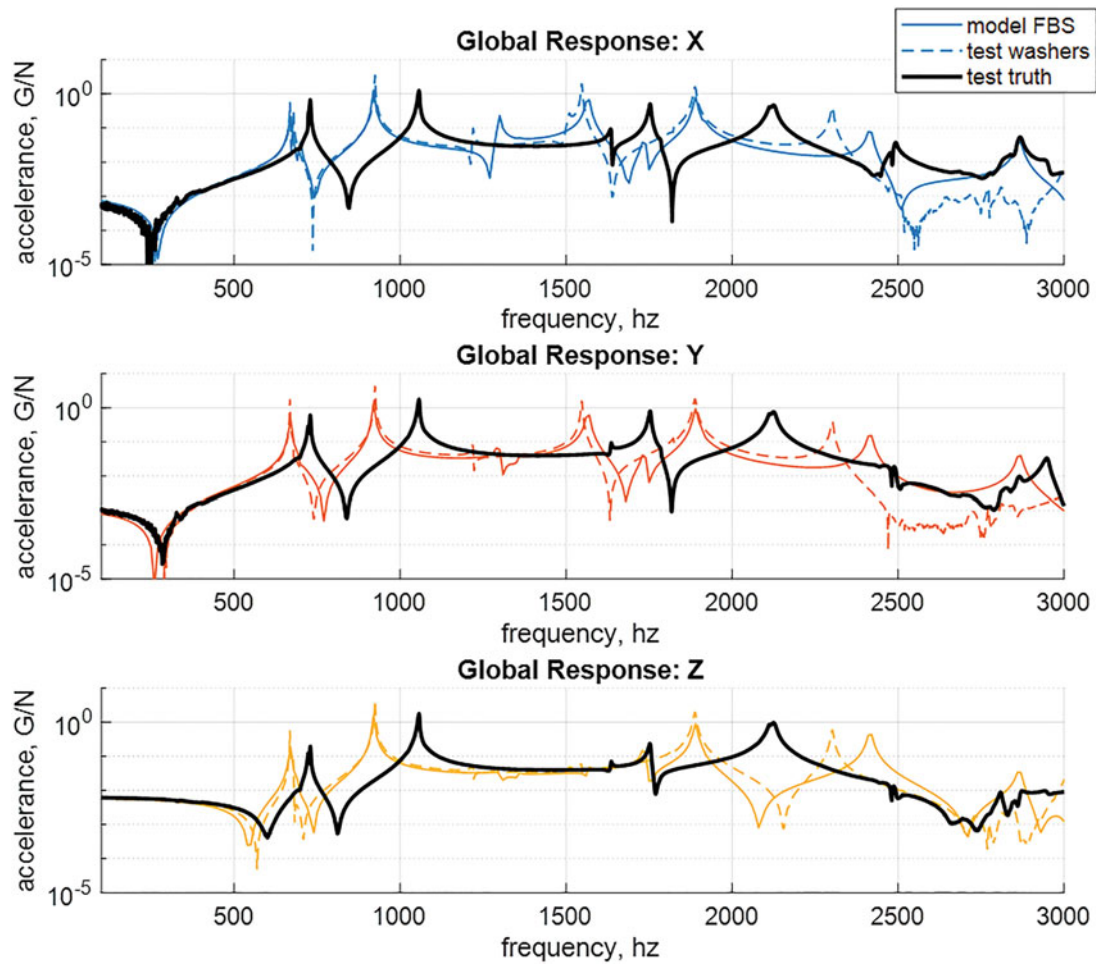


Fig. 30.5 Optimal configuration global payload response (+XYZ) comparing analytical substructured assembly, and experimental adjusted and truth assemblies

The experimental substructured assembly dynamics do not agree with any of the other methods. There is cross-axis sensitivity within the experimental plate dynamics, which in turn, alter the experimental substructured assembly FRFs. The accelerometers used to collect plate FRFs have a cross-axis sensitivity of $\leq 5\%$, per the specification sheets. However, cross-axis sensitivity issues can also come from imperfect orthogonal impacts. The FEM perfectly excites the in-axis modes, where, experimentally, the off-axis modal node must be impacted for that to occur. It is also difficult to impact in all orthogonal directions on the edge of a circular plate. For this reason, analytical FBS is recommended for any future implementation.

The goal is to use analytical FBS to predict the experimental test results, so the three methods to compare are analytical substructured assembly, experimental adjusted assembly, and experimental truth assembly (Fig. 30.5). The amplitudes and resonant frequencies of the analytical substructured assembly and experimental adjusted assembly correlate well around the knee frequency (around 1000 Hz). However, there is still a discrepancy between the former methods and the experimental truth assembly.

30.5 Conclusions

Using dynamics obtained from a FEM, LM-FBS can correctly determine the assembly dynamics. However, the proper interface conditions must be met. In the case of this research, more interface nodes per RBE3 group would increase the stiffness of the FBS dynamics and more accurately predict the experimental truth assembly dynamics. This would also increase computations time. Different methods to efficiently model the interface dynamics should be further investigated.

Next steps include looking at the mode shapes of the substructured assembly and truth assembly configurations, implementing modal substructuring, adding more parameters such as impact location/direction/magnitude, and investigating the equivalent damage of a multi-axis resonant plate pyroshock test. There is potential to define multiple objective functions to solve a case where the in- and off-axis responses have different knee frequencies. This would require investigation into how the mode shapes contribute to the off-axis response, since the response in this research is dominated by the circular plate “drum mode”. Most likely, the impact location/magnitude/direction will have to be added into the calculation process to excite key off-axis modes. In this case, the assumption that eliminating rotary DOFs has no significant impact on results should be re-evaluated.

Applicably, this process can be implemented in any resonant plate shock test laboratory. Ideally, a library of possible configurations would be constructed using FEMs of the available resonant plates. This would take time to initially set up, but this only has to be performed once. Then, once a component arrives for testing, the component dynamics are collected, either experimentally or analytically. The optimization algorithm is completed, allowing for custom parameters such as shock impulses, tolerance bands, and objective functions. The ideal configuration is solved for in a matter of minutes, eliminating the need for a “trial and error”. A single resonant plate shock test can be used to meet all three orthogonal axes specifications at once.

References

1. Jacobson, E.M.: Using frequency based substructuring to optimize multi-axis resonant plate shock tests. Master’s, Mechanical Engineering-Engineering Mechanics, Michigan Technological University (2019)
2. Hopkins, R., Sisemore, C.: Design of a resonant plate shock test for simultaneous multi-axis excitation. Presented at the Shock and Vibration Exchange, Dallas, TX, (2019)
3. Irvine, T.: An introduction to the shock response. *Spectrum*. July 9, 2012
4. Smallwood, D.O.: An improved recursive formula for calculating shock response spectra. In: *VibrationData.com* vol. August 2001, ed: Tom Irvine, (2001)
5. van der Seijs, M.V.: *Experimental Dynamic Substructuring*. (2016)
6. deKlerk, D., Rixen, D.J., Voormeeren, S.N.: General framework for dynamic substructuring: history, review, and classification of techniques. *AIAA*. **46**(5), (2008)

Erica recently completed her Master’s in Mechanical Engineering with focus in shock and vibration.



Chapter 31

A Data-Driven Approach to the Impedance Matched Multi-Axis Test Method

Kevin J. Moreno, Vijaya V. N. Sriram Malladi, and Pablo A. Tarazaga

Abstract Environmental testing is critical in certifying systems to operate and survive in harsh vibration environments. An example of this would be cargo rockets destined to deliver supplies to a low-earth orbiting space station. Aerodynamic effects would impose a distributed random excitation load onto the cargo rocket. It is imperative that test engineers perform an environmental test to replicate, as best as possible, the anticipated vibration loads on the rocket without subjecting it to the actual operational environment. Traditional in-lab environmental tests have shown to poorly reproduce the true response of a system subjected to distributed excitation loads. In recent literature, the Impedance Matched Multi-Axis Test (IMMAT) was developed to mitigate some of the current limitations of environmental tests through the use of finite element models (FEM) and multi-input multi-output (MIMO) control. As an extension of IMMAT, the present work investigates the use of a data-driven approach to supplement the creation of a numerical model used to predict optimal excitation locations and forces. The main advantage of this alternative approach to IMMAT removes the need for a FEM of the system being tested. This extends IMMAT to cases where a model of the subject being tested is not readily available and, yet, provides an opportunity for IMMAT to be deployed for certification. Additionally, a data-driven approach has the potential to capture more realistic test parameters, such as hard-to-recreate boundary conditions, material properties, and optimal excitation locations, as it is built directly from test data. There may be cases where this is advantageous, but may require better test designs. A preliminary numerical simulation is implemented to test the effectiveness and practicality of using vector fitted acceleration frequency response functions (FRF) to perform IMMAT.

Keywords Data-driven modeling · Environmental testing · MIMO · Vector fitting · System identification

31.1 Introduction

Environmental tests are implemented to ensure a system's proper functionality when subjected to experience a harsh vibration environment without risk of damage. The specific testing procedure typically depends on the excitation parameters of the system's operational environment and boundary conditions [1]. Unfortunately, these parameters are often difficult to obtain with a high degree of precision. Therefore, assumptions are made about the unknown testing parameters and tweaked through several trials until the desired results are obtained. This is often an inefficient and inaccurate method of environmental testing, which can result in over testing or under testing.

A typical environmental test would consist of using the acceleration data from environment capture trials at critical points in the system to control the test. Occasionally, the desired acceleration response would be enveloped to subject the system to a "worst-case" scenario [2]. The test engineer would proceed to excite the system multiple times in different orthogonal axis using electrodynamic shakers in an attempt to replicate the environmental acceleration response. The acceleration response at the control points would often show similar results to the environment capture trials or the spectral envelope. At this point, it is often assumed that the environmental tests were successful. However, this is often misleading as the acceleration response

K. J. Moreno (✉) · P. A. Tarazaga

Vibrations, Adaptive Structures, and Testing Lab, Department of Mechanical Engineering, Virginia Polytechnic Institute and State University, Blacksburg, VA, USA

e-mail: kjmoreno@vt.edu; ptarazag@vt.edu

V. V. N. Sriram Malladi

Department of Mechanical Engineering-Engineering Mechanics, Michigan Technological University, Houghton, MI, USA

e-mail: sriram@vt.edu

at non-control locations in the system may show signs of considerable over testing and under testing [3]. With this in mind, it can be considered that traditional environmental testing practices can produce unrepresentative system responses.

The IMMAT method improves upon traditional environmental testing methods by reliably replicating a more accurate system response to environmentally loaded excitation. It accomplishes this through the use of FEMs and MIMO control methods to drive the system using a discrete number of orthogonally placed electrodynamic shakers excited simultaneously [2]. However, the accuracy of the IMMAT can be diminished if the boundary conditions and material properties of the system are not faithfully replicated in the FEM to calculate the necessary natural frequencies and mode shapes in the frequency range of interest. Additionally, IMMAT would not be applicable to systems with intricate geometries difficult to reproduce in finite element software or older systems still in service without numerical or analytical models. The present work targets these specific cases where a model may not be available and where the test article's boundary conditions may be difficult to model accurately. This, this paper investigates the use of a data-driven model (DDM) via vector fitting as an FEM substitute in the IMMAT methodology. Vector fitting has been shown to provide realistic test parameters for dynamical systems using only frequency response data [4].

31.2 IMMAT Methodology

Similar to traditional environmental tests, the IMMAT method begins by using acceleration data from an environment capture trial to create a test specification. The test specification is the desired system response and is traditionally matched with or enveloped around the trial acceleration response at single or multiple locations on the system. A FEM of the test article is then created to estimate its natural frequencies, ω_r , and mode shapes, ϕ , and used to create a matrix of accelerance FRF elements, $A(\omega)$. Using the trial acceleration data and the matrix of accelerance FRFs, the IMMAT forces to be applied to each exciter, derived from linear system dynamics and multi-dimensional stationary stochastic process theory [5], is given by:

$$\left[S_{ff}^L(\omega) \right]_{Q \times Q} = [A(\omega)]_{Q \times P}^+ [S_{\ddot{x}\ddot{x}}(\omega)]_{P \times P} [A(\omega)]_{P \times Q}^{+H}, \quad (31.1)$$

where $S_{ff}^L(\omega)$ is the spectral density matrix of the force applied by the exciters, $S_{\ddot{x}\ddot{x}}(\omega)$ is the spectral density matrix of the acceleration obtained through the environment capture trial, $+$ is the pseudo-inverse, H is the Hermitian transpose, Q is the number of exciters, and P is the number of accelerometers. The system would then be driven by the exciters using the IMMAT forces. A concise framework of the IMMAT method can be seen in Fig. 31.1. A more detailed explanation of IMMAT can be found in [2].

31.3 Numerical Simulation of the IMMAT

In this study, the IMMAT methodology was implemented in a numerical study of a cantilever beam. The cantilever beam was modeled using the finite element method [6] and implemented in MATLAB. The beam itself is 6 feet long (1.83 meters) with a 1-inch (25.4 millimeters) square cross section and made of 6061-T6511 aluminum. Proportional damping was assumed and a 5% damping ratio was built into the model. The model contained 10 elements and included both translation and rotation degrees of freedom. For this study, only the first 3 modes were considered and, therefore, the spectrum band selected is from 0–150 Hz. The test specification was generated by assuming each of the translational degrees of freedom was excited by an excitation spectrum where the diagonal terms are a constant $5 \text{ N}^2/\text{Hz}$ and the off diagonal terms are 0. From this, the full acceleration response matrix was calculated and it consisted of auto spectral densities and cross spectral densities. The test specification was defined by the acceleration response at 5 arbitrary translational degrees of freedom shown as p_{1-5} in Fig. 31.2. The 3 excitation locations were chosen based on the mode shapes of the beam to ensure all of the modes of interest were being excited (no nodal points were chosen to guarantee energy transfer).

Given the testing parameters previously stated, the IMMAT was successfully able to closely replicate the acceleration response of a cantilever beam at two translational degrees of freedom for the first 3 modes when subjected to a distributed excitation load and can be seen in Fig. 31.3. At higher frequencies, the acceleration response from the IMMAT forces shows small deviations from the distributed excitation case around some resonances. This could be attributed to exciting the beam at too many locations where one exciter would be sufficient. This can simply be mitigated because changing input locations

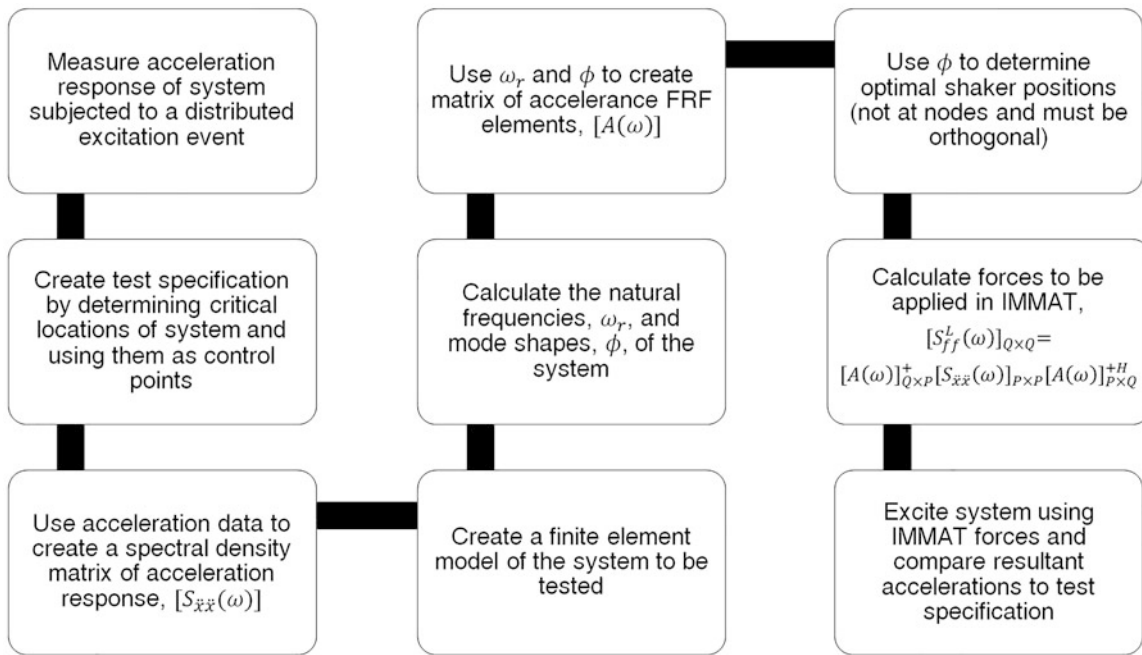


Fig. 31.1 Flow chart of the Impedance Matched Multi-Axis Test method

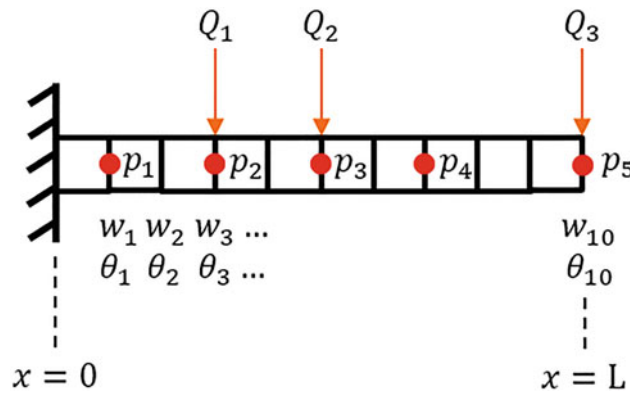


Fig. 31.2 Visual depiction of simulated cantilever beam where p_{1-5} are the accelerometer location and Q_{1-3} are the locations of the applied excitations

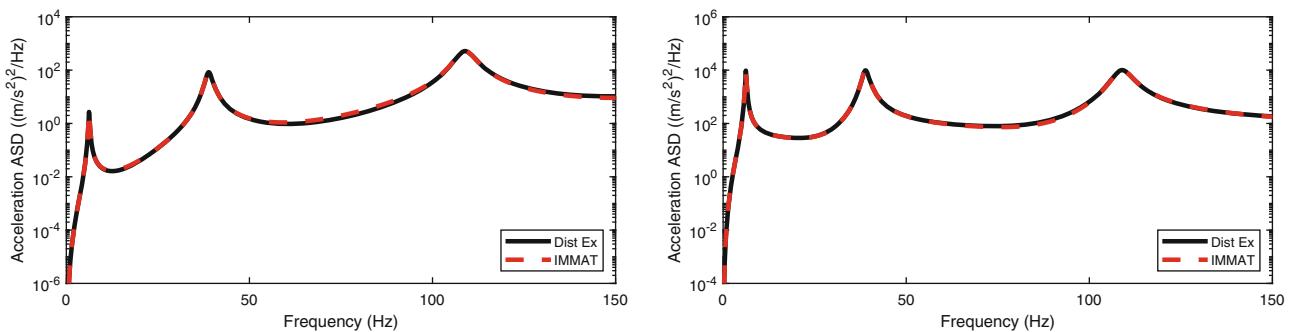


Fig. 31.3 Resultant acceleration response from IMMAT forces overlaid on top of acceleration response from distributed excitation load for translational degree of freedom 1 (left) and 10 (right)

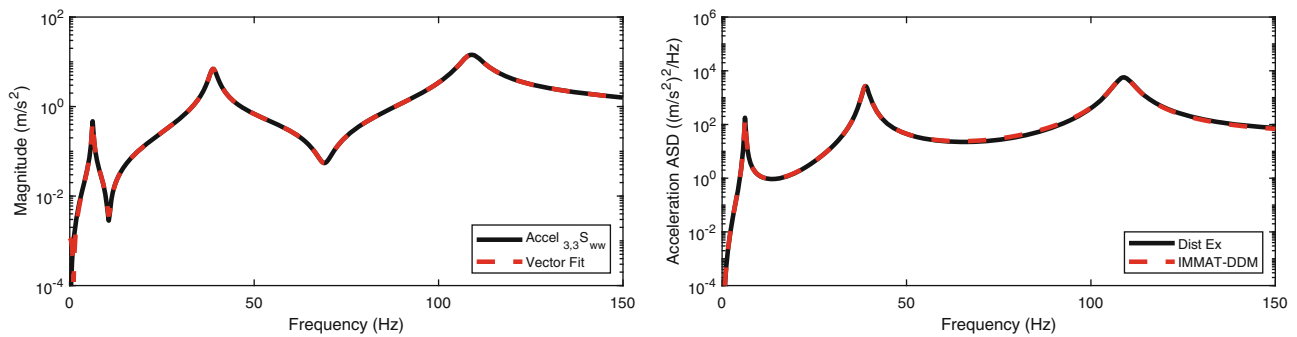


Fig. 31.4 Accelerance FRF calculated at the third translational degree of freedom overlaid with the vector fitted FRF (left) and the corresponding trial acceleration response overlaid with the data-driven IMMAT forces calculated at the same degree of freedom (right)

and performing numerous iterations is easily achieved using a FEM (one of the method's strengths when this is available). However, not having an easily obtainable model is always a possibility for a test engineer. Therefore, data driven modeling from vector fitting will be explored to investigate the feasibility of substituting them in place of an FEM in the IMMAT.

31.4 IMMAT Using a Data-Driven Model

A popular approach towards generating a DDM is through vector fitting of a rational function to FRF data. The methodology behind vector fitting FRF data starts with selecting an initial set of poles and iteratively relocating them to stable positions by solving a least square problem. Once the iterations have converged the poles have been selected, residue identification is implemented to finish the approximation of the FRF with a rational function in the form of:

$$f(s) \approx \sum_{m=1}^N \frac{c_m}{s - a_m} + d + se, \quad (31.2)$$

where terms d and e are optional terms and c_m and a_m are residues and poles respectively [7]. This form can be converted to a state space model of the system subjected to environmental tests. Vector fitting was applied to the accelerance spectral density matrix and the resultant vector fitted accelerance FRFs were used to calculate new IMMAT forces to replicate the trial acceleration data. As seen in Fig. 31.4, these new IMMAT-DDM forces can still closely reproduce the acceleration response of the beam subjected to a distributed excitation load.

31.5 Conclusion

Traditional environmental testing methods have been shown to produce inadequate system response replication at uncontrolled system locations. The IMMAT method addresses some of the limitations of environmental testing through the use of finite element models and MIMO control techniques to produce a more representative system response from different types of excitation characteristics. However, data driven modeling methods show promise in expanding IMMAT's range of applications to include those where precise testing parameters are difficult to obtain and where analytical and numerical models are infeasible to generate. Future work will include development of an algorithm using data driven interpolation methods to obtain FRFs at numerous points in between measurement locations to find the best possible drive points to optimally excite the system.

Acknowledgements Dr. Tarazaga would like to acknowledge the support provided by the John R. Jones III Faculty Fellowship.

References

1. Pusey, H.C.: An historic view of shock and vibration. In: Sound and Vibration, pp. 12–15. Franklin Watts, London (2008)
2. Daborn, P.: Smarter dynamic testing of critical structures. PhD Thesis, University of Bristol (2014)
3. Daborn, P., Ind, P. R., Ewins, D. J.: Replicating aerodynamic excitation in the laboratory. In: Conference proceedings of IMAC XXXI, (2013)
4. Malladi, V.V.N.S., Albakri, M. I., Tarazaga, P. A., Gugercin, S.: Data-driven modeling techniques to estimate dispersion relations of structural components. In: Proceedings of the ASME SMASIS 2018 (2018)
5. Harris, C.M.: Shock and Vibration Handbook, 6th edn, pp. 26.24–26.27. McGraw-Hill, New York (2010)
6. Inman, D.J.: Engineering Vibration, 4th edn, pp. 630–638, Boston, Pearson (2014)
7. Gustavsen, B., Semlyen, A.: Rational approximation of frequency domain responses by vector fitting. IEEE Trans. Power Delivery. **14**(3), (1999)

Kevin J. Moreno : My family is from El Salvador but I grew up in Central Maryland. I completed my B.S. in Mechanical Engineering at the University of Maryland. I am currently finishing up my M.S. in Mechanical Engineering at Virginia Tech and I hope to continue to work towards my Ph.D. immediately afterwards.



Chapter 32

An Automated Topology Optimization Platform Through a Collaborative Project Between Academia and Industry

Karolina Ohstrom, Seth Law, Alec Maxwell, Zhaoshuo Jiang, Juan Caicedo, Haley Sims, Nick Sherrow-Groves, and Nate Warner

Abstract The gap between research in academia and industry is narrowing as collaboration between the two becomes critical. Topology optimization has the potential to reduce the carbon footprint by minimizing material usage within the design space based on given loading conditions. While being a useful tool in the design phase of the engineering process, its complexity has hindered its progression and integration in actual design. As a result, the advantages of topology optimization have yet to be implemented into common engineering practice. To facilitate the implementation and promote the usage of topology optimization, San Francisco State University and the University of South Carolina collaborated with ARUP, a world leader in structural designs, to develop an Automated Topology Optimization Platform (ATOP) to synchronize commonly used industry software programs and provide a user-friendly and automated solution to perform topology optimization. ATOP allows for users to form a conceptual understanding of a structure's ideal shape and design in terms of ideal material placement by iterating various parameters such as volume fraction, and minimum and maximum member size at the start of a project. With developed platform, a high-rise building design from the literature was first adopted to validate the results from ATOP, after which an actual design project from ARUP was utilized to fully explore its functionality and versatility. Results show that ATOP has the potential to create aesthetic and structurally sound designs through an automated and intelligent process.

Keywords Topology optimization · Automated process · Academia-industry collaboration · Rhinoceros 3D · Altair

32.1 Introduction

Structural optimization has been attracting increasing attention in the design of structures to achieve efficient, lightweight, and thus economical designs [1]. Generally, structural optimization is classified into three categories, i.e. sizing optimization, shape optimization, and topology optimization. Sizing optimization treats the sizes of structural members as the design variables while shape optimization tries to find better shapes to satisfy the desired objectives. Topology optimization aims to find the optimal perimeter layout of a structure within a defined design domain [2]. In the design industry, the shape of the building is often pre-defined to achieve a desired aesthetic. The optimization of the structural member sizes could be done at a later stage after the determination of the structural system without changing much of the global behavior of the

K. Ohstrom
Cornell University, Ithaca, NY, USA
e-mail: ako24@cornell.edu

S. Law
University of Kansas, Lawrence, KS, USA

A. Maxwell · Z. Jiang (✉)
San Francisco State University, San Francisco, CA, USA
e-mail: awm@mail.sfsu.edu; zsjiang@sfsu.edu

J. Caicedo
University of South Carolina, Columbia, SC, USA
e-mail: CAICEDO@cec.sc.edu

H. Sims · N. Sherrow-Groves · N. Warner
Arup North America Limited, San Francisco, CA, USA
e-mail: Haley.Sims@arup.com; nick.sherrow-groves@arup.com; Nate.Warner@arup.com

structure. In contrast, the choice of the topology of a structure in the conceptual phase is generally the most decisive factor for the efficiency of a novel design [3]. Therefore, the focus of the optimization of structures in practice is typically placed on topology optimization.

Topology optimization is an important tool for designing an economical structure by allocating the materials to places that can efficiently transfer the loading acting on the structure. Beginning with Bendsøe and Kikuchi [4], the most common methods for topology optimization involve finite element analysis (FEA). Through FEA, the design space is divided into a series of small elements and each element is determined to either be part of the design or can be removed from the design. Topology optimization is useful for a wide range of fields, as techniques can be applied to large-scale structures as well as at micro- and nano-levels [5]. There is a significant gap between the engineering science with fundamental research in academia and engineering practice with potential implementation in the industry. Extensive research on topology optimization has been performed in academia [4, 6–17]. Although topology optimization techniques have been implemented in structural design in industry, it is not universally applied by all designers mainly due to the lack of integration with current design software and the tedious iteration process.

32.2 Proposed Solution

Through the opportunity provided by an NSF funded Research Experience for Undergraduates (REU) program established by San Francisco State University and the University of South Carolina, the REU participants were working together with faculty advisors in academia and industrial mentors in Arup North America LTD, an industrial leader in structural design, to develop an automated topology optimization platform (ATOP). The platform leverages the advantages of several commercial software platforms, including Rhinoceros 3D [18] and Altair HyperMesh/OptiStruct [19], to provide a user-friendly and automated process for topology optimization. Rhinoceros is a commonly used 3D modeling software which offers high accuracy, great compatibility with other software, and is highly accessible. Altair HyperMesh is a multi-disciplinary finite element pre-processor with advanced meshing capabilities. OptiStruct is an accurate and comprehensive structural solver that also provides innovative optimization technology. Figure 32.1 details the processes behind ATOP. The topology optimization process in ATOP is comprised of three main phases: modeling, pre-processing, and optimization. ATOP uses two programming languages, Python and tool command language (Tcl), to facilitate communication between Rhino and HyperMesh/OptiStruct. Python is a commonly used and highly versatile programming language and is used to communicate between the different components. Tcl is a high-level general-purpose programming language and is the default application program interface (API) for HyperMesh and OptiStruct. In the modeling phase, users will create geometry through the user-

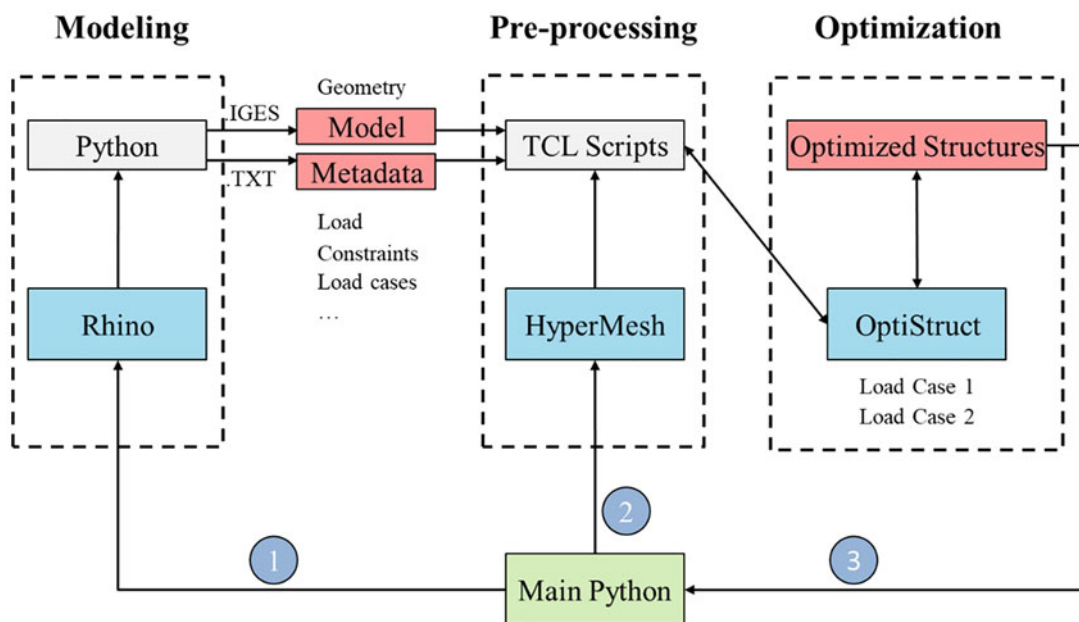
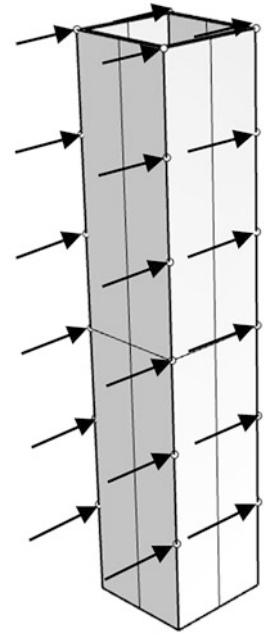


Fig. 32.1 Flowchart outlining ATOP process

Fig. 32.2 Model of high-rise structure case study with loading



friendly interface in Rhino and assign metadata (e.g., material properties, loading, and restraints conditions) to the model. During the pre-processing phase, the Main Python script will drive HyperMesh to import the stored model information and metadata from Rhino and create the corresponding model in HyperMesh. By doing so, the tedious model creating process in HyperMesh is avoided. In the optimization phase, Tcl scripts call the OptiStruct solver to perform topology optimization on the HyperMesh model that was set up in the pre-processing phase. Once that particular model has been optimized, ATOP returns to the pre-processing phase to set up a new load case, or optimization constraint. OptiStruct is then called again to carry out optimization on the next iteration HyperMesh model. This iterative process continues until all user specified combinations of load cases and optimization constraints have been achieved. Results of all user-specified combinations are then exported back to Rhino so that they may be easily viewed and compared.

32.3 Platform Validation

To validate the developed platform, a case study of a high-rise structure from literature [20] was adopted and the effects of several parameters, including volume fraction, and minimum and maximum member sizes were investigated. In the case study, Beghini et al. proposed a topology optimization framework to bridge the gap between architectural and structural engineering communities and performed topology optimization to maximize the stiffness of a tall high-rise building in Australia to serve as an example. In this particular example, the authors demonstrated the results without disclosing much detail on the parameters selection of the topology optimization, as it was not the focus of the study. With that, it is almost impossible to duplicate the results for the given design space without an automatic platform, as it might need an unlimited number of trials to find the unique combination of the parameters to produce the same results. Through the proposed ATOP platform, an attempt was made to iterate on multiple optimization parameters, including volume fraction, and maximum and minimum member size to obtain the same topology optimization results. A high-rise building model with a shell as shown in Fig. 32.2 was set up in this study. The model is constrained at the base both laterally and rotationally (in the x , y , and z directions). As was done in the literature, point loads P spanning multiple floors of the building with $P/2$ acting at its top were applied to represent wind loads. The optimization objective for this study is set to minimize the compliance. The compliance is defined as the inverse of stiffness. By default, OptiStruct performs optimization iterations until either the maximum number of 30 iterations is reached, or two consecutive iterations have a change in the objective function below the objective tolerance of 5%, the percent change in the objective function of two iterations. If a minimum member constraint is specified, the maximum number of iterations is increased to 80.

The following section discussed the selection process of the parameters and their effects on the optimization results.

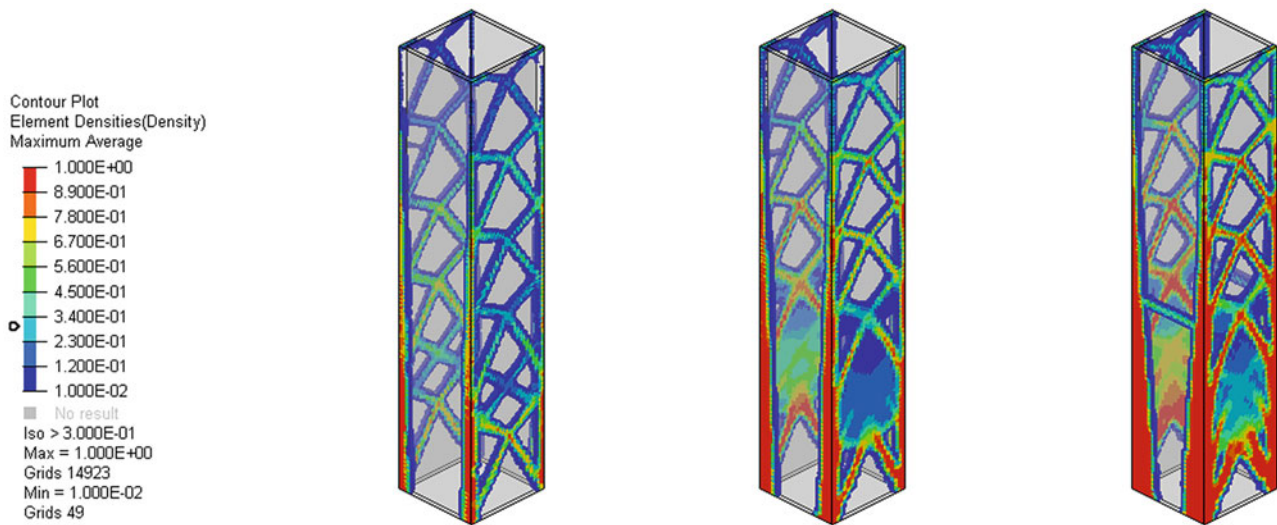


Fig. 32.3 High-rise structure case study showing the effects of different volume fractions: (from left to right) 0.1, 0.2, 0.3

1. Volume fraction is the percentage of the initial design volume that will be maintained in the optimized solid. This parameter guides the amount of material that may be placed within the design space of the final optimized shape. It limits the amount of overall material and is typically within the range of 10–30% of the original design material. Figure 32.3 shows the results of applying a volume fraction of 0.1, 0.2, and 0.3 (10%, 20%, and 30% of the original design volume) to demonstrate the effects that volume fraction has on the optimized results. As volume fraction increases, the amount of material allowed within the optimization continued to increase. The figures include a scale on the left side, which shows the density of material in the design space. The dark blue indicates an element density close to 0, while the red indicates an element density of 100%. Results can be further refined to only show material above a certain density threshold. In the figures of the optimized structures in this paper, a density threshold of 0.3 or 30% is used. This means that any element with a density less than 30% is not shown (becomes transparent) in the design space. Notably, because there are no other constraints on the optimization, as more material was added, a higher concentration was placed towards the bottom corners. This directly coincides with the objective of minimizing the compliance as these locations provide the highest amount of structural stiffness to the model.
2. Minimum Member Size is the lower limit for the diameter of elements in the final optimization. The minimum member size parameter narrows the scope of the topology optimization by assigning a factor that penalizes the formation of members smaller than the minimum member size. It is defined specifically to be a factor times the average element size within the model. An inherent function of the program exists that calculates the average size of the member within the optimization by comparing the sizes of the individually shaped elements that make up the finite element mesh. This parameter helps guide the program by ensuring that members of a reasonable size are created within the optimization. In HyperMesh, by default, the minimum member size must be at least 3 times the average element size but no greater than 12 times the average element size. Figure 32.4 shows the effects of applying a minimum member size of 3, 6, and 9 times the average element size. As the minimum member size increases, so does the size of the members. HyperMesh does take into consideration the necessity for members outside of the specified range. There may exist members whose sizes are smaller than the specific member size if these members are integral to the structural integrity of the model. As the minimum member size increases within the optimization, the number of members typically decreases as it takes more material to create each larger member.
3. Maximum Member Size, as the name indicated, is the opposite to the minimum member size parameter. It is defined as being 2 times the minimum member size within an optimization. While this parameter is not necessarily required in an optimization, it helps to further clean up the results. Figure 32.5 shows the effects of applying the maximum member size with the minimum member size. A small maximum member size creates members that may be deemed intangible. The maximum member size of 24 produced clear and legible members within the optimization which has better constructability in a real-life implementation.

Figure 32.6 provides a summary on the influence trend of the different parameters to the overall structural compliance. Figure 32.6a shows the correlation between volume fraction and compliance. As the volume fraction increases, the

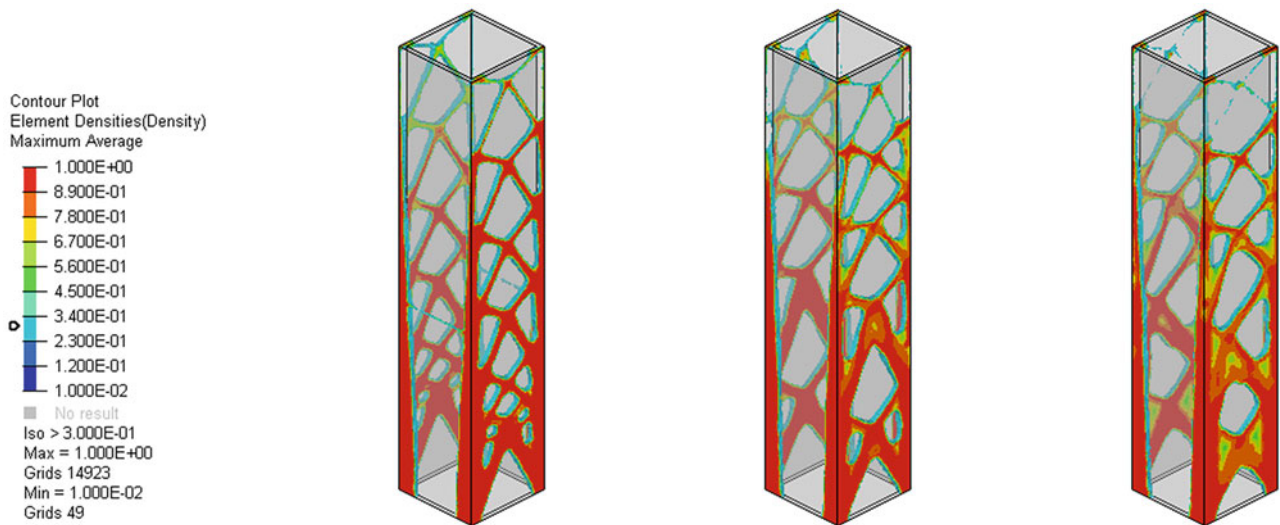


Fig. 32.4 High-rise structure case study showing the effects of different minimum member sizes: (from left to right) 3, 6, 9

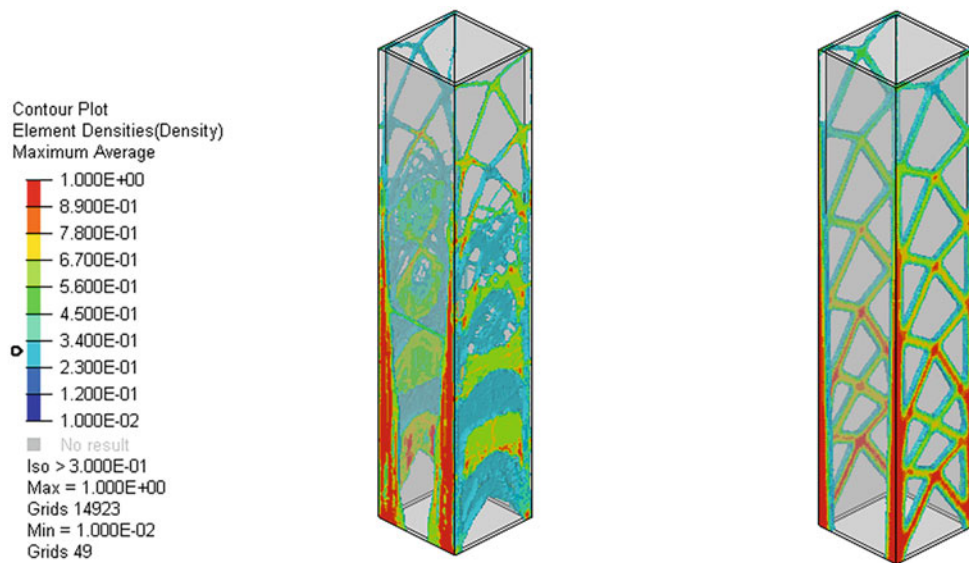


Fig. 32.5 High-rise structure case study showing the effects of different maximum member sizes: (from left to right) 6, 24

compliance decreases. The more material that may be used within the structure, the more it can be placed in various areas to increase stiffness. Figure 32.6b shows that an increase in minimum member size causes an increase in compliance because the larger members would find themselves more spaced out within the design field, which limits the area that the model may use to transfer the applied loads. The increase in compliance provides a tradeoff in the design aspect as members that are too small may not be realistically manufacturable. As shown in Fig. 32.6c, the maximum member size shares a similar correlation with compliance to that of the minimum member. As it increases, so does the compliance.

Through the 80 automated iterations using the ATOP platform to vary the parameters mentioned above, a result very similar to the design in Beghini et al. was achieved as shown in Fig. 32.7, which provided a validation and demonstrated the functionality of the platform. Without the use of the automated platform, each combination of parameters would have to be applied individually, which is a tedious and nearly impossible task to accomplish.

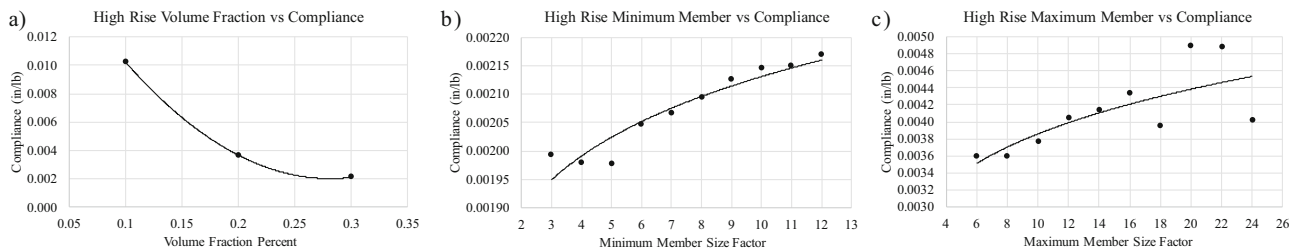
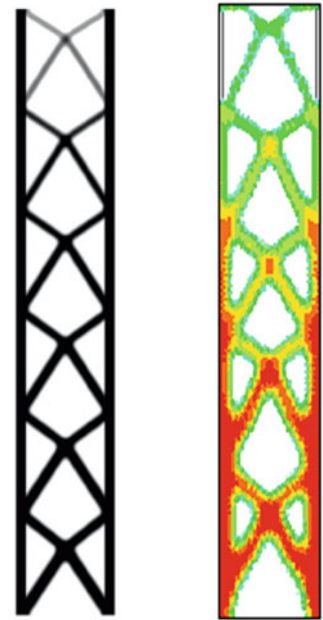


Fig. 32.6 High-rise Structure – (a) volume fraction (b) minimum member size (c) maximum member size

Fig. 32.7 High-rise structure case study results - design from Beghini et al. (left) vs ATOP results (right)



32.4 Case Study

After the validation of ATOP, the platform was used to perform topology optimization on an actual design project from Arup to fully explore its functionality and versatility. The design project is known as the Cosmos Sculpture, and its function is an artistic shade canopy. The cosmos sculpture has a skewed funnel shaped design space as can be seen in Fig. 32.8, with a height of 24.5 ft. and a 3-inch thick shell throughout the height of the sculpture. The top of the sculpture is an ellipse with a dimension of 30.5 ft. by 23.9 ft., and the bottom of the structure is circular with a diameter of 6.8 ft. Similar to the high-rise structure case study, the optimization results for the Cosmos Sculpture were created by iterating over volume fraction, minimum member sizes, and maximum member sizes. The loading for the Cosmos Sculpture is also shown in Fig. 32.8. In this study, only wind loads with a magnitude of 30psf were considered. The optimization objective and convergence criteria were the same as the high-rise case study.

1. Volume Fractions of 0.1, 0.2 and 0.3 were investigated for the Cosmos Sculpture. Results from iterating over volume fractions are shown in Fig. 32.9. It can be observed that, as the volume fraction increases, the amount of material was placed throughout the original design space with the concentration at the base of the sculpture. With only applying a volume fraction constraint, the optimized results did not display an aesthetic shape, nor any bracing pattern.
2. Same as the high-rise case study, the allowable minimum member sizes equal to 3–12 times the average element size were investigated. Results from applying minimum member size constraints of 3, 8, and 12 are shown in Fig. 32.10. In these results, the volume fraction remained consistently at 0.3. From Fig. 32.10, as minimum member size increases, the bracing pattern becomes clearer, and denser material is placed throughout the optimized result. For the Cosmos Sculpture, increasing minimum member size leads to a clearer conceptual starting point in the design phase. This information may be hidden without the automated process to explore a large variation of this parameter.

Fig. 32.8 Model of Cosmos Sculpture case study showing loading

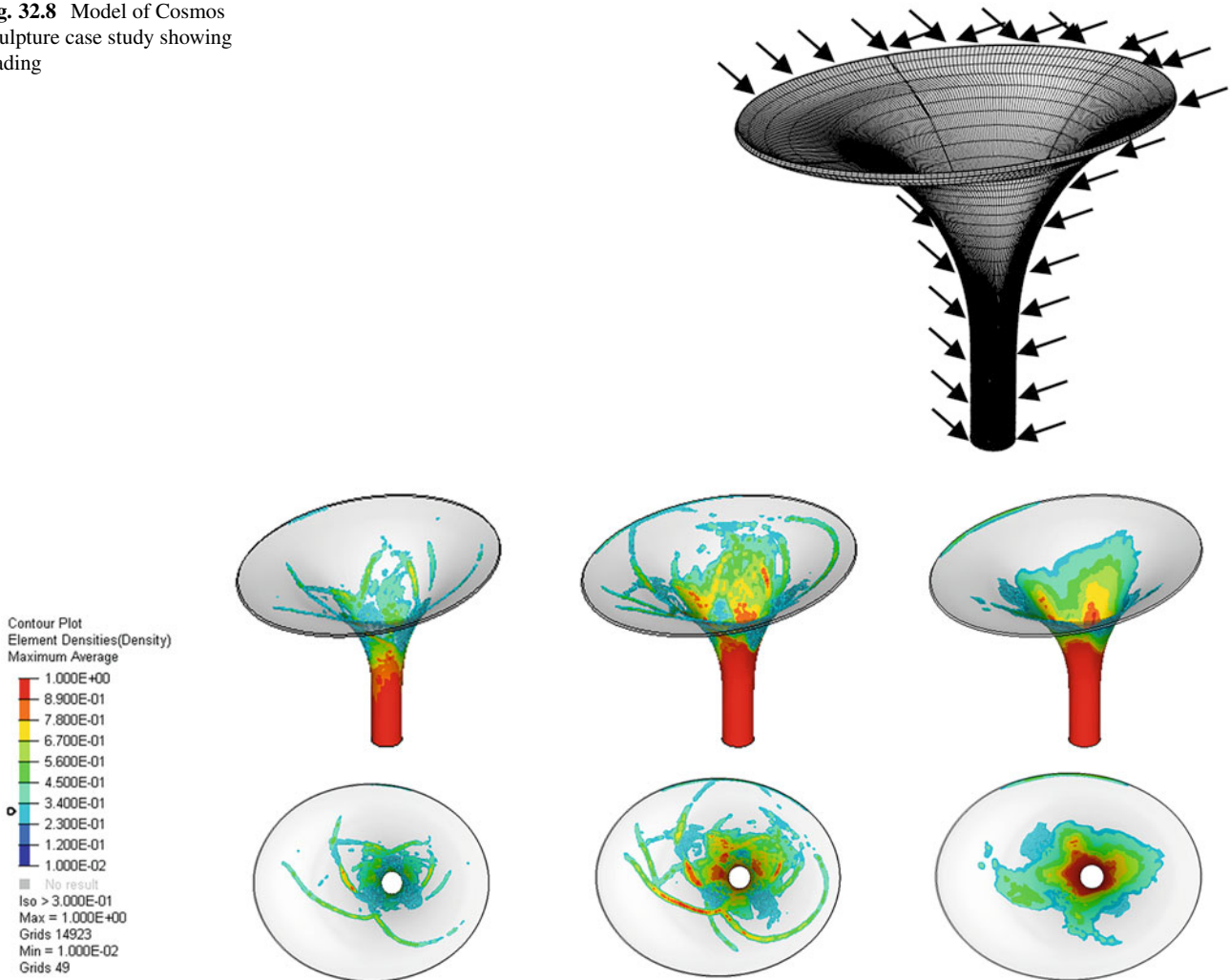


Fig. 32.9 Cosmos Sculpture case study (side and top view) showing the effects of three different volume fractions: (from left to right) 0.1, 0.2, 0.3

- The maximum member sizes were investigated in the range of 6–24 times the average element size of the finite element model. As maximum member size increases, the size of the members in the optimized shape increases while less dense material is available to be placed at the base of the structure to balance the increase of material placed at the top. For the Cosmos Sculpture, a maximum member size within the range of 12–16 times the average element size produces the best results since the design provides a more constructible brace pattern that covers more of the original design space (Fig. 32.11).

The previous results showed a lack of symmetry in the optimized results, evident by the lack of material in the lower left quadrant of the original design space. This is due to the fact that the loading is only applied at one side of the structure. To investigate the effects of possible loading from the other direction on the optimized shape, the Cosmos Sculpture was loaded with equivalent wind loads on the opposing sides, as seen in the bottom right of Fig. 32.12. When comparing results from the one side loading conditions, the full design space is used in this loading condition and the overall design is much more symmetrical.

Figure 32.13 shows the influence of optimization parameters on the structural compliance of the Cosmos Sculpture. Figure 32.13a demonstrates the effect of volume fraction on compliance. As volume fraction increases, the compliance decreases. By allowing more material to be placed throughout the design space, especially in critical areas, the optimized structure becomes stiffer. Figure 32.13b shows the effect of minimum member size on compliance. As minimum member size increases, compliance increases. As members are forced to become larger, it reduces the amount of area that the loads can be transferred over. The increase in compliance comes with the tradeoff of more manufacturable and aesthetic designs that

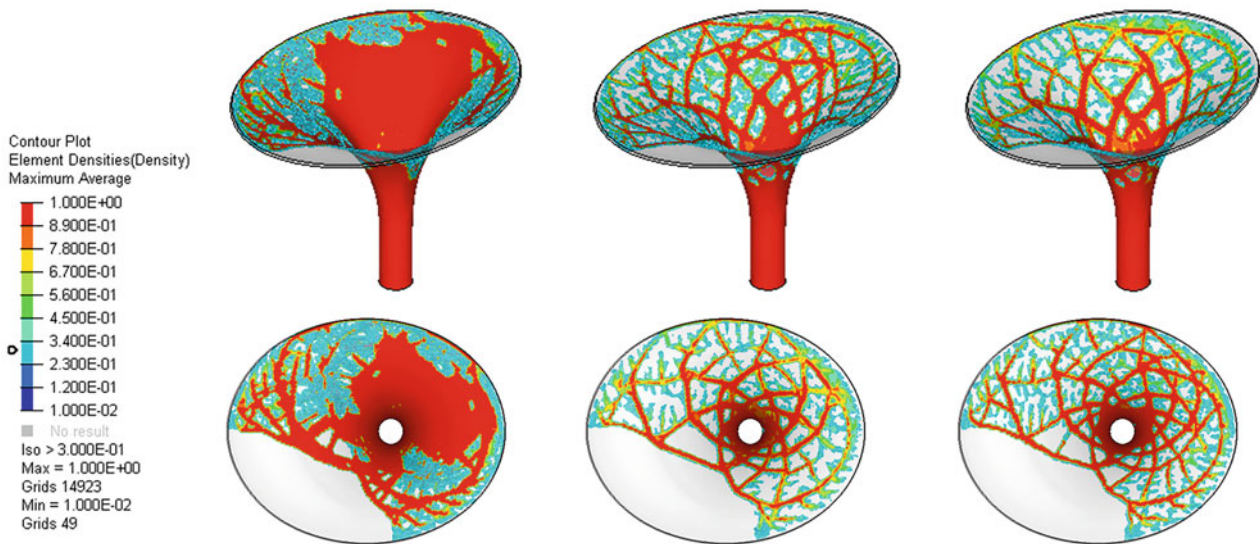


Fig. 32.10 Cosmos Sculpture case study (side and top views) showing the effects of applying different minimum member sizes: (from left to right) 3, 8, 12

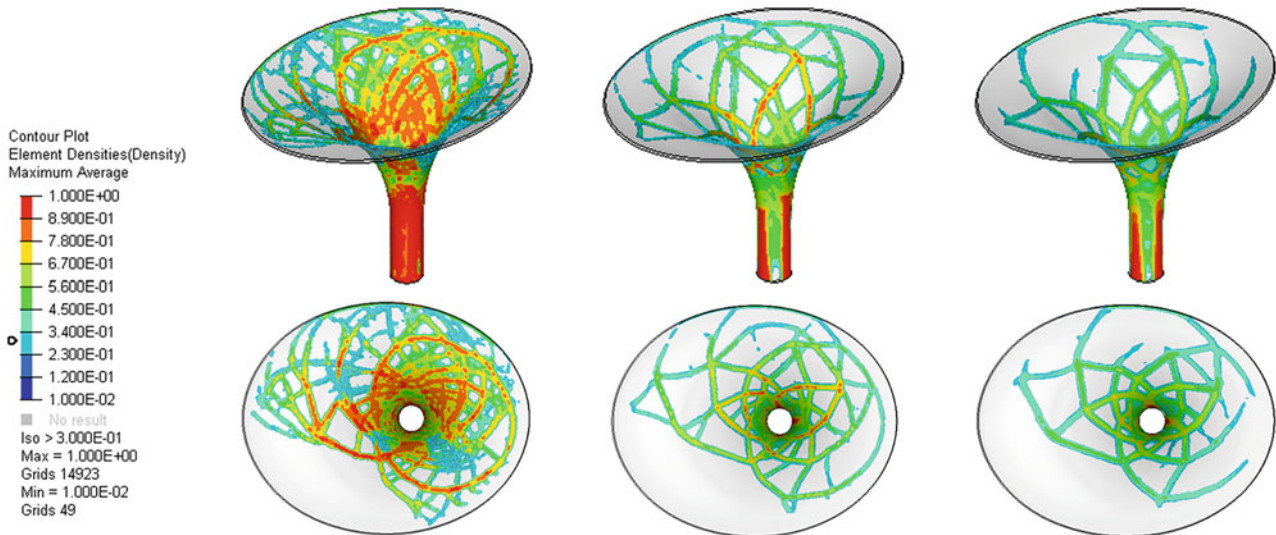


Fig. 32.11 Cosmos Sculpture case study (side and top views) showing the effects of different maximum member sizes: (from left to right) 6, 16, 24

could prove to be a more meaningful conceptual design. Figure 32.13c shows the relationship between maximum member size and compliance, which is similar to the relationship between minimum member size and compliance.

32.5 Conclusion

Structural optimization has been attracting increasing attention in the design of structures to achieve efficient, lightweight, and thus economical designs. Topology optimization has shown to have large effects on the global behavior of structures during the conceptual phase and have been intensively studied in academic world. Techniques on Topology optimization have been applied to structural design in industry, however, it is not universally applied by all designers mainly due to the lack of integration with current design software and the tedious iteration process. To bridge the gap between the fundamental research in academia and engineering practice in the industry, an NSF funded Research Experience for Undergraduates (REU)

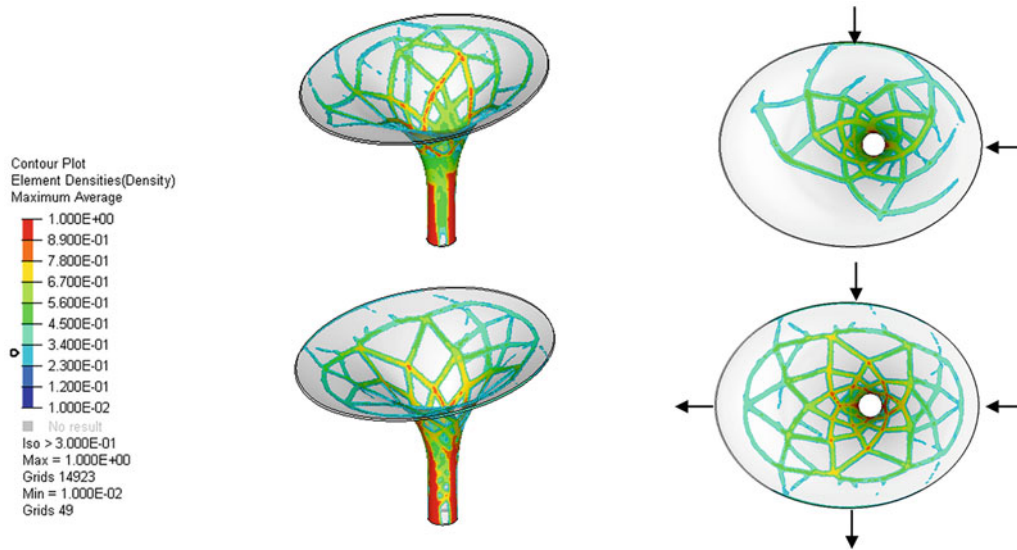


Fig. 32.12 Cosmos sculpture case study showing results from asymmetric loading (top) and symmetric loading (bottom)

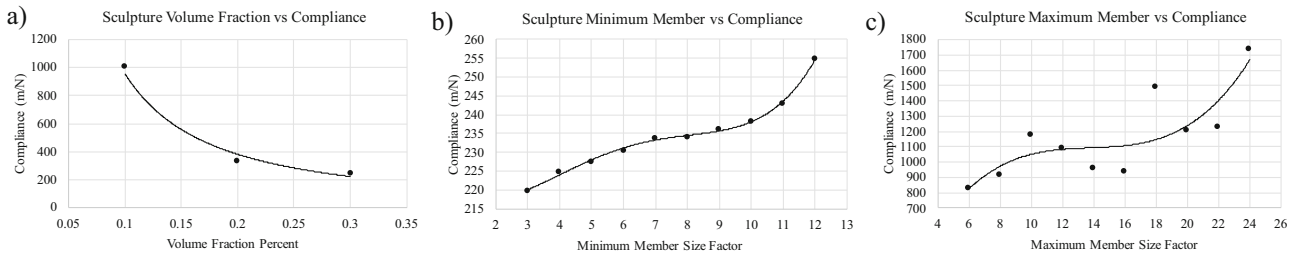


Fig. 32.13 Sculpture Structure – (a) volume fraction (b) minimum member size (c) maximum member size

program, was established by San Francisco State University and the University of South Carolina to provide an opportunity for the REU participants to experience research in both academic and industry settings and facilitate the knowledge exchange. In this study, the REU participants worked together with faculty advisors in academia and industry mentors at Arup North America Limited to develop ATOP, an automated topology optimization platform. The platform leverages the advantages of several commercial software platforms, including Rhinoceros 3D and Altair HyperMesh/OptiStruct, to provide a user-friendly and automated process for topology optimization that will incentivize implementation of topology optimization in structural design. After development, the platform was validated through performing optimizations on a high-rise structure in recent literature that was subjected to static wind loads. Even with limited information on the topology optimization parameters, the platform successfully achieved a similar optimized shape as in the literature case study, an almost impossible task without the help of automation. After the validation, ATOP was used to perform topology optimization on an actual design project from Arup. The design project was an artistic shade canopy subjected to wind loads and required to be aesthetically pleasing and have sufficient structural stiffness. ATOP was able to produce multiple optimized shapes by varying optimization parameters and investigating various loading conditions to provide the design team meaningful options on conceptual design. In these studies, analysis of the optimization parameters, including volume fraction, minimum member size and maximum member size, on the structure's compliance (inverse of stiffness) was investigated. The results of both studies showed similar trends on the effects of the various optimization parameters. When volume fraction is increased, compliance decreases as the increase in the allowable amount of material, especially in critical areas, increases the overall stiffness of the structure. The increase of minimum member size increases the compliance. As members are forced to become larger, it reduces the amount of area that the loads can be transferred over. The increase in compliance comes with a tradeoff of more manufacturable and aesthetic designs that could prove to be a more meaningful conceptual design. With the increase of the maximum member size, the overall compliance also increases. More aesthetically pleasing conceptual designs with well-defined members were produced when introducing some sort of member size constraint. Future work includes increasing

capabilities of the platform by providing more options on optimization objectives and optimization constraints, and to use this platform on different scale design problems to explore the scope of the platform.

Acknowledgements The authors would like to acknowledge the supports from National Science Foundation EEC-1659877/ECC-1659507, the College of Science and Engineering and the School of Engineering at San Francisco State University, and College of Engineering and Computing at the University of South Carolina. Supports from the industrial collaborator, Arup North America Limited, are also appreciated. In addition, the student cohort, Kaitlyn Chin and Alex Donner, who participated in the same NSF REU summer program in 2018 contributed greatly in creating the first version of the ATOP platform. Their efforts are also acknowledged and highly appreciated.

References

1. Beghini, A., Shook, D., Mazurek, A.: Material optimization for tall buildings. In: AEI, vol. 2015, pp. 567–580 (2015)
2. Tang, J., Xie, Y.M.: Conceptual design of buildings subjected to wind load by using topology optimization. *Wind Struct.* **18**(1), 021–035 (2014)
3. Eschenauer, H.A., Olhoff, N.: Topology optimization of continuum structures: a review. *Appl. Mech. Rev.* **54**(4), 331–390 (2001)
4. Bendsoe, M.P.: Optimal shape design as a material distribution problem. *Struct. Multidiscip. Optim.* **1**(4), 193–202 (1989)
5. Huang, X., Xie, M.: *Evolutionary Topology Optimization of Continuum Structures: Methods and Applications*. Wiley, Chichester (2010)
6. Zhou, M., Rozvany, G.I.N.: The COC algorithm, part II: topological, geometrical and generalized shape optimization. *Comput. Methods Appl. Mech. Eng.* **89**(1–3), 309–336 (1991)
7. Mlejnek, H.P.: Some aspects of the genesis of structures. *Struct. Multidiscip. Optim.* **5**(1), 64–69 (1992)
8. Sokolowski, J., Zochowski, A.: On the topological derivative in shape optimization. *SIAM J. Control. Optim.* **37**(4), 1251–1272 (1999)
9. Allaire, G., Jouve, F., Toader, A.M.: A level-set method for shape optimization. *Comptes Rendus Mathematique.* **334**(12), 1125–1130 (2002)
10. Allaire, G., Jouve, F., Toader, A.M.: Structural optimization using sensitivity analysis and a level-set method. *J. Comput. Phys.* **194**(1), 363–393 (2004)
11. Wang, M.Y., Wang, X., Guo, D.: A level set method for structural topology optimization. *Comput. Methods Appl. Mech. Eng.* **192**(1), 227–246 (2003)
12. Bourdin, B., Chambolle, A.: Design-dependent loads in topology optimization. *ESAIM: Control, Optimisation and Calculus of Variations.* **9**, 19–48 (2003)
13. Xie, Y.M., Steven, G.P.: A simple evolutionary procedure for structural optimization. *Comput. Struct.* **49**(5), 885–896 (1993)
14. Querin, O.M., Steven, G.P., Xie, Y.M.: Evolutionary structural optimisation (ESO) using a bidirectional algorithm. *Eng. Comput.* **15**(8), 1031–1048 (1998)
15. Li, Q., Steven, G.P., Xie, Y.M.: A simple checkerboard suppression algorithm for evolutionary structural optimization. *Struct. Multidiscip. Optim.* **22**(3), 230–239 (2001)
16. Kim, H., Querin, O.M., Steven, G.P., Xie, Y.M.: Improving efficiency of evolutionary structural optimization by implementing fixed grid mesh. *Struct. Multidiscip. Optim.* **24**(6), 441–448 (2002)
17. Yang, X.Y., Xie, Y.M., Liu, J.S., Parks, G.T., Clarkson, P.J.: Perimeter control in the bidirectional evolutionary optimization method. *Struct. Multidiscip. Optim.* **24**(6), 430–440 (2002)
18. Altair Engineering Inc.: *Introducing Altair HyperWorks 2019*. Retrieved September 28, 2019, from <https://altairhyperworks.com/>. (2019)
19. McNeel, R. & Associates.: *Rhino 6 for Windows and Mac*. Retrieved September 28, 2019, from <https://www.rhino3d.com/>. (2019)
20. Beghini, L.L., Beghini, A., Katz, N., Baker, W.F., Paulino, G.H.: Connecting architecture and engineering through structural topology optimization. *Eng. Struct.* **59**, 716–726 (2014). <https://doi.org/10.1016/j.engstruct.2013.10.032>

Chapter 33

Shaker-Amplifier System Characterization



Greta Colford, Kevin Craft, Andy Morello, Dustin Harvey, Colin Haynes, and Stuart Taylor

Abstract Equipment requirements for ground vibration testing of assemblies, sub-assemblies, and components are dependent on several factors. These include test configuration (e.g., size and mass), equipment performance parameters (e.g., stroke limit), and test architecture (e.g., single-axis or multi-axis). Equipment is historically selected based on similitude to past testing, engineering judgement, and/or rudimentary calculations based on Newton's second law of physics. From these methods alone it can be challenging to know if all desired test configurations and environments are achievable. As an alternative method to determine if a system is capable of running specific tests, a relationship can be developed between the electrical inputs and physical outputs to the system and used to predict if specific testing can be achieved. This paper explores and begins to quantify the relationship between the physical response of an electrodynamic shaker and DUT with the electrical signals of the power amplifiers and the data acquisition systems. Critical parameters of the system that impact shaker performance are identified using experimental data from three different ground vibration shaker tests. Understanding the relationship between the electrical and mechanical responses of an electrodynamic shaker system can provide test engineers with valuable information on the performance limitations of system, as well as knowledge to better utilize testing equipment resources and predict the testability of a proposed experiment. Objectives for this effort were fulfilled largely through experimental means, including post-processing of experimental data and reporting of findings to develop a knowledge database and technical approach, with an end-goal of developing metrics or tools upon which to base equipment requirements for future testing.

Keywords Electrodynamic shaker · Amplifier · Vibration · Environmental testing · Equipment requirements

33.1 Introduction and Motivation

Electrodynamic shaker systems are commonly used for a variety of vibration and shock testing applications. Choosing a vibration testing system that is mechanically and electrically capable of running the various tests on all test objects that need to be qualified can be challenging, especially if testing needs change over time. There are a multitude of parameters that can impact a shaker system's performance capability including test configuration and mounting fixtures, equipment performance parameters, and test design and architecture. Testing configuration parameters include the size, mass, and dynamic response of the device under test (DUT) and corresponding mounting fixtures. Shaker performance parameters are limited by the shaker stroke limit, peak velocity, peak force, material properties and thermal power limit of the armature coil, and armature size. The performance of a shaker system is also influenced by the maximum current and voltage outputs available from the power amplifier, as well as the outputs produced by the data acquisition drive or controller. To reduce the number of parameters that must be considered, manufacturers' rate their systems operating under a uniform set of conditions that are outlined in ISO 5344 and include a flat-band power spectral density from 20 to 2000 Hz using a non-resonant load made from a solid block of steel [1]. This approach allows shaker manufacturer ratings to be compared directly, and it defines performance capabilities under ideal conditions, but it does not clearly represent the capability of the shaker system under different conditions. Equipment for vibration testing also has been traditionally selected using basic calculations based on Newton's second law of physics and past testing experience, which can make it difficult to know if all required test configurations are mechanically or electrically possible.

G. Colford (✉) · K. Craft · A. Morello · D. Harvey · C. Haynes · S. Taylor
Los Alamos National Laboratory, Los Alamos, NM, USA

e-mail: gcolford@lanl.gov; kmcraft@lanl.gov; amorello@lanl.gov; harveydy@lanl.gov; cmhaynes@lanl.gov; sgtaylor@lanl.gov

The ultimate goal of this effort is to develop metrics or tools that predict shaker-amplifier testing capabilities of existing shakers currently in use for ground-vibration testing to better utilize shaker system equipment and provide test engineers insight to the testability of a specific DUT or test environment. This paper begins to investigate the relationship between the electrical outputs of the power amplifiers and the data acquisition system and the physical response of an electrodynamic shaker and DUT by looking at experimental data from three test series using three different shaker-amplifier systems.

33.2 Background

33.2.1 Physics of an Electrodynamic Shaker

An electrodynamic shaker works in a manner similar to a common loudspeaker, creating mechanical vibrations through the use of electrical current and the principals of electromagnetism [2]. At the center of the shaker there is a coil of wire suspended in a radial magnetic field, and when current is passed through the coil a force is generated and transferred to a structure that is often a table. The magnetic field is created using a permeable inner pole which transmits flux from one side of a magnet (or electromagnet), while the permeable outer pole transmits flux from the opposite side of the magnet. A radial flux field is created in the air gap between the inner and outer poles, and the interaction between the radial flux field and current from the coils is able to create vibrating motion [2]. The table, coil form, and coil together make up the armature assembly, to which the test object is mounted [3]. The armature is suspended and centered in the magnet structure through the use of springs or flexures. There is a proportional relationship between the current through the armature coil and the force applied by the shaker [4]. However, shaker manufacturers warn that this proportional relationship is not always accurate at all frequencies. Shaker systems consist of an electrodynamic shaker, a power amplifier, a measurement and control system, and an optional heat exchanger. The power amplifier's job is to take the drive signal from the controller and multiply the output by a fixed gain to be fed into the shaker. The heat exchanger can be used to cool the armature coil and amplifier so as to avoid overheating the hardware while in use, and it allows the shaker to operate at higher field levels. A basic schematic of an electrodynamic shaker is shown in Fig. 33.1.

33.2.2 How to Choose a Shaker

The traditional way to choose a shaker system that is mechanically capable of running a specific test uses a simple application of Newton's second law. Currently it is recommended by Senteck Dynamics, a shaker system manufacturer, to use the following method to choose a shaker system for a specific test:

First, determine the frequency range of the test, and then calculate the required peak values for displacement, velocity, and acceleration based on the test specification. The calculations to find the peak values are different depending on what type of test you are running, which can include sine, random, and shock [3]. Next, determine the total moving mass that the shaker will have to move, which includes the mass of the shaker armature, device under test (DUT), and any mounting fixtures or hardware needed to rigidly attach the DUT to the armature. Then, the total moving mass is compared to the shaker payload limits published by the manufacturer [3]. If it is within the recommended mass limits, then find the force required from the shaker by multiplying the total moving mass by the acceleration required by desired test profile, as seen in Eq. 33.1:

$$F_{required} = M_{total} * A_{peak} \quad (33.1)$$

Where M_{total} is the total moving mass that the shaker will have to move, A_{peak} is the peak acceleration determine by the desired test profile, and $F_{required}$ is the force required by the shaker. If the force required is more than the shaker is rated for, a different, more powerful shaker may be required [3].

Often shaker manufactures will suggest to apply at least a 30–40% margin of error on the calculated force (up to 100% margin in some specific test cases) to the specifications published by the manufacture to account for possibility of experiencing non-ideal conditions. However, shaker systems have been to known to exceed the published mechanical capabilities successfully in some test cases.

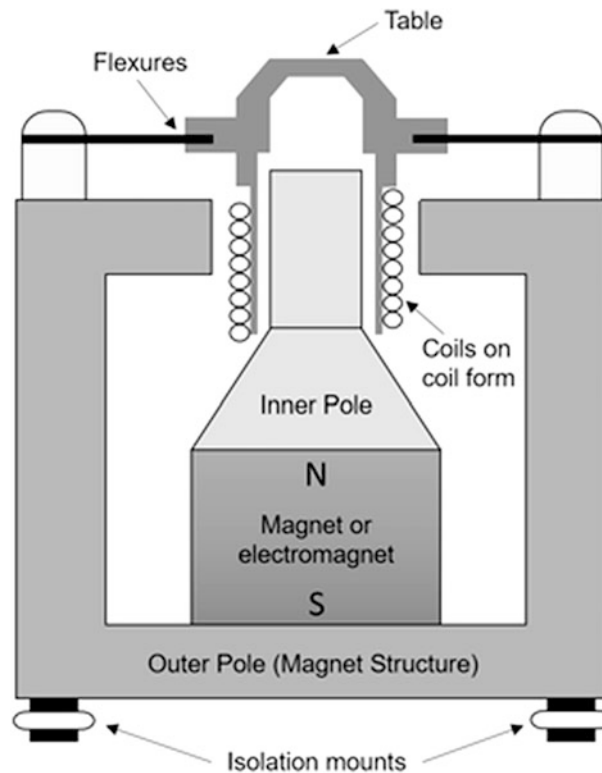


Fig. 33.1 Basic schematic of an electrodynamic shaker (cross-section)

33.2.3 Modeling of Electrodynamic Shaker Systems

Previous research efforts have modeled electrodynamic shaker systems for the purpose of characterizing the system, estimating parameters, and developing a virtual testing environment to exercise the testability of a test item. A popular approach to describe shaker-amplifier systems is the use of lumped parameter models coupled with electrical models. A basic electro-mechanical model was developed by Lang and Snyder to predict the shaker vibrational modes, the effects of isolating the shaker, and predicting maximum sine drive performance [2]. A mobility-based lumped parameters models was developed in Tiwari et al. for a medium-sized shaker, and Ricci et al. developed a coupled electro-mechanical lumped parameter model and vibration controller [5] [6]. Smallwood characterized an electrodynamic shaker system using a passive, two-port network where all variables considered are complex functions of frequency. Assumptions for this method include that the system is linear, and the output can be described by a single pair of output variables, force and acceleration of the shaker table [7]. Hoffait et al. developed a virtual shaker testing tool to predict the dynamic behavior of a coupled shaker-test specimen assembly for a specific shaker, though the methodology can be applied to other shaker systems [8]. Additionally, virtual shaker testing has been studied by Manzato et al. and Martina and Harri [9] [10].

Another method to define shaker system performance is through the use of “performance curves”, which are plots of acceleration versus frequency on a log scale and are also referred to as Q-curves. The performance curves are defined by displacement, velocity, and acceleration limits of the shaker under maximum ideal conditions. In general, at low frequencies the shaker is limited by the shaker stroke, mid-range frequencies are limited by the velocity of the shaker, and the higher frequencies are limited by the maximum force (acceleration) of the shaker. Performance curves are generated using Newton’s second law approach and are usually supplied by the shaker manufacturer.

These existing models (based on Newton’s second law) are helpful when applied to linear systems in a specific frequency range but might not be suitable for tests requiring higher frequency ranges or complex test fixtures. One intention behind developing an empirical model and using experimental data to derive shaker-amplifier system performance capabilities is to increase the fidelity of a predictive metric or tool to account for non-ideal responses during testing like armature resonance and test object dynamics.

33.3 Experimental Data

To develop a relationship between the mechanical and electrical components and responses of a shaker system, three different test series were analyzed. Each test series ran similar ground-testing, random-vibration environments in the X, Y, and Z axes, but utilized different test objects and shakers systems. For each test, data from the amplifier current, amplifier voltage, data acquisition drive, and accelerometer responses from the shaker table and test object were collected.

33.3.1 Test Set-up

Information about the testing set-up for each of the three ground vibration tests are in Table 33.1. Information on the rated shaker performance values as well as physical details of the shaker armatures is given in Appendix A.

Test A was a ground vibration test using an Unholtz-Dickie Corp. S452-16 shaker with a SAB30F power amplifier. The test ran two different environments along with a baseline random environment to characterize the test body during testing. A head expander and slip table was used to mount the test object to the armature for the X and Y/Z axes, respectively. Two different mounting fixtures were also used to attach the DUT to the head expander and slip table, and both were tested under all three environments (Fig. 33.2).

Test B was a ground vibration test utilizing an Unholtz-Dickie Corp T-1000 shaker with a SALL-300 power amplifier. Test B ran two environments in addition to the baseline environment. The DUT in this test was mounted directly on the armature plate, without a slip table or head expander. The DUT was rotated on the table to achieve all three test axes (Fig. 33.3).

Test C was a ground vibration test on the Unholtz-Dickie T-4000-3// shaker paired with a SAI-300 power amplifier. Test C had the largest total moving mass compared to Test A and B, and used a head expander and slip table with extension to mount the test object to the shaker armature. Three environments and the baseline random environments were run in Test C, and the DUT was also tested under multiple temperatures during the test series. The Test C DUT was also mounted to the slip table or head expander using two different mounting methods while testing the baseline environment (Fig. 33.4).

Table 33.1 Test configurations used for each test series

Test	Amplifier/Shaker System	Test Orientation	Total Moving Mass (kg)	Fixture/Mounting Method
A	Unholtz-Dickie Corp. SAB30F / S452-16	X	100	Head expander
		Y	163	Slip table
		Z	163	Slip table
B	Unholtz-Dickie Corp. SALL-100 / T-1000	X	178	Directly on armature
		Y	208	Directly on armature
		Z	208	Directly on armature
C	Unholtz-Dickie Corp. SAI-300 / T-4000-3" CSTA	X	1400	Slip table and slip table extension
		Y	1400	Slip table and slip table extension
		Z	923	Head expander

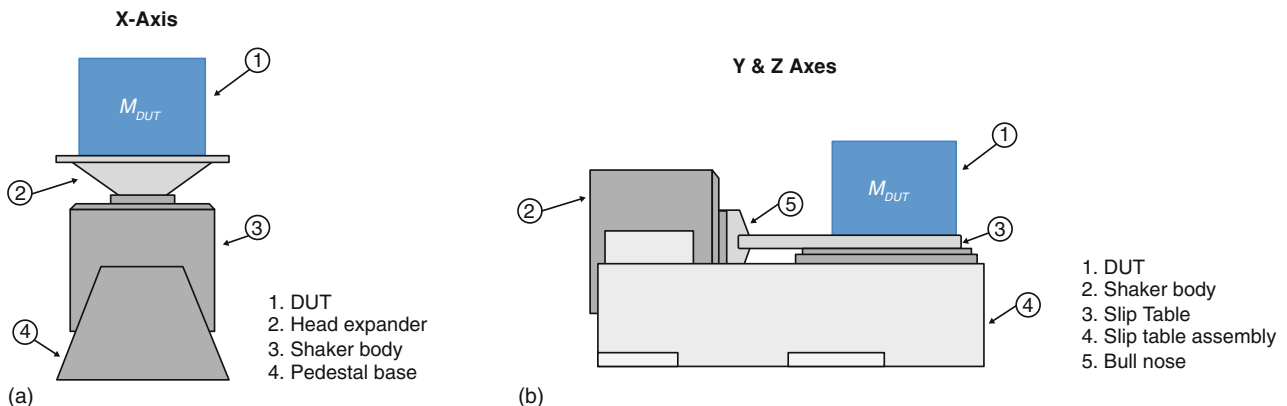


Fig. 33.2 (a) Test A: X-axis configuration. (b) Test A: Y and Z axes configuration

Fig. 33.3 Test B configuration. The test body was rotated to achieve testing on three axes

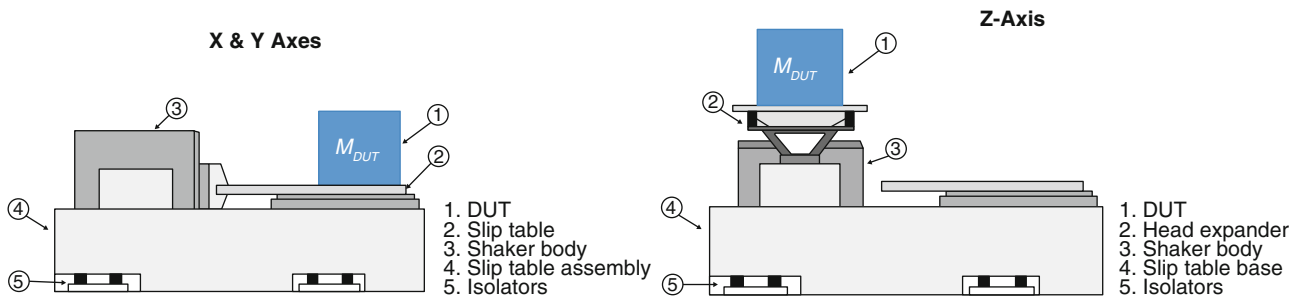
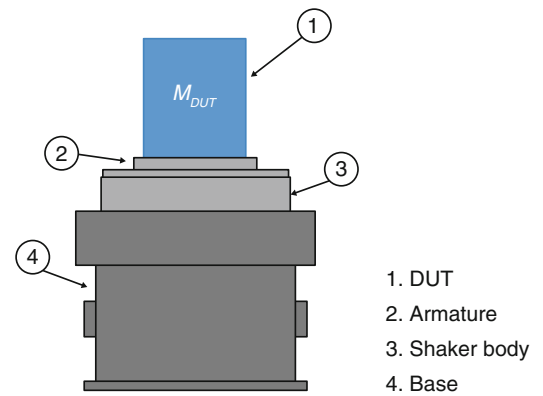


Fig. 33.4 (a) Test C: X and Y axis configuration. (b) Test C: Z-axis configuration

33.3.2 Test Environments

A total of five environments, plus the baseline environment, between the three tests were analyzed. The environments run for each test are outlined in Table 33.2. The table also outlines the input acceleration levels and frequency range of the test profile. The input, or control accelerometer location, was located on the shaker table for Test A and C, while the control accelerometer location was on the DUT for test B. It should also be noted that there were limits applied at other points on the DUT for some of the tests.

The baseline environment and Environment 1 were common between Tests A, B, and C and Environment 2 was common between Tests B and C. While the input acceleration may vary for each test within in a single environment, the environments are grouped together for comparison and represent similar environments across tests. For this analysis, the primary focus will be on Environment 1, Environment 2, and the baseline environment.

33.4 Analysis

For each of the three test series, the physical and electrical responses were compared and analyzed. Two different metrics were used to look at the relationship between the power amplifier electrical outputs and the physical response of the shaker and DUT and to start identifying testing parameters important to understanding shaker performance.

The first metric was computing transfer functions between the amplifier current and shaker table response, amplifier voltage and the shaker table response, and the data acquisition drive voltage and the shaker table response. This analysis provides insight on the frequency dependence of the relationship between electrical inputs to the shaker and the mechanical response. The second metric was computing the overall RMS values for each of the amplifier outputs and comparing to the overall RMS level of the acceleration response. The second approach explores the shaker-amplifier interactions under different testing conditions and environments. Applying these two metrics to experimental data under real testing conditions begins to reveal the complexities that a model must be able to capture to provide the desired predictive capabilities.

Table 33.2 Vibration environments for Test A, B, and C

Baseline				
The baseline environment was conducted in all test series and axes. It consisted of a flat spectrum random excitation from 10–2500 Hz. Each test/environment had varying levels of random excitation.				
Environment 1				
Test/ test orientation	X	Y	Z	Frequency range
Test A	0.805 G _{rms}	0.089 G _{rms}	0.418 G _{rms}	20–400 Hz
Test B	0.415 G _{rms}	0.904 G _{rms}	0.394 G _{rms}	8–1000 Hz
Test C	0.703 G _{rms}	1.46 G _{rms}	0.658 G _{rms}	10–1000 Hz
Environment 2				
Test/test orientation	X	Y	Z	Frequency range
Test B	0.123 G _{rms}	0.356 G _{rms}	0.305 G _{rms}	4–4000 Hz
Test C	0.784 G _{rms}	0.848 G _{rms}	0.570 G _{rms}	10–4000 Hz
Environment 3				
Test/test orientation	X	Y	Z	Frequency range
Test C	0.183 G _{rms}	0.082 G _{rms}	0.609 G _{rms}	4–1000 Hz
Environment 4				
Test/test orientation	X	Y	Z	Frequency range
Test B	2.78 G _{rms}	8.20 G _{rms}	9.00 G _{rms}	14–2300 Hz
Environment 5				
Test/test orientation	X	Y	Z	Frequency range
Test A	2.58 G _{rms}	0.636 G _{rms}	0.419 G _{rms}	20–1700 Hz

33.4.1 Transfer Functions

There are some trends in the literature and shaker system documentation in regard to the amplifier voltage and current outputs required by the shaker based on frequency that were seen while analyzing the data. At low frequencies, the voltage required is small, but the current required is large. At higher frequencies, the current required is less, and the voltage required is at a maximum, with the exception being at the resonant frequency. At the resonant frequency of the moving mass, the current and voltage requirements are at a minimum [11]. Another trend that was observed was the proportional relationship between the amplifier current and the force imparted on the shaker table and DUT. In Fig. 33.5, transfer functions between the amplifier current and DUT for the baseline environment event for Test A were computed for three different stages: -6 dB, -3 dB, and at full level. It can be observed that the transfer functions are overlapping, regardless of the level of the test, indicating a proportional relationship between the amplifier output current and the force produced by the armature which transfers to the acceleration response of the shaker table. This proportional trend was observed in all three test series, for all test axes and environments. Therefore, the analysis is focused on full-level events only when computing the transfer functions. The same trend can be seen for the amplified voltage and shaker acceleration response, as observed in Fig. 33.6.

Comparing Figs. 33.5 and 33.6, the overall shape of the transfer function is the same though at slightly different amplitudes. The same characteristics are present in both transfer functions, and when a transfer function between the accelerometer response and the data acquisition drive is plotted the same characteristics are observed. Electrically this makes sense, as current and voltage are related, and the voltage output from the amplifier is a scaled value of the output voltage of the data acquisition drive. Between each test environment, test axis, and test series, the relationships seen in the transfer functions for amplifier current, amplifier voltage, and data acquisition drive with the shaker acceleration response remain generally the same.

Figure 33.7 is a comparison of the baseline environment for the X test axis direction for each of the three tests, looking at the transfer function between the amplifier current and the table accelerometer response. There are different dynamic responses seen between each test, which could be attributed to the different shaker systems, testing configurations, or mounting methods used. For example, Test B had the test object attached directly to the armature table and had a flatter response over a greater frequency range compared to the other tests that had additional mounting hardware. This difference in response could possibly be connected to the DUT dynamics coupling less with the shaker or the design of the shaker system among other potential reasons. There are many complex responses seen in the experimental data, and the exact cause can be difficult to identify without additional testing. Characterizing these responses across tests and shaker systems can be helpful in understanding shaker performance and DUT response.

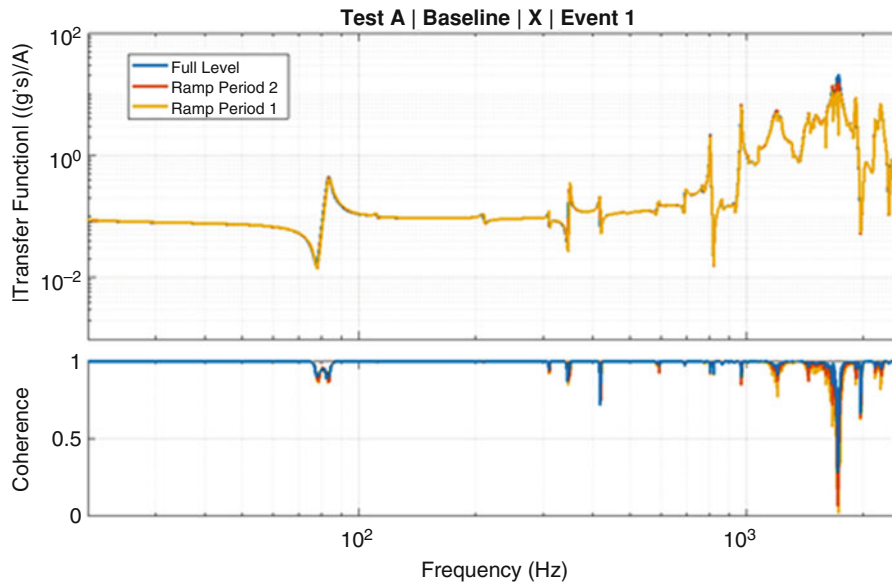


Fig. 33.5 Test A: transfer function between the accelerometer response and amplifier current for the baseline environment during ramp period 1 (-6 dB), ramp period 2 (-3 dB), and the full level test comparison

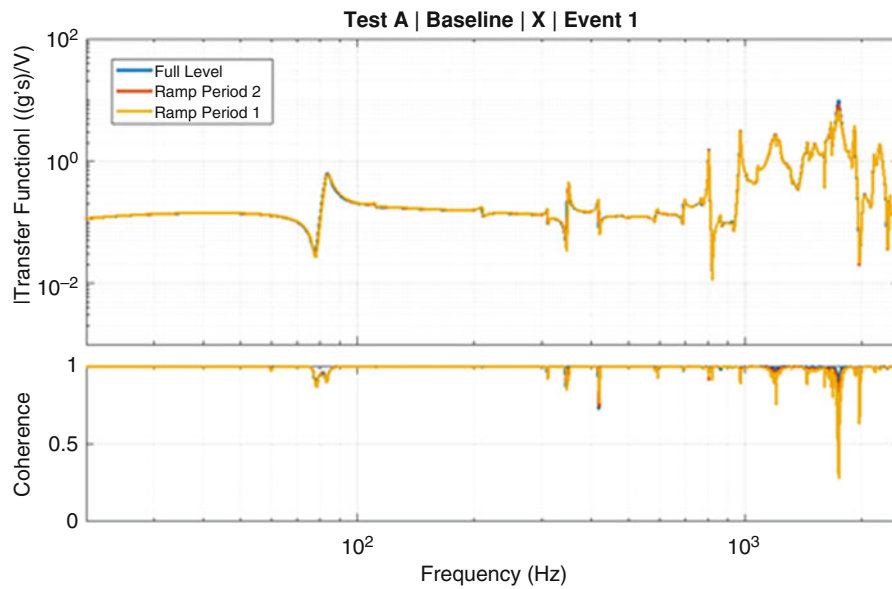


Fig. 33.6 Test A: transfer function between the accelerometer response and amplifier voltage for the baseline environment during ramp period 1 (-6 dB), ramp period 2 (-3 dB), and the full level test comparison

As expected, the largest peaks in the transfer functions are near the armature resonance values for the armature, slip table, or head expander, depending on the configuration used in the test. There is an interesting response for Tests A and C around 80 Hz, where there is a dip and rise in magnitude. The shifting seen around this same frequency in Test A and C over the course of each test may coincide with the different mounting methods used to attach the DUT to the slip table or head expander.

Figure 33.8 shows a comparison between Tests A, B, and C in the X axis for Environment 1. Similar trends can be seen in Environment 1 compared to the baseline environment, including the resonance values for the DUT, armature, and related mounting fixtures. There are some lower coherence values in this environment, but responses are slightly more similar between tests, especially between 0 and 400 Hz.

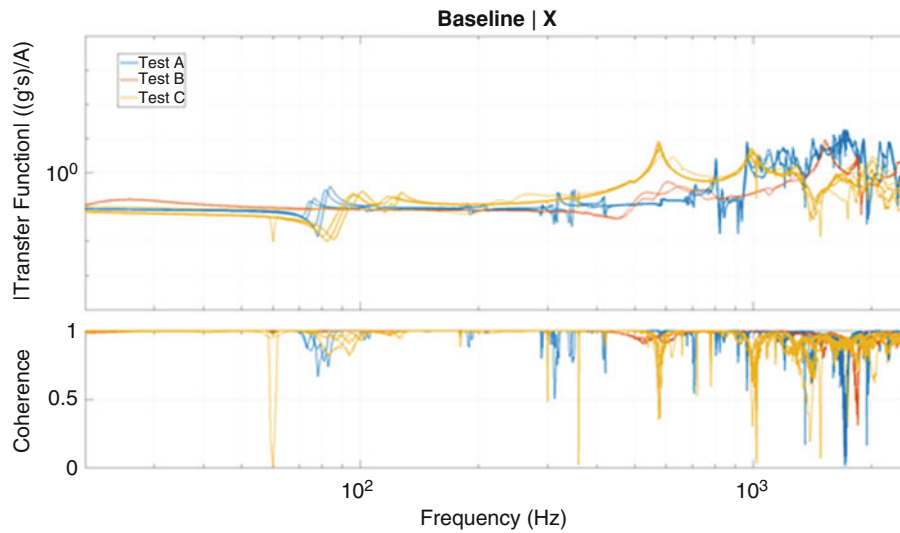


Fig. 33.7 Transfer functions between control response and amplifier current for the baseline environment

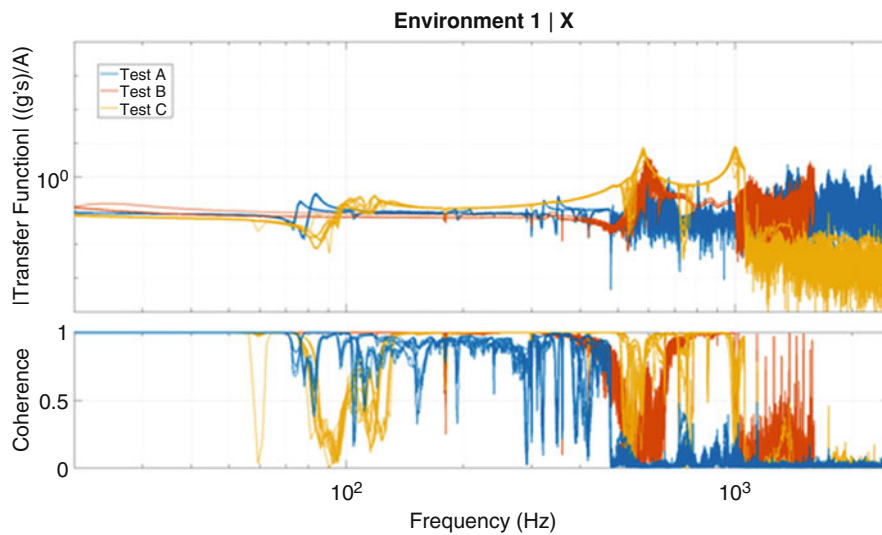


Fig. 33.8 Transfer functions between control response and amplifier current for Environment 1

33.4.2 RMS Plots

For each event in a test series, the RMS of the amplifier current, amplifier voltage, and data acquisition drive was computed and plotted with the RMS value of the corresponding acceleration response of the control locations for on-axis responses. The goal in this comparison was to find a method to map the amplifier limitations of the shaker. Fig. 33.9 is a plot of Test A with the RMS levels of all environments and test axes computed over the full frequency range of each environment. Each environment and test axis combination follows a linear trend, and the trend line could be extended and plotted with the limitations of the amplifier or shaker to find the maximum current or acceleration RMS values potentially available for a test environment. It should be recognized that these trend lines are for one DUT and will not necessarily encompass all desired DUTs for this specific shaker system since total moving mass is an important parameter that impacts shaker performance.

However, when the RMS values are computed to only include the common frequency range (0 to 400 Hz) between the three environments, the trend is linear between all the environments and test orientations, as seen in Fig. 33.10. This observation indicates a potential to use RMS values over specific frequency bands to predict the acceleration level response or the amplifier current and voltage requirements.

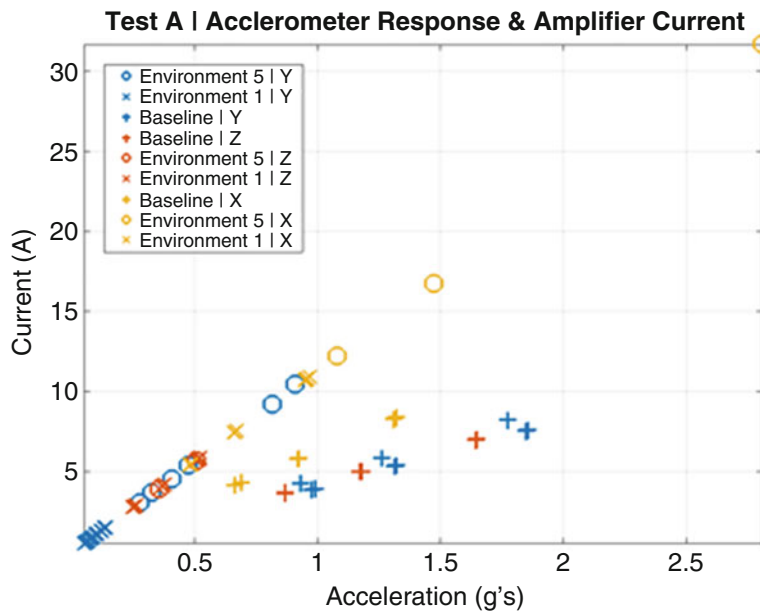


Fig. 33.9 RMS Acceleration vs. RMS Amplifier Current for Test A

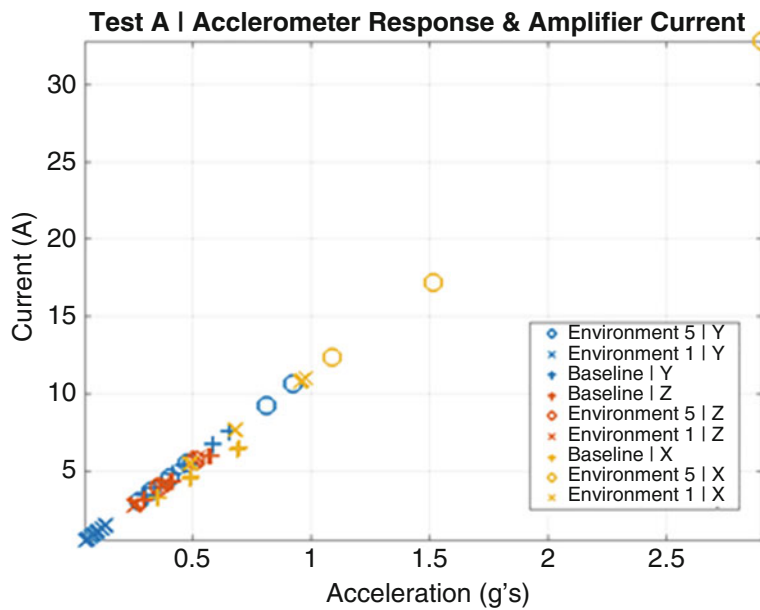


Fig. 33.10 RMS Acceleration vs. RMS Current for Test A, 0–400 Hz

33.5 Conclusion

The overall goal of this work is to develop metrics or tools to predict the electrical and mechanical limitations of a shaker amplifier system and a specific DUT for ground vibration testing applications. This paper provides initial analysis and characterization of the mechanical and electrical relationship between electrodynamic shakers and power amplifiers during vibration testing. Three different ground vibration tests with varying shaker systems, test objects, and mounting fixtures were evaluated using both transfer functions and RMS values to begin to understand critical parameters that can impact shaker performance. Ground vibration testing is complex, and there are many factors that influence the dynamic response of both the shaker and the DUT. Mass, DUT mounting fixtures, and resonant frequencies all had a significant effect on the shaker-amplifier system response. Future work includes continuing to identify significant parameters for the shaker-systems using additional methods and metrics, collecting and analyzing additional experimental data with different test objects and environments, and developing and deploying a predictive capability for future test planning.

Appendix A: Shaker System Performance Specifications

Test	A	B	C
System model	SAI30F-S452-16	SALL100-T1000	SALL300-T4000-3''
Sine force (pk)	5500 lbf (24.5 kN)	11,000 lbf (48.9 kN)	40,000 lbf (178 kN)
Random force (rms)	5500 lbf (24.5 kN) ¹	8000 lbf (35.6 kN) ²	40,000 lbf (178 kN) ³
Shock force (4 ms, half sine)	50 g: 120 lbs. (54 kg) 100 g: 36 lbs. (16 kg)	–	50 g: 1800 lbs. (818 kg) 100 g: 700 lbs. (318 kg)
Usable frequency range	DC to 3000 Hz	–	2 to 25,000 Hz
Maximum acceleration (sine, pk)	90 g	100 g	140 g
Maximum acceleration (random, rms)	75 g	–	135 g
Maximum velocity (sine sweep)	70 in/s	70 in/s	85 in/s
Maximum velocity (shock)	130 in/s	–	165 in/s
Stroke length (pk-pk)	2 in	1 in.	3 in (76 mm)
Armature weight	60 lbs	95 lbs	285 lbs
Armature diameter	17.5 in	–	25.5 in.
Armature resonance	2300 Hz	2300 Hz	2000 Hz
Amplifier model	SAI-30F	SALL-100	SALL-300

¹Random force rating based on flat spectrum from 20–2000 Hz with 160 lbs. (73 kg) non-resonant load

²Typical random rating with flat spectrum and load greater than 350 lbs. (158.8 kg)

³Typical random rating with flat spectrum and non-resonant load greater than 1000 lbs. (453.6 kg)

References

1. Electrodynamic vibration generating systems — Performance characteristics, Geneva, Switzerland: International Organization for Standardization (ISO), ISO 5344 (2004)
2. Lang, G.F., Snyder, D.: Understanding the physics of electrodynamic shaker performance. *Sound Vib.* **35**(10), 24–33 (2001)
3. Sentek Dymanics. How to Select a Vibration Testing System. Santa Clara (2016)
4. Lang, G.F.: Electrodynamic shaker fundamentals. *Sound Vib.* **34**(4), 14–23 (2001)
5. Tiwari, N., Puri, A., Saraswat, A.: Lumped parameter modelling and methodology for extraction of model parameters for an electrodynamic shaker. *J. Low Frequency Noise Vib. Active Control.* **36**(2), 99–115 (2017)
6. Ricci, S., Peeters, B., Fetter, R., Boland, D., Debille, J.: Virtual shaker testing for predicting and improving vibration test performance. In: *Conference Proceedings of the Society for Experimental Mechanics Series*, Orlando, FL (2009)
7. Smallwood, D.O.: Characterizing electrodynamic shakers. In: *Annual Technical Meeting and Exposition of the Institute of Environmental Sciences*, Los Angeles (1997)
8. Hoffait, S., Marin, F., Simon, D., Peeters, B., Golinval, J.-C.: Measured-based shaker model to virtually simulate vibration sine test. *Case Stud. Mech. Syst. Sig. Process.* **4**, 1–7 (2016)
9. Manzato, S., Bucciarelli, F., Arras, M., Coppotelli, G., Peeters, B., Carrella, A.: Validation of a Virtual Shaker Testing approach for improving environmental testing performance. In: *Proceedings of ISMA 2014 – international conference on noise and vibration engineering*, (2014)
10. Martino, J., Harri, K.: Virtual shaker modeling and simulation, parameters estimation of a high damped electrodynamic shaker. *Int. J. Mech. Sci.* **151**, 375–384 (2019)
11. Unholtz-Dickie Corporation: Operating and Maintenance Manual Model T-4000-1/CSTA. Unholtz-Dickie Corporation, Wallingford (2012)

Greta Colford graduated with a BS degree in mechanical engineering from Michigan Technological University in December 2018 and now works as a Post-Baccalaureate student engineer in the Engineering Technology and Design division at Los Alamos National Laboratory.